GDAŃSK UNIVERSITY OF TECHNOLOGY

INSTITUTE OF NAVAL ARCHITECTURE AND OCEAN ENGINEERING

Polish Maritime Research

No 2 (118) 2023
Vol. 30

ADDRESS OF PUBLISHER & EDITOR'S OFFICE:

GDAŃSK UNIVERSITY OF TECHNOLOGY

Institute of Naval Architecture and Ocean Engineering
G. Narutowicza 11/12
80-233 Gdańsk, POLAND

Price:
single issue: 25 PLN

Prices for abroad
single issue:
- in Europe EURO 15
- overseas USD 20

WEB:
pg.edu.pl/pmr

e-mail : pmr@pg.edu.pl

ISSN 1233-2585

CONTENS

ADDRESS OF PUBLISHER & EDITOR'S OFFICE:

GDAŃSK UNIVERSITY OF TECHNOLOGY

Institute of Naval Architecture and Ocean Engineering
G. Narutowicza 11/12
80-233 Gdańsk, POLAND

Editorial

POLISH MARITIME RESEARCH is the scientific journal with a worldwide circulation. This journal is published quarterly (four times a year) by Gdansk University of Technology (GUT). On September, 1994, the first issue of POLISH MARITIME RESEARCH was published. The main objective of this journal is to present original research, innovative scientific ideas, and significant findings and application in the field of **:**

Naval Architecture, Ocean Engineering and Underwater Technology,

The scope of the journal covers selected issues related to all phases of product lifecycle and corresponding technologies for offshore floating and fixed structures and their components.

All researchers are invited to submit their original papers for peer review and publications related to methods of the design; production and manufacturing; maintenance and operational processes of such technical items as:

- all types of vessels and their equipment,
- fixed and floating offshore units and their components,
- autonomous underwater vehicle (AUV) and remotely operated vehicle (ROV).

We welcome submissions from these fields in the following technical topics:

- ship hydrodynamics: buoyancy and stability; ship resistance and propulsion, etc.,
- structural integrity of ship and offshore unit structures: materials; welding; fatigue and fracture, etc.,
- marine equipment: ship and offshore unit power plants: overboarding equipment; etc.

POLISH MARITIME RESEARCH 2 (118) 2023 Vol. 30; pp. 4-10
10.2478/pomr-2023-0017

VESSEL ENERGY REQUIREMENT PREDICTION FROM ACCELERATION STAGE TOWING TESTS ON SCALE MODELS

Klaudia Wrzask
Gdansk University of Technology, Poland

* Corresponding author: *klaudia.wrzask@pg.edu.pl (Klaudia Wrzask)*

ABSTRACT

One of the most crucial tasks for naval architects is computing the energy required to meet the ship's operational needs. When predicting a ship's energy requirements, a series of hull resistance tests on a scale model vessel is carried out in constant speed stages, while the acceleration stage measurements are ignored. Another important factor in seakeeping analysis is the ship's hydrodynamic added mass. The second law of dynamics states that all this valuable information, that is, the dependence of the hull resistance on the vessel's speed and the added mass, is accessible from just one acceleration stage towing test done up to the maximum speed. Therefore, the acceleration stage, often overlooked in traditional towing experiments, can be a valuable source of information. For this reason, this work aims to generalise Froude's scaling procedure to full-scale vessels for the accelerated stage towing tests.

Keywords: ships energy requirement, towing tank tests, acceleration stage, hydrodynamic added mass

INTRODUCTION

In 1870, W. Froude initiated an investigation into ship resistance with the use of vessel models. The resistance is the horizontal component of the force opposing the forward motion of a vessel's hull. Froude noted that the wave configurations around geometrically similar forms were similar if compared at speeds proportional to the square root of the model length. He propounded that the total resistance could be divided into skin friction resistance and residuary – mainly wave-making – resistance. The specific residuary resistance would remain constant at corresponding speeds between the model and the full-scale vessel. Next, estimates of frictional resistance from a series of measurements on planks of different lengths and with different surface finishes were derived [1]. The scaling procedure proposed by Froude was based on towing experiments at constant speed on the model vessel. Further, in 1874 Froude carried out full-scale tests on HMS Greyhound (100 ft), and the results showed substantial agreement with the model predictions [2]. Finally, in 1877 he gave a detailed explanation of wave-making resistance, supporting his scaling methodology [3]. Froude's ideas still dominate this subject.

Nowadays, when predicting ships' energy requirements, resistance tests on model vessels are still conducted. For constant speed, the resistance is determined by towing force measurements. In the next step, the resistance test results are scaled from the model to the full-scale ship. A modification of Froude's scaling method by splitting the residual resistance into the form resistance and the wave-making resistance, suggested by Hughes [4], and known as the form factor (1+k) approach, was later adopted by the International Towing Tank Conference (ITTC).

The scaling procedures, as mentioned above, refer to towing tests at constant speed. Another important aspect is the derivation

of the hydrodynamic added mass of the ship, which may account for up to 30% of the ship's mass and therefore represents significant inertia for the accelerated motion. It follows from the laws of dynamics that all this information, i.e., the dependence of the resistance on the speed and the added mass, is accessible from the acceleration stage towing test done up to the maximum speed. The measuring apparatus in the 19th century did not allow Froude to conduct his research on the acceleration stage with the same level of precision as is possible now. Despite the development, great accuracy, and sampling rate of measurements, however, the author is unaware of any scaling procedures from the acceleration stage towing tests. Therefore, this paper derives a dynamical scaling proposition for the propulsion force needed to estimate the full-scale ship's energy consumption. A fully dynamic model can simulate any profile: constant speed, acceleration, deceleration, and gliding. Moreover, such an approach allows for optimisation of the required energy based on dynamical systems, which is especially desired for short-range vessels, where constant speed is not the major stage [5].

This paper is organised as follows. First, all the components of the ship's resistance in accelerated motion, with some historical background, are introduced. Next, the standard scaling procedure for the constant speed towing tank tests is described because most of the methodology used for the scaling from the accelerated motion tests is the same. Finally, a proposition for the towing tank tests in the accelerated stage and a scaling procedure for such tests are explained.

NEWTON'S SECOND LAW OF DYNAMICS FOR TOWING TESTS

To explain the concept of the proposed scaling procedure from the acceleration towing tank tests, let us start with Newton's second law of dynamics, which for any vessel takes the following form:

$$mv' = F_P(v, v') - R_T(v) \,. \tag{1}$$

Here m stands for the total mass, which is the sum of the mass of the vessel m_v and the hydrodynamic added mass of the water m_{add}, i.e.,

$$m = m_v + m_{add} \,. \tag{2}$$

In general, the added mass is a second-order tensor relating the fluid acceleration vector to the resulting force vector on the body. Only the surge added mass is taken into consideration in this work. Further, in formula (1), v' denotes the speed derivative over time, F_P is the propulsion force for the full-scale vessel, or the towing force in the case of the model vessel, and R_T is the total hull resistance force.

In the case of constant speed, i.e. $v' = 0$, the towing force is equal in magnitude to the total hull resistance, and the second law takes the following form:

$$F_P(v, 0) = R_T(v). \tag{3}$$

Then, after rewriting (1), we get

$$F_P(v, v') = F_P(v, 0) + (m_v + m_{add})\, v'. \tag{4}$$

Formula (4) shows that, from the acceleration stage towing tests, which give data $F_P(v, v')$, information on both the total hull resistance dependence on constant speed $F_P(v, 0)$ and the hydrodynamic added mass m_{add} are accessible.

THE ADDED MASS

In 1786 Du Buat found by experiment that the motion of spheres oscillating in water could only be described if an added mass was included in the equations of motion. In fluid mechanics, the added mass is defined as an extra fluid mass that accelerates with the body. It is the inertia added to a system because the accelerating body, to pass through, must move aside and then close in behind a specific volume of the surrounding fluid. The fluid thus possesses kinetic energy that it would lack if the immersed body were not in accelerated motion. The body has to impart this kinetic energy to the fluid by doing work on the fluid. Any corresponding equations of motion for the immersed body must take into account this loss of kinetic energy. This can be modelled in the equations of motion as some volume of fluid moving with the object although, in reality, the fluid will be accelerated to varying degrees. When the body moves at a constant speed, the corresponding motion of the fluid is steady; thus, the kinetic energy of the fluid is constant. It follows that for constant-speed motion, the added mass terms can be omitted in the equations of motion [6].

The added mass depends on the size and shape of the immersed body, the direction in which it moves through the fluid with respect to its axis, and the density and viscosity of the fluid. It can be described by a dimensionless coefficient which depends on the shape of the immersed body. The dimensionless added mass coefficient C_M is the added mass divided by the displaced fluid mass [7]; that is, divided by the fluid density ρ times the volume of the body under water V; therefore

$$m_{add} = C_M \rho V. \tag{5}$$

The same principles apply to ships. In the marine sector, added mass is referred to as hydrodynamic added mass. The hydrodynamic added mass has also been investigated in the maritime area. Motora first conducted model testing for a ship called Mariner to predict the added mass [8]. Ghassemi and Yari proposed a numerical calculation of the marine propeller's added mass using the boundary element method [9]. Zeraatgar et al. investigated the surge added mass of planing hulls by model vessel experiments and by approximations with a quasi-analytical method [10]. The conclusion was that the surge added water mass could account for 10% of the total mass for the investigated planing hulls.

Essentially for ships, the added mass can reach even one-third of their mass, representing significant inertia in addition to the viscous and wave-making drag forces. Thus, the energy required to accelerate the added mass should also be considered when performing a seakeeping analysis.

When conducting a towing test in the acceleration stage, the surge added mass can be obtained from the equations of motion by extrapolating the towing force to zero speed $F_P(0, v')$, i.e.,

$$(m_v + m_{add})v' = F_P(0, v') - R_T(0). \quad (6)$$

Then the total hull resistance can be neglected, $R_T(0) = 0$, and it follows that

$$m_{add} = \frac{F_P(0, v')}{v'} - m_v. \quad (7)$$

THE TOTAL HULL RESISTANCE

Even in calm water, a ship experiences the water's resistance to its motion. This force is referred to as the total hull resistance R_T. This resistance force is needed to calculate the ship's effective power. Many factors combine to form the total resistance force acting on the hull. The physical factors affecting ship resistance are the friction and viscous effects of the water acting on the hull and the energy required to create and maintain the ship's characteristic bow and stern waves. Finally, a minor contribution is made by the resistance that the air provides to the ship's motion. This may be written in the following form:

$$R_T = R_V + R_W + R_A, \quad (8)$$

where R_T is the total hull resistance, R_V is the viscous friction resistance, R_W is the wave-making resistance, and R_A stands for the air resistance.

The total hull resistance R_T can also be formulated by means of the dimensionless total resistance coefficient C_T with the following equation:

$$R_T = \frac{1}{2} C_T \rho S v^2. \quad (9)$$

Here ρ is the water density, S is the wetted surface area of the underwater hull, and v is the speed of the vessel.

As the total hull resistance R_T is the sum of the viscous R_V and wave-making R_W resistance, when neglecting the air resistance, one can write an equation for the total dimensionless resistance coefficient in terms of the viscous and wave-making coefficients, such that

$$C_T = C_V + C_W, \quad (10)$$

where C_T is the coefficient of the total hull resistance, C_V is the coefficient of the viscous frictional resistance, and C_W is the wave-making resistance coefficient.

To quantify these dimensionless resistance coefficients, two numbers are used. The Reynolds number *Re* quantifies the influence of viscous forces on the fluid's motion. It indicates the ratio of inertial to viscous forces and, for the ship, is defined as a dimensionless ratio

$$\mathcal{R}e = \frac{\mathrm{v}\rho L}{\mu} = \frac{\mathrm{v}L}{\nu}, \quad (11)$$

where v is the vessel's speed, L is the length of the wetted surface, μ is the dynamic viscosity, and ν is the kinematic viscosity.

The Froude number *Fr*, in hydrology and fluid mechanics, is used to quantify the influence of gravity on a fluid's motion. It indicates the ratio of the inertia forces to the gravitational forces related to the mass of water displaced by a floating vessel. It is defined by a dimensionless ratio:

$$\mathcal{F}r = \frac{\mathrm{v}}{\sqrt{gL}}. \quad (12)$$

Here g denotes the gravity acceleration. Then, the relationship between these two numbers can be written in the following form, which is practical for scaling purposes:

$$\mathcal{R}e = \frac{\rho}{\mu}\sqrt{g}\, L^{1.5}\, \mathcal{F}r. \quad (13)$$

THE VISCOUS RESISTANCE

Although water has low viscosity, it produces a significant friction force opposing the ship's motion. The viscous resistance R_V is made up of the skin friction resistance and the viscous pressure resistance. Experimental data have shown that water friction can account for most of the hull's total resistance at low speeds and is still dominant for higher speeds [11]. The ship's hull shape influences the magnitude of the viscous pressure drag. Vessels with a lower length-to-beam ratio will have greater drag than those with a higher length-to-beam ratio.

The dimensionless viscous coefficient C_V, taking into account both the skin friction and the viscous pressure resistance, can be derived from the formula

$$C_V = (1 + k)C_F. \quad (14)$$

Here $(1+k)$ is the form factor, which depends on the hull form, and C_F is the skin friction coefficient based on the flat plate results. The form factor $(1+k)$ can be derived from low-speed tests when, at low Froude numbers *Fr*, the wave resistance coefficient C_W tends to zero and therefore $(1+k) = C_T/C_F$. The skin friction resistance coefficient C_F is assumed to be dependent on the Reynolds number Re and is recommended to be calculated through the ITTC-1957 skin friction line as

$$C_F(\mathcal{R}e) = \frac{0.075}{(\log_{10}\mathcal{R}e - 2)^2}. \quad (15)$$

The ITTC-1978 powering prediction procedure for deriving the viscous coefficient C_V recommends the use of formula (15), together with the form factor $(1+k)$. The same methodology for calculating the C_V coefficient can be used for the proposed scaling procedure from the acceleration stage towing tests.

THE WAVE-MAKING RESISTANCE

When a submerged vessel travels through a fluid, pressure variations are created around the body. Near a free surface, the pressure variations manifest themselves through changes in the fluid level, creating waves. Such a wave system is made up of transverse and divergent waves. With a body moving through a stationary fluid, the waves travel at the same speed as the body. It follows that the transverse wavelength depends on the ship's speed. The mathematical form of such a wave system is called the Kelvin wave after Lord Kelvin [12]. The first step in formulating an analytical expression for the wave resistance was taken by Michell in 1898 [13]. A review of Michell's wave resistance approach and its impact on ship hydrodynamics

is given by Tuck [14]. Further, in 1909 wave resistance was investigated both theoretically and experimentally by Havelock [15] and elaborated in [16]. The findings are that the amplitudes of the waves directly depend on the ship's Froude number *Fr*. Thus the dimensionless coefficient for the wave-making resistance C_W is assumed to depend only on the Froude number. The wave resistance for low speeds is negligible, but for Froude numbers over 0.35, the wave resistance may exceed the viscous resistance for most vessels [11]. Setting equal Froude numbers for the model and full-scale ship, such that the wave resistance coefficients are equal, still dominates the subject of scaling procedures. This assumption will also be used in the proposed scaling procedure for the acceleration stage towing tests.

THE RESISTANCE BREAKDOWN

Within the subject of the resistance breakdown, it is worth emphasising the fundamental difference between the scaling methods proposed by Froude and Hughes. Froude assumed that all residuary resistance scales according to Froude's law, that is, for the same Froude number *Fr*. This is not physically correct because the viscous pressure drag included within the C_V dimensionless coefficient should scale according to Reynolds' law. Hughes assumes that the total viscous resistance, i.e., the friction and the form, scales according to Reynolds' law. This leads to the dimensionless resistance coefficient breakdown:

$$C_T(\mathcal{R}e, \mathcal{F}r) = C_V(\mathcal{R}e) + C_W(\mathcal{F}r). \tag{16}$$

This also needs to be adjusted, as the viscous resistance interferes with the wave-making resistance. The reason is that the boundary layer growth suppresses the stern wave; thus, the wave resistance can depend on *Re*. Moreover, the viscous resistance depends on the pressure distribution around the hull, which depends on wave-making [17]. Thus, an interaction term $C_{INT}(Re,Fr)$, depending on both numbers, is non-zero, i.e.

$$C_T(\mathcal{R}e,\mathcal{F}r)=C_V(\mathcal{R}e)+C_W(\mathcal{F}r)+C_{INT}(\mathcal{R}e,\mathcal{F}r). \tag{17}$$

Therefore, the resistance breakdown is an assumption made for the scaling practice rather than an exact physical representation. A detailed outline of the scaling effects and evidence supporting the existence of an interaction term is given by Terziev [18]. Nevertheless, the overall error caused by the resistance coefficient breakdown assumption (16) is sufficiently small. The form factor method proposed by Hughes and adopted by the ITTC is still an extremely valuable tool in predicting ships' energy requirements.

For the dynamical scaling purpose of this paper, certain assumptions, as mentioned above, will also be made; that is, the viscous friction coefficient C_V depends only on the Reynolds number *Re*, the wave-making coefficient C_W only on the Froude number *Fr*, and the interaction term will be neglected.

SCALING PROCEDURE FOR CONSTANT SPEED TOWING TESTS

Before explaining the scaling procedure from the acceleration stage, let us look at the constant speed stage towing tests because most assumptions will be the same for both approaches. To perform a scaling procedure for constant speeds, first, a geometric scale λ is set as the ratio of the full-scale ship length L_S to the model vessel length L_M, i.e.,

$$\lambda = \frac{L_S}{L_M} \tag{18}$$

Then for equal Froude numbers of both the full-scale ship and the model vessel: $Fr_M = Fr_S$, Froude's law of similarity sets the corresponding speeds:

$$\frac{\mathrm{v}_S}{\mathrm{v}_M} = \lambda^{0.5}. \tag{19}$$

Here v_S is the full-scale ship speed and v_M denotes the model vessel speed. Newton's second law of dynamics (1) for constant speeds takes the following form for both the full-scale and the model vessel:

$$0 = F_P(\mathrm{v}, 0) - R_T(\mathrm{v}). \tag{20}$$

Therefore, for constant vessel speeds, the towing force is equal in magnitude to the total hull resistance force; thus, Eq. (3) holds. Moreover, the propulsion force needed to assess the energy requirement for constant full-size vessel speeds is equal to the total resistance force acting on the full-size hull. In general, the scaling procedure for determining the total hull resistance of a full-scale ship from constant speed towing experiments on a geometrically scaled model vessel may be described in the following steps:

Step 1: Setting the range of the full-scale ship speed v_S, from the minimum to the desired maximum ship speed.

Step 2: Calculating the corresponding towing speeds for the model v_M using Froude's law of similarity (19).

Step 3: Recording, from the constant speed stage, the total hull resistance force $R_T(\mathrm{v}_M)$ of the model vessel towed in a series of tests at each speed v_M.

Step 4: Determining the coefficient of the total hull resistance for the model at each speed $C_T(\mathrm{v}_M)$ from formula (9).

Step 5: Determining the coefficient of the viscous resistance for the model vessel at each speed $C_V(\mathrm{v}_M)$ using the ITTC recommended formulas (14) and (15).

Step 6: Calculating the wave-making coefficient for the model vessel at each speed $C_W(\mathrm{v}_M) = C_T(\mathrm{v}_M) - C_V(\mathrm{v}_M)$.

Step 7: The wave-making resistance coefficients for the full-scale and the model vessel are equal: $C_W(\mathrm{v}_S) = C_W(\mathrm{v}_M)$.

Step 8: Determining the coefficient of the viscous resistance for the full-scale ship $C_V(\mathrm{v}_S)$, at speeds corresponding to the model towing speeds, with the use of the ITTC recommended formulas (14) and (15).

Step 9: Calculating the dimensionless coefficient of the total hull resistance for the full-scale vessel at each speed: $C_T(\mathrm{v}_S) = C_W(\mathrm{v}_S) + C_V(\mathrm{v}_S)$.

Step 10: Determining the total hull resistance of the full-scale vessel for each speed using formula (9).

PROPOSED SCALING PROCEDURE FROM THE ACCELERATION STAGE TOWING TESTS

The proposed scaling procedure for accelerated motion has the same methodology as Froude's scaling for constant speed mentioned above. The difference is that we are going to take a step back from the equation of motion (20) to full dynamics (1) because, in accelerated motion, the towing force is needed to overcome the total hull resistance and to accelerate the model vessel.

Table 1 presents the basic assumptions for the scaling rules needed in accelerated motion. Subscripts s correspond to the full-size vessel and M to the model vessel.

The geometric similarity and the Froude number for the full-size and model vessels remain the same for the acceleration stage scaling proposition. The difference is that, when accelerated, the mass of the vessel and the added mass of water have to be taken into account and scaled. Moreover, since the acceleration is the derivative of speed, for geometric scale λ, the acceleration scales as

$$\frac{\mathrm{d}v_S}{\mathrm{d}t} = \frac{\mathrm{d}(\lambda^{0.5}v_M)}{\mathrm{d}t} = \lambda^{0.5}\frac{\mathrm{d}v_M}{\mathrm{d}t}. \tag{21}$$

To derive the scaling formula for the acceleration stage, let us start from Newton's second law of dynamics in the following form:

$$mv' = F_P(v, v') - \frac{1}{2}\rho S C_T(\mathcal{F}r, \mathcal{R}e)v^2. \tag{22}$$

Further, the breakdown of the resistance coefficients (16) is assumed, i.e.,

$$mv' = F_P(v, v') - \frac{1}{2}\rho S\big(C_W(\mathcal{F}r) + C_V(\mathcal{R}e)\big)v^2. \tag{23}$$

Tab. 1. Scaling rules and basic assumptions

Physical quantity	Scaling rule	Assumptions
Length at the water line	$L_S = \lambda L_M$	Geometric similarity
Wetted surface area of hull	$S_S = \lambda^2 S_M$	Geometric similarity
Immersed volume	$V_S = \lambda^3 V_M$	Geometric similarity
Mass of the vessel	$m_{vS} = \lambda^3 m_{vM}$	The load of the model is prepared in such a way that the wetted volumes correspond to the geometric scaling.
Hydrodynamic added mass	$m_{addS} = \lambda^3 \frac{\rho_S}{\rho_M} m_{addM}$	The accelerating vessel moves a specific volume of the surrounding water and this volume scales with respect to geometric similarity.
Froude number	$\mathcal{F}r_S = \mathcal{F}r_M$	The ratio of the inertia forces to the gravitational forces related to the mass of water displaced by a floating vessel is the same for the model and full-scale ship.
Reynolds number	$\mathcal{R}e_S = \lambda^{0.5}\frac{\mu_M}{\mu_S}\frac{\rho_S}{\rho_M}\mathcal{R}e_M$	Same Froude number and geometric similarity
Speed	$v_S = \lambda^{0.5} v_M$	Same Froude number and geometric similarity
Acceleration	$a_S = \lambda^{0.5} a_M$	Same Froude number and geometric similarity

The wave resistance coefficient $C_W(Fr)$ is assumed to depend only on the Froude number and may be derived from Eq. (23), i.e.,

$$C_W(\mathcal{F}r) = \frac{2}{\rho S v^2}F_P(v, v') - \frac{2m}{\rho S v^2}v' - C_V(\mathcal{R}e). \tag{24}$$

When the Froude number is set to be the same for both the full-size and the model vessel, the partial dynamic similarity of the wave resistance coefficient $C_W(Fr)$ can also be used for accelerated motion; therefore

$$C_W(\mathcal{F}r) = \frac{2}{\rho_M S_M v_M^2}\big(F_{PM}(v_M, v_M') - m_M v_M'\big) - C_V(\mathcal{R}e_M), \tag{25}$$

$$C_W(\mathcal{F}r) = \frac{2}{\rho_S S_S v_S^2}\big(F_{PS}(v_S, v_S') - m_S v_S'\big) - C_V(\mathcal{R}e_S). \tag{26}$$

In formula (25), $F_{PM}(v_M, v_M')$ is the towing force from the acceleration stage towing tank test on the model vessel. Just one towing test up to the maximum speed is needed to access such information. $F_{PS}(v_S, v_S')$ in (26) is the propulsion force needed to predict the ship's energy requirement for accelerated motion. Further, it is assumed that the gravitational field g is the same for both the model and the full-scale vessels. Then, one can write the wave-making coefficient $C_W(Fr)$ for the full-scale vessel (26) using the scaling rules in Table 1:

$$C_W(\mathcal{F}r) = \frac{2}{\rho S_M v_M^2 \lambda^3}\Big(F_{PS}(v_S, v_S') - \lambda^{3.5}\big(m_{vM} + \frac{\rho_S}{\rho_M}m_{addM}\big)v_M'\Big) - C_V\Big(\lambda^{1.5}\frac{\mu_M}{\mu_S}\frac{\rho_S}{\rho_M}\mathcal{R}e_M\Big). \tag{27}$$

Below, let us write an equation where the upper part is the wave-making coefficient $C_W(Fr)$ for the full-size vessel with the scaling rules applied (27), and the bottom part is the wave-making coefficient for the model vessel (25):

$$\frac{2}{\rho S_M v_M^2 \lambda^3}\Big(F_{PS}(v_S, v_S') - \lambda^{3.5}\big(m_{vM} + \frac{\rho_S}{\rho_M}m_{addM}\big)v_M'\Big) - C_V\Big(\lambda^{1.5}\frac{\mu_M}{\mu_S}\frac{\rho_S}{\rho_M}\mathcal{R}e_M\Big) \tag{28}$$

$$=$$

$$\frac{2}{\rho S_M v_M^2}\Big(F_{PM}(v_M, v_M') - (m_{vM} + m_{addM})v_M'\Big) - C_V\big(\mathcal{R}e_M\big). \tag{29}$$

Then, after basic transformations on the above equation, the following scaling rules for obtaining the propulsion force for the full-scale vessel from the acceleration stage towing experiments on the scaled model are derived:

$$v_S = \lambda^{0.5}v_M,$$

$$v_S' = \lambda^{0.5}v_M',$$

$$m_S = \lambda^3\big(m_{vM} + \frac{\rho_S}{\rho_M}m_{addM}\big),$$

$$F_{PS}(v_S, v_S') = \lambda^3 F_{PM}(v_M, v_M') \tag{30}$$

$$+ \lambda^3(\lambda^{0.5} - 1)m_{vM}v_M' \tag{31}$$

$$+ \lambda^3(\lambda^{0.5}\frac{\rho_S}{\rho_M} - 1)m_{addM}v_M' \tag{32}$$

$$+ \lambda^3\frac{\rho S_M v_M^2}{2}\Big(C_V\big(\lambda^{1.5}\frac{\mu_M}{\mu_S}\frac{\rho_S}{\rho_M}\mathcal{R}e_M\big) - C_V\big(\mathcal{R}e_M\big)\Big). \tag{33}$$

Here, terms (30) and (33) are equivalent to the standard scaling procedures for constant speed when $v' = 0$, i.e.,

$$F_{PS}(\mathrm{v}_S,0) = \lambda^3 F_{PM}(\mathrm{v}_M,0)+$$
$$\lambda^3 \frac{\rho S_M \mathrm{v}_M^2}{2}\left(C_\mathrm{V}(\lambda^{1.5}\frac{\mu_M}{\mu_S}\frac{\rho_S}{\rho_M}\mathcal{R}e_M)-C_\mathrm{V}(\mathcal{R}e_M)\right). \quad (34)$$

Term (31) is the part of the propulsion force needed to accelerate a full-scale vessel. This part is equal to the part of the towing force needed to accelerate the model vessel with corresponding acceleration v'_M times the scaling factor $\lambda^3(\lambda^{0.5}-1)$. Finally, the term (32) is the part of the propulsion force that is needed to accelerate the added water mass of the full-scale vessel, and this is equal to the part of the towing force needed to accelerate the added water mass of the model vessel with the corresponding acceleration v'_M times the scaling factor $\lambda^3(\lambda^{0.5}-1\rho_M/\rho_M-1)$. Different water densities for the full-scale and model vessels were considered for the scaling factor in (32).

Therefore, the scaling approach for calculating the propulsion force of the full-scale vessel from the accelerated stage towing experiment on a scale model is proposed below:

Step 1: Setting the range of the full-scale ship speed v_S, from the minimum to the desired maximum speed.

Step 2: Calculating the towing speeds for the model v_M using Froude's law of similarity (19).

Step 3: Recording the towing force $F_{PM}(\mathrm{v}_M,\mathrm{v}'_M)$ of the model vessel from the acceleration stage towed up to the maximum speed.

Step 4: Calculating the added mass by extrapolating the towing force to zero speed and using formula (7).

Step 5: Determining the propulsion force $F_{PS}(\mathrm{v}_S,\mathrm{v}'_S)$ using formulas (30)–(33).

It should be noted that no time scale has been used in the proposed scaling procedure. The equations of motion for any profile can be derived from the second law of dynamics after determining the propulsion force of a full-size vessel $F_{PS}(\mathrm{v}_S,\mathrm{v}'_S)$.

CONCLUSIONS

This work derives a dynamical scaling proposition for the propulsion force required to estimate the full-scale vessel energy requirement. The towing force can be measured experimentally using the acceleration stage tests on a scale model vessel. This theoretical analysis demonstrates that such an approach may have advantages over constant speed towing tests. From the acceleration stage, it is possible to obtain information about the hydrodynamic added mass, which should also be considered when predicting the ship's energy consumption. Furthermore, all information about the constant speed stage is accessible from only one acceleration test done up to the maximum speed. Finally, the proposed testing and scaling procedure can be used for dynamic models when simulating various profiles of motion, including constant speed, accelerating, decelerating, and gliding.

REFERENCES

1. W. Froude, "Experiments on the surface-friction experienced by a plane moving through water," *British Association for the Advancement of Science*, vol. 42, pp. 118–124, 1872.

2. W. Froude, "On experiments with HMS Greyhound," *Transactions of the. Institution of Naval Architects*, vol. 15, 1874.

3. W. Froude, "Experiments upon the effect produced on the wave-making resistance of ships by length of parallel middle body," *Transactions of the Institution of Naval Architects*, vol. xviii, pp. 77–97, 1877.

4. G. Hughes, "Friction and form resistance in turbulent flow and a proposed formulation for use in model and ship correlation," *Transactions of the Royal Institution of Naval Architects*, vol. 96, pp. 314–376, 1954.

5. M. Kunicka and W. Litwin, "Energy demand of short-range inland ferry with series hybrid propulsion depending on the navigation strategy," *Energies*, vol. 12, no. 18, p. 3499, 2019. doi.org/10.3390/en12183499.

6. F. H. Imlay, *The complete expressions for added mass of a rigid body moving in an ideal fluid*. David Taylor Model Basin, Washington DC, 1961.

7. J. N. Newman, *Marine hydrodynamics*. The MIT Press, 2018.

8. S. Motora, "On the measurement of added mass and added moment of inertia of ships in steering motion," in *Proceedings of the First Symposium on Ship Maneuverability, David Taylor Model Basin Report*, vol. 1461, pp. 241–274, 1960.

9. H. Ghassemi and E. Yari, "The added mass coefficient computation of sphere, ellipsoid and marine propellers using boundary element method," *Polish Maritime Research*, 18, no. 1, pp. 17–26, 2011. doi.org/10.2478/v10012-011-0003-1.

10. H. Zeraatgar, A. Moghaddas, and K. Sadati, "Analysis of surge added mass of planing hulls by model experiment," *Ships and Offshore Structures*, vol. 15, no. 3, pp. 310–317, 2020. doi.org /10.1080/17445302.2019.1615705.

11. L. Birk, *Fundamentals of ship hydrodynamics: Fluid mechanics, ship resistance and propulsion*. John Wiley & Sons, 2019.

12. W. Thomson, "On ship waves," *Proceedings of the Institution of Mechanical Engineers*, vol. 38, no. 1, pp. 409–434, 1887, doi. org/10.1243/PIME_PROC_1887_038_028_02.

13. J. H. Michell, "XI. The wave-resistance of a ship," *The London, Edinburgh, and Dublin Philosophical Magazine and Journal of Science*, vol. 45, no. 272, pp. 106–123, 1898.

14. E. O. Tuck, "The wave resistance formula of JH Michell (1898) and its significance to recent research in ship hydrodynamics," *The ANZIAM Journal*, vol. 30, no. 4, pp. 365–377, 1989. doi.org/10.1017/S0334270000006329.

15. T. H. Havelock, "The wave-making resistance of ships: a theoretical and practical analysis," *Proceedings of the Royal Society of London. Series A, Containing Papers of a Mathematical and Physical Character*, vol. 82, no. 554, pp. 276–300, 1909. doi.org/10.1098/rspa.1909.0033.

16. T. H. Havelock, "The theory of wave resistance," *Proceedings of the Royal Society of London. Series A, Containing Papers of a Mathematical and Physical Character*, vol. 138, no. 835, pp. 339–348, 1932. doi.org/10.1098/rspa.1932.0188.

17. A. F. Molland, S. R. Turnock, and D. A. Hudson, *Ship resistance and propulsion*. Cambridge University Press, 2017.

18. M. Terziev, T. Tezdogan, and A. Incecik, "Scale effects and full-scale ship hydrodynamics: A review," *Ocean Engineering*, vol. 245, p. 110496, 2022. doi.org/10.1016/j.oceaneng.2021.110496.

POLISH MARITIME RESEARCH 2 (118) 2023 Vol. 30; pp. 11-27
10.2478/pomr-2023-0018

NUMERICAL ANALYSIS OF RESISTANCE CHARACTERISTICS OF A NOVEL HIGH-SPEED QUADRAMARAN

Xin Liu
Jimei University, School of Marine Engineering, Xiamen, China
Jinglei Yang
Jimei University, School of Marine Engineering, Xiamen, China
Defeng Wu
Jimei University, School of Marine Engineering, Xiamen, China
Liang Hou
Shanghai Xiyi Marine Technology Co., Ltd, Shanghai, China
Xiaowen Li
Jimei University, School of Marine Engineering, Xiamen, China
Qian Wan
Dalian Shipbuilding Industry Co., Ltd, Dalian, China

* Corresponding author: *yangjinglei1220@126.com (Jinglei Yang)*

ABSTRACT

This paper utilised computational fluid dynamics (CFD) technology to calculate the resistance of a novel high-speed quadramaran in calm water using the Navier–Stokes (N–S) equation, analysed the total resistance, frictional resistance, and residual resistance characteristics of this novel high-speed quadramaran at different length Froude numbers, and compared them with the results of a conventional high-speed catamaran with the same displacement. The results showed that the total resistance of the quadramaran had a significant hump at the Froude number of 0.6, due to the complexity of the wave interference among the four demihulls, and the hump value was about 1.6 times that of the catamaran. Above the hump speed, the total resistance of the quadramaran decreased with the increase of the Froude number, until reaching the Froude number of 1.06, when the curve became flat, and it showed a maximum resistance reduction of 40% at the Froude number of 1.66 compared with the catamaran, where the total resistance curve was steep. The frictional resistance of the quadramaran increased gradually with the growth of the Froude number, which was basically consistent with the change trend of the catamaran. The residual resistance of the quadramaran first rose and then reduced with the rising Froude number, the curve showed a large hump due to the adverse wave interference, and the hump value was about 1.7 times that of the catamaran. Above the Froude number of 1.06, as the wave interference changed from adverse to favourable, the quadramaran had lower residual resistance than the catamaran. The bow and stern demihulls of the quadramaran were also analysed for their resistance characteristics. The total resistance of the bow demihulls increased gradually with the increase of the Froude number, the curve had a small hump at the Froude number of 0.7, and above the hump speed, the curve was steep. The total resistance of the stern demihulls first increased and then decreased with the growth of the Froude number, the hump value at the Froude number of 0.85 was significant and was about 2 times that of the bow demihulls, and the curve became flat above the Froude number of 1.51.

Keywords: high-speed quadramaran; high-speed catamaran; resistance characteristic; wave-making interference; resistance hump

INTRODUCTION

In recent years, multi-hulls have been widely studied by a large number of researchers because of their wide deck area, excellent speed, and seakeeping performance. The catamaran is one of the most widely studied and applied hull forms, with relatively variable designs, including the small waterline catamaran (SWATH), wave-piercing catamaran, partial air cushion support catamaran (PACSCAT) [1–2], asymmetric catamaran [3–5], supercritical catamaran [6], etc. Trimarans and pentamarans mostly use the form of a large main hull in the middle and small demihulls distributed on both sides of the main hull, while the hull forms are mostly slender or small waterline hulls. However, there is not much research on the quadramaran, and most researchers who study quadramarans generally take slender or small waterline hulls as the hull forms. Peng [7] utilised the boundary element method in terms of the Green function to compute the resistance and motion responses of a slender catamaran, trimaran, quadramaran, and pentamaran by altering the configurations of the demihulls. Fang et al. [8] took the small waterline quadramaran (SLICE) as the research object to investigate its resistance characteristics, compared with a SWATH of the same scale, and concluded that the SLICE had certain resistance advantages only under the condition of shallow draft. Michell's linear wave resistance theory method was adopted by Cai et al. [9] to study the wave-making resistance characteristics of a SWATH, trimaran, SLICE, and pentamaran at different Froude numbers, and obtain the proportion of wave-making resistance. A series of numerical simulations based on FLUENT software was performed by Zhang et al. [10], and the total resistance characteristics and flow field distributions of a small waterline catamaran, trimaran, and quadramaran were analysed. Based on Neumann–Michell theory, Liu et al. [11] used the self-developed NMShip-SJTU solver to numerically calculate the wave-making resistance of a staggered quadramaran with slender demihulls at different Froude numbers and different longitudinal and transverse positions, analysing the wave interference characteristics. Yanuar et al. [12-13] conducted a set of experiments in calm water to investigate the effect of the quadramaran configurations on the total resistance coefficient and interference factor.

As a prominent research method, computational fluid dynamics (CFD) technology is widely applied by many researchers in the process of ship design, and can accurately and effectively forecast the hydrodynamic performance of ships. Farkas et al. [14] performed a number of numerical simulations of an S60 catamaran at different separations to obtain the characteristics of the total resistance and the wave interference factor, and the numerical results showed good agreement with the experimental results. Hu et al. [15] developed an asymmetric catamaran and investigated its resistance, rise-up, and dynamic trim angle by altering the lateral separation and longitudinal stagger based on the CFD method, and the deviations of the numerical results from the experimental results were less than 6%. Ebrahimi et al. [16] proposed a planing catamaran with transverse steps, analysed the aero-hydrodynamic effect in calm water at different displacements, and numerically calculated the resistance, the results of which agreed well with the experimental data. Li et al. [17] investigated the seakeeping characteristics of a slender trimaran equipped with and without a T-foil near the bow by experimental and numerical methods. The numerical simulations were validated by comparisons with the experimental tests. A range of numerical simulations were carried out by Heidari et al. [18], and the effects of the trim, heel, and yaw angles of the side hulls on the resistance and flow field characteristics of a trimaran were investigated; by contrast with the experimental values, the maximum numerical error was only 5%. Yildiz et al. [19] analysed the total resistance and wave profiles of a trimaran with nine different outrigger configurations by using the CFD method, and obtained good agreements when compared with the experimental results. To reduce the resistance in calm water and wavy conditions, Nazemian et al. [20] took the numerical results as the objective function, which were computed by CFD simulation and matched well with the experimental data, and utilised an arbitrary shape deformation method to optimise the hull shape of a wave-piercing trimaran. All the studies mentioned above applied the STAR CCM+ solver to perform numerical calculations, and good consistencies were shown between the numerical and experimental results, which verified the validity of the CFD method. So, this indicates that the CFD method could meet the requirements of practical engineering applications and reliably and accurately predict the hydrodynamic performance of multi-hulls.

In this paper, a novel high-speed quadramaran with a service speed above 30 kn is developed. A high-speed V-shaped hull form is applied to the demihull, which is different from the slender or small waterline quadramaran studied by previous researchers. It is undeniable that the slender hull or small waterline hull is conducive to reducing the wave-making resistance of multi-hulls, but the draft of the hull at the same displacement is deep, which is not conducive to navigating in a shallow fairway and is detrimental to the development of the hull form towards heavy loads and large sizes. Compared with a slender hull, the shape of the demihull makes the hull space more spacious, facilitates the arrangement of equipment, and makes the draft shallower. As the most widely used, the V-shaped hull form has excellent high-speed performance, but its seakeeping performance is unsatisfactory in a rough sea state. The advantage of multi-hulls is that they have great seakeeping and stability performance in rough sea states, but the wave-making resistance will be larger than that of monohulls due to the wave interference among the demihulls at high speed. The ship type proposed is based on the quick reach needs of windfarm maintenance and ocean transportation, which require a service speed above 30 kn. The hull form integrates the advantages of the V-shaped hull and multi-hull, which means that the quadramaran has not only a remarkable high-speed performance, but also excellent seakeeping in rough sea states. This paper studies the resistance characteristics

of the quadramaran in calm water, including the resistance, rise-up, dynamic trim angle, and wave-making interference. Analyses are carried out with several numerical simulations based on the mature STAR CCM+ solver. The computed results could provide data support for the further study of ship model experiments.

NUMERICAL SIMULATION METHOD

GOVERNING EQUATIONS AND THEORIES

Considering the influence of turbulent pulsation, the governing equations of fluids are commonly based on the time-averaged method [21–22]. The continuous equation and the Reynolds-Averaged Navier–Stokes equation are expressed as follows:

$$\frac{\partial \rho}{\partial t} + \frac{\partial}{x_i}(\rho u_i) = 0 \tag{1}$$

$$\frac{\partial(\rho u_i)}{\partial t} + \frac{\partial}{\partial x_j}(\rho u_i u_j) = -\frac{\partial P}{\partial x_i} + \frac{\partial}{\partial x_j}\left(\mu \frac{\partial u_i}{\partial x_j} - \overline{\rho u_i' u_j'}\right) + S_i \tag{2}$$

where u_i and u_j are the time-averaged value of the velocity component, and the value range of subscript i and j is (1,2,3); P is the time-averaged value of the pressure; ρ is the fluid density; μ is a hydrodynamic viscosity coefficient; $-\overline{\rho u_i' u_j'}$ is the Reynolds stress; and S_i is the generalised source term of the momentum equation.

The standard $k-\varepsilon$ model is used as the turbulence model in this paper. The equation of the turbulent kinetic energy k and turbulent dissipation rate ε are expressed as follows:

$$\frac{\partial(\rho k)}{\partial t} + \frac{\partial(\rho k u_i)}{\partial x_i} = \frac{\partial}{\partial x_j}\left[\left(\mu + \frac{\mu_t}{\sigma_k}\right)\frac{\partial k}{\partial x_j}\right] + G_k - \rho\varepsilon \tag{3}$$

$$\frac{\partial(\rho\varepsilon)}{\partial t} + \frac{\partial(\rho\varepsilon u_i)}{\partial x_i} = \frac{\partial}{\partial x_j}\left[\left(\mu + \frac{\mu_t}{\sigma_\varepsilon}\right)\frac{\partial \varepsilon}{\partial x_j}\right] + C_{1\varepsilon}\frac{\varepsilon}{k}G_k - C_{2\varepsilon}\rho\frac{\varepsilon^2}{k} \tag{4}$$

where G_k is the generation term of turbulent kinetic energy k caused by the average velocity gradient; $\mu_t = \rho C_\mu \frac{k^2}{\varepsilon}$; C_μ=0.09; σ_k=1.0; and σ_ε=1.3.

The volume of fluids (VOF) method [23–24] was utilised to capture the free liquid surface. The phase distribution and position at the interface are described by the field of phase volume fraction a_j, where the phase j is defined as follows:

$$a_j = \frac{V_i}{V} \tag{5}$$

where V_i is the volume of the phase j in the mesh cell and V is the volume of the mesh cell.

The sum of the volume fractions of all the phases in a mesh cell must be 1; that is, $\sum_{i=1}^{N} a_i = 1$, where N is the total number of phases. According to the value of the volume fraction, it can distinguish whether there are different phases or fluids in the mesh cell; that is, when a_i=0, the mesh cell has no phase i at all. When a_i=1, this mesh cell is completely filled by the phase i; 0< a_i <1, where the value between the two limits indicates the existence of an interface between the phases.

COMPUTATIONAL MODEL

The ship type studied in this paper was inspired by a catamaran with a step [16]. Using a step on the hull could separate the water, create a dry section from step to transom, and reduce the resistance at high speed [25–26]. The stepped hull is viewed as two regular hulls following each other closely, so that the catamaran turns into a quadramaran. A high-speed V-shaped catamaran (Fig. 1b) is selected to separate at midship, the first demihulls are used as the bow demihulls of the quadramaran, and the second demihulls are replaced by other V-shaped hulls used as the stern demihulls of the quadramaran, where the centre lines of the bow and stern demihulls are aligned. Before the ship type in this paper was proposed, a hull form optimisation study was carried out, and it was found that a large deadrise angle at the bow demihull was beneficial to improve the wave interference and reduce the total resistance. So that the bow and stern demihulls are of different V-shaped hull forms, the bow hull has leaner lines, larger deadrise angles, and smaller waterline entrance angles than those of the stern hull.

A full-scale model has been chosen as the study objective, and the main parameters of the catamaran and quadramaran in full scale are listed in Table 1. They have the same displacement and same waterline length, and the geometry models are established as shown in Fig. 1.

Tab. 1 The main parameters of the quadramaran and catamaran

High-speed quadramaran		High-speed catamaran	
Parameters	Value	Parameters	Value
Length overall of bow demihull L_{bOA} (m)	11.76	Length overall of demihull L_{OA} (m)	22.5
Length overall of stern demihull L_{sOA} (m)	12.32		
Waterline length of bow demihull L_b (m)	11.00	Waterline length of demihull L (m)	21.72
Waterline length of stern demihull L_s (m)	10.72		
Moulded breadth of bow demihull B_b (m)	3.92	Moulded breadth of demihull B (m)	3.38
Moulded breadth of stern demihull B_s (m)	4.1		
Deadrise angle in the midship of bow demihull β_b (°)	40.9	Deadrise angle in the midship of demihull β (°)	27.3
Deadrise angle in the midship of stern demihull β_s (°)	18.9		

High-speed quadramaran		High-speed catamaran	
Parameters	Value	Parameters	Value
Transverse spacing of the centreline of demihulls K_c (m)	5.55	Transverse spacing of the centreline of demihulls K_c (m)	5.2
Longitudinal spacing of demihulls K_l (m)	0.05	Longitudinal spacing of demihulls K_l (m)	/
Length overall of quadramaran L_{OA} (m)	24.13	Length overall of catamaran L_{OA} (m)	22.5
Breadth overall of quadramaran B_{OA} (m)	9.65	Breadth overall of catamaran B_{OA} (m)	8.44
Moulded depth D (m)	2.4	Moulded depth D (m)	3.5
Draft T (m)	1.13	Draft T (m)	1.2
Displacement of bow demihulls Δ_b (t)	27	Displacement of bow demihulls Δ_b (t)	/
Displacement of stern demihulls Δ_s (t)	43	Displacement of stern demihulls Δ_s (t)	/
Total displacement of quadramaran Δ (t)	70	Total displacement of catamaran Δ (t)	70

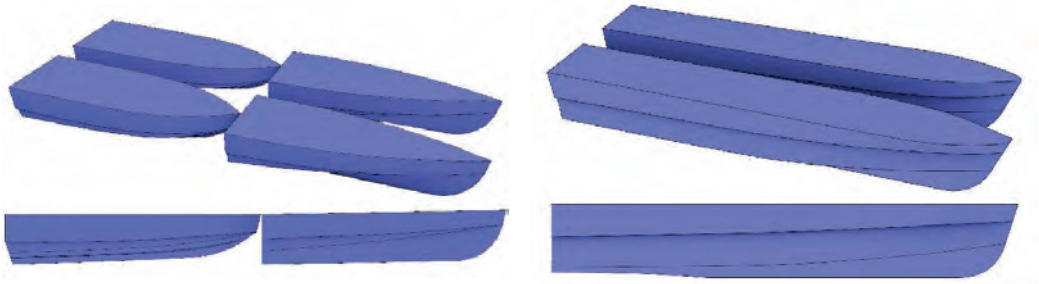

(a) quadramaran *(b) catamaran*

Fig. 1. The geometry models

NUMERICAL SCHEME

Boundary conditions

The computational domain is extended 1.5 L to the front of the bow, 3 L to the rear of the stern, L to the side, L above the free surface, and 1.5 L below the free surface. The boundary conditions of the inlet, top, and bottom of the computational domain are set as the velocity inlet, the outlet is set as the pressure outlet, both sides are set as the symmetry plane, and the hull surface is set as a no-slip wall surface.

Calculation setup

The implicit unsteady state is selected as the time model, the material is selected as Euler multiphase flow, the motion of the hull is set as six degrees of freedom rigid body motion, the VOF wave is set as calm water, the time step is set to 0.001 s, and the iteration step is 10 steps.

The studied speed ranges between 3.6 m/s and 24.18 m/s, because the total waterline length of the quadramaran, that is, the sum of the bow and stern demihulls' waterline length, is the same as that of the catamaran, so that they have the same length Froude number, represented by the symbol F_r. Besides, the symbols F_{rb} and F_{rs} represent the length Froude number of the bow and stern demihull, respectively. Table 2 shows the corresponding speeds of the computational model.

Tab. 2 Corresponding speeds of computational model

Speed V (m/s)	Speed V (kn)	Length Froude number of entire hull F_r	Volume Froude number of entire hull $F_{r\nabla}$	Length Froude number of bow demihull F_{rb}	Length Froude number of stern demihull F_{rs}
3.60	7	0.25	0.41	0.35	0.35
5.14	10	0.35	0.57	0.50	0.50
6.69	13	0.46	0.81	0.64	0.65
7.72	15	0.53	1.06	0.74	0.75
8.74	17	0.60	1.22	0.84	0.85
10.29	20	0.71	1.38	0.99	1.00
11.83	23	0.81	1.63	1.14	1.15
12.86	25	0.88	1.87	1.24	1.25
13.89	27	0.95	2.03	1.34	1.36
15.43	30	1.06	2.19	1.49	1.51
16.98	33	1.17	2.44	1.64	1.66
18.00	35	1.23	2.69	1.73	1.76
19.03	37	1.30	2.84	1.83	1.86
20.58	40	1.41	3.01	1.98	2.01
22.12	43	1.52	3.25	2.13	2.16
23.15	45	1.59	3.49	2.23	2.26
24.18	47	1.66	3.66	2.33	2.36

Grid convergence study

To boost confidence in the CFD computation results, a grid convergence study is needed before systematic computations according to ITTC recommended procedures [27–28]. Three sets of grids corresponding to fine, medium, and coarse grids are established, respectively. The grid refinement ratio is $r_G = \sqrt{2}$. Taking the quadramaran speed 20.58 m/s as an example, the grids from the finest to the coarsest grids are illustrated in Fig. 2, and the grid cell numbers are given in Table 3. The calculated results using different grid strategies are shown in Table 4.

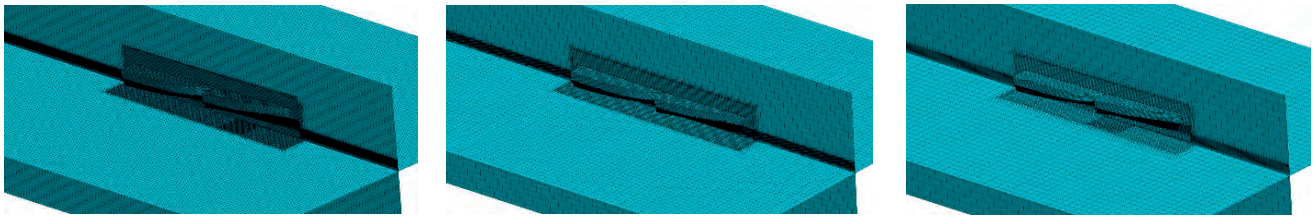

(a) fine grid *(b) medium grid* *(c) coarse grid*

Fig. 2. Grids from finest to coarsest

Tab. 3 Number of cells for three grids

Grid scheme	(a) fine grid S_1	(b) medium grid S_2	(c) coarse grid S_3
Number of grids	38775148	16133326	6091183

Tab. 4 Calculated results using different grid strategies

Grid scheme	(a) fine grid S_1	(b) medium grid S_2	(c) coarse grid S_3
Bow total resistance (kN)	43.40	44.18	45.17
Stern total resistance (kN)	39.64	41.26	43.61
Total resistance (kN)	83.08	85.46	88.77
Dynamic trim angle (°)	1.397	1.427	1.469
Rise-up (m)	0.418	0.419	0.421

Tab. 5 Grid uncertainty analysis

Grid scheme	Bow total resistance	Stern total resistance	Total resistance	Dynamic trim angle	Rise-up
Convergence ratio R_G	0.787	0.686	0.718	0.697	0.451
Convergence condition	Monotonic	Monotonic	Monotonic	Monotonic	Monotonic
Accuracy P_G	0.693	1.086	0.957	1.042	2.298
Grid error $\delta^*_{RE_G}$	2.867	3.529	6.042	0.068	0.0007
Correction factor C_G	0.271	0.457	0.393	0.435	1.218
$\lvert 1 - C_G \rvert$	0.729	0.543	0.607	0.565	0.218
Uncertainty U_G	7.045	7.363	13.376	0.145	0.0099
Uncertainty $U_G(\% S_G)$	16.23%	18.57%	16.10%	10.34%	0.24%
Correction error δ^*_G	0.778	1.613	2.375	0.0295	0.0008
Correction error $\delta^*_G(\% S_G)$	1.83%	4.24%	2.94%	2.16%	0.20%
Correction uncertainty U_{C_G}	2.089	1.917	3.667	0.038	0.0001
Correction uncertainty $U_{G_C}(\% S_G)$	4.90%	5.04%	4.54%	2.80%	0.04%

The differences in the results between the different grid schemes are defined as follows:

$$\begin{cases}\varepsilon_{21} = S_2 - S_1 \\ \varepsilon_{32} = S_3 - S_2\end{cases} \tag{1}$$

The convergence ratio R_G is defined as

$$R_G = \frac{\varepsilon_{21}}{\varepsilon_{32}} \tag{2}$$

According to [27], three convergence conditions are possible:
(1) Monotonic convergence: $0 < R_G < 1$;
(2) Oscillatory convergence: $R_G < 0$;
(3) Divergence: $R_G > 1$.

The results of the convergence ratio R_G shown in Table 5 are less than 1, so the grid convergence is monotonic.

For monotonous convergence, the Generalized Richardson extrapolation is used to estimate the grid error $\delta^*_{RE_G}$.

$$\delta^*_{RE_G} = \frac{\varepsilon_{21}}{r_G^{P_G} - 1} \tag{3}$$

The order of accuracy P_G is estimated as

$$P_G = \frac{In\left(\varepsilon_{32}/\varepsilon_{21}\right)}{In(r_G)} \tag{4}$$

The correction factor C_G is defined as

$$C_G = \frac{r_G^{P_G} - 1}{r_G^{P_{Gest}} - 1} \tag{5}$$

where $P_{Gest} = 2$ was used according to [28].

For C_G considered as sufficiently less than or greater than 1 and lacking confidence, the error δ_G is not estimated, and the uncertainty U_G is estimated as follows:

$$U_G = \begin{cases}[9.6(1 - C_G)^2 + 1.1]\left|\delta^*_{RE_G}\right| & |1 - C_G| < 0.125 \\ [2|1 - C_G| + 1]\left|\delta^*_{RE_G}\right| & |1 - C_G| \geq 0.125\end{cases} \tag{6}$$

For C_G considered close to 1 and having confidence, the correction error δ^*_G and the correction uncertainty U_{G_C} are estimated as follows:

$$\delta^*_G = C_G \delta^*_{RE_G} \tag{7}$$

$$U_{G_C} = \begin{cases}[2.4(1 - C_G)^2 + 0.1]\left|\delta^*_{RE_G}\right| & |1 - C_G| < 0.25 \\ [|1 - C_G|]\left|\delta^*_{RE_G}\right| & |1 - C_G| \geq 0.25\end{cases} \tag{8}$$

The correction simulation result S_C is defined as

$$S_C = S_G - \delta^*_G \tag{9}$$

where S_G is the result of numerical simulation under the finest grid S_1.

Table 5 shows the results of the grid uncertainty analysis. δ^*_G and U_{G_C} are relatively small, so the level of verification is relatively small, < 6%. This indicates that the errors in the results caused by grid discretisation are very small. Thus, as a trade-off between accuracy and efficiency, the grid density S_2 is selected for calculation.

Mesh generation

The overset mesh method is applied to the computational mesh. Mesh encryption is performed on the free liquid surface and the area around the hull, respectively, and boundary layer meshes are set around the hull, where 6 boundary layers are created with a growth rate of 1.1. The specific computational meshes are shown in Fig. 3. The y+ distribution obtained for the speed of 20.58 m/s from the full-scale simulation is shown in Fig. 4, where the value for y+ around the hull is about 100–1500.

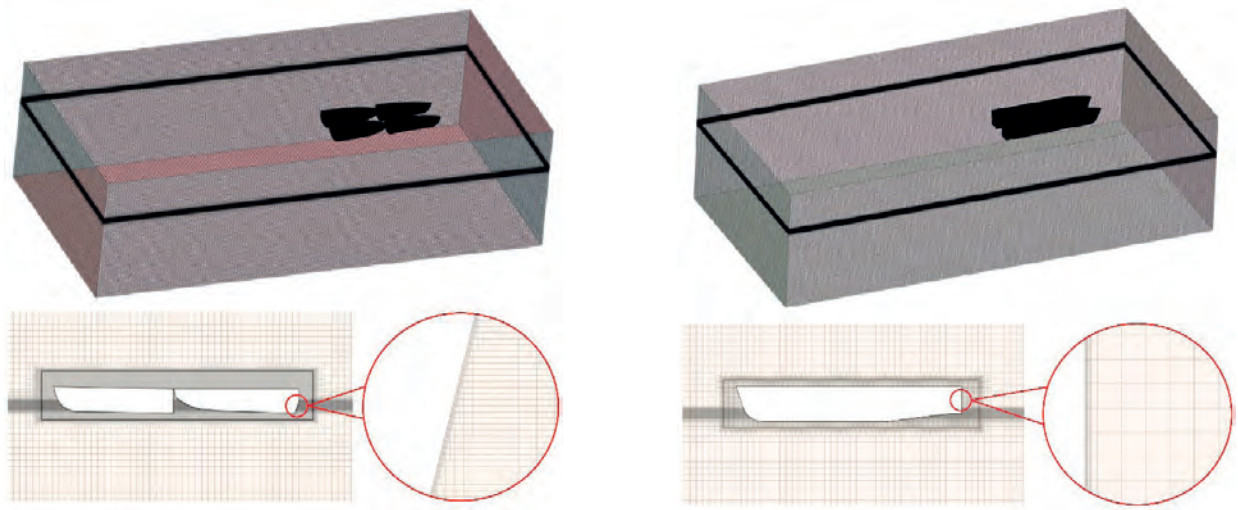

(a) quadramaran *(b) catamaran*

Fig. 3. Computational mesh

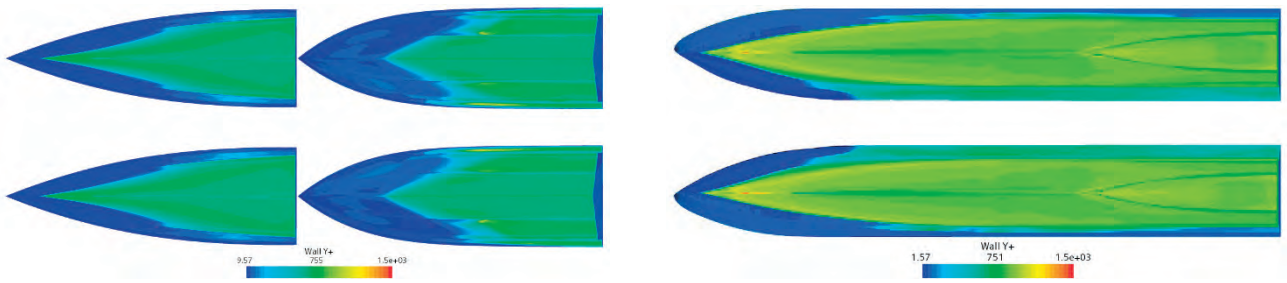

(a) quadramaran *(b) catamaran*

Fig. 4. The distribution of y+ for the speed of 20.58 m/s

Validation of the numerical method

Considering the absence of publicly available ship model test results, a V-shaped high-speed boat from the M_1 ship type proposed by Parviz Ghadimi [26] is selected to carry out a comparative study to assess the accuracy of the numerical methods. Table 6 lists the principal dimensions of hull M_1 while Fig. 5 illustrates the geometry of the model.

The results are compared with experimental and CFD data for the total resistance, dynamic trim angle and rise-up, as given in Figs. 6-8. It is seen that the numerical results of the total resistance and dynamic trim angle agree well with the experimental results. The maximum deviation of the total resistance is 10.9% at 7 m/s, and the maximum deviation of the dynamic trim angle is 18.76% at 7 m/s. Although the overall deviation of the rise-up is large, the general trend is consistent with the experimental value. It can be seen that the CFD numerical calculation method used in this paper is suitable and has reliable calculation accuracy.

Tab. 6 The principal dimensions of hull

Parameters	Value
Length overall L_{OA} (m)	2.64
Maximum beam B (m)	0.551
Displacement Δ (kg)	86
Longitudinal distance of gravity centre L_{CG} (m)	0.791
Vertical distance of gravity centre V_{CG} (m)	0.185
Speed V (m/s)	1-7

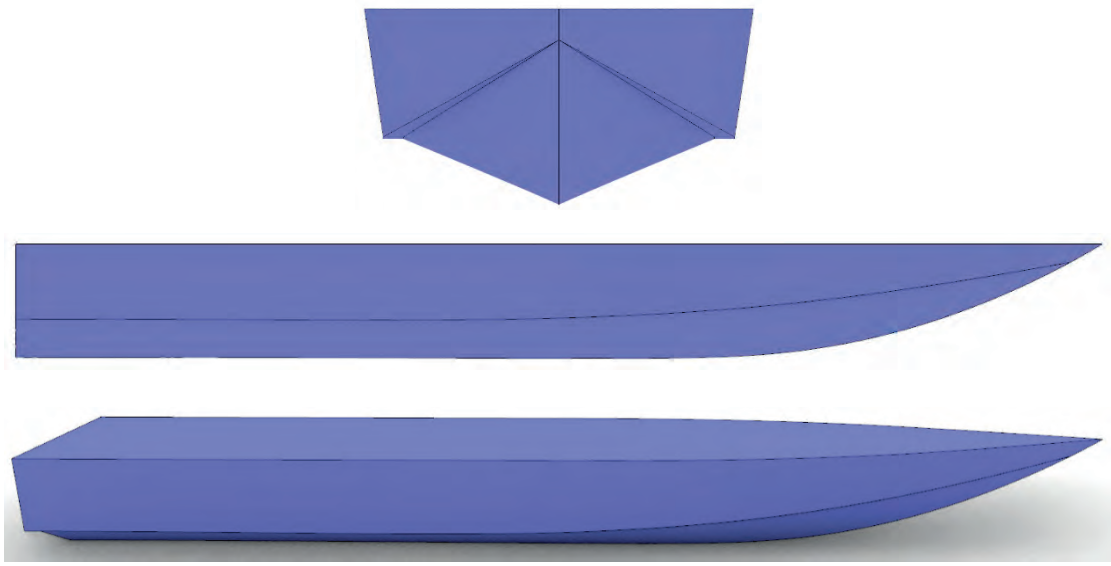

Fig. 5. The geometry of the model

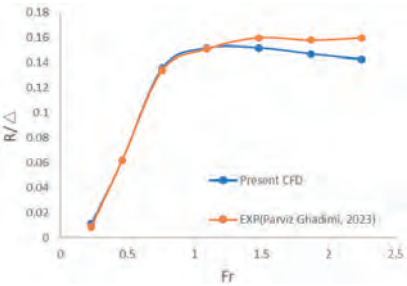

Fig. 6. Comparison of total resistance

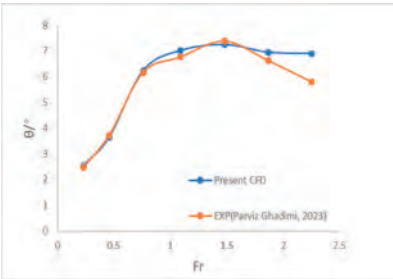

Fig. 7. Comparison of dynamic trim angle

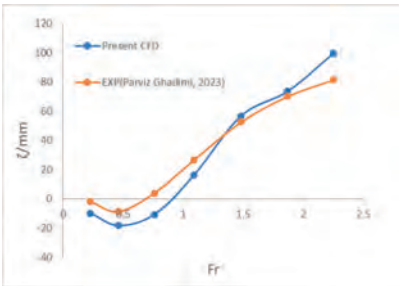

Fig. 8. Comparison of rise-up

CALCULATION RESULTS AND ANALYSIS

For high-speed ships, resistance can be divided into two parts: frictional resistance and residual resistance [29]. The calculation formula of the total resistance is expressed as follows.

$$R_t = C_t \frac{1}{2} \rho S V^2 \tag{10}$$

where C_t is the total resistance coefficient, $C_t = C_f + C_r + \Delta C_F$; C_f is the frictional resistance coefficient; C_r is the residual resistance coefficient; ΔC_F is the correction coefficient, which is 0.0004; ρ is the density of seawater, kg/m^3; S is the wet surface area of the hull, m^2; V is the hull speed, m/s.

The frictional resistance coefficient C_F is obtained based on the equivalent plank assumption, which was determined by the International Towing Tank Conference (ITTC) [30], that is:

$$C_f = \frac{0.075}{(\lg Re - 2)^2} \tag{11}$$

where Re is the Reynolds number.

For high-speed ships, although the viscous pressure resistance accounts for a small proportion of the residual resistance, most of the residual resistance is composed of the wave-making resistance, so the characteristics of the wave-making resistance can be reflected by the residual resistance [31].

According to [32], when the length Froude number $F_r < 0.4$, the buoyancy force dominates relative to the hydrodynamic force effect, and vessels in this Froude number range are called displacement vessels; vessels with a length Froude number in the range of $0.4 - 0.5 < F_r < 1.0 - 1.2$ are called semi-planing vessels, which means that high-speed submerged hull-supported vessels denote vessels in which the buoyancy force is not dominant; vessels with a length Froude number in the range of $F_r > 1.0 - 1.2$ are called planing vessels, which means that the hydrodynamic force mainly carries the weight. However, there is no clear line of demarcation between planing and nonplaning conditions just by referring to the length Froude number, as individual circumstances alter cases.

In this paper, the calculation results were analysed by using non-dimensional parameters. The speed is represented by the length Froude number F_r, which is defined as $F_r = \frac{V}{\sqrt{gL}}$, and the resistance is represented by the resistance to weight ratio, which is defined as R/Δ, where V is the hull speed, m/s L is the waterline length, m; g is the acceleration of gravity, with a value of 9.8 m/s^2; R is the resistance value, N; and Δ is the hull weight, kg.

ANALYSIS OF RESISTANCE CHARACTERISTICS OF INTEGRATED HULL

Figs. 9–13 show the comparison curves of the characteristics of the rise-up ζ, dynamic trim angle θ, frictional resistance R_f/Δ , residual resistance R_r/Δ and total resistance R_t/Δ of the quadramaran and catamaran as a function of the length Froude number F_r, respectively.

From the curves of the quadramaran, it can be seen that at low speed ($F_r < 0.53$), the motion turns from the displacement regime into the semi-planing regime, the dynamic trim angle increases with the increase of , the bow rises and the stern descends, so the rise-up is negative. The frictional resistance, residual resistance, and total resistance increase constantly. Because the hydrodynamic force is not enough to support the hull in this regime, the dynamic trim angle keeps increasing and the hull keeps descending until reaching the Froude number of 0.53, when the curve of the rise-up shows its hump, and the hull begins to rise. The dynamic trim angle, the residual resistance, and the total resistance have a significant hump at the Froude number of 0.6. Above the hump speed, due to the hydrodynamic force effect, the dynamic trim angle, the residual resistance, and the total resistance begin

to decrease until reaching the Froude number of 1.06, when the motion enters the planing regime, the dynamic trim angle becomes relatively steady, and the rise-up continues to increase gradually due to the hydrodynamic force effect. So the residual resistance keeps decreasing, while, because of the rapid growth of frictional resistance, the total resistance curve becomes remarkably flat and shows no upward trend.

Fig. 9 shows the comparison between the rise-up curves of the quadramaran and catamaran, where it can be seen that the two hulls have roughly the same change trend. Both hulls first descend and then rise, and both have a large hump at the Froude number of 0.53. However, because the quadramaran makes the flow separate from the middle and generates multiple planing surfaces leading to the hydrodynamic force being multiplied and greater, the rise-up value of the quadramaran is significantly higher than that of the catamaran.

Fig. 10 presents the comparison between the dynamic trim angle curves of the quadramaran and catamaran. It can be seen that both hulls also have roughly the same change trend. The dynamic trim angle of the two hulls first increases and then decreases; the quadramaran shows the hump at the Froude number of 0.6, while the catamaran shows the hump at the Froude number of 0.53. Because the bow and stern demihulls of the quadramaran generate multiple planing surfaces, causing the hydrodynamic force to be decentralised rather than concentrated like the catamaran, the angle amplitude of the catamaran is greater than that of the quadramaran, which is the opposite of the curve of the rise-up due to the special ship type.

Fig. 11 illustrates that the frictional resistance curves of both hulls have similar change trends on account of the similar main scales of the hulls.

Fig. 12 shows the comparison between the residual resistance curves of the quadramaran and catamaran. At low speed ($F_r < 0.53$), the residual resistance of both hulls increases constantly with the growth of F_r. The catamaran shows the hump at the Froude number of 0.53, while the quadramaran shows the hump at the Froude number of 0.6. The complexity of the wave interference among the four demihulls leads to the quadramaran having a significant hump, the value of which is about 1.7 times that of the catamaran. Above the hump speed, the residual resistance of both hulls reduces until reaching the Froude number of 1.06. The adverse wave interference makes the residual resistance of the catamaran increase again, while the residual resistance of the quadramaran continues to decrease due to the increase of the rise-up and the occurrence of favourable wave interference.

Fig. 13 shows the comparison between the total resistance curves of the quadramaran and catamaran. At low speed ($F_r < 0.53$), the two hulls turn from the displacement regime into the semi-planing regime, and the total resistance of both hulls increases constantly with the growth of F_r. The catamaran shows the hump at the Froude number of 0.53, while the quadramaran shows the hump at the Froude number of 0.6. The complexity of the wave interference among the four demihulls leads to the quadramaran having a significant hump, the value of which is about 1.6 times that of the catamaran. Above the hump speed, the total resistance of the catamaran still increases gently, while the quadramaran begins to decrease, until reaching the Froude number of 1.06, when the two hulls enter the planing regime, and the total resistance of the catamaran increases steeply, while for the quadramaran it becomes flat. Above the Froude number of 1.06, the quadramaran starts to have less total resistance than the catamaran, with a maximum resistance reduction of 40% at the Froude number of 1.66. This indicates that the quadramaran has a remarkable resistance advantage above the Froude number of 1.06 (at a service speed above 30 kn).

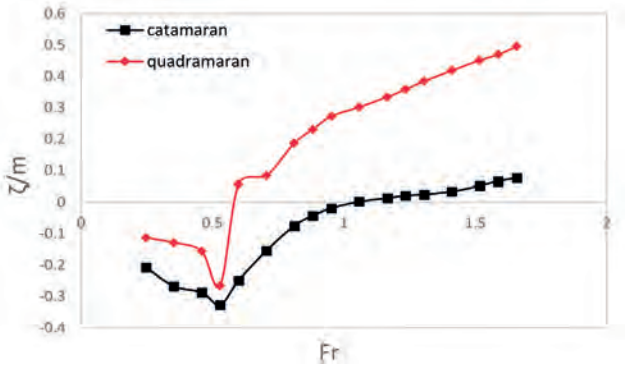

Fig. 9. Comparison of curves of rise-up

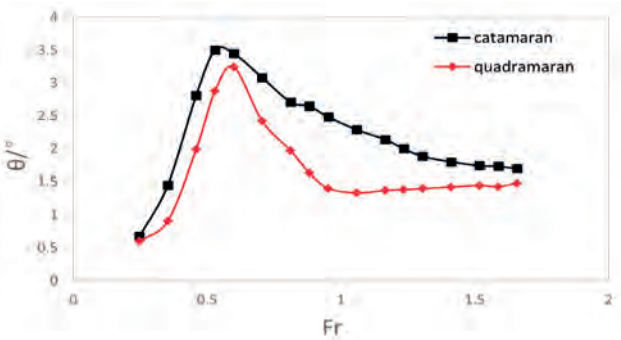

Fig. 10. Comparison of curves of dynamic trim angle

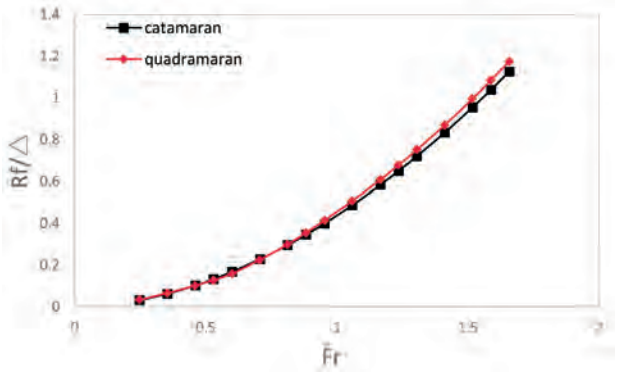

Fig. 11. Comparison of curves of frictional resistance

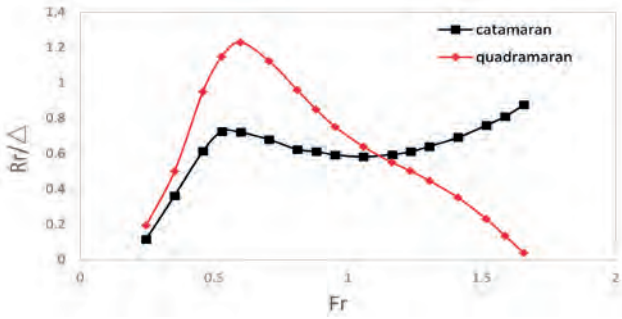

Fig. 12. Comparison of curves of residual resistance

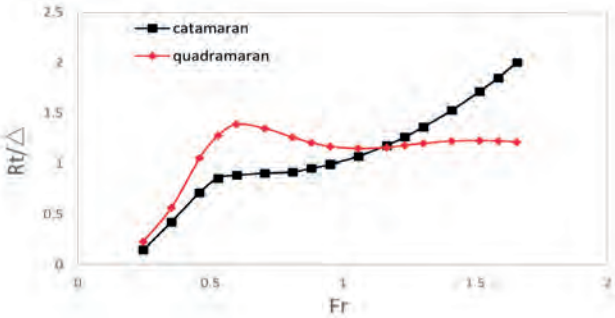

Fig. 13. Comparison of curves of total resistance

ANALYSIS OF RESISTANCE CHARACTERISTICS OF DEMIHULLS

The resistance of the demihulls is monitored independently by decomposing from the quadramaran hull. Figs. 14–19 show the resistance calculation results of the bow and stern demihulls of the quadramaran, in which the lower corner labels b and s represent the bow and stern, respectively.

Figs. 14 and15 present the frictional resistance curves of the bow and stern demihulls. It can be seen that the trends of frictional resistance of the bow and stern demihulls change similarly, as both increase constantly with the increase of the Froude number, which reflects that the frictional resistance is directly proportional to the square of speed. The leaner hull form, leading to a smaller wetted surface, makes the bow demihulls have lower values of frictional resistance.

Figs. 16 and 17 show the residual resistance curves of the bow and stern demihulls. At low speed (V < 7.72 m/s), the residual resistance of both demihulls rises gradually with the growth of the Froude number. The bow demihulls show the hump at the Froude number of 0.74, while the stern demihulls show the hump at the Froude number of 0.85. The reason is that the stern demihulls are located in the flow field of the bow demihulls, so the complexity of the wave interference makes the stern have a significant hump, the value of which is about 2 times that of the bow demihulls. Above the hump speed, as the hull rises, the residual resistance of both demihulls decreases with the increase of the Froude number.

Figs. 18 and 19 illustrate the total resistance curves of the bow and stern demihulls. At low speed (V < 7.72 m/s), the total resistance of both demihulls rises gradually with the growth of the Froude number. The bow demihulls show the hump at the Froude number of 0.74, while the stern demihulls show the hump at the Froude number of 0.85. The complexity of the wave interference makes the stern have a significant hump, the value of which is about 1.8 times that of the bow demihulls. Above the hump speed, the total resistance of the bow demihulls keeps increasing, while the total resistance of the stern demihulls begins to decrease until reaching the Froude number of 1.51, at which the hull enters planing mode and the curve becomes flat.

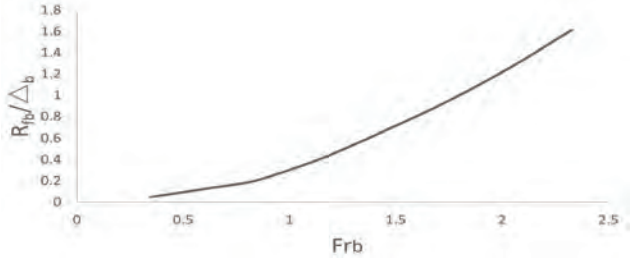

Fig. 14. Frictional resistance curve of bow demihulls

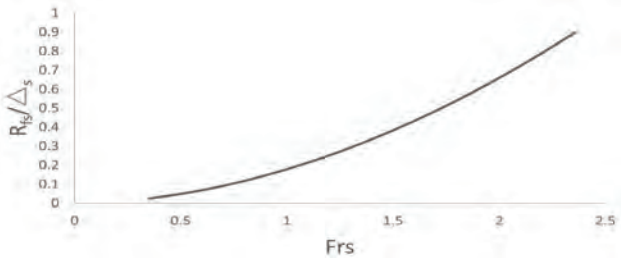

Fig. 15. Frictional resistance curve of stern demihulls

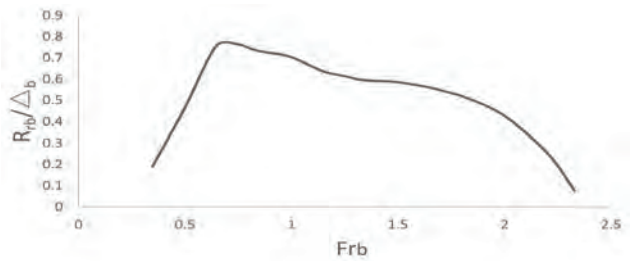

Fig. 16. Residual resistance curve of bow demihulls

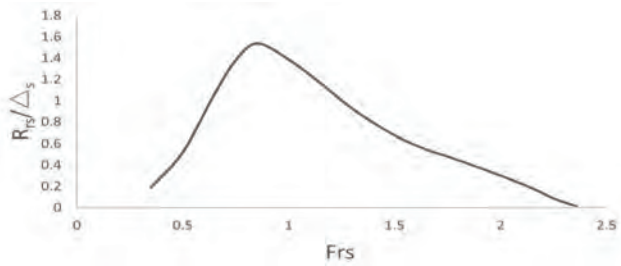

Fig. 17. Residual resistance curve of stern demihulls

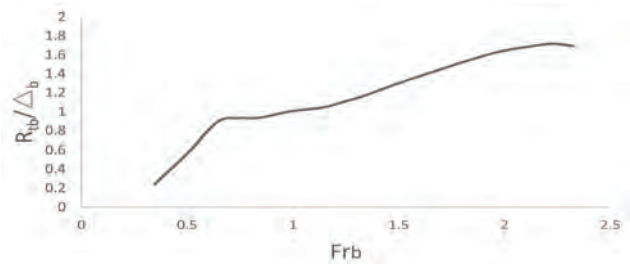

Fig. 18. Total resistance curve of bow demihulls

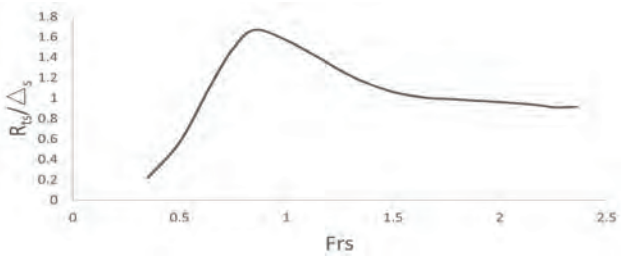

Fig. 19. Total resistance curve of stern demihulls

ANALYSIS OF WAVE-MAKING CHARACTERISTICS

Figs. 20 and 21 compare the contour and side view of the wave-making characteristics of the quadramaran and catamaran at different Froude numbers. It can be seen that, at low speed ($F_r < 0.53$), the two hulls turn from the displacement regime into the semi-planing regime. Both hulls descend and the dynamic trim angle increases. Transverse waves and divergent waves occur and reinforce each other, which makes the flow fields among the demihulls quite disorderly and adverse wave interference occurs. The flow in the stern region does not separate cleanly off the transom and therefore produces a large stern wake due to the sudden change in flow direction. Besides, the flows over the demihulls affect one another, which makes the flow asymmetric, so adverse viscous interference occurs. Having two more demihulls and a narrower separation than the catamaran results in complex flow fields, such that the quadramaran has worse wave and viscous interference and a higher wake, so that the total resistance of the quadramaran has a significant hump. Above the hump speed, as the hull rises and the dynamic trim angle decreases, the wave and viscous interference both improve, the flow fields gradually become orderly, the tail wake of the main hull extends backwards, the wake height decreases, and the flow under the transom is sufficient for separation. This results in cavitation being generated, which is equivalent to increasing the hull length and reducing the resistance, and the hydrodynamic force gradually dominates relative to the buoyancy force. As the hull of the quadramaran is separated in the middle by the bow and stern demihulls, the effect of the hydrodynamic force is greater than on the catamaran, so the total resistance of the quadramaran decreases in this regime, while for the catamaran it increases gently. Above the Froude number of 1.06, both hulls enter the planing regime. The wave pattern created behind the hulls is lengthened and narrower, and the length of cavitation becomes longer with the growth of the Froude number. The cavitation formed by the quadramaran is longer than that of the catamaran, and

the hydrodynamic force makes the quadramaran rise more, so the resistance curve is remarkably flat, while the wave-making at the bow of the catamaran rises, increasing its wave-making resistance, so the resistance curve is steep. In general, the quadramaran has worse wave-making characteristics at low speed but better characteristics at high speed compared to the catamaran.

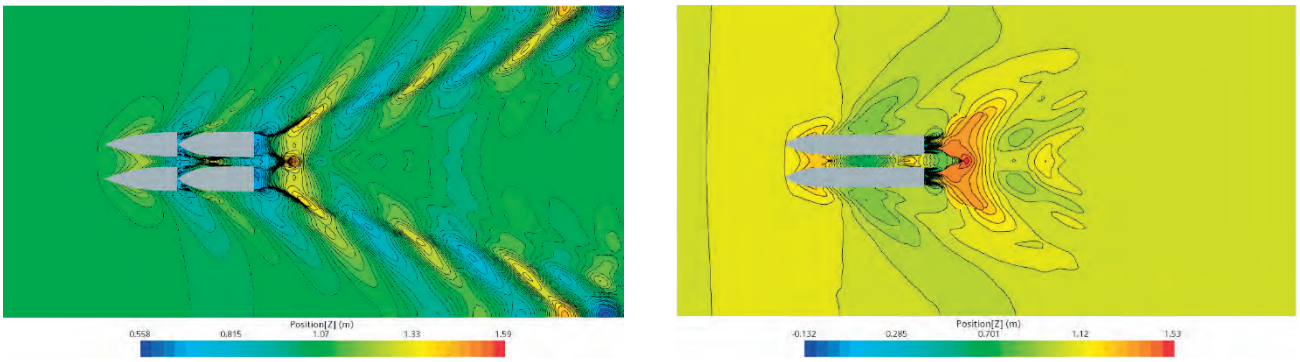

$F_r = 0.35$

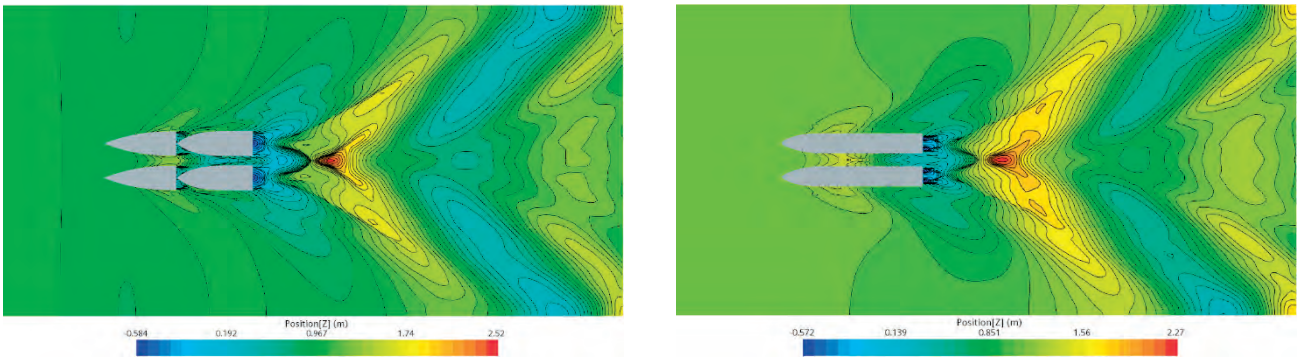

$F_r = 0.53$

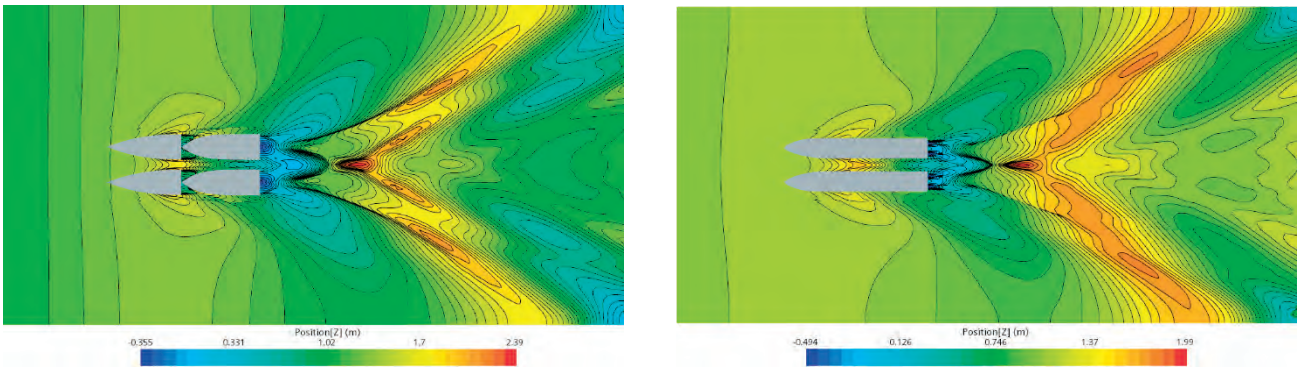

$F_r = 0.6$

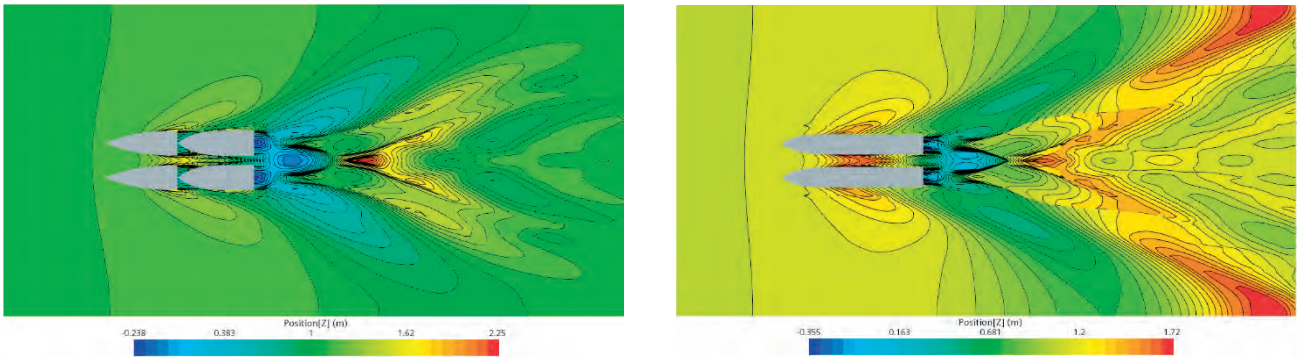

$F_r = 0.71$

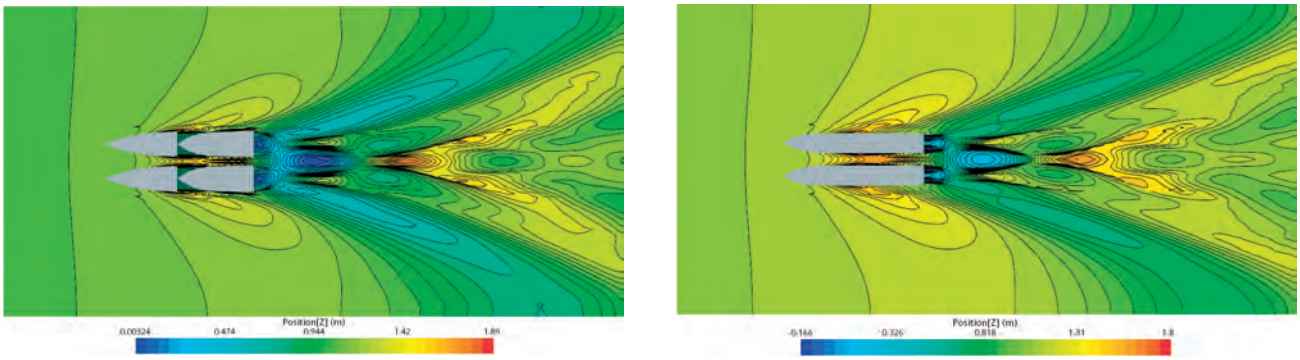

$F_r = 0.88$

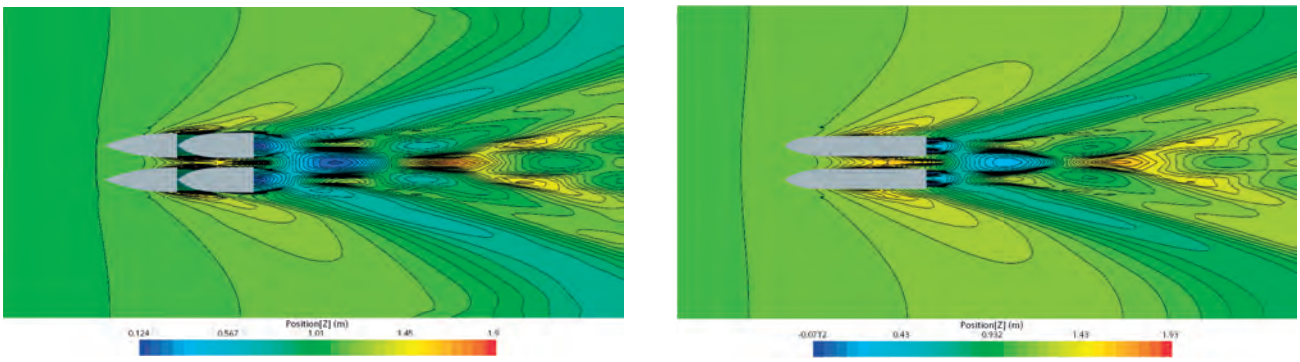

$F_r = 1.06$

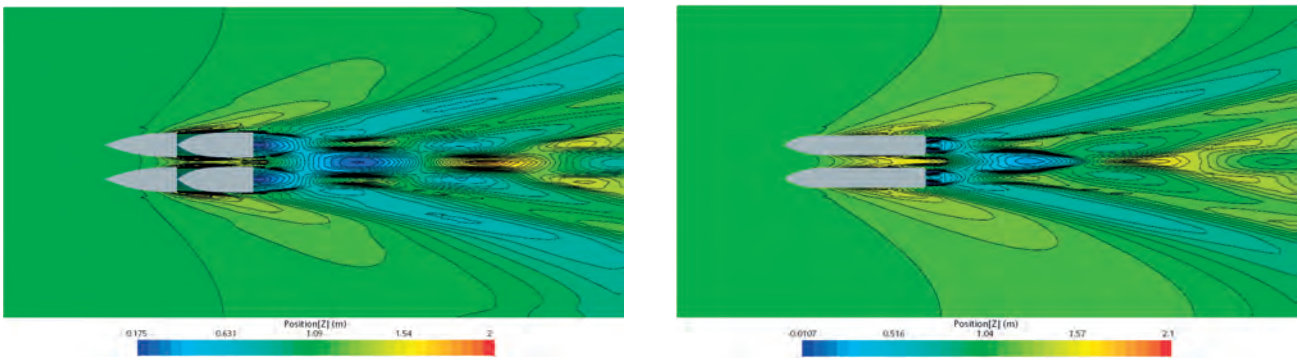

$F_r = 1.23$

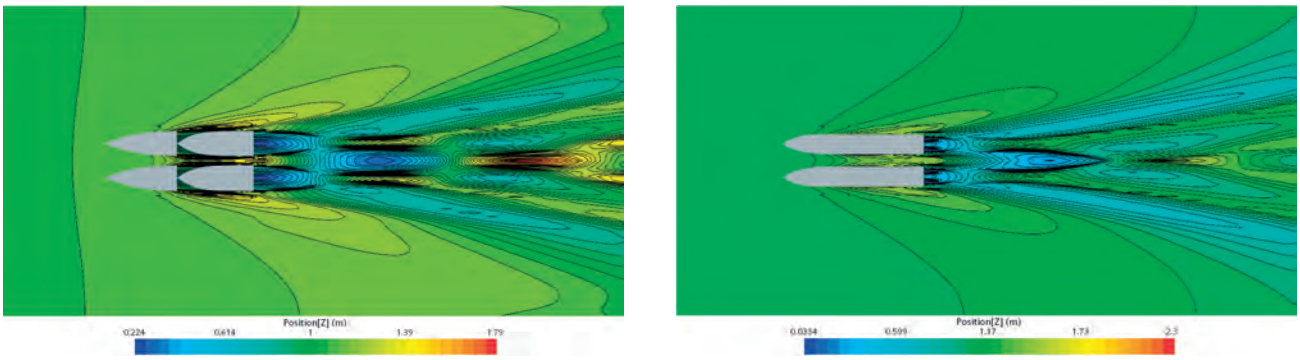

$F_r = 1.41$

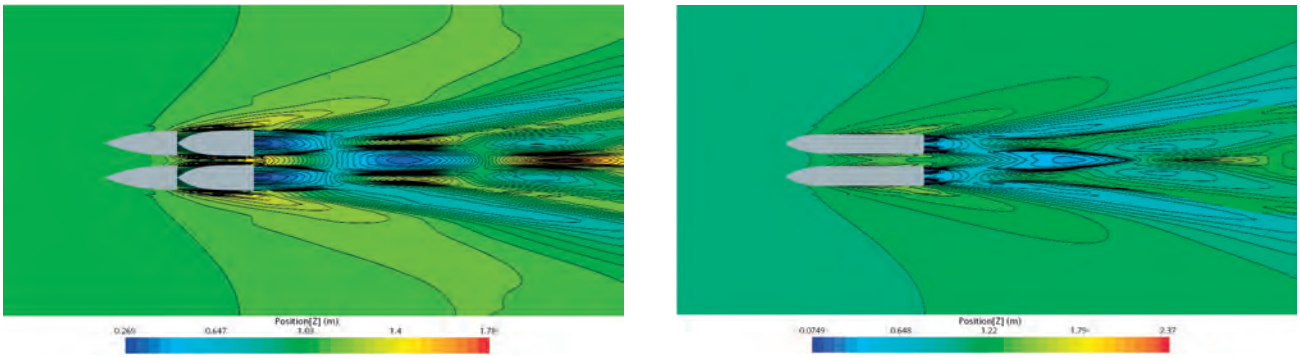

$F_r = 1.59$

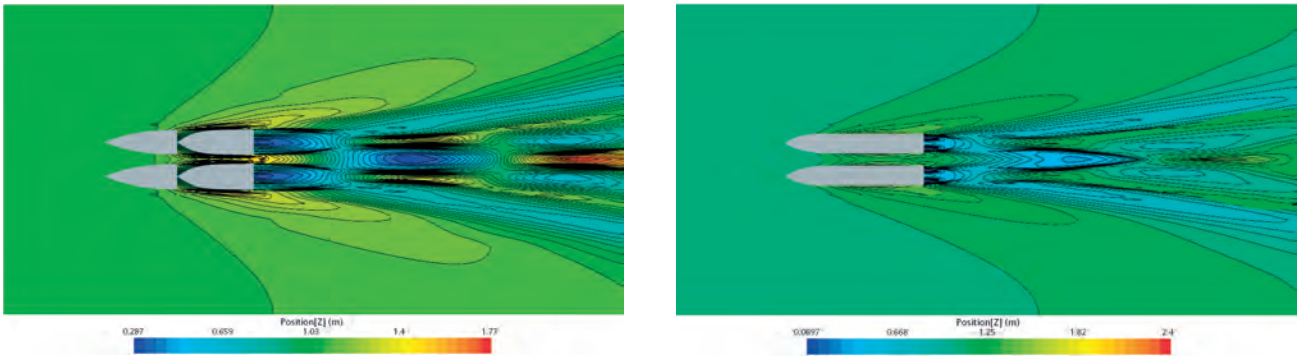

$F_r = 1.66$

(a) quadramaran *(b) catamaran*

Fig. 20. Wave contour comparison of two hulls at different F_r

$F_r = 0.35$

$F_r = 0.53$

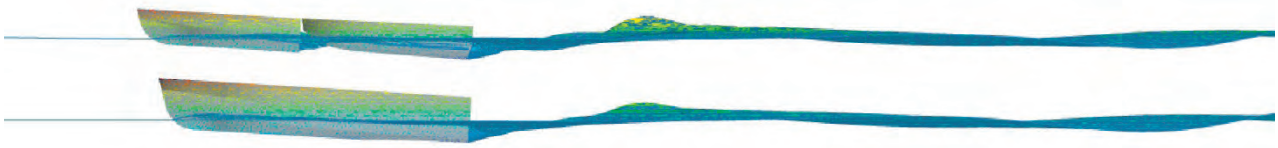

$F_r = 0.6$

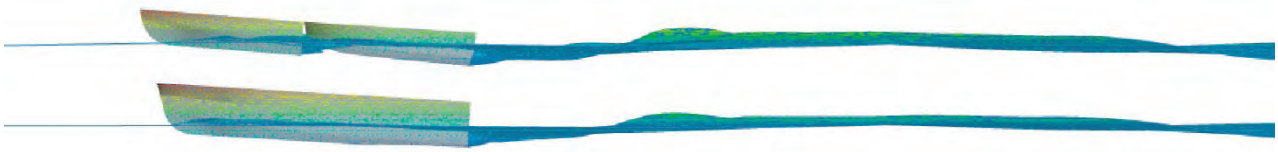

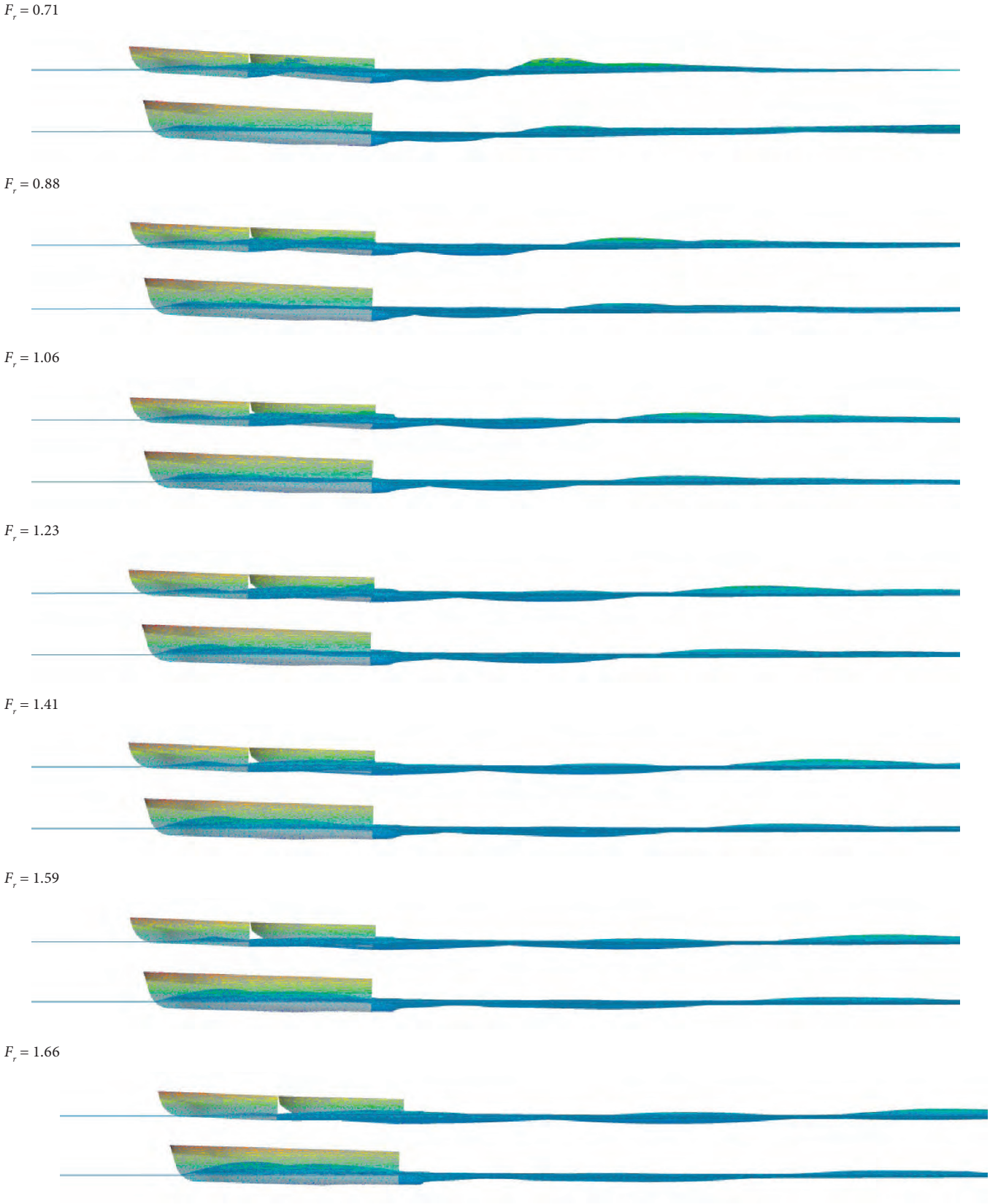

Fig. 21. Wave side view comparison of two hulls at different F_r

CONCLUSIONS

In this paper, a novel high-speed quadramaran is proposed, its resistance in calm water is calculated based on the CFD method, and the resistance characteristics are analysed. The following conclusions are obtained:

a) Due to the complex wave interference among the demihulls, the total resistance of the high-speed quadramaran has a significant hump at the Froude number of 0.6, the value of which is about 1.6 times that of the high-speed catamaran, for which the hump occurs at the Froude number of 0.53. Above the hump speed, the total resistance of the quadramaran does not increase but decreases, and the change trend of the total resistance tends to be flat when F_r = >1.06, which is different from that of the catamaran, where the total resistance curve was steep. The total resistance is significantly less than that of the catamaran, with a maximum reduction of 40% at the Froude number of 1.66, which indicates that the quadramaran has an obvious resistance advantage above the Froude number of 1.06 (at a service speed above 30 kn), and its high-speed performance is outstanding.

b) The frictional resistance curves of the quadramaran and catamaran have a similar change trend on account of the similar main scales of the two hulls. The residual resistance of the quadramaran first increases and then decreases with the increase of the Froude number. At low speed (F_r = < 0.53), the intricate wave interference of the quadramaran makes the hump value of residual resistance about 1.7 times that of the catamaran. However, at high speed (F_r = > 1.06), the residual resistance of the quadramaran is much less than that of the catamaran. This is mainly because, with the increase of the Froude number, the rise-up increases, the length of cavitation at the stern region is longer, and the wave interference is more favourable, which greatly reduces the wave-making resistance of the quadramaran.

c) The change trends of the frictional resistance on the bow and stern demihulls of the quadramaran are similar Both of them increase gradually as the Froude number rises, but the bow demihulls have lower values due to the smaller wetted surface. The change trends of the residual resistance on the bow and stern demihulls are also similar. Both of them increase first and then decrease with the growth of the Froude number, but the hump value of the stern is about 2 times that of the bow demihulls due to the intricate wave interference. The total resistance characteristics of the bow and stern demihulls are different. The total resistance of the bow demihulls increases gradually with the increase of the Froude number and has a small hump at the Froude number of 0.74. The total resistance of the stern demihulls first increases and then decreases with the increase of the Froude number and has a significant hump at the Froude number of 0.85 due to the complexity of the wave interference. Above the hump speed, as the hull rises and the wave interference changes from adverse to favourable, the total resistance of the stern demihulls decreases until reaching the Froude number of 1.51, when it tends to be flat.

ACKNOWLEDGEMENT

This work is supported by the Xiamen Natural Science Foundation (3502Z20227210) and Fujian Provincial Department of Education (JAT210227).

REFERENCES

1. J. L. Yang, H. B. Sun, X. W. Li, and X. Liu, "Flow field characteristic analysis of cushion system of partial air cushion support catamaran in regular waves," *Polish Maritime Research*, vol. 29, no. 3, pp. 35–46, 2022. doi: 10.2478/pomr-2022-0024.

2. J. L. Yang, Z. Lin, P. Li, Z. Q. Guo, H. B. Sun, and D. M. Yang, "Experimental investigations on the resistance performance of a high-speed partial air cushion supported catamaran," *International Journal of Naval Architecture and Ocean Engineering*, vol. 12, pp. 38–47, 2020. doi: 10.1016/j.ijnaoe.2019.05.004.

3. S. W. Kim, G. W. Lee, and K. C. Seo, "The comparison on resistance performance and running attitude of asymmetric catamaran changing shape of tunnel stern exit region," in *Proc. 1st International Joint Conference on Materials Science and Mechanical Engineering, Bangkok, Thailand, February 2018*. doi: 10.1088/1757-899X/383/1/012047.

4. A. Honaryar, M. Ghiasi, P. F. Liu, and A. Honaryar, "A new phenomenon in interference effect on catamaran dynamic response," *International Journal of Mechanical Sciences*, vol. 190, 106041, 2021. doi: 10.1016/j.ijmecsci.2020.106041.

5. H. Wang, R. C. Zhu, L. Zha, and M. X. Gu, "Experimental and numerical investigation on the resistance characteristics of a high-speed planing catamaran in calm water," *Ocean Engineering*, vol. 258, 11837, 2022. doi: 10.1016/j.oceaneng.2022.111837.

6. Z. S. Dong, X. P. Gao, W. C. Dong, and X. P. Lu, "Supercritical twin-planing-hull (in Chinese)," *Shipbuilding of China*, vol. 41, no. 3. pp. 1–7, Sep. 2000. doi: 10.3969/j.issn.1000-4882.2000.03.001.

7. H. X. Peng, *Numerical computation of multi-hull ship resistance and motion*. Ph.D. thesis, Dalhousie University, Canada, 2001. URI: http://hdl.handle.net/10222/55750.

8. B. Fang, X. P. Gao, and Z. S. Dong, "Performance of small waterplane area quad-hull's resistance (in Chinese)," *Journal of Naval University of Engineering*, vol. 15, no. 1, pp. 70–75, Feb. 2003. doi: 10.3969/j.issn.1009-3486.2003.01.018.

9. X. G. Cai, H. B. Chang, and P. Wang, "Research about the wave-making resistance of multi-hull ship in the calm water (in Chinese)," *Journal of Hydrodynamics*, vol. 24, no. 6, pp. 713–723, 2009. doi: 10.16076/j.cnki.cjhd.2009.06.009.

10. Y. Zhang, L. Chen, Z. Y. Zhang, F. Yang, and L. Zheng, "Research on resistance of multi-hull ships with FLUENT (in Chinese)," *Ship & Boat*, vol. 23, no. 5, pp. 23–30, Oct. 2012. doi: 10.3969/j.issn.1001-9855.2012.05.005.

11. X. W. Liu and D. C. Wan, "Numerical analysis of wave interference among demihulls of high-speed quadramarans (in Chinese)," *Shipbuilding of China*, vol. 58, Special Issue, pp. 140–151, Nov. 2017. [Online]. Available: http://qikan.cqvip.com/Qikan/Article/Detail?id=673742485&from=Qikan_Search_Index

12. Yanuar, Gunawan, A. Muhyi, and A. Jamaluddin, "Ship resistance of quadramaran with various hull position configurations," *Journal of Marine Science and Application*, vol. 15, pp. 28–32, 2016. doi: 10.1007/s11804-016-1340-3.

13. Yanuar, K. T. Waskito, and M. P. Widjaja, "Energy efficiency of high speed tetramaran ship model with minimum resistance configuration," *International Journal of Mechanical Engineering and Robotics Research*, vol. 6, no. 4, pp. 263–267, 2017. doi: 10.18178/ijmerr.6.4.263-267.

14. A. Farkas, N. Degiuli, and I. Martic, "Numerical investigation into the interaction of resistance components for a series 60 catamaran," *Ocean Engineering*, vol. 146, pp. 151–169, 2017. doi: 10.1016/j.oceaneng.2017.09.043.

15. J. F. Hu, Y. H. Zhang, P. Wang, and F. Qin, "Numerical and experimental study on resistance of asymmetric catamaran with different layouts," *Brodogradnja*, vol. 71, no. 2, pp. 91–110, 2020. doi: 10.21278/brod71206.

16. A. Ebrahimi, R. Shafaghat, A. Hajiabadi and M. Yousefifard, "Numerical and experimental investigation of the aero-hydrodynamic effect on the behavior of a high-speed catamaran in calm water," *Journal of Marine Science and Application*, vol. 21, pp. 56–70, 2022. doi: 10.1007/s11804-022-00295-6.

17. A. Li and Y. B. Li, "Numerical and experimental study on seakeeping performance of a high-speed trimaran with T-foil in head waves," *Polish Maritime Research*, vol. 26, no. 3, pp. 65–77, 2019. doi: 10.2478/pomr-2019-0047.

18. M. Heidari, Z. Razaviyan, F. Yusof, E. Mohammadian, A. B. Alias, M. H. Akhbari, A. Akbari, and F. Movahedi, "Numerical analysis of side hull configuration in trimaran," *Revista Internacional de Métodos Numéricos para Cálculo y Diseño en Ingeniería*, vol. 35, no. 2, pp. 1–31, 2019. doi: 10.23967/j.rimni.2019.06.004.

19. B. Yildiz, B. Sener, S. Duman, and R. Datla, "A numerical and experimental study on the outrigger positioning of a trimaran hull in terms of resistance," *Ocean Engineering*, vol. 198, 106938, 2020. doi: 10.1016/j.oceaneng.2020.106938.

20. A. Nazemian and P. Ghadimi, "CFD-based optimization of a displacement trimaran hull for improving its calm water and wavy condition resistance," *Applied Ocean Research*, vol. 113, 102729, 2021. doi: 10.1016/j.apor.2021.102729.

21. J. D. Anderson, *Computational Fluid Dynamics: The Basics with Applications*. New York: McGraw-Hill, 1995.

22. J. H. Ferziger, M. Perić, and R. L. Street, *Computational Methods for Fluid Dynamics*, 4th ed. 2020 Edition. Springer, 2019.

23. User Guide, 2022. STAR CCM+ version 2022. SIEMENS Simcenter.

24. K. V. Meredith, A. Heather, J. de Vries, and Y. Xin, "A numerical model for partially-wetted flow of thin liquid films," *Computational Methods in Multiphase Flow VI*, vol. 70, pp. 239–250, 2011. doi:10.2495/MPF110201.

25. H. Kazemi, M. M. Doustdar, A. Najafi, H. Nowruzi, and M. J. Ameri, "Hydrodynamic performance prediction of stepped planing craft using CFD and ANNs," *Journal of Marine Science and Application*, vol. 20, pp. 67–84, 2021. doi.org/10.1007/s11804-020-00182-y.

26. P. Ghadimi, S. M. Sajedi, and M. Sheikholeslami, "Experimental study of the effects of V-shaped steps on the hydrodynamic performance of planing hulls," *Journal of Engineering for the Maritime Environment*, vol. 237(1), pp. 238–256, 2023. doi: 10.1177/14750902221098304.

27. ITTC, 2021. *Recommended Procedures and Guidelines. Uncertainty Analysis in CFD Verification and Validation Methodology and Procedures*. 7.5-03-01-01.

28. ITTC, 2017. *Recommended Procedures and Guidelines. Uncertainty Analysis in CFD, Examples for Resistance and Flow*. 7.5-03-02-01.

29. L. Birk, *Fundamentals of Ship Hydrodynamics: Fluid Mechanics, Ship Resistance and Propulsion*. UK, Chichester: John Wiley, 2019.

30. ITTC, 2014. *Recommended Procedures and Guidelines. Practical Guidelines for Ship CFD Applications*. 7.5-03-02-03.

31. Z. H. Liu, W. T. Liu, Q. Chen, F. Y. Luo, and S. Zhai, "Resistance reduction technology research of high-speed ships based on a new type of bow appendage," *Ocean Engineering*, vol. 206, 107246, 2020. doi.org/10.1016/j.oceaneng.2020.107246.

32. O. Faltinsen, *Hydrodynamics of High-Speed Marine Vehicles*. Cambridge University Press, 2010.

POLISH MARITIME RESEARCH 2 (118) 2023 Vol. 30; pp. 28-38
10.2478/pomr-2023-0019

DYNAMIC POSITIONING CAPABILITY ASSESSMENT BASED ON OPTIMAL THRUST ALLOCATION

Agnieszka Piekło
Maritime Advanced Research Centre, Poland
Anna Witkowska
Poland
Tomasz Zubowicz*
Gdańsk Uniwersity of Technology, Poland

* Corresponding author: *tomasz.zubowicz@pg.edu.pl (Tomasz Zubowicz)*

ABSTRACT

The article presents an efficient method of optimal thrust allocation over the actuators in a dynamically positioned ship, according to the DNV-ST-0111 standard, Level 1. The optimisation task is approximated to a convex problem with linear constraints and mathematically formulated as quadratic programming. The case study is being used to illustrate the use of the proposed approach in assessing the DP capability of a rescue ship. The quadratic programming-based approach applied for dynamic positioning capability assessment allows for fast calculations to qualitatively compare different ship designs. In comparison with the DNV tool, it gives 100% successful validation for a ship with azimuth thrusters and a pessimistic solution for a ship equipped with propellers with rudders. Therefore, it can be safely applied at an early design stage.

Keywords: optimal thrust allocation, dynamic positioning, quadratic programming

INTRODUCTION

Dynamic positioning (DP) is one of the ship's operational states in which its relative or absolute position and heading are automatically maintained at desired set points. This goal is achieved by using only the ship's own, active thrusters without any mooring lines or other equipment. For safety reasons, the DP propulsion system configuration is maintained over-actuated. In turn, the DP control system (DPCS) applied solves continuously the stabilising control task by utilising advanced, closed-loop, model-based algorithms with the aim of achieving high disturbance rejection capabilities to cope with the vast influence of the environmental conditions at sea.

A DP capability defines a ship's station-keeping ability under given environmental conditions. The assessment of a vessel's ability to keep its position is critical for planning and executing safe and reliable DP operations. A leading classification society, Det Norske Veritas (DNV), has developed a standard for DP station-keeping capability assessments, provided in DNV-ST-0111 [1]. The standard identifies DP capability as numbers corresponding to the Beaufort scale and capability plots (in polar form). The main drawback of [1] is that it does not formulate explicitly the calculation procedures for DP assessment. Three different DP capability levels are defined, each requiring a specific assessment method. *Level 1*, considered in this paper, is specified for mono-hull ships. The calculation method at this level shall be based on a static balance of environmental and the vessel's actuator forces, assuming the same specified environmental data for all vessels. The static balance shall

determine the thrust distribution among thrusters (both magnitude and direction), called thrust allocation (TA). In some specific cases, it comes down to a simple solution of a 3-DOF problem with three unknown parameters, as implemented in [2] and [3]. However, in most cases, this task has no unique solution since the DP-capable ships are usually over-actuated. Considering thrust vector components as more than the equilibrium equations, the DP capability assessment task evolves to an optimal TA problem.

A general overview of marine control systems and an optimal TA problem are given in [4], [5]. Considering the task formulation and the approach to finding its solution, two categories of methods are identified based on the available literature. The first consists of gradient-based optimisation techniques. Here, the quadratic programming (QP) or Lagrangian multipliers-based methods are typically used [6]. Both assume that the objective function and constraints are smooth, and guarantee reaching a global minimum in a finite time. In turn, the second group of methods consists of the so-called non-gradient (derivative-free) methods. This group is represented by the meta-heuristic algorithms [7]. These include, e.g., particle swarm optimisation [8], genetic or evolutionary algorithms [9], [10], [11], [12], [13], [14], and direct-search algorithms [15]. A multi-objective optimisation-based approach to the TA problem is typically considered with application of the NSGAII algorithm [16], [17], In the latter group of algorithms, if certain requirements are met, the algorithms tends to converge to a global optimum. However, the convergence is relatively slow and there is no guarantee of reaching the solution in a finite time. In addition, different non-optimal TA strategies are also presented. These include deterministic and pseudo-inverse-based matrix methods [18], [19]. The model-based predictive control allocation [20] and adaptive control allocation [21], [22] are quite complex and, though time-consuming, allow one to take into account the actuator dynamics and uncertainties in the calculations. The subject of *optimal thrust allocation* using QP approximation is covered in [6], [23], [24], [25], [26], [27]. Related to this work, the convex optimisation approach is discussed in [8].

In this paper, the authors consider the TA problem as an optimisation task set up using the QP framework. The objective is to optimise the ship's propulsion power consumption during DP operations. The presented optimal TA method is inspired by [6]. The QP formulation is achieved by applying approximation techniques to reformulate the originally non-linear problem. With that goal, the azimuth thrusters, tunnel thruster and propeller with rudder constraints, as well as the objective function, are adopted accordingly. The proposed approach meets DNV standards and is easily adapted for the purposes of the DP capability assessment of mono-shaped ships. In this manner, the proposed solution fills the gap of the lack of calculation method details in [1]. The advantage of applying the QP-based approach is the guarantee of reaching the optimal solution in a finite time – if the solution exists. This feature is considered important for practical reasons, e.g., fast prototyping during the initial stage of a project. The structure of the underlying algorithm and the computational complexity of the calculations to be performed are also encouraging for considering the development of (online) designers' support tools. Moreover, the effect of thruster failure can also be analysed by using the DP capability plot. The presented methodology allows for a complete (all kinds of thrusters, including a propeller with the rudder) and fast in-house DP capability assessment for ship concept design. In this study, a rescue ship is used with different thruster configurations as an example. The DP capability results were compared with the existing tools offered by DNV.

The remaining section of this research work is organised in the following manner. In the *Problem Formulation* section, the DP capability assessment problem is formulated. The *Methodology* section provides information on the applied method used to propose a solution to the formulated problem. The results obtained with comparison to available external tools are discussed in the *Results* section, followed by the final *Conclusions*.

PROBLEM FORMULATION

A DP capability analysis enables one to determine the maximum environmental impact of the forces and moment that the DP system can counteract, or to design a DP actuation system that is able to withstand the prescribed disturbances. Therefore, the aim is to balance the environmental conditions by the thrust forces and moments provided by the propulsion system, which, by considering planar movement, yields:

$$\begin{aligned} \textstyle\sum_{i=1}^{N} T_{\mathrm{x}\,i} &= F_{\mathrm{env\,x}}\,, \\ \textstyle\sum_{i=1}^{N} T_{\mathrm{y}\,i} &= F_{\mathrm{env\,y}}\,, \\ \textstyle\sum_{i=1}^{N}(-T_{\mathrm{x}\,i}\cdot y_i + T_{\mathrm{y}\,i}\cdot x_i) &= M_{\mathrm{env\,z}} \end{aligned} \tag{1}$$

where $F_{\mathrm{env\,x}}$, $F_{\mathrm{env\,y}}$ and $F_{\mathrm{env\,z}}$ denote the x and y direction net force components [N] and z direction moment [Nm] resulting from the environmental influences (wind, wave and current), also considered as disturbance inputs; $T_{\mathrm{x\,i}}$ and $T_{\mathrm{y\,i}}$ indicate the x and y direction force components generated by the *i*th thruster [N], considered as control inputs; x_i and y_i define the position of the *n*th thruster in the ship-centred coordinate frame [1]; and *N* denotes the total number of thrusters.

Since the DPCS belongs to the class of over-actuated systems, Eq. (1) has no unique solution in terms of thruster-generated forces $T_{\mathrm{x\,i}}$ and $T_{\mathrm{y\,i}}$, $\forall i$. Therefore, instead of solving Eq. (1), the thrust is to be allocated while optimising the total power consumption (P_{total}), considering the balance equation as equality constraints. With that goal, a constrained QP formulation is applied. For the mentioned purpose, the following set of assumptions is considered.

Assumption 1. *The DP capability is achieved at the given operational conditions whenever Eq. (1) holds.*

Assumption 2. *The environmental forces in Eq. (1) are assumed to be scenario-driven, depending on the DP capability table* [1].

Assumption 3. *The relation between power and thrust can be expressed as a quadratic function with satisfactory accuracy.*

Assumption 4. *The thrust constraints imposed by the physical limits of the propulsion configuration and type can be approximated by a set of convex polygons.*

Assumptions 1 and 2 are a consequence of physical laws and do not introduce artificial limitations to the problem. From [4], it is found that the physical relationship between the produced thrust T and consumed power P can be given by the non-linear relation $P = T^{3/2}$, but it can be effectively approximated by a function of at most second degree (Assumption 3). Notably, different thruster types will have different thrust region shapes. In the general case, the constraints on the thrust form non-convex regions. By virtue of Assumptions 3 and 4, the problem is reduced to a convex one. However, this simplification can lead to a loss of precision in the power assessment.

METHODOLOGY

In the following subsection, the QP approach to thrust allocation is defined, including the propeller with rudder and thrust loss of the spoiled zone of the azimuth thruster.

DECISION VARIABLES

Considering the problem (1), a vector of decision variables is defined in the following lines.

$$\boldsymbol{u} \stackrel{\text{def}}{=} \left[T_{\mathrm{x}\,1}, T_{\mathrm{y}\,1}, T_{\mathrm{x}\,2}, T_{\mathrm{y}\,2}, \ldots, T_{\mathrm{x}\,\mathrm{N}}, T_{\mathrm{y}\,\mathrm{N}}\right]^T \quad (2)$$

The value of $\boldsymbol{u}$ is not arbitrary but is subject to constraints resulting from the propulsion type and respective location in the considered coordinate frame.

CONSTRAINTS

A direct approach to constraint formulation based on DNV-ST-0111 leads to non-linear expressions. Invoking Assumption 4, by utilising linearisation mechanisms, allows one to modify the constraints to linear form, as shown in the following lines.

Azimuth thruster

The azimuth thruster constraints arise from operational restrictions. First, flushing another operating thruster is forbidden (Fig. 1a). Second, directing the thruster to the skeg or another non-working (dead) thruster (Fig. 1a) causes a loss of thrust. The first case introduces the so-called forbidden zones, where the thruster capacity is assumed to be equal to zero (Fig. 1b). The second one introduces spoiled zones, where the capacity of the thruster is reduced to a fraction of its maximum value (Fig. 1b).

Flushing another working thruster in the DP causes a drop in the efficiency of both the thruster that is doing the flushing and the one being flushed. The former is associated with the interaction of the propeller (thruster) jet with the other thruster (obstacle). The water jet hits the obstacle, disturbing the wake behind. The obstacle could also be a skeg or another non-working thruster. The latter is due to the drastically changed inflow to the flushed thruster and its propeller. The accelerated flow causes a drop in the propeller thrust as the angle of the inflow to the propeller blades increases, which in turn causes a change in the operational point of the propeller on the propeller characteristics curves. This phenomenon is complex to take into account as clearly defined losses. Therefore, the forbidden zone is applied to completely avoid the interaction.

An example of handling constraints for the azimuth thruster is shown in Fig. 1b. The approach is to divide the thrust constraint region into a set of convex safe zones (labelled and then into linearly approximated polygons. From these considerations, the zone boundary and saturation inequalities arise.

Zones Boundary Inequality Constraint. Following Assumption 4, the boundary conditions are formulated as linear inequalities [6]:

$$\begin{aligned} T_{\mathrm{x}\,i} \sin \beta_{\mathrm{start}\,z_i} - T_{\mathrm{y}\,i} \cos \beta_{\mathrm{start}\,z_i} \leq 0 \\ -T_{\mathrm{x}\,i} \sin \beta_{\mathrm{end}\,z_i} + T_{\mathrm{y}\,i} \cos \beta_{\mathrm{end}\,z_i} \leq 0 \end{aligned} \quad (3)$$

where $\beta_{\mathrm{start}\,z_i}$, $\beta_{\mathrm{end}\,z_i}$ denote the angles at which the zth zone of the ith thruster starts and ends, respectively

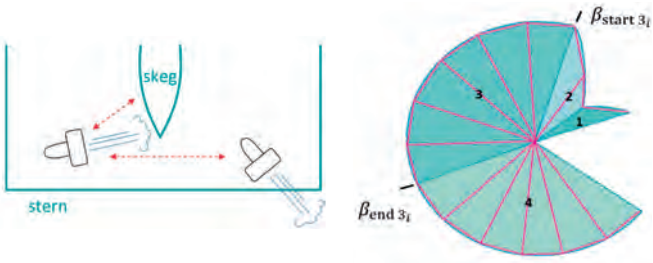

(a) Thruster flushing skeg and another working thruster *(b) th thruster capacity (background) and convex safe zones*

Fig. 1. Forbidden, spoiled zones and safe zones of azimuth thruster

Saturation Inequality Constraints. Two mechanisms of polygon description are provided, depending on the zone shape. First is for the circle-shaped zone (e.g., Fig. 1b, zones 3, 4) [6]:

$$T_{\mathrm{x}\,i} \cos\left(\varphi_j\right)_i + T_{\mathrm{y}\,i} \sin\left(\varphi_j\right)_i \leq r_i \quad (4)$$

where r_i is the maximum effective thrust of the ith thruster and φ_j refers to the ith middle angle of the polygon. An

illustration of the resulting polygon is provided in Fig. 2a. Second is for the spoiled zones (e.g., Fig. 1b, zones 1,2) [6]:

$$T_{\mathrm{x}\,i}(y_{k+1} - y_k) + T_{\mathrm{y}\,i}\,(x_{k+1} - x_k) \leq x_k y_{k+1} - x_{k+1} y_k \quad \textbf{(5)}$$

where x_k, y_k are the coordinates of the first point, while x_{k+1}, y_{k+1} are the coordinates of the subsequent point. An illustration is provided in Fig. 2b.

Taking m_{z_i} as the total number of polygons within the ith zone of the ith thruster to describe a single zone, a system of m_{z_i} linear inequalities is needed. In practice, the number of polygons into which the zone is divided determines the accuracy of the method and shall be chosen individually for each case [6].

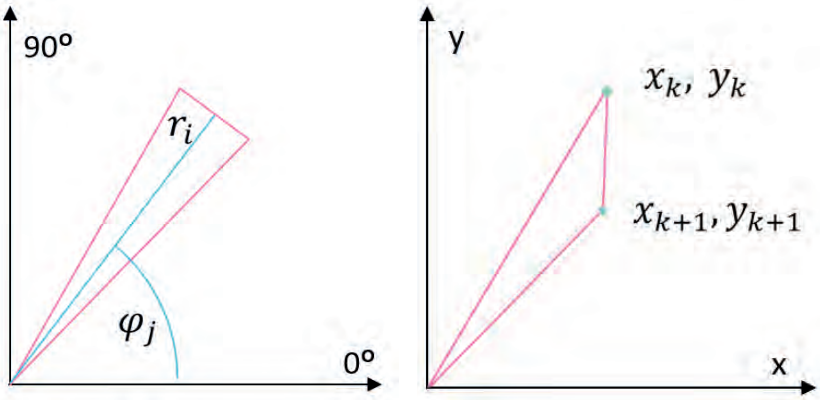

(a) Saturation – circle-shaped zone *(b) Saturation - spoiled zone*

Fig. 2. Inequality constraints - azimuth thruster

Propeller with rudder

In the presented approach, the rudder angle is not a decision variable as it cannot be approximated to a quadratic relation to power. Instead, a thrust region of the propeller representing all possible rudder angles is introduced, and the thrust-power quadratic relation can be maintained. Considering the boundaries of the maximum angle of the rudder on both sides, a convex thrust region can be defined by application of the methodology given in Eq. (3) and Eq. (5). Two convex thrust regions of the propeller with rudder are depicted in Fig. 3 with the linearisation mechanism applied. Region I is the reverse mode of the propeller and region II is the forward mode, accounting for rudder angle settings from -30° to 30°. After the optimisation, the rudder angle can be found by application of the approximately linear relation between the thrust angle and rudder angle. Another constraint needs to be defined for the reverse mode of the propeller, as described below. This creates two separate convex zones of the propeller with the rudder and these are to be taken into the optimisation process separately.

$$-T_{\max i} \leq T_{\mathrm{x}\,i} \leq 0 \;\cap\; T_{\mathrm{y}\,i} = 0 \quad \textbf{(6)}$$

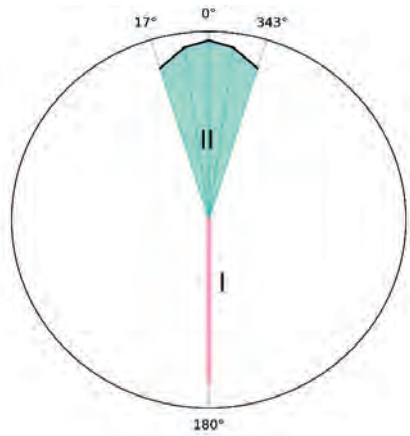

Fig .3. Propeller with rudder convex thrust regions

System of equations

The number of sub-problems to solve separately with the QP solver will be equal to the combination of all the convex zones of all the thrusters. In the case of the azimuth thruster, it could be up to 5 to 6 zones per thruster, and for the propeller with rudder it is 2. Matrices of constraints are built to define a system of equations. For the azimuth thruster for each thruster, they consist of two equations defined in Eq. (3) together with the set of equations defined in Eq. (4) or Eq. (5) in the case of spoiled zones. For the propeller with rudder, the system of equations is Eq. (3) with the set of equations defined in Eq. (5) and, in the case of a reverse mode, the set of equations corresponding to Eq. (6) is applied.

OBJECTIVE FUNCTION

By virtue of Assumption 3, the TA is assessed by considering an objective function (P_{total}) that yields a quadratic approximation of the total power consumption as a function of the generated forces:

$$P_{\mathrm{total}}(\boldsymbol{u}) \stackrel{\text{def}}{=} \boldsymbol{u}^T \boldsymbol{W} \boldsymbol{u} \quad \textbf{(7)}$$

where $\boldsymbol{W} \stackrel{\text{def}}{=} diag(w_1, w_1, w_2, w_2, \ldots, w_{\mathrm{N}}, w_{\mathrm{N}})$ is a diagonal matrix of weight coefficients w_i, $\forall_i$, corresponding to each mounted thruster. The weight coefficients are determined according to [1] with the exception that the maximum thrust loss in the case of spoiled zones is also considered.

OPTIMISATION TASK DECOMPOSITION

Due to the nature of the constraints, e.g., free variables, the problem of thrust allocation is decomposed into several sub-problems to be solved independently using a QP approach. The best amongst all the solutions found is selected by comparison. Considering all possible combinations of the thruster's convex zones and rudder angle cases, the number of optimisation tasks is given by $L = \prod_{i=1}^{N} Z_i$, where Z_i represents the total number of zones of the ith thruster. In the case of the azimuth thruster, the possible interactions impose decomposition of the optimisation task into Z_i convex sub-problems as in Eq. (3). Subsequently, in the case of the propeller with the rudder, Z_i denotes the total number of sub-problems, which is two (forward and reverse mode). The QP-based thrust allocation task for the ith sub-problem yields:

$$\begin{aligned} \mathrm{QP}_l: \quad & \boldsymbol{u}_l := \arg\min_{\boldsymbol{u}} P_{\mathrm{total}}(\boldsymbol{u}) \\ s.t. \quad & \boldsymbol{A}_l \boldsymbol{u} = \boldsymbol{b} \\ & \boldsymbol{G}_l \boldsymbol{u} \leq \boldsymbol{h}_l \end{aligned} \tag{8}$$

where $\boldsymbol{A}_l$ and $\boldsymbol{G}_l$ are the equality and inequality constraints matrices; $\boldsymbol{b}$ denotes a vector encompassing forces and moments; $\boldsymbol{h}_l$ represents the thrust saturation and limiting operation angle. The internal structure of the vectors and matrices results directly from Eq. (3) – (6).

The best thrust allocation ($\boldsymbol{u}^*$) is found by comparison between the L results as stated below:The best thrust allocation is found by comparison between the results as stated below:

$$\begin{aligned} & \boldsymbol{u}^* := \arg\min_{\boldsymbol{u}_l} \{P_{\mathrm{total}}(\boldsymbol{u}_l)\} \\ & s.t. \;\; \boldsymbol{u}_l \leftarrow \mathrm{QP}_l \;\wedge l \in \overline{1, L} \end{aligned} \tag{9}$$

where $P_{\mathrm{total}}(\boldsymbol{u}_l)$ is the total power related to the solution of Eq. (8).

DP CAPABILITY ASSESSMENT

Finally, the ship's DP capability is assessed in the following manner. The problem Eq. (8) – (9) is solved for discrete values of angle (from 0° to 360°) and increasing levels of the impact of environmental forces. The exact number of combinations varies from ship to ship, to cover the whole considered domain of interest. Consequently, a population of results is obtained for each environmental angle considered. In each case, the result is obtained by applying the minimum operator. The DP capability results are typically presented in graphic form, as a polar plot, where each circle in the plot represents a DP number corresponding to a specific weather condition [1].

PROGRAM FLOWCHART

The DP Capability plot program has been coded using Python 3.8 programming language extended with the *qpsolvers* library, delivering the *quadprog* solver used to handle the optimisation problem of Eq. (9) [28]. The flowchart illustrating the program data flow is presented in Fig. 4. Fig. 4a presents the main part of the program routine, while the sub-process directly invoking the optimisation task (Eq. (8)) is illustrated in Fig. 4b. The logic of the program is as follows. First, the program reads the user-generated inputs, namely the basic hull and thruster data (Fig. 4a). In the same step, the propeller coefficients /or azimuth thruster's losses are calculated based on the DNV standard, while the loop of environmental angles (γ) and DP numbers ($k_{\mathrm{DP}} \in \overline{1, n_{\mathrm{DP}}}$) is initiated.

Second, the environmental force calculation combines the basic hull data and environmental (wind, current and wave) coefficients. The maximum ventilation losses and maximum effective thrust for each thruster are calculated. Third, the DP Capability Assessment sub-process is called. Within the sub-process (Fig. 4b), all the combinations of linear matrices $\boldsymbol{G}_l$,$\boldsymbol{h}_l$, $\boldsymbol{A}_l$, $\boldsymbol{b}$ and $\boldsymbol{W}_l$, for $l = 1 : L$ are calculated. These define all (L) possible combinations of the convex sets comprising the constraints. The process loops through these combinations, solving each time the problem defined by Eq. (8). The DP Capability Assessment sub-process ends by finding vector u^*, which corresponds to the minimal power consumption as defined by Eq. (9). At this point, the control flow is returned to the main routine and the program continues until the environmental angle and DP number conditions are satisfied. Fourth and last, the solution – DP Capability plot data – is saved and plots are generated. In the case of a loss of one of the thrusters, one must simply consider the only remaining thruster, noting that, in the case of the azimuth thruster, a spoiled zone due to flushing a dead thruster needs to be considered, as given in Eq. (5).

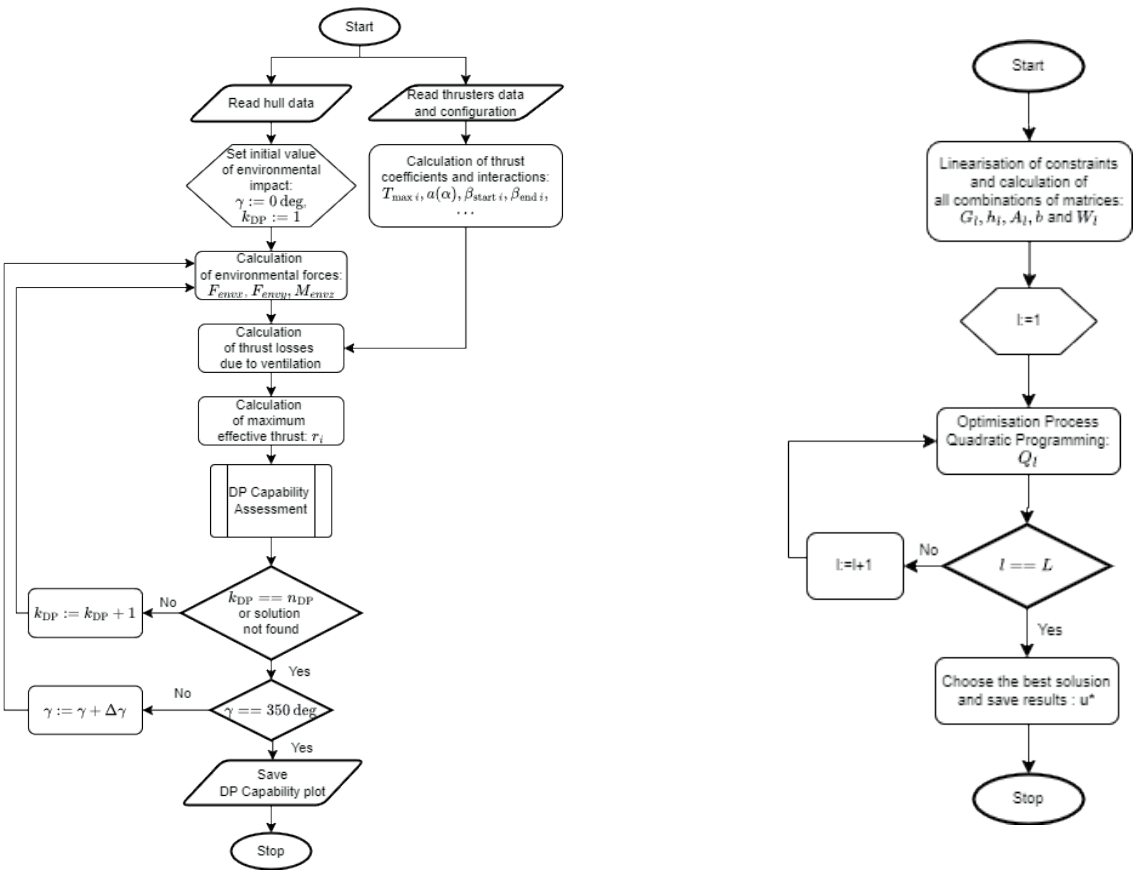

(a) DP Main routine *(b) DP Capability Assessment sub-process*

Fig. 4. Flowchart of DP capability plot program

RESULTS

To illustrate the proposed approach, a case study was used to evaluate the DP capability of a rescue ship with an overall length of 96 m. The required data for the experiment regarding the ship's geometry are included in Tab. 1. The ship under analysis is equipped with five propellers (see Table 2). These include two azimuth thrusters at the stern, one azimuth thruster with a nozzle at the bow, and two tunnel thrusters at the bow. The discussed distribution of the propulsion system components is illustrated in Fig. 5a.

Tab. 1. General ship data

Symbol	Value	Unit	Description[1]
L_{pp}	86.6	*m*	Length between perpendiculars
B	18.8	*m*	Maximum breadth at waterline
T	5.0	*m*	Summer load line draft
L_{os}	95.85	*m*	Longitudinal distance between the foremost and aftmost point under water
X_{os}	-0.13	*m*	Longitudinal position of $L_{os}/2$
Bow_{angle}	27.4	°	Half bow angle of entrance
$A_{F,\,wind}$	392.0	m^2	Frontal projected wind area
$A_{L,\,wind}$	1203.0	m^2	Longitudinal projected wind area
$X_{L,\,wind}$	6.014	*m*	Longitudinal position of the area centre of $A_{L,\,wind}$
$A_{L,\,current}$	441.0	m^2	Longitudinal projected submerged current area
$X_{L,\,current}$	4.717	*m*	Longitudinal position of the area centre of $A_{L,\,current}$
x_{skeg}	-37.8	*m*	*x* position of the skeg aft edge
y_{skeg}	0	*m*	*y* position of the skeg aft edge

[1] Full definition of variables with the coordinate system is available in DNV standard [1].

Tab. 2. Thrusters main data

Description	Unit	Thruster 1	Thruster 2	Thruster 3	Thruster 4	Thruster 5
Thruster type	–	Azimuth thruster without nozzle / Shaft line with open FPP propeller	Azimuth thruster without nozzle / Shaft line with open FPP propeller	Azimuth thruster with nozzle	Tunnel thruster	Tunnel thruster
Rudder type	–	Not applicable / NACA	Not applicable / NACA	Not applicable	Not applicable	Not applicable
x	m	-41.076	-41.076	34.12	37.12	40.72
y	m	4.690	-4.690	0	0	0
x	m	1.540	1.540	-1.100	2.000	2.000
Propeller diameter, D	m	3.100	3.100	1.650	1.740	1.740
Engine brake power, P_{brake}	Kw	1325	1325	880	900	900
Rudder surface A_r	m^2	Not applicable / 6.000	Not applicable / 6.000	Not applicable	Not applicable	Not applicable

This section reports the results of the DP capability assessment obtained based on the approach described in the Methodology section. A tool developed using the Python programming language has been used for this purpose. It is important to note that the tool is in line with the DNV standard [1] Level 1, in which a so-called DP number is assigned to specific environmental conditions (wind, waves and currents). To improve legibility, firstly, an elementary example for two arbitrary angles is presented in the Optimal thrust allocation sub-section. Secondly, the evaluation of DP capabilities is discussed. Thirdly, the results obtained are compared with those obtained using the DNV on-line tool[2].

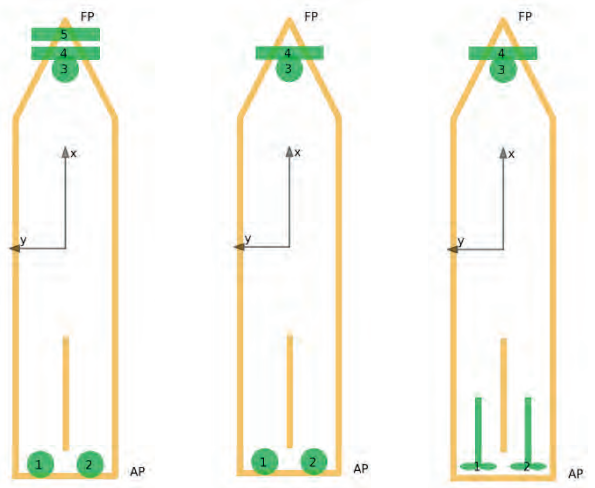

(a) Main thrusters – 5 azimuth thrusters

(b) Main thrusters – 4 azimuth thrusters

(c) Main thrusters – propeller with rudder – 4 thrusters

Fig. 5. Thrusters layout for analysed vessel

[2] The free version of the application is limited to analysis of a maximum four thrusters and does not share detailed results, just the DP capability plot.

The results analysed in this section include three cases. A comparative layout of the three cases is shown in Fig. 5. The first case (no. 1) includes all five thrusters presented in Table 3 with the layout depicted in Fig. 5a. In Fig. 6 and Fig. 7, the results of the DP capability evaluation for this case are presented. The second case (no. 2) considers the layout depicted in Fig. 5b and includes only the azimuthal thrusters in the analysis. The third case (no. 3), with the layout depicted in Fig. 5c, considers the azimuth, tunnel and rudder propellers as the main thrusters. In order to compare the results obtained by the presented method with those obtained from the free online application provided by DNV, the bow thruster was excluded from the analysis (in cases no. 2 and 3). This is due to the fact that the version of the DNV application provided allows analysis of ships with only up to four propellers. In addition, the efficiency of the propulsion system with azimuthal thrusters was compared with the system where the propulsion system consists of thrusters with rudders. The results of the DP capability assessment for the second and third cases are compared in Fig. 8 with the DNV online application.

OPTIMAL THRUST ALLOCATION

The direct result of the calculation is the thrust allocation (thrust components in the and direction for all thrusters). An example of optimal thrust allocation for two distinct angles, namely 10° and 90°, calculated under environmental conditions set to DP number 6 [1], is presented in Fig. 6 for case no. 1 and the TA results are listed in Table 3.

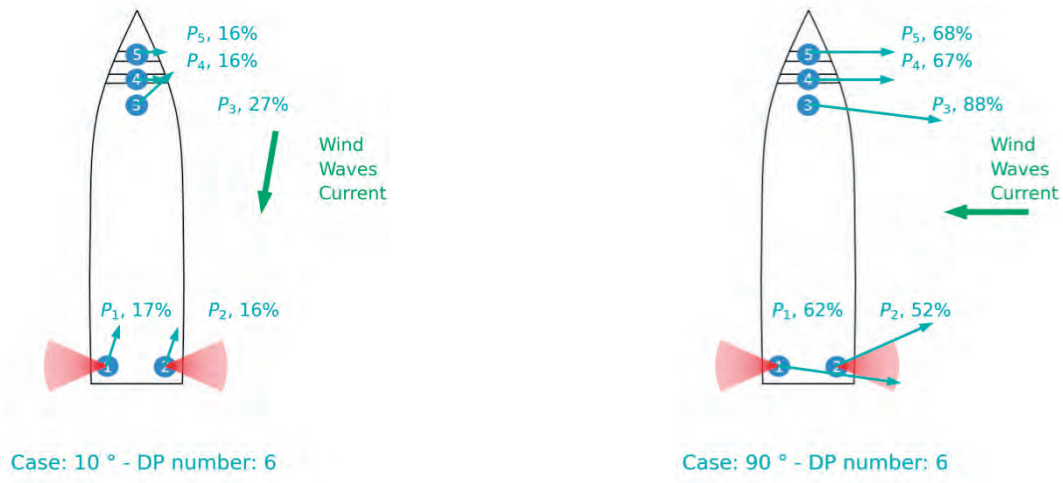

(a) Environmental angle 10°

(b) Environmental angle 90°

Fig. 6. Optimal thrust allocation

Tab. 3. Results of optimal thrust allocation as effective thrust vector values

Effective thrust [kN]										
Thruster	1		2		3		4		5	
Force component	$T_{x,1}$	$T_{y,1}$	$T_{x,2}$	$T_{y,2}$	$T_{x,3}$	$T_{y,3}$	$T_{x,4}$	$T_{y,4}$	$T_{x,5}$	$T_{y,5}$
Case 10 °	28	-9.5	25.6	-9.5	23.7	-25.6	0	-15.9	0	-16.4
Case 90 °	-15.4	-108.6	37.4	-84.1	-14.8	-113	0	-68.2	0	-68.6

The location of the thrusters is indicated with blue numbered dots. The red areas near the rear thrusters indicate the forbidden zones. The result of the thrust allocation is indicated by the turquoise arrows attached to the thrusters. For legibility of the result, the percentage of maximum thrust is displayed to clearly characterise the magnitude of the thrust vectors

As a result of the analysis, one can clearly identify that the environmental impact from the 90° direction causes higher engagement of the thrusters. In both cases, it can be observed that the most utilised thruster is the bow azimuth thruster. At the 10° direction, the thrust utilisation is significantly reduced. This directly relates to the ship's geometry, both under and above the water level, and the exerted environmental forces and moments that depend on it.

DP CAPABILITY ASSESSMENT

The DP capability plot is a result of a true/false solution of the QP solver. In the case of true, the solution is found, the thrust allocation is performed allowing for the power consumption to be determined, and the ship is capable of keeping its position. In the case of false, the ship cannot maintain its position. The solver loops through the environmental angles and conditions (in total up to 396 cases) to return the DP capability plot.

Fig. 6 presents the results of the DP capability assessment (case no. 1), showcasing both the DP capability and the power envelope for a selected scenario (DP number 3). Three DP operation modes have been investigated. First is "intact", where all the thrusters are considered operational. Second is a single failure, where one of the thrusters failed, and two scenarios were explored, one considering the failure of thruster 2 and second of thruster 3 (location given in Fig. 5). Third is the worst-case scenario which, in this case, is loss of the switchboard. In both failure scenarios and the worst-case scenario, the DP capability is significantly reduced. The DP system is more effective at DP number 3 in the intact case than in other cases, especially the worst-case scenario, which is the most power-consuming.

The results from the developed tool were compared to those obtained using the on-line application by DNV (Fig. 7). It was found that, in the case of using azimuth thrusters as the main propulsion (case no. 2), the results obtained from both tools are the same (Fig. 7a). However, the results obtained considering propellers with the rudder as the main thruster (case no. 3) vary significantly (Fig. 7b). In general, the methodology presented in this work shows a more pessimistic outcome in comparison to the DNV web application. Further investigation of the discrepancies is required to gain a better understanding of the matter.

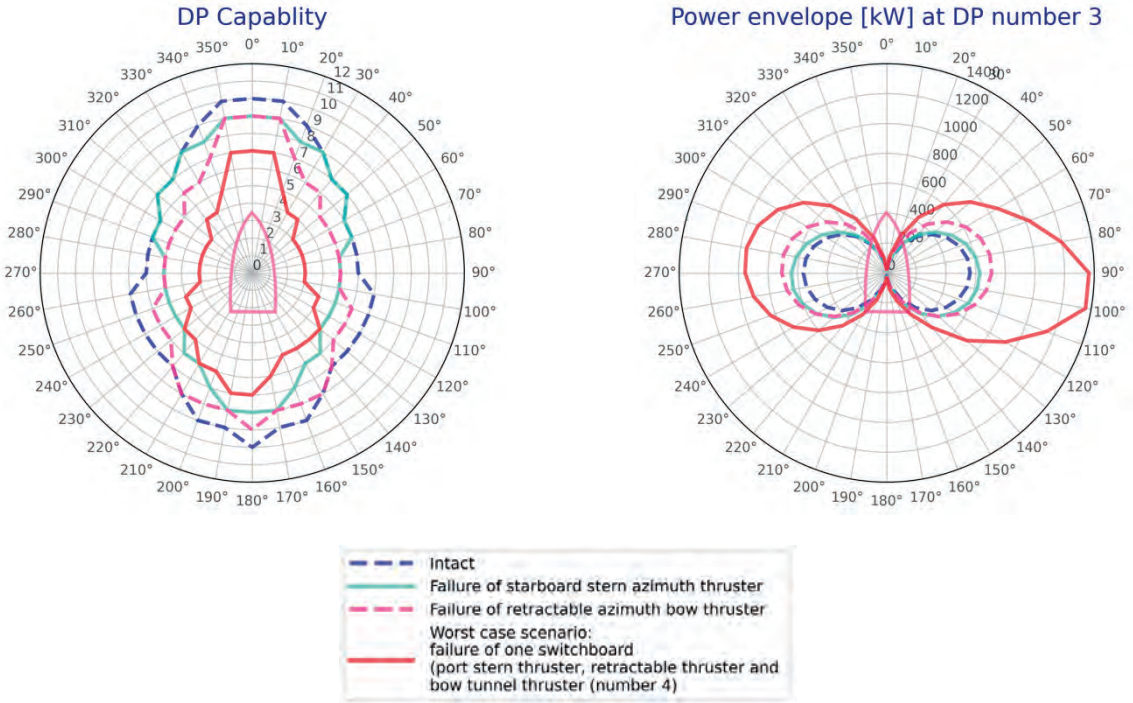

(a) DP capability plot *(b) Power consumption polar plot*

Fig. 7. Comparison of selected cases

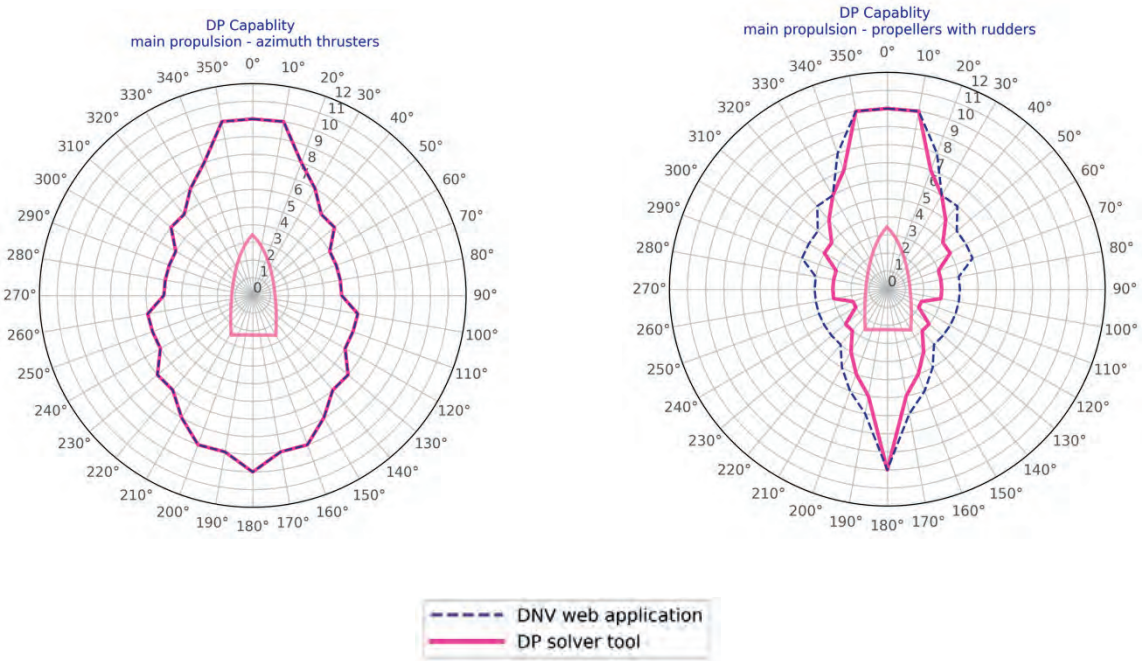

(a) 4 thrusters - two aft propulsors: azimuth thrusters *(b) 4 thrusters - two aft propulsors: propellers with rudders*

Fig. 8. Comparison of DP capability plots

CONCLUSIONS

The recently increasing need for DP assessment tools, both fast rough calculations as well as time-domain simulations for the early stage of the design, was the motivation for the study. The quadratic programming method used in optimal thrust allocation provided relevant results when applied to DNV rules (DNV-ST-0111 standard). This was evident while concerned with handling the influences between the thrusters and the skeg. The guidelines and rules provided by the DNV classification society are very popular and are often applied in the ship design phase in typical design offices around the world. Thus, the presented method could be effectively used by designers for rough initial calculations without a need for investment in expensive software.

The presented method is handy while making comparisons between different designs and especially when selecting the size and power of the thrusters at the early design stage. However, it should be treated only as the initial evaluation before contracting for making an offer. This is due to the lack of sufficient validation data for the TA evaluation. Moreover, the DNV guidelines are based on the empirical formulas and therefore the results should be treated as an approximation of the DP performance. The DP capability assessment of a ship equipped with propellers with rudders reveals some discrepancies when compared with the results obtained using DNV's online application. Further research in this area, including validation with a broader group of ships of different types, is likely to yield a better insight into this problem.

It is important to mention that, due to the adopted methodology (thrust forces being the decision variables), it was not possible to apply the ventilation losses according to DNV-DT-0111 correctly. Among other factors, the losses depend on the propeller loading (thrust), but the thrust is the result of the optimisation, therefore it was not possible to take it into account when preparing the input to the QP solver. Losses are not dependent on thrust loading for sufficiently deep draughts or lower sea states. This varies from ship to ship. The maximum losses (for the maximum loading) are adopted instead, which can lead to an extremely pessimistic result in the case of a vessel with very low draught relative to the propeller's vertical position.

An important element of future research will be the evaluation of the accuracy of the method based on time-domain simulation and model tests. Verification of the simulation is planned based on experiments on the dedicated test stand of the Maritime Advanced Research Centre, using the physical model of the ship, equipped with a DP system.

REFERENCES

1. DNV, DNV-ST-0111, Assessment of station keeping capability of dynamic positioning vessels, DNV, 2021.
2. M. Tomera, "Dynamic positioning system for a ship on harbour manoeuvring with different observers. Experimental Results," Polish Maritime Research, 2014.
3. M. Tomera, "Dynamic positioning system design for "Blue Lady". Simulation tests," Polish Maritime Research, 2012.
4. T. Fossen, Handbook of Marine Craft Hydrodynamics and Motion Control, 1st ed. New York: John Wiley, 2011.
5. A. Sørensen, „Marine Control Systems. Propulsion and Motion Control of Ships and Ocean Structures," Lecture Notes, Department of Marine Technology. Norwegian University of Science and Technology, 2013.
6. C. de Wit, „Optimal thrust allocation methods for dynamic positioning of ships," M.Sc. thesis, Delft University of Technology, 2009.
7. S. Luke, "Essentials of Metaheuristics," in Lecture Notes, Second Edition , 2016.
8. J. Ming and Y. Bowen, „The optimal thrust allocation based on QPSO algorithm for dynamic positioning vessels," Tianjin, China, 2014, doi: 10.1109/ICMA.2014.6885898.
9. X. Yang, "Optimization and metaheuristic algorithms in engineering," in Metaheuristics in Water, Geotechnical and Transport Engineering, Elsevier, 2013, pp. 1-23.
10. G. Ding, P. Gao, X. Zhang, and Y. Wang, "Thrust allocation of dynamic positioning based on improved differential evolution algorithm," in Proc. 39th Chinese Control Conference, Shenyang, China, doi: 10.23919/CCC50068.2020.9188704, 2020.
11. R. Storn and K. Price, "Differential evolution - A simple and efficient adaptive scheme for global optimization over continuous spaces," Journal of Global Optimization, vol. 23, no. 1, 1995.
12. D. Goldberg, Genetic Algorithms in Search, Optimization & Machine Learning. Addison-Wesley, 1989.
13. T. Baetz-Beielstein, „Overview: Evolutionary Algorithms," Ph.D. project, Cologne University of Applied Sciences, 2014.
14. M. Kochenderfer and T. Wheeler, Algorithms for Optimisation. MIT Press, 2019.
15. E. Baeyens, A. Herreros, and J. Perán, "A direct search algorithm for global optioptimization," Algorithms, vol. 9, no. 2, p. 40, 2016, https://doi.org/10.3390/a9020040.
16. K. Deb, A. Pratap, S. Agarwal, and T. Meyarivan, "A fast and elitist multiobjective genetic algorithm: NSGA-II," IEEE Transactions on Evolutionary Computation, vol. 6, no. 2, pp. 182-197, 2002, doi: 1109/4235.996017.

17. D. Gao, X. Wang, T. Wang, Y. Wang, and X. Xu, "Optimal thrust allocation strategy of electric propulsion ship based on improved non-dominated sorting genetic algorithm II," IEEE Access, vol. 7, no. 1, pp.135247-135255, 2019, doi: 10.1109/ACCESS.2019.2942170, 2019.

18. F. Mauro and R. Nabergoj, "Advantages and disadvantages of thruster allocation procedures in preliminary dynamic positioning predictions," Ocean Eng., vol. 123, pp. 96-102, 2016, https://doi.org/10.1016/j.oceaneng.2016.06.045.

19. O. Harkegard, "Dynamic control allocation using constrained quadratic programming," J. Guid. Contr. Dynam., vol. 27, no. 6, pp. 1028–1034, 2004, https://doi.org/10.2514/1.11607.

20. Y. Luo, A. Serrani, S. Yurkovich, D. B. Doman, and M. W. Oppenheimer, "Model predictive dynamic control allocation with actuator dynamics," in IEEE Proc. 2004 American Control Conference, pp. 1695–1700, 2004, doi: 10.23919/ACC.2004.1386823.

21. A. Witkowska and R. Śmierzchalski, "Adaptive backstepping tracking control for an over-actuated DP marine vessel with inertia uncertainties," Int. J. Appl. Math. Comput. Sci., vol. 28, no. 4, pp. 679–693, 2018, doi: 10.2478/amcs-2018-0052.

22. J. Tjønnås and T. Johansen, "Adaptive control allocation," Automatica, vol. 44, pp. 2754-2766, 2008, https://doi.org/10.1016/j.automatica.2008.03.031.

23. M. Valčič, „Optimization of thruster allocation for dynamically positioned marine vessels," Doctoral thesis, University of Rijeka, 2020.

24. E. Ruth, „Propulsion control and thrust allocation on marine vessels," Doctoral thesis, Norwegian University of Science and Technology, 2008.

25. L. Wang, J. Yang, and S. Xu, "Dynamic positioning capability analysis for marine vessels based on a DPCap polar plot program," China Ocean Eng., vol. 32, no. 1, pp. 90-98, 2018, doi: 10.1007/s13344-018-0010-4.

26. P. Zalewski, "Constraints in allocation of thrusters in a DP simulator," Sci. J. Mar.Univ. Szczecin, vol. 52, no. 124, pp. 45-50, 2017, doi: 10.17402/244.

27. P. Zalewski, "Convex optimization of thrust allocation in a dynamic positioning system," Sci. J. Mar.Univ. Szczecin, vol. 48, no. 120, pp. 58-62, 2016, doi: 10.17402/176.

28. D. Goldfarb and A. Idnani, "A numerically stable dual method for solving strictly convex quadratic programs," Mathematical Programming, vol. 27, pp. 1-33, 1983.

POLISH MARITIME RESEARCH 2 (118) 2023 Vol. 30; pp. 39-60
10.2478/pomr-2023-0020

USING ARTIFICIAL NEURAL NETWORKS FOR PREDICTING SHIP FUEL CONSUMPTION

Van Giao Nguyen [1]
Sakthivel Rajamohan [2]
Krzysztof Rudzki [3]
Janusz Kozak [4]
Prabhakar Sharma [5*]
Nguyen Dang Khoa Pham [6]
Phuoc Quy Phong Nguyen [6]
Phuong Nguyen Xuan [6*]

[1] Institute of Engineering, HUTECH University, Ho Chi Minh City, Viet Nam
[2] Department of Mechanical Engineering, Amrita School of Engineering, Coimbatore, Amrita Vishwa Vidyapeetham, India
[3] Gdynia Maritime University, Faculty of Marine Engineering, Poland
[4] Gdansk University of Technology, Poland
[5] Mechanical Engineering Department, Delhi Skill and Entrepreneurship University, India
[6] PATET Research Group, Ho Chi Minh City University of Transport, Ho Chi Minh City, Viet Nam

* Corresponding authors: *phuong@ut.edu.vn (X.P. Nguyen)*
prabhakar.sharma@dseu.ac.in (P. Sharma)

ABSTRACT

In marine vessel operations, fuel costs are major operating costs which affect the overall profitability of the maritime transport industry. The effective enhancement of using ship fuel will increase ship operation efficiency. Since ship fuel consumption depends on different factors, such as weather, cruising condition, cargo load, and engine condition, it is difficult to assess the fuel consumption pattern for various types of ships. Most traditional statistical methods do not consider these factors when predicting marine vessel fuel consumption. With technological development, different statistical models have been developed for estimating fuel consumption patterns based on ship data. Artificial Neural Networks (ANN) are some of the most effective artificial methods for modelling and validating marine vessel fuel consumption. The application of ANN in maritime transport improves the accuracy of the regression models developed for analysing interactive relationships between various factors. The present review sheds light on consolidating the works carried out in predicting ship fuel consumption using ANN, with an emphasis on topics such as ANN structure, application and prediction algorithms. Future research directions are also proposed and the present review can be a benchmark for mathematical modelling of ship fuel consumption using ANN.

Keywords: Artificial Neural Networks; Fuel management; Marine engine; Ship fuel consumption; Energy efficiencys

INTRODUCTION

In recent years, the maritime transport sector and maritime activities, such as container depots and port activities, have experienced a rise in greenhouse gas (GHG) emissions [1], [2]. This rise can be correlated with the increasing trend in shipping vessel fossil fuel consumption [3]–[5] and serious environmental pollution, including oil spillage [6]–[8]. Consequently, these significant increases in GHG emissions due to the use of fossil fuels are thought to further exacerbate the rise in global average temperature and potentially irreversible ecological impacts related to climate change [9], [10]. Given the fact that a major portion of global cargo is carried by ships, improving the overall energy efficiency of marine transport promises to yield positive results, in terms of GHG emissions relating to fuel consumption [11]–[13]. According to the 2019 data published by the International Maritime Organisation (IMO), emissions from maritime transportation accounts for 2.5% of global GHG emissions. The emissions of these various heat-trapping gases are known to be the main driver behind anthropogenic global warming and changes in global weather patterns, yielding potentially harmful effects on the Earth's ecological systems and human society [14]–[16]. As the main international regulatory body of

maritime shipping activities, the IMO has developed the Ship Energy Efficiency Management Plan (SEEMP) and Energy Efficiency Design Index (EEDI) as two crucial measures aimed at lowering GHG emissions and curbing environmental pollution through the more efficient use of fuels in marine vessels [17]–[22].

Consequently, lower emissions of common air pollutants from ships, such as sulphur oxide (SOx) and nitrogen oxide (NOx), as well as major GHG were observed with the introduction of these regulations [23], [24]. Considering the direct relationship between fossil fuel consumption and GHG emissions, several studies have explored different strategies to deliver more efficient ship operations, such as hull cleaning and design [25]–[28], and the incorporation of renewable energy sources including wind energy [29]–[31], solar energy [32]–[35], wave energy [36], [37], and fuel cells [38], [39]. Ship energy management plans provide critical inputs for the continuous monitoring and analysis of marine vessel performance by taking the design and operational measures into account [40]–[42]. Data-driven performance monitoring provides an effective solution to holistic system management including real-time decision making, assessment and evaluation, and cost-effective resource management [43], [44]. Other factors driving the need for better energy efficiency management on marine vessels stem from economics, compliance, and stakeholder requirements [45], [46]. A ship's energy consumption accounts for a significant portion of its operating costs [47]. It has been observed that up to two-thirds of shipping costs and one-quarter of total operating costs depend on fuel consumption [48], [49]. Hence, predicting fuel consumption and energy inputs provides a good measurement of energy efficiency management within marine transport [50], [51]. Besides these proposed strategies, estimation models have been proved effective in identifying the key variables that influence fuel consumption [52], [53]. The availability of estimation models not only provides the total system recognition, but also enhances the capability of monitoring operating conditions and forecasting potential malfunctions [54]–[56]. In general, the characteristics and application of prediction models for ship fuel consumption are illustrated in Fig. 1.

Since fuel costs account for the largest portion of ship operating costs [58], better fuel consumption also means higher energy efficiency and greater profitability for the marine vessel's owner [59]. Therefore, accurately predicting the rate of fuel consumption is a challenging task because there are several external influencing factors. Access to the estimation model has yielded key advantages for fleet owners and companies when optimising fuel consumption and operational costs, by efficiently tracking and analysing the key parameters [60], [61]. Considering these facts, computer-assisted tools would be more appropriate for assisting decision-making [62]. There are several statistical techniques, algorithms, and artificial intelligence methods that are commonly used, and these include polynomial regression (PR), support vector machine (SVM), fuzzy logic, artificial neural network (ANN), and other algorithms [63]–[65]. Among these, PR is the most popular method and it uses polynomial functions to approximate data points. One of the advantages of this method is its simplicity and a high degree of flexibility when applied to a general dataset. In the marine transport and shipping industry, PR is typically used to analyse the hull-propeller's performance loss and reconstruct ship trajectories for automatic identification system data [64]. On the other hand, SVM has gained special interest among the machine learning tools used in classification and regression models. The main objective of SVM is to map input vectors to a higher dimensional space, in which an optimal discriminant hyperplane is constructed. The use of kernel functions is relevant in mapping input data. Within SVM, the ship detection images are divided into small blocks of pixels [66] that can be categorised, based on colour and texture. Using regression models, outliers can then be identified, polluted ship tracks can be regressed [67] and a ship's motion can be predicted [63]. The strong preference for this technique over other learning methods stems from better generalisation that could alleviate overfitting problems.

Grounded in mathematical models, these tools make

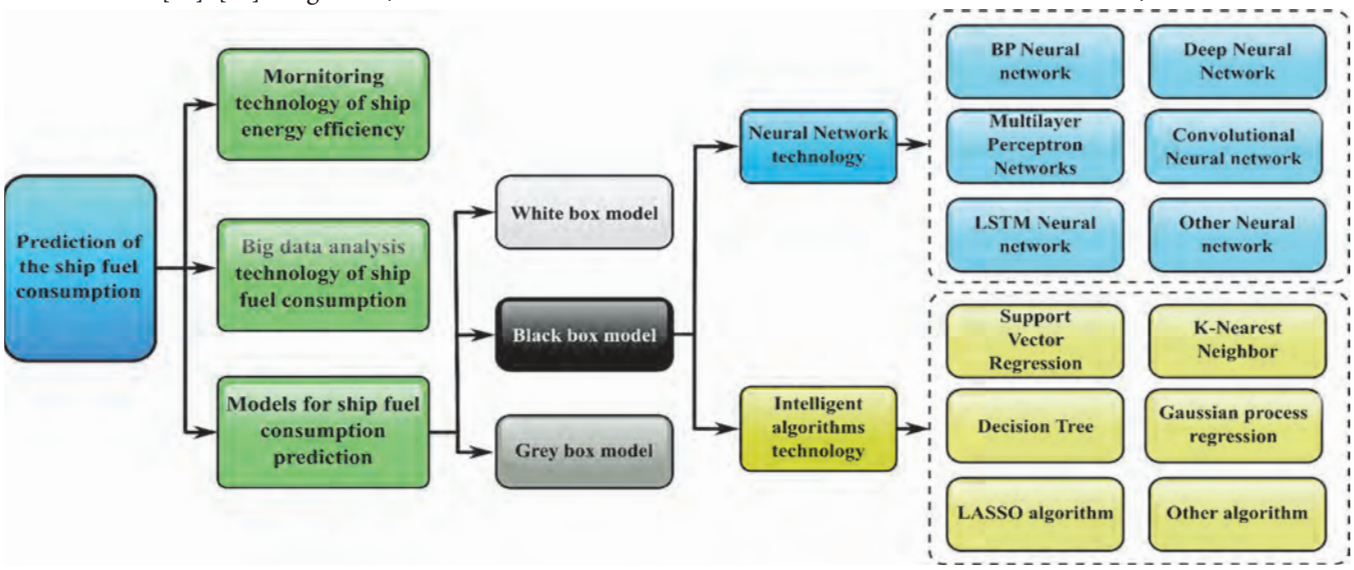

Fig. 1. Topology of models for predicting ship fuel consumption [57]

the connection between the input variables, such as fuel consumption and estimated travel time to the destination, and the outputs, based on command and current operational conditions related to the ship propulsion thrust [68]. In analysing bibliographic references relating to the various techniques of displaying the commanded outputs, Rudzki et al. [69] revealed the inadequacy of the present models that formalise the required heuristic knowledge. According to the authors, the use of ANNs could be applied to attain such models with better predictive power, concerning the estimation of ship fuel consumption and travel time to the destination, for given commanded outputs and operational parameters. ANN is a better approach due to its better accuracy and capability when being applied in practice. In this scenario, the absence of the requirement of mathematical relations between the input and output data gives the ANN technique a key advantage [70]. As a subset of artificial intelligence, ANN enables systems to learn from previous experience and available historical data, and improve on current conditions [71]. Based on recorded system performance, system conditions could then be assessed and further improved upon [72]. First, a model algorithm is run (training mode) on a partial set of data before being fully examined (testing mode) with a full set of data. By combining advanced statistical methods, realistic estimation models can be formulated by applying the train-test process based on the ANN algorithms. Estimating a vessel's fuel consumption with minimal error rates could be useful, while providing ship operators with important insights. For these reasons, ANN is an integral instrument in managing marine vessel operations and energy efficiency [73]. Therefore, the current work reviewed a data analysis framework based on ANN used to predict ship fuel consumption. In addition, the use of ANN to derive a regression model for ship fuel consumption, as well as the performance and accuracy of ANN, were also thoroughly analysed through various inputs and outputs of the ANN model.

ANN STRUCTURE

Machine learning (ML) is a subfield of artificial intelligence that uses algorithms and statistical models to allow computer systems to improve their performance on a given job by learning from data, without being explicitly programmed [74]. The objective of machine learning is to create algorithms that can recognise patterns in data and utilise those patterns to make predictions or conduct actions [75], [76]. ANNs are a type of machine learning algorithm inspired by the anatomy and functioning of the human brain. ANNs are made up of linked layers of nodes, or neurons, which process information and transmit it on to other neurons to be processed [78-79]. ANNs are utilised in a range of applications, including picture and speech recognition, natural language processing, and financial market prediction [79]–[83]. ANNs are a form of supervised learning algorithm that, with training, can learn to recognise patterns in data. During training, the ANN is given a set of inputs as well as the desired outputs [84]. To minimise the difference between the actual output and the required output, the ANN modifies the strength of the connections between its neurons. Once trained, the ANN can be used to make forecasts on previously unknown data [85].

ANNs have proven to be extremely effective in a wide range of machine learning tasks, particularly those involving enormous volumes of data. ANNs are highly versatile and can be used to solve a wide range of problems; they are a strong tool for solving a wide range of challenging issues in machine learning and artificial intelligence [86]–[88]. ANNs can, on the other hand, be difficult to train and demand a large amount of computer power, particularly for deep neural networks with many layers [89]. ANNs are constructed from a collection of small computational units, known as neurons, organised into layers. The neurons in one layer communicate with the neurons in the next layer, establishing a network which is capable of processing complicated information. Each neuron in an ANN gets input from neurons in the previous layer, analyses that information, and generates an output signal that is sent to neurons in the following layer [90]. Each neuron processes its inputs by computing a weighted sum, adding a bias term, and sending the result via a nonlinear activation function. ANNs can simulate complicated nonlinear interactions between inputs and outputs using this nonlinear activation function [91][92]. A neuron's basic mathematical operation can be described as [80]:

$$y = f(\Sigma(w * x) + b). \tag{1}$$

Herein, y denotes the total of all inputs f is the activation function, w is the weight associated with each input x, b is the bias term, and Σ denotes the total of all inputs.

During training, the weights and biases of an ANN are modified to minimise a cost function that assesses the difference between the network's expected and intended outputs [93]. The weights and biases are commonly adjusted using a backpropagation method, which computes the gradient of the cost function with respect to the weights and biases and updates them in the direction of decreasing cost. ANNs have been shown to be extremely effective in applications involving vast amounts of data, such as deep learning [94]. In contrast to the simple linear regression method, which portrays the relationship between input and output variables with a single equation, fuzzy logic-based regression models rely on local functions and provide global approximations in a nonlinear relationship [95]. Consequently, local functions or membership functions are combined into a single expression. Besides this, fuzzy logic models have the capability to capture highly nonlinear and multidimensional interactions among the different factors.

On the contrary, the application of ANN models offers key benefits, including a generalisation and extrapolation capability [96]. Furthermore, ANN models can be constructed without the prior knowledge of the type of function. These systems can be trained by a process called machine learning, through which the performance of simple tasks can be taught

and improved over time. There are several basic elements in ANNs, including processing elements (i.e. inputs, outputs, and weights) and activation (neuron/transfer) functions [98-99]. These components closely resemble the makeup of biological neurons which form the basis for the ANN [99]. After inputs are received from one end and processed/summed, the outputs are generated on the other end of the artificial neuron. Within this process, the weight factor for each input is calculated according to the strength of the input signal [100]. The weighted sum of all inputs is processed via a nonlinear function, known as the activation linear function [101]. The activation function can take several forms, including sigmoid, nonlinear, piecewise linear, and step functions. These continuous and monotonically increasing functions are often differentiable and bounded. Based on these models, a computer-assisted decision support system can be constructed to select the ship driveline commanded output to deliver the optimal ship fuel consumption. Besides this, ship logs (which contain ship records such as managing events, ship operation and navigation information) are important sources of historical data which have been used in ANN models to estimate ship fuel consumption [102], [103].

In practice, the ship operators often rely on their knowledge, experience, and instinct when setting the appropriate values for the commanded outputs [104]. As stated earlier, it is impractical to choose one appropriate method that allows for the selection of commanded outputs, based on formalised heuristic knowledge. In certain situations, there is the potential that the chosen settings can be illogical and unsuitable [105]. To minimise the potential risk of such incidences, the availability of a decision support system (Fig.2) is highly desirable, in which the decision support system was constructed based on the following key parts:

- A data acquisition module containing several uncontrollable inputs and one output variable vector based on normalised ANN data;
- An identification module containing the input, based on the normalised ANN output values obtained from the prior module and one matrix-represented output capturing the internal data representation of the ANN used in the estimation of ship fuel consumption;
- An optimisation module containing two input and two output variables. The two-input data include: (i) the output from the preceding module in the form of ANN matrix data, and (ii) the vector value of the weight factors of the two-objective optimisation model. The two outputs correspond with the optimal commanded outputs.

Fig. 2. Structure of decision support system block [105]

The available literature on ship fuel use estimation considers three commonly used models: white-box models (WBMs), black-box models (BBMs), and grey-box models (GBMs) [106], [107]. Based on prior knowledge of the system, a WBM relies on the physical understanding of a system, as well as its identifiable or known structure and parameters in the decision making [70,109]. On the contrary, the use of BBM occurs in the absence of a priori knowledge of the system when making output decisions based on a few key input data [107]. Researchers have found higher accuracy in well-trained BBMs, compared to WBMs. Nevertheless, the training of BBMs often necessitates the collection and input of large amounts of high-quality data [109]. BBMs also fail to provide interpretability and extrapolating capability compared to WBMs [110]. As reported, BBM (which includes Back Propagation Neural Network, Multilayer Perceptron Network, Long Short-term Memory, Convolutional Neural Network, and Deep Neural Network) performs well in terms of ship fuel consumption prediction [96,112]. GBM is a hybrid model constructed on the basis of the system's underlying physical processes, while some parameters can be estimated using input data [70,109]. GBMs leverage the key advantages of the prior two modelling techniques [109]. Referencing several studies, Table 1 provides comparisons between WBMs, BBMs and GBMs, highlighting the advantages of GBMs over the other two methods.

Even though the technique offers several important advantages, GBMs have not been very well studied in the estimation of ship fuel consumption. One of the reasons for the lack of research on GBMs in this context could be that the system is modelled as a piecewise function; whereas, the ship's sailing motion provides the variables in determining the outcomes [122]. Hence, external environmental factors, such as changing wind direction and wave motion, strongly affect the vessel's resistance. Traditional GBM used in the estimation of ship fuel consumption is based on a set of four sub-functions, accounting for each of the weather directions [123]. Besides the common parameters, there are also individual parameters for each of the sub-functions. Considering this fact, the use of derivative-based techniques, such as the Gauss–Newton algorithm and the Levenberg–Marquardt algorithm, is insufficient for providing estimations of all common parameters together. To overcome this obstacle, researchers have come up with sequential parameter estimation procedures at the cost of global optimality [124].

Meng et al. [125] constructed a SPEP, in which the common parameters of the piecewise function were first estimated and then used as fixed variables in other sub-functions (i.e. bow sea, beam sea and following sea). Nevertheless, this approach has not been fully taken advantage of in the collected data. As shown in Fig. 3, only 25% of the data were utilised in the estimation of the common parameters in the sequential parameter estimation procedures. Furthermore, the lack of optimality in the estimation of the common parameters will affect the level of accuracy, when estimating the other parameters included in the remaining sub-functions.

Table 1. Characteristics of WBM, BBM and GBM applied for prediction of fuel consumption for ships

Methods	Advantage	Disadvantage	References
WBM	- Obtained results and system behaviours can be interpreted and predicted. - Data can be extrapolated in addition to the given data. - Historical data are not required.	- Potential uncertainties and assumptions significantly affect the accuracy of predictions. - Required prior knowledge. - Low accuracy.	[109][112][106][113]
BBM	- BBM has higher accuracy than WBM. - Prior knowledge is not required.	- Historical data are required in large amounts. - Model interpretability and extrapolation capacity are poor. - Unreasonable results might be received.	[109][114][115][116][117][118][119][120]
GBM	- GBM has a higher accuracy than WBM. - Less historical data is required for GBM compared to BBM and WBM. - High model interpretability. - Unreasonable results might be avoided.	- Extrapolation capacity is not high.	[109][121]

Hence, the use of GBMs in the current context of ship fuel consumption estimation is restricted, based on its quality and accuracy [126]. In an attempt to mitigate the shortcomings related to GBMs, a new genetic algorithm-based grey-box model (GA-based GBM) is presented as a possible method for estimating ship fuel consumption [109]. The present GA-based GBM approach differs from conventional GBMs, in that 100% of the collected data are used in the estimation of the common parameters, as shown in Fig. 3. The new approach also allows for the concurrent estimation of all common parameters of the GBM that further enhance the accuracy and reliability of the GBM. Studies by Coraddu et al. [106] and Aldous et al. [127] supported these conclusions. Nevertheless, due to the inclusion of piecewise structures in GBMs subject to the segregated weather directions, it is more difficult to estimate the parameters of GBMs. SPEP has been able to resolve this problem at the expense of the global optimality that inevitably affects the accuracy of GBMs in estimating ship fuel consumption.

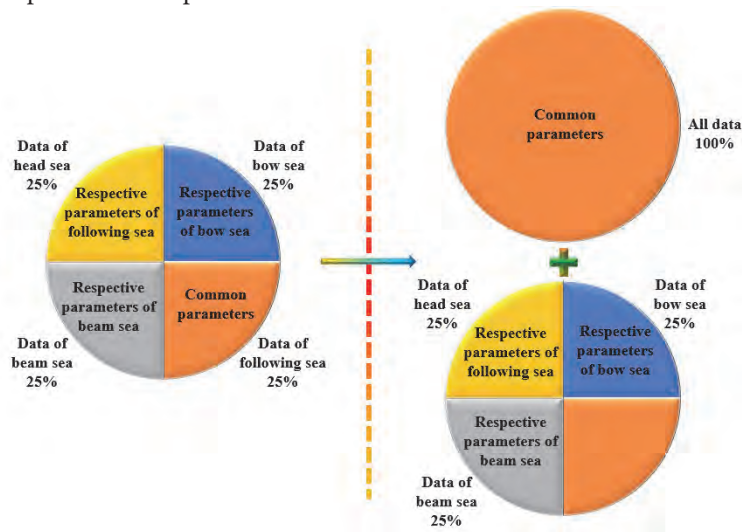

Fig. 3. Data utilisation of GBM based on existing SPEP (Left) and the proposed GA (Right) [109]

Previous studies have been successful in using heuristic and metaheuristic algorithms in solving highly complex problems [129,130]. These methods are potential solutions for the aforementioned problem while taking into account their flexibility. Among the available literature, applications of heuristic and metaheuristic methods in estimating parameters are found in complex (piecewise, nonlinear, etc.) models among various fields. Some examples include the study of evolutionary strategies of biochemical pathways [130], applications of particle swarm optimisation in chemical engineering [131], grasshopper optimization algorithm in engine area [132], [133], simulated annealing algorithms used in the Muskingum routing model [134], and a flower pollination algorithm for solar PV application [135]. Despite the prevalence of heuristic and metaheuristic algorithms in different fields, their use as the main tool in estimating the parameters in ship fuel consumption prediction models has remained relatively limited. They offer a new perspective in the current knowledge gap by proposing a GA-based GBM to be used in the estimation of parameters in the fuel ship consumption model. Compared to existing SPEP-based GBMs, these improved GA-based GBMs have several key advantages.

Furthermore, the GA-based GBM reflects higher reliability in capturing the relationship between ship fuel consumption rate and its determinants. These benefits further strengthen the model application in performing energy efficiency and sustainability analysis in the study of marine vessel operation. From an industrial perspective, the GA-based GBM presented in the current research can be integrated as part of the ship energy efficiency programs, to optimise ship fuel consumption and reduce GHG emissions, because of its better predictive capability.

In the construction of the decision support system, it was found that the following requirements are important: (i) state the input and variables related to the

ship driveline system models, (ii) construct models predicting ship fuel consumption and speed based on ANN; and (iii) construct a decision-making model based on multi-objective optimisation [65], [136], [137]. In the development of these models, a ship was identified as a solid object placed at the water-air boundary. Along with the partial immersion position and maintained relative motion, these factors enabled the selection of appropriate variables for both the black box and the decision-making models. Fig. 4 shows the problem captured in the 'black box' form, under the influence of several different factors [105].

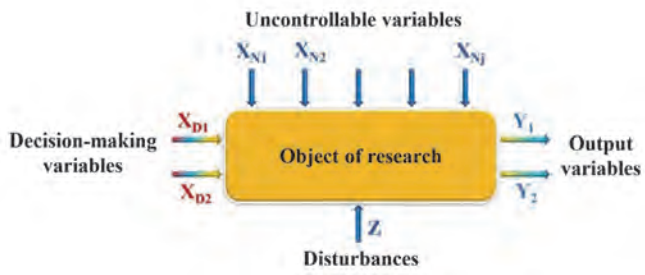

Fig. 4. 'Black box' model [105]

Fig. 4 shows that, in terms of decision-making variables (X_{Di}), the two main selected variables were the combustion engine rotational speed and the CPP pitch. On the other hand, the uncontrollable input variables (X_{Nj}) were identified among a range of factors influencing the ship sailing motion [118]. These factors played an important role in the commanded outputs of the ship driveline system that determined the desired ship motion and speed via the propeller thrust. Last but not least, the model output variables are Y_k, (the combustion engine fuel consumption) [105]. The other factors that were difficult to capture and had minimal variance (with respect to the ship's motion) were denoted as Z or the model disturbances. In formulating the decision-making problem, the distinct variables contained in the black box model were considered. The main problem statement is to determine the values of the decision-making variables X_{Di} subjected to the uncontrollable variables X_{Nj} in order to achieve the anticipated values of the output variables, Y_k. The values obtained for the model output variables Y_k make up the objectives for the optimisation function. The function is set up in order to minimise the ship's fuel consumption. Taking into account the distinguished variables of the black box model, the decision-making problem can be formulated as follows: what should the values of the decision-making variables X_{Di} be for the given values of the uncontrollable variables X_{Nj}, in order to provide the desired values of the output variables, Y_k.

Researchers have constructed models using GBMs, which integrate both partial theoretical structure and input data [138]. WBMs, also known as cause-effect models, can explain the relationship between the different variables and the studied phenomenon, as well as the underlying processes. To quantify these processes, equations were set up based on existing knowledge of the relationships. For dynamic systems, the balance method is the preferred method used in the construction of WBMs [140-141]. In addressing systems containing physical quantities, the balancing of parameters occurs for those that are subjected to the conservation law of momentum and energy. Despite the advantage of the balance method, it is impractical to rely on such a method when modelling both fuel consumption and ship sailing, in implementing a decision-making support model subjected to the commanded output of the ship driveline system. Due to the extraordinary complexity of the equations that are used in describing these relationships and processes, they are impossible to solve. Furthermore, the varying influence of several parameters over the processes and the studied phenomenon also complicate the problem. Even though these equations could be simplified in linear, parabolic or hyperbolic forms, the complexity of the studied processes does not allow for generalisation or linearisation procedures. Besides this, the results obtained from solving these equations through approximation, falls short of being useful in practice. Given these reasons, the need for alternative modelling techniques is highly warranted. In particular, the use of the BBM method could provide important insight into the existing relationships and fundamental processes. In contrast to the WBMs, the use of BBMs does not require the full analysis of the causes when understanding the studied phenomenon. In constructing this type of model, the necessary steps are carried out as follows: performing measurements; analysing the results and identifying the required parameters for the considered issue; examining the validity of the initial conditions; searching for a functional dependency or providing guesses based on the researcher's instinct; fitting the function with the appropriate parameters; comparing the results of measurements and the fitted model [70-142]. In the case of non-conformity, one or several of the following steps or additional measurements can be conducted. Data collection is first carried out using actual measurements or historical records. By the rules of thumb, these data should be grouped into dependent (i.e. those to be estimated) and independent variables (i.e. those to be used in necessary conditions).

ROLE OF ANN AND MACHINE LEARNING IN PREDICTING SHIP FUEL CONSUMPTION

Among the recent advances in research, applications of ANN have been found in several fields, highlighting the latest developments [142]–[147], as well as issues related to the marine industry [148]–[150]. The method based on ANN is known to be a widely applied prediction model. Besikci et al. [151] employed the ANN model to predict fuel consumption by modelling the relationship between engine speed and the outside variables, aiming to predict the fuel consumption of a tanker. Wang et al. [152] used a wavelet neural network (WNN) to optimise the energy efficiency of a ship. By using this developed WNN, engine speed could reach the optimal value under various navigation environments and working

conditions; thus, energy efficiency and the ship's sailing were optimised, resulting in optimised fuel consumption of the ship. Arslan et al. [153] and Bal et al. [117] developed decision support systems grounded in ANN prediction models. In these models, there were seven main input variables, including ship speed, main engine rotational speed, mean draft, trim, number of cargos, wind and sea conditions, as depicted in Fig. 5a. These parameters were used as the determinants in predicting the output variable, which was ship fuel consumption. The authors relied on ship noon reports to gather the ship's main operating data. Both studies utilised the Neural Network Toolbox in MATLAB 2010a software to construct the neural network models. In terms of data set, they used data obtained from 7 tanker ships, respectively. 70% of these data were randomly chosen for training, while the rest were utilised to validate the results. The main ANN modelling approach relied on the backpropagation algorithm, which performed learning on a feed-forward neural network consisting of one hidden layer. In these studies, the main learning algorithm was Levenberg–Marquardt, in which hyperbolic tangent sigmoid transfer function was the activation function and the training epochs were limited to 10,000. In comparison with the multiple regression model [118,154], the ANN model performed significantly better, based on the observed correlation of actual and predicted fuel consumption data in both training and validation data groups, as depicted in Fig. 5b and 5c.

Conventional statistical methods have been commonly used in modelling various phenomena. The study by Rudzki et al. [118] provided an assessment of the application of a statistical regression technique in modelling optimal parameters for the ship drive's propulsion. Using multiple regression techniques, a BBM was developed for the decision-making system considered and similar types of data were used in constructing the ANN models utilised in this case [154]. These data are key for explaining the relationship among the different operational parameters (i.e. related to ship propulsion thrust) and the fuel consumption and travel time to the destination subjected to the commanded outputs. As reported in the literature, the Gaussian processes model is a supervised probabilistic machine learning framework, which could be used for regression and classification applications [155]. Therefore, Petersen et al. [116] applied single-input variables with an ANN and a Gaussian process method in predicting ship propulsion efficiency performance. In another study, Li et al. [156] used a neural network in their modelling, analysis, and prediction of ship motion. Utilising another type of neural network, Perera et al. [157,158] was able to capture the compression and expansion of ship performance data. Despite the existence of several ANN studies in the ship and maritime field, they all failed to provide an adequate validation of the entire big data analysis process, as well as the regression models used in predicting ship performance and fuel consumption. In the study conducted by Pedersen et al. [114], a method was proposed for predicting a ship's propulsive power, based on ANN and subject to the external factors affecting the ship resistance and propulsion. These different factors included ship speed, wind speed and direction relative to ship sailing, air and ocean temperature. Based on the hindcast approach, the built model was trained to estimate a ship's propulsive power using input data from three different sources, including onboard measurements, noon reports, and sea state and weather conditions. The authors compiled the data set from 323 different noon report samples. As stated in their methodology, Pedersen et al. [114] only set 5 and 20 hidden layers as the two extremes to train the model. As a result, a 7% accuracy level was achieved when using the ANN model from noon report data in estimating ship fuel consumption. Because the model used 'time' as one of the input variables, it was suggested that the trend line of ship fuel consumption could be identified over time.

In another study, a model was constructed by Du et al. [159,160] to predict a ship's propulsive power. The proposed model was able to capture the synergetic effects of the various

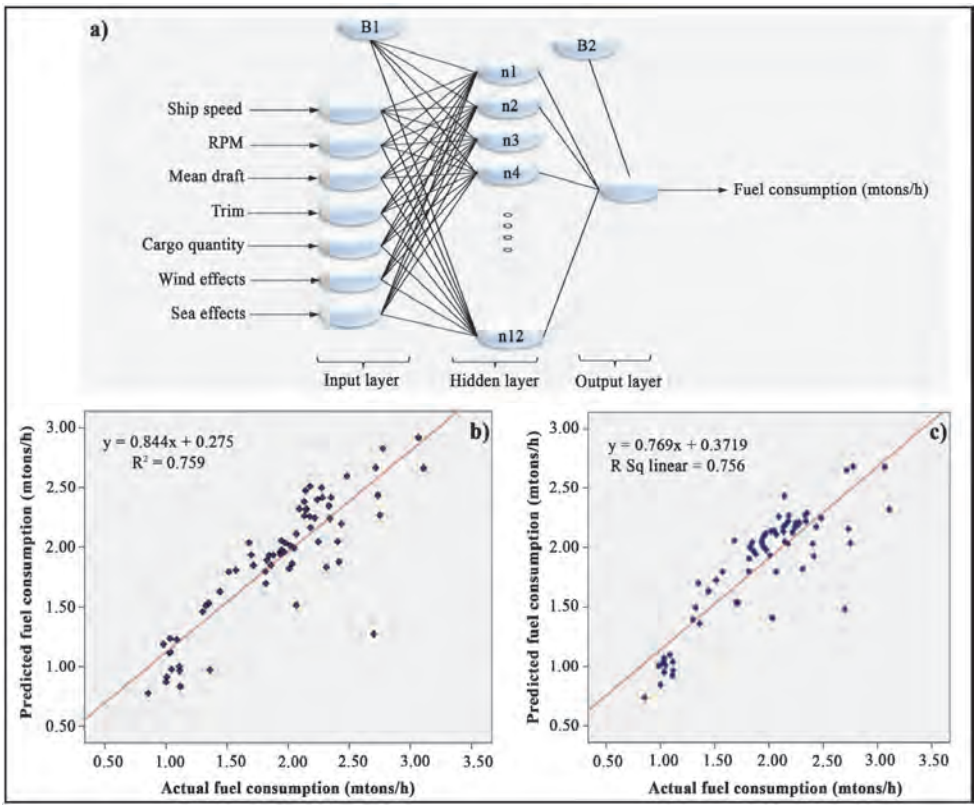

Fig. 5. (a) – ANN structure for predicting fuel consumption of a ship with 7 input data; (b) - Relationships between actual and predicted fuel consumption using ANN model; and (c) - multiple regression model [117]

independent factors affecting ship fuel efficiency. The authors also proposed an ANN-based framework for managing ship fuel consumption which included a two-step procedure. The process began with the estimation of the ship engine rotation speed and then the engine power was subjected to the obtained speed. The calculation of ship fuel consumption was based on a set of estimated parameters. Besides, there are several required variables for the ANN model, such as ship speed, displacement tonnage, wind force, wind wave height, swell height, sea current factor and ship trim [161,162]. Samples of noon reports were collected from 3 different ships, totally 121, 160 and 153 reports, respectively. As a result, the authors concluded that a simple single hidden layer ANN model had the best fit performance among other tested models. In another study, Rudzki et al. [163] developed a two-criteria optimisation algorithm, including both the objective function and the set of acceptable solutions, allowing the rational management of a ship's fuel consumption and navigation time on the basis of the combination ANN and MATLAB package. As a result, they presented the relationship between engine speed and fuel consumption, allowing vessel owners to find the lowest possible operating costs.

As a subject of study, researchers have yet to fully investigate the use of ANN models in predicting ship speed under varying operating conditions. Without the presence of propulsive force, variable speed towing tank experiments could be utilised in estimating the amount of power needed to propel the ship hull. In the analysis of ANN models, the authors have examined those models which take into account the ship resistance or power and their main determinants. In a study by Couser et al. [164], they examined the appropriateness of using ANN for predicting ship resistance compared to conventional statistical methods. In their experiments, the researchers utilised the ANN network as an interpolation strategy in predicting ship residual resistance in various types of catamaran. It was observed that results from ANN models met the accuracy threshold to be applied when making preliminary estimates of ship resistance. In particular, the building of the ANN model was based on a single hidden layer and 15 neurons comprised a hidden layer. The authors arrived at two main conclusions: (i) the added hidden layers did not yield any additional benefits in terms of improving model accuracy and only increased the model complexity and training time; (ii) the availability of specific computer-aided software allowed for the fast training and running of the ANN model in solving the ship resistance problems, relative to traditional statistical techniques.

Using an ANN model, Grabowska et al. [165] followed a similar strategy in their research on ship resistance prediction. In their experiment, the authors applied the parameters from seven available offshore marine vessels to the model parameters obtained from the test results carried out in a towing tank (i.e. a ship model basin used to conduct physical and hydrodynamic tests on ship models). They also compared seven different training algorithms with different hidden layer configurations, to evaluate their performance and identify possible effects of network architecture on the model outcomes. As a result, the Quick Propagation algorithm was selected for additional examination due to the best potential for favourable results, in terms of the correlation between target and output values (i.e. correlation coefficient R2 and absolute validation error). To determine the optimal network design architecture, several cases used 4 to 24 neurons in a hidden layer because the 24-neuron configuration gave the lowest absolute validation error. In this methodology, the study set the required input and output layers according to the input data dimensionality (i.e. the number of input variables in a dataset) and the required output values. Hence, the authors were able to select the number of hidden layer neurons from the geometric mean values obtained from the formula provided by Bishop [166]. Through the automated network architecture design, 24 neurons were identified as the optimal number delivering the highest level of accuracy. In brief, the authors concluded a satisfactory level of accuracy obtained from the constructed network compared to the model test results. However, additional studies on the network architecture are warranted that could offer a potential improvement on the model result. In a different experiment, Mason et al. [167] tested ANN model configurations using the data obtained from the original towing tank tests that had been previously conducted using the method proposed by Holtrop et al. [168]. In the initial test network design configuration, the number of layers was limited to three: the input, hidden and output layer. Utilising a quasi-Newton method, the training runs were set to 50,000 iterations. To lower the potential model errors, 10 retrains were conducted for each tested neural network topology, including 4 inputs, 4 neuron-hidden layers combined with 1 output to 4 inputs, 17 neuron-hidden layers and 1 output. The authors confirmed the effectiveness of the feedforward ANN used in fitting an extra data set containing a fair degree of random and meaningless information.

Consequently, a proposed model containing two hidden layers might be more optimal than one, as depicted in Fig. 6a [169]. Le et al. [169] presented the method of designing a multilayer perceptron artificial neural network (MLP-ANN) and used MLP-ANN to predict ship fuel consumption. They employed data from 100–143 container ships, while sailing time, speed, cargo weight, and capacity were considered as input parameters. As a result, they indicated that MLP-ANN could be used to predict the container ship fuel consumption by fitting lines very close to the actual results, as plotted in Fig. 6b. In another study, Ortigosa et al. [170,171] proposed an ANN model to predict two different ship resistance variables. The authors applied the multilayer perceptron (MLP) in training both synthetically generated and experimental datasets to estimate the different coefficients, including form and wave coefficients subjected to ship hull geometry coefficients and the Froude number. Based on the outlined methodology, an ANN-based empirical model was designed and tested using data produced by the Holtrop and Mennen method [168]. The model aimed to deliver an estimation of the components directly related to the ship resistance. In this case, the authors tested the proposed model using

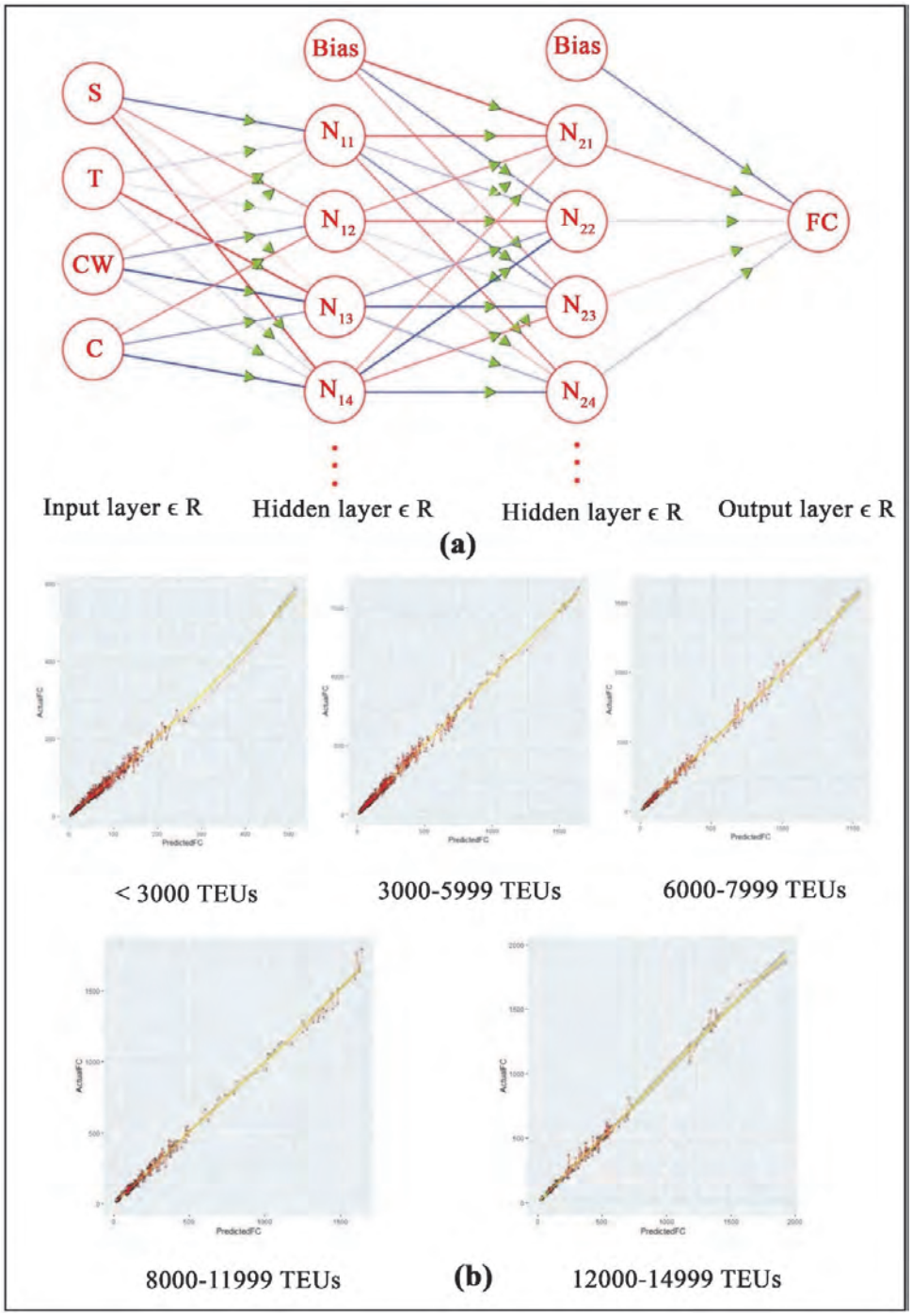

Fig. 6. *(a) – ANN model with 2 hidden layers; (b) - Actual and estimated fuel consumption* [169]

MLP containing a sigmoid hidden layer and two linear output layers. Subsequently, the quasi-Newton method with Broyden–Fletcher–Goldfarb–Shanno train direction and Brent optimal train rate (as proposed in Bishop [166]) were utilised in training the constructed algorithm. The model was tested with a different number of hidden layer network configurations. In the process, the authors selected the network design that achieved the best optimal generalisation and validation errors. As a result, an ANN network model containing 5 inputs, 9 hidden layer neurons and 2 outputs was selected as the best configuration.

Comparing the results obtained from the selected ANN model to those produced by the Holtrop and Mennen method, there were overall improvements, in terms of model performance over the whole dataset. In reviewing the available literature on the application of ANN in predicting ship fuel consumption and hull resistance, several conclusions were reached:

(i) Input data used in training the model to predict ship fuel consumption were based on data extracted from actual ship logs, also known as noon reports;

(ii) Most studies relied on design data (geometric parameters of ship hull design) or experimental data obtained from tank tests as input variables for modelling ship resistance;

(iii) There needs to be more information on measurement methods and the types of propellers used in marine driveline systems. The bulk of available references concerning the application of ANNs were found in Bishop [166]. Regarding the strategy in the present research, a detailed experiment was proposed for planning and building sufficient ANN models to estimate ship fuel consumption and desired speed. The specific experiment was tested using various commanded outputs of the marine vessel driveline system while being subjected to a range of different off-shore environmental conditions. However, the collected data from the shipping company was limited, leading to difficulties in predicting to a high accuracy by using ANN. These limitations could be overcome by the integration of ANN with other algorithms, such as expert knowledge [172], the Cognitive Reliability and Error Analysis Method [173], or an Adaptive Neuro-Fuzzy Inference System combined with fuzzy logic theory [174]. In general, the use of ANN for predicting ship fuel consumption is summarised in Table 2.

Table 2. Various models based on neural network for prediction of ship fuel consumption

Parameters of concern	Data sources	Method	Accuracy	Reference
Engine load, operating parameters, weather conditions	-	ANN	0.9055	[175]
Weather and current conditions, engine speed	Voyage data		-	[176]
Engine load, operating parameters, weather conditions	AMS		0.9709–0.9936	[177]
Weather and current conditions, engine speed	Route software		-	[178]
Weather and current conditions	LAROS system		0.9870	[179]
Weather and current conditions	ACMS, AIS, and weather forecast		0.9960	[103]
Weather and current conditions, engine speed	-	BPNN	R^2 = 0.9817	[180]
Weather and current conditions, engine speed	Ship monitoring system		R^2 = 0.9843	[101]
Weather and current conditions, engine speed	-	MLPN	R^2 = 0.8340	[151]
Weather and current conditions, rudder angle	Sensors		Relative error = 0.02	[181]
Engine speed, shaft power	Sensors	LSTM	RMSE = 2.714	[182]
Weather and current conditions	-		-	[161]
Weather and current conditions, engine speed	Multisource sensors		-	[51]
Weather and current conditions, engine speed	ADLM and CMEMS	DNN	R^2 = 0.8940	[111]
Weather and current conditions, engine speed	Shipping company, and CMEMS		0.95	[183]
Weather and current conditions, engine speed	Ship monitoring system	DBN	MRE = 0.3539	[184]

The ANN model is found to be cheap in computation; however, it does not seem to have any rule for selecting the feature variables or avoiding the overfitting cases in the training process. For this reason, Wang et al. [185] developed a new model to describe the fuel consumption of a specific ship, in relationship to surrounding environments and ship states. Indeed, they used the LASSO regression algorithm to implement the variable selection of feature variables, such as wind speed and wave height, air pressure and wind force, cargo weight and draft etc., with the aim of evaluating the ship fuel consumption, as illustrated in Fig. 7a. More importantly, they compared the performance of the proposed LASSO model with others like ANN, SVR, and GP in predicting the ship fuel consumption. As a result, the developed LASSO model outperformed the others, as depicted in Fig. 7b. Hu et al. [180] employed the back-propagation neural network (BPNN) and Gaussian process regression (GPR) techniques for the prediction of the fuel consumption of a ship. They found that the two above-mentioned techniques could be used to predict the ship's fuel consumption with high accuracy, especially with the consideration of the effects of marine environmental factors. As a result, BPNN (T = 14.7 s) was found to provide shorter runtime than GPR (T = 2236.4 s), while GPR (R^2 = 0.9887) offers higher accuracy than BPNN (R^2 = 0.9817).

Big data is well-known as an emerging tool in maritime and intelligent transport applications [186]–[188]. Indeed, ship fuel consumption is associated with a large number of ship parameters such as navigational environment [189], sailing state [112], ship loading [190], hull fouling [191], and applied antifouling coating [192], showing that the related data are diverse, complex and huge [193]. For these reasons, the application of big data could provide a foundation for the establishment of a model for ship fuel consumption [58,197]. In recent years, the use of big data combined with ANN and machine learning techniques was considered as a feasible method to predict the ship fuel consumption more exactly [58,198]. As illustrated in Fig. 8, the following four steps are included in the big data analysis process for ship performance and operational efficiency. They include (1) data denoising, (2) data clustering, (3) data compression and expansion, and (4) regression analysis using a neural network [196].

The input data required for big data analysis include a range of time series data, as well as equipment, navigation, and weather-related data. Upon collection of these data, the data cleaning step, also known as data denoising, is essential in eliminating unnecessary noise, bias, and outliers found in the raw data [197]. Within this step, any abnormalities are extracted from the dataset, once detected. Such types of data are identified as any unusually large differences between two adjacent values or any detectable deviation outside of the normal value range of input or output variables that can be confirmed using the domain knowledge about the variables [198]. In the present research, the authors utilised a smoothing algorithm to clean and refine the raw dataset by minimising any discernibly large differences between two neighbouring data values. Data denoising is then followed by the data clustering step, in which the post-cleaning data are categorised based on the high-frequency operation regions using the Gaussian mixture model [199]. After this initial clustering step, an additional silhouette analysis is conducted to validate the prior classification of data according to the operation regions. The resulting number of clusters is then modified several times, until the highest possible estimated silhouette value is attained. The final number of clusters is identified that corresponds to the highest possible silhouette value. In

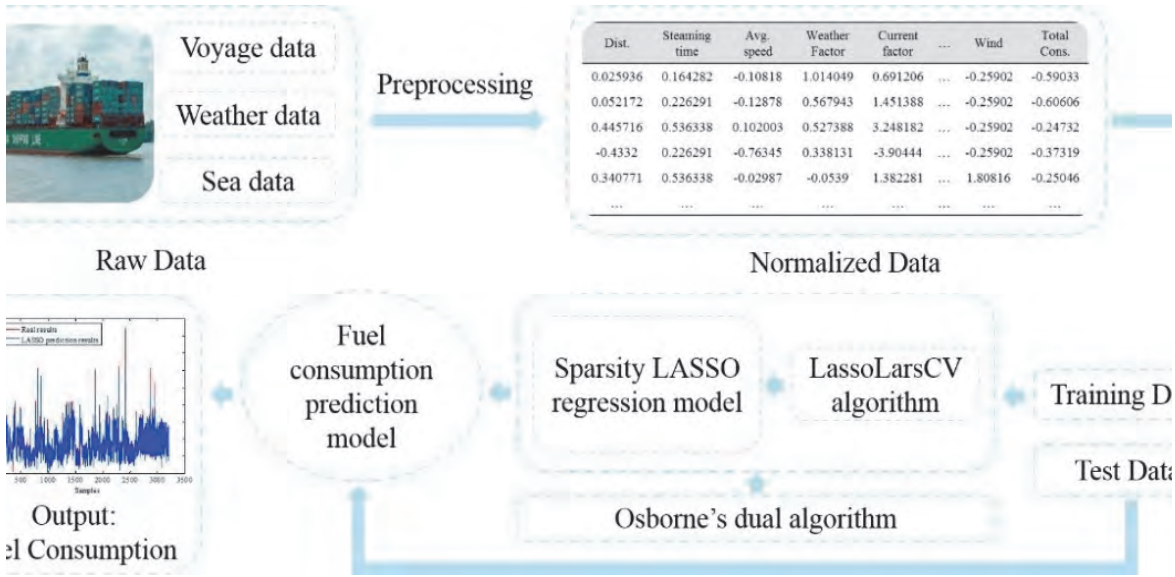

(a)

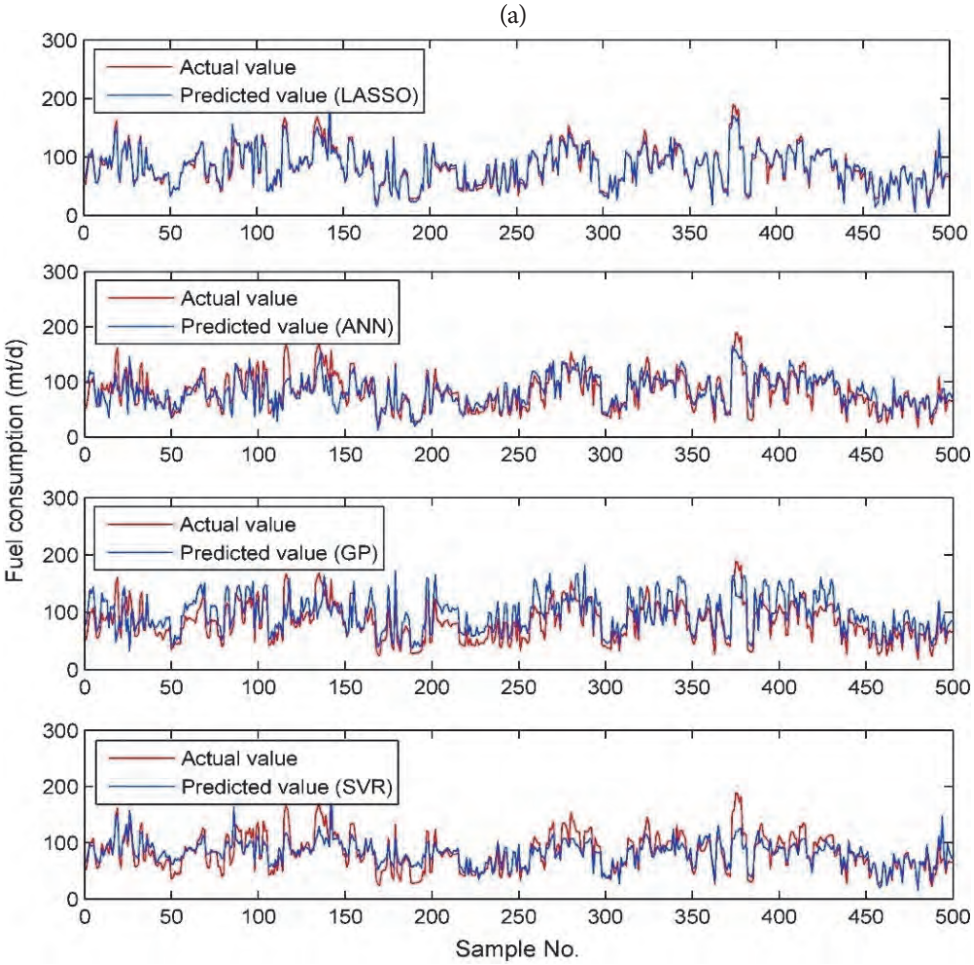

(b)

Fig. 7. (a) - Framework for ship fuel consumption based on LASSO regression algorithm; (b) – Comparison of model performance between LASSO and ANN, SVR, and GP [185]

the next phase, compression and expansion processes are performed on the clustered data in order to get them ready for transmission and storage. To ensure minimal data loss, mean squared errors (MSE) are used as a tool to compare the quality of the pre and post-compression datasets. Thus, the MSE between these two datasets is checked against the user-defined

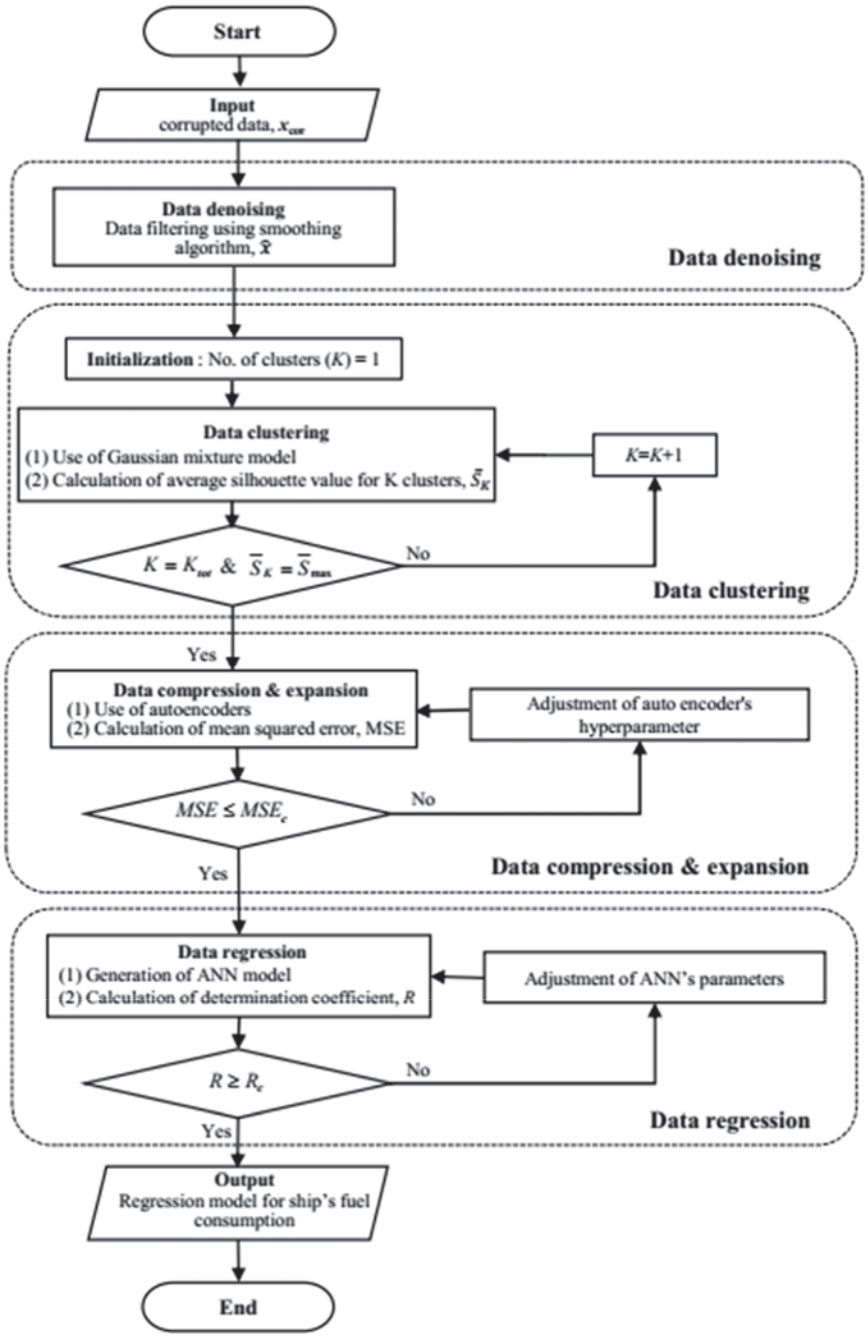

Fig. 8. Big data analysis process for managing ship fuel consumption [196]

MSE. Once the data compression and restoration ratios are examined and the conditions for specific user-defined values are met, the data pre-processing part is complete. Next, the regression analysis is performed using ANN to predict ship fuel consumption. In the process of validating the results, the parameters of the ANN model are modified until the calculated value from the regression function exceeds the user-defined value. The outcome of the analysis provides the regression model for estimating ship fuel consumption.

In recent years, the internet of things (IoT) technology has been applied to the maritime industry with the of improving energy management, ship management, and environmental management [200]. With the integration of IoT technology, the introduction of remote-control systems has allowed for the monitoring of a new generation of smart ships from command centres located on land. With recent advances in IoT technology, the availability of Wi-Fi-enabled sensors mounted on ship equipment and machinery has provided access and continuous collection of a ship's navigational information and operational data [201], [202]. Once collected, this large amount of time-series data must be processed and analysed to reveal insights on ship performance. A big data framework was constructed by Perera et al. [203], which can be used in the pre-processing (e.g. error detection, classification, and data compression) and post-processing (e.g. data expansion, integration verification, and data regeneration) of large volumes of time-series data. In their study, the authors utilised a simple regression model to explain the relationship between the different parameters, despite the lack of verification of the accuracy of fuel consumption data. Because of the high number of dimensions and interactions among variables in most big data analysis, it is important to ensure the accuracy of the final regression model.

CONCLUSIONS AND FUTURE RECOMMENDATIONS

In the present study, a broader literature review has been carried out on developing a prediction model for fuel consumption using ANN. The knowledge gap in the field of research has been addressed. The salient findings of the present review are given below:

1. Most of the present research focuses on machine learning methods to predict fuel consumption with a significant objective of saving energy and reducing emissions.
2. WBMs are suited for conditions with fewer data to process i.e. insufficient voyage data. The workload of the model can be increased by augmenting data sets. So, WBMs can be suited to conditions where the prediction accuracy is not an important factor and voyage data is limited.
3. On the other hand, BBMs can be used effectively and with high accuracy by combining machine learning and

statistics. ANN is one of the most commonly used and accurate methods for BBM. Even though BBMs require highly accurate data, they are preferred for ship fuel prediction applications owing to their reliability.

4. The application of ANN models in predicting ship fuel consumption provides key advantages, including their generalisation and extrapolation capability. From an industrial point of view, the GA-based GBM can be integrated as part of a ship's energy efficiency programs to optimise ship fuel consumption and reduce GHG emissions, as a result of its better predictive capability.
5. The ANN model is cheap, in computation terms; however, it does not have any rule for selecting the feature variables, as well as avoiding the overfitting cases in the training process. As the data collected from the shipping company, for model development, was limited, the accuracy of the prediction model by ANN was affected to a greater extent. These limitations could be overcome by the integration of ANN with other algorithms, such as expert knowledge.

Based on the current status of research into fuel consumption models, the following directions for future research can be proposed:

1. The various alternate sources of marine fuels can be explored. The predictive modelling of data obtained from using alternate fuels can be analysed.
2. The future prediction models may consider additional non-navigational field parameters. Some parameters, such as berth allocation, inventory and market trends, can be added while modelling the system.
3. The fuel consumption models may be integrated with energy efficiency optimisation methods for better results. The developed models can also be used as tools for evaluating the marine vessel fuel consumption study by combining all the factors of cruising.

NOMENCLATURE

ANN	Artificial Neural Networks
GHG	Greenhouse gas
IMO	International Maritime Organisation
LSTM	Long Short Term Memory
BP	Back Propagation
LASSO	Least Absolute Shrinkage and Selection Operator
SEEMP	Ship Energy Efficiency Management Plan
EEDI	Energy Efficiency Design Index
SOx	Sulphur oxide
NOx	Nitrous oxide
PR	Polynomial regression
SVM	Support vector machine
DSS	Decision support system
WBMs	White-box models
BBMs	Black-box models
GBMs	Grey-box models
SPEPs	Sequential parameter estimation procedures
GA-based GBM	Genetic algorithm-based grey-box model
XDi	Decision-making variables
XNj	Uncontrollable input variables
WNN	Wavelet neural network
MLP	Multilayer perceptron
MLP-ANN	Multilayer perceptron artificial neural network
GPR	Gaussian process regression
BPNN	Backpropagation neural network
GMM	Gaussian mixture model
MSE	Mean squared errors
IoT	Internet of things

REFERENCES

1. V. J. Jimenez, H. Kim, and Z. H. Munim, "A review of ship energy efficiency research and directions towards emission reduction in the maritime industry," J. Clean. Prod., vol. 366, p. 132888, Sep. 2022, doi: 10.1016/j.jclepro.2022.132888.

2. A. T. Hoang, "Applicability of fuel injection techniques for modern diesel engines," in International Conference on Sustainable Manufacturing, Materials and Technologies, ICSMMT 2019, 2020, p. 020018. doi: 10.1063/5.0000133.

3. T. a Boden, G. Marland, and R. J. Andres, "Global, Regional, and National Fossil-Fuel CO2 Emissions," Carbon Dioxide Inf. Anal. Cent. Oak Ridge Natl. Lab. USA Oak Ridge TN Dep. Energy, 2009.

4. I. A. Fernández, M. R. Gómez, J. R. Gómez, and L. M. López-González, "Generation of H2 on Board Lng Vessels for Consumption in the Propulsion System," Polish Marit. Res., vol. 27, no. 1, 2020, doi: 10.2478/pomr-2020-0009.

5. V. D. Bui and H. P. Nguyen, "Role of Inland Container Depot System in Developing the Sustainable Transport System," Int. J. Knowledge-Based Dev., vol. 12, no. 3/4, p. 1, 2022, doi: 10.1504/IJKBD.2022.10053121.

6. A. Urbahs and V. Zavtkevics, "Oil Spill Detection Using Multi Remote Piloted Aircraft for the Environmental Monitoring of Sea Aquatorium," Environ. Clim. Technol., vol. 24, no. 1, pp. 1–22, Jan. 2020, doi: 10.2478/rtuect-2020-0001.

7. X. P. Nguyen, D. T. Nguyen, V. V. Pham, and V. D. Bui, "Evaluation of the synergistic effect in wastewater treatment from ships by the advanced combination system," Water Conserv. Manag., vol. 5, no. 1, pp. 60–65, 2021.

8. D. T. Vo, X. P. Nguyen, T. D. Nguyen, R. Hidayat, T. T. Huynh, and D. T. Nguyen, "A review on the internet of thing (IoT) technologies in controlling ocean environment," Energy Sources, Part A Recover. Util. Environ. Eff., pp. 1–19, Jul. 2021, doi: 10.1080/15567036.2021.1960932.

9. E. Lindstad, B. Lagemann, A. Rialland, G. M. Gamlem, and A. Valland, "Reduction of maritime GHG emissions and the potential role of E-fuels," Transp. Res. Part D Transp. Environ., vol. 101, p. 103075, Dec. 2021, doi: 10.1016/j.trd.2021.103075.

10. P. Sharma et al., "Using response surface methodology approach for optimizing performance and emission parameters of diesel engine powered with ternary blend of Solketal-biodiesel-diesel," Sustain. Energy Technol. Assessments, vol. 52, p. 102343, Aug. 2022, doi: 10.1016/j.seta.2022.102343.

11. Z. Wu and X. Xia, "Tariff-driven demand side management of green ship," Sol. Energy, 2018, doi: 10.1016/j.solener.2018.06.033.

12. W. Tarełko, "The effect of hull biofouling on parameters characterising ship propulsion system efficiency," Polish Marit. Res., 2014, doi: 10.2478/pomr-2014-0038.

13. H. P. Nguyen, N. D. K. Pham, and V. D. Bui, "Technical-Environmental Assessment of Energy Management Systems in Smart Ports," Int. J. Renew. Energy Dev., vol. 11, no. 4, pp. 889–901, Nov. 2022, doi: 10.14710/ijred.2022.46300.

14. V. V. Pham and A. T. Hoang, "Analyzing and selecting the typical propulsion systems for ocean supply vessels," 2020. doi: 10.1109/ICACCS48705.2020.9074276.

15. A. T. Hoang, V. D. Tran, V. H. Dong, and A. T. Le, "An experimental analysis on physical properties and spray characteristics of an ultrasound-assisted emulsion of ultra-low-sulphur diesel and Jatropha-based biodiesel," J. Mar. Eng. Technol., vol. 21, no. 2, pp. 73–81, Mar. 2022, doi: 10.1080/20464177.2019.1595355.

16. H. P. Nguyen, P. Q. P. Nguyen, and T. P. Nguyen, "Green Port Strategies in Developed Coastal Countries as Useful Lessons for the Path of Sustainable Development: A case study in Vietnam," Int. J. Renew. Energy Dev., vol. 11, no. 4, pp. 950–962, Nov. 2022, doi: 10.14710/ijred.2022.46539.

17. V. V. Pham, A. T. Hoang, and H. C. Do, "Analysis and evaluation of database for the selection of propulsion systems for tankers," 2020. doi: 10.1063/5.0007655.

18. International Maritime Organization(IMO), "Third IMO GHG study executive summary," 2014.

19. International Maritime Organization(IMO), "MEPC 213 63."

20. International Maritime Organization(IMO), "Guıdelınes For The Development Of A Shıp Energy Effıcıency Management Plan (SEEMP)."

21. International Maritime Organization(IMO), "MEPC 214 63."

22. International Maritime Organization(IMO), "Guıdelınes On The Method Of Calculatıon Of The Attaıned Energy Effıcıency Desıgn Index (EEDI) For New Shıps."

23. International Maritime Organization(IMO), "Prevention of Air Pollution from Ships," 2005.

24. V. D. Tran, A. T. Le, and A. T. Hoang, "An Experimental Study on the Performance Characteristics of a Diesel Engine Fueled with ULSD-Biodiesel Blends.," Int. J. Renew. Energy Dev., vol. 10, no. 2, pp. 183–190, 2021.

25. R. Adland, P. Cariou, H. Jia, and F. C. Wolff, "The energy efficiency effects of periodic ship hull cleaning," J. Clean. Prod., 2018, doi: 10.1016/j.jclepro.2017.12.247.

26. H. Zeraatgar and M. H. Ghaemi, "The Analysis of Overall Ship Fuel Consumption in Acceleration Manoeuvre Using Hull-Propeller-Engine Interaction Principles and Governor Features," Polish Marit. Res., vol. 26, no. 1, 2019, doi: 10.2478/pomr-2019-0018.

27. H. Islam and G. Soares, "Effect of trim on container ship resistance at different ship speeds and drafts," Ocean Eng., 2019, doi: 10.1016/j.oceaneng.2019.03.058.

28. X. P. Nguyen, "A simulation study on the effects of hull form on aerodynamic performances of the ships," in Proceedings of the 2019 1st International Conference on Sustainable Manufacturing, Materials and Technologies, 2020, p. 020015. doi: 10.1063/5.0000140.

29. R. D. Ionescu, I. Szava, S. Vlase, M. Ivanoiu, and R. Munteanu, "Innovative Solutions for Portable Wind Turbines, Used on Ships," Procedia Technol., 2015, doi: 10.1016/j.protcy.2015.02.102.

30. W.-H. Chen et al., "Optimization of a vertical axis wind turbine with a deflector under unsteady wind conditions via Taguchi and neural network applications," Energy Convers. Manag., vol. 254, p. 115209, Feb. 2022, doi: 10.1016/j.enconman.2022.115209.

31. L. Pascali, "The Wind of Change: Maritime Technology, Trade, and Economic Development," Am. Econ. Rev., vol. 107, no. 9, pp. 2821–2854, Sep. 2017, doi: 10.1257/aer.20140832.

32. H. Wang, E. Oguz, B. Jeong, and P. Zhou, "Life cycle and economic assessment of a solar panel array applied to a short route ferry," J. Clean. Prod., 2019, doi: 10.1016/j.jclepro.2019.02.124.

33. W. Yu, P. Zhou, and H. Wang, "Evaluation on the energy

efficiency and emissions reduction of a short-route hybrid sightseeing ship," Ocean Eng., 2018, doi: 10.1016/j.oceaneng.2018.05.016.

34. M. N. Nyanya, H. B. Vu, A. Schönborn, and A. I. Ölçer, "Wind and solar assisted ship propulsion optimisation and its application to a bulk carrier," Sustain. Energy Technol. Assessments, vol. 47, p. 101397, Oct. 2021, doi: 10.1016/j.seta.2021.101397.

35. X. P. Nguyen and V. H. Dong, "A study on traction control system for solar panel on vessels," 2020, p. 020016. doi: 10.1063/5.0007708.

36. N. Alujevic, I. Catipovic, S. Malenica, I. Senjanovic, and N. Vladimir, "Ship roll control and energy harvesting using a U-tube anti-roll tank," 2018.

37. Y. Huo, X. Dong, and S. Beatty, "Cellular Communications in Ocean Waves for Maritime Internet of Things," IEEE Internet Things J., vol. 7, no. 10, pp. 9965–9979, Oct. 2020, doi: 10.1109/JIOT.2020.2988634.

38. N. C. Shih, B. J. Weng, J. Y. Lee, and Y. C. Hsiao, "Development of a 20 kW generic hybrid fuel cell power system for small ships and underwater vehicles," 2014. doi: 10.1016/j.ijhydene.2014.01.113.

39. H. Xing, C. Stuart, S. Spence, and H. Chen, "Fuel Cell Power Systems for Maritime Applications: Progress and Perspectives," Sustainability, vol. 13, no. 3, p. 1213, 2021.

40. M. Jelić, V. Mrzljak, G. Radica, and N. Račić, "An alternative and hybrid propulsion for merchant ships: current state and perspective," Energy Sources, Part A Recover. Util. Environ. Eff., pp. 1–33, Oct. 2021, doi: 10.1080/15567036.2021.1963354.

41. O. Konur, C. O. Colpan, and O. Y. Saatcioglu, "A comprehensive review on organic Rankine cycle systems used as waste heat recovery technologies for marine applications," Energy Sources, Part A Recover. Util. Environ. Eff., vol. 44, no. 2, pp. 4083–4122, Jun. 2022, doi: 10.1080/15567036.2022.2072981.

42. L. Mihanović, M. Jelić, G. Radica, and N. Račić, "EXPERIMENTAL INVESTIGATION OF MARINE ENGINE EXHAUST EMISSIONS," Energy Sources, Part A Recover. Util. Environ. Eff., pp. 1–14, Dec. 2021, doi: 10.1080/15567036.2021.2013344.

43. Y. A. chaboki, A. Khoshgard, G. Salehi, and F. Fazelpour, "Thermoeconomic analysis of a new waste heat recovery system for large marine diesel engine and comparison with two other configurations," Energy Sources, Part A Recover. Util. Environ. Eff., pp. 1–26, Jun. 2020, doi: 10.1080/15567036.2020.1781298.

44. S. Vakili, A. I. Ölçer, A. Schönborn, F. Ballini, and A. T. Hoang, "Energy-related clean and green framework for shipbuilding community towards zero-emissions: A strategic analysis from concept to case study," Int. J. Energy Res., vol. 46, no. 14, pp. 20624–20649, Nov. 2022, doi: 10.1002/er.7649.

45. V. N. Armstrong and C. Banks, "Integrated approach to vessel energy efficiency," Ocean Eng., 2015, doi: 10.1016/j.oceaneng.2015.10.024.

46. N. H. Phuong, "What solutions should be applied to improve the efficiency in the management for port system in Ho Chi Minh City," Int. J. Innov. Creat. Chang., vol. 5, no. 2, pp. 1747–1769, 2019.

47. V. Glavatskhih, A. Lapkin, L. Dmitrieva, I. Khodikova, and A. Golovin, "Ships' energy efficiency management: organizational and economic aspect," MATEC Web Conf., vol. 339, p. 01020, Jul. 2021, doi: 10.1051/matecconf/202133901020.

48. M. Stopford, Maritime economics: Third edition. 2008. doi: 10.4324/9780203891742.

49. M. H. Ghaemi and H. Zeraatgar, "Impact of Propeller Emergence on Hull, Propeller, Engine, and Fuel Consumption Performance in Regular Head Waves," Polish Marit. Res., vol. 29, no. 4, pp. 56–76, Dec. 2022, doi: 10.2478/pomr-2022-0044.

50. M. S. Eide, T. Longva, P. Hoffmann, Ø. Endresen, and S. B. Dalsøren, "Future cost scenarios for reduction of ship CO2 emissions," Marit. Policy Manag., 2011, doi: 10.1080/03088839.2010.533711.

51. Z. Yuan, J. Liu, Q. Zhang, Y. Liu, Y. Yuan, and Z. Li, "Prediction and optimisation of fuel consumption for inland ships considering real-time status and environmental factors," Ocean Eng., vol. 221, p. 108530, Feb. 2021, doi: 10.1016/j.oceaneng.2020.108530.

52. T. Uyanık, Ç. Karatuğ, and Y. Arslanoğlu, "Machine learning approach to ship fuel consumption: A case of container vessel," Transp. Res. Part D Transp. Environ., vol. 84, p. 102389, Jul. 2020, doi: 10.1016/j.trd.2020.102389.

53. E. Işıklı, N. Aydın, L. Bilgili, and A. Toprak, "Estimating fuel consumption in maritime transport," J. Clean. Prod., vol. 275, p. 124142, Dec. 2020, doi: 10.1016/j.jclepro.2020.124142.

54. F. Cipollini, L. Oneto, A. Coraddu, A. J. Murphy, and D. Anguita, "Condition-Based Maintenance of Naval Propulsion Systems with supervised Data Analysis," Ocean Engineering. 2018. doi: 10.1016/j.oceaneng.2017.12.002.

55. Y. Raptodimos and I. Lazakis, "Using artificial neural

network-self-organising map for data clustering of marine engine condition monitoring applications," Ships Offshore Struct., 2018, doi: 10.1080/17445302.2018.1443694.

56. H. Bakır et al., "Forecasting of future greenhouse gas emission trajectory for India using energy and economic indexes with various metaheuristic algorithms," J. Clean. Prod., vol. 360, p. 131946, Aug. 2022, doi: 10.1016/j.jclepro.2022.131946.

57. K. Wang et al., "A comprehensive review on the prediction of ship energy consumption and pollution gas emissions," Ocean Eng., vol. 266, p. 112826, Dec. 2022, doi: 10.1016/j.oceaneng.2022.112826.

58. K. A. Chrysafis, I. N. Theotokas, and I. N. Lagoudis, "Managing fuel price variability for ship operations through contracts using fuzzy TOPSIS," Res. Transp. Bus. Manag., vol. 43, p. 100778, Jun. 2022, doi: 10.1016/j.rtbm.2021.100778.

59. A. Fan, J. Yang, L. Yang, D. Wu, and N. Vladimir, "A review of ship fuel consumption models," Ocean Eng., vol. 264, p. 112405, Nov. 2022, doi: 10.1016/j.oceaneng.2022.112405.

60. J.-G. Kim, H.-J. Kim, and P. T.-W. Lee, "Optimizing ship speed to minimize fuel consumption," Transp. Lett., vol. 6, no. 3, pp. 109–117, Jul. 2014, doi: 10.1179/1942787514Y.0000000016.

61. S. Sherbaz and W. Duan, "Operational options for green ships," J. Mar. Sci. Appl., vol. 11, no. 3, pp. 335–340, Sep. 2012, doi: 10.1007/s11804-012-1141-2.

62. J. A. Reggia and S. Tuhrim, Computer-assisted medical decision making. Springer Science & Business Media, 2012.

63. B. Kawan, H. Wang, G. Li, and K. Chhantyal, "Data-driven Modeling of Ship Motion Prediction Based on Support Vector Regression," Sep. 2017, pp. 350–354. doi: 10.3384/ecp17138350.

64. L. Zhang, Q. Meng, Z. Xiao, and X. Fu, "A novel ship trajectory reconstruction approach using AIS data," Ocean Eng., vol. 159, pp. 165–174, Jul. 2018, doi: 10.1016/j.oceaneng.2018.03.085.

65. O. B. Öztürk and E. Başar, "Multiple linear regression analysis and artificial neural networks based decision support system for energy efficiency in shipping," Ocean Eng., vol. 243, p. 110209, Jan. 2022, doi: 10.1016/j.oceaneng.2021.110209.

66. J. Hadi, Z. Y. Tay, and D. Konovessis, "Ship Navigation and Fuel Profiling based on Noon Report using Neural Network Generative Modeling," J. Phys. Conf. Ser., vol. 2311, no. 1, p. 012005, Jul. 2022, doi: 10.1088/1742-6596/2311/1/012005.

67. B. Ban, J. Yang, P. Chen, J. Xiong, and Q. Wang, "Ship Track Regression Based on Support Vector Machine," IEEE Access, vol. 5, pp. 18836–18846, 2017, doi: 10.1109/ACCESS.2017.2749260.

68. M. Bentin, D. Zastrau, M. Schlaak, D. Freye, R. Elsner, and S. Kotzur, "A New Routing Optimization Tool-influence of Wind and Waves on Fuel Consumption of Ships with and without Wind Assisted Ship Propulsion Systems," Transp. Res. Procedia, vol. 14, pp. 153–162, 2016, doi: 10.1016/j.trpro.2016.05.051.

69. M. Haranen, P. Pakkanen, R. Kariranta, and J. Salo, "White, Grey and Black-Box Modelling in Ship Performance Evaluation," 1st Hull Performence Insight Conf., 2016.

70. M. L. Fam, Z. Y. Tay, and D. Konovessis, "An Artificial Neural Network for fuel efficiency analysis for cargo vessel operation," Ocean Eng., vol. 264, p. 112437, Nov. 2022, doi: 10.1016/j.oceaneng.2022.112437.

71. "The MIT encyclopedia of the cognitive sciences," Choice Rev. Online, 1999, doi: 10.5860/choice.37-1902.

72. I. H. Witten, E. Frank, and M. a. Hall, Data Mining: Practical Machine Learning Tools and Techniques, Third Edition. 2011.

73. P. Karagiannidis and N. Themelis, "Data-driven modelling of ship propulsion and the effect of data pre-processing on the prediction of ship fuel consumption and speed loss," Ocean Eng., vol. 222, p. 108616, Feb. 2021, doi: 10.1016/j.oceaneng.2021.108616.

74. G. Lampropoulos, "Artificial Intelligence, Big Data, and Machine Learning in Industry 4.0," in Encyclopedia of Data Science and Machine Learning, IGI Global, 2022, pp. 2101–2109. doi: 10.4018/978-1-7998-9220-5.ch125.

75. K. Karunamurthy, A. A. Janvekar, P. L. Palaniappan, V. Adhitya, T. T. K. Lokeswar, and J. Harish, "Prediction of IC engine performance and emission parameters using machine learning: A review," J. Therm. Anal. Calorim., Jan. 2023, doi: 10.1007/s10973-022-11896-2.

76. P. Sharma, "Data-driven predictive model development for efficiency and emission characteristics of a diesel engine fueled with biodiesel/diesel blends," in Artificial Intelligence for Renewable Energy Systems, Elsevier, 2022, pp. 329–352. doi: 10.1016/B978-0-323-90396-7.00005-5.

77. M. B. Patel, J. N. Patel, and U. M. Bhilota, "Comprehensive Modelling of ANN," in Research Anthology on Artificial Neural Network Applications, IGI Global, 2022, pp. 31–40. doi: 10.4018/978-1-6684-2408-7.ch002.

78. Z. Tian and S. Fong, "Survey of meta-heuristic algorithms

for deep learning training," Optim. algorithms—methods Appl., 2016.

79. W.-H. Chen et al., "A comparative analysis of biomass torrefaction severity index prediction from machine learning," Appl. Energy, vol. 324, p. 119689, Oct. 2022, doi: 10.1016/j.apenergy.2022.119689.

80. O. I. Abiodun, A. Jantan, A. E. Omolara, K. V. Dada, N. A. Mohamed, and H. Arshad, "State-of-the-art in artificial neural network applications: A survey," Heliyon, vol. 4, no. 11, p. e00938, Nov. 2018, doi: 10.1016/j.heliyon.2018.e00938.

81. O. I. Abiodun et al., "Comprehensive Review of Artificial Neural Network Applications to Pattern Recognition," IEEE Access, vol. 7, pp. 158820–158846, 2019, doi: 10.1109/ACCESS.2019.2945545.

82. J.-H. Kim, Y. Kim, and W. Lu, "Prediction of ice resistance for ice-going ships in level ice using artificial neural network technique," Ocean Eng., vol. 217, p. 108031, Dec. 2020, doi: 10.1016/j.oceaneng.2020.108031.

83. S. Gan, S. Liang, K. Li, J. Deng, and T. Cheng, "Ship trajectory prediction for intelligent traffic management using clustering and ANN," in 2016 UKACC 11th International Conference on Control (CONTROL), Aug. 2016, pp. 1–6. doi: 10.1109/CONTROL.2016.7737569.

84. N. Gupta, "Artificial neural network," Netw. Complex Syst., vol. 3, no. 1, pp. 24–28, 2013.

85. I. Veza et al., "Review of artificial neural networks for gasoline, diesel and homogeneous charge compression ignition engine," Alexandria Eng. J., vol. 61, no. 11, pp. 8363–8391, Nov. 2022, doi: 10.1016/j.aej.2022.01.072.

86. M. Sharifzadeh, A. Sikinioti-Lock, and N. Shah, "Machine-learning methods for integrated renewable power generation: A comparative study of artificial neural networks, support vector regression, and Gaussian Process Regression," Renew. Sustain. Energy Rev., vol. 108, pp. 513–538, Jul. 2019, doi: 10.1016/j.rser.2019.03.040.

87. A. Gopi, P. Sharma, K. Sudhakar, W. K. Ngui, I. Kirpichnikova, and E. Cuce, "Weather Impact on Solar Farm Performance: A Comparative Analysis of Machine Learning Techniques," Sustainability, vol. 15, no. 1, p. 439, Dec. 2022, doi: 10.3390/su15010439.

88. P. Sharma and B. J. Bora, "A Review of Modern Machine Learning Techniques in the Prediction of Remaining Useful Life of Lithium-Ion Batteries," Batteries, vol. 9, no. 1, p. 13, Dec. 2022, doi: 10.3390/batteries9010013.

89. I. . Basheer and M. Hajmeer, "Artificial neural networks: fundamentals, computing, design, and application," J. Microbiol. Methods, vol. 43, no. 1, pp. 3–31, Dec. 2000, doi: 10.1016/S0167-7012(00)00201-3.

90. A. D. Dongare, R. R. Kharde, and A. D. Kachare, "Introduction to artificial neural network," Int. J. Eng. Innov. Technol., vol. 2, no. 1, pp. 189–194, 2012.

91. P. Dey, A. Sarkar, and A. K. Das, "Development of GEP and ANN model to predict the unsteady forced convection over a cylinder," Neural Comput. Appl., vol. 27, no. 8, pp. 2537–2549, Nov. 2016, doi: 10.1007/s00521-015-2023-8.

92. B. Maleki, B. Singh, H. Eamaeili, Y. K. Venkatesh, S. S. A. Talesh, and S. Seetharaman, "Transesterification of waste cooking oil to biodiesel by walnut shell/sawdust as a novel, low-cost and green heterogeneous catalyst: Optimization via RSM and ANN," Ind. Crops Prod., vol. 193, p. 116261, Mar. 2023, doi: 10.1016/j.indcrop.2023.116261.

93. A. G. R. Vaz, B. Elsinga, W. G. J. H. M. van Sark, and M. C. Brito, "An artificial neural network to assess the impact of neighbouring photovoltaic systems in power forecasting in Utrecht, the Netherlands," Renew. Energy, vol. 85, pp. 631–641, Jan. 2016, doi: 10.1016/j.renene.2015.06.061.

94. R. J. Kuo, C. H. Chen, and Y. C. Hwang, "An intelligent stock trading decision support system through integration of genetic algorithm based fuzzy neural network and artificial neural network," Fuzzy Sets Syst., vol. 118, no. 1, pp. 21–45, Feb. 2001, doi: 10.1016/S0165-0114(98)00399-6.

95. J. C. Fernández, L. B. Corrales, I. F. Benítez, and J. R. Núñez, "Fault Diagnosis of Combustion Engines in MTU 16VS4000-G81 Generator Sets Using Fuzzy Logic: An Approach to Normalize Specific Fuel Consumption," 2022, pp. 17–29. doi: 10.1007/978-3-030-98457-1_2.

96. C. W. Mohd Noor, R. Mamat, G. Najafi, M. H. Mat Yasin, C. K. Ihsan, and M. M. Noor, "Prediction of marine diesel engine performance by using artificial neural network model," J. Mech. Eng. Sci., vol. 10, no. 1, pp. 1917–1930, Jun. 2016, doi: 10.15282/jmes.10.1.2016.15.0183.

97. Keh-Kim Kee, Boung-Yew Lau Simon, and K.-H. Y. Renco, "Artificial neural network back-propagation based decision support system for ship fuel consumption prediction," in 5th IET International Conference on Clean Energy and Technology (CEAT2018), 2018, pp. 13 (6 pp.)-13 (6 pp.). doi: 10.1049/cp.2018.1306.

98. B. Panda and A. Ghoshal, "An ANN based switching network for optimally selected photovoltaic array with battery and supercapacitor to mitigate the effect of intermittent solar irradiance," Energy Sources, Part A Recover. Util. Environ. Eff., vol. 44, no. 3, pp. 5784–5811, Sep. 2022, doi: 10.1080/15567036.2022.2088897.

99. J. Zou, Y. Han, and S.-S. So, "Overview of Artificial Neural Networks," in Artificial Neural Networks. Methods in Molecular Biology, 2008, pp. 14–22. doi: 10.1007/978-1-60327-101-1_2.

100. S. Al-Dahidi, J. Adeeb, O. Ayadi, M. Alrbai, and L. Al-Ghussain, "A feature transformation and extraction approach-based artificial neural network for an improved production prediction of grid-connected solar photovoltaic systems," Energy Sources, Part A Recover. Util. Environ. Eff., vol. 44, no. 4, pp. 9232–9254, Dec. 2022, doi: 10.1080/15567036.2022.2128475.

101. Z. Yuan, J. Liu, Y. Liu, Y. Yuan, Q. Zhang, and Z. Li, "Fitting Analysis of Inland Ship Fuel Consumption Considering Navigation Status and Environmental Factors," IEEE Access, vol. 8, pp. 187441–187454, 2020, doi: 10.1109/ACCESS.2020.3030614.

102. T. Cepowski and P. Chorab, "The Use of Artificial Neural Networks to Determine the Engine Power and Fuel Consumption of Modern Bulk Carriers, Tankers and Container Ships," Energies, vol. 14, no. 16, p. 4827, Aug. 2021, doi: 10.3390/en14164827.

103. Y. B. A. Farag and A. I. Ölçer, "The development of a ship performance model in varying operating conditions based on ANN and regression techniques," Ocean Eng., vol. 198, p. 106972, Feb. 2020, doi: 10.1016/j.oceaneng.2020.106972.

104. T. Zhou, Q. Hu, Z. Hu, and R. Zhen, "An adaptive hyper parameter tuning model for ship fuel consumption prediction under complex maritime environments," J. Ocean Eng. Sci., vol. 7, no. 3, pp. 255–263, Jun. 2022, doi: 10.1016/j.joes.2021.08.007.

105. W. Tarelko and K. Rudzki, "Applying artificial neural networks for modelling ship speed and fuel consumption," Neural Computing and Applications, vol. 32, no. 23. 2020. doi: 10.1007/s00521-020-05111-2.

106. A. Coraddu, L. Oneto, F. Baldi, and D. Anguita, "Vessels fuel consumption forecast and trim optimisation: A data analytics perspective," Ocean Engineering. 2017. doi: 10.1016/j.oceaneng.2016.11.058.

107. L. T. Leifsson, H. Sævarsdóttir, S. T. Sigurdsson, and A. Vésteinsson, "Grey-box modeling of an ocean vessel for operational optimization," Simul. Model. Pract. Theory, 2008, doi: 10.1016/j.simpat.2008.03.006.

108. L. Ljung, "Black-box models from input-output measurements," 2001. doi: 10.1109/imtc.2001.928802.

109. L. Yang, G. Chen, N. G. M. Rytter, J. Zhao, and D. Yang, "A genetic algorithm-based grey-box model for ship fuel consumption prediction towards sustainable shipping," Ann. Oper. Res., 2019, doi: 10.1007/s10479-019-03183-5.

110. F. Baldi, Modelling, analysis and optimisation of ship energy systems. Chalmers University of Technology, 2016.

111. C. Gkerekos and I. Lazakis, "A novel, data-driven heuristic framework for vessel weather routing," Ocean Eng., vol. 197, p. 106887, Feb. 2020, doi: 10.1016/j.oceaneng.2019.106887.

112. R. Lu, O. Turan, E. Boulougouris, C. Banks, and A. Incecik, "A semi-empirical ship operational performance prediction model for voyage optimization towards energy efficient shipping," Ocean Eng., vol. 110, 2015, doi: 10.1016/j.oceaneng.2015.07.042.

113. F. Tillig, J. W. Ringsberg, W. Mao, and B. Ramne, "A generic energy systems model for efficient ship design and operation," Proc. Inst. Mech. Eng. Part M J. Eng. Marit. Environ., vol. 231, no. 2, 2017, doi: 10.1177/1475090216680672.

114. B. P. Pedersen and J. Larsen, "Modeling of Ship Propulsion Performance," World Marit. Technol. Conf., 2009.

115. B. P. Pedersen and J. Larsen, "Prediction of full-scale propulsion power using artificial neural networks," Proc. 8th Int. Conf. Comput. IT Appl. Marit. Ind., pp. 537–550, 2009.

116. J. P. Petersen, D. J. Jacobsen, and O. Winther, "Statistical modelling for ship propulsion efficiency," J. Mar. Sci. Technol., 2012, doi: 10.1007/s00773-011-0151-0.

117. E. Bal Beşikçi, O. Arslan, O. Turan, and A. I. Ölçer, "An artificial neural network based decision support system for energy efficient ship operations," Comput. Oper. Res., 2016, doi: 10.1016/j.cor.2015.04.004.

118. K. Rudzki and W. Tarelko, "A decision-making system supporting selection of commanded outputs for a ship's propulsion system with a controllable pitch propeller," Ocean Eng., 2016, doi: 10.1016/j.oceaneng.2016.09.018.

119. J. P. Petersen, O. Winther, and D. J. Jacobsen, "A Machine-Learning Approach to Predict Main Energy Consumption under Realistic Operational Conditions," Sh. Technol. Res., vol. 59, no. 1, pp. 64–72, Jan. 2012, doi: 10.1179/str.2012.59.1.007.

120. B. P. Pedersen and J. Larsen, "Gaussian Process Regression for Vessel Performance Monitoring," Compit, 2013.

121. Journée, J. M. J., Rijke, R. J., Verleg, and G. J. H., "Marine performance surveillance with a personal computer," Delft, Netherlands Delft Univ. Technol., 1987.

122. X. Wang, Z. Zou, L. Yu, and W. Cai, "System identification

modeling of ship manoeuvring motion in 4 degrees of freedom based on support vector machines," China Ocean Eng., vol. 29, no. 4, pp. 519–534, Jun. 2015, doi: 10.1007/s13344-015-0036-9.

123. L. Þ. Leifsson, H. Sævarsdóttir, S. Þ. Sigurðsson, and A. Vésteinsson, "Grey-box modeling of an ocean vessel for operational optimization," Simul. Model. Pract. Theory, vol. 16, no. 8, pp. 923–932, Sep. 2008, doi: 10.1016/j.simpat.2008.03.006.

124. C.-K. Lin and H.-J. Shaw, "Preliminary parametric estimation of steel weight for new ships," J. Mar. Sci. Technol., vol. 21, no. 2, pp. 227–239, Jun. 2016, doi: 10.1007/s00773-015-0345-y.

125. Q. Meng, Y. Du, and Y. Wang, "Shipping log data based container ship fuel efficiency modeling," Transp. Res. Part B Methodol., 2016, doi: 10.1016/j.trb.2015.11.007.

126. L. Chen, P. Yang, S. Li, Y. Tian, G. Liu, and G. Hao, "Grey-box identification modeling of ship maneuvering motion based on LS-SVM," Ocean Eng., vol. 266, p. 112957, Dec. 2022, doi: 10.1016/j.oceaneng.2022.112957.

127. L. G. Aldous, "Ship operational efficiency: performance models and uncertainty analysis." UCL (University College London), 2016.

128. S. K. Paul, S. Asian, M. Goh, and S. A. Torabi, "Managing sudden transportation disruptions in supply chains under delivery delay and quantity loss," Ann. Oper. Res., 2019, doi: 10.1007/s10479-017-2684-z.

129. A. Rezaei Somarin, S. Chen, S. Asian, and D. Z. W. Wang, "A heuristic stock allocation rule for repairable service parts," Int. J. Prod. Econ., 2017, doi: 10.1016/j.ijpe.2016.11.013.

130. C. G. Moles, P. Mendes, and J. R. Banga, "Parameter estimation in biochemical pathways: A comparison of global optimization methods," Genome Research. 2003. doi: 10.1101/gr.1262503.

131. M. Schwaab, E. C. Biscaia, J. L. Monteiro, and J. C. Pinto, "Nonlinear parameter estimation through particle swarm optimization," Chem. Eng. Sci., 2008, doi: 10.1016/j.ces.2007.11.024.

132. I. Veza et al., "Multi-objective optimization of diesel engine performance and emission using grasshopper optimization algorithm," Fuel, vol. 323, p. 124303, Sep. 2022, doi: 10.1016/j.fuel.2022.124303.

133. I. Veza et al., "Grasshopper optimization algorithm for diesel engine fuelled with ethanol-biodiesel-diesel blends," Case Stud. Therm. Eng., vol. 31, p. 101817, Mar. 2022, doi: 10.1016/j.csite.2022.101817.

134. H. Orouji, O. B. Haddad, E. Fallah-Mehdipour, and M. A. Mariño, "Estimation of Muskingum parameter by meta-heuristic algorithms," Proc. Inst. Civ. Eng. Water Manag., 2013, doi: 10.1680/wama.11.00068.

135. D. F. Alam, D. A. Yousri, and M. B. Eteiba, "Flower Pollination Algorithm based solar PV parameter estimation," Energy Convers. Manag., 2015, doi: 10.1016/j.enconman.2015.05.074.

136. H. Lee, N. Aydin, Y. Choi, S. Lekhavat, and Z. Irani, "A decision support system for vessel speed decision in maritime logistics using weather archive big data," Comput. Oper. Res., vol. 98, pp. 330–342, Oct. 2018, doi: 10.1016/j.cor.2017.06.005.

137. K. Fagerholt, "A computer-based decision support system for vessel fleet scheduling—experience and future research," Decis. Support Syst., vol. 37, no. 1, pp. 35–47, 2004.

138. M. H. Shamsi, U. Ali, E. Mangina, and J. O'Donnell, "A framework for uncertainty quantification in building heat demand simulations using reduced-order grey-box energy models," Appl. Energy, vol. 275, p. 115141, Oct. 2020, doi: 10.1016/j.apenergy.2020.115141.

139. O. Loyola-Gonzalez, "Black-Box vs. White-Box: Understanding Their Advantages and Weaknesses From a Practical Point of View," IEEE Access, vol. 7, pp. 154096–154113, 2019, doi: 10.1109/ACCESS.2019.2949286.

140. M. Nasr, R. Shokri, and A. Houmansadr, "Comprehensive Privacy Analysis of Deep Learning: Passive and Active White-box Inference Attacks against Centralized and Federated Learning," in 2019 IEEE Symposium on Security and Privacy (SP), May 2019, pp. 739–753. doi: 10.1109/SP.2019.00065.

141. Y.-Y. Zhang, Z.-H. Wang, and Z.-J. Zou, "Black-box modeling of ship maneuvering motion based on multi-output nu-support vector regression with random excitation signal," Ocean Eng., vol. 257, p. 111279, 2022.

142. N. Asproulis and D. Drikakis, "An artificial neural network-based multiscale method for hybrid atomistic-continuum simulations," Microfluid. Nanofluidics, 2013, doi: 10.1007/s10404-013-1154-4.

143. N. Asproulis and D. Drikakis, "Nanoscale materials modelling using neural networks," J. Comput. Theor. Nanosci., vol. 6, no. 3, pp. 514–518, 2009.

144. G. Rajchakit, A. Pratap, R. Raja, J. Cao, J. Alzabut, and C. Huang, "Hybrid control scheme for projective lag synchronization of Riemann-Liouville sense fractional

order memristive BAM neural networks with mixed delays," Mathematics, 2019, doi: 10.3390/math7080759.

145. G. Rajchakit, P. Chanthorn, P. Kaewmesri, R. Sriraman, and C. P. Lim, "Global mittag-leffler stability and stabilization analysis of fractional-order quaternion-valued memristive neural networks," Mathematics, 2020, doi: 10.3390/math8030422.

146. P. Niamsup, M. Rajchakit, and G. Rajchakit, "Guaranteed cost control for switched recurrent neural networks with interval time-varying delay," J. Inequalities Appl., 2013, doi: 10.1186/1029-242X-2013-292.

147. H. Zhang, W. Xiong, R. Zhang, and H. Su, "Prediction of gas consumption based on LSTM-BPNN hybrid model," Energy Sources, Part A Recover. Util. Environ. Eff., vol. 44, no. 4, pp. 10665–10680, Dec. 2022, doi: 10.1080/15567036.2022.2157520.

148. A. Radonjić, D. Pjevčević, and V. Maraš, "Neural Network Ensemble Approach to Pushed Convoys Dispatching Problems," Polish Marit. Res., vol. 27, no. 1, 2020, doi: 10.2478/pomr-2020-0008.

149. L. Pan, "Exploration and Mining Learning Robot of Autonomous Marine Resources Based on Adaptive Neural Network Controller," Polish Marit. Res., 2018, doi: 10.2478/pomr-2018-0115.

150. L. Qiang, Y. Bing-Dong, and H. Bi-Guang, "Calculation and Measurement of Tide Height for the Navigation of Ship at High Tide Using Artificial Neural Network," Polish Marit. Res., 2018, doi: 10.2478/pomr-2018-0118.

151. E. Bal Beşikçi, O. Arslan, O. Turan, and A. I. Ölçer, "An artificial neural network based decision support system for energy efficient ship operations," Comput. Oper. Res., vol. 66, pp. 393–401, Feb. 2016, doi: 10.1016/j.cor.2015.04.004.

152. K. Wang, X. Yan, Y. Yuan, and F. Li, "Real-time optimization of ship energy efficiency based on the prediction technology of working condition," Transp. Res. Part D Transp. Environ., vol. 46, pp. 81–93, Jul. 2016, doi: 10.1016/j.trd.2016.03.014.

153. O. Arslan, E. Besikci, and A. Olcer, "Improving energy efficiency of ships through optimisation of ship operations," No. FY2014-3 IAMU, 2014.

154. K. Rudzki, "Two-objective optimization of engine ship propulsion settings with controllable pitch propeller using artificial neural networks," Gdynia Maritime University, 2014.

155. Z. Said et al., "Application of novel framework based on ensemble boosted regression trees and Gaussian process regression in modelling thermal performance of small-scale Organic Rankine Cycle (ORC) using hybrid nanofluid," J. Clean. Prod., vol. 360, p. 132194, Aug. 2022, doi: 10.1016/j.jclepro.2022.132194.

156. G. Li, H. Zhang, B. Kawan, H. Wang, O. L. Osen, and A. Styve, "Analysis and modeling of sensor data for ship motion prediction," 2016. doi: 10.1109/OCEANSAP.2016.7485648.

157. L. P. Perera and B. Mo, "Marine Engine Operating Regions under Principal Component Analysis to evaluate Ship Performance and Navigation Behavior," IFAC-PapersOnLine, 2016, doi: 10.1016/j.ifacol.2016.10.487.

158. L. P. Perera and B. Mo, "Data compression of ship performance and navigation information under deep learning," 2016. doi: 10.1115/OMAE2016-54093.

159. M. Q. Yuquan D, "Models for ship fuel efficiency with applications to in-service ship fuel consumption management," National University of Singapore, 2016.

160. W. Y. Du Y, Meng Q, "Artificial neural network models for ship fuel efficiency with applications to in-service ship fuel consumption management," 2016.

161. Y. Zhu, Y. Zuo, and T. Li, "Predicting Ship Fuel Consumption based on LSTM Neural Network," in 2020 7th International Conference on Information, Cybernetics, and Computational Social Systems (ICCSS), Nov. 2020, pp. 310–313. doi: 10.1109/ICCSS52145.2020.9336914.

162. M. Chaal, "Ship operational performance modelling for voyage optimization through fuel consumption minimization," 2018.

163. K. Rudzki, P. Gomulka, and A. T. Hoang, "Optimization Model to Manage Ship Fuel Consumption and Navigation Time," Polish Marit. Res., vol. 29, no. 3, pp. 141–153, Sep. 2022, doi: 10.2478/pomr-2022-0034.

164. P. R. Couser, A. P. Mason, G. Mason, C. R. Smith, and B. R. Von Konsky, "Artificial Neural Networks for Hull Resistance Prediction," 2004.

165. K. Grabowska and P. Szczuko, "Ship resistance prediction with Artificial Neural Networks," in 2015 Signal Processing: Algorithms, Architectures, Arrangements, and Applications (SPA), 2015, pp. 168–173.

166. C. M. Bishop, Neural networks for pattern recognition. Oxford university press, 1995.

167. A. P. Mason, P. R. Couser, G. Mason, C. R. Smith, and B. R. Von Konsky, "Optimisation of Vessel Resistance using Genetic Algorithms and Artificial Neural Networks," Compit 05, 2005.

168. J. Holtrop and G. G. J. Mennen, "APPROXIMATE POWER PREDICTION METHOD.," 1982. doi: 10.3233/isp-1982-2933501.

169. L. T. Le, G. Lee, K.-S. Park, and H. Kim, "Neural network-based fuel consumption estimation for container ships in Korea," Marit. Policy Manag., vol. 47, no. 5, pp. 615–632, Jul. 2020, doi: 10.1080/03088839.2020.1729437.

170. I. Ortigosa, R. Lopez, and J. Garcia, "A neural networks approach to residuary resistance of sailing yachts prediction," in Proceedings of the international conference on marine engineering MARINE, 2007, vol. 2007, p. 250.

171. I. Ortigosa, R. López, and J. García, "Prediction of total resistance coefficients using neural networks," J. Marit. Res., vol. 6, no. 3, pp. 15–26, 2009.

172. G. Zhang, V. V. Thai, K. F. Yuen, H. S. Loh, and Q. Zhou, "Addressing the epistemic uncertainty in maritime accidents modelling using Bayesian network with interval probabilities," Saf. Sci., vol. 102, pp. 211–225, Feb. 2018, doi: 10.1016/j.ssci.2017.10.016.

173. Q. Zhou, Y. D. Wong, H. S. Loh, and K. F. Yuen, "A fuzzy and Bayesian network CREAM model for human reliability analysis – The case of tanker shipping," Saf. Sci., vol. 105, pp. 149–157, Jun. 2018, doi: 10.1016/j.ssci.2018.02.011.

174. Q. Zhou, Y. D. Wong, H. S. Loh, and K. F. Yuen, "ANFIS model for assessing near-miss risk during tanker shipping voyages," Marit. Policy Manag., vol. 46, no. 4, pp. 377–393, May 2019, doi: 10.1080/03088839.2019.1569765.

175. J. Tran et al., "Systematic review and content analysis of Australian health care substitute decision making online resources," Aust. Heal. Rev., vol. 45, no. 3, pp. 317–327, Jan. 2021, doi: 10.1071/AH20070.

176. C. Sun, H. Wang, C. Liu, and Y. Zhao, "Dynamic Prediction and Optimization of Energy Efficiency Operational Index (EEOI) for an Operating Ship in Varying Environments," J. Mar. Sci. Eng., vol. 7, no. 11, p. 402, Nov. 2019, doi: 10.3390/jmse7110402.

177. Y.-R. Kim, M. Jung, and J.-B. Park, "Development of a Fuel Consumption Prediction Model Based on Machine Learning Using Ship In-Service Data," J. Mar. Sci. Eng., vol. 9, no. 2, p. 137, Jan. 2021, doi: 10.3390/jmse9020137.

178. L. Moreira, R. Vettor, and C. Guedes Soares, "Neural Network Approach for Predicting Ship Speed and Fuel Consumption," J. Mar. Sci. Eng., vol. 9, no. 2, p. 119, Jan. 2021, doi: 10.3390/jmse9020119.

179. P. Karagiannidis, N. Themelis, G. Zaraphonitis, C. Spandonidis, and C. Giordamlis, "Ship fuel consumption prediction using artificial neural networks," in Proceedings of the Annual meeting of marine technology conference proceedings, Athens, Greece, 2019, pp. 46–51.

180. Z. Hu, Y. Jin, Q. Hu, S. Sen, T. Zhou, and M. T. Osman, "Prediction of Fuel Consumption for Enroute Ship Based on Machine Learning," IEEE Access, vol. 7, pp. 119497–119505, 2019, doi: 10.1109/ACCESS.2019.2933630.

181. R. Ye and J. Xu, "Vessel fuel consumption model based on neural network," Sh. Eng., vol. 38, no. 3, pp. 85–88, 2016.

182. Z. Wang and S. Chen, "Real-time Forecast of Fuel Consumption of Ship Main Engine Based on LSTM Neural Network [J]," J. Wuhan Univ. Technol. (Transportation Sci. Eng., vol. 44, no. 05, pp. 923–927, 2020.

183. L. Bui-Duy and N. Vu-Thi-Minh, "Utilization of a deep learning-based fuel consumption model in choosing a liner shipping route for container ships in Asia," Asian J. Shipp. Logist., vol. 37, no. 1, pp. 1–11, Mar. 2021, doi: 10.1016/j.ajsl.2020.04.003.

184. X. Q. Shen, S. Z. Wang, T. Xu, C. J. Shi, and B. X. Ji, "Ship Fuel Consumption Prediction under Various Weather Condition Based on DBN," in Safety of Sea Transportation, CRC Press, 2017, pp. 69–74. doi: 10.1201/9781315099088-11.

185. S. Wang, B. Ji, J. Zhao, W. Liu, and T. Xu, "Predicting ship fuel consumption based on LASSO regression," Transp. Res. Part D Transp. Environ., vol. 65, pp. 817–824, Dec. 2018, doi: 10.1016/j.trd.2017.09.014.

186. V. D. Bui and H. P. Nguyen, "A Comprehensive Review on Big Data-Based Potential Applications in Marine Shipping Management," Int. J. Adv. Sci. Eng. Inf. Technol., vol. 11, no. 3, pp. 1067–1077, Jun. 2021, doi: 10.18517/ijaseit.11.3.15350.

187. Z. H. Munim, M. Dushenko, V. J. Jimenez, M. H. Shakil, and M. Imset, "Big data and artificial intelligence in the maritime industry: a bibliometric review and future research directions," Marit. Policy Manag., vol. 47, no. 5, pp. 577–597, Jul. 2020, doi: 10.1080/03088839.2020.1788731.

188. H. P. Nguyen, P. Q. P. Nguyen, and V. D. Bui, "Applications of Big Data Analytics in Traffic Management in Intelligent Transportation Systems," JOIV Int. J. Informatics Vis., vol. 6, no. 1–2, pp. 177–187, May 2022, doi: 10.30630/joiv.6.1-2.882.

189. A. Fan, Z. Wang, L. Yang, J. Wang, and N. Vladimir, "Multi-stage decision-making method for ship speed optimisation considering inland navigational environment," Proc. Inst. Mech. Eng. Part M J. Eng. Marit. Environ., vol. 235, no. 2, pp. 372–382, May 2021, doi: 10.1177/1475090220982414.

190. A. V. Goodchild and C. F. Daganzo, "Double-Cycling

Strategies for Container Ships and Their Effect on Ship Loading and Unloading Operations," Transp. Sci., vol. 40, no. 4, pp. 473–483, Nov. 2006, doi: 10.1287/trsc.1060.0148.

191. R. Adland, P. Cariou, H. Jia, and F.-C. Wolff, "The energy efficiency effects of periodic ship hull cleaning," J. Clean. Prod., vol. 178, pp. 1–13, Mar. 2018, doi: 10.1016/j.jclepro.2017.12.247.

192. A. Farkas, N. Degiuli, I. Martić, and M. Vujanović, "Greenhouse gas emissions reduction potential by using antifouling coatings in a maritime transport industry," J. Clean. Prod., vol. 295, p. 126428, May 2021, doi: 10.1016/j.jclepro.2021.126428.

193. Y. Zhu, Y. Zuo, and T. Li, "Modeling of Ship Fuel Consumption Based on Multisource and Heterogeneous Data: Case Study of Passenger Ship," J. Mar. Sci. Eng., vol. 9, no. 3, p. 273, Mar. 2021, doi: 10.3390/jmse9030273.

194. Y. Man, T. Sturm, M. Lundh, and S. N. MacKinnon, "From Ethnographic Research to Big Data Analytics—A Case of Maritime Energy-Efficiency Optimization," Appl. Sci., vol. 10, no. 6, p. 2134, Mar. 2020, doi: 10.3390/app10062134.

195. Ø. J. Rødseth, L. P. Perera, and B. Mo, "Big data in shipping-Challenges and opportunities," 2016.

196. J. L. and Y. N. M. Jeon, "A study on big data technology and collection, processing and analysis method for ship," in The Korean Society of Mechanical Engineers Annual Conference, Korea, pp. 3083–3085.

197. T. Varelas and S. Plitsos, "Real-Time Ship Management through the Lens of Big Data," in 2020 IEEE Sixth International Conference on Big Data Computing Service and Applications (BigDataService), 2020, pp. 142–147.

198. T. Anan, H. Higuchi, and N. Hamada, "New artificial intelligence technology improving fuel efficiency and reducing CO2 emissions of ships through use of operational big data," Fujitsu Sci. Tech. J, vol. 53, no. 6, pp. 23–28, 2017.

199. B. Mishachandar and S. Vairamuthu, "Diverse ocean noise classification using deep learning," Appl. Acoust., vol. 181, p. 108141, Oct. 2021, doi: 10.1016/j.apacoust.2021.108141.

200. H. P. Nguyen, P. Q. P. Nguyen, D. K. P. Nguyen, V. D. Bui, and D. T. Nguyen, "Application of IoT Technologies in Seaport Management," JOIV Int. J. Informatics Vis., vol. 7, no. 1, p. 228, Mar. 2023, doi: 10.30630/joiv.7.1.1697.

201. J. Chen, "IOT Monitoring System for Ship Operation Management Based on YOLOv3 Algorithm," J. Control Sci. Eng., vol. 2022, pp. 1–7, Jun. 2022, doi: 10.1155/2022/2408550.

202. C. Wang, J. Shen, P. Vijayakumar, and B. B. Gupta, "Attribute-Based Secure Data Aggregation for Isolated IoT-Enabled Maritime Transportation Systems," IEEE Trans. Intell. Transp. Syst., pp. 1–10, 2021, doi: 10.1109/TITS.2021.3127436.

203. L. P. Perera and B. Mo, "Machine intelligence based data handling framework for ship energy efficiency," IEEE Trans. Veh. Technol., 2017, doi: 10.1109/TVT.2017.2701501.

POLISH MARITIME RESEARCH 2 (118) 2023 Vol. 30; pp. 61-67
10.2478/pomr-2023-0021

HIGH QUALITY MULTI-ZONE AND 3D CFD MODEL OF COMBUSTION IN MARINE DIESEL ENGINE CYLINDER

Dominika Cuper-Przybylska [1]
Van Nhanh Nguyen [2]
Cao Dao Nam [3]
Jerzy Kowalski [4*]
[1] Central Office of Measures POLAND, Poland
[2] Institute of Engineering, HUTECH University, Ho Chi Minh City, Viet Nam
[3] Institute of Mechanical Engineering, Ho Chi Minh City University of Transport, Ho Chi Minh City, Viet Nam
[4] Gdansk University of Technology, Poland

* Corresponding author: *jerzy.kowalski@pg.edu.pl (J. Kowalski)*

ABSTRACT

The paper presents a 3D model of the processes taking place in the cylinder of a large 4-stroke marine engine. The model is based on CFD calculations performed on the moving mesh. The modelling range includes the full duty cycle (720° crankshaft position) and the complete geometry of the cylinder with inlet and exhaust ducts. The input data, boundary conditions and validation data were obtained by direct measurements on the real object. Fuel injection characteristics were obtained by Mie scattering measurements in a fixed-volume chamber. The modelling results have been validated in terms of the pressure characteristics of the engine's cylinder within the entire range of its loads. The mean error did not exceed 1.42% for the maximum combustion pressure and 1.13% for the MIP (Mean Indicated Pressure). The model was also positively validated in terms of the O_2 and NO_X content of the exhaust gas. The mean error in this case was 1.2% for NO_X fractions in the exhaust gas and 0.4% for O_2 fractions. The complete model data has been made available in the research data repository on an open access basis.

Keywords: CFD combustion model, large 4-stroke engine, diesel engine, emission, NO_X concentration

INTRODUCTION

Proper evaluation of the processes taking place in the piston engine cylinder is necessary for the design of structures with high energy and environmental performance. A mathematical model, the results of which are verified by real-world measurements, is used increasingly often. This model enables modification of the engine design to improve its performance without incurring significant financial expenses for experimental research. CFD models based on FEM are a common class of models used for this purpose and the use of these types of models in design is basically a standard. It should be noted, however, that the mathematical description of the phenomena occurring in the engine combustion chamber for the modelling of the exhaust gas composition is very complex. During the operation of the diesel engine, injection, spraying and evaporation of the fuel, fuel mixing with air, self-ignition, combustion and turbulent propagation of flame occur simultaneously in the combustion chamber. In addition, the thermodynamic conditions of these phenomena are determined by the movement of the piston, the movement of the valves and the exchange of heat with the engine components. Therefore, despite significant advances in information technology, such models are a kind of compromise between the simplicity of the model and the accuracy of the modelling results.

Because the modelling of the key phenomena requires considerable computer resources, combustion process models are often greatly simplified [1]. Unfortunately, the simplifications used so far to assess the composition of exhaust gases, such as the limitation of the size of the mesh [2], 0-, 1- and 2-dimensional

models [2–4], or the simplified description of combustion phenomena [5–6], etc., result in significant discrepancies between the calculation results and the values measured.

Due to limited computer resources, most of the research available in the literature concerns the design of engine sizes that are relatively small in relation to marine engines [7]. The design of marine engines is different from the design of small engines. The most important differences are the cubic capacity of 10–30 litres per cylinder, the speed below 1,500 rpm, the extended piston stroke, the high boost pressure, the start of ignition before the upper dead point of the piston, and the operation of the engine at a constant speed or according to the propeller characteristics [8].

These differences between relatively small engines and those used in shipbuilding produce significant changes in the measured thermodynamic parameters and in the composition of the exhaust gases. Sarvi *et al.* [9] presented an extensive study in which they set out the characteristics of exhaust gas emissions from a large medium-speed compression ignition engine with a design similar to that used in shipbuilding. According to their findings, an increase in engine load when operating at a constant speed results in a reduction in NO_X emissions. This trend is the inverse of the emission characteristics presented for a relatively small engine [10]. In both cases, a reduction in the engine speed resulted in an increase in NO_X emissions [11–13]. The marine engine load parameters, similar to fixed pitch propeller conditions, cause varied changes in NO_X emissions [14].

In principle, it is possible to find only relatively few 3D CFD models of the combustion processes taking place in piston engines with dimensions and thermodynamic parameters similar to marine engines. The author of [15] used a simplified 0-dimensional heat evolution model for a large-capacity 2-stroke engine. A multi-zone combustion model for a marine engine is also presented in [16], but it is not a model that reproduces the shape of the whole 3D combustion chamber. A model of mean values for a marine engine was presented by Alegret *et al.* [17] to assess the impact of the bypass valve and the EGR system on engine operation. On the other hand, comprehensive multidimensional models are available only for relatively small designs [18–19].

For these reasons, the aim of this study was to build 3D and CFD models of the phenomena occurring in the cylinder of a marine 4-stroke diesel engine for assessment of the composition of the exhaust gases. The presented model is unique in the research literature due to its complexity and suitability for the modelling of large marine engines. This model is available for use on an open access basis in the scientific data repository of Gdansk University of Technology [20].

EXPERIMENT – INPUT DATA AND DATA FOR MODEL VERIFICATION

To achieve our goal, input data needs to be collected to identify the model and to verify the modelling results. For this purpose, laboratory tests on a direct-injection 3-cylinder turbocharged 4-stroke diesel engine were carried out. The test bench layout is shown in Fig. 1 and the basic specifications of the Sulzer 3AL25/30 engine are provided in Table 1.

Tab. 1. Specifications of the Sulzer 3AL25/30 engine

Parameter	Unit	Value
MIP max	MPa	1.15
Speed	rpm	750
Number of cylinders	–	3
Bore	mm	250
Stroke	mm	300
Cylinder capacity	dm^3	14.7
Compression ratio	–	12.7
Injector		
Number of nozzles	–	9
Nozzles diameter	mm	0.325
Open pressure	MPa	25

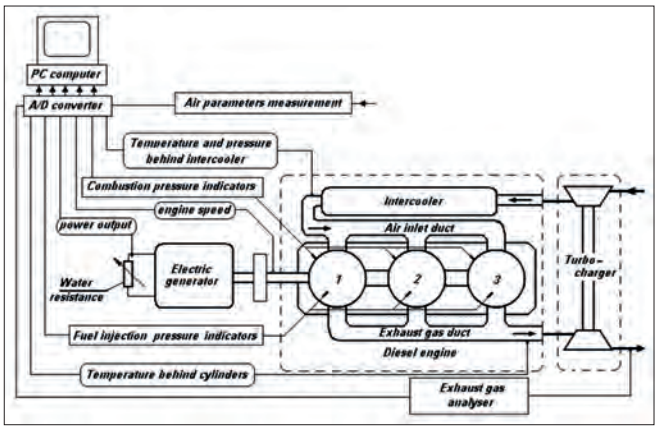

Fig. 1. Layout of the measuring station [21]

During the tests, the engine was charged using a generator electrically connected to a water resistor. A charge air cooler was also used. During the measurements the engine was powered by diesel oil of a known specification. The fuel apparatus of the engine consisted of mechanically controlled Bosch-type pumps combined with multiple-hole injectors. The engine design presented is commonly used on ships as the propulsion of generators or as the main propulsion of the ship together with the variable-pitch propeller [8]. Fifty-six laboratory station parameters were measured during the tests, including the engine speed and load, the speed of the turbocharger and the temperatures and pressures of the cooling water, lubricating oil, charge air, exhaust gas and fuel parameters. Exhaust gases were analysed using an electrochemical analyser with an infrared sensor to measure the CO_2 fractions. The air humidity, temperature, and pressure were also measured. The air flow rate was measured using a Venturi orifice to determine the emissions of exhaust gas ingredients. All these parameters were measured with a sampling time of 1 second. The engine cylinder pressure and fuel pressure in the fuel lines in front of the injectors were measured with a resolution equal to 0.5° of the rotation of the

crankshaft. Fuel consumption was measured by the volumetric method. A detailed description of the tests and their results can be found, e.g., in [21].

MODELLING

THE MOVING MESH

The building of the moving mesh of the engine cylinder requires a compromise between the accuracy of the representation of the phenomena occurring in the engine cylinder and the calculation time. Increasing the size of the finite volumes used in the mesh reduces the required processing power but also the accuracy of the modelling. This problem is particularly important in the case of modelling combustion processes in relatively large marine engines. Assuming that the mean diameter of the droplets of fuel injected into the cylinder is in the order of 10–50 μm [5] and that the cylinder diameter is 250 mm, it is necessary to create a moving mesh consisting of about 10^{15} finite volumes. This size, combined with the complexity of the phenomena occurring in the engine cylinders, would result in calculation times measured in weeks or months, however, even using the latest computation servers. Therefore, the number of finite elements was reduced to 10^6, which shortened the computation time for a single cycle of the 4-stroke engine (720° crankshaft position), using 32 CPU cores and 192 GB RAM, to about 500 hours. The mesh, presented schematically in the form of sections in Fig. 2, occupies a storage space exceeding 8 GB.

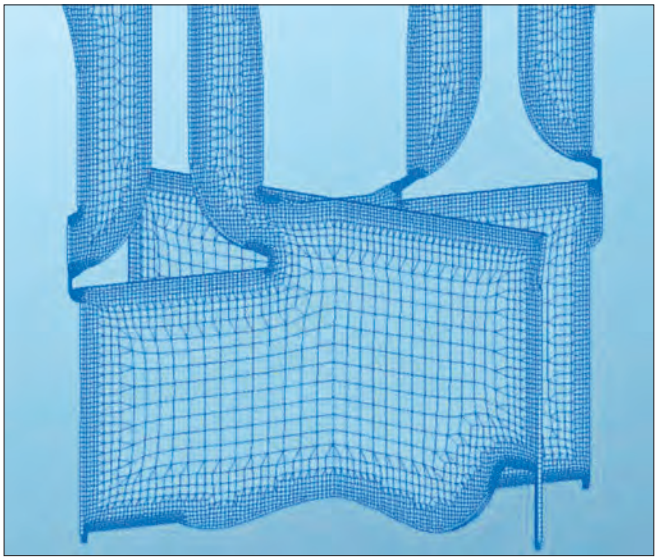

Fig. 2. Diagram of the moving mesh

To analyse the calculation time, three moving meshes were defined, from which the optimal solution was ultimately selected. The course of the mesh preparation is described in [22]. This mesh consists of 500,000 finite volumes for the combustion chamber and 1,500,000 finite volumes when the inlet and outlet ducts are opened during the modelling of the working medium replacement. The maximum finite volume size of 8 mm was used. In places where there was intensification of the modelled phenomena (fuel injection, ignition, high flow rate, turbulence, etc.), the size of the finite volumes was limited to 1–2 mm. The size of the finite volumes of the moving mesh also required a compaction to a dimension equal to 0.125 mm in the vicinity of the valve faces, at the time of opening and closing. Examples of the densities are shown in Fig. 3. This mesh allowed the full engine cycle to be calculated using 25,110 iterations. The mesh and the complete configuration files are provided in the open access data [20] and the calculation performance analysis using this grid in [22].

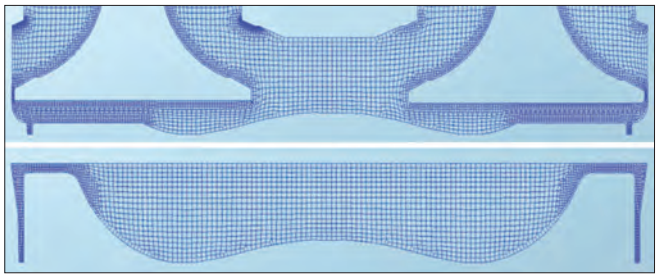

Fig. 3. Perpendicular sections in the mesh at the time of flushing

FUEL INJECTION

The building of the model of the delivery of fuel to the cylinder requires determination of the shape of the fuel jet and its quantitative characteristics.

The shape of the injected fuel jet was determined experimentally. The tests consisted in installing the injector in the fixed-volume chamber filled with nitrogen to the pressures of 3.2 and 4.3 MPa. These pressures correspond to the pressure in the engine cylinder at the start of the fuel injection for the minimum load and the maximum load, respectively. Fuel was delivered to the injector at a constant pressure of 50 MPa, with the injector opening pressure set at 25 MPa (see Table 1). The injection flow was recorded using the Mie scattering method [23–24] with a sampling rate of 40 kHz and a resolution of 512 x 256 pixels. The detailed course of the tests and the results are presented in [25].

The quantitative characteristics of the fuel injection depend on the injection start time and on its progress in time. In the classic self-ignition engine fuel apparatus design, the start of fuel injection into the cylinders is constant and depends on the angular position of the camshaft. This time was identified by determining the change in the fuel level in the transparent vertical tube mounted directly on the fuel pump during the slow rotation of the shaft. The reading was made with an accuracy of 0.5° of the crankshaft position. As a result of the observations made, the angle of the start of the fuel injection into the cylinders was set at 18° bTDC. The mass flow rate of the fuel injection into the cylinder was determined based on an analysis of the fuel pressure characteristics measured on the fuel lines before the injectors of the test facility. Assuming a constant flow rate from the nozzle, it can be assumed that the mass flow rate of the fuel is directly proportional to the pressure in the fuel line. This solution was proposed due to

the lack of technical possibilities to install an injector needle position sensor.

COMBUSTION

The fuel supplied to the engine cylinder is sprayed and evaporated. The WAVE model [26] along with the modification by Wakisaki [27] and Dukowicz's evaporation model [28] were used. The TAB [29], Chu [30] and FIPA [31] models were also taken into account but the verification of the calculation results led to their rejection.

Many models of combustion processes are described in the literature on the subject, but the most popular models in the last 15 years are based on Coherent Flame Models [32]. These models describe the combustion process on the assumption that the scale of the chemical reactions is many times smaller than the phenomena associated with the turbulent mass flow of the gas mixture in the engine cylinder. This assumption allows for a separate description of both phenomena. This approach was used by Colin and Benkenida [12]. The model modified by these authors, called the 3-Zones Extended Coherent Flame Model (ECFM-3Z or 3Z-ECFM), allows for correct combustion process modelling results for compression ignition engines. This model has been positively verified, e.g., in studies [33–38], and assumes that ignition and combustion take place in a certain volume containing a homogeneous mixture of fuel and air. The proportions of the mixture are determined based on the results of calculations using equations of the turbulent mixing of evaporated fuel with air and the resulting mixture with air and combustion products. This model also determines the delay of the self-ignition. The flame propagation in the combustion chamber is also described in the 3Z-ECFM model, with the flame areas being defined by the emission model based on fuel oxidation reactions.

Thus, in the proposed model, fuel with the accepted substitute composition of the $C_{13}H_{23}$ hydrocarbons, evaporating according to Dukowicz's model, is mixed with air in the cylinder space. The quantity and composition of the mixture in each finite volume of the moving mesh are calculated based on the averaged Navier–Stokes and flow continuity equations. The Reynolds Averaged Navier–Stokes equations (RANS) method was chosen due to its relatively short computation time. The k-zeta-f model proposed by Hanjalyc, Popovac and Hadziabdic in 2004 [39] was used to average the turbulent flow in the finite volumes. This iterative SIMPLE calculation algorithm [40] was used to correct the pressures in the finite volumes. Under-relaxation factors were selected for each of the balance equations considered and for each crankshaft position. The selection of these factors allowed for correct results in no more than 100 iterations for each equation, with an assumed calculation accuracy of 1%. Methods for solving first-order hyperbolic equations in the form of the "upwind" differential scheme [41] were used to calculate the energy balances and turbulent flows, and the central differential scheme [42] was applied to the calculation of the flow continuity equations. A variable calculation step was also defined. During the compression stroke the calculation step was equal to 1° of the crankshaft position. This step was reduced to 0.02° when the fuel was sprayed, ignited and when the outlet valve was opened.

This study used the combination of two NO_X formation mechanisms: Zeldowicz's thermal mechanism and Fenimore's mechanism of quick nitrogen oxides. Other NO_X formation mechanisms, including the mechanism of formation from the nitrogen contained in the fuel, were omitted due to the negligible nitrogen content in the fuel used.

HEAT EXCHANGE MODEL

The course of the phenomena occurring in the engine cylinders during the combustion process depends on the prevailing thermodynamic conditions. These, in turn, result from the combustion process itself and from the exchange of heat with the structural elements of the cylinders [43].

In the presented combustion process model, the heat transfer model is implemented into each finite volume located on the outer surfaces of the mobile mesh. Boundary conditions of the third type [44] were applied in the form of the determination of the heat flow rate through the structural components of the engine cylinder to the cooling system due to radiation and heat conduction. Fixed values for the heat take-over factor, $\alpha=3.5\bullet10^4$ W/(m²•K), thermal resistance, R=37 (m²•K)/W, and emissivity, $\varepsilon=0.79$, were adopted. It should be borne in mind that the values of these coefficients depend, inter alia, on the temperature of the combustion process, the specific heat and viscosity of the mixture in the cylinder, as well as the speed of flows. However, the introduction of these dependencies would require an additional iterative loop to be introduced into the calculation algorithm to determine the temperature of the cylinder walls. The result would be a significant increase in the computation time. The calculations described were done with the AVL Fire package.

The complete model data has been made available in the research data repository on an open access basis, as a tool to be used in research by a wide range of scientists [20].

MODELLING RESULTS AND VALIDATION

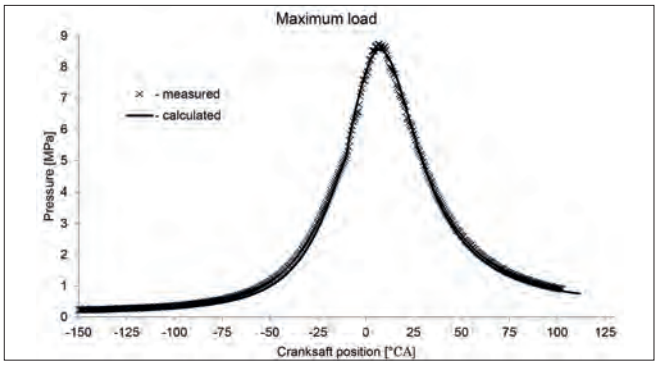

Fig. 4. Calculated combustion pressure and measured engine cylinder pressure for the maximum load

Fig. 4 illustrates an example of the combustion pressure characteristics in a cylinder, obtained by modelling and by direct measurements. The continuous line shows the results obtained by calculation. An example visualisation of the

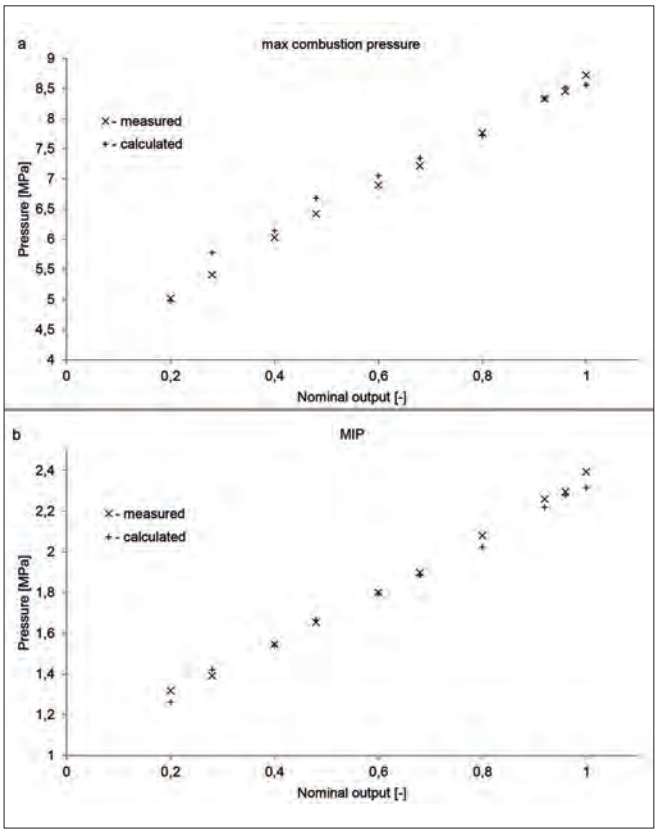

Fig. 5. Calculated and measured (a) max. pressure and (b) MIP in engine cylinders

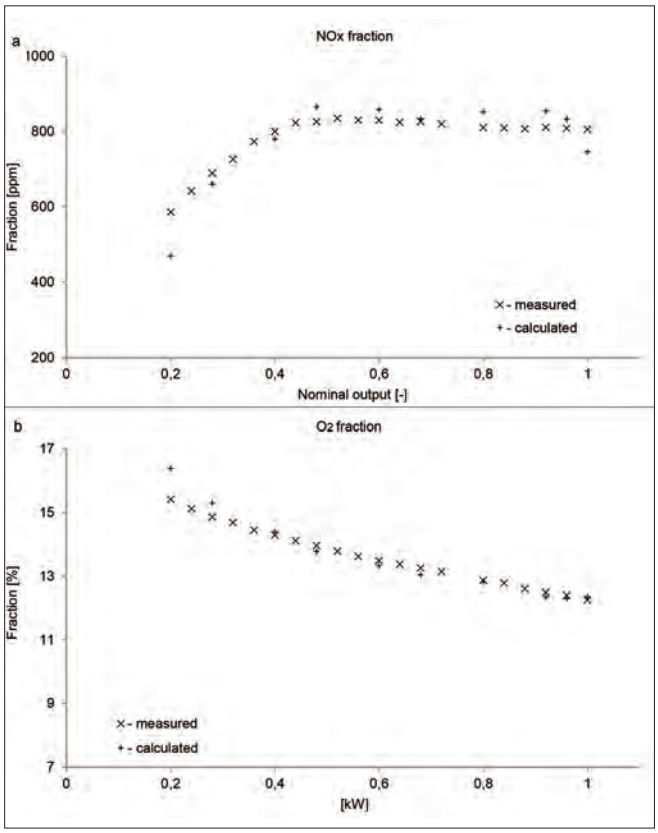

Fig. 6. Calculated and measured fractions of (a) NO_X and (b) O_2 in combustion gases

temperature distribution in the engine cylinder during fuel injection with a self-ignition focus is also shown. Fig. 5 presents the aggregate results of the calculations and measurements of the combustion pressure in the engine cylinders. A comparison was made between the calculated and measured MIP values and the maximum combustion pressure. According to the above results, the largest relative error for MIP, 4.3%, was achieved for a test facility load of 50 kW. The mean error in the values calculated in relation to the values measured for the entire load range considered for the test facility was 1.42% for the maximum pressure and 1.13 % for the MIP, respectively.

The results of the calculations obtained were also validated based on the composition of the exhaust gases emitted. Fig. 6 shows the results of the calculations and measurements of the NO_X and O_2 fractions in the exhaust gases of the test facility, being recognised as efficient. According to the results presented, the mean error in the values calculated in relation to the values measured for the whole engine load range equals 1.2% for the NO_X fractions in the exhaust gases and 0.4% for the O_2 fractions. It should be noted that, in this case too, the largest calculation errors were obtained for the minimum engine load considered.

The accuracy of the exhaust gas analyser measuring lines used in the experimental tests was used as a criterion for accepting the validation of the results for the NO_X and O_2 fractions. This accuracy is 5% of the indication for the NO_X probe and 0.2% of the absolute O_2 fractions in the exhaust gas. According to the considerations presented, the modelling results in Fig. 6 fall within the established validation criterion.

CONCLUSIONS

The aim of the study was to build a model of the combustion process of a 4-stroke marine engine. For this purpose, a moving mesh was built covering the cylinder space and the inlet and outlet ducts. The model is based on partial models including the WAVE fuel spraying model, Dukowicz's fuel evaporation model and the 3Z-ECFM combustion model. The initial and boundary conditions and data necessary for the validation of the calculation results were obtained by direct experimental measurements. As a result of the work carried out, it was possible to create a model mapping the fractions of NO_X and O_2 in exhaust gases.

The validation results presented allow the use of the resulting model to look for relations between the parameters of the combustion process in a 4-stroke marine engine and the composition of the exhaust gases. This model calculates the NO_X and O_2 fractions with an accurate quantitative analysis. According to the results presented, the mean error in the values calculated in relation to the values measured for the entire engine load range considered was 1.2% for the NO_X fractions in the exhaust gases and 0.4% for the O_2 fractions. The model has also been successfully validated in terms of the pressure characteristics of the engine cylinder during the combustion process. The complete model data has been made available in the research data repository on an open access basis, as a tool to be used in research by a wide range of scientists.

CREDITS

The work was supported by AVL, the FIRE software developer, under the "University Partnership" affiliate program.

REFERENCES

1. M. H. Ghaemi, "Performance and emission modelling and simulation of marine diesel engines using publicly available engine data," *Polish Maritime Research*, vol. 28(4), pp. 63–87, 2021. https://doi.org/10.2478/pomr-2021-0050

2. J. Shu, J. Fu, J. Liu, Y. Ma, S. Wang, B. Deng, and D. Zeng, "Effects of injector spray angle on combustion and emissions characteristics of a natural gas (NG)-diesel dual fuel engine based on CFD coupled with reduced chemical kinetic model," *Applied Energy*, vol. 233–234, pp. 182–195, 2019. https://doi.org/10.1016/j.apenergy.2018.10.040

3. T. Poinsot and D. Veynante, *Theoretical and numerical combustion*. Edwards, 2005.

4. F. Payri, P. Olmeda, J. Martín, and A. García, "A complete 0D thermodynamic predictive model for direct injection diesel engines," *Applied Energy*, vol. 88, pp. 4632–4641, 2011. https://doi.10.1016/j.apenergy.2011.06.005

5. K. K. Kuo, *Principles of combustion*. New Jersey, Wiley, 2005.

6. S. Wang and L. Yao, "Effect of engine speeds and dimethyl ether on methyl decanoate HCCI combustion and emission characteristics based on low-speed two-stroke diesel engine," *Polish Maritime Research*, vol. 27(2), pp. 85–95, 2020. https://doi.org/10.2478/pomr-2020-0030

7. H. Eichlseder and A. Wimmer, "Potential of IC-engines as minimum emission propulsion system," *Atmos. Environ.*, vol. 37(37), pp. 5227–5236, 2003. https://doi.org/10.1016/j.atmosenv.2003.05.001

8. J. Carlton, *Marine Propellers and Propulsion*, 3rd ed. Elsevier Ltd., 2012.

9. A. Sarvi, C. J. Fogelholm, and R. Zevenhoven, "Emissions from large-scale medium-speed diesel engines: 1. Influence of engine operation mode and turbocharger," *Fuel Processing Technology*, vol. 89, pp. 510–519, 2008. https://doi.org/10.1016/j.fuproc.2007.10.006

10. D. Agarwal, S. K. Singh, and A. K. Agarwal, "Effect of exhaust gas recirculation (EGR) on performance, emissions, deposits and durability of a constant speed compression ignition engine," *Applied Energy*, vol. 88, pp. 2900–2907, 2011. https://doi.org/10.1016/j.apenergy.2011.01.066

11. A. Sarvi, C. J. Fogelholm, and R. Zevenhoven, "Emissions from large-scale medium-speed diesel engines: 2. Influence of fuel type and operating mode," *Fuel Processing Technology*, vol. 89, pp. 520–527, 2008. https://doi.org/10.1016/j.fuproc.2007.10.005

12. O. Colin and A. Benkenida, "The 3-zones extended coherent flame model (ECFM3Z) for computing premixed/diffusion combustion," *Oil & Gas Science and Technology*, vol. 59(6), pp. 593–609, 2004. https://doi.org/10.2516/ogst:2004043

13. C. Rodriguez, M. Lamas, J. Rodriguez, and A. Abbas, "Analysis of the pre-injection system of a marine diesel engine through multiple-criteria decision-making and artificial neural networks," *Polish Maritime Research*, vol. 28(4), pp. 88–96, 2021. https://doi.org/10.2478/pomr-2021-0051

14. Z. Korczewski, "Test method for determining the chemical emissions of a marine diesel engine exhaust in operation," *Polish Maritime Research*, vol. 28(3), pp. 76–87, 2020. https://doi.org/10.2478/pomr-2021-0035

15. Z. Yang, Q. Tan, and P. Geng, "Combustion and emissions investigation on low-speed two-stroke marine diesel engine with low sulfur diesel fuel," *Polish Maritime Research*, vol. 26(1), pp. 153–161, 2011. https://doi.org/10.2478/pomr-2019-0017

16. R. Zhao, L. Xu, X. Su, S. Feng, C. Li, Q. Tan, and Z. Wang, "A numerical and experimental study of marine hydrogen–natural gas–diesel tri-fuel engines," *Polish Maritime Research*, vol. 27(4), pp. 80–90, 2020. https://doi.org/10.2478/pomr-2020-0068

17. G. Alegret, X. Llamas, M. Vejlgaard-Laursen, and L. Eriksson, "Modeling of a large marine two-stroke diesel engine with cylinder bypass valve and EGR system," *IFAC-PapersOnLine*, vol. 48(16), pp. 273–278, 2015. https://doi.org/10.1016/j.ifacol.2015.10.292

18. F. Payri, J. Benajes, X. Margot, and A. Gil, "CFD modeling of the in-cylinder flow in direct-injection diesel engines," *Computers & Fluids*, vol. 33, pp. 995–1021, 2004. https://doi.org/10.1016/j.compfluid.2003.09.003

19. Z. Sahin and O. Durgun, "Multi-zone combustion modeling for the prediction of diesel engine cycles and engine performance parameters," *Applied Thermal Engineering*, vol. 28, pp. 2245–2256, 2008. https://doi.org/10.1016/j.applthermaleng.2008.01.002

20. J. Kowalski, *Complete input data to CFD 3D model of combustion in the large marine 4-stroke engine*, 2018. [Dataset]. https://doi.org/10.34808/0kbc-ny83.

21. J. Kowalski, "An experimental study of emission and combustion characteristics of marine diesel engine with fuel pump malfunctions," *Appl. Therm. Eng.*, vol. 65(1–2), pp. 469–79, 2014. https://doi.org/10.1016/j.applthermaleng.2014.01.028

22. J. Kowalski and P. Jaworski, "3D mesh model for RANS numerical research on marine 4-stroke engine," *Journal of Polish CIMAC*, vol. 9(1), pp. 87–94, 2014.

23. S. N. Soid and Z. A. Zainal, "Spray and combustion characterization for internal combustion engines using optical measuring techniques – A review," Energy, vol. 36(2), pp. 724–741, 2011. https://doi.org/10.1016/j.energy.2010.11.022

24. E. Delacourt, B. Desmet, and B. Besson, "Characterisation of very high pressure diesel sprays using digital imaging techniques," *Fuel*, vol. 84(7–8), pp. 859–867, 2005. https://doi.org/10.1016/j.fuel.2004.12.003

25. J. Grochowalska, J. Kowalski, Ł. J. Kapusta, and P. Jaworski, *The experimental results of diesel fuel spray with marine engine injector*, 2021. [Dataset]. https://doi.org/10.34808/c3aw-dq41.

26. A. B. Liu and R. D. Reitz, *Modeling the Effects of Drop Drag and Break-up on Fuel Sprays*. SAE Technical Paper. 1993; 930072.

27. T. Wakisaka et al., *Numerical Prediction of Mixture Formation and Combustion Processes in Premixed Compression Ignition Engines*. COMODIA, 2001.

28. J. K. Dukowicz, *Quasi-steady droplet change in the presence of convection*. Informal Report, Los Alamos Scientific Laboratory, LA7997-MS.

29. P. O'Rourke and A. Amsden, *The TAB Method for Numerical Calculation of Spray Droplet Breakup*. SAE Technical Paper, 1987, 872089.

30. C. C. Chu and M. L. Corradini, "One-dimensional transient fluid model for fuel/coolant interaction analysis," *Nuclear Science and Engineering*, vol. 101, pp. 48–71, 1989.

31. C. Habchi and D. Verhoeven, *Modeling Atomization and Break Up in High-Pressure Diesel Sprays*. SAE Technical Paper, 1997, 970881.

32. F. E. Marble and J. E. Broadwell, *The Coherent Flame Model for Turbulent Chemical Reactions*. Technical Report TRW-29314-6001-RU-00, USA, 1977.

33. R. Mobasheri, Z. Peng, and S. M. Mirsalim, "Analysis the effect of advanced injection strategies on engine performance and pollutant emissions in a heavy duty DI-diesel engine by CFD modeling," *International Journal of Heat and Fluid Flow*, vol. 33, pp. 59–69, 2012. https://doi.org/10.1016/j.ijheatfluidflow.2011.10.004

34. R. Mobasheri and Z. Peng, "CFD investigation into diesel fuel injection schemes with aid of homogeneity factor," *Computers & Fluids*, vol. 77, pp. 12–23, 2013. https://doi.org/10.1016/j.compfluid.2013.02.013

35. H. Taghavifar, S. Khalilarya, and S. Jafarmadar, "Engine structure modifications effect on the flow behavior, combustion, and performance characteristics of DI diesel engine," *Energy Conversion and Management*, vol. 85, pp. 20–32, 2014. https://doi.org/10.1016/j.enconman.2014.05.076

36. S. Jafarmadar, "Exergy analysis of hydrogen/diesel combustion in a dual fuel engine using three-dimensional model," *International Journal of Hydrogen Energy*, vol. 39, pp. 9505–9514, 2014. https://doi.org/10.1016/j.ijhydene.2014.03.152

37. W. Park, J. Lee, K. Min, J. Yu, S. Park, and S. Cho, "Prediction of real-time NO based on the in-cylinder pressure in diesel engines," in *Proc. of the Combustion Institute*, vol. 34, pp. 3075–3082, 2013. https://doi.org/10.1016/j.proci.2012.06.170

38. R. Lebas, T. Menard, P. A. Beau, A. Berlemont, and F. X. Demoulin, "Numerical simulation of primary break-up and atomization: DNS and modelling study," *International Journal of Multiphase Flow*, vol. 35, pp. 247–260, 2009. https://doi.org/10.1016/j.ijmultiphaseflow.2008.11.005

39. K. Hanjalić, M. Popovac, and M. Hadžiabdić, "A robust near-wall elliptic relaxation eddy-viscosity turbulence model for CFD," *International Journal of Heat and Fluid Flow*, vol. 25(6), pp. 1047–1051, 2004. https://doi.org/10.1016/j.ijheatfluidflow.2004.07.005

40. B. Kaludercic, "Parallelisation of the Lagrangian model in a mixed Eulerian–Lagrangian CFD algorithm," *J. Parallel Distrib. Comput.*, vol. 64(2), pp. 277–284, 2004. https://doi.org/10.1016/j.jpdc.2003.11.010

41. J. Donea and A. Huerta, *Finite Element Methods for Flow Problems*. Wiley, 2003.

42. R. W. Lewis, P. Nithiarasu, and K. N. Seetharamu, *Fundamentals of the Finite Element Method for Heat and Fluid Flow*. Wiley, 2004.

43. R. J. Goldstein, W. E. Ibele, and S. V. Patankar, "Heat transfer – A review of 2003 literature," *Int. J. Heat Mass Transf.*, vol. 49(3–4), pp. 451–534, 2006. https://doi.org/10.1016/j.ijheatmasstransfer.2005.11.001

44. F. P. Incropera and D. P. DeWitt, *Fundamentals of Heat and Mass Transfer*. Wiley, 2001.

POLISH MARITIME RESEARCH 2 (118) 2023 Vol. 30; pp. 68-75
10.2478/pomr-2023-0022

INVESTIGATION OF THE EFFICIENCY OF A DUAL-FUEL GAS TURBINE COMBUSTION CHAMBER WITH A PLASMA-CHEMICAL ELEMENT

Serhiy Serbin [1*]
Badri Diasamidze [1]
Marek Dzida [2]
Daifen Chen [3]
[1] Admiral Makarov National University of Shipbuilding, Mikolayiv, Ukrain
[2] Gdansk University of Technology, Poland
[3] Jiangsu University of Science and Technology, Zhenjiang, China

* Corresponding author: *serbin1958@gmail.com (Serhiy Serbin)*

ABSTRACT

The study is devoted to the possibility of increasing the efficiency of the working process in dual-fuel combustion chambers of gas turbine engines for FPSO vessels. For the first time, it is proposed to use the advantages of plasma-chemical intensification of the combustion of hydrocarbon fuels in the dual-fuel combustion chambers, which can simultaneously operate on gaseous and liquid fuels. A design scheme of a combustion chamber with a plasma-chemical element is proposed. A continuous type mathematical model of a combustion chamber with a plasma-chemical element has been developed, which is based on the solution of a system of differential equations describing the processes of chemical reactions in a turbulent system, taking into consideration the initiating effect of the products of plasma-chemical reactions on the processes of flame propagation. A modified six-stage kinetic scheme of hydrocarbon oxidation was used to simultaneously predict the combustion characteristics of the gaseous and liquid fuels, taking into account the decrease in the activation energy of carbon monoxide oxidation reactions when the products of the plasma-chemical element are added. The results reveal that the addition of plasma-chemical products significantly reduces CO emissions in the outlet section of the flame tube (from 25-28 ppm to 3.9-4.6 ppm), while the emission of nitrogen oxides remains practically unchanged for the studied combustion chamber. Further research directions are proposed to enhance the working process efficiency of a dual-fuel combustion chamber for gas turbine engines as part of the power plant of FSPO vessels.

Keywords: gas turbine engine; power plant; dual-fuel combustion; combustion chamber; liquid and gaseous fuels, plasma-assisted combustion

INTRODUCTION

Contemporary challenges have led to increased research and development of marine infrastructure, particularly related to FPSO vessels [1-3]. The use of gas turbine engines on such vessels [4-6] has emerged as a promising approach to improving their technical and economic performance. Previous studies [7-8] have shown that the simultaneous operation of gas turbine engines with fuels differing in phase state is possible, and the problems arising during the simultaneous operation of low-emission gas turbine combustion chambers on different fuels have been identified. To address these problems, the plasma-chemical method of combustion intensification [9-10] offers a promising way to improve the efficiency of using various hydrocarbon fuels. Several studies [11-12] have shown the benefits of this approach, including an extended range of stable operation, increased completeness of fuel combustion, reduced non-uniformity of temperature fields at the outlet of the combustion chamber, and reduced emissions of toxic components [13-14].

The method of plasma-chemical burning of fuels in the combustion chambers of heat engines [15-17] is implemented by systems containing low-temperature plasma generators (plasma torches), power sources, devices for supplying plasma gas, fuel, means of regulating and controlling parameters and operating modes. The key elements of the systems are plasma torches, or plasma-chemical elements developed on their basis, plasma-fuel nozzles, plasma-chemical generators of hydrogen-containing gas, and plasma igniters. Moreover, in [18], the results of research on plasma-fuel nozzles are presented, showing a significant reduction in nitrogen oxide emissions during the combustion of a fuel-air mixture in an experimental reverse-vortex combustion chamber, as well as the possibility of expanding the range of stable operation of the chamber as a result of plasma assistance.

The set of studies carried out in [19, 20] on increasing the efficiency of gas turbine engines made it possible to create systems of plasma-chemical ignition and combustion, which significantly increase the reliability of starting power plants, increase the completeness of combustion of hydrocarbon fuels, and also reduce the emission of carcinogenic substances. The plasma-chemical combustion intensification system is designed for flame stabilisation in devices for fuel burning (gaseous, liquid, alternative) and consists of a plasma-chemical element and its energy supply source. When fuel is fed into the plasma air jet, thermochemical reactions occur, which determine a significant yield of active components (radicals, atoms, intermediate compounds).

The completed works on the creation of plasma-chemical systems allowed us to carry out experimental and industrial testing of several systems of plasma-chemical combustion intensification for energy equipment. It was found that similar systems provide a 2-3 times expansion of the range of stable ignition and burning of fuel in the combustion chamber even when using liquid fuel, increase the stability of combustion in transient modes, increase the completeness of combustion during the start-up process, improve the flame propagation conditions, increase the reliability of operation, and prevent combustion chamber extinction during operation [10, 19].

The reactions that occur when mixing low-temperature air plasma with fuel in the volume of a plasma-chemical element or on the surface of a swirling plasma jet under certain conditions lead to the formation of over-equilibrium concentrations of atoms and radicals (H, CH_3, O, OH, etc.) and a large number of products of incomplete conversion of hydrocarbons (CO, H_2). Reaction products from the zone of direct contact of the plasma with part of the fuel quickly diffuse into the zone of the main fuel-air mixture and contribute to the intensification of its combustion.

The current level of development of low-current plasma generators of direct current (arc current less than 2 A) makes it possible to use their advantages (long service life of electrodes, no need for their water cooling, significant thermal efficiency, small dimensions, the possibility of working at high pressure) to increase the efficiency of dual-fuel combustion chambers.

An innovative approach to the implementation of reliable ignition of various fuels in any conditions, including starting at high pressures, smooth adjustment of the air excess coefficient, temperature, and thermal power, flameout prevention, the use of gaseous and liquid fuels, including with high moisture content, allows plasma-chemical devices with low-current plasma generators to be considered as promising for dual-fuel combustion chambers of gas turbine engines.

Therefore, the purpose of the work is to increase the efficiency of a gas turbine dual-fuel combustion chamber, intended for operation as part of the power plant of an FPSO vessel, through the use of a plasma-chemical element.

MATHEMATICAL MODELLING

In recent years, several studies have investigated various aspects of the modelling and thermodynamic analysis of the effects of low-temperature plasma on combustion processes, specifically for gaseous fuels [21], liquid hydrocarbons [22], and coal [23]. However, these studies have primarily focused on fuel-burning devices operating on a single fuel type. To theoretically analyse the combustion processes of liquid and gaseous fuels and the effects of air plasma on the physicochemical mechanisms in dual-fuel gas turbine combustion chambers, a three-dimensional modelling method was employed. This method considered the mechanisms of plasma-chemical combustion intensification for hydrocarbon fuels that vary in physical state. A continuum-type mathematical model was developed, which describes the laws of mass, energy, momentum, and chemical component conservation and transfer in a chemically reacting turbulent two-phase system. It is worth noting that this model enables numerical experiments to be conducted with virtual models of fuel combustion devices and provides new insights into the structure of turbulent flows under non-isothermal conditions, turbulent pulsations, plasma activation, and complex geometric shapes of dual-fuel combustion chambers. For modelling of the physical and chemical processes inside the dual-fuel combustion chamber with plasma assistance, a generalised method based on a numerical solution of the combined conservation and transport equations for a multi-component chemically reactive turbulent system was employed [9-16]. This method provides a procedure for numerical integration of the differential equations, which describe the reacting viscous gas flows. A 3D model of the reacting flows has been used which enables the prediction of the plasma-chemical influence and optimisation parameters taking into consideration mixing, turbulence, radiation, and combustion features [24-26].

The mass conservation equation may be represented as follows:

$$\frac{\partial \rho}{\partial t} + \nabla(\rho \vec{v}) = S_m , \tag{1}$$

where ρ is the flow mass density, ρ is the local flow velocity vector, and S_m is the mass added to the continuous phase from the dispersed second phase.

The momentum conservation equation in a fixed system of reference may be formed as follows:

$$\frac{\partial}{\partial t}(\rho \vec{v}) + \nabla(\rho \vec{v}\vec{v}) = -\nabla p + \nabla \cdot (\tau_{st}) + \rho \vec{g} + \vec{F} , \tag{2}$$

where p is the static pressure, τ_{st} is the stress tensor, and $\rho\vec{g}$ and $\vec{F}$ are the gravitational and external body forces, respectively.

For aerodynamic prediction, the RNG-based k-ε-turbulence model was used [27].

In a general form, the energy conservation equation is written as follows:

$$\frac{\partial}{\partial t}(\rho E) + \nabla\cdot\left(\vec{v}\,(\rho E + p)\right) = \nabla\cdot\left(k_{eff}\,\nabla T - \Sigma_j \vec{J}_j + (\bar{\bar{\tau}}_{eff}\cdot\vec{v})\right) + S_h\,, \quad (3)$$

where E is the total energy, k_{eff} is the effective conductivity, $\vec{J}_j$ is the diffusion flux of species j, and $\bar{\bar{\tau}}_{eff}$ is the effective viscosity coefficient. The term S_h includes the heat of the chemical reaction inside the combustion chamber, and any other volumetric heat sources.

For the liquid fuel burning calculations in the dual-fuel combustion chamber, the coupled discrete phase model (DPM) was used. The Lagrangian discrete phase model [22, 28, 29] follows the Euler–Lagrange approach. The fluid phase is treated as a continuum by solving the time-averaged Navier–Stokes equations, while the dispersed phase is solved by tracking a large number of droplets through the calculated flow field. The coupling between the phases and their impact on both the discrete phase trajectories and the continuous phase flow has been included.

This force balance equates the particle inertia with the forces acting on the particle and can be written (for the direction in Cartesian coordinates) as

$$\frac{du_p}{dt} = F_D(u - u_p) + \frac{g_x(\rho_p - \rho)}{\rho_p} + F_x\,, \quad (4)$$

where F_x is the additional acceleration term, $F_D(u - u_p)$ is the drag force per unit particle mass, and

$$F_D = \frac{18_\mu}{\rho_p d_p^2}\frac{C_D Re}{24}\,.$$

Here, u is the fluid phase velocity, u_p is the particle velocity, μ is the molecular viscosity of the fluid, ρ is the fluid density, ρ_p is the density of the particle, d_p is the particle diameter, and Re is the relative Reynolds number.

The inert heating model is applied when a particle temperature is less than the vaporisation temperature and after the volatile fraction of the particle has been consumed. This procedure uses a simple heat balance to relate the particle temperature to the convective heat transfer and the absorption/emission of radiation at the particle surface:

$$m_p c_p \frac{dT_p}{dt} = hA_p(T_\infty - T_p) + \varepsilon_p A_p \sigma(\theta_R^4 - T_p^4)\,, \quad (5)$$

where m_p is the mass of the particle, c_p is the heat capacity of the particle, A_p is the surface area of the particle, T_∞ is the local temperature of the continuous phase h is the convective heat transfer coefficient, ε_p is the particle emissivity, σ is the Stefan–Boltzmann constant, and θ_R is the radiation temperature.

The droplet vaporisation model is initiated when the temperature of the droplet reaches the vaporisation temperature and continues until the droplet reaches the boiling point T_{bp}.

Heat transfer to the particle during the vaporisation process includes contributions from convection, radiation, and the heat value consumed during vaporisation:

$$m_p c_p \frac{dT_p}{dt} = hA_p(T_\infty - T_p) + \frac{dm_p}{dt} h_{fg} + \varepsilon_p A_p \sigma(\theta_R^4 - T_p^4)\,, \quad (6)$$

where h_{fg} is the latent heat.

The mass of the droplet is reduced according to the equation

$$m_p(t + \Delta t) = m_p(t) - \dot{N}_{Mi} A_p M_{w,i}\,\Delta t, \quad (7)$$

where is the molecular weight of species .

The rate of vaporisation is governed by gradient diffusion with the flux of droplet vapour into the gas phase

$$\dot{N}_{Mi} = k_c(C_{i,S} - C_{i,\infty})\,, \quad (8)$$

where $\dot{N}_{Mi}$ is the molar flux of the vapour, k_c is the mass transfer coefficient, $C_{i,S}$ is the vapour concentration at the droplet surface, and $C_{i,\infty}$ is the vapour concentration in the bulk gas.

When the droplet temperature reaches the boiling point, a boiling rate equation is applied:

$$-\frac{d(d_p)}{dt} = \left[\frac{2k_\infty[1 + 0.23\sqrt{Re_d}]}{d_p}(T_\infty - T_p) + \varepsilon_p\sigma(\theta_R^4 - T_p^4)\right]. \quad (9)$$

The particle size distribution after injection of a liquid fuel is defined by fitting the size distribution data to the Rosin–Rammler equation. The Rosin–Rammler distribution function is based on the assumption that an exponential relationship exists between the droplet diameter d and the mass fraction of droplets with diameter greater than d:

$$Y_d = e^{-(d/\bar{d})^n}, \quad (10)$$

where $\bar{d}$ is the size constant and n is the size distribution parameter.

The boundary conditions in the combustion chamber inlets, symmetry axes, walls, and outlet were set in accordance with the conditions for carrying out physical experiments and recommendations for modelling the turbulent burning processes. The method for the system solution of Eqs. (1)–(10), the finite difference scheme, and the solution stability analysis are explained in detail in [30].

Note that the acts of chemical transformation in the combustion chamber occur when molecules collide, while their kinetic energy turns into potential energy and is spent on breaking the bonds in the molecules. However, bond destruction will occur only when the value of the potential energy exceeds a certain limit – the activation energy E. Not all collisions in which the energy exceeds the activation energy lead to a chemical reaction. For this, the appropriate orientation of the molecules among themselves is also necessary. Thus, activation involves the conversion of an average molecule into an active molecule. The smaller the value of E, the higher the reaction rate usually is [31].

The uniqueness of the chain reactions occurring within combustion chambers lies in their multi-step transformation process, leading to the production of various intermediate products such as atomic fragments, radicals, intermediate compounds, etc. It is worth noting that one of the factors of the plasma-chemical impact on hydrocarbon oxidation processes

is the formation of a large number of intermediate and unstable compounds in the process of plasma activation. The addition of plasma-chemical products to the primary zone of the gas turbine combustion chamber leads to a decrease in the activation energy of the hydrocarbon oxidation reactions. As a result, there is a change in the distribution of the flow parameters inside the burning device [19, 20]. Based on the data presented in [19], a correlation was deduced to quantify the effect of the amount of plasma-chemical products β (by volume) on the reduction of the activation energy ΔE for the resulting reaction between the fuel and oxidiser, as depicted in Fig. 1.

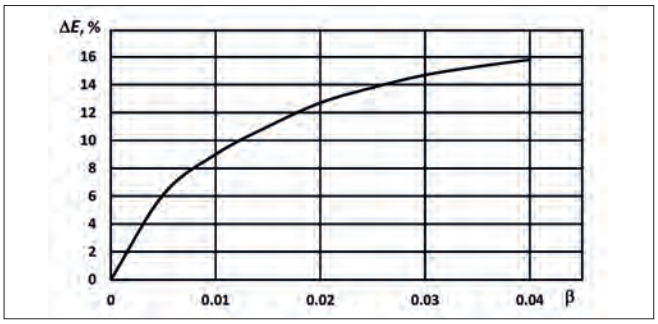

Fig. 1. Dependence of the decrease in the activation energy of the hydrocarbon oxidation reaction on the amount of plasma-chemical products β (by volume)

Approximation of this graphic dependence made it possible to obtain the following formula for reducing the activation energy ΔE depending on the amount of additives (by volume) of plasma-chemical products (reliability of approximation $R^2 = 0.996$):

$$\Delta E = 3.87 \cdot 10^5 \beta^3 - 3.51 \cdot 10^4 \beta^2 + 1.17 \cdot 10^3 \beta + 0.363. \quad (11)$$

This dependence was used when performing three-dimensional calculations of the parameters of a dual-fuel combustion chamber, taking into consideration plasma activation.

To simulate the hydrocarbon oxidation processes in a dual-fuel combustion chamber with plasma assistance, a six-stage burning scheme was used that simulates the oxidation processes of light distillate fuel ($C_{16}H_{29}$) and gaseous methane CH_4 [7, 32]. The simplified kinetic mechanism of combustion is as follows:

$$2C_{16}H_{29} + 16O_2 \rightarrow 32CO + 29H_2;$$
$$2H_2 + O_2 \rightarrow 2H_2O;\ CO + O_2 \rightarrow 2CO_2;$$
$$2H_2O \rightarrow 2H_2 + O_2;\ 2CO_2 \rightarrow 2CO + O_2;$$
$$2CH_4 + O_2 \leftrightarrow 2CO + 4H_2O.$$

Eqs. (1)-(10) represent a closed system that, under appropriate initial conditions and known characteristics of the gaseous and liquid phases, determines the distribution of the parameters inside the volume of a dual-fuel combustion chamber and the change in time of the transport characteristics of liquid fuel droplets.

STUDY OF THE PARAMETERS OF A DUAL-FUEL COMBUSTION CHAMBER WITH A PLASMA-CHEMICAL ELEMENT

The design scheme of the combustion chamber of a 25 MW gas turbine produced by the "Zorya"-"Mashproekt" research and production complex (Mykolaiv, Ukraine) with a modified front-end device and an installed plasma-chemical element is shown in Fig. 2.

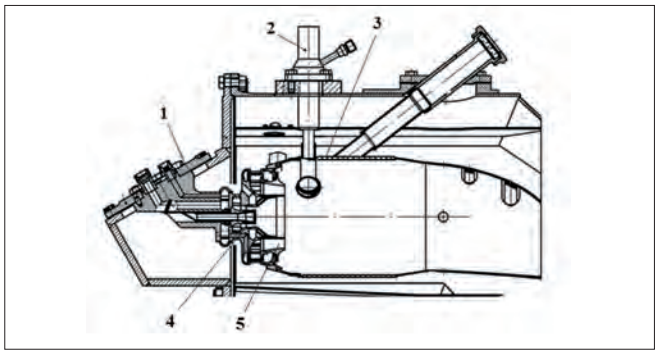

Fig. 2. Location of a plasma-chemical element in the low-emission combustion chamber: 1 – burner device; 2 – plasma-chemical element; 3 – flame tube; 4 – internal radial swirler; 5 – external radial swirler

Compared with the serial combustion chamber, the following design changes are proposed:

1. For more convenient installation, the plasma-chemical element is installed on the outer body of the combustion chamber, and the products of the plasma-chemical transformations are fed into the primary zone of the combustion chamber through the openings of the flame transfer pipes.
2. The supply of liquid fuel to the channels of the internal and external swirlers of the flame tube is carried out via a total of 30 tubes or nozzles, which are evenly distributed throughout the channels of the swirlers.
3. The film cooling system of the serial flame tube is replaced by a convective one, which allows the relative air consumption for cooling the flame tube to be reduced by 1-1.5% [16].

Table 1 presents the initial parameters of a dual-fuel combustion chamber.

Tab. 1. Input parameters for calculating the combustion chamber in nominal mode

Parameter	Value
1. Airflow through the flame tube, kg/s	4.355
2. Average pressure at the outlet of the high-pressure compressor, Pa	2052300
3. Air temperature at the inlet of the chamber, K	770
4. Temperature of the gaseous fuel at the inlet of the chamber, K	288
5. Temperature of the diesel fuel at the inlet of the chamber,	313

The flow rate of plasma-forming air supplied through the plasma-chemical element is 0.5-1.0 g/s and the average temperature of the plasma jet is 2500-4000 K (depending on the electrical power consumed). Inside the plasma-chemical element, a re-enriched fuel-air mixture is provided with air excess coefficients of 0.2-0.4.

To determine the influence of a plasma-chemical element on the characteristics of a dual-fuel gas turbine combustion chamber, calculations of the fuel combustion and emissions of the main pollutants (NO and CO) were carried out for three different modes of fuel supply (1, 2 and 3 in Table 2), which correspond

to the following distributions of the mass consumption of hydrocarbons: mode 1 - 50% liquid and 50% gaseous, mode 2 - 70% liquid and 30% gaseous, mode 3 - 100% liquid. The effect of the plasma-chemical products added to the primary zone of the combustion chamber was analysed, varying the quantity β: 0 (without additives), 0.005, 0.01, 0.015, and 0.02. These quantities correspond to a reduction in the activation energy of the hydrocarbon oxidation reactions by 0%, 6%, 9%, 11%, and 12%, respectively (refer to Fig. 1).

Tab. 2. Fuel consumption through the flame tube for the investigated modes of fuel supply

Mode of operation	Fuel consumption through the flame tube, kg/s			
	Gaseous fuel		Liquid fuel	
	External swirler	Internal swirler	External swirler	Internal swirler
1	0.0472	0.00248	0.00314	0.000165
2	0.0283	0.00149	0.00440	0.000232
3	0	0	0.0944	0.00497

The results of numerical modelling of the processes in a dual-fuel low-emission combustion chamber showed that the addition of plasma-chemical products positively affects the nature of the fuel combustion along the flame tube. The most rational - from the point of view of the energy consumption for the functioning of the plasma system - are the modes of operation at $\beta = 0.01$ and 0.015.

Figs. 2-3 present the temperature distribution of the combustion products in the outlet section of the flame tube for two typical fuel supply modes 3 and 1, respectively. It can be seen that, with the addition of the plasma-chemical products, the average integral temperature of the outlet gases practically does not change.

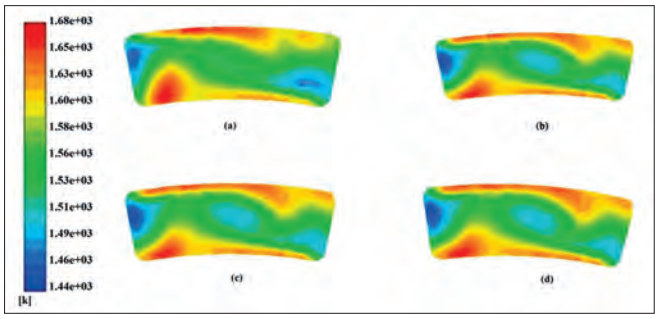

Fig. 2. Distribution of temperatures (K) in the outlet section for the third mode of fuel supply: a – the basic variant without additions of plasma-chemical products; b – β = 0.005; c –β = 0.01; d – β = 0.02

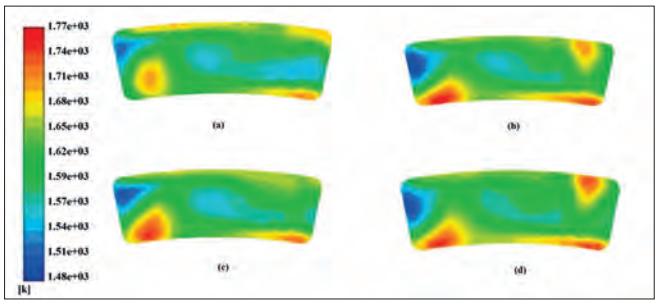

Fig. 3. Distribution of temperatures (K) in the outlet section for the first mode of fuel supply: a – the basic variant without additions of plasma-chemical products; b – β = 0.005; c –β = 0.01; d – β = 0.02

Figs. 4–5 present the distribution of the carbon monoxide CO concentrations in the outlet section of the flame tube for fuel supply modes 3 and 1, respectively. It can be seen that the addition of plasma-chemical products in the amount $\beta \geq 0.005$ causes a significant decrease in CO emissions as a result of the acceleration of the carbon monoxide oxidation reactions and intensification of the mixture formation processes in the primary zone of the combustion chamber. This effect is especially evident when burning liquid fuel.

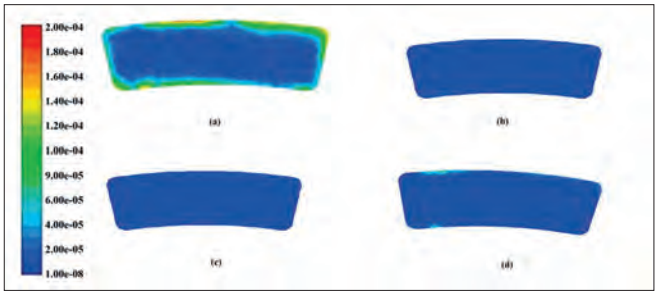

Fig. 4. Distribution of carbon monoxide concentrations at outlet section for the third mode of fuel supply: a – basic version without additions of plasma-chemical products; b – β = 0.005; c –β = 0.01; d – β = 0.02

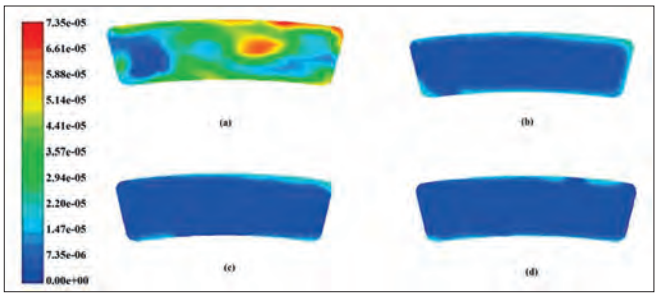

Fig. 5. Distribution of carbon monoxide concentrations at outlet section for the first mode of fuel supply: a – basic version without additions of plasma-chemical products; b – β = 0.005; c –β = 0.01; d – β = 0.02

The following graphs show the temperature distributions (Fig. 6), and the volumetric concentrations of carbon monoxide CO (Fig. 7) and nitrogen oxides NO (Fig. 8) in the outlet cross-section of a dual-fuel low-emission combustion chamber of a 25 MW gas turbine engine for different fuel supply options (without and with the addition of plasma-chemical products into the primary zone of the chamber).

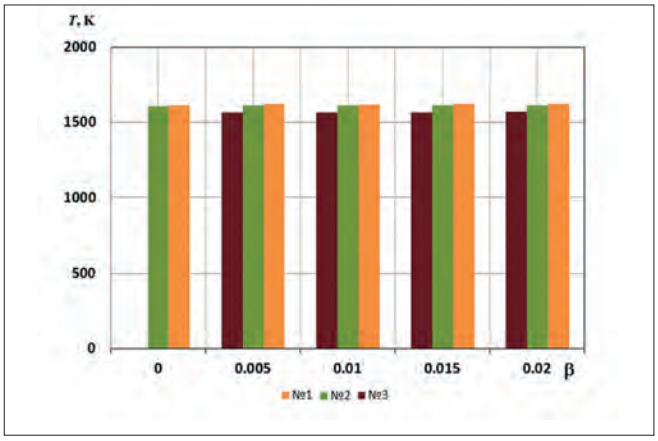

Fig. 6. Dependencies of temperatures in the outlet section of the flame tube on the amount of additives of plasma-chemical products for modes 1-3

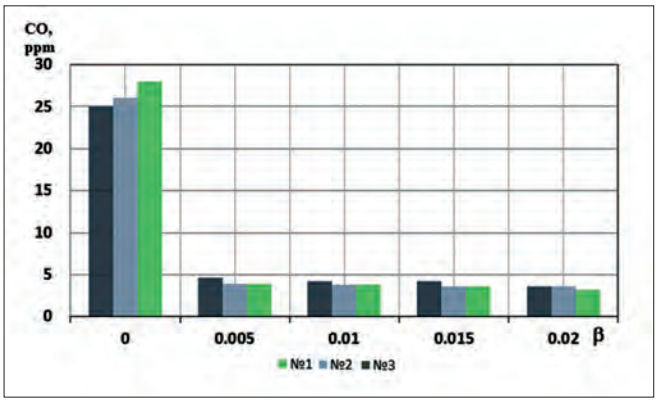

Fig. 7. Dependencies of volume concentrations of CO in the outlet section on the amount of additives of plasma-chemical products for modes 1-3

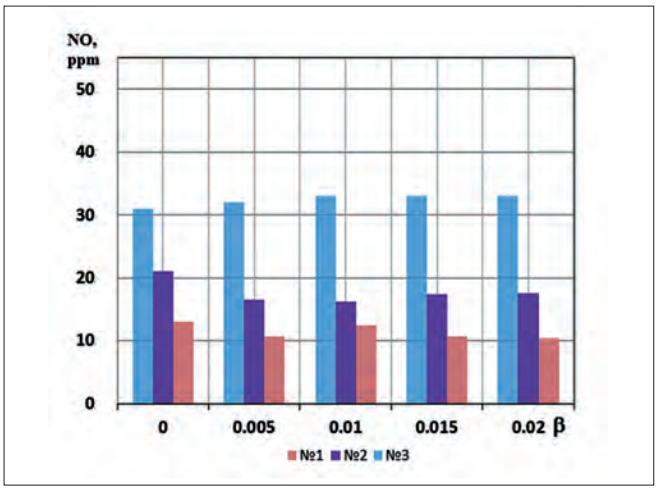

Fig. 8. Dependencies of volume concentrations of NO in the outlet section of the flame tube on the amount of additives of plasma-chemical products for modes 1-3

The analysis of the obtained data revealed that the addition of products of a plasma-chemical element to the primary zone of a dual-fuel gas turbine combustion chamber causes the temperature of the gases at the exit of the flame tube to increase slightly (less than 1%) compared to the variant without the addition of plasma-chemical products. For all three investigated modes of fuel supply (1-3), a significant decrease in the content of carbon monoxide (from 25-28 ppm to 3.9-4.6 ppm) is observed, even with a small amount of plasma-chemical products ($\beta = 0.005$). Further increase in the amount of plasma-chemical products to $\beta = 0.02$ has practically no effect on the CO emissions, as they are at a minimal (practically zero) level. It can be seen that, with the addition of plasma-chemical products, the distribution of nitrogen oxides at the exit of the combustion chamber changes slightly. Moreover, when the combustion chamber operates in transient modes with the use of plasma-chemical elements, an increase can be expected in the burning stability of lean fuel-air mixtures, together with a decrease in the probability of the formation of pulsating combustion modes, and flame extinction.

FINAL CONCLUSION

A study of the combustion efficiency of fuels differing in phase state in a dual-fuel gas turbine combustion chamber with a plasma-chemical element was carried out, allowing new data to be obtained on the distribution of the main parameters of the flow in the volume of the flame tube and at its outlet for different modes of supply of liquid and gaseous fuels, taking into consideration the amount of plasma-chemical products supplied to the primary zone of the chamber. The intensifying effect of low-temperature air plasma on the environmental parameters of the combustion chamber with preliminary mixing of fuels with an oxidiser in the channels of the radial-axial swirlers of the flame tubes is confirmed. It was established that the addition of plasma-chemical products in the amount of $\beta \geq 0.005$ (by volume) provides a significant reduction in carbon monoxide emissions at the outlet section of the flame tube: from 25-28 ppm to 3.9-4.6 ppm. Also, with the addition of plasma-chemical products, the concentration of nitrogen oxides at the outlet of the combustion chamber changes slightly. We note a significant positive effect of the products of plasma-chemical reactions in expanding the range of stable operation of the combustion chamber. Experimental studies of the system of plasma-chemical intensification for the combustion of hydrocarbon fuels on natural objects should be considered a further direction of the research.

REFERENCES

1. "Gas turbine power solutions minimize weight, footprint on FPSOs." Accessed: Mar. 15, 2023. [Online]. Available: https://assets.siemens-energy.com/siemens/assets/api/uuid:91faa9eb-0a1e-4f9f-91c8-5a632f89c0da/offshoremag-fpsos-eprint-1811off58-61.pdf

2. M. Hammer, P. E. Wahl, R. Anantharaman, D. Berstad, and K. Y. Lervåg, "CO2 capture from off-shore gas turbines using supersonic gas separation," *Energy Procedia*, vol. 63, pp. 243–252, 2014, doi: https://doi.org/10.1016/j.egypro.2014.11.026.

3. Y. Gu and Y. Ju, "LNG-FPSO: Offshore LNG solution," *Frontiers of Energy and Power Engineering in China*, vol. 2, no. 3, pp. 249–255, Jul. 2008, doi: https://doi.org/10.1007/s11708-008-0050-1.

4. O. Cherednichenko, S. Serbin, and M. Dzida, "Application of thermo-chemical technologies for conversion of associated gas in diesel-gas turbine installations for oil and gas floating units," *Polish Maritime Research*, vol. 26, no. 3, pp. 181–187, Sep. 2019, doi: https://doi.org/10.2478/pomr-2019-0059.

5. O. Cherednichenko, S. Serbin, and M. Dzida, "Investigation of the combustion processes in the gas turbine module of an FPSO operating on associated gas conversion products," *Polish Maritime Research*, vol. 26, no. 4, pp. 149–156, Dec. 2019, doi: https://doi.org/10.2478/pomr-2019-0077.

6. S. Serbin, N. Washchilenko, M. Dzida, and J. Kowalski, "Parametric analysis of the efficiency of the combined gas-steam turbine unit of a hybrid cycle for the FPSO vessel," *Polish Maritime Research*, vol. 28, no. 4, pp. 122–132, Dec. 2021, doi: https://doi.org/10.2478/pomr-2021-0054.

7. S. Serbin, B. Diasamidze, and M. Dzida, "Investigations of the working process in a dual-fuel low-emission combustion chamber for an FPSO gas turbine engine," *Polish Maritime Research*, vol. 27, no. 3, pp. 89–99, Sep. 2020, doi: https://doi.org/10.2478/pomr-2020-0050.

8. S. Serbin, B. Diasamidze, V. Gorbov, and J. Kowalski, "Investigations of the emission characteristics of a dual-fuel gas turbine combustion chamber operating simultaneously on liquid and gaseous fuels," *Polish Maritime Research*, vol. 28, no. 2, pp. 85–95, Jun. 2021, doi: https://doi.org/10.2478/pomr-2021-0025.

9. A. J. Harrison and F. J. Weinberg, "Flame stabilization by plasma jets," *Proceedings of the Royal Society of London. A. Mathematical and Physical Sciences*, Jan. 19, 1971. https://royalsocietypublishing.org/doi/abs/10.1098/rspa.1971.0015 [Accessed: Mar. 15, 2023].

10. N. A. Gatsenko and S. I. Serbin, "Arc plasmatrons for burning fuel in industrial installations," *Glass and Ceramics*, vol. 51(11–12), pp. 383–386, 1994, doi: https://doi.org/10.1007/BF00679821

11. S. I. Serbin, "Features of liquid-fuel plasma-chemical gasification for diesel engines," *IEEE Trans. Plasma Sci.*, vol. 34, no. 6, pp. 2488–2496, Dec. 2006, doi: https://doi.org/10.1109/tps.2006.876422.

12. A. Yu. Starikovskii, N. B. Anikin, I. N. Kosarev, E. I. Mintoussov, S. M. Starikovskaia, and V. P. Zhukov, "Plasma-assisted combustion," *Pure and Applied Chemistry*, vol. 78, no. 6, pp. 1265–1298, Jan. 2006, doi: https://doi.org/10.1351/pac200678061265.

13. L. Massa and J. B. Freund, "Plasma-combustion coupling in a dielectric-barrier discharge actuated fuel jet," *Combustion and Flame*, vol. 184, pp. 208–232, Oct. 2017, doi: https://doi.org/10.1016/j.combustflame.2017.06.008.

14. D. K. Dinh, H. S. Kang, S. Jo, D. H. Lee, and Y.-H. Song, "Partial oxidation of diesel fuel by plasma – Kinetic aspects of the reaction," *International Journal of Hydrogen Energy*, vol. 42, no. 36, pp. 22756–22764, Sep. 2017, doi: https://doi.org/10.1016/j.ijhydene.2017.07.164.

15. S. Serbin, A. Mostipanenko, I. Matveev, and A. Tropina, "Improvement of the gas turbine plasma assisted combustor characteristics," *49th AIAA Aerospace Sciences Meeting including the New Horizons Forum and Aerospace Exposition*, Jan. 2011, doi: https://doi.org/10.2514/6.2011-61.

16. S. Serbin, A. Kozlovskyi, and K. Burunsuz, "Influence of plasma-chemical products on process stability in a low-emission gas turbine combustion chamber," *International Journal of Turbo & Jet-Engines*, Jan. 2021, doi: https://doi.org/10.1515/tjj-2020-0046.

17. S. I. Serbin, A. V. Kozlovskyi, and K. S. Burunsuz, "Investigations of nonstationary processes in low emissive gas turbine combustor with plasma assistance," *IEEE Trans. Plasma Sci.*, vol. 44, no. 12, pp. 2960–2964, Dec. 2016, doi: https://doi.org/10.1109/tps.2016.2607461.

18. I. B. Matveev, S. A. Matveeva, E. Y. Kirchuk, S. I. Serbin, and V. G. Bazarov, "Plasma fuel nozzle as a prospective way to plasma-assisted combustion," *IEEE Trans. Plasma Sci.*, vol. 38, no. 12, pp. 3313–3318, Dec. 2010, doi: https://doi.org/10.1109/tps.2010.2063716.

19. S. I. Serbin, "Modeling and experimental study of operation process in a gas turbine combustor with a plasma-chemical element," *Combustion Science and Technology*, vol. 139, no. 1, pp. 137–158, Oct. 1998, doi: https://doi.org/10.1080/00102209808952084.

20. S. I. Serbin, I. B. Matveev, and G. B. Mostipanenko, "Investigations of the working process in a 'lean-burn' gas turbine combustor with plasma assistance," *IEEE Trans. Plasma Sci.*, vol. 39, no. 12, pp. 3331–3335, Dec. 2011, doi: https://doi.org/10.1109/tps.2011.2166811.

21. S. M. Mousavi, R. Kamali, F. Sotoudeh, N. Karimi, and B. J. Lee, "Numerical investigation of the plasma-assisted MILD combustion of a CH4/H2 fuel blend under various working conditions," *Journal of Energy Resources Technology*, vol. 143, no. 6, Oct. 2020, doi: https://doi.org/10.1115/1.4048507.

22. I. B. Matveev and S. I. Serbin, "Theoretical and experimental investigations of the plasma-assisted combustion and reformation system," *IEEE Trans. Plasma Sci.*, vol. 38, no. 12, pp. 3306–3312, Dec. 2010, doi: https://doi.org/10.1109/TPS.2010.2063713.

23. I. B. Matveev and S. I. Serbin, "Modeling of the coal gasification processes in a hybrid plasma torch," *IEEE Trans. Plasma Sci.*, vol. 35, no. 6, pp. 1639–1647, Dec. 2007, doi: https://doi.org/10.1109/tps.2007.910134.

24. B. E. Launder and D. B. Spalding, *Lectures in Mathematical Models of Turbulence.* London: Academic Press, 1972, ISBN 0124380506.

25. I. B. Matveev, S. I. Serbin, V. V. Vilkul, N. A. Goncharova, "Synthesis gas afterburner based on an injector type plasma-assisted combustion system," *IEEE Trans. Plasma Sci.*, vol. 43, no. 12, pp. 3974–3978, 2015, doi: https://doi.org/10.1109/TPS.2015.2475125.

26. S. I. Serbin, I. B. Matveev, G. B. Mostipanenko, "Plasma-assisted reforming of natural gas for GTL: Part II – Modeling of the methane-oxygen reformer," *IEEE Trans. Plasma Sci.*, vol. 43, no. 12, pp. 3964–3968, 2015, doi: https://doi.org/10.1109/TPS.2015.2438174.

27. V. Yakhot and S. A. Orszag, "Renormalization group analysis of turbulence: I. Basic theory," *Journal of Scientific Computing*, vol. 1, no. 1, pp. 3–51, 1986.

28. G. M. Faeth, "Structure and atomization properties of dense turbulent sprays," *Symp. (Int.) Combust.*, vol. 23, no. 1, pp. 1345–1352, 1991, https://doi.org/10.1016/S0082-0784(06)80399-1.

29. G. Faeth, "Spray combustion models – A review," *17th Aerospace Sciences Meeting*, New Orleans, USA, 1979, https://doi.org/10.2514/6.1979-293.

30. ANSYS Fluent Theory Guide. ANSYS, Inc., 2013.

31. A. H. Lefebvre and D. R. Ballal, *Gas turbine combustion: alternative fuels and emissions.* CRC Press, 2010.

32. K. Meredith and D. Black, "Automated global mechanism generation for use in CFD simulations," *44th AIAA Aerospace Sciences Meeting and Exhibit*, Jan. 2006, doi: https://doi.org/10.2514/6.2006-1168.

POLISH MARITIME RESEARCH 2 (118) 2023 Vol. 30; pp. 76-84
10.2478/pomr-2023-0023

GUIDED WAVES IN SHIP STRUCTURAL HEALTH MONITORING – A FEASIBILITY STUDY

Emil Roch [1*]
Beata Zima [1]
Krzysztof Woloszyk [1]
Yordan Garbatov [2]
[1] Gdańsk University of Technology, Poland
[2] Universidade de Lisboa, Portugal

* Corresponding author: *emil.roch@pg.edu.pl (Emil Roch)*

ABSTRACT

Ships and offshore structures operate in a severe corrosion degradation environment and face difficulty in providing long-lasting corrosion protection. The Classification Societies recommend regular thickness measurements leading to structural component replacements, to ensure structural integrity during service life. The measurements are usually performed using ultrasonic thickness gauges and such an approach requires multiple measurements of the corroded structural components. Otherwise, the collected data are insufficient to precisely assess the corrosion degradation level. This study aims to perform numerical and experimental analyses to verify the use of guided ultrasonic waves in defining the corrosion degradation level of the corroded structural components of a ship. The study incorporates the fundamental antisymmetric Lamb mode, excited by piezoelectric transducers attached at the pre-selected points on stiffened panels, representing typical structural ship components. The specimens are exposed to accelerated marine corrosion degradation, the influence of the degree of degradation on the wave time of flight being analysed. The study indicates that guided waves are a promising approach for diagnosing corroded structural components. The signals characterised by a high signal-to-noise ratio have been captured, even for relatively long distances between the transducers. This proves that the proposed approach can be suitable for monitoring more extensive areas of ship structures by employing a single measurement.

Keywords: Corrosion, Guided Waves, Non-destructive Testing, Ship Structures

INTRODUCTION

The current recommendations of the International Association of Classification Societies (IACS) specify the number of gauge measurements as being three per plate in maritime structures. Det Norske Veritas guidelines [1], based on the IACS requirements [2], recommend increasing the measures for more severe corrosion found in the investigated area and additional surveys when pitting corrosion is observed. However, those gauged measurements often do not provide enough information due to the high non-regularity of the geometry of corroded structural components [3], introducing a high level of uncertainty, and they do not provide enough information to analyse the severity level of corrosion degradation. Therefore, there is a need to develop alternative methods that could be more effective and inexpensive and allow for the monitoring of significant areas during a single measurement.

The guided wave propagation approach has recently attracted significant attention from researchers as a promising tool for non-destructive diagnostics. Due to the ability of the guided wave to travel long distances with insignificant amplitude reduction and their high sensitivity to defects, they are commonly used

for diagnostics in different industrial applications. For this purpose, the arrays of piezoelectric transducers are mounted on the surface of the tested structure or are embedded directly into the structure. They are used for data collection and generating mechanical guided waves (GW) [4, 5].

Some algorithms are dedicated to the detection, localisation and size estimation of various damage types, such as localised damages [4], debonding [6], deterioration of the structural parameters [7], etc. Special attention was paid to the non-destructive evaluation of the corrosion degradation level, as it is one of the most common degradation types of structures subjected to aggressive environmental conditions. Pitting and general corrosion were recently investigated by [7–14]. The method of corrosion pit detection and visualisation using the dispersion curve regression method was proposed by Tian et al. [9]. Ervin and Reis investigated the case of general corrosion of steel reinforcing bars embedded in concrete [10, 11]. Pulse-echo and pulse transmission methods were used by Sharma and Mukherjee [12] to monitor the corrosion process of the reinforcing bar. Moustafa et al. [13] proposed a method to evaluate the corrosion level in post-tensioned systems based on the fractal analysis of guided ultrasonic waves. The normalised acoustic nonlinearity parameter of the second and third harmonics was incorporated by Ding et al. [7], to evaluate the level of corrosion degradation. Laser-induced guided waves were used to estimate the corrosion pit size, location, and depth by Gao et al. [8].

The thickness reduction caused by corrosion degradation is currently measured using an ultrasonic gauge, which is time-consuming. Several studies have proved the potential of guided waves in non-destructive diagnostics of corrosion impact. Precise measurements of corroded element geometry are possible using other methods, such as photogrammetry or laser scanning. Nevertheless, those methods are expensive and challenging to use in the case of ship hull thickness measurements. Also, both sides of the plate need to be scanned and, thus, additional problems might occur because of the permanent deflection, buckling or residual post-welding stresses. Guided wave-based methods may increase the efficiency of the measuring process and reduce the associated costs of the time-consuming traditional inspections.

This study aims to perform numerical and experimental feasibility analyses to evaluate the use of guided ultrasonic waves in estimating the degradation level of corroded stiffened panels as a part of ship hulls. Contrary to our previous studies [15, 16], where only distances of approximately 300 mm were investigated, this proves the possibility of using the guided waves on longer distances (up to 1250 mm), which is crucial for increasing the effectiveness and reducing the total cost of the state assessment. Previous work was devoted to analysing the possibility of monitoring plate corrosion degradation. The current study is the next step towards a more realistic scenario of inspecting a ship's structural components when the whole of the plates, with complex geometry and additional obstacles like stiffeners, need to be tested. The study incorporates a fundamental antisymmetric Lamb mode excited by piezoelectric transducers attached to pre-selected locations on stiffened panels. Before non-destructive testing, the stiffened panels are exposed to accelerated natural marine corrosion in a specially designed and prepared corrosion tank.

CORRODED SAMPLE SET-UP

Experimental testing of guided wave propagation was conducted on mild steel specimens with an initial plate thickness of t = 6 mm. The geometry of the specimens is presented in Fig. 1. These stiffened plates (plates reinforced by stiffeners) are typical structural components of ship hull structures.

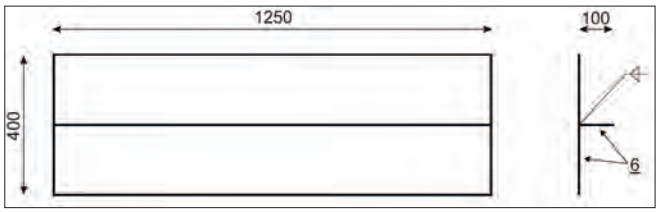

Fig.1. Intact specimen geometry (dimensions in mm)

The experiment includes one intact sample and three specimens with different degrees of corrosion degradation (*DoD*). The *DoD* is considered as the percentage loss of the initial mass of the specimen (m_{intact}) which is reduced due to corrosion degradation (mass after corrosion – $m_{corroded}$):

$$DoD = \frac{m_{intact} - m_{corroded}}{m_{intact}} \cdot 100\% \quad (1)$$

Therefore, only the specimen's mean thickness loss is captured, without considering the irregular character of the corrosion damage. Corrosion of the specimens was accelerated in a specially designed tank with corrosion process parameters: salinity 3.5%, temperature 55°C and increased dissolved air (fully saturated conditions). The *DoD* achieved were 12% (specimen *c*12) and 24% (specimen *c*24) and were taken from mass measurements. The mean thickness reduction, calculated based on mass reduction, is presented in Table 1. Thickness measurements were also performed using a micrometre screw along both long edges. The thickness measurements were made alongside the edges because of the transducer configuration, which will be presented later in this paper, and the mean thicknesses are presented in Table 1. Finally, ultrasonic thickness gauge measurements were also performed on the plates, resulting in a thickness map, as shown in Figure 2. Due to the significant difference between UT measurements and micrometre screws, UT measurements were only used to represent corrosion irregularity.

Tab. 1. DoD and mean specimen thickness.

Specimen	*DoD* [%]	Path (as seen in Fig. 7)	Mean thickness based on *DoD* [mm]	Mean thickness on edge [mm]
intact	0	–	6.00	6.00
c12	12	I	5.28	5.34
		II		5.46
c24	24	I	4.56	4.76
		II		4.98

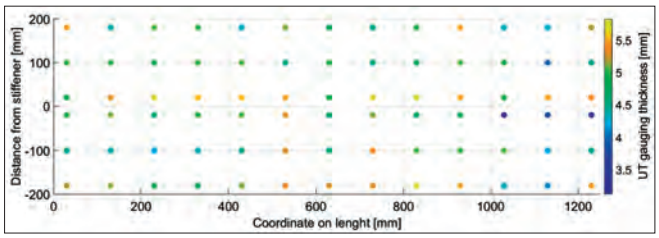

Fig. 2. Plate thickness distribution, specimen c24, UT gauging

Figures 3 and 4 present photos of selected specimens. Figure 3 shows a close-up view of the intact and corroded plate surface. On the intact plate, the surface was as it arrived from the steel mill. The corroded surface was dried out and so the authors removed loose corrosion products and dusted up the surface. Figure 4 presents a stiffener side view on the *c*12 sample, with magnifications on given parts of the plate. Apart from specimen markings, there are visible white dots on the sample, indicating places where UT gauging was performed.

Fig. 3. Plate surface close-up. Left: intact plate. Right: c24 plate corroded and cleaned from corrosion products

Fig. 4. Sample c12 (12% DoD): stiffener side view with close-ups of surface.

BACKGROUND OF GUIDED WAVES

One of the essential features of guided waves is their dispersive nature. The relationship between their velocity and the number of wave modes is usually presented as a dispersion curve, which can be traced by solving dispersion equations. For the plate-like structures, the dispersion relationships were formulated by Lamb [17]. Thus, the waves are called Lamb waves. Two Lamb wave families can be distinguished: antisymmetric (Eq. (2)) and symmetric (Eq. (3)). The dispersion relations are as follows:

$$\frac{tan(qd)}{tan(pd)} = \frac{(k^2-q^2)^2}{4k^2pq} \tag{2}$$

$$\frac{tan(qd)}{tan(pd)} = \frac{4k^2pq}{(k^2-q^2)^2} \tag{3}$$

The parameters d and k indicate the plate thickness and the wavenumber, respectively, while q and p depend on longitudinal and transverse wave velocities in an infinite medium. Based on the equations, the curves illustrating the relationships between velocity and excitation frequency can be traced, as shown in Fig. 5.

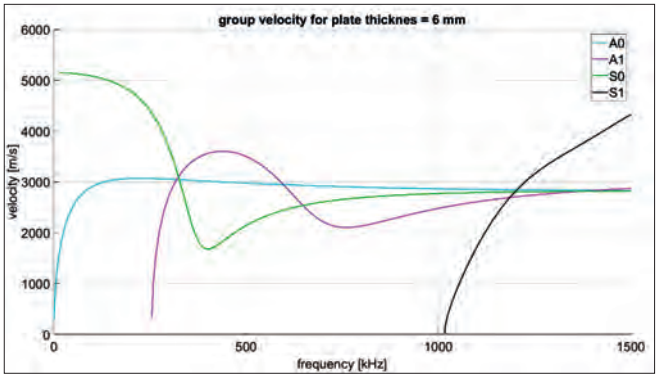

Fig. 5. Group velocity against frequency for 6 mm steel plate (A-antisymmetric, S-symmetric mode)

Piezoelectric transducers were mounted at pre-selected points on the plate surface to generate guided waves. Because the transducers were attached to the plate surface, and the excitation applied perpendicular to it, antisymmetric modes were mainly excited. The significant difference between velocities (for the antisymmetric A0 and S0 modes for frequencies incorporated in the experimental tests, the velocity of S0 mode is higher than A0 mode by about 2000 m/s for a frequency of 140 kHz) result in the mode family being easily recognised, based on the difference in the time of flight. The scheme of deformation forms an antisymmetric wave (A0), as seen in Fig. 6.

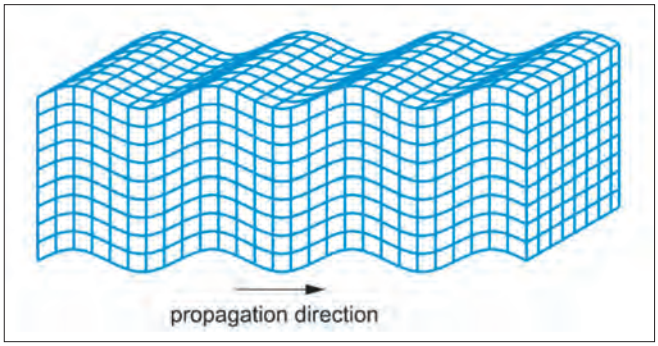

Fig. 6. Deformation form of antisymmetric wave propagation

In the presented paper, we use the commonly known guided wave feature, i.e. its velocity strongly depends on the plate thickness. Therefore, if the wave propagation velocity is known, we can determine the average thickness of the specimen alongside the propagation path. Eq. (2) was solved to demonstrate the velocity-thickness dependency and a good curve representing this relationship, for a frequency of 140 kHz, was plotted (Fig. 7).

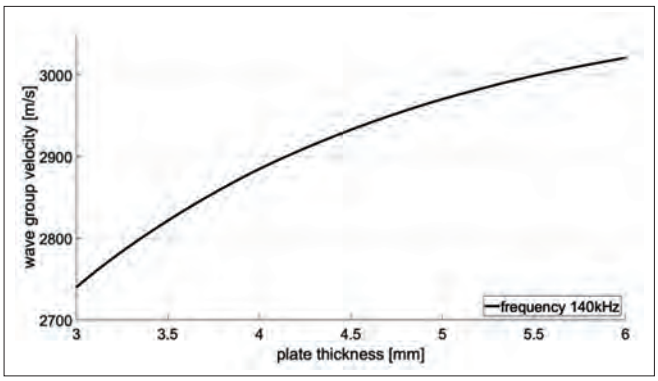

Fig. 7. Antisymmetric group wave velocity to plate thickness curve

Since the distance between measurement points is constant, the change in the flight time may be associated with corrosion degradation and thickness reduction. This assumption is the basis of the presented analysis. Later in the paper, the thickness reduction will be estimated, based on the time of flight (ToF), which is the time needed to travel from an actuator to the sensor. Therefore, for an exemplary frequency of 140 kHz, the relationship between the ToF measured on the distance of 1250 mm, which is the length of the considered ship hull structural element, is presented in Fig. 8. It should be noted that the dispersive equations (Eq. (2) and (3)) are nonlinear and the ToF-thickness relationship is also nonlinear.

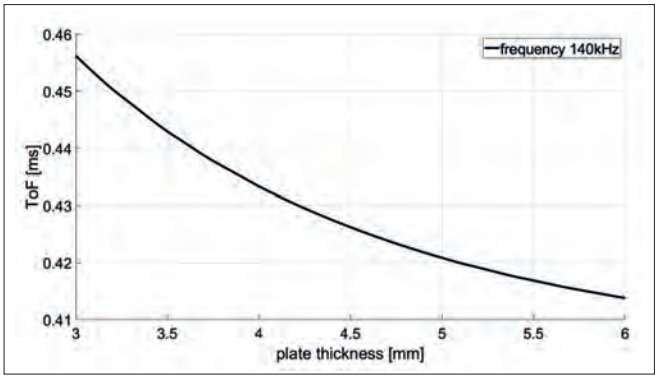

Fig. 8. Antisimetric 140 kHz wave ToF in different plate thicknesses at 1250 mm distance

MATERIALS AND METHODS

ANALYSED STRUCTURAL COMPONENTS

Piezoelectric transducers were mounted in plate corners as pairs, the first for path I and the second for path II. Transducers were attached on the right hand corner of the plate by using special wax as a coupling medium. Transducer positions and the geometry of the tested plate can be seen in Fig. 9.

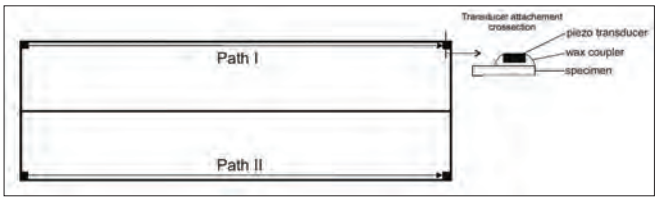

Fig. 9. Transducer locations and paths (left) and cross-section of transducer (right)

EXPERIMENTAL SET-UP AND TRANSDUCER CONFIGURATIONS

Transducers were connected to a wave generator, amplifier, and oscilloscope, as presented in Fig. 10. The signal measured from a series of the same signals was then averaged at an oscilloscope, filtered using an oscilloscope-integrated low pass filter (with double base cut-off frequency), and stored as a voltage-time relationship.

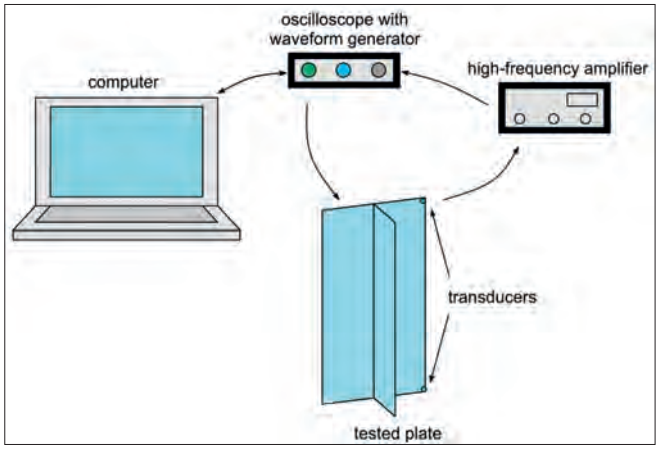

Fig. 10. Guided wave experimental set-up.

Two paths were investigated in the study, both along the longer sides of the plates. The signal generated by the wave generator was a packet consisting of a five-cycle sine modulated by the Hanning window, as presented in Fig. 11.

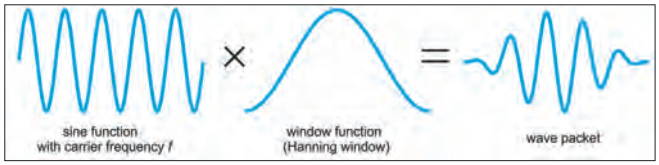

Fig. 11. Windowing sine signal using the Hanning window

In the study, the piezoelectric transducers were attached near the corners of the plate for two reasons. First, fewer reflections provide a cleaner, more readable signal; second, energy only disperses at a quarter of the circle instead of the entire circular wavefront. Thus, the signal energy was about four times higher than in the case of attachment in the middle part of the plate [18]. Parts of the ship structure have free edges; however, applying the method to plates limited by stiffeners or girders should be possible. It is expected that the signal-to-noise ratio might be lower but the basic operating principle should be kept the same.

SELECTION OF EXCITATION PARAMETERS

In the first step, the sensitivity analysis aimed at determining the influence of excitation frequency on signal amplitude, was carried out to investigate corroded plates. A waterfall chart is presented in Fig. 12, registering signals for frequencies in the range 60-300 kHz, with a step of 20 kHz. It can be seen that the amplitude of the incident wave significantly decreases for a frequencies lower than 100 kHz and higher than 160 kHz.

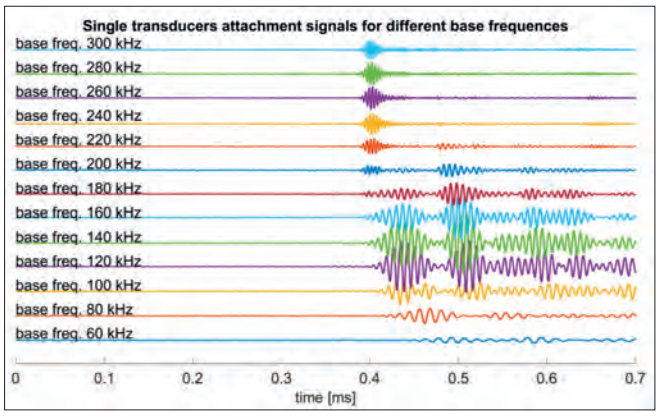

Fig. 12. Waterfall chart of signal received for different base frequencies.

Maximal amplitudes of the received signals were registered and are presented in Fig. 13. The highest amplitudes of the incident waves lead to the highest signal-to-noise ratios and were achieved for the frequency 140 kHz. The final data were only collected and analysed for this frequency because it provided the clearest and the most readable signals.

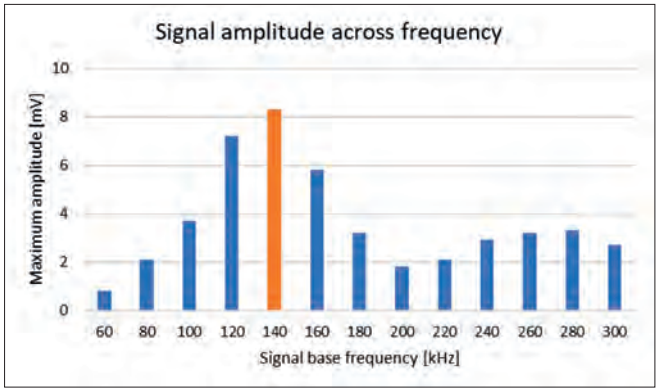

Fig. 13, Column chart of registered amplitudes for base frequencies.

NUMERICAL MODEL

Numerical simulations were performed using commercial FEM (finite element method)-based software (Abaqus) [19], to demonstrate and recreate experiments on the wave propagation phenomena in the stiffened plate. The dynamic/Explicit module was used to accurately model mechanical wave propagation. Guided waves were simulated in intact and corroded specimens modelled as a constant-thickness shell structure. Four node shell elements were applied with reduced integration (S4R). A convergence study preceded the numerical analysis, to determine the element size. Finally, each element had the same dimensions (1 mm x 1 mm). The transient wave propagation problem was solved with a 10-7 s time step, adjusted according to CFL (Courant–Friedrichs–Lewy) conditions [20] related to frequency and wavelength. The mechanical properties were a Poisson's ratio of 0.3 and a material density equal to 7800 kg/m³, which was established based on previously conducted experimental destructive tests performed on specimens of the same steel. An elastic modulus of 188.5 GPa was calculated non-destructively, based on the Lamb equation for the intact plate. Because Poisson's ratio has a relatively small influence on the shape of the dispersion curves, only elastic modulus was considered during the calibration procedure and curve fitting. The geometry was consistent with the dimensions of the intact specimen presented in Fig. 1. The simulations were made for plate thicknesses taken as average thickness from the measurements with the use of micrometer, of each path (see Fig. 9).

RESULTS AND DISCUSSION

VISUALISATION OF WAVE PROPAGATION IN SHIP STRUCTURE

Figure 14 presents the numerical simulation results in snapshots collected for selected time instants. After wave excitation at the corner of the plate, the circular wavefront was observed propagating within the structure. The material is assumed to be isotropic and homogeneous, which means that the propagation velocity is the same in each direction. The presence of the stiffener triggers additional reflections, affecting the wave propagation patterns. As a result, surface waves (Rayleigh waves) are observed, propagating along the plate edges. Therefore, the diagnostic procedures dedicated to ship structures should consider the more complex geometry and the presence of additional waves affecting registered signals.

Even though the numerical model did not consider thickness variability along the propagation path, and the thickness was assumed to be constant, the influence of modelled corrosion degradation is visible in visualisation. The wave propagates with a higher velocity in the intact plate (see Fig. 14, $t = 0.46$ ms). The difference in wave velocity can be explained by the dispersive character of guided waves (see Eq. (2) and (3)).

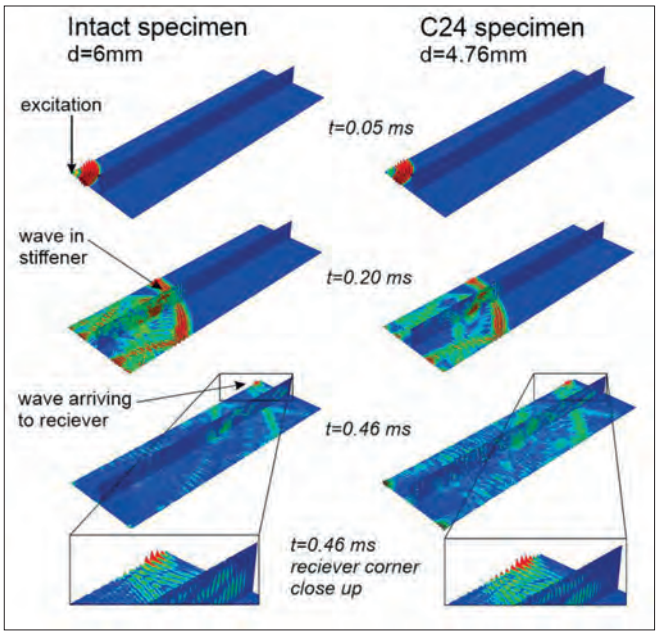

Fig. 14. Visualisation of wave propagation – deformation: intact specimen and specimen characterised by DoD of 24%

EXPERIMENTAL RESULTS

Figure 15 shows the received signal from two measurements, both for the intact plate but at opposite sides. Since the transducer's ability to actuate and receive a signal depends on the attachment and the wax used for transducer mounting, signal amplitude cannot be compared directly. To make signals possible to compare, they were all normalised to a 1V amplitude at the peak of the first packet received after about 0.4-0.5 ms.

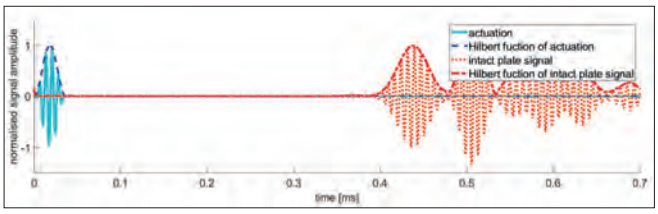

Fig. 15. The comparison of the signals measured alongside both edges of the intact plate

The envelopes of the signals were determined by using Hilbert transform to interpret and present signals more clearly. Figure 16 presents the actuation signal, registered signal, and Hilbert transforms, as well as the interpretation of the ToF, which is used in further analysis. This study measures the ToF as the peak-to-peak value between the actuation and registered signals. As the lengths of both paths are equal, ToF can be used for group velocity comparison.

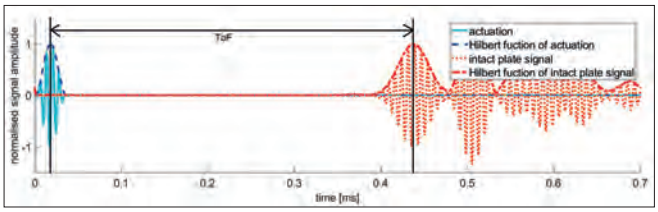

Fig. 16. Excitation and received signal for intact sample, excitation 140 kHz

Figures 17 and 18 show the Hilbert transforms of the normalised signal received for intact and corroded specimens. All signals were triggered in a similar way, i.e. for the time $t = 0$ ms. Figure 17 presents the results for the first path of all three plates. As predicted by theoretical analysis, the signal travelled with a higher velocity in an intact plate. Next, the waves propagating in plates *c*12 and *c*24 were registered.

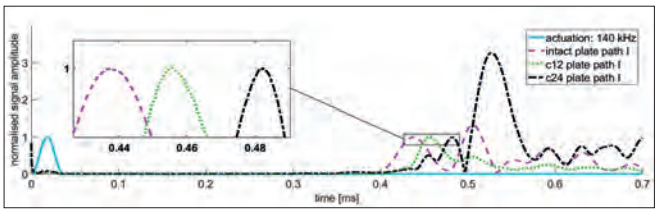

Fig. 17. Hilbert transforms of actuation and signals received at path I

Figure 18 presents the results for the second path alongside the opposite edge. As path I, the wave travelled with the highest velocity in an intact plate. The clear relationship between increasing ToF and the degree of degradation is demonstrated in Fig. 18. For comparison, the ToF for all registered signals was determined and is summarised in Table 2.

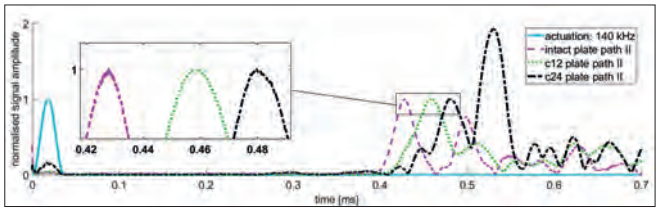

Fig. 18. Hilbert transforms of actuation and signals received at path II

Tab. 2. Values of Time of Flight (ToF) measured at Hilbert transform peak [ms]

Specimen	Path	Mean thickness on edge [mm]	ToF [ms]
intact	I	6.00	0.419
	II	6.00	0.409
c12	I	5.34	0.437
	II	5.46	0.441
C24	I	4.76	0.463
	II	4.98	0.461

NUMERICAL RESULTS

The results of the FEM simulations, in the form of Hilbert transforms of registered signals, are presented in Fig. 19. The thickness chosen to calculate ToF with FEM corresponds with the mean path thickness from micrometer screw measurements. The same relation between ToF and thickness can be observed: the smaller the plate thickness, the greater ToF.

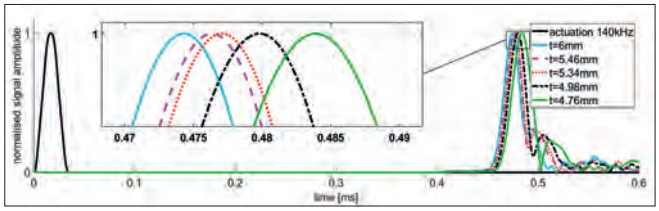

Fig. 19. Hilbert transform of received signals from FEM analysis: both for intact and 24% DoD plate

Figure 20 presents the experimental and numerical ToFs. FEM values were calculated based on the mean thickness of the path from the micrometer. It can be seen that all ToFs for the FEM-tested plates are more significant than in the experimental plates. This can be explained by the fact that the constant average thickness was adopted in the numerical model, while the corroded surface was irregular in the real case. However, in both cases, the same decreasing trend is noted.

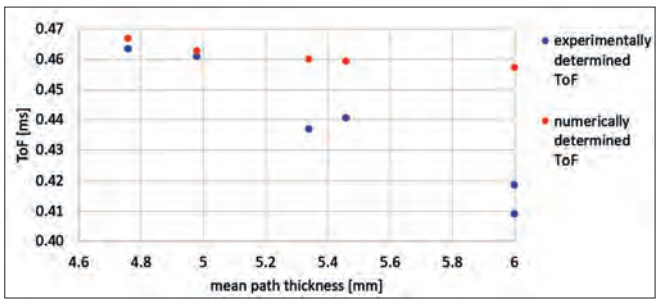

Fig. 20. Twenty FEM results compared with experimental results

COMPARISON OF EXPERIMENTAL AND THEORETICAL RESULTS FROM LAMB EQUATIONS

As previously mentioned, the relationship between ToF and the plate thickness is strongly nonlinear and requires the solving of dispersion equations. Based on the experimentally determined material parameters, the theoretical curve representing the thickness-ToF relationship was calculated for an incorporated frequency of 140 kHz and compared with experimental results (Fig. 21).

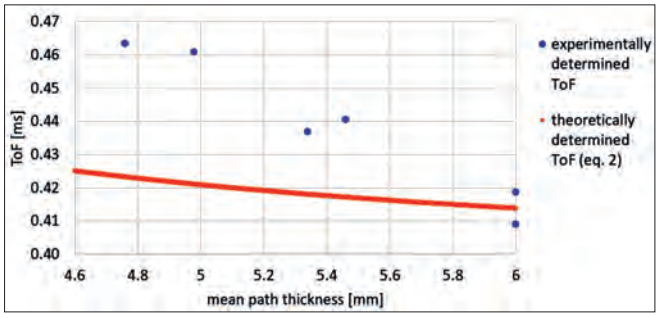

Fig. 21. ToF to thickness curve from equations in front of ToF measured in the experiment

In the last stage, an algorithm was developed in the MATLAB environment, to fit the theoretical curve to the experimental results. The theoretical curve was calculated based on solving Eq. (2), using material parameters from the paragraph describing the numerical model. This was used to fit the dispersion curve based on the regression analysis, using the least square method. The algorithm considers plate thickness and the systematic error of the ToF measurements. Because several approaches for ToF determination give slightly different results, it was assumed that the results could be burdened with some systematic errors. Moreover, the delay resulting from signal transmission between the components of the experimental set-up might also affect the ToF values. Based on the regression analysis results, the error value was estimated at 0.036 ms.

The discrepancies between experimental and numerical results may also result from the differences between the material parameters determined using the fitting Lamb equation to the experimental results. The difference between the actual specimen's average thickness, alongside the propagation paths and the thickness obtained by solving the inverse problem using Lamb equations, was checked and calculated. The inverse calculation was based on the wave propagation velocity for a given average path thickness. The final inaccuracy was calculated as 2.8 mm. This means that, based on the non-destructive results and fitting curve procedure, the plate is thinner by 2.8 mm .

The results of the curve fitting (after considering the inaccuracies) that translates the curve by translation vector [ToF; d] = [-0.036 ms; 2.8 mm], are presented in Fig. 22. The solid curve represents the theoretically determined thickness-ToF relationship, while experimental results are marked with green markers. It can be seen that the experimental and theoretical results coincide well with each other. The absolute average difference between experimental results and the fitted curve equals 0.005 ms, and the maximum difference between observed ToF values equals 0.054 ms.

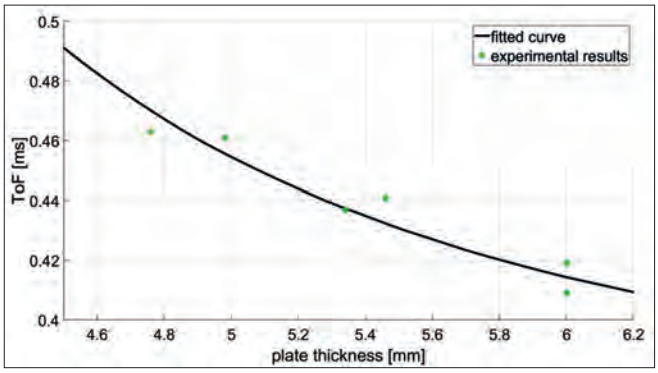

Fig. 22. Translated curve fitted to experimental results, non-translated curve for reference.

CONCLUSIONS

This study analysed the possibility of applying guided waves to the health monitoring of a ship's structural components subjected to corrosion degradation. The correlation between ToF and mean plate thickness can be easily observed in naturally accelerated corroded plates. This ensures that the guided wave dispersion might be used to estimate the mean value of the thickness loss of the plate, which was proven in many previous papers. However, it was observed that guided waves could easily travel significant distances on the plates, which is promising when analysing the large-scale structural components typically found in ship structures. The experiments presented were performed on a simpler geometry. However, they can be performed for other, more complex geometries. Signals would differ due to different distances or additional reflections. As a feasibility study, the paper proves the concept of structural health monitoring based on the time of flight. Testing this possibility was also important in the context of the reliability of the wave-based method. It could be observed that even a relatively high degradation level was associated with insignificant differences in the ToF. In the case of short distances, the difference would be invisible, and the state assessment would be more challenging to perform.

In the next stage, we could observe the influence of the inaccuracies of ToF determination, as well as the complex geometry of the corroded plates. Developed FEM models, theoretical dispersion curves and experimental results do not overlap perfectly. It should be noted that FEM and Lamb's curves are biased. After determining the translation vector, the results were matched with high accuracy. The main source of the discrepancies between numerical, theoretical and experimental results is an incorrect assumption commonly applied in the literature about the reduced constant thickness plate. In real cases, the corroded plates are characterised by irregular surfaces, while thickness variability entails variable velocity alongside the propagation path. The second important aspect, which should be considered in further investigations, is the complex structure of the corroded plate. Because corrosion products and coatings differ in terms of their parameters, the plate should be regarded

as a multi-layered structure, with layers varying in thickness and material parameters.

The next problem discussed in the paper concerned the influence of material parameters (elastic modulus) on the theoretical reference curve. A solution for this might be the opportunity to calibrate measurement techniques on the intact element. In this study, we have not compared the results for the same specimen but for various degradation levels, i.e. several specimens varying in *DoD*. In the case of monitoring the same element, the influence of inaccuracies in material parameter estimation would have a much smaller impact on the final results.

To understand the wave propagation phenomenon in multi-layered plate-like structures with variable thickness, more samples need to be tested, with a detailed knowledge of the surface topography, determined with the support of photogrammetry or CMM, and defined by statistical parameters. It is worth mentioning that, in the initial stages of introducing the method to diagnosing the construction, support from the mentioned methods may still be necessary. However, such an approach would allow for the further development of a mathematical model, describing the relationship between average wave velocity and surface parameters.

The paper demonstrates the possibilities of using guided waves, even for the more complex specimens. The tested plates were stiffened with an additional web in the middle parts. The incident wave was easily identified despite the additional obstacles and the ToF was calculated. This is essential in the ToF-based methods because, very often, the interference of several different wave packets efficiently identifies the first peak and, consequently, estimates the ToF. The results presented here prove that the sensor network can be set in a way that facilitates the non-destructive testing procedure.

Future work should also consider comprehensive research on the wave's ability to overcome obstacles, such as stiffeners or deep girders. Also, research about plate measurements reinforced by stiffeners and deep girders is necessary for possible practical applications using wave-guided methods.

A potential problem with the in situ application of this method is the necessity to specify the Young modulus, which strongly influences group speed.

ACKNOWLEDGEMENTS

The research was carried out within project No. 2021/43/D/ST8/00786, financed by the National Science Centre, Poland. Abaqus calculations were carried out at the Academic Computer Centre in Gdańsk.

The third author would like to thank for the support of the Foundation for Polish Science (FNP).

REFERENCES

1. DNV GL, *CLASS GUIDELINE Ultrasonic thickness measurements of ships*, 2016. [Online]. Available: http://www.dnvgl.com.
2. ACS, "IACS UR Z7," *UR Z7 Hull classification surveys*, 2020.
3. K. Woloszyk, Y. Garbatov, and J. Kowalski, "Indoor accelerated controlled corrosion degradation test of small and large-scale specimens," *Ocean Engineering*, vol. 241, p. 110039, Dec. 2021, doi: 10.1016/j.oceaneng.2021.110039.
4. B. Zima and R. Kędra, "Debonding Size Estimation in Reinforced Concrete Beams Using Guided Wave-Based Method," *Sensors*, vol. 20, no. 2, p. 389, Jan. 2020, doi: 10.3390/s20020389.
5. B. Zima and M. Rucka, "Guided waves for monitoring of plate structures with linear cracks of variable length," *Archives of Civil and Mechanical Engineering*, vol. 16, no. 3, pp. 387–396, May 2016, doi: 10.1016/j.acme.2016.01.001.
6. A. Farhidzadeh and S. Salamone, "Reference-free corrosion damage diagnosis in steel strands using guided ultrasonic waves," *Ultrasonics*, vol. 57, no. C, pp. 198–208, Mar. 2015, doi: 10.1016/j.ultras.2014.11.011.
7. X. Ding, C. Xu, M. Deng, Y. Zhao, X. Bi, and N. Hu, "Experimental investigation of the surface corrosion damage in plates based on nonlinear Lamb wave methods," *NDT & E International*, vol. 121, p. 102466, Jul. 2021, doi: 10.1016/j.ndteint.2021.102466.
8. T. Gao, H. Sun, Y. Hong, and X. Qing, "Hidden corrosion detection using laser ultrasonic guided waves with multi-frequency local wavenumber estimation," *Ultrasonics*, vol. 108, p. 106182, Dec. 2020, doi: 10.1016/j.ultras.2020.106182.
9. Z. Tian, W. Xiao, Z. Ma, and L. Yu, "Dispersion curve regression – assisted wideband local wavenumber analysis for characterising three-dimensional (3D) profile of hidden corrosion damage," *Mech Syst Signal Process*, vol. 150, p. 107347, Mar. 2021, doi: 10.1016/j.ymssp.2020.107347.
10. B.L. Ervin and H. Reis, "Longitudinal guided waves for monitoring corrosion in reinforced mortar," *Meas Sci Technol*, vol. 19, no. 5, p. 055702, May 2008, doi: 10.1088/0957-0233/19/5/055702.
11. B.L. Ervin, D.A. Kuchma, J.T. Bernhard, and H. Reis, "Monitoring Corrosion of Rebar Embedded in Mortar Using High-Frequency Guided Ultrasonic Waves," *J Eng Mech*, vol. 135, no. 1, pp. 9–19, Jan. 2009, doi: 10.1061/(ASCE)0733-9399(2009)135:1(9).
12. S. Sharma and A. Mukherjee, "Longitudinal Guided Waves for Monitoring Chloride Corrosion in Reinforcing Bars in Concrete," *Struct Health Monit*, vol. 9, no. 6, pp. 555–567, Nov. 2010, doi: 10.1177/1475921710365415.
13. A. Moustafa, E.D. Niri, A. Farhidzadeh, and S. Salamone, "Corrosion monitoring of post-tensioned concrete structures

using fractal analysis of guided ultrasonic waves," *Struct Control Health Monit*, vol. 21, no. 3, pp. 438–448, Mar. 2014, doi: 10.1002/stc.1586.

14. L. Xiao, J. Peng, J. Zhang, Y. Ma, and C.S. Cai, "Comparative assessment of mechanical properties of HPS between electrochemical corrosion and spray corrosion," *Constr Build Mater*, vol. 237, p. 117735, Mar. 2020, doi: 10.1016/j.conbuildmat.2019.117735.

15. B. Zima, K. Woloszyk, and Y. Garbatov, "Experimental and numerical identification of corrosion degradation of ageing structural components," Ocean Engineering, vol. 258, p. 111739, Aug. 2022, doi: 10.1016/j.oceaneng.2022.111739.

16. B. Zima, K. Woloszyk, and Y. Garbatov, "Corrosion degradation monitoring of ship stiffened plates using guided wave phase velocity and constrained convex optimisation method," *Ocean Engineering*, vol. 253, p. 111318, Jun. 2022, doi: 10.1016/j.oceaneng.2022.111318.

17. Z. Su, L. Ye, and Y. Lu, "Guided Lamb waves for identification of damage in composite structures: A review," *J Sound Vib*, vol. 295, no. 3–5, pp. 753–780, Aug. 2006, doi: 10.1016/j.jsv.2006.01.020.

18. B. Zima and R. Kędra, "Detection and size estimation of crack in plate based on guided wave propagation," *Mech Syst Signal Process*, vol. 142, p. 106788, Aug. 2020, doi: 10.1016/j.ymssp.2020.106788.

19. Smith M., *ABAQUS/Standard User's Manual*. Dassault Systèmes Simulia Corp, 2009.

20. Courant R., Friedrichs K, and Lewy H., "On the partial difference equations of mathematical physics," *IBM*, no. 11, pp. 215–234, 1967.

POLISH MARITIME RESEARCH 2 (118) 2023 Vol. 30; pp. 85-94
10.2478/pomr-2023-0024

HEALTH MONITORING OF A COMPRESSION IGNITION ENGINE FED WITH DIFFERENT LOW-SULPHUR MARINE FUELS BY ENDOSCOPIC IMAGE PROCESSING AND ANALYSIS

Zbigniew Korczewski*
Gdansk University of Technology, Poland

* Corresponding author: *zbikorcz@pg.edu.pl (Zbigniew Korczewski)*

ABSTRACT

This article characterises the methodology for the endoscopic testing of a laboratory diesel engine used for testing marine fuels. The 'Shadow' measurement method used in the XLG3 type EVEREST digital endoscope, for quantitative and qualitative identification of detected surface defects, was approximated. Representative endoscopic images of the elements limiting the working space of the research engine are demonstrated, having been recorded during the usable quality testing of newly produced, low-sulphur marine fuels, so-called 'modified fuels'. The main purpose of the endoscopic examinations was the final verification of the tested fuel's suitability for feeding full-size marine engines.

Keywords: low-sulphur marine fuels, usable quality, engine tests, health monitoring, endoscopic examinations

INTRODUCTION

Permanently inflated emission standards, with respect to the release of harmful toxic components in the exhaust gases of marine engines, enforce the application of various types of exhaust purifying (neutralising) devices, e.g. wet 'scrubbers' or dry 'sorbers', as well as non-standard marine fuels [1]. These are usually low-sulphur fuels, the so-called 'modified (blended) fuels', produced by the mechanical mixing of Marine Gasoil (MGO) type distillate based fuel with RMG380 type residual marine fuel oil in an appropriate mass ratio [6]. The propellant oils obtained in this way should be subjected to comprehensive numerical tests, by means of accessible utility computer programs that enable simulating engine working processes, within:

- energy performance [14],
- fuel combustion [10],
- exhaust chemical emissions [7] [11],
- fuel injection [13], and
- working medium exchange [9].

Experimental engine tests should then be carried out in laboratory conditions. Their main purpose should be to determine the usable quality of the non-standard fuel before it enters use in ship operations. Experimental testing of the fuel is most often carried out on specially designed small-scale engine stands, which imitate the essential design and parametric features of a real object [5] [15] and, very rarely, on full-size marine engines [4] [16].

In order to carry out a comparative analysis of the impact of various types of modified marine fuels on the energy state of a diesel research engine (in terms of its performance, efficiency and chemical emissivity of exhaust gases), parametric tests should be conducted according to the established program. The methodology for carrying out this type of research was developed at the Department of Ship Power Plant in the Gdańsk University of Technology [6]. This research makes it possible to determine the nature of the impact of the elemental composition and the calorific and ignition properties of the applied fuel on the selected performance and emission parameters of the research engine. It also enables

determination of the position of the fuel when ranking the usable quality of the previously tested marine fuels [5]. Engine tests are preceded by the proper preparation of a fuel sample, delivered by the manufacturer (or shipowner) in an appropriate amount; this includes its purification and initial assessment of the combustion process quality in the bomb calorimeter [20].

After completing the program of parametric tests on the laboratory engine powered by the tested marine fuel, direct, optical assessment (verification) of its technical condition should be started, in terms of the injection apparatus, as well as working space. Until then, the engine should be started several times from a cold state, with manual switching of the fuel fed system from distillate fuel to the modified marine fuel under test (and vice versa). The engine should be also loaded according to the propeller or regulator characteristics in the adjusted range of torque and crankshaft rotational speed variations. The structural verification of the engine should be carried out after at least 20 hours running time.

First, the injector and the injection pump should be removed from the engine, which are subjected to further diagnostic examinations on specialised test beds, and then disassembled and optically verified, particularly their precise couples (friction nodes) [6].

In the last stage of the research, an endoscopic assessment of the working space and technical state of the engine is carried out, in accordance with the previously developed methodology for conducting this type of diagnostic test [5].

RESEARCH METHODOLOGY AND APPLIED MEASURING APPARATUS

Detection of the material surface defects of elements limiting the working spaces of a piston internal combustion engine, by means of optical and digital endoscopes, is one of the youngest methods of technical diagnostics [2] [12]. Today this kind of measuring apparatus is widely applied to the operation of automotive engines [8]. Its high diagnostic efficiency is also known, in terms of industry and marine engine operation [3] [18]. This is particularly important in the early stages of their development, when the observed parameters of the diagnostic systems are not sufficiently sensitive to changes in the state of the surface layers. On the basis of the nature and size of the identified surface defects and damage, it is not only possible to assess the technical condition of directly accessible structural elements of the engine's working space, but also (indirectly) to assess the technical condition of those structural elements of the engine that are not directly accessible and which cooperate with workspaces. Thus, on the basis of the endoscopic examination of the cylinder surface and the nature of the surface defects detected on it, an indirect diagnosis can be made regarding the technical condition of the ring or guiding part of the piston, although it is not possible to make a direct endoscopic assessment of the technical condition of these areas of the piston. The basic condition for reliable endoscopic diagnoses of the technical condition of engine working spaces is the ability to make, not only a qualitative, but also a quantitative, assessment of the detected surface defects. Digital endoscopy brings completely new possibilities in this regard. Digital image analysers, cooperating with the 'StereoProbe', 'ShadowProbe', 'Laser-Dots' and 'PhaseProbe' measuring heads, allow for digital processing of stereoscopic effects, which enables dimensioning of the seen images of surface defects in such a way that they give the impression of quasi-three-dimensionality, with their depth, solidity and mutual arrangement (Fig. 1). Analysis of the literature on the subject indicates that there is a great importance for the diagnosis of such a method of identifying damage. On the basis of the available statistical data and the results of the author's own research, it can be concluded that the application of endoscopic methods can now detect most of the operational damage to the working spaces of the engine (also identified by other diagnostic methods).

The qualitative (optical) and quantitative (digital) assessment of the technical condition of the working space of a Farymann Diesel D10 type single-cylinder diesel research engine with a pre-combustion chamber, presented in this article, was carried out using the Everest XLG3 type industrial video endoscope equipped with a 'ShadowProbe' measuring head [17]. Endoscopic diagnostic examinations were aimed at estimating the intensity of the degradation process of an engine's structural elements under feeding conditions with various types of distillation and residual marine fuels, including low-sulphur, modified (blended) ones [6]. So far, six different low-sulphur marine fuels have been tested; the basic physical and chemical properties are summarised in Table 1.

a) b)

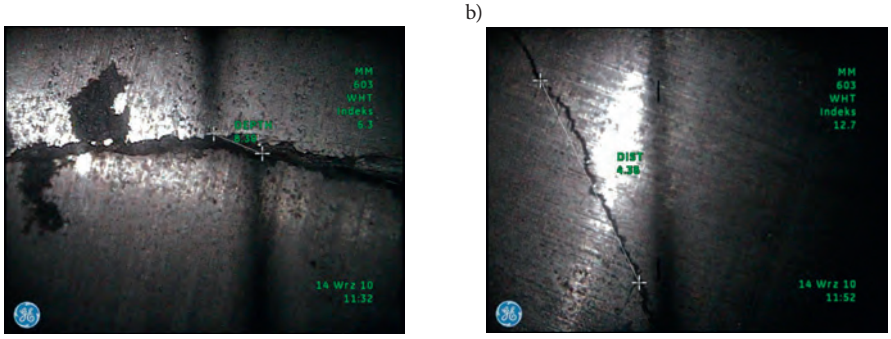

Fig. 1. Endoscopic image of crack in the cylinder liner of the Bukh Diesel E100 engine, dimensioned with the 'Shadow' method: a) step of the cracked cylinder surface layer – 8.30 mm, b) length of the step crack – 4.38 mm

Tab. 1. Measurement results of elemental composition, as well as energy and ignition properties, of the considered low-sulphur marine fuels

PARAMETER	MGO	MDO	RMD 80/L	RMD 80/S	RME 180	RMG 380
The content of carbon *C*, % m/m	86.26	86.63	86.14	86.54	86.12	86.10
The content of hydrogen *H*, % m/m	11.10	11.20	11.72	11.75	11.80	11.90
The content of nitrogen *N*, % m/m	0.05	0.04	0.027	0.02	0.02	0.02
The content of sulphur *S*, % m/m	0.09	0.008	0.028	0.10	0.01	0.01
Gross calorific value, MJ/kg	46.20	45.68	46.01	45.41	46.19	46.03
Net calorific value, MJ/kg	43.23	42.70	43.04	42.44	43.20	43.08
Cetane Number (CN) / Calculated Carbon Aromaticity Index (CCAI)	57.2	51.0	755.0	791.0	750.0	747.0
Density at 15°C, kg/m^3	827.1	820.0	872.7	885.0	878.7	884.5
Kinematic viscosity at 40°C (dist.) / 50 C (res.), mm/s	2.99	2.37	77.83	16.48	165.30	308.00

During the endoscopic examination, special attention was paid to the cleanliness of the whole working space. In addition, one should pay attention to the presence of surface corrosion and erosion defects, as well as products of incomplete fuel combustion on the piston crown, bottom plate of the cylinder head, cylinder liner surface and on the valve heads and seats (faces).

Figure 2 shows a general view of the XLG3 video endoscope ready for usage. This device comprises a complex diagnostic system and enables the inspection of the internal spaces of the engine through existing or specially made technological openings, with a diameter of at least 7 mm. The XLG3 was equipped with a replaceable inspection probe with the following parameters: diameter 6.1 mm, length 3.0 m. The probe tip was controlled by a joystick located on the handle (articulation control, with electronic position lock function and automatic return to the straightened position of the probe) and allowed the probe to be bent by 120° in any direction (up-down / left-right).

The optical image was converted into an electronic image by means of a CCD SUPER HEAD TM camera, with a diameter of 4.2 mm and a resolution of 440,000 pixels, placed in the head of the speculum. This provided continuous digital zoom and left-right image reversal. The digital recording of the colour image was sent via the transmission rail (signal wires) of the inspection probe to the central unit of the endoscopic set. Then, the image 'passed' through digital processors and was sent to the LCD monitor mounted in the handle of the video probe, above the manual panel. The inspection probe of the video endoscope has replaceable tips, enabling observation in the frontal and lateral sectors at different angles and, because of this, the possibility of manually inspecting the internal spaces of the engine are significantly increased. It is also possible to replace the lenses of the speculum head from standard to measuring ones in operating conditions, without the need for additional tools and breaks in testing. This way of dimensioning surface defects by means of the 'Shadow' method (or any other) is ensured; the probe is protected against mechanical damage by an external tungsten braid.

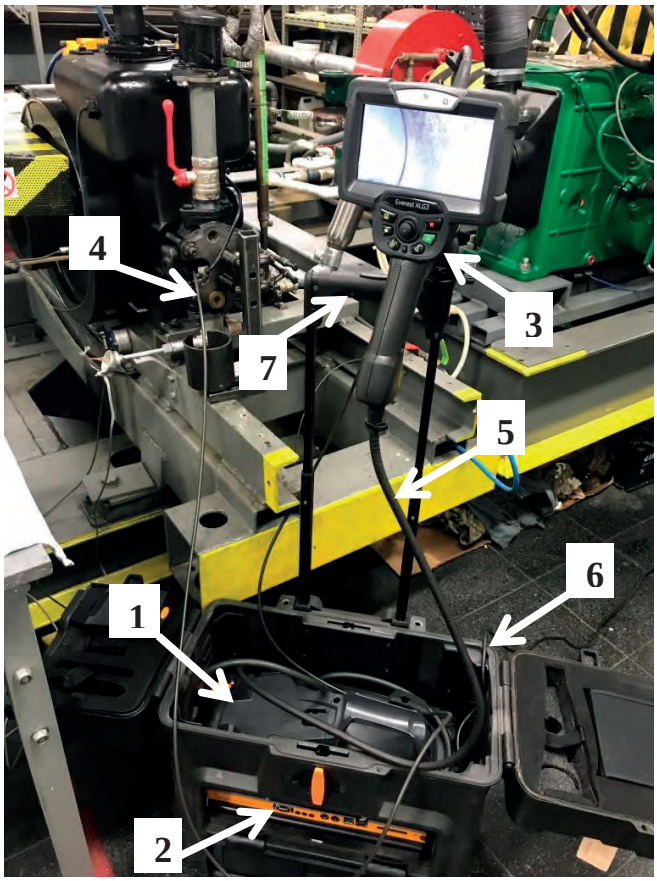

Fig. 2. General view of the Everest XLG3 measuring video endoscope ready for usage (Farymann Diesel D10 type research engine in the background): 1 – central unit, 2 – control panel, 3 – videoprobe handle with a manual panel and monitor, 4 – inspection probe, 5 – optical fibre of the object illumination, 6 – suitcase, 7 – transport (assembly) handle

The XLG3 video endoscope is equipped with a source of cold white light (a 75W HID discharge lamp – the arc tube), with a guaranteed life span of 1000 hours, which is placed in the device's housing. The light is white and the colour temperature of the light source is about 5000 K. The video endoscope application software enables the measurement of detected damage and surface defects using the 'Shadow' method, as well as digitally saving recorded images (photos and videos) in the following formats: BMP, JPG, and MPEG4. These can be saved in the internal memory (50 GB) or on a removable USB drive.

In order to gain access to the working space of the research engine, the injector was removed from the cylinder head and the sight glass probe of the video endoscope was introduced (Fig. 3 and 4). Endoscopic examination should be carried out with special precautions. Failure to comply with the basic procedures of conduct during the endoscopic examinations may result in the destruction of the video probe, damage to the structural elements of the engine, and, even, its complete immobilisation, as a result of accidental entry into the working spaces of the so-called 'foreign objects' (e.g. the cut end of the inspection probe). The most important principles and methodological recommendations, which must be categorically followed in order to ensure rational usage of the endoscopic system for diagnosing internal combustion engines, were described in the publication devoted to the operational diagnostics of marine engines [6].

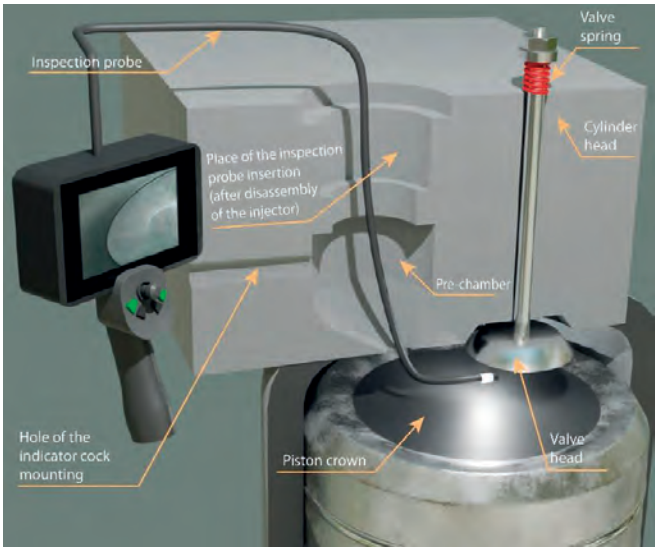

Fig. 4. Longitudinal section of the cylinder head of the Farymann Diesel D10 engine with the marked place of entering the video endoscope inspection probe

SURFACE DEFECT DIMENSIONING TECHNOLOGY

The tip of the video endoscope's 'Shadow' inspection head is equipped with specialized optics, generating a straight-line shadow in the luminous flux (like a projector) on the surface of the examined element. The projection of the shadow takes place at a known angle of the sighting head in relation to the observed surface and a known angle of the observation sector. The shadow generated near the detected defect is then located and recorded by a CCD camera placed in the assembly head. The closer the inspection head is to the observed surface, the closer the shadow line is to the left hand side of the monitor screen. Since the position of the shadow generating the image on the matrix of the LCD monitor screen is known, it is possible to easily calculate the magnification of this image and determine the linear dimension of the distance between individual pixels, as well as the actual dimensions of the detected surface defects, from dependencies (1) and (2) (Fig. 5).

a) b)

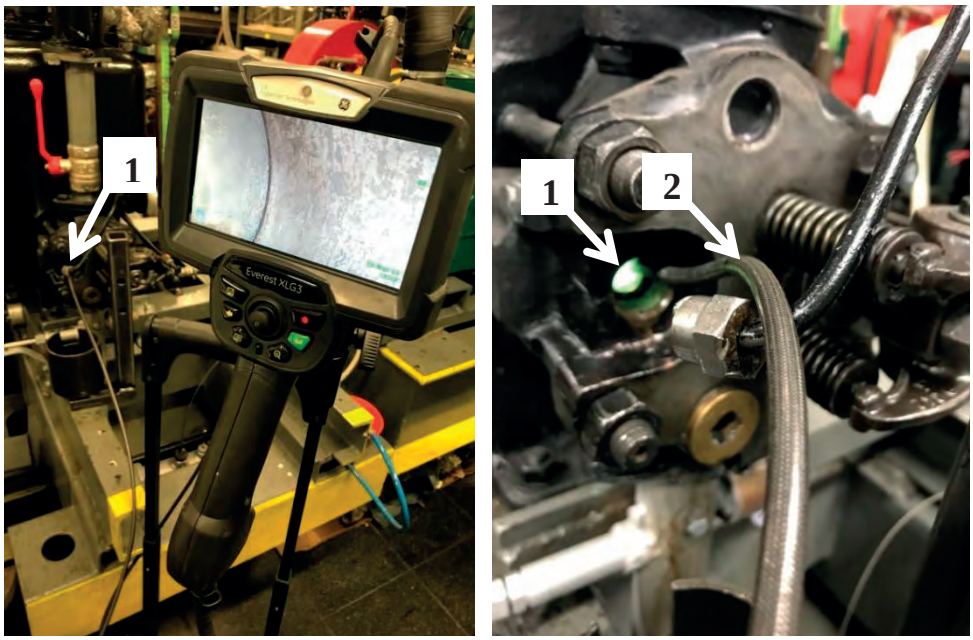

Fig. 3. View of the XLG3 manual endoscope panel with a visible image of the cylinder space of the Farymann Diesel research engine type D10 (a) way of inserting the inspection probe of the video endoscope into the research engine working space (b) 1 – inspection hole after removing the fuel injector, 2 – inspection probe

The diagnostician confirms the position of the shadow line on the monitor matrix by superimposing the cursor line on the shadow (dashed line in Fig. 5). In this way, the digital coordinates of the shadow line are determined. In Fig. 5, the

digital position of the shadow line on the monitor matrix corresponds to X=150 pixels, counted from the left side of the screen. The calibration data of the applied measuring head, stored in the computer database of the video endoscope, show that this corresponds to the distance of the probe lens from the observed surface of (for this example) 20 mm.

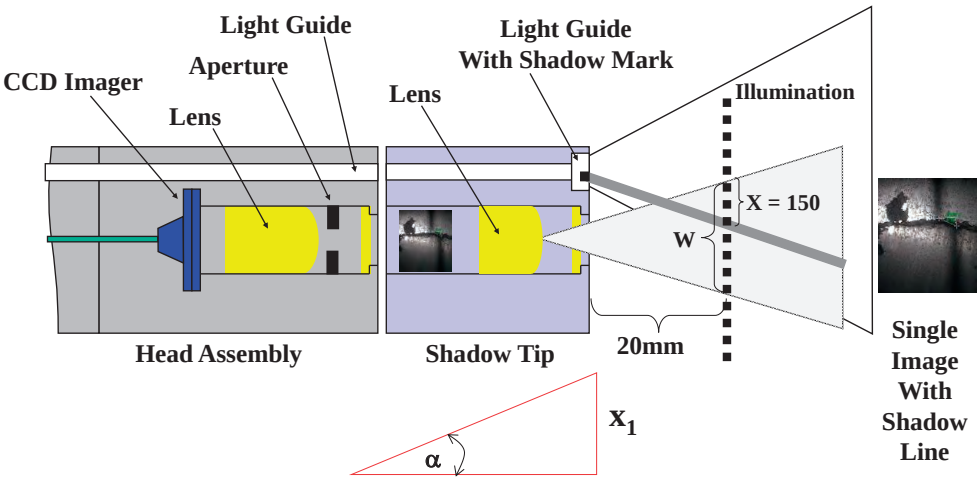

Fig. 5. Schematic diagram of the 'Shadow' measurement method [19]

The calculation algorithm of the video endoscope computer, by using simple trigonometric relationships for the field of view angle of the measuring head 50° (α = 50°/2), determines the X_1 coordinate on the monitor matrix from the equation:

$$X_1 = tg\alpha \cdot 20\ mm = tg25^o \cdot 20\ mm = 9.32\ mm \quad (1)$$

Hence, the dimension W is:

$$W = 2 \cdot X_1 = 2 \cdot 9.32\ mm = 18.64\ mm \quad (2)$$

For a given resolution of the LCD monitor matrix (X 640 pixels, which corresponds to a dimension of 18.64 mm), it can be determined, from the aspect ratio, that the distance between individual pixels is 0.029 mm. Therefore, the actual dimension of the detected surface defect L represents the distance between the dimensional cursors. This is calculated by multiplying the conversion factor of 0.029 mm/pixel by the number of pixels between the dimensional cursors marked by the diagnostician (vertical and horizontal coordinates), read by the computer from the monitor matrix.

The following measurement options are available in the 'Shadow' method [19]:

- length;
- skew length;
- multi-segment length, broken length (circumference);
- distance of the point from the base line;
- depth (protrusion); and
- diameter of the marked area (using a circular ruler).

A very important diagnostic advantage of the 'Shadow' method is the possibility of immediate resolution of doubts regarding the correct interpretation (unambiguous distinction) of surface defects, resulting in material loss or build-up. Diagnostic problems of this type accompany the assessment of the working spaces' technical conditions within combustion engines. Due to optical and light effects, the usual contamination of the surface of the air or exhaust passages, in the form of mineral deposits or fuel combustion products (carbon deposits), is often interpreted as corrosive or erosive defects in the structural material. Figure 1 shows that such doubts are easily resolved by the nature of the shadow line deviation observed on the video endoscope monitor. The surface indentation (the greater distance of the speculum head to the surface) is accompanied by a refraction and shift of the shadow line to the right hand side of the screen, whilst its convexity (its greater approximation to the speculum head) comprises refraction and a shift of the shadow line to the left hand side of the screen. Figure 1a shows an example of the result of measuring the depth of a concave surface profile of a crack in the cylinder surface, made with the Everest XLG3 video endoscope. In turn, for the measurement of the crack length (Fig. 1b) of 4.38 mm, the accuracy index is 12.7, which corresponds to a measurement error of 0.1 mm. The method of determining the accuracy index of the measurements carried out is shown in Fig. 6.

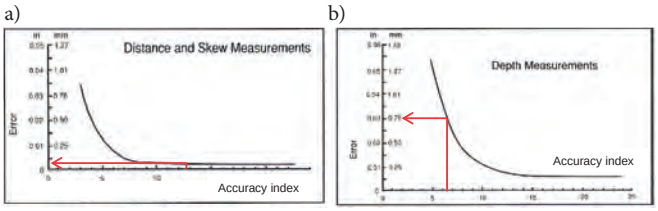

Fig. 6. The method of determining the measurement error from the measurement accuracy index using the'Shadow' method: a) measurement of the distance and skew length; b) depth measurement (protrusion) [19]

It should also be taken into account that in the 'Shadow' method, the measurement of the depth (protrusion) of the surface profile is only possible along the shadow line generated perpendicular to the tested surface.

The 'shadow' method is particularly characterised by the utilitarian values confirmed in diagnostic examinations of marine engines, as well as high accuracy, which (while maintaining the required measurement conditions) might reach 95% [17]. The most important factor of high measurement accuracy is the maximum approximation of the

speculum head to the tested surface (the shadow line moves to the left as it approaches the surface of the speculum head) and maintaining the position of the speculum head perpendicular to this surface (the shadow line runs perpendicular to the base of the monitor's screen).

RESULTS AND DISCUSSION

Before the video endoscope can begin recording, the appropriate optical lens on the sight glass head of the inspection probe has to be installed. Two optical lenses are used for engine examinations:

- standard probe XLG3T61120FG type, 6.1 mm in diameter, straight-on observation, 120° field of view and 5-100 mm depth of field;
- measuring ShadowProbe XLG3TM6150FG type, with a diameter of 6.1 mm, straight ahead observation, angle of view 50° and depth of field 12–30 mm.

Each endoscopic examination of the engine begins with a standard lens, while the detected surface defects are identified with a measuring lens. During the examination, special attention should be paid to the condition of the valve heads and seats, as well as the condition of the internal surfaces of the cylinder liner (surface layer), as well as the piston head and bottom. The recorded results (endoscopic images) are related to the reference state of the working space of the research engine fed with MDO fuel, for each test of a new type of low-sulphur marine fuel (Fig. 7). Additionally, a comparative analysis of endoscopic images of the same structural elements of the engine working space is carried out, being recorded immediately before and after the parametric tests of the marine fuel (Fig. 8).

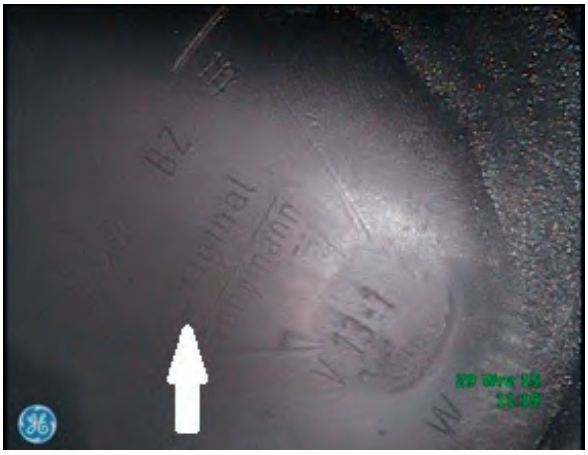

a) Piston head with visible identification number

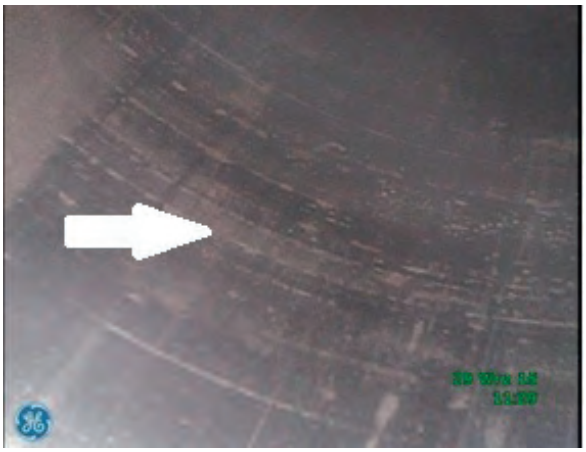

b) Cylinder sliding surface in the vicinity of BDC – traces of abrasive wear, no traces of the liner 'honing'

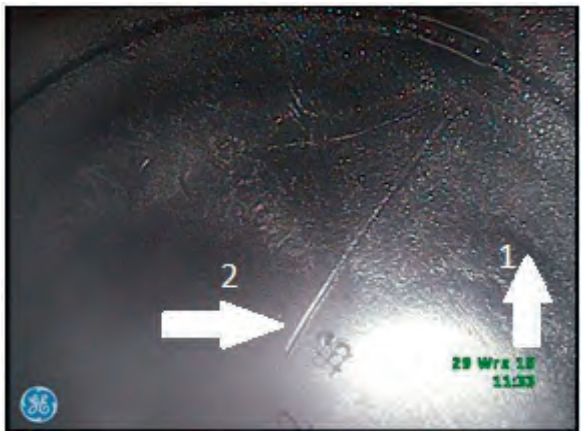

c) Piston crown – visible traces of carbon deposits (1) and scratches on the surface (2)

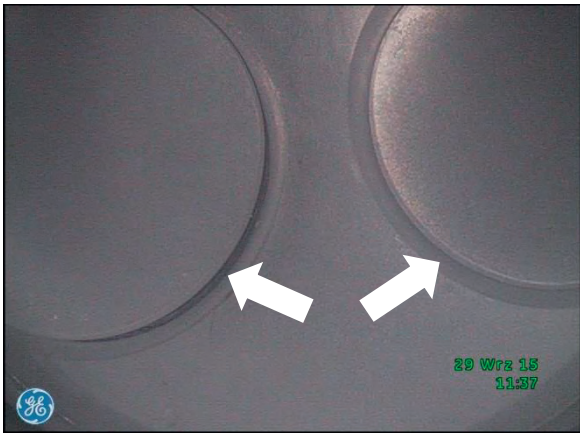

d) Bottom plate of the cylinder head with valve seats

e) Measurement of the scratch length on the piston crown made by the 'Shadow' method – 7.52 mm, with an accuracy index of 4.9, corresponding to an absolute error of 0.3 mm

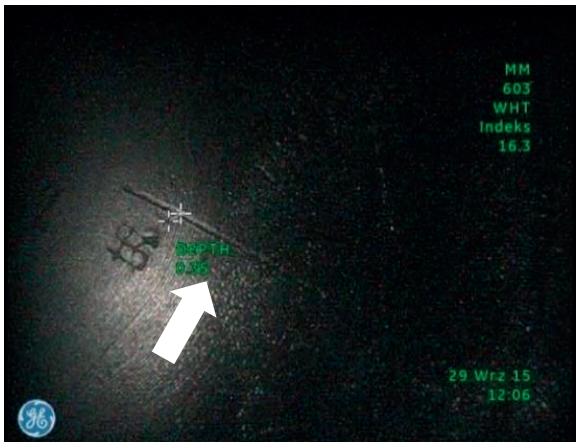

f) Measurement of the scratch depth on the piston crown made by the 'Shadow' method – 0.35 mm, with an accuracy index of 16.3, corresponding to an absolute error of 0.1 mm

Fig. 7. Endoscopic image of the in-cylinder space of the Farymann Diesel D10 engine fed with MDO standard fuel in the reference condition (a-d) and the results of measurement of surface defects detected on the piston crown (e-f)

As a result of endoscopic examinations of the research engine in the reference condition, the following were found:

- the presence of longitudinal traces of slight abrasive wear of the cylinder liners
- (microslicings, scratchings, ploughings);
- the presence of small surface defects on the piston crown (mainly scratchings);
- slight deposits of impurities (mainly soot) on the bottom plate of the cylinder head, as well
- as on the surfaces of the cylinder's intake and exhaust valve heads.

The quality of the combustion process is reflected in the technical condition of the surfaces limiting the working space of the research engine. For example, as a result of the parametric tests while using low-sulphur MGO distillate fuel, significantly exceeded emissions of unburnt hydrocarbons and carbon monoxide were found. This diagnostic symptom proves its incomplete combustion [5]. Comparing the endoscopic examination results recorded for the engine working space carried out immediately before and after parametric tests, an increased amount of soot and ash is evident on the piston crown, bottom plate of the cylinder head and valve heads (Fig. 8). These are unambiguous symptoms of an incorrect fuel dose or injection advance angle, which indicate the need for engine adjustment. However, no additional surface defects were detected and earlier traces of abrasive, corrosive and erosive wear identified on the cylinder liner surface (i.e. at the beginning of the research engine operation) were conservative. Interestingly, the working space of the engine was self-cleaned of soot after switching to a different type of low-sulphur residual RMG380 marine fuel, with significantly lower chemical emissivity of exhaust gases [5] (Fig. 9). The registered results of the engine's endoscopic examinations were verified during direct inspection of its working space, after removal of the cylinder head at the end of the whole testing program for all marine fuels, see Fig. 10. The results confirmed the satisfactory technical condition of the engine, without any symptoms of destructive impacts on its structure from any of the tested low-sulphur marine fuels (apart from carbon deposits).

BEFORE THE PARAMETRIC EXAMINATIONS

a) Cylinder surface in the lower part of the liner – traces of abrasive and erosive wear, no visible traces of honing of the liner

c) Piston crown – identification numbers visible

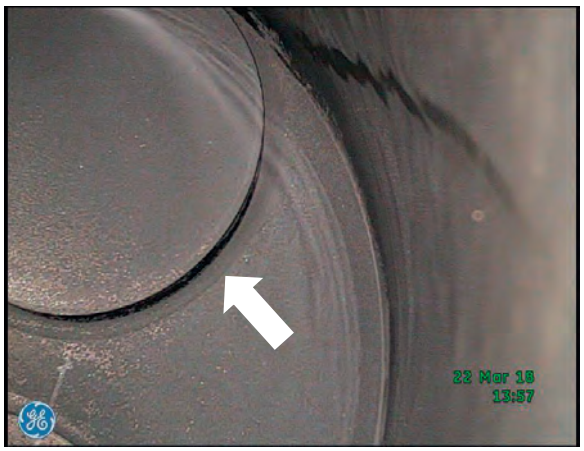

e) Bottom plate of the cylinder head – ajar outlet valve, closed inlet valve

AFTER THE PARAMETRIC EXAMINATIONS

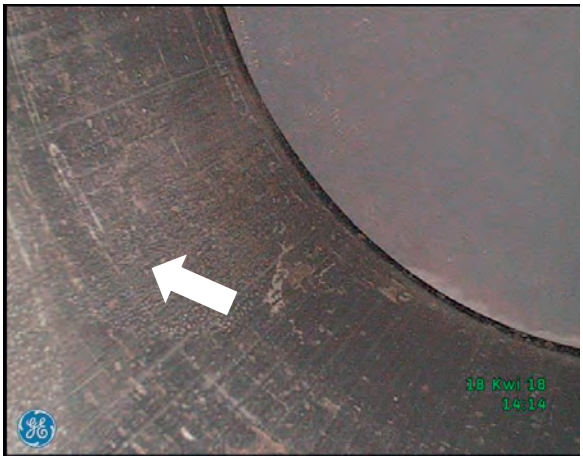

b) Cylinder surface in the middle part of the liner – traces of abrasive and erosive wear, no visible traces of honing of the liner

d) Piston crown – thick layer of soot, identification numbers not visible (visible trace after moving the video endoscope probe)

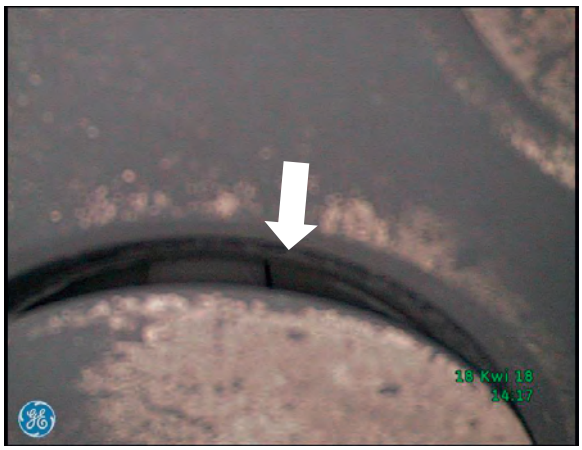

f)) Bottom plate of the cylinder head – ajar outlet valve, closed inlet valve (magnification), carbon deposits on the valve face

BEFORE THE PARAMETRIC EXAMINATIONS **AFTER THE PARAMETRIC EXAMINATIONS**

g) Fuel injector spray tip fitted immediately prior to parametric examinations

h) Fuel injector removed from the cylinder head – thick layer of soot on the spray tip

Fig. 8. Endoscopic image of the cylinder working space (a–l) and view of the fuel injector spray tip (g–h) of the Farymann Diesel D10 research engine before and after parametric examinations in the conditions of feeding MGO type marine fuel

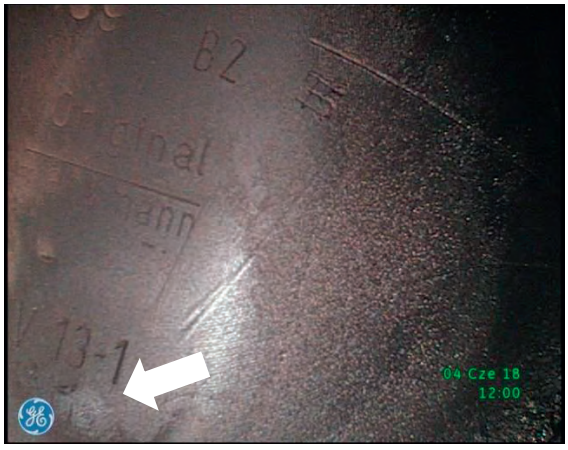

Fig. 9. Endoscopic image of the piston crown of the Farymann Diesel D10 research engine after testing RMG380 type marine fuel– surface clean, free of defects and contamination, identification numbers visible again

Cylinder liner closed by the piston head – clean surface, identification numbers visible

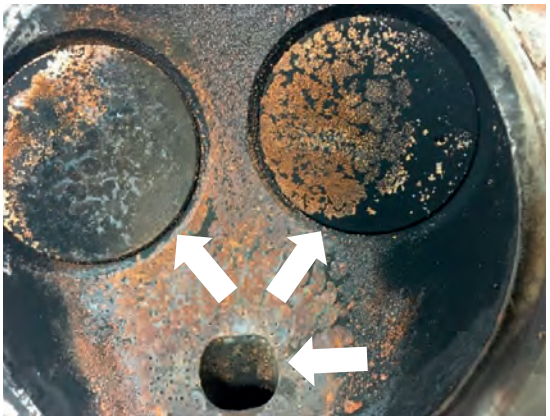

Bottom plate of the cylinder head – closed cylinder valves, a passage connecting the cylinder working space with the combustion pre-chamber, no traces of working medium leakage through the valve faces

Fig. 10. View of the in-cylinder space of the Farymann Diesel D10 engine after removing the cylinder head

FINAL REMARKS AND CONCLUSIONS

On the basis of the results recorded from the endoscopic examinations of the laboratory diesel engine after the completion of the entire testing program for low-sulphur marine fuels, it can be concluded that the technical condition of the available structural elements limiting its working space is satisfactory. The condition did not undergo significant changes under the influence of changes in the elemental composition of the fuel or the additives used to improve its lubricity. Also, changes in temperature and viscosity, during the implementation of transient processes in particular (e.g. rapid changes in a fuel dose during engine running), did not result in noticeable wear of the surface layers of the available structural elements of the working space. The detected surface defects, in the form of carbon deposits, indicate the need to adjust the fuel dose and the injection advance angle.

REFERENCES

1. K. Andersson, S. Brynolf, E. Fridell, and M. Magnusson, *Compliance possibilities for the future ECA regulations through the use of abatement technologies or change of fuels.* Transportation Research Part D: Transport and Environment, 2014, 28, pp. 6-18. https://doi.org/10.1016/j.trd.2013.12.001.

2. J. Breen and M. Stellingwerff, *Application of optical and digital endoscopy.* Proceedings 2nd EAEA–Conference, Vienna, 1995.

3. J. Hlebowicz, *Industrial endoscopy.* Gamma Office. Warszawa 2000 (in Polish).

4. Z. Korczewski, *Test method for determining the chemical emissions of a marine Diesel engine exhaust in operation.* Polish Maritime Research, 2021, 28, pp. 76-87. https://doi.org/10.2478/pomr-2021-0035.

5. Z. Korczewski, *Energy and emission quality ranking of newly produced low-sulphur marine fuels.* Polish Maritime Research, 2022, 29, pp. 77-87. https://doi.org/10.2478/pomr-2022-0045.

6. Z. Korczewski, *Methodology of testing marine fuels in real operating conditions of the compression-ignition engine.* Gdańsk University of Technology, PL, 2022 (in Polish).

7. J. Kowalski, *ANN based evaluation of the NOx concentration in the exhaust gas of a marine two-stroke diesel engine.* Polish Maritime Research, 2009, 16, pp. 60-66. https://doi.org/10.2478/v10012-008-0023-7.

8. L. Kukiełka, D. Woźniak and J. Woźniak, *Endoscopy in automotive technology chosen aspects.* Autobusy, 2015, 6, pp. 292–298.

9. M.I. Lamas, C.G. Rodriguez and J.M. Rebollido, *Numerical model to study the valve overlap period in the Wartsila 6L 46 four-stroke marine engine.* Polish Maritime Research, 2012, 19, pp. 31-37. https://doi.org/10.2478/v10012-012-0004-8.

10. M.I. Lamas and C.G. Rodriguez, *Numerical model to study the combustion process and emissions in the Wartsila 6L 46 four-stroke marine engine.* Polish Maritime Research, 2013, 20, pp. 61-66. https://doi.org/10.2478/pomr-2013-0017.

11. M.I. Lamas, C.G. Rodriguez, J. Telmo, and J.D. Rodríguez, *Numerical analysis of emissions from marine engines using alternative fuels.* Polish Maritime Research, 2015, 22, pp. 48-52. https://doi.org/10.1515/pomr-2015-0070.

12. M.E. Rainer, *Philipp Bozzini – the father of endoscopy.* Journal of Endourology, 2003, 10, pp. 859-862. https://doi.org/10.1089/089277903772036145.

13. C.G. Rodriguez, M.I. Lamas, J.D. Rodríguez, and A. Abbas, *Analysis of the pre-injection system of a marine diesel engine through multiple-criteria decision-making and artificial neural networks.* Polish Maritime Research, 2021, 28, pp. 88-96. https://doi.org/10.2478/pomr-2021-0051.

14. N. Zamiatina, *Comparative overview of marine fuel quality on Diesel engine operation.* Procedia Engineering, 2016, 134, pp. 157-164.

15. R. Zhao, L. Xu, X. Su, S. Feng, C. Li, Q. Tan, and Z. Wang, *A numerical and experimental study of marine hydrogen–natural gas–diesel tri–fuel engines.* Polish Maritime Research, 2020, 27, pp. 80-90. https://doi.org/10.2478/pomr-2020-0068.

16. Z. Yang, Q. Tan and P. Geng, *Combustion and emissions investigation on low-speed two-stroke marine diesel engine with low sulphur diesel fuel.* Polish Maritime Research, 2019, 26, pp. 153-161. https://doi.org/10.2478/pomr-2019-0017.

17. Everest VIT GE. XLG3 VideoProbe measurement system. USA 2011.

18. Europen Motorii Marini srl. The optical fibres industrial endoscopy for marine and industrial engines. Italy 2022.

19. General Electric Company Inspection Technologies. The Everest XLG3 VideoProbe System. Manual Guide. USA 2011.

20. IKA WERKE CALORIMETERS. IKA designed for scientists. IKA-Werke GmbH & Co. KG, Germany 2022.

POLISH MARITIME RESEARCH 2 (118) 2023 Vol. 30; pp. 95-104
10.2478/pomr-2023-0025

ENERGY MANAGEMENT STRATEGY CONSIDERING ENERGY STORAGE SYSTEM DEGRADATION FOR HYDROGEN FUEL CELL SHIP

Wei Cao[1]
Pan Geng[1]
Xiaoyan Xu[1]
Tomasz Tarasiuk[2] *
[1] Shanghai Maritime University, Logistics Engineering College, China
[2] Gdynia Maritime University, Poland

* Corresponding author: *t.tarasiuk@we.umg.edu.pl (Tomasz Tarasiuk)*

ABSTRACT

A hybrid energy system (HES) including hydrogen fuel cell systems (FCS) and a lithium-ion (Li-ion) battery energy storage system (ESS) is established for hydrogen fuel cell ships to follow fast load transients. An energy management strategy (EMS) with hierarchical control is presented to achieve proper distribution of load power and enhance system stability. In the high-control loop, a power distribution mechanism based on a particle swarm optimization algorithm (PSO) with an equivalent consumption minimization strategy (ECMS) is proposed. In the low-level control loop, an adaptive fuzzy PID controller is developed, which can quickly restore the system to a stable state by adjusting the PID parameters in real time. Compared with the rule-based EMS, hydrogen consumption is reduced by 5.319%, and the stability of the power system is significantly improved. In addition, the ESS degradation model is developed to assess its state of health (SOH). The ESS capacity loss is reduced by 2% and the daily operating cost of the ship is reduced by 1.7% compared with the PSO-ECMS without considering the ESS degradation.

Keywords: Hydrogen fuel cell ship, Energy management, Fuzzy PID, Equivalent energy consumption minimum, Energy storage system degradation

INTRODUCTION

The data show that international shipping released about 796 million tons of CO_2 in 2012. As a result, the International Maritime Organization has developed regulations to reduce CO_2 emissions from ships [1, 2]. Therefore, all-electric ships with fuel cells and energy storage systems have gained great attention in various countries due to their high efficiency, but chiefly their pollution-free characteristics have to be underlined [3]. Hydrogen fuel cells are now widely used in the fuel cell vehicle industry, but their application in the marine industry is still in its infancy. However, this trend is expected to grow in the future [4].

The power distribution mechanism is the core part of the HES, and can coordinate the output power of power sources and improve power system stability. Intelligent algorithms such as the sine and cosine algorithm, model predictive control, and deep reinforcement learning algorithm are being implemented to achieve a reasonable distribution of the load power among different power sources. For example, Mehdi et al. [5] developed a zero-emission ship model with FCS, Li-ion batteries, as well as shore power, in addition to proposing an EMS based on an improved sine and cosine algorithm. The objective is to reduce hydrogen consumption and prolong the lifetime of the power sources. In [6], the authors proposed a controller consisting of an intelligent algorithm, filters,

and state logic control for a ship with a gas turbine, battery, and supercapacitors (SUC) to achieve real-time control. In [7, 8], a multi-objective deep reinforcement learning-based algorithm is presented for an emission-free ship to optimize the load power allocation among the FCS and ESS. In [9], the authors developed a nonlinear ship model considering the sea state and weather, with the model predictive control being used to solve the optimization problem. In [10], the authors argue that the parameters of the hybrid ESS are critical for the power system. So recursive least squares are applied for online parameter identification and the model predictive control is used to share the load power between the battery and SUC. In [11], the output power of the FCS and battery is determined by minimizing the operation cost. In [12], to reduce the ESS capacity loss, a deep reinforcement learning algorithm is used to jointly optimize the ESS sizing and power distribution mechanism.

The control methods of DC/DC converters have been optimized to improve the stability of the power system. In [13], the authors proposed a controller for DC/DC converters based on a sliding mode control and PI control to minimize bus voltage fluctuations. In [14], a bus voltage control method based on drop control is proposed. This method solves the voltage drop by adding the voltage correction value to the reference voltage. In [15], the authors present an adaptive fuzzy logic controller, and it can be adapted to different operation conditions by adjusting the parameters in real time.

For ship power systems, the EMS consists of two key aspects: the power distribution mechanism and the controller for the DC/DC converter; however, most articles focus on one aspect alone and ignore the impact of ESS degradation on the power system. Therefore, an EMS with hierarchical control is proposed in this paper.

STRUCTURE AND MODEL OF FUEL CELL SHIP

POWER SYSTEM STRUCTURE

For the article purpose, the conventional radial distribution architecture is considered. It is assumed that the system consists of 2×135 kW hydrogen FCS, 2×550 V/100Ah ESS, which can be currently bought on the market, completed by converters, control units, propulsion load, and hotel load. The topology of the analyzed shipboard power system (SPS) is shown in Fig. 1. As the FCS suffers from a slow dynamic response, it requires a couple with ESS, which is applied for covering the fast load variations [16]. During the period of high load power, to meet the load power requirement, the output power of the FCS and ESS is greater than zero. During the period of low load power, the ESS absorbs excess energy to maintain the bus voltage stability [17]. During the entire operation, the ESS has two states, charging and discharging. It is connected to a boost/buck DC/DC converter. Since the FCS does not absorb energy from the system, it is connected to a boost DC/DC converter.

According to the FCS data, when the rated power of the fuel cell system is 135kW, the optimal output power during operation is in the range of 27 kW-120 kW. Both low and high operating conditions will cause incomplete chemical reactions and subsequent damage to the reactor, resulting in a shortened lifetime. Therefore, for subsequent analyses the minimum output power of the fuel cell system is set to 27kW.

The energy storage system (ESS) is to account for the fast load variation. For subsequent analyses, it was assumed that the peak load will equal to 110 kW and single ESS should meet this demand. Therefore, according to recommendation ref. [18], the nominal energy of single ESS was set to 55 kWh.

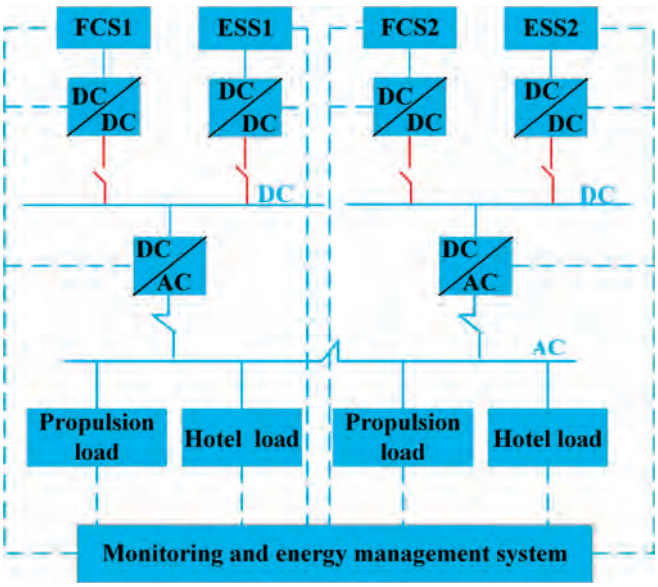

Fig. 1. The topology of the SPS

FC model

The equivalent circuit of a fuel cell (FC) is shown in Fig. 2 and the expression of the fuel cell output voltage is shown in Eq. (1) [19].

$$V_{fc} = E_{oc} - NAln\left(\frac{i_{fc}}{i_0}\right) \times \frac{3}{sT_d+3} - (R_{ohm} \times i_{fc}) \quad (1)$$

where V_{fc} and i_{fc} are the output voltage and output current of the fuel cell respectively. E_{oc} is the open circuit voltage, N is the number of cells, T_d is the response time and R_{ohm} represents the internal resistance.

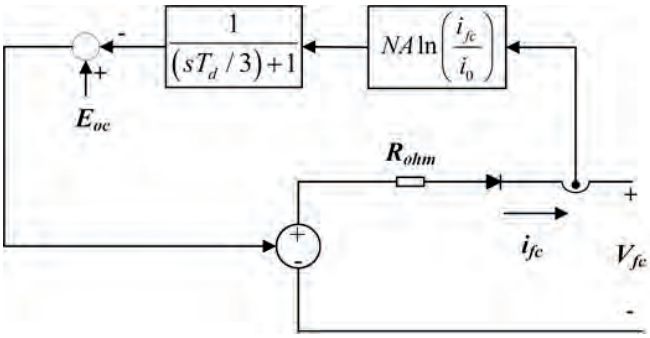

Fig. 2. The equivalent circuit of a fuel cell stack

Li-ion battery model

The dynamic feature of the Li-ion battery is represented by the Thevenin model as shown in Fig 3. The terminal voltage of the battery is shown in Eq. (2) [20].

$$\begin{cases} C\frac{d}{dt}U_C = i_B - \frac{U_C}{R_2} \\ U_B = U_{OC} - (U_C + i_B R_1) \end{cases} \quad (2)$$

where R_1 is the ohmic resistance, R_2 is the polarization resistance, U_C is the polarization voltage. U_B and i_B are the output voltage and output current of the Li-ion battery, U_{oc} is the open circuit voltage of the Li-ion battery.

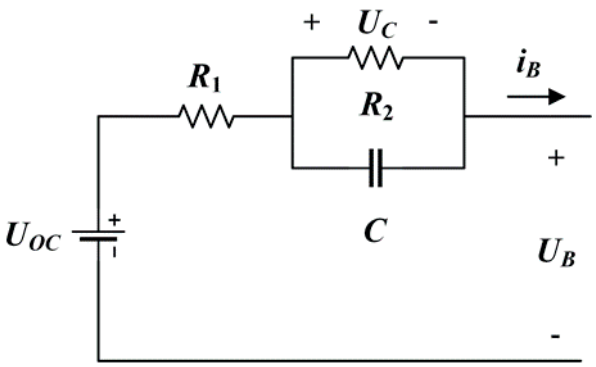

Fig 3. Thevenin model

THE ESS DEGRADATION MODEL

The methods for assessing the SOH include physical model-based methods, semi-empirical life models, and data-driven methods [21]. The ESS must be replaced when its actual capacity is 80% of the rated capacity. The semi-empirical long-term cycle life model is developed in [22]. In this paper, an ESS degradation model based on the semi-empirical life model is developed to calculate the loss of ESS capacity.

$$Q_{loss} = m\sum_{i=1}^{N}[q(i)]^{0.554} \times e^{(-\frac{E}{RT})} \quad (3)$$

$$\begin{cases} q = |I_{ESS}| \times t \\ I_{ESS} = \frac{P_{ESS}}{U_{ESSnom}} \end{cases} \quad (4)$$

$$\begin{gathered} ESS_{int} = C_{power} \times P_{rate} + C_{capacity} \times Q_{rate} \\ C_{loss} = ESS_{int} \times (\frac{Q_{loss}}{0.2}) \end{gathered} \quad (5)$$

where m is a constant, E is the activation energy, and both of them are linearly related to the current rate (C_{rate}). R is the gas constant. It is assumed that the operating voltage of the ESS is stable at the rated value and the temperature (T) is kept constant during the operation, q is the amount of charge absorbed and released by the ESS per unit of time. C_{power} is the cost per unit power of the ESS (\$200/kW). $C_{capacity}$ is the cost per unit capacity of the ESS (\$125/kWh). C_{loss} is the ESS capacity loss cost. ESS_{int} is the installation cost of the ESS. The values of the parameters are listed in Table 1 [23].

Tab. 1. The parameters for ESS degradation model

Parameter	Value
C_{rate}	2C
m	19300
E	-31000
R	8.31 J/mol/K
T	25°C

ENERGY MANAGEMENT STRATEGY

The EMS with hierarchical control presented in this paper involves two layers of control loops: the high-level control loop realizes the reasonable distribution of load power between different power sources depending on the load power and the state of charge (SOC) of the ESS; the low-level control loop suppresses power system fluctuations by controlling the DC/DC converter. The overall structure diagram is shown in Fig. 4.

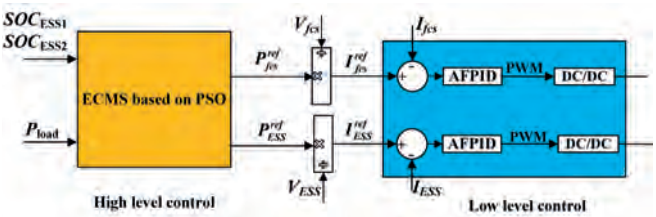

Fig. 4. Hierarchical control structure

HIGH-LEVEL CONTROL

In the high-level control loop, two power distribution mechanisms are designed:

(i) A power allocation mechanism based on the Support Vector Machine (SVM); (ii) An equivalent consumption minimization strategy (ECMS) based on PSO.

The core idea of the ECMS is to equate the energy demand of the ESS with the same amount of hydrogen consumption, which is regarded as indirect hydrogen consumption. The energy demand of the hydrogen FCS is direct hydrogen consumption. The model is solved to minimize the total hydrogen consumption [24]. The algorithm flow chart of the PSO-ECMS is shown in Fig. 5. The instantaneous hydrogen consumption can be defined as the following formula:

$$\begin{cases} minJ_{H_2,eqv}(t) = C_{price} \times \sum_{i=1}^{2}\left(m_{fcsi}(t) + m_{ESSi}(t)\right) \\ m_{fcsi}(t) = \frac{P_{fcsi}(t)}{LHV\eta_{fcs}(t)} \\ \eta_{fcs} = (-0.1123 \times P_{fcs} + 54.1)/100 \\ m_{ESSi}(t) = \frac{n(t)}{LHV}P_{ESSi}(t)p(SOC) \end{cases} \quad (6)$$

where C_{price} is the price of hydrogen ($4.5/kg); n(t) is the equivalence factor, which serves to convert the electrical energy consumed by the ESS into an equivalent amount of hydrogen consumption, $p(SOC)$ is the penalty factor, which is used to ensure that the SOC remains in a specific range. $\eta_{fcs}(t)$ is the efficiency of the FCS at time t, the relationship between the output power and efficiency of the FCS is shown in Fig. 6. P_{fcs}(t) is the output power of the hydrogen FCS at time t; LHV is the low heat value of hydrogen (120MJ/kg); P_{ESS}(t) is the output power of the ESS at time t.

$$\mathrm{n(t)} = 1 - 2\mu \times \left[\frac{SOC(t)}{SOC_{max}+SOC_{min}} - 0.5\right] \quad (7)$$

$$\mathrm{p(SOC)} = 1 - \left[\frac{SOC(t)-SOC_{target}}{SOC_{max}-SOC_{min}}\right]^3 \quad (8)$$

where μ is the equilibrium coefficient; SOC_{max}, SOC_{target}, and SOC_{min} are the maximum, target, and minimum values of the SOC respectively. When $SOC>SOC_{target}$ and $p(SOC)<1$, the cost of ESS energy is lower and the ESS is biased towards discharge; when $SOC>SOC_{target}$ and $p(SOC)>1$, the cost of ESS energy increases and the ESS is biased towards charging.

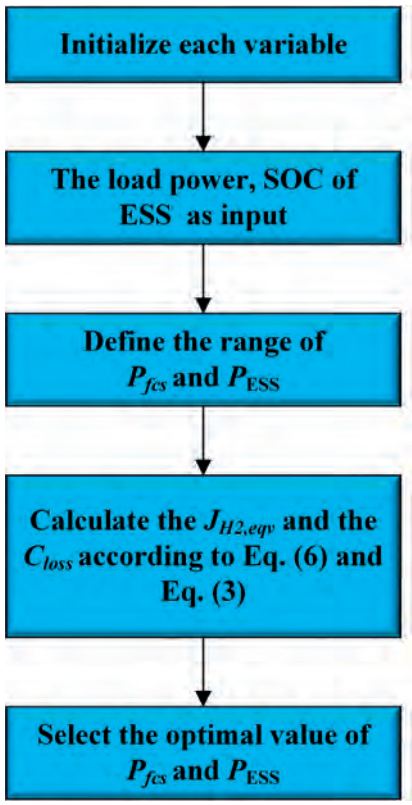

Fig. 5. The flowchart for PSO-ECMS

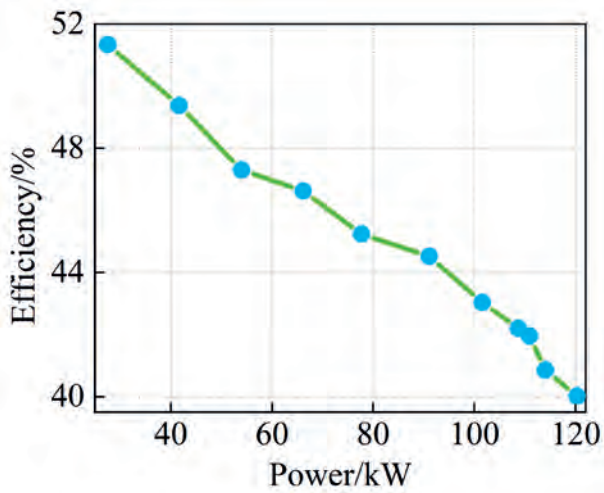

Fig .6. The relationship between the output power and efficiency of the FCS

The following equation about the SOC of the ESS must be satisfied:

$$30\% \leq \mathrm{SOC} \leq 90\% \quad (9)$$

The following equation about P_{fcs} must be satisfied:

$$\mathrm{P}_{fcs,min} \leq P_{fcs} \leq \mathrm{P}_{fcs,max} \quad (10)$$

The following equation about P_{ESS} must be satisfied:

$$|P_{ESS}| \leq P_{ESS,max} \tag{11}$$

The change rate of the FCS output power must satisfy Eq. (12):

$$\left|P_{fcs}(t+1) - P_{fcs}(t)\right| \leq \triangle P_{fcs,max} \tag{12}$$

The power system must maintain a real-time power balance:

$$P_{load} = \sum_i^2 \left(\eta_{DC1} P_{fcsi} + \eta_{DC2} \max\left(P_{ESSi}, 0\right) + \frac{1}{\eta_{DC2}} \min\left(P_{ESSi}, 0\right)\right) \tag{13}$$

where η_{DC1} is the efficiency of the boost DC/DC converter (0.98); η_{DC2} is the efficiency of the boost/buck DC/DC converter (0.9).

The principle of the SVM is to define the reference value of the output power of the FCS and ESS based on the SOC of the ESS and load power. In this paper, the SOC is divided into three stages, and the power distribution mechanism is shown in Fig. 7.

The total output power of ESS is obtained according to Eq. (14).

$$P_{ESS} = P_{load} - P_{fcs1,ref} - P_{fcs2,ref} \tag{14}$$

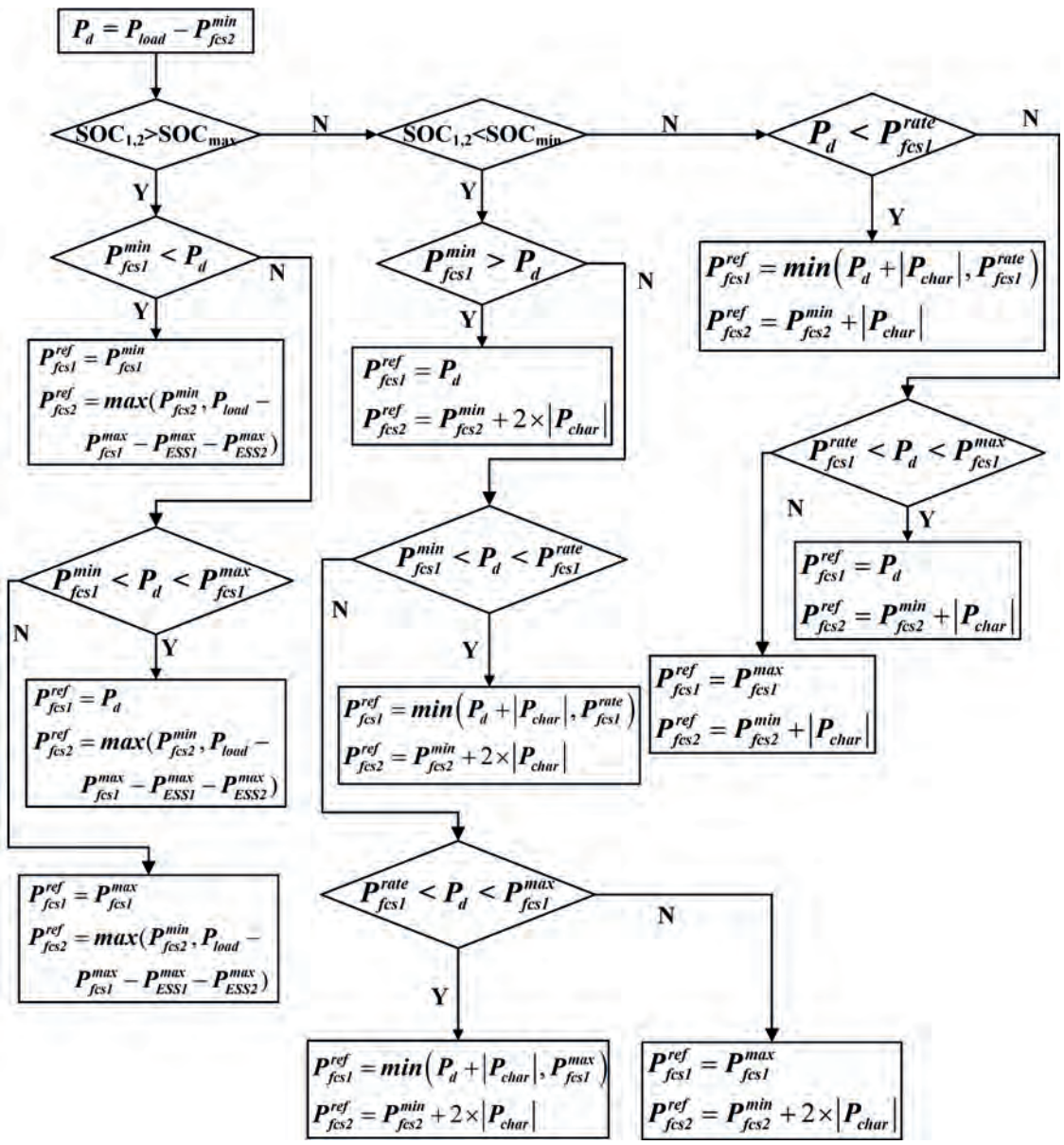

Fig. 7. Power distribution mechanism based on SVM

The output power of ESS1 and ESS2 are determined according to Eq. (15) and Eq. (16).

$$P_{ESS1,ref} = \begin{cases} \frac{SOC_1}{SOC_1+SOC_2} \times P_{ESS}, P_{ESS} > 0 \\ \frac{|SOC_1-SOC_{target}|}{|SOC_1-SOC_{target}|+|SOC_2-SOC_{target}|} \times P_{ESS}, P_{ESS} < 0 \end{cases} \quad (15)$$

$$P_{ESS2,ref} == \begin{cases} \frac{SOC_2}{SOC_1+SOC_2} \times P_{ESS}, P_{ESS} > 0 \\ \frac{|SOC_2-SOC_{target}|}{|SOC_1-SOC_{target}|+|SOC_2-SOC_{target}|} \times P_{ESS}, P_{ESS} < 0 \end{cases} \quad (16)$$

LOW-LEVEL CONTROL

An adaptive fuzzy PID controller (AFPID) is presented in this paper by combining fuzzy control with PID control. The structure of the AFPID is shown in Fig. 8. The AFPID takes the error and the rate of change of the error as input, and corrects the control parameters of the PID in real time by fuzzification, fuzzy inference machine, and defuzzification so that the controller has good dynamic and static characteristics. The fuzzy domains of the variables and the values of the quantization factors are summarized in Table 2.

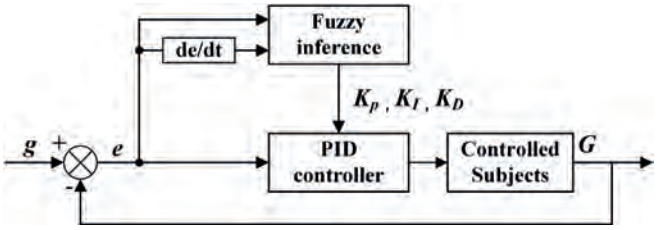

Fig. 8. AFPID controller

Tab. 2. The parameters for AFPID

	e	ec	ΔK_P	ΔK_I	ΔK_D
Fuzzy domains	[-2,6]	[-4,4]	[0,6]	[6,12]	[0,6]
Quantization factors	0.05	0.01	29	30	5
Affiliation function	Triangles	Triangles	NB/PB is Gaussian, the rest is triangular	Triangles	Triangles

RESULT

The EMS with hierarchical control is verified using Matlab/Simulink software, and the main parameters of the model are shown in Table 3.

For further analyses, authors assumed that the considered load profile would correspond to the load profile registered onboard of the hydrogen fuel cell passenger ship "Alsterwasser" [25]. There are four operation states during the voyage, namely, cruising, docking, anchoring and sailing (accelerating). However, this paper focuses on the effect of load fluctuation on the ship power system, so only the docking and sailing are considered, when the high load variations and peak values are observed. The load profiles for the considered states are shown in Fig. 9 [25]. According to the ship operation profile, there are ten such states during one hour. For anchoring state the load is low and for cruising it is constant, more or less 40 kW. Finally, during the docking phase, the load power fluctuates in a wide range, and the peak load power reaches a maximum during the sailing phase.

Tab. 3. The main parameters of the model

	Parameter	Value
FCS	$P_{fcs,min}$	27 kW
	$P_{fcs,max}$	137.5 kW
	$P_{fcs,rate}$	135 kW
	Power ramp rate limit of FCS	±4.24 kW/s
ESS	Nominal voltage/capacity	550V/100Ah
	$P_{ESS,max}$	110 kW
	SOC_{max}	100%
	SOC_{min}	30%
	SOC_{target}	80%

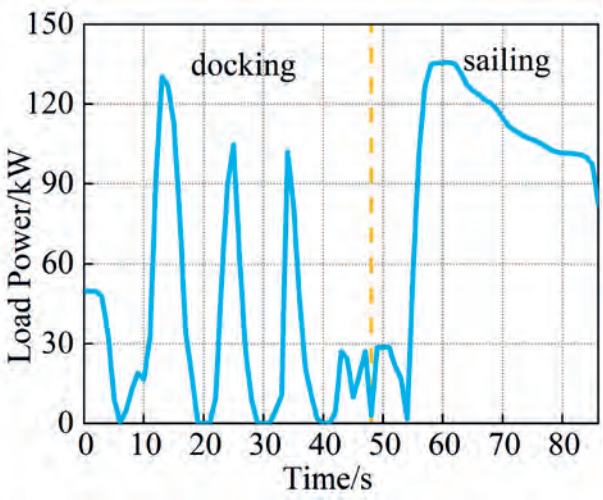

Fig. 9. Load profile

COMPARISON OF THE DIFFERENT POWER DISTRIBUTION MECHANISMS

SVM

The output power of the power sources and the SOC of the ESS are shown in Fig. 10. Fig. 10(a) and Fig. 10(b) indicate that the output power of FCS1 fluctuates greatly since the SVM fails to consider the characteristics of the hydrogen FCS, which will reduce its lifetime. The load power does not exceed the maximum output power of FCS1, ESS1, and ESS2, so during the entire operation the FCS2 works with constant output power of 27 kW, according to control (Fig. 7). Finally, the energies provided by FCS1 and FCS2 are 1.1 kWh and 0.65 kWh, respectively.

The initial values of the SOC of ESS1 and ESS2 are the same, so the output power curves of ESS1 and ESS2 are the same. The average output power of ESS1 and ESS2 is smaller during the entire operation. The results indicate that the power distribution mechanisms based on SVM do not consider the characteristics of each power source and cannot achieve optimal power distribution. When the output power of the ESS is greater than zero, it implies a release of energy and vice versa. From Fig. 10(c), the SOC of ESS1 and ESS2 fluctuates within the bounded range and the final SOC of ESS1 and ESS2 is 79.52%.

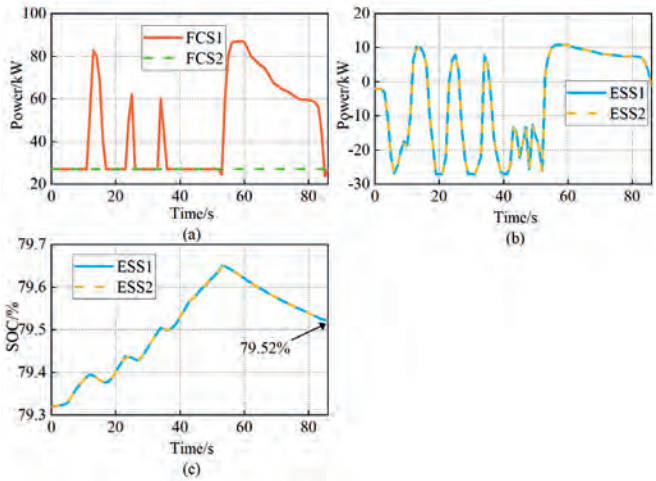

Fig. 10. (a) FCS output power; (b) ESS output power; (c) SOC of the ESS

PSO-ECMS without considering ESS degradation

The output power of the power sources and the SOC of the ESS are shown in Fig. 11. From Fig. 11(a), FCS1 and FCS2 operate in the highest efficiency range and the output power does not fluctuate greatly over the entire operation. During the docking phase, the PSO-ECMS can control the rate of change of the FCS output power, so the output power curve of the FCS is smoother and the peak output power of FCS1 reduces by 50.6% compared with SVM, which can prolong the lifetime of the FCS. From Fig. 11(b), due to the ESSs being used to track the fast load variations, the output power of ESS1 and ESS2 fluctuate greatly during the operation. Fig. 11(c) shows that, during the docking phase, the load power is lower. During this period, ESS1 and ESS2 are charging for more periods, so the SOC reaches the maximum value after the docking phase ends. During the sailing phase, the load power reaches its maximum, and the output power of ESS1 as well as ESS2 reaches peak values. Therefore, the SOC keeps falling. The final SOC of ESS1 and ESS2 is 79.5% and 79.38%, respectively. Both of these values are close to the target SOC.

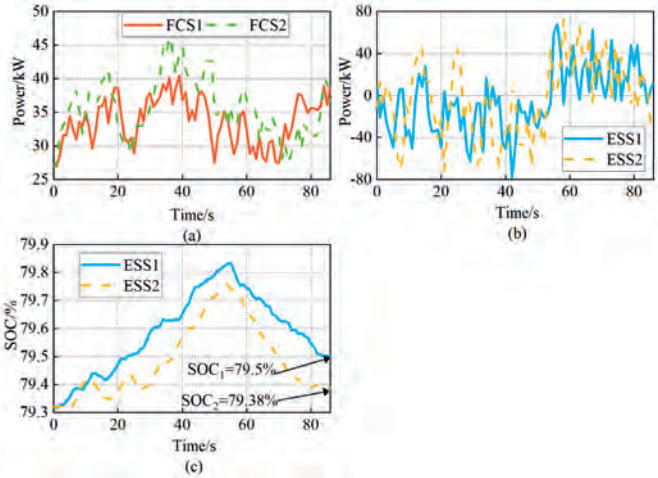

Fig. 11. (a) FCS output power; (b) ESS output power; (c) SOC of the ESS

PSO-ECMS considering ESS degradation

The loss of ESS capacity is calculated based on its output power. From Fig. 12(a) and Fig. 12(b), it is clear that, although the output power of FCS1 and FCS2 does not fluctuate greatly when considering the ESS degradation, it has been rising slowly to reduce the output power of the ESS. Hence, the average output power of the FCS is higher compared with PSO-ECMS when ESS degradation is not considered. From Fig. 12(c), during the docking phase, the ESS SOC keeps increasing. However, during the sailing phase, the SOC of the ESS is smoother. This indicates that the output power of the ESS is smaller, which can reduce the ESS capacity loss. The SOC fluctuates within a reasonable range and the final SOC of ESS1 and ESS2 is 79.8% and 79.63%, respectively. Both of them are approximated target values.

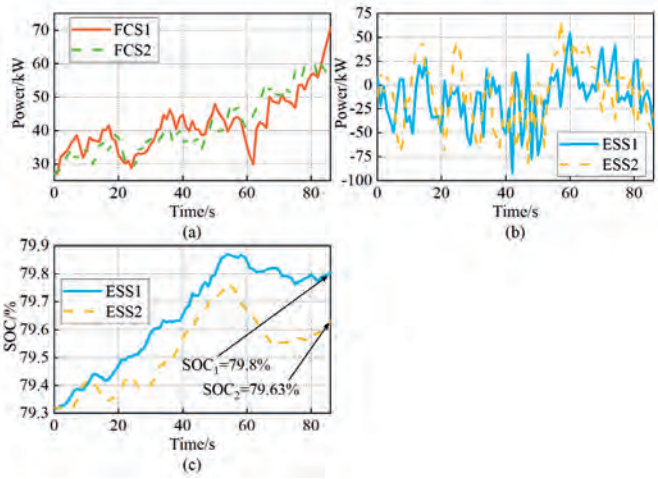

Fig. 12. (a) FCS output power; (b) ESS output power; (c) SOC of the ESS

The hydrogen consumption

Fig. 13(a) indicates the hydrogen consumption increase since the SVM-based power allocation mechanism is an empirical rule-based approach. Although hydrogen consumption is lower during some periods, it cannot achieve the global optimum. The hydrogen consumption is 101.7 g in one cycle and the operation cost is $0.45765 with SVM. From Fig. 13(b), the PSO-ECMS-based power allocation mechanism makes the hydrogen FCSs feed the remaining energy back to the ESS during the docking phase, so the instantaneous hydrogen consumption is higher in some periods. During the sailing phase, the energy stored in the ESS is effectively utilized, and the instantaneous hydrogen consumption is low. Without considering ESS degradation, the hydrogen consumption is 96.29 g in one cycle and the operation cost is $0.4333 with the PSO-ECMS. Compared with SVM, the operation cost reduces by 5.319%. Fig. 13(c) indicates that the hydrogen consumption is 99.63 g in one cycle and the operation cost is $0.44833 with the PSO-ECMS when considering the ESS degradation. Compared with SVM, the operation cost reduces by 2%.

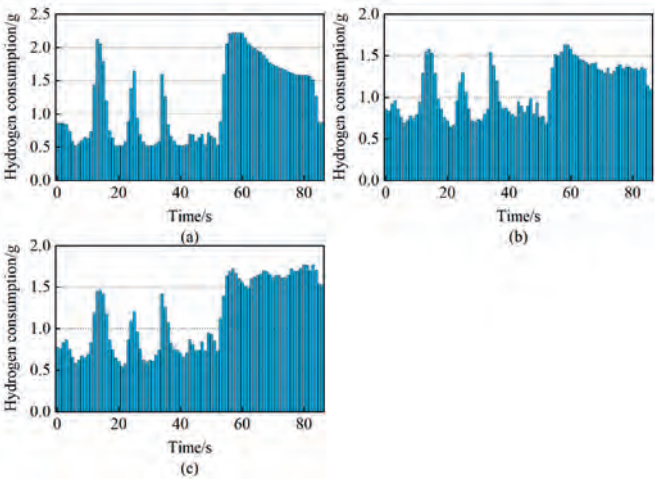

Fig. 13. (a) Hydrogen consumption of SVM; (b) Hydrogen consumption with PSO-ECMS without considering ESS degradation; (c) Hydrogen consumption with PSO-ECMS considering ESS degradation

ESS degradation

From Fig. 14(a), the total capacity loss is 0.00883% in one cycle without considering ESS degradation. From Fig. 14(b), when the ESS degradation constraint is considered, the output power of the ESS is reduced and the total capacity loss of the ESS is 0.00866% in one cycle. The capacity loss is reduced by 2% compared to that without considering ESS degradation. The hydrogen consumption is $0.4333 and the cost of the ESS capacity loss is $12.74 without considering ESS degradation. However, when ESS degradation is taken into account, the hydrogen consumption is $0.44833 and the cost of the ESS capacity loss is $12.5, with the daily operation cost being reduced by 1.7%.

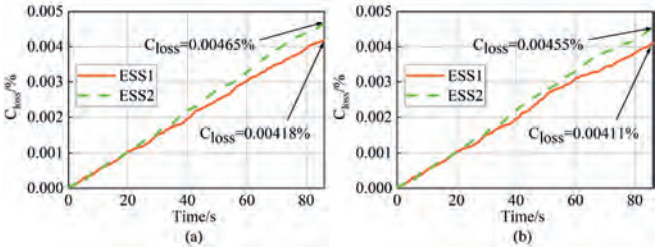

Fig. 14. (a) The ESS capacity loss without considering ESS degradation; (b) The ESS capacity loss considering ESS degradation

Bus voltage

The fluctuation curve of the bus voltage on the DC side of the ship power system is shown in Fig. 15. From Fig. 15(a), it can be observed that the AFPID controller makes the bus voltage fluctuations smaller and closer to the desired value. Fig. 15(b) shows that the deviation of the bus voltage from the reference value is reduced by 7.22% compared to PID control by between 10s and 30s. The result shows that the bus voltage is smoother and the stability of the ship power system is significantly improved when AFPID control is used for the low-level control loop.

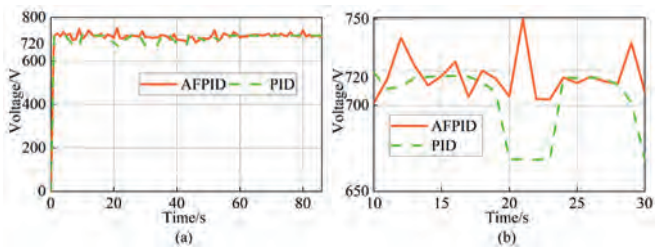

Fig. 15. (a) The bus voltage; (b) The bus voltage between 10s and 30s

CONCLUSIONS

In this paper, the EMS with hierarchical control is presented. In addition, an ESS degradation model is developed to assess the ESS SOH and reduce capacity loss. The key findings can be summarized as below:

(i) The FCS output power is constant or increases slowly with the PSO-ECMS. Compared to the SVM-based EMS, the output power curve of the FCS is smoother and the hydrogen consumption reduces by 5.319% without considering ESS degradation during the entire operation.

(ii) The AFPID controller can adjust the three parameters of PID in real time according to the change in the system state. Compared to the conventional PID controller, the bus voltage fluctuation is smaller and the bus voltage can be restored to the reference value within a shorter time when the load changes suddenly. The dynamic and static performance of the shipboard power system is significantly improved.

(iii) An ESS degradation model is developed to calculate the capacity loss. Although hydrogen consumption has increased, the total operating cost reduces by 1.7% after adding the capacity loss to the objective function.

REFERENCES

1. Z. Korczewski, "Test method for determining the chemical emissions of a marine diesel engine exhaust in operation," *Polish Maritime Research*, 2021. doi:10.2478/pomr-2021-0035.

2. M. Barakat, B. Tala-Ighil, H. Chaoui, H. Gualous, D. Hissel, "Energy Management of a Hybrid Tidal Turbine-Hydrogen Micro-Grid: Losses Minimization Strategy," *Fuel Cells*, 2020. doi:10.1002/fuce.201900082.

3. P. Geng, X. Y. Xu, T. Tarasiuk, "State of charge estimation method for lithium-ion batteries in all-electric ships based on LSTM neural network," *Polish Maritime Research*, 2020. doi:10.2478/pomr-2020-0051.

4. R. Zhao *et al.*, "A numerical and experimental study of marine hydrogen-natural gas-diesel trifuel engines," *Polish Maritime Research*, 2020. doi:10.2478/pomr-2020-0068.

5. M. Rafiei, J. Boudjadar, M. H. Khooban, "Energy Management of a Zero-Emission Ferry Boat With a Fuel-Cell-Based Hybrid Energy System: Feasibility Assessment," *IEEE Trans. Ind. Electron.*, 2021. doi:10.1109/tie.2020.2992005.

6. S. Faddel, A. A. Saad, M. E. Hariri, O. A. Mohammed, "Coordination of Hybrid Energy Storage for Ship Power Systems With Pulsed Loads," *IEEE Trans. Ind. Appl.*, 2020. doi:10.1109/tia.2019.2958293.

7. S. Hasanvand, M. Rafiei, M. Gheisarnejad, M. H. Khooban, "Reliable Power Scheduling of an Emission-Free Ship: Multiobjective Deep Reinforcement Learning," *IEEE Trans. Transport. Electrif.*, 2020. doi:10.1109/tte.2020.2983247.

8. P. Wu, J. Partridge, R. Bucknall, "Cost-effective reinforcement learning energy management for plug-in hybrid fuel cell and battery ships," *Applied Energy*, 2020. doi:10.1016/j.apenergy.2020.115258.

9. M. Banaei, J. Boudjadar, M. H. Khooban, "Stochastic Model Predictive Energy Management in Hybrid Emission-Free Modern Maritime Vessels," *IEEE Trans. Ind. Inform.*, 2021. doi:10.1109/tii.2020.3027808.

10. J. Hou, Z. Y. Song, H. Hofmann, J. Sun, "Adaptive model predictive control for hybrid energy storage energy management in all-electric ship microgrids," *Energy Conversion and Management*, 2019. doi:10.1016/j.enconman.2019.111929.

11. M. Banaei, M. Rafiei, J. Boudjadar, M. H. Khooban, "A Comparative Analysis of Optimal Operation Scenarios in Hybrid Emission-Free Ferry Ships," *IEEE Trans. Transport. Electrif.*, 2020. doi:10.1109/tte.2020.2970674.

12. J. Nunez Forestieri, M. Farasat, "Energy flow control and sizing of a hybrid battery/supercapacitor storage in MVDC shipboard power systems," *IET Electrical Systems in Transportation*, 2020. doi:10.1049/iet-est.2019.0161.

13. M. H. Khooban, M. Gheisarnejad, H. Farsizadeh, A. Masoudian, J. Boudjadar, "A New Intelligent Hybrid Control Approach for DC-DC Converters in Zero-Emission Ferry Ships," *IEEE Trans. Power. Electron.*, 2020. doi:10.1109/tpel.2019.2951183.

14. T. H. Wang *et al.*, "A Power Allocation Method for Multistack PEMFC System Considering Fuel Cell Performance Consistency," *IEEE Trans. Ind. Appl.*, 2020. doi:10.1109/tia.2020.3001254.

15. J. Chen, C. Xu, C. Wu, W. Xu, "Adaptive Fuzzy Logic Control of Fuel-Cell-Battery Hybrid Systems for Electric Vehicles," *IEEE Trans. Ind. Inform.*, 2018. doi:10.1109/tii.2016.2618886.

16. F. Balsamo, P. De Falco, F. Mottola, M. Pagano, "Power Flow Approach for Modeling Shipboard Power System in Presence of Energy Storage and Energy Management Systems," *IEEE Trans. Energy Convers.*, 2020. doi:10.1109/tec.2020.2997307.

17. H. Ahmadi, M. Rafiei, M. A. Igder, M. Gheisarnejad, M. H. Khooban, "An Energy Efficient Solution for Fuel Cell Heat Recovery in Zero-Emission Ferry Boats: Deep Deterministic Policy Gradient," *IEEE Trans. Veh. Technol.*, 2021. doi:10.1109/tvt.2021.3094899.

18. [18] A. Boveri, F. Silvestro, M. Molinas, E. Skjong. Optimal Sizing of Energy Storage Systems for Shipboard Applications. *IEEE Trans. Energy Convers.* 2019. doi:10.1109/TEC.2018.2882147.

19. Y. Z. Zhang *et al.*, "Real-Time Energy Management Strategy for Fuel Cell Range Extender Vehicles Based on Nonlinear Control," *IEEE Trans. Transport. Electrif.*, 2019. doi:10.1109/tte.2019.2958038.

20. C. Lin, H. Mu, R. Xiong, W. X. Shen, "A novel multi-model probability battery state of charge estimation approach for electric vehicles using H-infinity algorithm," *Applied Energy*, 2016. doi:10.1016/j.apenergy.2016.01.010.

21. X. Y. Lu, H. Y. Wang, "Optimal Sizing and Energy Management for Cost-Effective PEV Hybrid Energy Storage Systems," *IEEE Trans. Ind. Inform.*, 2020. doi:10.1109/tii.2019.2957297.

22. J. Park *et al.*, "Semi-empirical long-term cycle life model coupled with an electrolyte depletion function for large-format graphite/LiFePO4 lithium-ion batteries," *Journal of Power Sources*, 2017. doi:10.1016/j.jpowsour.2017.08.094.

23. J. Wang *et al.*, "Cycle-life model for graphite-LiFePO4 cells," *Journal of Power Sources*, 2011. doi:10.1016/j.jpowsour.2010.11.134.

24. M. Kalikatzarakis, R. D. Geertsma, E. J. Boonen, K. Visser, R. R. Negenborn, "Ship energy management for hybrid propulsion and power supply with shore charging," *Control Engineering Practice*, 2018. doi:10.1016/j.conengprac.2018.04.009.

25. H. Chen, Z. H. Zhang, C. Guan, H. B. Gao, "Optimization of sizing and frequency control in battery/supercapacitor hybrid energy storage system for fuel cell ship," *Energy*, 2020. doi:10.1016/j.energy.2020.117285.

POLISH MARITIME RESEARCH 2 (118) 2023 Vol. 30; pp. 105-113
10.2478/pomr-2023-0026

BEHAVIOUR OF A TORSIONAL VIBRATION VISCOUS DAMPER IN THE EVENT OF A DAMPER FLUID SHORTAGE

Andrzej Chmielowiec*
Rzeszow University of Technology, Poland
Adam Michajłyszyn
Rzeszow University of Technology, Poland
Wojciech Homik
Rzeszow University of Technology, Rzeszow, Poland

* Corresponding author: *achmie@prz.edu.pl (Andrzej Chmielowiec)*

ABSTRACT

Abstract: This article presents the analysis of a damping fluid deficiency in a torsional vibration viscous damper. The problem is analysed both qualitatively and quantitatively. Experimental results are presented, showing what happens to the damper in a situation where the design of the housing is inadequate and the inertia forces prevent the formation of an oil film. In addition, the article deals with the problem of the proper design of the oil channel and the dimensions required to enable the damper to operate reliably. The results of the article may be useful to the constructors of torsional vibration viscous dampers for marine engines.

Keywords: ngine vibrations; Torsional vibration; Viscous damper; Oil channel; Damper design

INTRODUCTION

The problem of vibrations and their damping occurs in all types of internal combustion engine. In these engines, the reciprocating motion is converted into rotational motion by means of a piston-crank system. During this process, the engine's crankshaft is affected by gas forces arising in the combustion process of the fuel-air mixture and inertia forces originating from the masses in motion. Periodic changes in force generates vibrations in the entire system, the most dangerous of which are torsional vibrations [2, 8, 18]. This problem particularly concerns large engines, especially ships' engines, for which the above-mentioned loads may even lead to engine destruction in extreme conditions. This is evidenced by numerous publications reporting damage to crankshafts in marine engines. In recent years, such events have been described, among others, by Fonte et al. [5, 6], Gomes et al. [7] and Kutay and Kamal [16]. Contemporary failures motivated scientists to develop risk assessments related to torsional vibrations of ship propulsion systems. Liberacki [17] defined the risk associated with crankshaft failure and Senjanović et al. [22] and Murawski and Dereszewski [19] presented methods for assessing and monitoring torsional vibrations in a ship's power plant. To address issues associated with the generation of torsional vibrations, a properly selected damper should be installed as a solution. In the case of marine engines, the dominant device is a viscous torsional vibration damper [10]. The authors Komada and Honda [14, 15], Dziurdź and Pakowski [4], Pasricha [20] and Homik [11] all described the characteristics of the damper operation and its impact on the amplitude of torsional vibrations in the propulsion system of a ship. The conditions for the reliable operation of a torsional vibration viscous damper is the formation of

an oil film between the housing and the inertial ring. Such an oil film makes it possible to dissipate energy through internal friction in fluid particles, with no wearing of the damper parts. Considering the above, it should be stated that one important issue is the level to which the damper is filled with fluid of an appropriate viscosity. The right level of filling ensures effective and reliable operation. Improper, or too little, filling of the damper causes accelerated wear on the active surfaces, which reduces its effectiveness. In connection with the above, constructors use various types of procedures that allow this problem to be solved. One solution is to reduce wear by using appropriate materials [1, 9]. The second solution is to ensure fluid friction through the correct design of the oil channel.

This article presents the behaviour of silicone oil during the start-up of a torsional vibration viscous damper. Formulas for the volume of the oil channel have also been determined, the proper execution of which guarantees the formation of the oil film carrier layers. The information contained herein may be useful for the constructors of torsional vibration viscous dampers for marine engines.

DESIGN AND PRINCIPLE OF TORSIONAL VIBRATION VISCOUS DAMPER OPERATION

The torsional vibration viscous damper is a relatively simple device in its design and its individual parts are shown in Fig. 1. The basic elements responsible for its proper functioning are: housing connected to the cover, an inertia ring and silicone oil. The interaction of these three parts makes it possible to dissipate the energy of torsional vibrations in the form of heat. In Fig. 1, the oil channel (item 8) is highlighted. This element is often overlooked in various types of torsional vibration viscous damper analysis. This article shows that the oil channel is a key element, from the point of view of proper functioning of the device.

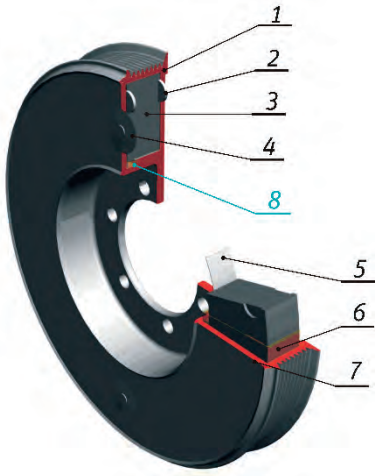

Fig. 1. Torsional vibration viscous damper: 1 - damper housing, 2 - thrust bearing, 3 - inertia ring, 4 - plug, 5 - radial bearing, 6 - silicone oil, 7 - cover, 8 - oil channel.

The essence of the effective operation of a torsional vibration viscous damper is the relative movement of the inertia ring and the housing. This movement is shown in Fig. 2, by the angular velocity of the housing ω_H and the angular velocity of the inertia ring ω_I. If only $\omega_H \neq \omega_H$, then the viscosity of the fluid between the ring and the housing creates a frictional force. This force is proportional to the speed difference between the housing and the inertia ring at a given point, and inversely proportional to the distance between them. This mechanism creates a braking force that counteracts sudden changes in the angular velocity of the housing. This makes it possible to suppress torsional vibrations. Fig. 2 shows a diagram of a working torsional vibration viscous damper. All of the necessary geometric properties are marked on it, which allow description of the movement of the ring, assuming that the empty spaces are completely filled with silicone oil.

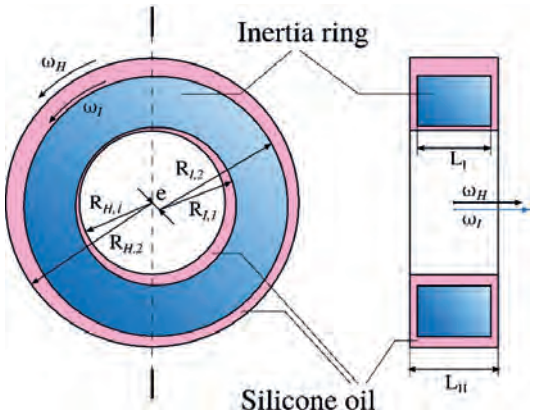

Fig. 2. Overview of a torsional vibration viscous damper, in which the inertial ring rotates with an angular velocity ω_I, the housing rotates with an angular velocity ω_H, and the eccentricity of the housing and the inertia ring has the value e.

It is worth noting that the radial internal clearance $c_1 = R_{I,1} - R_{H,1}$ is smaller than the external radial clearance $c_2 = R_{H,2} - R_{I,2}$. The c_2/c_1 ratio is generally so large that the weight of the ring is mainly supported by the hydrodynamic force generated in the inner oil layer. To generate this hydrodynamic lift, (poly)dimethylsiloxane is used, which is characterised by high viscosity. Depending on the application, its kinetic viscosity generally varies from 10,000 cSt (0.01 m^2s^{-1}) to 1,000,000 cSt (1 m^2s^{-1}). Such large values are obtained by creating very long polymer chains, the structure of which is shown in Fig. 3.

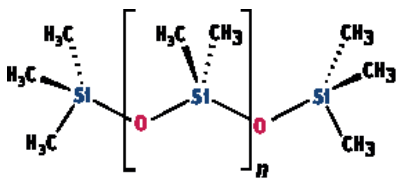

Fig. 3. Structural formula of a silicone oil molecule - (poly)dimethylsiloxane, whose viscosity is closely related to the length of the chain of repeating dimethyl groups [3].

The aforementioned viscosities require the synthesis of chains consisting of 500 to 2,000 dimethyl groups. In addition, this type of fluid is characterised by highly variable viscosity, as afunction of temperature. As shown in [3], the (poly) dimethylsiloxanes used in damping devices differ in their characteristics from the commonly used models of viscosity as a function of temperature. Another very important feature of silicone oil is its relative volumetric expansion ($930 \cdot 10^{-6}$ per °C), i.e. about 4.5 times the volumetric expansion of water. This means that, in the operating temperature range from –30 °C to about 70 °C, its volume changes by about 10%. Thus, there is never a situation in which the damper is completely filled with viscous fluid. This is the main reason for using an oil channel in the design of the damper. It is intended as a kind of buffer into which excess oil is drained during operations at high temperatures and from which it is drawn during operations at low temperatures. The main task of the channel is to provide oil in the layer between the radii $R_{H,1}$ and $R_{I,1}$, which is the main carrying layer for the inertia ring. A lack of oil in this layer causes dry friction and mixed friction (dry and wet) between the housing and the inertia ring. This leads to the wear of inner damper surfaces and contamination of the oil. In addition, such a damper loses its damping properties and, in extreme cases, may even act as a vibration exciter.

HYDRODYNAMIC FORCES IN THE DAMPER

In order for the damper to fulfill its task, it is necessary to lift the ring by hydrodynamic forces. To model this phenomenon, a method based on the bearings theory is adopted [12]. The basis of this theory is the Reynolds equation [21] which, among other things, assumes laminar fluid flow. As evidenced by the experimental results discussed later in the article, the relative velocity between the inertia ring and the housing is small. Therefore, it was assumed that the movement of the fluid is laminar and the hydrodynamic pressure of the oil film is described by the formula

$$p(\varphi_i) = p_0 + 6\eta|\omega_H - \omega_I|\left(\frac{R_i}{c_i}\right)^2 \frac{\varepsilon_i(2+\varepsilon_i\cos\varphi_i)\sin\varphi_i}{(2+\varepsilon_i^2)(1+\varepsilon_i\cos\varphi_i)^2} \quad (1)$$

where φ_i is the angular coordinate shown in Fig. 5, p_0 is the pressure of the air enclosed in the housing, η is the dynamic viscosity of the silicone oil, R_i is, in accordance with the Reynolds condition, set to $\frac{1}{2}(R_{H,i} + R_{I,i})$, c_i is the radial clearance defined in the previous parts, and ε_i is the relative eccentricity, defined as the ratio e/c_i. It is worth noting here that adopting such a formula for R_i is purely arbitrary. The values of the radii $R_{H,i}$ and $R_{I,i}$ are so close that one may as well assume $R_i = R_{H,i}$ or $R_i = R_{I,i}$ as it will not have a significant impact on the obtained numerical results. By introducing the dimensionless function

$$\gamma(\varepsilon_i, \varphi_i) = \frac{\varepsilon_i(2+\varepsilon_i\cos\varphi_i)\sin\varphi_i}{(2+\varepsilon_i^2)(1+\varepsilon_i\cos\varphi_i)^2} \quad (2)$$

we get the following relation

$$p(\varphi_i) = p_0 + 6\eta|\omega_H - \omega_I|\left(\frac{R_i}{c_i}\right)^2 \gamma(\varepsilon_i, \varphi_i) \quad (3)$$

In accordance with the Gümbel condition, we now assume that the distribution of pressure in the inner ($i = 1$) and outer ($i = 2$) layers is given by the formula

$$p_i(\varphi_i) = \begin{cases} p(\varphi_i), & \varphi_i \in [0, \pi], \\ 0, & \varphi_i \in (\pi, 2\pi) \end{cases} \quad (4)$$

The behaviour of the hydrodynamic pressure function p_i is strictly dependent on the course of the dimensionless function $\gamma(\varepsilon_i,\varphi_i)$. This function, for several selected values of ε_i, is presented on the graph in Fig. 4. This graph presents a good picture of how the silicone oil pressure is distributed in the inner and outer layers. Note that the pressure function has exactly one maximum. By equating the derivative $\rho(\varphi_i)'$ to zero, it can be shown that this maximum is realised for a certain angle $\varphi_{i,m}$, satisfying the following relations

$$\sin(\varphi_{i,m}) = \frac{\left[(\varepsilon_i^2-1)(\varepsilon_i^2-2)\right]^{1/2}}{\varepsilon_i^2+2} \quad (5)$$

$$\cos(\varphi_{i,m}) = \frac{-3\varepsilon_i}{\varepsilon_i^2+2} \quad (6)$$

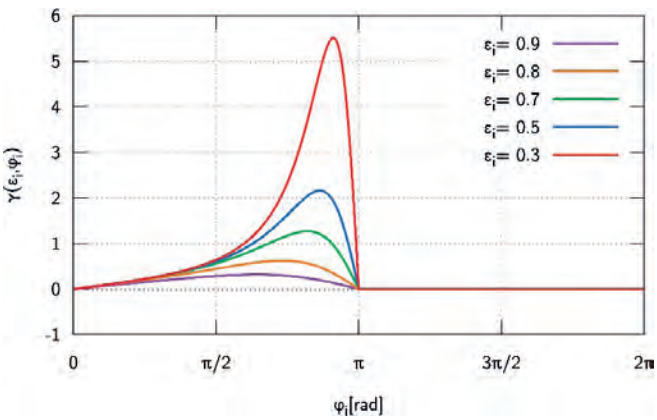

Fig. 4. Graph of the dimensionless function $\gamma(\varepsilon_i,\varphi_i)$ according to the Gümbel condition for example values of ε_i.

By integrating the pressure of the inner layer p_1 and the pressure of the outer layer p_2 around the circumference of the inertia ring, we obtain the values of hydrodynamic forces acting on the inertia ring. During the operation of the damper, these forces are set at a level and in a position that balances the weight of the inertia ring. This situation is illustrated in Fig. 5, where the angle θ is the deviation angle of the axis $\varphi_i = 0$ from the vertical. Thus, in the equilibrium, the angle θ and the relative eccentricities ε_i must satisfy the relations

$$Q\cos\theta = -L_I R_1 \int_0^{2\pi} p_1 \cos\varphi_1 \; d\varphi_1 - L_I R_2 \int_0^{2\pi} p_2 \cos\varphi_2 \; d\varphi_2 \quad (7)$$

$$Q\sin\theta = L R_1 \int_0^{2\pi} p_1 \sin\varphi_1 \; d\varphi_1 + L R_2 \int_0^{2\pi} p_2 \sin\varphi_2 \; d\varphi_2 \quad (8)$$

By integrating by parts we get the following relations

$$Q\cos\theta = 12\eta|\omega_H - \omega_I| L_I \sum_{i=1}^{2} \frac{\varepsilon_i^2 R_i^3}{(2+\varepsilon_i^2)(1-\varepsilon_i^2)c_i^2} \quad (9)$$

$$Q\sin\theta = 6\pi\eta|\omega_H - \omega_I| L_I \sum_{i=1}^{2} \frac{\varepsilon_i R_i^3}{(2+\varepsilon_i^2)(1-\varepsilon_i^2)^{1/2} c_i^2} \quad (10)$$

It is true that three variables θ, ε_1 and ε_2 appear in the above equations, but the latter two are related by the equation $\varepsilon_1 = \varepsilon_2 \frac{c_2}{c_1}$. This means that Eqs. (9) and (10) give complete information about the equilibrium position of the inertia ring.

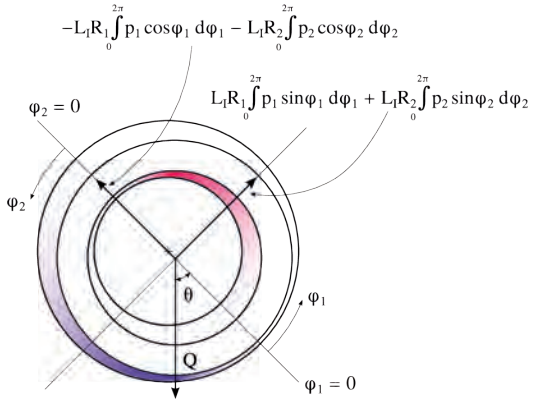

Fig. 5. Hydrodynamic forces balancing the weight of the inertia ring Q, given by the Gümbel condition for rotating elements (the intensity of the colour reflects the magnitude of the hydrodynamic pressure).

The adopted model does not take into account the movement of the fluid in the axial direction. Its great advantage, however, is the fact that it has analytical solutions and this makes it possible to quickly estimate the hydrodynamic pressure in both load-bearing layers. In future, the two-dimensional Reynolds equation may be used. Although it does not have analytical solutions, it will probably give a better picture of what is happening with the oil film inside the damper. Unfortunately, at the moment the authors do not have sufficient experimental data to determine reasonable boundary conditions for the numerical model.

DAMPER BEHAVIOUR IN THE CASE OF OIL SHORTAGE

Analysis of the torsional vibration viscous damper was performed on a specially prepared stand. This stand was first equipped with a damper designed with an error. This error consisted of the lack of an oil channel. In addition, the damper was deprived of bearings. This element was deliberately eliminated so that, during the experiments, it was possible to detect the difference in the operation of the damper without an oil channel and with an oil channel.

a) *b)*

Fig. 6. Position of silicone oil and air inside the damper: a) before starting work, b) after the oil is pushed out by the centrifugal force and the pressure of the inertia ring during operation.

Fig. 6a shows how the silicone oil fills the inside of the damper housing after 24 hours of rest in the vertical position. In contrast, Fig. 6b shows the position of the oil after only 3 minutes of damper operation. The photographs clearly show the displacement of the silicone oil in the circumferential direction due to the centrifugal force. Due to the lack of an oil channel, the inner support layer is stripped of oil and the inertia ring and housing are put into a dry and mixed friction state. After the tests, the damper housing was reworked and an oil channel was made in it. The modified damper was subjected to the same series of tests as the version without an oil channel. The cross-sections of the housing of both versions of the damper are shown in Fig. 7. The experiments clearly showed how important the oil channel is in the design. Its appropriate geometry guarantees the presence of silicone oil in both carrier layers, enabling the proper operation of the damper.

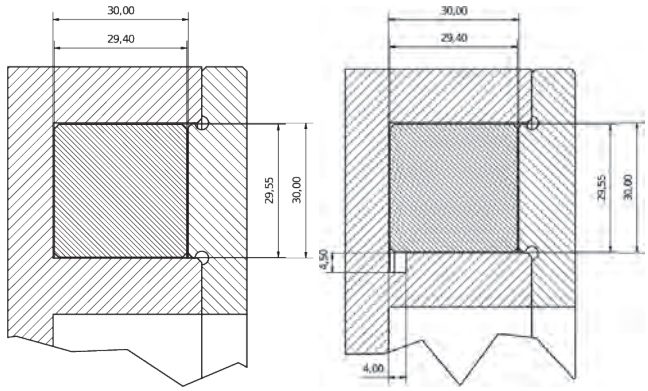

a) *b)*

Fig. 7. Damper model: a) without oil channel, b) with oil channel.

The results of the conducted experiments show which geometrical parameters of the damper are the most important, from the point of view of operational modelling, and they are shown in Fig. 8. The diagram includes two hydrodynamic pressures in both carrying layers and the pressure generated by the inertia force.

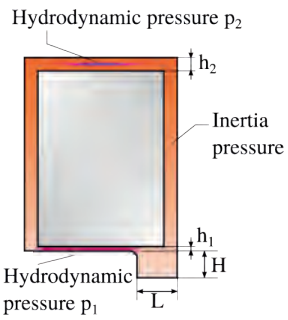

Fig. 8. Diagram of the oil channel's geometrical parameters in the torsional vibration viscous damper with the designation of the main areas of hydrodynamic pressure.

MEASUREMENT STAND

The measurement stand is presented in Fig. 9, the tested damper being marked with the number '4'. During each test, the damper was filled with silicone oil with a kinematic nominal viscosity $\nu_{25}^{30} = 0.03$ m^{2}s^{-1} at a temperature of 25 °C. During the first series of tests, the stand was equipped with a damper without an oil channel. The second series of tests was carried out after modifying the housing and making an oil channel in it. The entire station was driven by an electric squirrel-cage motor marked with the number '1'. The motor power was 0.75 kW and its maximum rotational speed was 1400 rpm, regulated by the motor controller. A two-piston compressor marked with the number '6' was used to generate torsional vibrations. Rigid couplings marked with the number '2' were used to connect all the elements of the stand. Their design guarantees the transfer of torsional vibrations without damping, which is crucial from a measurement point of view. A digital torque meter '5' was placed on the shaft, enabling the recording of the torque with a frequency of up to 2600 Hz. The amplitude-frequency characteristics of the compressor were then determined.

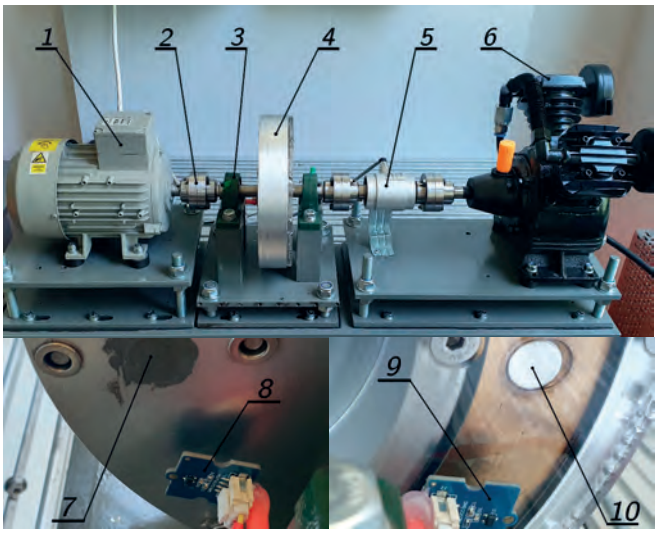

Fig. 9. Measuring stand: 1 - electric motor with adjustable rotational speed, 2 - rigid coupling, 3 - bearing supporting the shaft, 4 - vibration damper, 5 - torque meter, 6 - two-piston compressor for excitation of torsional vibrations, 7 - neodymium magnet in the damper housing, 8 - Hall sensor for the housing, 9 - Hall sensor for the inertia ring, 10 - neodymium magnet in the inertia ring.

The main parts responsible for the measurements are magnets '7' and '10', which are placed in the housing and inertia ring, respectively. The appearance of the magnet in a certain position is registered by the Hall sensors '8' and '9' and this makes it possible to study the relative position of the housing and the inertia ring. The sensors were connected to a recorder with a microcontroller. The system is able to measure the time when the magnet appears in the sensor area with an accuracy of 10^{-5} s. Because of this, it is possible to precisely determine the angular position of both damper elements over time. The recording of the time events takes place asynchronously, based on interruptions generated by the microcontroller's Timer/Counter signals from the sensors. The microcontroller measures the time for full rotation and the time between recording the signal from both Hall sensors. Based on these data, it is possible to determine the relative change in the angular position of the housing and the inertia ring.

RESEARCH RESULTS AND THEIR INTERPRETATION

Experiments were carried out for three rotational speeds of the shaft: n_1 = 426 rpm, n_2 = 702 rpm, and n_3 = 1014 rpm. During the tests, both a damper without a channel and a damper with an oil channel were tested. The time of a single experiment was 1000 s. The damper had a temperature of 25 °C at the beginning of the test and, after its completion, it did not change by more than 1.5 °C. Therefore, it is possible to ignore changes in the viscosity and volume of the silicone oil inside the device.

a) Rotation speed n_1 = 426 rpm.

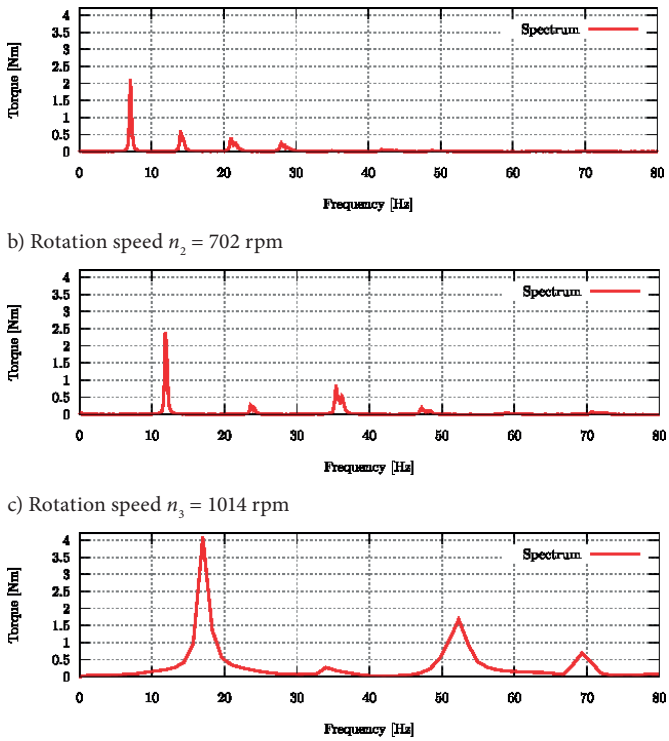

Fig. 10. Spectral characteristics of a two-piston compressor forcing torsional vibrations for individual rotational speeds.

Torsional vibrations were forced by a two-piston compressor; the spectral characteristics for individual rotational frequencies are shown in Fig. 10. The first four harmonics are clearly visible in the spectral image, with the first and third clearly dominating. This is quite natural because the compressor has two pistons and the angle between the cylinders is 90°.

Fig. 11 presents the results of the measurements obtained for rotational speeds $n1$,n_2, and n_3. The graphs show the change in the angular position ϕ of the housing relative to the inertia ring as a function of time. They show that the inertia ring

in the damper without an oil channel in the first phase of the movement performs a follow-up movement relative to the housing. When the oil in the inner carring layer is pushed out in the circumferential direction by the inertia force, the ring stops and does not make any further movement relative to the housing. The relative change in the angular position of the housing and the ring is marked with a red line on the graphs.

a) Rotation speed n_1 = 426 rpm.

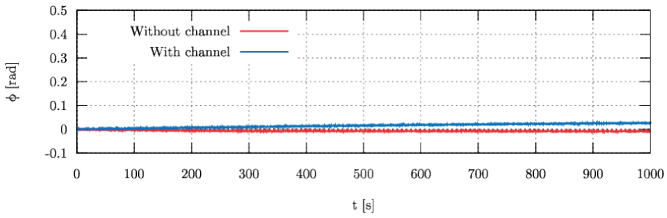

b) Rotation speed n_2 = 702 rpm

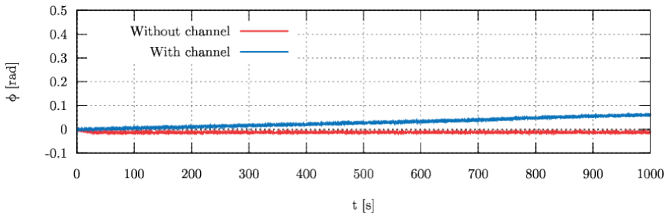

c) Rotation speed n_3 = 1014 rpm

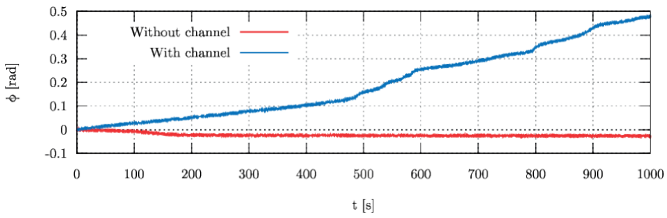

Fig. 11. Graphs of the housing and the inertia ring's relative angular position for a damper without a channel and with an oil channel for different rotation speeds.

The situation is completely different in the case of a damper with an oil channel. In this case, the inertia ring moves in the opposite direction. i.e. it performs an overtaking movement relative to the housing. In addition, the existence of the oil channel means that the inner carrying layer is constantly supplied with oil. Therefore, systematic, relative movement of the inertia ring and housing is observed, which is marked with a blue line in the graphs. This is the state of correct operation of the damper, which dissipates the energy of torsional vibrations through the continuous relative movement of the housing and inertia ring. In Fig. 11c, for a rotational speed of 1014 rpm, there is instability in the increase of the relative angular position ϕ. This results from overheating of the motor due to excessive load and its unstable operation after 500 seconds of the test. The graph shows a large difference between the ϕ variability at 702 rpm and 1014 rpm. For this reason, a decision was made to perform an additional measurement for the rotational speed of 804 rpm. The relationship between ϕ and time t for all four measurements, in the case of a damper with an oil channel, is shown in Fig. 12, which clearly shows the increase in the average relative angular velocity $\overline{\omega} = \frac{\Delta\phi}{\Delta t}$ and this accompanies the increase in rotational speed.

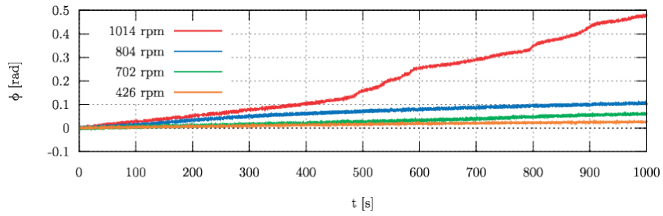

Fig. 12. Plots of the relative angular position of the housing and inertia ring for different rotation speeds.

Table 1 presents the numerical values of the relative position angle ϕ for times t equal to 200, 400, 600, 800 and 1000 s. In addition, the average relative angular velocity $\overline{\omega}$ for the entire test duration and the average relative angular velocity $\overline{\omega}_{200}$ for the time interval [200,1000] is also presented.

The speed $\overline{\omega}_{200}$ is particularly important because it shows how the housing and the inertia ring move relative to each other after the oil is pushed out by the inertia force in the circumferential direction. From the determined values (Table 1), it is clear that in the absence of a channel, the ring practically does not move. In practice, this results in dry or mixed friction between the housing and the inertia ring. During operation, this will lead to excessive wear of the contact surface and damage to the damper. The situation is completely different in the case of a damper with an oil channel. In this case, the movement is visible, which suggests that an oil film has formed that separates the housing from the inertia ring. It should also be noted that the small value of the relative angular velocity justifies the correctness of the assumption

Tab. 1. Numerical summary of selected measurements.

	With channel				Without channel		
rpm	426	702	804	1014	426	702	1014
ϕ(200) rad	0.007	0.010	0.033	0.052	-0.005	-0.014	-0.022
ϕ(200) rad	0.013	0.020	0.062	0.104	-0.006	-0.013	-0.026
ϕ(200) rad	0.018	0.032	0.080	0.255	-0.006	-0.013	-0.026
ϕ(200) rad	0.023	0.047	0.094	0.348	-0.007	-0.012	-0.027
ϕ(200) rad	0.026	0.061	0.106	0.479	-0.007	-0.012	-0.027
$\overline{\omega}$ rad/s	26×10^{-6}	61×10^{-6}	106×10^{-6}	479×10^{-6}	-7×10^{-6}	-12×10^{-6}	-27×10^{-6}
$\overline{\omega}_{200}$ rad/s	24×10^{-6}	64×10^{-6}	91×10^{-6}	534×10^{-6}	-2.5×10^{-6}	2.5×10^{-6}	-6×10^{-6}

about the laminarity of the oil flow. The experimental results therefore confirm that the assumptions made for the model presented in the previous section are correct. It should also be noted that the size of the relative velocity obtained is in line with the results mentioned by Klimczyk et al. [13]. Unfortunately, this two-page publication does not contain detailed numerical information about the results obtained but only focuses on the experiment description, concluding that a single rotation of the inertia ring relative to the housing lasts from several minutes to several hours, depending on the temperature.

CONCLUSIONS REGARDING THE CORRECT DESIGN OF A TORSIONAL VIBRATION VISCOUS DAMPER

As already mentioned, the oil channel is supposed to be a kind of buffer for silicone oil. Therefore, its geometrical parameters, such as depth H and width L (Fig. 8), are strictly dependent on the dimensions of the damper and the temperatures at which it operates. Therefore, we assume that T_F is the damper filling temperature and T_L and T_H are the lowest and highest damper operating temperatures, respectively. In further considerations, we will assume that the damper is filled in thermally stable conditions. This means that both the damper and the oil is filled at a constant temperature T_F. We assume that, in such conditions, the damper can be filled to the degree $\delta \in (0,1)$. This is the part of the volume occupied by the silicone oil at the temperature T_F after the filling process is completed. In general, this factor is approximately 0.9, which means that the damper can be filled to 90%. In addition, we assume that the relative volumetric expansion of silicone oil is independent of temperature and is $\kappa = 0.00093$ °C^{-1}. By using the introduced notations and modifying the formula given in [3], it is possible to determine the volume occupied by the oil in the viscous damper at a given temperature T:

$$V(T) = V_F(1 + \kappa(T - T_F)) \tag{11}$$

where V_F is the volume of fluid poured into the damper during filling.

As a result of this, it is possible to determine the minimum $V_H = V_F(1 + \kappa\ (T_H - T_F))$ and maximum $V_L = V_F(1 + \kappa\ (T_L - T_F))$ volume that will be occupied by the fluid in the damper. This assumes that the volume of the viscous fluid space in the damper is $V_0 + V$, where V_0 is the volume of the free space around the inertia ring and V is the volume of the oil channel.

From the previous considerations, it follows that

$$V_F = \delta(V_0 + V) \tag{12}$$

$$V_L = \delta(V_0 + V)(1 + \kappa(T_L - T_F)) \tag{13}$$

$$V_H = \delta(V_0 + V)(1 + \kappa(T_H - T_F)) \tag{14}$$

The condition for the formation of an oil film in the inner layer is the fulfillment of the following inequalities: $V_0 < V_L < V_H < V_0 + V$. The inequality $V_L < V_H$ is fulfilled automatically, because the temperature T_L is lower than T_H, which translates into the appropriate relationship for the above volumes. From the inequality $V_H < V_0 + V$ we can derive a dependence:

$$T_H < T_F + \frac{1-\delta}{\kappa\delta} \tag{15}$$

Interestingly, this condition is completely independent of the volume V_0. For silicone oil $\kappa = 0.00093$ °C^{-1} and, assuming that the damper is filled to 90% ($\delta = 0.9$), we obtain the condition $T_H < T_F + 119.47$. This means that the maximum operating temperature of the damper cannot exceed the filling temperature by more than 119.47 °C.

From the second inequality $V_0 < V_L$ we obtain the dependence on the minimum volume of the oil channel

$$V > V_0\left(\frac{1}{\delta(1+\kappa(T_L - T_F))} - 1\right) \tag{16}$$

It should be noted that the value in brackets is positive, provided that Eq. (15) and the inequality $T_L < T_H$ are met. Thus, the volume of the oil channel should be an appropriate fraction of the volume V_0. This fraction can be treated as nless function χ of the variable T_F with the parameters δ, κ and T_L.

$$\chi(T_F) = \frac{1}{\delta(1+\kappa(T_L - T_F))} - 1 \tag{17}$$

The graph of the χ function for exemplary parameter values is presented in Fig. 13.

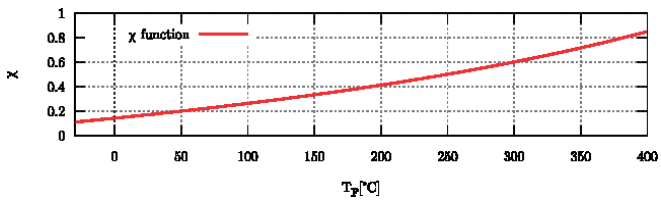

Fig. 13. Graph of the dimensionless function for parameters , and C.

This shows the rate at which the volume of the oil channel increases as a function of the filling temperature. This is especially important for high viscosity silicone oils. In their case, it is necessary to significantly heat the damper and oil so that the injected fluid has the lowest possible viscosity. The numerical value of the volume V_0 is determined on the basis of the geometric parameters of the damper, using the following formula:

$$V_0 = \pi(R_{H,2}^2 - R_{H,1}^2)L_H - \pi(R_{I,2}^2 - R_{I,1}^2)L_I \tag{18}$$

On the other hand, the geometric dimensions H and L of the channel are selected in such a way that they meet the relation $V = \pi HL\ (2R_{H,1} - H)$.

SUMMARY

This article presents a simple analytical model, the task of which is to theoretically justify the reliable operation of a torsional vibration viscous damper. It was found that such a reliable operation requires the formation of an oil film in both gaps of the damper (inner and outer). This model can be the basis for determining the value of the hydrodynamic pressure in a working damper. It also provides the ability to determine the relative position of the housing and the inertia ring. In order to be able to apply this model in a quantitative way, further experimental work is needed to determine the nature of the relative angular velocity.

Next, the authors presented the design and operation of the measuring stand, which was used to test the properties of a medium-size torsional vibration viscous damper. On this stand, a damper made without an oil channel was tested, followed by a modified damper, which already had such a channel. The obtained measurement results clearly show (Fig. 12) that the lack of an oil channel results in stopping the relative movement of the housing and the inertia ring. In practice, this means that there is no vibration damping. The use of a transparent cover also made it possible to show how the force of inertia pushes the oil towards the outer gap.

In summary, the authors derived analytical equations for the volume of the oil channel, which would guarantee the correct formation of an oil film in both carrying layers. The volume of the channel can be calculated as the product of the free space for oil and a certain dimensionless characteristic function . This function was introduced by the authors and depends on four values: the lowest damper operating temperature, the damper filling temperature, the degree of filling of the damper and the relative volumetric expansion of the viscous fluid (in this case, silicone oil).

REFERENCES

1. D. Baranovskyi, S. Myamlin, M. Bulakh, D. Podosonov, and L. Muradian, 'Determination of the Filler Concentration of the Composite Tape', Applied Sciences. vol. 12, no. 21, 11044, 2022. doi: 10.3390/app122111044

2. P. Charles, J. Sinha, F. Gu, L. Lidstone, and A. Ball, 'Detecting the crankshaft torsional vibration of diesel engines for combustion related diagnosis', Journal of sound and vibration, vol. 321, no. 3-5, pp. 1171-1185, 2009. doi: 10.1016/j.jsv.2008.10.024

3. A. Chmielowiec, W. Woś, and J. Gumieniak, 'Viscosity Approximation of PDMS Using Weibull Function', Materials, vol. 14, no. 20, 6060, 2021. doi: 10.3390/ma14206060

4. J. Dziurdź and R. Pakowski, 'Analysis of action viscous torsional vibration damper of the crankshaft based on transverse vibration the engine block', in Solid State Phenomena, vol. 236, pp. 145-152, 2015. doi: 10.4028/www.scientific.net/SSP.236.145

5. M. Fonte and M. De Freitas, 'Marine main engine crankshaft failure analysis: a case study', Engineering Failure Analysis, vol. 16, no. 6, pp. 1940-1947, 2009. doi: 10.1016/j.engfailanal.2008.10.013

6. M. Fonte, P. Duarte, V. Anes, M. Freitas, and L. Reis, 'On the assessment of fatigue life of marine diesel engine crankshafts', Engineering failure analysis, vol. 56, pp. 51-57, 2015. doi: 10.1016/j.engfailanal.2015.04.014

7. J. Gomes, N. Gaivota, R. Martins, and P. Silva, 'Failure analysis of crankshafts used in maritime V12 diesel engines', Engineering Failure Analysis, vol. 92, pp. 466-479, 2018. doi: 10.1016/j.engfailanal.2018.06.020

8. H. Han, K. Lee, and S. Park, 'Parametric study to identify the cause of high torsional vibration of the propulsion shaft in the ship', Engineering Failure Analysis, vol. 59, pp. 334-346, 2016. doi: 10.1016/j.engfailanal.2015.10.018

9. W. Homik, 'Diagnostics, maintenance and regeneration of torsional vibration dampers for crankshafts of ship diesel engines', Polish Maritime Research, vol. 17, no. 1, pp. 62-68, 2010. doi: 10.2478/v10012-010-0007-2

10. W. Homik, 'Damping of torsional vibrations of ship engine crankshafts-general selection methods of viscous vibration damper', Polish Maritime Research, vol. 18, no. 3, pp. 43-47, 2011. doi: 10.2478/v10012-011-0016-9

11. W. Homik, 'The effect of liquid temperature and viscosity on the amplitude-frequency characteristics of a viscotic torsion damper', Polish Maritime Research, vol. 19, no. 4, pp. 71-77, 2012. doi: 10.2478/v10012-012-0042-2

12. Y. Hori,'Hydrodynamic Lubrication'. Springer, Tokyo, 2006. doi: 10.1007/4-431-27901-6

13. S. Klimczyk, A. Szymański, and A. Lipiński, 'Isotope method for determining the displacement of the inertia ring of a torsional vibration damper' (in Polish), in Fizyka dla przemysłu - materiały V konferencji, Poznań, pp. 114-115, 1986.

14. T. Kodama and Y. Honda, 'Study on torsional vibration characteristics of small high-speed marine diesel engine crankshaft system with viscous friction damper: Numerical calculation method of torsional angular displacement and stress using simultaneous measurement values at two points', Journal of the Korean Society of Marine Engineering, vol. 41, no. 8, pp. 723-731, 2017. doi: 10.5916/jkosme.2017.41.8.723

15. T. Kodama and Y. Honda, 'A Study on the Modeling and Dynamic Characteristics of the Viscous Damper Silicone Fluid Using Vibration Control of Engine Crankshaft Systems', International Journal of Mechanical Engineering and Robotics Research, vol. 7, no. 3, 2018. doi: 10.18178/ijmerr.7.3.273-278

16. S. Kutay and B. Kamal, 'Assessment of marine diesel engine crankshaft damages', Ships and Offshore Structures, vol. 17, no. 9, pp. 2130-2139, 2022. doi: 10.1080/17445302.2022.2050522

17. R. Liberacki, 'Risk criteria for sea-going ships arising from the operation of the main engines' crankshaft-connecting rod-piston systems', Journal of Polish CIMAC, vol. 7, no. 2, pp. 115-121, 2012.

18. L. Murawski, 'Axial vibrations of the ship power transmission system: propulsion shaftline engine crankshaft', Polish Maritime Research, vol. 3, no. 9, pp. 21-28, 1996.

19. L. Murawski and M. Dereszewski, 'Theoretical and practical backgrounds of monitoring system of ship power transmission systems' torsional vibration', Journal of Marine Science and Technology, vol. 25, no. 1, pp. 272-284, 2020. doi: 10.1007/s00773-019-00646-z

20. M. Pasricha, 'Effect of damping on parametrically excited torsional vibrations of reciprocating engines including gas forces', Journal of ship research, vol. 50, no. 02, pp. 147-157, 2006. doi: 10.5957/jsr.2006.50.2.147

21. O. Reynolds, 'On the Theory of Lubrication and its Application to Mr.B. Tower's Experiments', Philosophical Transaction of Royal Society of London, vol. 177, no. 1, pp. 157-234, 1886.

22. I. Senjanović, N. Hadzić, L. Murawski, N. Vladimir, N. Alujević, and D.-S. Cho, 'Analytical procedures for torsional vibration analysis of ship power transmission system', Engineering Structures, vol. 178, pp. 227-244, 2019. doi: 10.1016/j.engstruct.2018.10.035

POLISH MARITIME RESEARCH 2 (118) 2023 Vol. 30; pp. 114-120
10.2478/pomr-2023-0027

IMAGE PROCESSING METHOD FOR CARGO CONTAINER IDENTIFICATION IN A STACK WITHIN THE CARGO TEMPERATURE CONTROL AND FIRE SAFETY SYSTEM ON CONTAINER SHIPS

Vladyslav Konon *
National University „Odessa Maritime Academy", Odesa, Ukraine

* Corresponding author: *science.est@hotmail.com*

ABSTRACT

The current research is focused on the identification of cargo containers in a stack from their images in the infrared and visible spectra, in order to locate the container-origin of ignition within the cargo temperature control and fire safety system. The relevance of the topic is reinforced by the functional requirements for shipboard safety, which are embodied in Chapter II-2 of the Safety of Life at Sea (SOLAS) Convention, and demanded by the necessity of enhancing safety measures during cargo transportation by the world container fleet. The thermal imager's field of view (FOV) and the coordinate dependencies between the object and its image have been studied and modelled, and an algorithm for fire detection has been defined within the scope of the current research in connection with the containers within the camera's FOV. A corresponding verification has been carried out by means of simulation modelling using the Unity and C# programming language capabilities.

Keywords: shipboard safety, cargo transportation, cargo temperature control, image processing, fire detection

ABBREVIATIONS

SOLAS – Safety of Life at Sea
FSS Code – International Code on Fire Safety Systems
TEU – twenty-foot equivalent unit
IMDG – International Maritime Dangerous Goods
MFAG – Medical First Aid Guide for use in accidents involving dangerous goods
EmS – Emergency response procedures for ships carrying dangerous goods
ULCS – ultra-large container ship
PIR – passive infrared
RoPax – roll-on/roll-off passenger ship/ferry
RGB – red, green and blue
CCFSS – cargo temperature control and fire safety system
FOV – field of view
IDE – integrated development environment
ROI – region of interest
UI – user interface

INTRODUCTION

The occurrence of high-profile incidents, such as the cases of the MSC Zoe and X-Press Pearl, with the loss of almost 350 containers at sea or the fire, respectively, have emphasised the following two issues in the consideration of safety tasks on container ships: loss of containers at sea and fires associated with cargo ignition [1]. The constant increase in the size of ships of this type in the last decade is related to an effect of scale in the world trade of containerised cargoes. This trend brings additional design variables and operational factors into

the analysis of the abovementioned safety challenges. Between 2011 and 2019, the volume of the container fleet increased by about 15%, while the share of vessels larger than 10,000 TEU increased by approximately 500%.

Thus, the excessive number and density of containers on deck and in holds, the limited space between the stacks and the ship's configuration, which, despite a significant increase in size, has generally remained unchanged, means that a fire or explosion in a container can be very difficult to detect, control and extinguish at an early stage. At the same time, particular attention needs to be paid to the transportation of special cargoes, namely dangerous goods. Although such IMDG cargoes should be stowed in accordance with the relevant regulations and ship's certificates (e.g., the Document of Compliance for the Carriage of Dangerous Goods), in practice, there are cases of undeclared or incorrectly declared dangerous goods [2]. Thus, the Master and crew become more vulnerable to the associated risks and cannot take the appropriate actions and measures required by the relevant instructions and documents (Cargo Securing Manual, MFAG, EmS guide, etc.). In accordance with Regulation 3 of Chapter VII of the SOLAS Convention, the transportation of dangerous goods in containers must comply with the provisions of the IMDG Code.

According to the information provided in [3], 58% of the 36 contributing factors in twelve fire/explosion reports were related to emergency actions on board during the emergency response, equipment failure, its installation/design and incorrectly declared or missing information regarding IMDG cargoes.

The requirements for providing ships with fire safety systems are stipulated by the SOLAS Convention [4] and the International Code on Fire Safety Systems (FSS Code) [5] in accordance with Chapter II-2 of the mentioned Convention. Notwithstanding the other requirements for the transportation of IMDG cargoes, such fire systems must ensure the protection of the ship from the dangers associated with the carriage of dangerous goods in accordance with Regulation 19 of Part G of Chapter II-2 of the SOLAS Convention.

In order to achieve the fire safety goals set by the SOLAS Convention, the following functional requirements are listed in Chapter II-2 [6]:

- division of the ship into main vertical and horizontal zones by thermal and structural boundaries;
- separation of living quarters from the rest of the ship's premises by thermal and structural boundaries;
- restrictions on the use of flammable materials;
- detection of fire in the area of origin;
- provision of means of evacuation and access to fire-fighting equipment;
- availability of fire-fighting appliances and minimisation of the risk of ignition of flammable cargo vapour.

However, the opinion has been expressed that "...the legal requirements prescribed by SOLAS were originally developed for fires on board general cargo vessels, and these ships are structurally very different to a container vessel, and cargo is stored differently. We believe the mode of fire-fighting set out in SOLAS is not suitable for a modern container ship...", as stated by the chairman of the International Union of Marine Insurance forum [7].

On the other hand, there have been a number of studies aimed at improving the fire safety on board ships of different types and applying a wide variety of methods and approaches.

The research in [8] is focused on the issue of engine room fires, highlighting the inherent dangers and defining fire safety management as an important factor in efficient fire prevention. In this regard, a survey on fire safety in the engine room was carried out, resulting in proposals for the improvement of engine room fire safety management.

The study [9] presents a comparison between the predictions of three different fire models and the experimental results of a model-scale fire test as a fire scenario on a vehicle deck on board a RoPax ship. The results obtained from this research may be useful for ship design and engineering in order to reduce the risks of accidents occurring.

Paying particular attention to the subject of cruise ship fires, an attention-backpropagation neural network model is proposed in [10]. The model designed can provide a decision-making reference for subsequent fire-fighting measures and personnel evacuation. The results obtained showed the effective and early fire warning generation.

However, it should also be noted that commercial and safety concerns are usually opposed to each other. This problem is no less relevant for the container fleet too. In practice, the crews on board ULCS may differ slightly from those on vessels of smaller sizes. Consequently, safety issues become more susceptible to the negative influence of the human factor, inter alia. In this context, the need to develop new methods and systems of firefighting and fire-detection, as well as to improve the existing ones, is further justified. Since firefighting is much simpler at the early stages of fire detection, the current research is focused in the direction of temperature control of containerised cargoes.

Generally, conventional fire-detection systems consist of a central module and a monitoring panel (additional repeater panels are possible); combinations of heat detectors, smoke and flame sensors, etc.; manual fire detectors; and sound and light alarm signalling devices. They can be both fairly simple and more complex to implement. According to the principle used to determine ignition, the following types of fire sensors can be distinguished [6]: thermal sensors, ionisation smoke sensors, optical smoke sensors, photo-thermal sensors, flame sensors, beam sensors, linear thermal sensors, and intrinsically safe systems.

At the same time, a number of studies have been devoted to the problem of the development and improvement of fire-detection systems for various applications.

The study [11] presents a differential passive infrared (PIR) sensor and a method based on deep neural networks for real-time fire detection. The developed method uses a one-dimensional continuous wavelet transform to process the signals received from the sensor, with subsequent conversion of the resulting coefficients into RGB spectrum images and processing by a convolutional neural network. However, despite the declared effectiveness of the proposed system, its implementation on board a container ship with the purpose of cargo monitoring raises several issues that require further research. These include, but are not limited to, the following: the ability to detect unopened flames, such as ignition inside a cargo container; the number of

sensors required since, based on the calculation of one sensor per container, a 3,000 TEU container ship may need 3,000 sensors, which raises subsequent issues of their placement and further maintenance.

Trying to solve the problem of false positives, [12] describes a method for quick detection of fire by smoke. The proposed algorithm relies on the colour and diffusion characteristics of smoke and counts the number of pixels in each potential smoke region by processing its video image. However, as noted by the authors, this model has a drawback that requires further study, expressed in the independent generation of false signals due to the features of the algorithm.

The authors of [13] propose to use video images in order to detect flames, providing regular monitoring, and saving the received image at the time of the fire alarm, which may also be used for investigations. However, the implementation of such a system for cargo control on board a container vessel also raises additional issues. Besides, its effectiveness in the case of smoke or flames located inside a cargo container requires a separate study.

In [14], a cargo temperature control and fire safety system (CCFSS) is proposed and its relevance is outlined. CCFSS is based on the implementation of thermographic tools, such as thermal imagers, for efficient and early-stage fire detection in a real-time mode on board container ships. However, the proposed concept still requires solutions for a number of sub-tasks, such as:

- definition of the most efficient layout of the thermal cameras to cover the area monitored;
- development of an algorithm that is able to predict and assess the potential hazardous situation at an early stage;
- development of a method for identifying the container that is the ignition source in a stack by its images in both the thermal and visible spectra.

The first two of these sub-tasks are discussed in [15]. It was therefore decided to conduct further research on the described system in relation to a cargo identification method.

The purpose of the current research is to propose a method for the identification of cargo containers within the stack from images in both the thermal and visible spectra within the CCFSS. Such a method may contribute to the identification of the heat/ignition origin at an early stage, namely to define its exact position. The relevance of this study is reinforced by the functional requirements listed in the SOLAS Convention, namely, determination of the fire in the area of origin and minimisation of the ignition risk of flammable cargo.

THERMAL IMAGER'S FIELD OF VIEW

In order to solve this task, the general idea of an installation pattern, the minimum number of thermal cameras required, the corresponding algorithm for data processing within the CCFSS, an instrument's field of view (FOV) and other parameters/limitations are considered, as well as the vessel's configuration in the area where the system is installed. The parameters of the thermal camera used during the on-site observations are shown in Table 1.

Tab. 1. Specifications of the thermal camera module

Camera module	
Thermal sensor	17 µm pixel size
Thermal resolution	80x60
Visual resolution	640x480
Horizontal / vertical FOV	46° ± 1° / 35° ± 1°
Focus	Fixed 15 cm – infinity
Radiometry	
Scene dynamic range	-20°C – 120°C
Accuracy	± 5°C or ± 5% of the difference between the ambient and scene temperature. Applicable 60s after start-up when the unit is within 15°C – 35°C and the scene is within 10°C – 120°C
Thermal image analytics	– Movable spot meters – Whole image region of interest (ROI) – Editable in saved images
Palettes	Iron, Black hot, White hot, Rainbow, Contrast, Arctic, Lava, Coldest, Hottest

As installation within, for example, a cargo hold may encounter some difficulties such as bulkheads or other configuration features that may obscure the view of the sensor, it is proposed to install cameras in accordance with such configurations in order to cover all the objects of interest through the common FOV of several thermal imagers. In this way, one camera can monitor a determined number of containers.

As a first approximation, a camera's FOV can be presented as a pyramid with a rectangle at the base. Thus, the FOV can be determined by the pyramid's height and the angles at its vertex. In the context of the set task, the angles at the pyramid's vertex are the horizontal and vertical angles of the FOV, given from the imager's specifications.

Fig. 1 schematically shows the thermal camera in relation to the cargo containers: the thermal camera is located within the cross-deck (3) of the ship's cargo area in such a way that the pyramid of its FOV (2), rotated by an angle α, covers a predetermined number of containers (1). Thus, the height of the pyramid will depend on the distance from the camera to measurable objects.

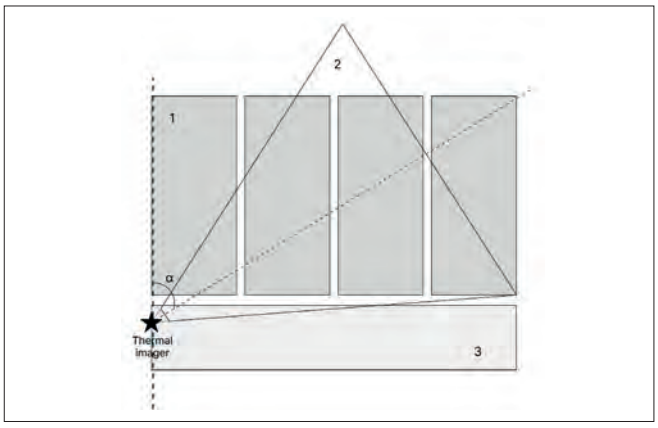

Fig. 1. Schematic representation of thermal imager's location in relation to cargo containers (top view)

During the on-site observations, it was determined that the distance from the camera to the observable object, which is more than about 12 m, is practically inexpedient within the framework of the set task. Thus, based on the initial data available and trigonometric transformations, a pyramid's edge can be obtained by the formula:

$$a = \sqrt{h^2 \cdot \tan^2 \frac{H_{fov}}{2} + \frac{h^2}{\cos^2 \frac{V_{fov}}{2}}} \quad , \tag{1}$$

where:

a – side edge of the pyramid with a rectangle at the base;
h – height of the pyramid;
H_{fov} – horizontal angle of the FOV;
V_{fov} – vertical angle of the FOV.

Thus, the FOV pyramid, considering the camera specifications from Table 1, namely, H_{fov} = 46° and V_{fov} = 35° for a maximum object distance of 12 m and a camera's focus of 15 cm, becomes the frustum [16] at the value of the focus, as plotted in Fig. 2.

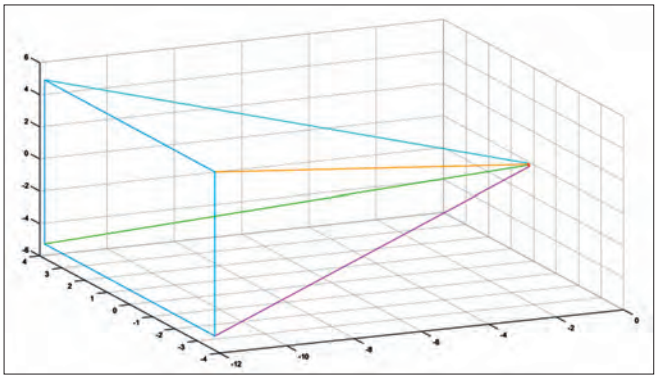

Fig. 2. Plot of the view frustum for thermal camera used during the on-site observations

DEPENDENCY BETWEEN THE COORDINATE SYSTEMS OF AN OBJECT AND ITS IMAGE

The position of the image at the time of photographing is determined by three elements of the interior and six elements of the exterior orientations (Fig. 3). The interior elements include: a camera's focus f and coordinates x_0, y_0 of a main point *o*. At the same time, the exterior elements are: the coordinates of a projection centre *S* – *XS*, *YS*, *ZS*, and the longitudinal, transverse and rotation angles ω, α and κ, respectively [17]. *OXYZ* is the coordinate system of the object *M*; oxyz – the coordinate system of the image; *m* is the projection (image) of the object *M* in the plane of the image. Vector $\vec{R}$ determines the position of the object *M* in relation to the coordinate system of the image. Vector $\vec{R_S}$ determines the position of the projection centre *S* in the object's coordinate system. Vector $\vec{R_M}$ determines the position of the object *M* in relation to the coordinate system of the object. Vector $\vec{r'}$ determines the position of the image *m* in the coordinate system of the image. Thus, the elements of the internal orientation are defined by the internal geometry of the camera at the time of data collection and can be obtained from the instrument's specifications and through its calibration. The elements of the external orientation are determined by the position and angular orientation of the camera in relation to the measurable object's coordinate system [18].

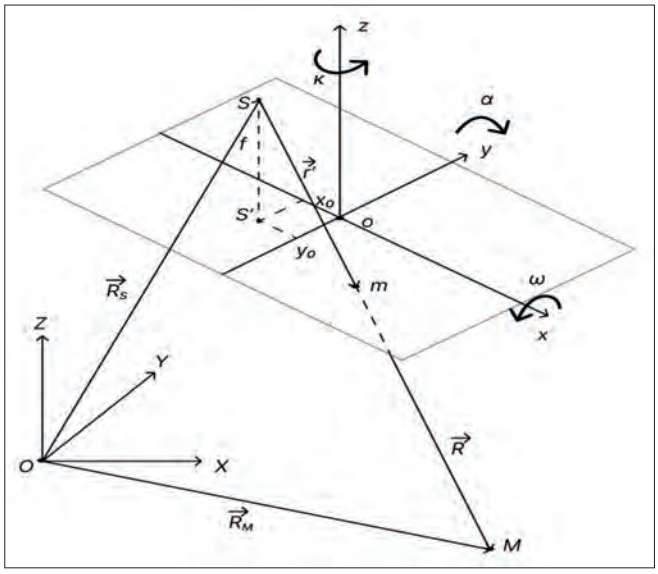

Fig. 3. Elements of the interior and exterior orientation

The coordinates of the object and its image are thus connected through the collinearity equation, which may be presented as follows:

$$\begin{cases} X = X_S + (Z - Z_S)\dfrac{X'}{Z'} \\ Y = Y_S + (Z - Z_S)\dfrac{Y'}{Z'} \end{cases} , \tag{2}$$

where:

X, Y, Z – coordinates of the object M in the object's coordinate system;
X_S, Y_S, Z_S – coordinates of the projection centre S;
X', Y', Z' – coordinates of the vector $\vec{r'}$ in the object's coordinate system, which may be defined by the formula:

$$\begin{bmatrix} X' \\ Y' \\ Z' \end{bmatrix} = A \begin{bmatrix} x - x_0 \\ y - y_0 \\ -f \end{bmatrix} , \tag{3}$$

where:

x_0, y_0, f – elements of the interior orientation;
x, y – coordinates of the image;
A – coordinate transformation matrix (direction cosine matrix), the values a_{ij} of which are determined by the values of the angle elements of the exterior orientation (ω, α, κ).

The direction cosine matrix A may be presented as follows:

$$A = \begin{bmatrix} \cos\alpha \cdot \cos\kappa - \sin\alpha \cdot \sin\omega \cdot \sin\kappa & -\cos\alpha \cdot \cos\kappa - \sin\alpha \cdot \sin\omega \cdot \cos\kappa & -\sin\alpha \cdot \cos\omega \\ \cos\omega \cdot \sin\kappa & \cos\omega \cdot \cos\kappa & -\sin\omega \\ \sin\alpha \cdot \cos\kappa + \cos\alpha \cdot \sin\omega \cdot \sin\kappa & -\sin\alpha \cdot \sin\kappa + \cos\alpha \cdot \sin\omega \cdot \cos\kappa & \cos\alpha \cdot \cos\omega \end{bmatrix} \tag{4}$$

Considering Eq. (3), the collinearity equation Eq. (2) takes the following form:

$$\begin{cases} X = X_S + (Z - Z_S)\dfrac{a_{11}(x-x_0)+a_{12}(y-y_0)-a_{13}f}{a_{31}(x-x_0)+a_{32}(y-y_0)-a_{33}f} \\ Y = Y_S + (Z - Z_S)\dfrac{a_{21}(x-x_0)+a_{22}(y-y_0)-a_{23}f}{a_{31}(x-x_0)+a_{32}(y-y_0)-a_{33}f} \end{cases} \quad (5)$$

In the case of the CCFSS, the elements of the exterior orientation can be determined at the stage of the thermal imager's installation. Also, the coordinate systems of each camera's position within the common FOV pattern can be defined individually, as they are to be synchronised by a general data processing algorithm of the CCFSS. Thus, the allocation of the object's coordinate system for each camera's position can be presented with the origin in the corresponding projection centre *S* (*XS*; *YS*; *ZS*), both rotated at the same values of ω, α, and κ. Thus, the angle elements between the respective axes of the coordinate systems acquire zero values, as also do the coordinates of the projection centre *S*. So the coordinate transformation matrix *A* from Eq. (4) becomes a third-order identity matrix, and Eq. (2) considering A as the identity matrix in Eq. (3) take the following form:

$$\begin{cases} X_M = \dfrac{Z_M \cdot (x_i - x_0)}{-f} \\ Y_M = \dfrac{Z_M \cdot (y_i - y_0)}{-f} \end{cases}, \quad (6)$$

where:

X_M, Y_M – coordinates of the object M in relation to the camera's position;

x_i, y_i – coordinates of the object's image in the plane of the image;

f – camera's focus;

Z_M – distance from the camera to the measurable object.

SIMULATION MODELLING OF CONTAINER DETECTION BY THERMAL IMAGING

A simulation environment developed by means of the Unity IDE and C# programming language capabilities, which are also described in [14, 15], was used in this research in order to perform the simulation modelling of the current task.

Ignition source identification is performed by matching the dynamic infrared data of the object from its thermal image with static coordinate dependencies using images in both the infrared and visible spectra. The data of the visible spectrum are used to distinguish containers within the FOV of the camera, namely, by defining regions of interest (ROI) on the respective image. Therefore, several ROIs can be defined in regard to the respective containers within the camera's FOV. The camera's coordinates are predetermined, based on the elements of the external and internal orientation by means of the defined dependency between the coordinate systems of an object and its image. The thermal data layer of the infrared picture, which contains the temperature information for each pixel and its corresponding palette colour, can be used in order to analyse the real-time condition of the cargo container being monitored. A colour chart or *colour palette* is required for a better match of the pixel's intensity values, which results in better detailing of the image. Moreover, these are used as an effective instrument for thermal data visualisation [19]. Thus, the container in which the ignition originates can be defined by a colour (temperature) change. When such a change is detected inside the respective ROI, the location of the origin of ignition can be identified and presented in bay/row/tier form, using data on the camera's location within the vessel's cargo area. An example of a thermal image in relation to the visible spectrum, taken during the on-site observations with the thermal imager, is presented in Fig. 4. It shows the possibility of thermal data processing by using appropriate commercial software. Spot 1, which is marked as "Sp1" in the infrared spectrum, corresponds to a temperature of 68.8°C. The instrument's calibration and evaluation of the accuracy are the subjects of a separate study and are partially reviewed in [14].

Fig. 4. Reefer-container's compressor in visible and infrared spectra

Fig. 5 presents the viewing frustum of the virtual camera, which is located inside the simulated cargo hold within the virtual environment. The camera's view is rendered as a virtual texture plane, which is equivalent to the image. Within the designed simulation, the cargo containers have a thermal layer, which changes colour depending on the temperature settings of the application. One virtual camera is set to monitor four containers, which are identified within the camera's coordinate system by numbers from left to right and from 0 to 3 (Fig. 6).

When the application is started, the colour values of the texture within the ROIs are saved to an array and used as the reference point. This is compared to the values obtained in each frame and, in the case of detecting a colour change, a warning message is issued that fire has been detected in the respective container, indicating the number from 0 to 3. In this context, each frame can be considered as an iteration of the cycle, which is stopped by a respective command from the operator.

Fig. 6 displays the above-mentioned virtual texture on the left ("Scene") for visual data analysis during the simulation process. On the right ("Game"), a general overview of the simulated cargo hold with the user interface (UI) is presented. The UI allows the user to set the temperature of a fire source and start/stop the calculations. In the bottom tab ("Console"), the warnings generated are shown in accordance with the algorithm. The monitored containers are numbered for clarity.

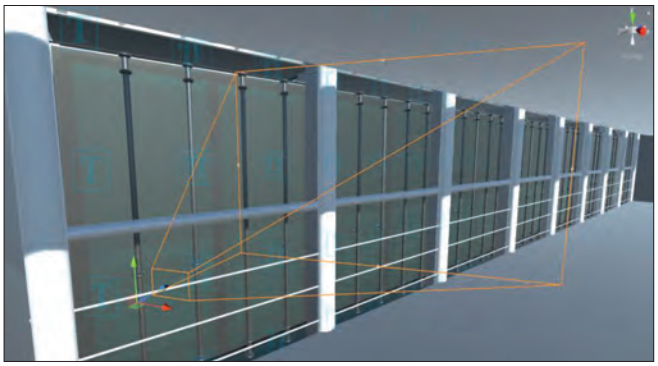

Fig. 5. Virtual camera's viewing frustum

In the presented results, colour changes have been detected only in containers 2 and 3, with the respective warning messages displayed in the "Console" tab.

The proposed algorithm is considered satisfactory within the framework of the set task. However, it still requires enhancement and further research in order to implement the use of multiple cameras, and for determination of the container with the highest temperature value within the common FOV and data synchronization arrangement.

Fig. 6. Simulation of container identification

CONCLUSIONS

The relevance of the safety issues inherent to cargo transportation by container ships has motivated research in the field, which is aimed at safety improvements through implementing a wide variety of methods and approaches. The increase in the size of container ships only reinforces the need for such improvements, particularly in the context of fire safety.

The current study proposes an image processing method to identify cargo containers in a stack within the CCFSS. This method is based on the use of thermal imagers as instruments for cargo monitoring. The algorithm developed uses images in both the thermal and visible spectra in order to detect the container that is the source of ignition and its exact position by matching the dynamic infrared data of the object from its thermal image with static coordinate dependencies. The thermal camera's FOV used during the on-site observations has been modelled during the research. The method for identifying a container's position is based on elements of its external and internal orientation, and can be implemented through the defined dependency between the coordinate systems of an object and its image. The obtained position is determined in relation to the camera's coordinate system and can potentially be transformed into a "bay/row/tier" form by comparing the placement data of the respective camera in the cargo area being monitored. The simulation modelling was carried out using the Unity and C# programming language capabilities. The results obtained, as presented in the current work, are considered satisfactory within the set task.

However, additional research should be carried out in order to implement the use of multiple cameras, enabling the determination of the container with the highest temperature value within the common FOV and data synchronization arrangements. It should be noted that, while the simulation performed was carried out for the placement of imagers in a cargo hold, the proposed image processing method may also be used on deck. Therefore, the issue of the cameras' installation pattern, as well as the other features and tasks of the CCFSS, will be the subject of further studies.

REFERENCES

1. European Maritime Safety Agency, "European Maritime Safety Report 2022," *European Maritime Safety Agency*, EMSA TN-AA-22-00, 2022. [Online]. Available: https://emsa.europa.eu/publications/item/4735-emsafe-report.html. [Accessed: Feb. 18, 2023].

2. J. Ellis, "Undeclared dangerous goods – Risk implications for maritime transport," *WMU Journal of Maritime Affairs*, vol. 9(1), pp. 5–27, 2010, doi: 10.1007/bf03195163.

3. European Maritime Safety Agency, "Safety Analysis of Data Reported in EMCIP – Analysis on Marine Casualties and Incidents involving Container Vessels," *European Maritime Safety Agency*, EMSA, 2020. [Online]. Available: https://www.emsa.europa.eu/newsroom/latest-news/item/4276-safety-analysis-of-data-reported-in-emcip-analysis-onmarine-casualties-and-incidents-involving-container-vessels.html. [Accessed: Feb. 18, 2023].

4. IMO, *Consolidated Text of the International Convention for the Safety of Life at Sea, 1974, and its Protocol of 1988: Articles, Annexes and Certificates*. Incorporating all amendments in effect from 1 January 2020. London: IMO, 2020.

5. IMO, *International Code for Fire Safety Systems*. London: IMO, 2015.

6. *Fire Training Manual including Fire Safety Operations*, 2nd ed. Broadstone: I.C. Brindle, 2011.

7. The Maritime Executive, "Call for Better Fire Fighting Systems on Container Ships," *The Maritime Executive*, Sep. 19, 2017. [Online]. Available: https://maritime-executive.com/article/call-for-better-fire-fighting-systems-on-container-ships. [Accessed: Feb. 18, 2023].

8. W. Zeńczak and A. Krystosik-Gromadzińska, "Improvements to a fire safety management system," *Polish Maritime Research*, vol. 26, no. 4, pp. 117–123, Dec. 2019, doi: 10.2478/pomr-2019-0073.

9. A. Salem, "Vehicle-deck fires aboard Ropax ships: A comparison between numerical modelling and experimental results," *Polish Maritime Research*, vol. 26, no. 2, pp. 155–162, Jun. 2019, doi: 10.2478/pomr-2019-0035.

10. Z. Xiong, B. Xiang, Y. Chen, and B. Chen, "Research on the risk classification of cruise ship fires based on an Attention-Bp Neural Network," *Polish Maritime Research*, vol. 29, no. 3, pp. 61–68, Sep. 2022, doi: 10.2478/pomr-2022-0026.

11. K. L. B. L. Xavier and V. K. Nanayakkara, "Development of an early fire detection technique using a passive infrared sensor and deep neural networks," *Fire Technology*, vol. 58, pp. 3529–3552, 2022, doi: 10.1007/s10694-022-01319-x.

12. H. Wang, Y. Zhang, and X. Fan, "Rapid early fire smoke detection system using slope fitting in video image histogram," *Fire Technology*, vol. 56, pp. 695–714, 2020, doi: 10.1007/s10694-019-00899-5.

13. X. Cheng, J. Wu, X. Yuan, and H. Zhou, "Principles for a video fire detection system," *Fire Safety Journal*, vol. 33(1), pp. 57–69, 1999, doi: 10.1016/s0379-7112(98)00047-2.

14. V. Konon and V. Savchuk, "Infrared thermography in the context of fire safety in container transportation by sea," *Shipping & Navigation*, vol. 33, pp. 43–53, 2022, doi: 10.31653/2306-5761.33.2022.43-53.

15. V. Konon and N. Konon, "Application perspective of digital neural networks in the context of marine technologies," *TransNav, The International Journal on Marine Navigation and Safety of Sea Transportation*, vol. 16, no. 4, pp. 743–747, 2022, doi:10.12716/1001.16.04.16.

16. D. F. Rogers, *Procedural Elements of Computer Graphics*. New York: WCB/McGraw-Hill, 1997.

17. T. Szkodny, "Calculation of the Location Coordinates of an Object Observed by a Camera," in *Man-Machine Interactions 3. Advances in Intelligent Systems and Computing*, vol. 242, D. Gruca, T. Czachórski, S. Kozielski, Eds. Cham: Springer, 2014, pp. 139–151, doi: 10.1007/978-3-319-02309-0_15.

18. J. Duh, "Photogrammetry: DTM Extraction & Editing," Portland State University, 2017. [Online]. Available: https://web.pdx.edu/~jduh/courses/geog493f17/Week03.pdf [Accessed: Feb. 18, 2023].

19. A. Berg, *Detection and Tracking in Thermal Infrared Imagery*. Licentiate [Dissertation]. Linköping, Sweden: Linköping University Electronic Press, 2016. [Online]. Available: DiVA – Academic Archive Online, doi: 10.3384/lic.diva-126955.

POLISH MARITIME RESEARCH 2 (118) 2023 Vol. 30; pp. 121-129
10.2478/pomr-2023-0028

AN INSTALLATION ANGLE ERROR CALIBRATION METHOD IN AN ULTRA-SHORT BASELINE SYSTEM BASED ON A DUAL TRANSPONDER

Baoheng Liu [1] *
Xiaochuan Zhang [1]
Shuyang Jia [1]
Sichen Zou [1]
Deyan Tian [1]
Lianglong Da [2]
[1] The PLA Navy Submarine Academy, China
[2] Naval Submarine Academy, China

* Corresponding author: *1094480943@qq.com (Baoheng Liu)*

ABSTRACT

The installation error of an acoustic transceiver array is one of the important error sources in an ultra-short baseline (USBL) system. In a USBL system with a positioning accuracy of 0.5%, an installation error angle of 1° will lead to a positioning error of 1.7% times the slant distance. In this paper, a dual transponder-based installation angle error calibration method for USBL is proposed. First, the positioning errors induced by various installation angles are deduced and analysed using the linear measurement of seafloor targets. Then, an iterative algorithm is proposed that estimates the rolling alignment error, pitching alignment error, and heading alignment error, in that order. The simulation and experienced results show that, after three iterations, the estimates of the three alignment errors can converge quickly, all of the estimates converge to within 0.001° and the estimated values are very close to the true values. The horizontal positioning error caused by the installation error angle can be reduced by nearly 75%. The method has good effectiveness and robustness, and can greatly improve the positioning accuracy of the USBL system.

Keywords: USBL, installation angle error, misalignment calibration, numerical algorithm, hydrolocation

INTRODUCTION

The benefits of an ultra-short baseline positioning system (USBL) are a small array size, easy installation, adaptability, and low cost. As a result, it has significant social value and practical potential and can be instrumental in modern ocean mapping, resource exploration, the development of marine national security, and the detection of undersea targets (1). The installation error of an acoustic transceiver array is one of the important error sources in USBL systems (1). The installation error can be divided into coordinate offset error and angle rotation error, and the angle rotation error has a great influence on the positioning accuracy of USBL. Relevant literature shows that, in a USBL system with a positioning accuracy of 0.5%, an installation error angle of 1° will lead to a positioning error of 1.7% times the slant distance, so it is important to accurately calibrate the installation angle before using the USBL system (2). Moreira et al. (2007) (3) first proposed the need to calibrate the error angle before USBL positioning. Yu (2010) (4) applied GPS-RTK (Global Positioning System real-time Kinematic) to the angle error calibration and used the least square method to calculate the installation error angle, but this method had special requirements for the selection of sampling points. Li et al. (2013) (5) verified the feasibility of the least square method to experimentally estimate the error angle of USBL installations in the sea, and the accuracy of the positioning system after error compensation could reach 5‰ of the slant distance. Morgado et al. (2013) (6) pointed out that the installation error angle of

the USBL system can be estimated by the multi-circle detour method with different navigation radii. However, this method requires the centre of the mother ship's orbit trajectory to be located above the underwater transponder, which is difficult to be directly applied in practical engineering. Chen (2008) (7) studied the USBL installation error calibration method for ships sailing along a straight line and (8) verified the feasibility of the straight track method through theory and experiment. Jinwu et al. (2018) [(10)] proposed a fast calibration algorithm for USBL installation error angle based on a laid out multi-transponder but this algorithm has strict requirements on the placement of transponders, limiting its application.

It is often difficult for ships to perform complex manoeuvres, and so they typically follow circular or straight paths in order to collect USBL, GPS, or other gyro compass observation data. Both the circular path and the straight path are simple manoeuvres but the disadvantage of the circular path scheme is that the rotational acceleration will reduce the performance of the gyro compass and motion sensor, and it needs to use different radii to circumnavigate many times, which is complicated. As a result, this paper suggests a dual transponder-based installation angle error calibration method for the USBL system. The positioning errors caused by various installation angles are first deduced and analysed. Based on this, an iterative approach is proposed, correcting the positioning errors of each angle sequentially by first estimating the rolling alignment error, then the pitching alignment error, and, finally, the heading alignment error.

PRINCIPLE AND ERROR ANALYSIS OF USBL POSITIONING COORDINATE SYSTEMS

The schematic of a ship navigating along a straight line path to locate an underwater transponder is shown in Fig. 1, where d represents the horizontal distance between the transponder and the ship track, θ represents the ship heading, (d, l) represents the position of O_S relative to the origin O_a, and the depths of transponder 1 and 2 are h_1 and h_2, respectively.

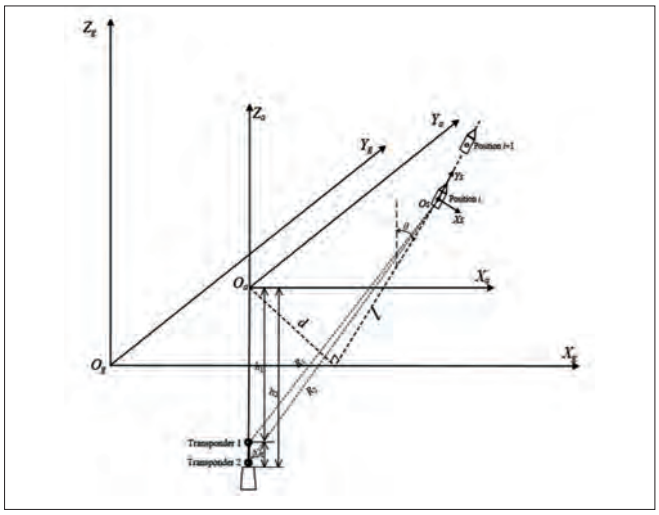

Fig. 1. The geometry of a straight path survey for positioning an underwater transponder

This paper employs several coordinate systems. The global coordinate system $O_gX_gY_gZ_g$ can obtain the absolute coordinate position of the object and $O_sX_sY_sZ_s$ is the base coordinate system, including the gyro compass and motion sensor. The auxiliary coordinate system $O_aX_aY_aZ_a$ is defined to simplify the derivation and its origin is located on the sea surface, above the transponder. The global coordinate system $O_gX_gY_gZ_g$ is a common earth-fixed coordinate system, e.g. the world geodetic system 1984 (WGS-84). The auxiliary coordinate system $O_aX_aY_aZ_a$ is an imaginary local coordinate system with the set point as the origin. The USBL acoustic array is installed under the base array and, due to the installation error, the base coordinate system and the acoustic array coordinate system cannot completely coincide. To study the impact of installation error on the USBL positioning, the USBL acoustic array coordinate system $O_tX_tY_tZ_t$ is defined as shown in Fig. 2, where the alignment errors of heading, pitch, and roll are α, β and γ, respectively.

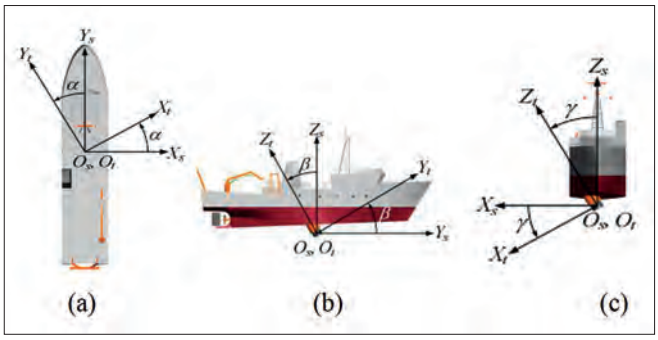

Fig. 2. The USBL acoustic array coordinate system $O_tX_tY_tZ_t$. (a) heading misalignment, (b) pitch misalignment, and (c) roll misalignment

THE BASIC POSITIONING PRINCIPLE

The USBL positioning system sends an inquiry signal to an underwater target transponder by a transducer array. The transponder receives the signal and sends a positioning signal; the transducer array measures the phase difference or delay difference between the base array elements to determine the target orientation. The slant distance between the measured target and the transducer array is then calculated by measuring the round-trip time between the query signal and the positioning signal. By measuring the orientation and slant distance, the underwater target location may be finalised. The commonly used geometric diagram of the USBL positioning principle is shown in Fig. 3.

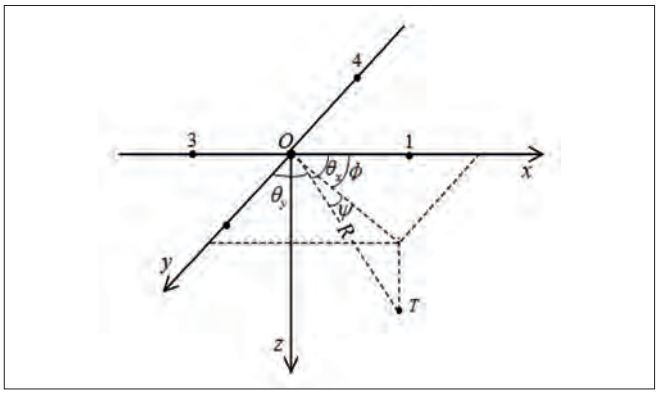

Fig. 3. The geometric diagram of the USBL positioning principle

The North-East-Earth rectangular coordinate system (x, y, z) is used, with the array's centre at coordinate origin O. The No. 1 and No. 3 transducers are located on the x-axis, and the No. 2 and No. 4 transducers are located on the y-axis. The included angles between the target T and the x-and y-axes are θ_x and θ_y, respectively, and the slant range between the coordinate origin O and the target T is R.

Then, the coordinates of target T can be expressed as:

$$P_t = [R\cdot\cos\theta_x, R\cdot\cos\theta_y, R\cdot\sqrt{1-(\cos^2\theta_x+\cos^2\theta_y)}\,] \quad (1)$$

The distance between the target and the coordinate origin is much larger than the array spacing, so the signal can be considered to be the far-field plane wave propagation. Then, the delay difference τ_{13} of the No. 1 and No. 3 transducers, and the delay differences τ_{24} of the No. 2 and No. 4 transducers are, respectively:

$$\tau_{13} = \frac{d_{13}\cos\theta_x}{c}, \quad \tau_{24} = \frac{d_{24}\cos\theta_y}{c}, \quad (2)$$

where c is the sound velocity in water, d_{13} is the distance between the No. 1 and No. 3 transducers, and d_{24} is the distance between the No. 2 and No. 4 transducers. Substituting Eqs. (2) into Eq. (1) gives the coordinates of T as:

$$P_t = \left[\frac{cR\tau_{13}}{d_{13}}, \frac{cR\tau_{24}}{d_{24}}, R\cdot\sqrt{1-c^2[(\frac{\tau_{13}}{d_{13}})^2+(\frac{\tau_{24}}{d_{24}})^2]}\,\right] \quad (3)$$

When the baseline length and sound speed in seawater are known, Eq. (3) states that the coordinate position of the target may be determined by computing the time delay and slant range, allowing for USBL positioning of the underwater target.

In addition, the slant range (R), bearing (ϕ), and depression angle (ψ) from the underwater transponder to the USBL centre can also be used to calculate the position. The coordinate of the transponder T is shown in Eq. (4). It can be seen that, by this method, the position of the transponder in the USBL acoustic array coordinate can be determined by simply measuring the slant range, horizontal bearing, and depression angle.

$$P_t = [R\cos\psi\cos\phi, R\cos\psi\sin\phi, -R\sin\psi] \quad (4)$$

AN INSTALLATION ANGLE ERROR CALIBRATION BASED ON A DUAL TRANSPONDER

USBL POSITIONING ERRORS DUE TO ANGULAR MISALIGNMENTS

The position of transponder 1 in the $O_aX_aY_aZ_a$ coordinate system can be written as: $\boldsymbol{P}_a = [0, 0, -h_1, 1]$. When there is no alignment error between the attitude sensor and USBL acoustic array, $O_tX_tY_tZ_t$ and $O_sX_sY_sZ_s$ completely coincide, and the position of the seabed transponder in the $O_tX_tY_tZ_t$ coordinate system is: $\boldsymbol{P}_t = \boldsymbol{T}_{sa}(d, l, \theta)\cdot\boldsymbol{P}_a = [-d, -l, -h_1, 1]$. When there is a heading alignment error α between the $O_tX_tY_tZ_t$ coordinate system and $O_sX_sY_sZ_s$ coordinate system, the position of the seabed transponder is:

$$\boldsymbol{P}_t^{\alpha} = \boldsymbol{T}_{ts}(\alpha)\,\boldsymbol{T}_{sa}(d, l, \theta)\,\boldsymbol{P}_a \begin{bmatrix} -d\cos\alpha - l\sin\alpha \\ d\sin\alpha - l\cos\alpha \\ -h_1 \\ 1 \end{bmatrix} \quad (5)$$

Similarly, when there is pitch alignment error β and roll alignment error γ, between the USBL acoustic base coordinate system and the carrier base coordinate system, respectively, the position of the transponder in the $O_tX_tY_tZ_t$ coordinate system is:

$$\boldsymbol{P}_t^{\beta} = \boldsymbol{T}_{ts}(\beta)\,\boldsymbol{T}_{sa}(d, l, \theta)\,\boldsymbol{P}_a \begin{bmatrix} -d \\ -l\cos\beta - h_1\sin\beta \\ l\sin\beta - h_1\cos\beta \\ 1 \end{bmatrix},$$

$$\boldsymbol{P}_t^{\gamma} = \boldsymbol{T}_{ts}(\gamma)\,\boldsymbol{T}_{sa}(d, l, \theta)\,\boldsymbol{P}_a \begin{bmatrix} -d\cos\gamma + h_1\sin\gamma \\ -l \\ -d\sin\gamma - h_1\cos\gamma \\ 1 \end{bmatrix} \quad (6)$$

In order to analyse the influence of alignment errors on the USBL positioning in the $O_tX_tY_tZ_t$ coordinate system, the positioning error caused by the heading misalignment α is:

$$\boldsymbol{\varepsilon}^{\alpha} = \boldsymbol{P}_t^{\alpha} - \boldsymbol{P}_t = \begin{bmatrix} -d\cos\alpha - l\sin\alpha + d \\ d\sin\alpha - l\cos\alpha + l \\ 0 \\ 0 \end{bmatrix} \quad (7)$$

Similarly, the positioning errors of transponders $\boldsymbol{\varepsilon}^{\beta}$ and $\boldsymbol{\varepsilon}^{\gamma}$, caused by the pitch and roll misalignments under the coordinate system $O_tX_tY_tZ_t$, are, respectively:

$$\boldsymbol{\varepsilon}^{\beta} = \boldsymbol{P}_t^{\beta} - \boldsymbol{P}_t = \begin{bmatrix} 0 \\ -l\cos\beta - h_1\sin\beta + l \\ l\sin\beta - h_1\cos\beta + h_1 \\ 0 \end{bmatrix},$$

$$\boldsymbol{\varepsilon}^{\gamma} = \boldsymbol{P}_t^{\gamma} - \boldsymbol{P}_t = \begin{bmatrix} -d\cos\gamma + h_1\sin\gamma + d \\ 0 \\ -d\sin\gamma - h_1\cos\gamma + h_1 \\ 0 \end{bmatrix} \quad (8)$$

To analyse the influence of angular misalignments on positioning accuracy, the following simulation was conducted. Suppose the depth of transponder 1 is 100 m, the horizontal distance d from the transponder to the ship's straight track is 50, 100, 200, and 300 m, l is –100 m to 100 m, and the heading, pitch, and roll misalignments are all set to 10°. Figs. 4-6 show the positioning error diagram caused by the misalignment of heading, pitch, and roll.

$\boldsymbol{\varepsilon}_x^{\alpha}$ and $\boldsymbol{\varepsilon}_y^{\alpha}$ are the positioning errors in the x-direction and y-direction caused by heading misalignment, respectively. According to Eq. (8), we can obtain:

$$\boldsymbol{\varepsilon}_x^{\alpha} = \cot\frac{\alpha}{2}\cdot\boldsymbol{\varepsilon}_y^{\alpha} + \csc\frac{\alpha}{2}\cdot d \quad (9)$$

It can be seen from Eq. (9) and Fig. 4 that the positioning error in the x-direction, caused by heading misalignment, has

a linear relationship with the positioning error in the y-direction, and the error increases with the increase of horizontal distance d, while there is no positioning error in the z-direction.

Similarly, $\boldsymbol{\varepsilon}_y^{\beta}$ and $\boldsymbol{\varepsilon}_z^{\beta}$ are the positioning errors in the y-direction and z-direction caused by pitch misalignment, and $\boldsymbol{\varepsilon}_x^{\gamma}$ and $\boldsymbol{\varepsilon}_z^{\gamma}$ are the positioning errors in the x-direction and z-direction caused by roll misalignment. According to Eq. (8), we can obtain:

$$\boldsymbol{\varepsilon}_y^{\beta} = \tan\frac{\beta}{2} \cdot \boldsymbol{\varepsilon}_z^{\beta} + \sec\frac{\beta}{2} \cdot h, \quad \boldsymbol{\varepsilon}_x^{\gamma} = -\tan\frac{\gamma}{2} \cdot \boldsymbol{\varepsilon}_z^{\gamma} + \sec\frac{\beta}{2} \cdot h \quad \textbf{(10)}$$

It can be seen that the positioning error in the y-direction, caused by pitch misalignment, has a proportional linear relationship with the error in the z-direction, and the error is independent of the horizontal distance d, while there is no positioning error in the x-direction. In addition, the positioning errors in the x-direction and z-direction, caused by roll misalignment, are independent of l, and the errors increase with the increase of horizontal distance d, while there is no positioning error in the y-direction.

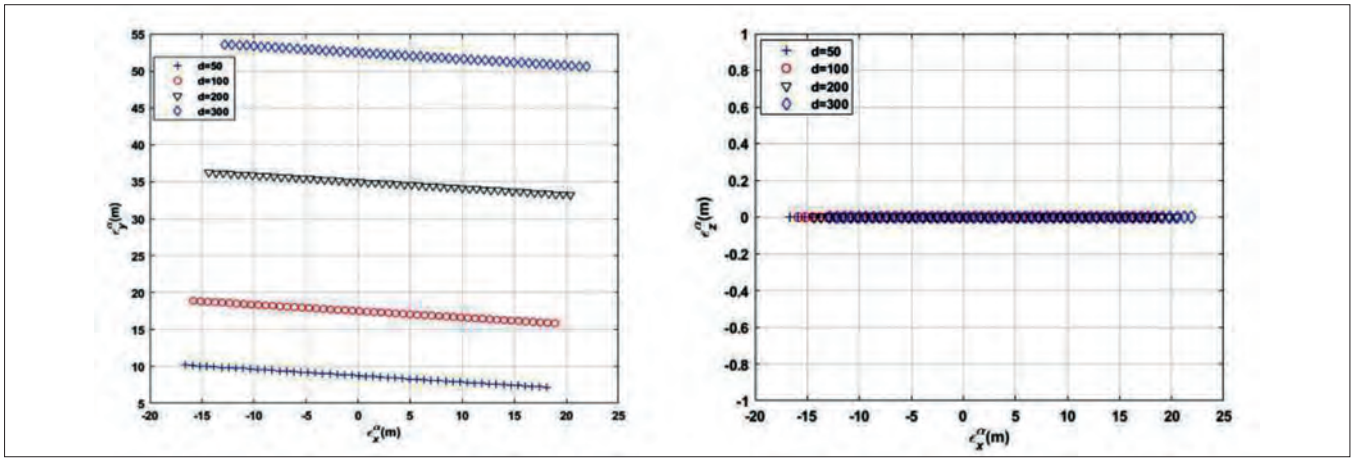

Fig. 4. The positioning error diagram caused by heading misalignment

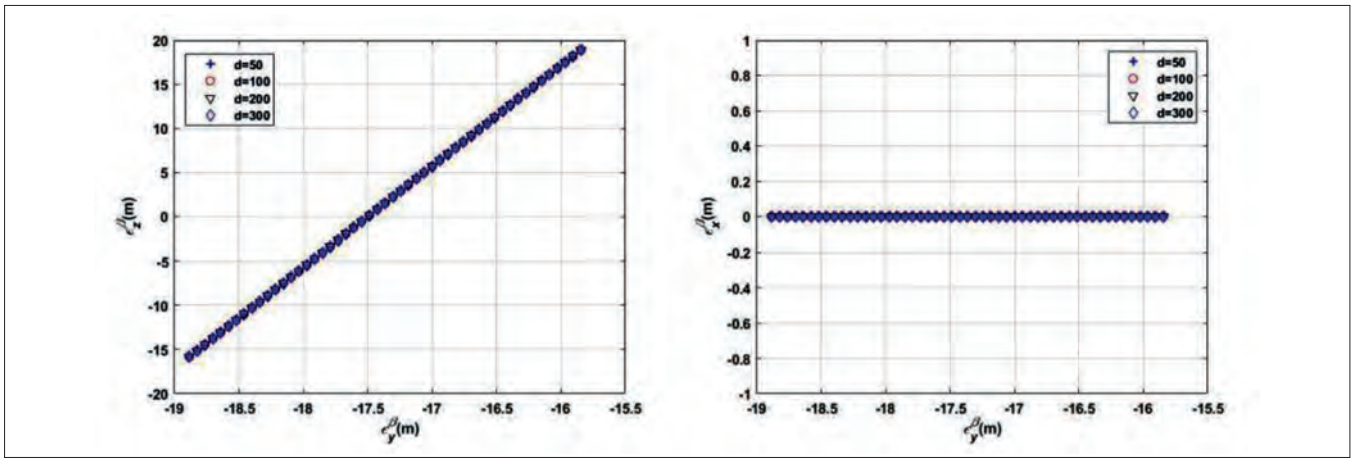

Fig. 5. The positioning error diagram caused by pitch misalignment

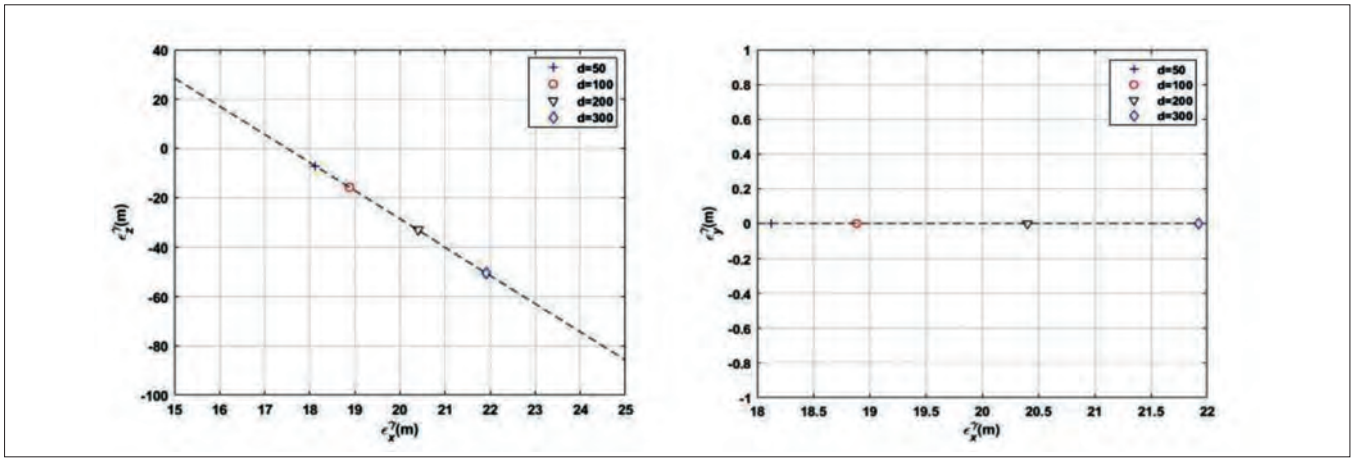

Fig. 6. The positioning error diagram caused by roll misalignment

ITERATIVE ALGORITHM

When the USBL acoustic coordinate system and the carrier base coordinate system have alignment errors of heading, pitch, and roll, the position of the seabed transponder 1 is:

$$\boldsymbol{P}'_{t1} = \boldsymbol{T}_{ts}(\alpha)\ \boldsymbol{T}_{ts}(\beta)\ \boldsymbol{T}_{ts}(\gamma)\ \boldsymbol{T}_{sa}(d, l, \theta)\ \boldsymbol{P}_a = \\ = \begin{bmatrix} -d\cos\gamma\cos\alpha - l\cos\gamma\sin\alpha + h_1\sin\gamma \\ -d(\sin\beta\sin\gamma\cos\alpha - \cos\beta\sin\alpha) - l(\sin\beta\sin\gamma\sin\alpha + \cos\beta\cos\alpha) - h_1\sin\beta\cos\gamma \\ -d(\sin\gamma\cos\beta\cos\alpha + \sin\beta\sin\alpha) - l(\sin\gamma\cos\beta\sin\alpha - \sin\beta\cos\alpha) - h_1\cos\beta\cos\gamma \\ 1 \end{bmatrix} \tag{11}$$

Similarly, the coordinate of the seabed transponder 2 is:

$$\boldsymbol{P}'_{t2} = \begin{bmatrix} -d\cos\gamma\cos\alpha - l\cos\gamma\sin\alpha + h_2\sin\gamma \\ -d(\sin\beta\sin\gamma\cos\alpha - \cos\beta\sin\alpha) - l(\sin\beta\sin\gamma\sin\alpha + \cos\beta\cos\alpha) - h_2\sin\beta\cos\gamma \\ -d(\sin\gamma\cos\beta\cos\alpha + \sin\beta\sin\alpha) - l(\sin\gamma\cos\beta\sin\alpha - \sin\beta\cos\alpha) - h_2\cos\beta\cos\gamma \\ 1 \end{bmatrix} \tag{12}$$

For the characteristics of positioning errors caused by each installation angle, an algorithm for iterative calculation and estimation of heading, pitch, and roll misalignments is proposed. The specific steps are as follows:

(1) The installation error angle of roll is solved by the error component in the x-direction of the $O_tX_tY_tZ$ coordinate system. According to Eq. (11) and Eq. (12), when the ship sails in a straight line, the x-axis values of transponder 1 and transponder 2 are:

$$\boldsymbol{P}'_{t1\_x} = -d\cos\gamma\cos\alpha - l\cos\gamma\sin\alpha + h_1\sin\gamma, \\ \boldsymbol{P}'_{t2\_x} = -d\cos\gamma\cos\alpha - l\cos\gamma\sin\alpha + h_2\sin\gamma \tag{13}$$

From Eq. (13), we can get the following equation:

$$\boldsymbol{P}'_{t1\_x} - \boldsymbol{P}'_{t2\_x} = (h_1 - h_2)\sin\gamma \tag{14}$$

Then, the roll misalignment is given as:

$$\gamma = \arcsin\frac{\boldsymbol{P}'_{t1\_x} - \boldsymbol{P}'_{t2\_x}}{h_1 - h_2} = \arcsin\frac{\boldsymbol{P}'_{t2\_x} - \boldsymbol{P}'_{t1\_x}}{\Delta h} \tag{15}$$

where $\boldsymbol{P}'_{t1\_x}$ and $\boldsymbol{P}'_{t2\_x}$ represent the x-axis coordinate values of transponder 1 and transponder 2, respectively, in the USBL array coordinate system. Δh is the depth difference between transponder 1 and transponder 2.

(2) After correcting the roll error, it can be found that the pitch installation error angle can be solved by the error component in the y-direction. According to Eq. (11) and Eq. (12), the y-axis values of transponder 1 and transponder 2 are:

$$\boldsymbol{P}'_{t1\_y} = -d(\sin\beta\sin\gamma\cos\alpha - \cos\beta\sin\alpha) - \\ -l(\sin\beta\sin\gamma\sin\alpha + \cos\beta\cos\alpha) - h_1\sin\beta\cos\gamma \tag{16}$$

$$\boldsymbol{P}'_{t2\_y} = -d(\sin\beta\sin\gamma\cos\alpha - \cos\beta\sin\alpha) - \\ -l(\sin\beta\sin\gamma\sin\alpha + \cos\beta\cos\alpha) - h_2\sin\beta\cos\gamma \tag{17}$$

When there is no roll error, it can be seen from Eq. (16) and Eq. (17) that:

$$\boldsymbol{P}'_{t1\_y} - \boldsymbol{P}'_{t2\_y} = (h_2 - h_1)\sin\beta \tag{18}$$

Then, the pitch misalignment is calculated as:

$$\beta = \arcsin\frac{\boldsymbol{P}'_{t1\_y} - \boldsymbol{P}'_{t2\_y}}{h_2 - h_1} = \arcsin\frac{\boldsymbol{P}'_{t1\_y} - \boldsymbol{P}'_{t2\_y}}{\Delta h} \tag{19}$$

where $\boldsymbol{P}'_{t1\_y}$ and $\boldsymbol{P}'_{t2\_y}$ represent the y-axis coordinate values of transponder 1 and transponder 2, respectively, in the USBL array coordinate system.

(3) After both the roll and pitch misalignments are corrected, it should be noted that the heading error angle can be solved by combining the error component in the x-direction and y-direction of a transponder. When there is no roll and pitch error, it can be seen that:

$$\boldsymbol{P}'_{t1\_x} = -d\cos\alpha - l\sin\alpha,\ \ \boldsymbol{P}'_{t1\_y} = d\sin\alpha - l\cos\alpha \tag{20}$$

Then, the heading misalignment is given as:

$$\alpha = \arcsin\frac{\boldsymbol{P}'_{t1\_y}\cdot d - \boldsymbol{P}'_{t1\_x}\cdot l}{d^2 + l^2} \tag{21}$$

(4) However, the above analysis is carried out under the assumption that the deviations of the other two angles have been corrected when calculating each installation error angle, which is not the case in engineering practice. Therefore, the above method cannot directly estimate the error angle and so the above steps must be repeated. An incremental iterative algorithm is proposed to estimate the error angle, as shown in Fig. 7. The iterative algorithm starts from $\alpha = \beta = \gamma = 0$ and, in each iteration, the increments $\Delta\alpha$, $\Delta\beta$, and $\Delta\gamma$ of the installation error angle are calculated and accumulated. Then the original positioning data of the positioning observations are modified with the updated estimation of roll, pitch and heading. The iterative process is continued until all estimates of the angular deviations converge.

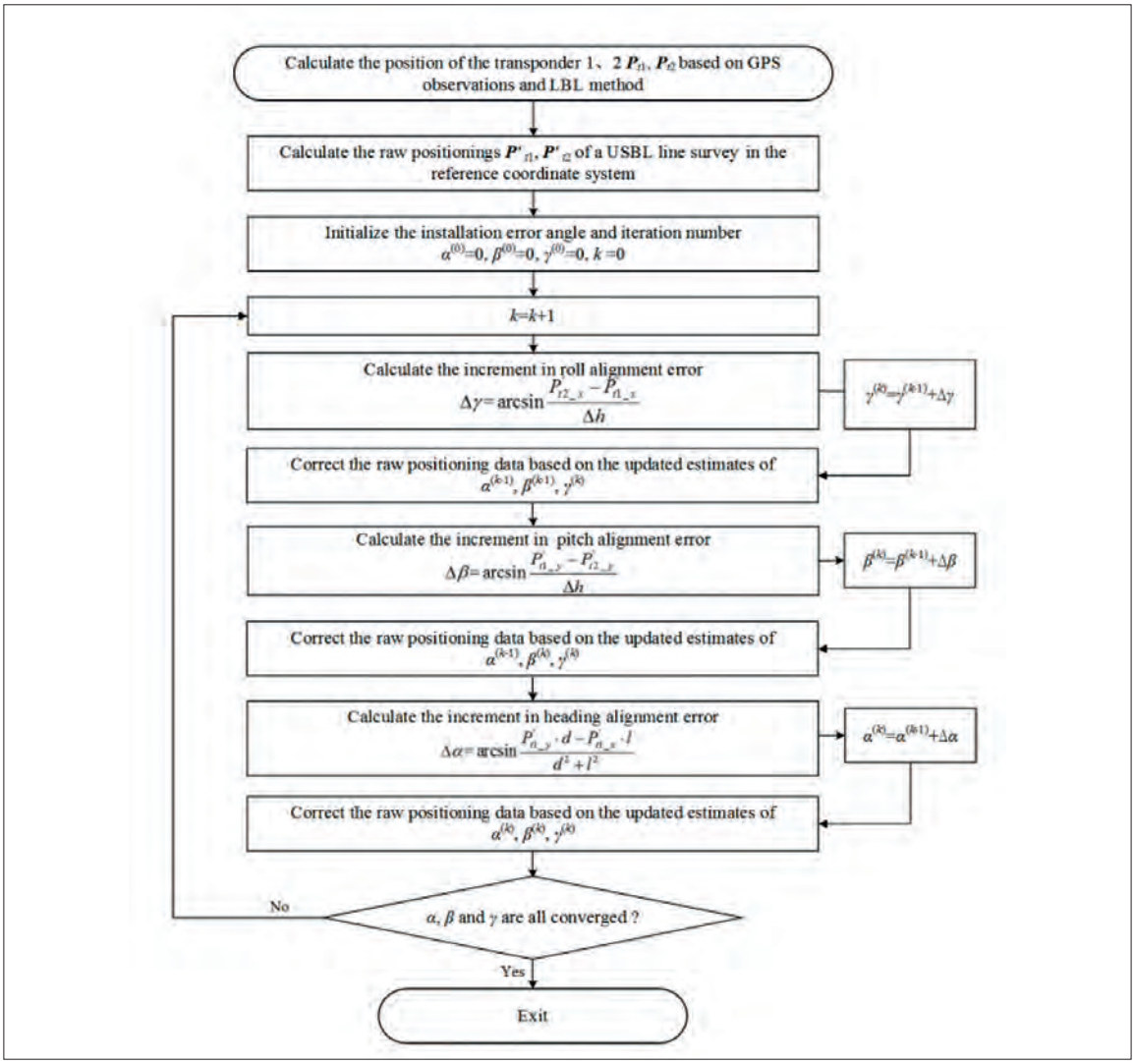

Fig. 7. The incremental iterative algorithm

NUMERICAL SIMULATIONS

According to Eq. (4), the position of the transponder can be calculated by measuring the oblique distance R, bearing ϕ, and depression angle ψ. The effectiveness and robustness of the new algorithm to noise are analysed by adding random Gaussian noise. The simulation conditions are as follows: the depths of transponder 1 and 2 are 100 m and 150 m, respectively, and the horizontal distance d from the transponder to the ship's straight track is 50 m, l is −100 m to 100 m, the values of three installation angle errors α, β, and γ are 7°, 3°, and 5°, respectively. The values of R, ϕ, and ψ all follow a normal distribution with zero mean, the standard deviation of R is 0.25 m, and the standard deviation of ϕ and ψ is 0.2°.

When the alignment error is not corrected, the x and y coordinates of the two transponders are as shown in Fig. 8(a), the position after one iteration is shown in Fig. 8(b), and the result after five iterations is shown in Fig. 8(c). It can be seen that, after correction, the x and y coordinates of the two transponders tend to be approximately the same as the number of iteration increases. The number of iterations ranges from one to five and the iterative estimations of the alignment error for 200 observed positions are calculated and averaged according to Eqs. (22), (26), and (29), and the results are shown in Table 1. It can be seen from the table that the estimates of roll, pitch, and heading converge to their true values with a small error. In addition, the algorithm is robust, even with measurement errors, and all of the estimates converge to within 0.001° after three iterations.

Tab. 1. The iterative estimates of alignment errors

Iteration number	$\Delta\alpha$	$\Delta\beta$	$\Delta\gamma$	α	β	γ
1	6.968°	2.495°	4.512°	6.968°	2.495°	4.512°
2	0.024°	0.426°	0.443°	6.992°	2.921°	4.955°
3	0.008°	0.079°	0.045°	7.000°	3.000°	5.000°
4	3.6e-5°	6.8e-4°	5.3e-4°	7.000°	3.000°	5.000°
5	1.5e-7°	2.2e-5°	3.8e-5°	7.000°	3.000°	5.000°

EXPERIENCE AND ANALYSIS

A USBL localisation experiment was conducted to further verify the effectiveness of the proposed installation angle error calibration method in practical applications. The test equipment

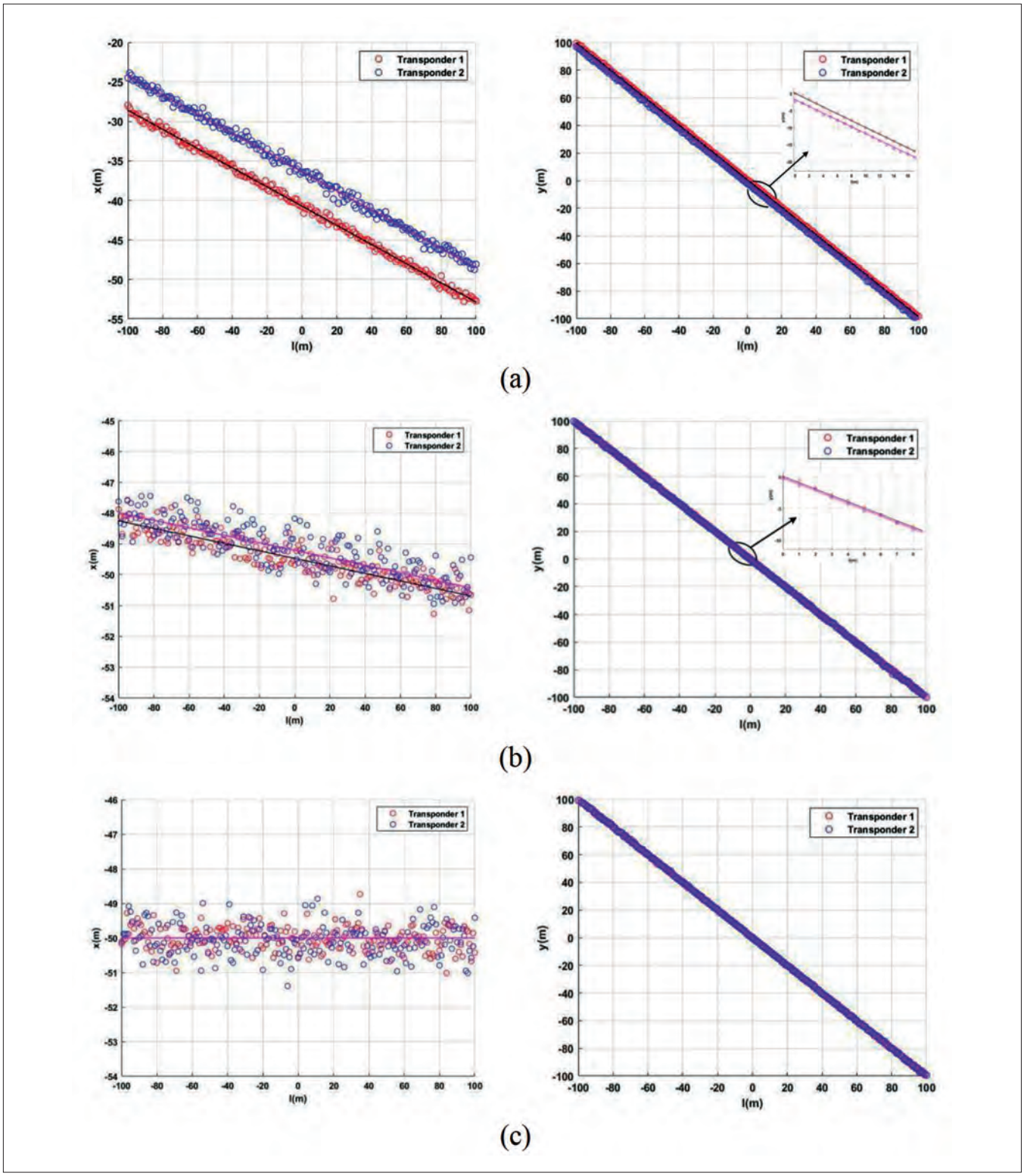

Fig. 8. The x and y coordinates of the two transponders. (a) No iteration; (b) one iteration; (c) five iterations

included the USBL system, Real Time Kinematical Global Positioning System (RTK-GPS), and Attitude and Heading Reference System (AHRS). The transducer array has a four-element planar array structure, with four elements located on the horizontal axis of the acoustic array, and the transmitter head is located at the geometric centre of the four arrays. The transducer array is mounted on the starboard side of the mother ship at a depth of 2 m and is rigidly connected to the connecting rod. The RTK-GPS is used to measure the horizontal position of the two transponders and take it as the origin. Since the accuracy of RTK reaches the centimetre level, this coordinate could be taken as the true value of algorithm verification. In the experiment, the ship sailed in a straight line near the transponders, and eight navigation tracks were seen (Fig. 9).

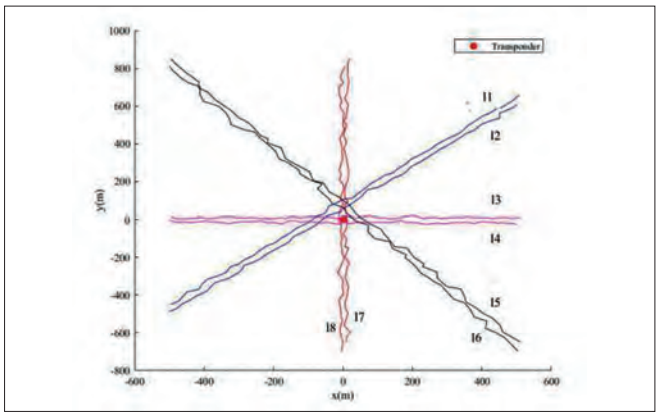

Fig. 9. The eight navigation tracks

The pitch, roll, and heading alignment errors were estimated using the USBL observations measured along path *l*1, according to the installation angle error calibration method proposed in the previous section and shown in Fig. 10. As can be seen from the figure, the estimates of the three alignment errors can converge quickly, and the estimates are very close to the true values when the number of iterations is three. Then, these three alignment errors were estimated using the USBL observations collected along paths *l*1–18 and the results are shown in Table 2. It can be seen that the standard deviations of the pitch, roll and heading alignment error estimates are small, which indicates that the algorithm is robust for all three error estimates. It should be noted that the USBL installation angle error can be caused by surface ambient noise and hull self-noise, artificial incorrect installation operation, and measurement errors of devices such as RTK-GPS and OCTANS. These factors have different effects on heading angle, pitch angle and roll angle, so the horizontal and heading installation errors are different.

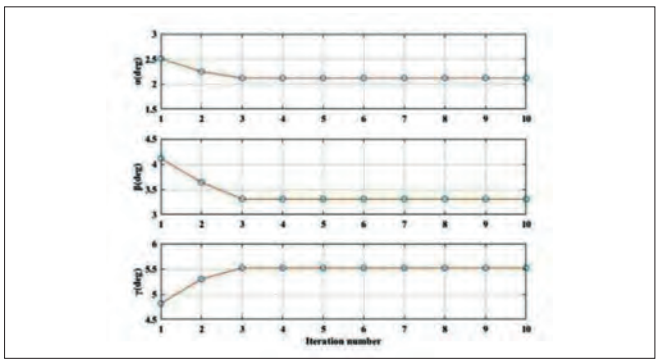

Fig. 10. Convergence of the estimates based on the observations collected along path l1.

Tab. 2. Estimates of alignment errors from different paths

Survey path	α	β	γ	Survey path	α	β	γ
11	2.12°	3.31°	5.52°	15	2.03°	3.15°	5.55°
12	2.05°	3.25°	5.45°	16	2.20°	3.40°	5.44°
13	2.25°	3.36°	5.61°	17	1.99°	3.33°	5.42°
14	2.18°	3.22°	5.37°	18	2.28°	3.13°	5.51°
Mean	2.14°	3.27°	5.48°	Std. dev.	0.10°	0.09°	0.07°

Based on the results in Table 2, the USBL observations were corrected, and the seabed transponder positioning before and after the error correction is shown in Fig. 11. The point distribution shows that there is a large horizontal positioning error before the correction and after the error correction, the positioning results are more concentrated at the true position of the transponder. The horizontal position error is reduced by nearly 75% after the error angle correction of the USBL installation, and the horizontal positioning accuracy of USBL has been significantly improved.

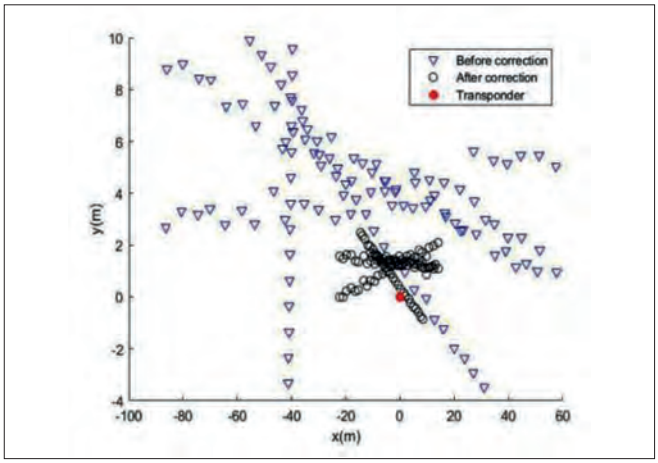

Fig. 11. The seabed transponder positioning before and after t he error correction

CONCLUSION

This paper deduces and analyses the influencing laws of heading, pitch, and roll on positioning errors. Then, an iterative calibration algorithm of USBL installation angle error, based on dual transponders, is proposed, which first estimates the rolling alignment error, then estimates the pitch alignment error, and, finally, estimates the heading alignment error. Simulations and experience show that the convergence speed of the three alignment errors is very fast; only a few iterations are needed to accurately calculate the alignment errors, and the new algorithm has good effectiveness and stability, which can greatly improve the positioning accuracy of the USBL system.

ACKNOWLEDGEMENTS

The authors would like to acknowledge the support of the National Natural Science Foundation of China, under Grant Numbers 41906005 and 41705081.

REFERENCES

1. L. Paull, S. Saeedi, M. Seto and L. Howard, "AUV navigation and localisation: A review," *IEEE Journal of Oceanic Engineering*, vol. 39, no. 1, pp. 131–149, 2013, doi:10.1109/JOE.2013.2278891.

2. D. Zhong, D. Yang and M. Zhu, "Improvement of sound source localisation in a finite duct using beamforming methods," *Applied Acoustics*, vol. 103, no. 1, pp. 37–46, 2016, doi:10.1016/j.apacoust.2015.10.007.

3. W. Gierusz, N. Cong Vinh and A. Rak, "Manoeuvring control and trajectory tracking of very large crude carrier," *Ocean Engineering*, vol. 34, no. 7, pp. 932-945, 2007, doi:10.1016/j.oceaneng.2006.06.003.

4. L. Moreira, T.I. Fossen and C. Guedes Soares, "Path following control system for a tanker ship model," *Ocean Engineering*, vol. 34, no. 14, pp. 2074-2085, 2007, doi:10.1016/j.oceaneng.2007.02.005.

5. M. Yu, "In-situ calibration of transceiver alignment for a high-precision USBL system," in *Proc. Int. Conf. Comput. Appl. Syst. Modeling (ICCASM)*, pp. V11-84–V11-87, 2010, doi:10.1109/ICCASM.2010.5623256.

6. Z. Li, C. Zheng and D. Sun, "Track analysis and design for Ultra Short Baseline installation error calibration," in *Proc. OCEANS*, San Diego, CA, USA, 2013, pp. 1–5, doi:10.23919/OCEANS.2013.6741035.

7. M. Morgado, P. Oliveira, and C. Silvestre, "Tightly coupled ultra-short baseline and inertial navigation system for underwater vehicles: An experimental validation," *J. Field Robot.*, vol. 30, no. 1, pp. 142–170, 2013, doi:10.1002/rob.21442.

8. H.H. Chen, "In-situ alignment calibration of attitude and ultra-short baseline sensors for precision underwater positioning," *Ocean Engineering*, vol. 35, no. 14-15, pp. 1448-1462, 2008, doi:10.1016/j.oceaneng.2008.06.013.

9. Y. Meng, S. Gao, Y. Zhong, H. Gaoge and S. Aleksandar, "Covariance matching based adaptive unscented Kalman filter for direct filtering in INS/GNSS integration," *Acta Astron*, vol. 120, pp. 171–181, 2016, doi:10.1016/j.actaastro.2015.12.014.

10. T. Jinwu, X. Xiaosu, Z. Tao, Z. Liang and L. Yao, "Study on Installation Error Analysis and Calibration of Acoustic Transceiver Array Based on SINS/USBL Integrated System," in *IEEE Access*, vol. 6, pp. 66923-66939, 2018, doi:10.1109/ACCESS.2018.2878756.

POLISH MARITIME RESEARCH 2 (118) 2023 Vol. 30; pp. 130-145
10.2478/pomr-2023-0029

EVALUATION OF GEOMETRICAL INFLUENCE ON THE HYDRODYNAMIC CHARACTERISTICS AND POWER ABSORPTION OF VERTICAL AXISYMMETRIC WAVE ENERGY CONVERTERS IN IRREGULAR WAVES

Wanchao Zhang*
College of Naval Architecture and Ocean Engineering, Jiangsu University of Science and Technology, Zhenjiang, China
Yang Zhu
Jiangsu University of Science and Technology, China
Shuxu Liu
Jiangsu University of Science and Technology, China
Jianhua Wang
The PLA Troops 92228, China
Wentian Zhang
The PLA Troops 92228, China

* Corresponding author: *zhangwanchao@just.edu.cn (Wanchao Zhang)*

ABSTRACT

To obtain the mechanical energy of waves from arbitrary directions, the vibration absorbers of wave energy converters (WEC) are usually vertically axisymmetric. In such case, the wave-body interaction hydrodynamics is an essential research topic to obtain high-efficiency wave energy. In this paper, a semi-analytical method of decomposing the complex axisymmetric boundary into several ring-shaped stepped surfaces based upon the boundary approximation method (BAM) is introduced and examined. The hydrodynamic loads and parameters, such as the wave excitation forces, added mass and radiation damping of the vertical axisymmetric oscillating buoys, can then be achieved by using the new boundary discretisation method. The calculations of the wave forces and hydrodynamic coefficients show good convergence with the number of discretisation increases. Comparison between the constringent results and the results of the conventional method also verifies the feasibility of the method. Then, simulations and comparisons of the hydrodynamic forces, motions and wave power conversions of the buoys with series draught and displacement ratios in regular and irregular waves are conducted. The calculation results show that the geometrical shape has a great effect on the hydrodynamic and wave power conversion performance of the absorber. In regular waves, though the concave buoy has the lowest wave conversion efficiency, it has the largest frequency bandwidth for a given draught ratio, while in irregular waves, for a given draught ratio, the truncated cylindrical buoy has the best wave power conversion, and for a given displacement of the buoy, the concave buoy shows the best wave power conversion ability.

Keywords: Vertical axisymmetric, Ring-shaped stepped surface, Boundary approximation, Constringent, Geometrical shape

INTRODUCTION

Slow-speed ocean waves have now been proved to be a promising renewable resource that can promote the periodic vibration of the floating structure or the periodic compression and release of air, thus converting energy [1]. For this reason, and based on this principle, many wave energy converter (WEC) concepts have been developed for efficient and economic power absorption, such as the point absorber (PA), which utilises the heave mode of the oscillating buoy in waves. At the same time, the wave–body interaction hydrodynamics, as well as the performance analysis of the power take-off (PTO) mechanism, have also been continuously studied to facilitate the design of equipment and achieve the best operation in the considered environment.

The influence of the geometry influence on hydrodynamic characteristics has been evaluated on traditional marine structures to minimise their motion and improve their sea-keeping ability [2]-[3]. In contrast, the same efforts have been made in the case of PAWECs in order to make the absorber oscillate harmoniously in random sea waves, allowing maximum motion amplitudes to absorb more wave power. Many works on improving the wave power conversion efficiency by optimising the geometrical shape or parameters of PAWECs have been conducted in view of the increasing interest in ocean renewable energy [4]-[6]. Mavrakos and Katsaounis [7] explored the effect of the floaters' geometries on the power conversion performance of tightly moored vertical axisymmetric wave energy converters. The absorbers, considering a bottom-mounted vertical or horizontal skirt in the single-body and piston-like arranged WECs, were examined and comparatively assessed. They found that the conical absorber with a vertical skirt, considering the same displacement, has a better power conversion ability as the significant wave height increases. A surge–pitch wave energy converter with bi-cubic B-spline surfaces of parametric description was examined by McCabe et al. [8]. The elementary cost function was used to determine the performance, and the optimal shape of the collector was obtained by using genetic algorithms. They found that the optimal collector shape with the best cost function value overall was asymmetrical, with a bulbous body and 'wings' that slope backwards from the bottom upwards. Similar research on shape optimisation using a genetic algorithm was also conducted later by McCabe [9], considering the constraint regimes defined by the displacement and power rating limits based on wave data from the North-East Atlantic Ocean. Zhang et al. [10] introduced a new hydrodynamic evaluation method for vertical axisymmetric absorbers and explored several cases for the optimisation of wave energy conversion. They found that, among absorbers with the same outer radius and draught, the cylindrical type shows an excellent wave energy conversion ability at certain given frequencies, while in random sea waves, the parabolic and conical ones have better stabilisation and applicability in wave power conversion. Shadman et al. [11] presented a methodology for the geometrical optimisation of wave energy converters based on statistical analysis methods and the hydrodynamics of the system in the frequency domain. They tested this method on an axisymmetric heaving point absorber for a nearshore region of the Rio de Janeiro coast and obtained the optimal geometrical configuration. Esmaeilzadeh and Alam [12] calculated the optimum shape for a submerged planar pressure differential wave energy converter through a systematic method based on high-performance computing and considering different kinds of incident waves. A new parametric description of the absorber shape with Fourier decomposition of geometrical shapes is introduced in their research. Very recently, Erselcan and Kükner [13] conducted a parametric optimisation study to find an optimal design for a heaving point absorber wave energy converter located off the Turkish coast of the Black Sea. The effects of the geometry, mass, and the dimensions of the floats and the parameters of the power take-off system are considered and evaluated.

The above series of optimisation studies are based upon the accurate simulation of the hydrodynamics of wave power harvesting structures. For those oscillating absorbers with a simple configuration, the traditional potential flow algorithm, dividing the encircled fluid domain into several subdomains, can be employed. In such case, the expressions of the velocity potentials, added mass, radiation damping and wave forcing can be analytically presented by using the eigenfunction expansion method as shown in Mavrakos et al. [14] and Bachynski et al. [15]. Thus, the hydrodynamic performance as affected by the geometrical parameters can be systematically described. However, for absorbers with a complex wetted surface, numerical calculation methods (boundary element method, finite element method, etc.) should be used. Based on these methods, many studies have been carried out to improve the wave power conversion performance of the device, though it needs large quantities of grid data and a huge number of calculations. For example, to optimise the absorber's wave power conversion for a targeted location in the Atlantic off the west coast of Ireland, Goggins and Finnegan [16] introduced a methodology considering geometric configuration contrasts with massive hydrodynamic numerical calculations using ANSYS-AQWA. To systematically analyse the effects of the geometric constraints of an oscillating water column wave energy converter for power optimisation in irregular waves, Gomes et al. [17] calculated extensive hydrodynamic data using the BEM-based code WAMIT. Later, Koh et al. [18] conducted a multi-objective optimisation considering the constraints of PTO damping and the production cost of the required sheet plate volume. Because of the requirement for sufficient relevant hydrodynamic data corresponding to the power conversion of geometrical parameter selection, the commercial program ANSYS-AQWA was employed, which resulted in the establishment of a vast amount of grid data and models. Related float configuration optimisation research considering more complex structures and more advanced methods is still ongoing, such as by Garcia-Teruel et al. [19]-[20], Esmaeilzadeh et al. [21], Sergiienko et al. [22], Berenjkoob et al. [23], and Rodríguez et al. [24]. However, the researches on the influence of the PTO damping and

geometrical configurations on the power conversion of the harvesting buoy with heave motion are still not sufficiently thorough and comprehensive.

In this context, a semi-analytical solution, first put forward by Kokkinowrachos et al. [25] and explored further by Zhang et al. [10], was employed for the relatively fast and simple hydrodynamic calculation and systematic wave power conversion evaluation of a vertical axisymmetric absorber with heave motion. The lateral section shapes of the buoy were described by different power series equations, such as half for concave and one for conical. Having divided the fluid domain under the float into coaxial annular fluid domains, a general eigenfunction expansion matching method was then understandably employed. A convergence and accuracy test for the hydrodynamic calculation of a hemisphere was conducted by increasing the number of discretisations. Further, a set of hydrodynamic coefficients and wave excitation forces for the oscillating absorbers with continuous draught ratios were calculated conveniently. Then, the corresponding captured wave power in regular and irregular waves, considering the general and optimised PTO mechanical damping coefficients, was calculated. The effect of the geometrical configuration of the buoys on the wave power conversion was systematically analysed and evaluated, and can be referred to in future work to improve the wave energy conversion performance.

Table 1. Variables and their definitions

Variable	Definition	Variable	Definition
ω	Wave frequency (rad/s)	A	Wave amplitude (m)
$\ddot{O}$	Velocity potential (m²/s)	g	Gravity acceleration (m/s²)
h	Water depth (m)	m	Mass of the floater (kg)
k	Wave number	ρ	Water density (kg/m³)
F_{d3}	Wave force in heave (N)	R	Radius of the floater (m)
μ_{33}	Added mass in heave (kg)	d	Draught of the floater (m)
λ_{33}	Radiated damping in heave (Ns/m)	t	Straight wall height of the floater (m)
k_{33}	Hydrostatic restoring stiffness coefficient (N/m)	η	Wave energy conversion efficiency
RAO_3	Response amplitude operator in heave	c_p	PTO damping coefficient (Ns/m)
$\bar{F}_{d3}$	Non-dimensional wave force in heave	P0	Incident wave power (W)
$\bar{\mu}_{33}$	Non-dimensional added mass in heave	Pa	Average captured wave power (W)
$\bar{\lambda}_{33}$	Non-dimensional radiated damping in heave	ω_p	Peak frequency (rad/s)
$S(\omega)$	Wave spectral density	H_S	Significant wave height (m)

HYDRODYNAMIC FORMULATIONS

The oscillating absorber considered in this study is shown in Fig. 1. We define the cylindrical coordinated system (r,θ,z) by its origin located at the centre of the absorber and on the mean plane of the free surface. The axis *oz* is vertically upward. The wetted surface of the absorber is assumed to comprise a cylindrical surface and a vertical axisymmetric curved surface. The outer radius of the two surfaces is the same and denoted as R. The cylinder height, the whole draught and the water depth are denoted as t, d and h, respectively, in which $0 \le t \le d$. For convenience, the variables and their definitions are displayed in Table 1.

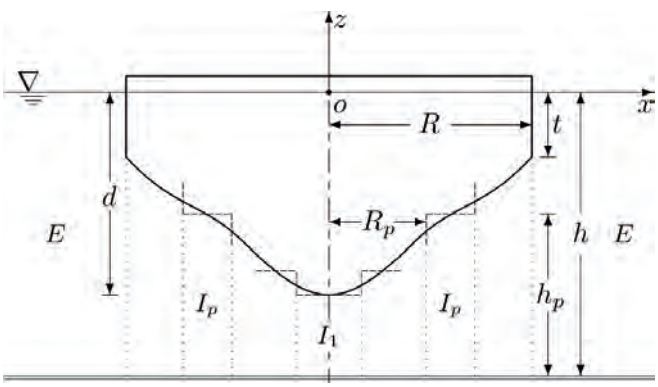

Fig. 1. Definition of fluid subdomains of boundary approximation method

For incompressible and inviscid fluid, and for small amplitude wave theory with irrotational motion, we can introduce a velocity potential $\Psi(r,\theta,z,t)$ to describe the fluid flow. Assuming harmonic motion in frequency domain, for the sake of simplicity, the time variation can be omitted and the velocity potential can be written as

$$\Psi(r,\theta,z,t) = \mathrm{Re}[\Phi(r,\theta,z)e^{-i\omega t}] \tag{1}$$

According to the line plane wave theory, the spatial velocity potential Φ can be decomposed as the undisturbed incident wave velocity potential Φ_0, scattered potential Φ_7 for a fixed body and radiation potential Φ_j(j = 1,3,5) induced by the body motion oscillation in otherwise calm water. The velocity potentials Φ_0 and Φ_7 comprise the diffracted potential Φ_D around the structure with constraints. Then, we have

$$\begin{aligned}\Phi(r,\theta,z) &= \Phi_0(r,\theta,z) + \Phi_7(r,\theta,z) + \sum_{j=1}^{6} -i\omega\xi_j\Phi_j(r,\theta,z)\\ \Phi_D(r,\theta,z) &= \Phi_0(r,\theta,z) + \Phi_7(r,\theta,z)\end{aligned} \tag{2}$$

where ξ_j (j = 1-6) is the j-th mode motion amplitude and only $j = 3$ for heave is considered in this paper. The aforementioned velocity potentials should satisfy the
Laplace equation:

$$\nabla^2\Phi = 0 \tag{3}$$

free surface condition:

$$\omega^2\Phi - g\partial_z\Phi = 0 \quad z = 0, r \geq R \tag{4}$$

seabed condition:

$$\partial_z\Phi = 0 \quad z = -h \tag{5}$$

hull boundary condition:

$$\partial_n\Phi_3 = V_n, \quad \partial_n(\Phi_0 + \Phi_7) = 0 \tag{6}$$

radiation condition:

$$\lim_{r\to\infty}\sqrt{kr}(\partial_r\Phi - ik\Phi) = 0 \tag{7}$$

where i is an imaginary unit and k is the wave number, which comes from the dispersion relation, and the symbol $\partial_n()$ indicates the derivative in the normal vector pointing always outwards from the wetted surface of the device.

ADDED MASS, RADIATION DAMPING AND WAVE FORCING

Assuming that an undisturbed incident sinusoidal wave with amplitude A and frequency w propagates along the positive x-axis direction, this can be expressed in cylindrical coordinates as

$$\begin{aligned}\Phi_0(r,\theta,z) &= \frac{Ag}{i\omega}\sum_{l=0}^{\infty}\varphi_{0\ell}(r,z)\cos\ell\theta \quad \text{with} \quad \varphi_{0\ell}(r,z) =\\ &= \varepsilon_\ell i^\ell \mathbf{J}_\ell(kr)\cosh k(z+h)/\cosh kh\end{aligned} \tag{8}$$

where $J_\ell(\cdot)$ is the Bessel function of the first kind, of order $\ell(\ell = 0,1,2,\cdots)$ and ε_ℓ is the Neumann symbol, defined by $\varepsilon_0 = 1$ and $\varepsilon_\ell = 2$ for $\ell \geq 1$. In accordance with , the velocity potential of the diffraction potential field caused by the fixed device can be written in the form

$$\Phi_7(r,\theta,z) = \frac{Ag}{i\omega}\sum_{\ell=0}^{\infty}\varepsilon_\ell i^\ell\varphi_{7\ell}(r,z)\cos\ell\theta \tag{9}$$

In the unbounded fluid domain with finite water depth, the radiation velocity potential caused by the forced oscillated vertical axisymmetric body in heave can be expressed as

$$\Phi_3(r,\theta,z) = \varphi_{3\ell}(r,z) \text{ with } \ell = 0 \tag{10}$$

The newly introduced velocity potential expressions $\varphi_{D\ell}$ and $\varphi_{3\ell}$ should also satisfy the former boundary conditions, and their solution will be the key problem in the hydrodynamic analysis of the oscillating buoy. To obtain the hydrodynamic characteristics of the absorbers, the velocity potentials around the vertical axisymmetric body should be confirmed. Before decomposing the Laplace equation with the method of separation of variables, we should first divide the fluid domain around the device into several subdomains. For the complex axisymmetric wetted surface, we decompose it into ring-shaped stepped surfaces by dividing the projection curve on the vertical plane averagely. Thus, the velocity potentials in each domain can be expressed in the form of Fourier series.

(a) Velocity potential in domain $E\,(r \geq R, -h \leq z \leq 0)$

$$\begin{aligned}\varphi_{j\ell}^E(r,z) &= \alpha_{j\ell 0}^E\Gamma_0(z)\mathbf{H}_\ell(k_0r)/\mathbf{H}'_\ell(k_0R) +\\ &+ \sum_{n=1}^{\infty}\alpha_{j\ell n}^E\Gamma_n(z)\mathbf{K}_\ell(k_nr)/\mathbf{K}'_\ell(k_nR) + \Re_{j\ell}^E(r,z)\end{aligned} \tag{11}$$

with $j = 3,7$, and $\mathbf{H}_\ell(\cdot)$ and $\mathbf{K}_\ell(\cdot)$ are the Hankel function of the first kind and the modified Bessel function of the second kind of order ℓ separately. Here and hereafter, a prime denotes taking the differentiation of a function with respect to its argument. The wave numbers k_0, $k_n(n = 1,2,3\cdots)$ are defined by $\omega^2 = gk_0\tanh k_0h = -gk_n\tan k_nh$. The function expressions $\tilde{A}(\cdot)$ and $\Re(\cdot)$ are given as

$$\Gamma_0(z)=\cos k_0h\cosh k_0(z+h)/[2k_0h+\sinh 2k_0h]\quad \Gamma_n(z)=[\cos k_n(z+h)]/[2k_nh+\sin 2k_nh]$$
$$\Re_{30}^{E}(r,z)=0\quad \Re_{D\ell}^{E}(r,z)=[\cosh k_0(z+h)]/\cosh k_0h\,\varepsilon_\ell i^\ell \mathbf{J}_\ell(k_0r) \tag{12}$$

(b) Velocity potential in domain $I_1\ (0\le r\le R_1,-h\le z\le h_1-h)$ and $I_p\ (2\le p\le N, R_{p-1}\le r\le R_p,-h\le z\le h_p-h)$

$$\varphi_{j\ell}^{I_1}(r,z)=\alpha_{j\ell 0}^{I_1}G_{j\ell}^{I_1}(r)+\sum_{n=1}^{\infty}[\alpha_{j\ell n}^{I_1}\mathbf{I}_\ell(\lambda_{n1}r)/\mathbf{I}_\ell(\lambda_{n1}R_1)\cos\lambda_{n1}(z+h)]+\Re_{j\ell}^{I_1}(r,z) \tag{13}$$

$$\begin{aligned}\varphi_{j\ell}^{I_p}(r,z)=&\alpha_{j\ell 0}^{I_p}G_{j\ell}^{I_p}(r)+\sum_{n=1}^{\infty}\alpha_{j\ell n}^{I_p}Q_{n\ell}^{I_p}(r)\cos\lambda_{np}(z+h)+\tilde{\alpha}_{j\ell 0}^{I_p}\tilde{G}_{j\ell}^{I_p}(r)+\\&+\sum_{n_p=1}^{\infty}\tilde{\alpha}_{j\ell n}^{I_p}\tilde{Q}_{n\ell}^{I_p}(r)\cos\lambda_{np}(z+h)+\Re_{j\ell}^{I_p}(r,z)\end{aligned} \tag{14}$$

In the eigenfunction expansions for the velocity potentials, similarly, the unknown function expressions of λ, $G(\cdot)$, $Q(\cdot)$ and $\Re(\cdot)$ are given as

$$\begin{aligned}&\Re_{D\ell}^{I_p}(r,z)=0,\ \Re_{30}^{I_p}(r,z)=[2(z+h)^2-r^2]/(4h_p)\\&\lambda_{np}=n\pi/h_p,\ G_{D\ell}^{I_1}(r)=(r/R_1)^\ell,\ G_{30}^{I_1}(r)=1\\&G_{j\ell}^{I_p}(r)=\begin{cases}\ln(r/R_{p-1})/\ln(R_p/R_{p-1})\\[(r/R_{p-1})^\ell-(R_{p-1}/r)^\ell]/(R_p/R_{p-1})^\ell-(R_{p-1}/R_p)^\ell\end{cases}\quad p\ge 2\\&\tilde{G}_{j\ell}^{I_p}(r)=\begin{cases}\ln(R_p/r)/\ln(R_p/R_{p-1})\\[(R_p/r)^\ell-(r/R_p)^\ell]/[(R_p/R_{p-1})^\ell-(R_{p-1}/R_p)^\ell]\end{cases}\quad p\ge 2\\&Q_{n\ell}^{I_p}(r)=[\mathbf{K}_\ell(\lambda_{np}R_{p-1})\mathbf{I}_\ell(\lambda_{np}r)-\mathbf{K}_\ell(\lambda_{np}r)\mathbf{I}_\ell(\lambda_{np}R_{p-1})]/\mathbf{\Pi}_{p\ell n}\quad p\ge 2\\&\tilde{Q}_{n\ell}^{I_p}(r)=[\mathbf{K}_\ell(\lambda_{np}r)\mathbf{I}_\ell(\lambda_{np}R_p)-\mathbf{K}_\ell(\lambda_{np}R_p)\mathbf{I}_\ell(\lambda_{np}r)]/\mathbf{\Pi}_{p\ell n}\quad p\ge 2\\&\mathbf{\Pi}_{p\ell n}=\mathbf{K}_\ell(\lambda_{np}R_{p-1})\mathbf{I}_\ell(\lambda_{np}R_p)-\mathbf{K}_\ell(\lambda_{np}R_p)\mathbf{I}_\ell(\lambda_{np}R_{p-1})\quad p\ge 2\end{aligned} \tag{15}$$

The sets of unknown Fourier coefficients *a* are determined by taking advantage of orthogonality, in the so-called Garrett method, according to matching of the potentials and its normal derivative on the juncture boundaries surface shared by the subdomains. For the detailed matching procedure, the reader can refer to Zhang et al. [10]. Considering the heave motion applied in the wave energy conversion, the wave forcing and radiation damping coefficients in heave need to be obtained. Thus, by defining $R_0=0$, the non-dimensional wave excitation forces and hydrodynamic coefficients of the absorber in heave can be calculated and defined by

$$\begin{aligned}\bar{F}_{d3}=&\frac{F_{d3}}{\rho gAR^2}=-\frac{i2\pi}{R^2}\sum_{p=1}^{N}\int_{R_{p-1}}^{R_p}\varphi_{30}^{I_p}(r,h_p-h)rdr\\=&-i\pi\alpha_{700}^{I_1}-\pi\sum_{n=1}^{\infty}\alpha_{70n}^{I_1}\frac{(-1)^n}{\lambda_{n1}R^2}\frac{\mathbf{I}_0(k_0r)}{\mathbf{I}_0'(k_0R)}\\&-\frac{i2\pi}{R^2}\sum_{p=2}^{N}\left\{\alpha_{700}^{I_p}[1-\frac{R_p^2-R_{p-1}^2}{2R_p^2\ln(R_p/R_{p-1})}]+\sum_{n=1}^{\infty}\alpha_{70n}^{I_p}(-1)^n\frac{R_pQ_{n0}^{I_p}(R_{p-1})}{\lambda_{np}}\right\}\\&-\frac{i2\pi}{R^2}\sum_{p=2}^{N}\left\{\tilde{\alpha}_{700}^{I_p}[\frac{R_{p-1}^2}{R_p^2}-\frac{R_p^2-R_{p-1}^2}{2R_p^2\ln(R_p/R_{p-1})}]+\sum_{n=1}^{\infty}\tilde{\alpha}_{70n}^{I_p}(-1)^n\frac{R_p\tilde{Q}_{n0}^{I_p}(R_{p-1})}{\lambda_{np}}\right\}\end{aligned} \tag{16}$$

$$\begin{aligned}\bar{\mu}_{33}+i\bar{\lambda}_{33}=&\frac{\mu_{33}}{\rho R^3}+i\frac{\lambda_{33}}{\rho\omega R^3}=-\frac{i2\pi d}{R^3}\sum_{p=1}^{N}\int_{R_{p-1}}^{R_p}\varphi_{30}^{I_p}(r,h_p-h)rdr\\=&-\frac{i\pi d}{R}\alpha_{300}^{I_1}-\frac{\pi d}{R}\sum_{n=1}^{\infty}\alpha_{30n}^{I_1}\frac{(-1)^n}{\lambda_nR_1^2}\frac{\mathbf{I}_0(k_0r)}{\mathbf{I}_0'(k_0R)}\\&-\frac{i2\pi d}{R^3}\sum_{p=2}^{N}\left\{\alpha_{300}^{I_p}[1-\frac{R_p^2-R_{p-1}^2}{2R_p^2\ln(R_p/R_{p-1})}]+\sum_{n=1}^{\infty}\alpha_{30n}^{I_p}(-1)^n\frac{R_pQ_{n0}^{I_p}(R_{p-1})}{\lambda_{np}}\right\}\\&-\frac{i2\pi d}{R^3}\sum_{p=2}^{N}\left\{\tilde{\alpha}_{3}^{I_p,0}[\frac{R_{p-1}^2}{R_p^2}-\frac{R_p^2-R_{p-1}^2}{2R_p^2\ln(R_p/R_{p-1})}]+\sum_{n=1}^{\infty}\tilde{\alpha}_{30n}^{I_p}(-1)^n\frac{R_p\tilde{Q}_{n0}^{I_p}(R_{p-1})}{\lambda_{np}}\right\}\end{aligned} \tag{17}$$

WAVE ENERGY CONVERSION

Having obtained the hydrodynamic parameters and wave-excited forces, the wave energy conversion ability of the buoys can be further investigated. The power take-off (PTO) mechanism assembled between the absorber and the solid platform or seabed is composed of a linear damper, which can be activated to output electric energy under the absorber's heave reciprocating motion [26]. In such case, the motion of the buoy with the PTO mechanism in waves can be expressed as

$$(m+\mu_{33})\ddot{z}+(\lambda_{33}+c_p)\dot{z}+k_{33}z=f_{d3} \tag{18}$$

where c_p denotes the damper's damping coefficient, which can be regulated, k_{33} is the hydrostatic restoring stiffness coefficient and is expressed as ρgS, with water density ρ, gravity acceleration *g* and waterline area *S*. The variables $\ddot{z}$, $\dot{z}$, z and f_{d3} contain the common time factor $e^{i\omega t}$, which can be unified as $\phi=\Phi e^{-\omega t}$. By separating the time factor from these variables into the frequency domain, the response amplitude operator (RAO) of the buoy in heave can be obtained and given as

$$RAO_3=\frac{Z}{A}=\frac{F_{d3}}{-\omega^2(m+\mu_{33})+i\omega(\lambda_{33}+c_p)+k_{33}} \tag{19}$$

In this paper, the wave-excited motion amplitude *A* here is unit, so the calculated RAO will also be the motion amplitude. According to Falnes [28], for an oscillating-buoy wave energy converter, the captured wave energy with a linear PTO mechanism can be defined as

$$P_a=\int_{\Delta t}^{T+\Delta t}c_p\dot{z}\cdot\dot{z}dt=\frac{1}{2}c_p\omega^2Z^2 \tag{20}$$

Therefore, the optimal PTO damping coefficient can be obtained by solving the extreme value problem of the power expression about the damping coefficient. Then, we have the optimal expression of the damping coefficient:

$$c_{p,opt}=[\lambda_{33}^2+(\omega m+\omega\mu_{33}-\frac{k_{33}}{\omega})^2]^{1/2} \tag{21}$$

To better understand the wave conversion ability of the buoy with different geometries, we define the capture width ratio η to describe the wave energy conversion efficiency, expressed as

$$\eta = P_a / P_0 \tag{22}$$

with the incident wave power defined as

$$P_0 = \rho g B \omega A / (4k_0) \cdot (1 + 2k_0 h / \sinh 2k_0 h) \tag{23}$$

where B denotes the heave wave width of the buoy and is defined as twice the radius of the buoy in this paper. k_0 is the zero order wave number for a given wave frequency ω.

NUMERICAL RESULTS

CONVERGENCE AND VERIFICATION

The numerical work in this section is involved in the choice of the number of terms used in the infinite simulations. The former 30 terms of the unknown Fourier coefficients are adopted in the infinite summations to compute the numerical results because the infinite summations have excellent truncation characteristics, as depicted in Yeung [29]. A quintessential hemisphere with radius $R=5m$ and draught $5\,\mathrm{m}$ in the water depth of $h = 50\,\mathrm{m}$ with different incident wave frequencies is adopted here to verify the feasibility and validity of this semi-analytical solution.

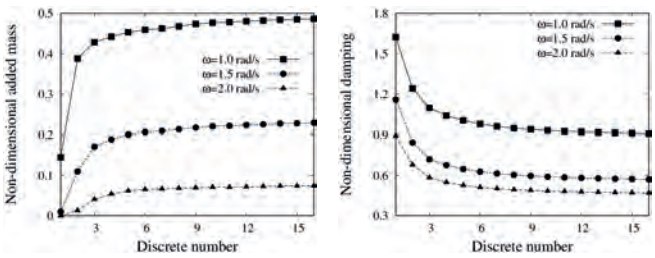

Fig. 2. Non-dimensional hydrodynamic calculation results with different incident wave frequencies for a hemisphere

The examinations on the convergence of the wave forces and hydrodynamic coefficients of the above-mentioned hemisphere in the presence of regular waves of different frequencies in a water depth of $h = 50\,\mathrm{m}$ are shown in Fig. 2. It can be concluded that convergent results can be achieved when the number of discretization reaches 15.

The analytical solution method based upon the multipole theory for a hemisphere has been developed by Hulme [30]. In such case, the correctness of the present semi-analytical method can be verified by calculating the hydrodynamic parameters of the above-mentioned absorber with these two methods. Comparisons of the wave excitation forces and hydrodynamic coefficients of the absorber in heave in Table 2 show good agreement, which can be regarded as validation of the present method.

Tab. 2. Verification of the solution method

Frequency (rad/s)	1.0		1.5		2.0	
Method	Present	Analytical	Present	Analytical	Present	Analytical
$F_{d3}/(\rho g A R^2)$	0.9925	0.9895	0.3736	0.3745	0.1388	0.1367
$\mu_{33}/(\rho R^3)$	0.488	0.4903	0.2311	0.2297	0.0756	0.0763
$\lambda_{33}/(\rho R^3 \omega)$	0.9058	0.9042	0.5676	0.5667	0.4668	0.4701
Maximum error (%)	0.47		0.61		1.54	

HYDRODYNAMIC PERFORMANCE

Based upon the above verified hydrodynamic calculation method, the hydrodynamic characteristics of the vertical axisymmetric absorbers can be analysed. In such case, four kinds of vertical axisymmetric absorbers are considered for evaluation of the influence of the geometry on the hydrodynamic characteristics and wave energy conversion performance. The complex wetted surface of the absorber comprises a vertical cylindrical surface and a vertical axisymmetric curved surface. The geometrical parameters and lateral views of the absorbers are shown in Fig. 3. They are concave, conical, parabolic and ellipsoidal surfaces, and we define them in turn as cases 1–4, respectively. The curves in the semi-section lateral views in the dashed frames are described with curvilinear equations in their local coordinate systems as

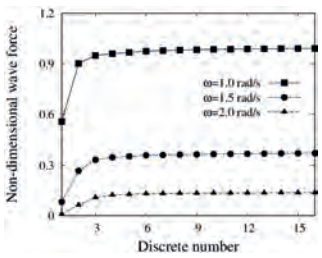

$$\begin{aligned}
&\text{Case } 1 \rightarrow z/(d-t) = \sqrt{x/R} \\
&\text{Case } 2 \rightarrow z/(d-t) = x/R \\
&\text{Case } 3 \rightarrow z/(d-t) = (x/R)^2 \\
&\text{Case } 4 \rightarrow z/(d-t) = 1 - \sqrt{1-(x/R)^2}
\end{aligned} \tag{24}$$

in which $0 \le x \le R$, $0 \le t < d$, and, to describe the absorber's geometrical characteristics more conveniently, we define the draught ratio $(d-t)/d$ as $d_r (0 \le d_r \le 1)$. When the draught ratio equals 0, the absorbers will be vertical truncated cylinders. In addition, the buoys are defined as concave, conical, paraboloid and ellipsoid buoys in turn.

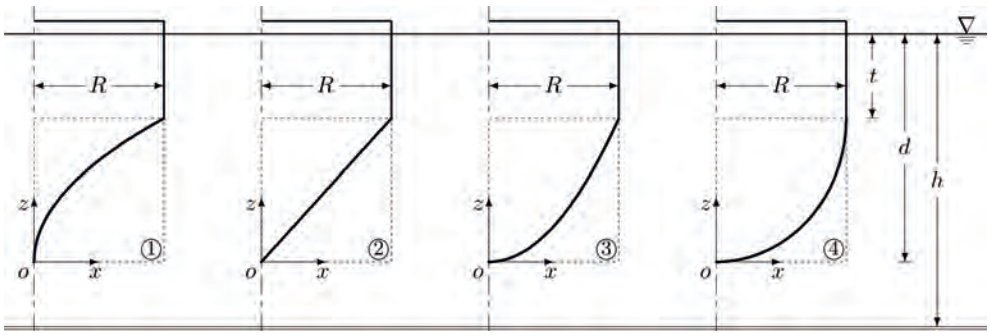

Fig. 3. Geometrical parameters description and semi-section lateral views of the considered absorbers

In this paper, we define the four types of buoys with the same outer radius $R = 5$ m and draught $d = 6$ m, in water with depth $h = 50$ m, to estimate the hydrodynamic and wave power conversion performance impartially. The response amplitude operators of the buoys in heave motion with free vibration, considering consecutive incident wave frequencies and draught ratios, are given in Fig. 4. It can be clearly seen that the motion RAOs in heave for the chosen absorbers have nearly identical trends to the incident wave frequencies and draught ratios. For a given draught ratio, there will be a peak value of the RAO with the increase of wave frequencies. However, in the range of the draught ratios, the concave type buoy shows a relatively high-frequency bandwidth, and when the draught ratio reaches 0.8, the resonance characteristics are not so obvious. In such case, the motion characteristics, as well as their formation mechanism at higher draught ratios, take on added importance. For a better understanding, the heave RAO and hydrodynamic parameters are also described with the given draught ratio equal to 0.8 and 1.0 for the four kinds of buoys.

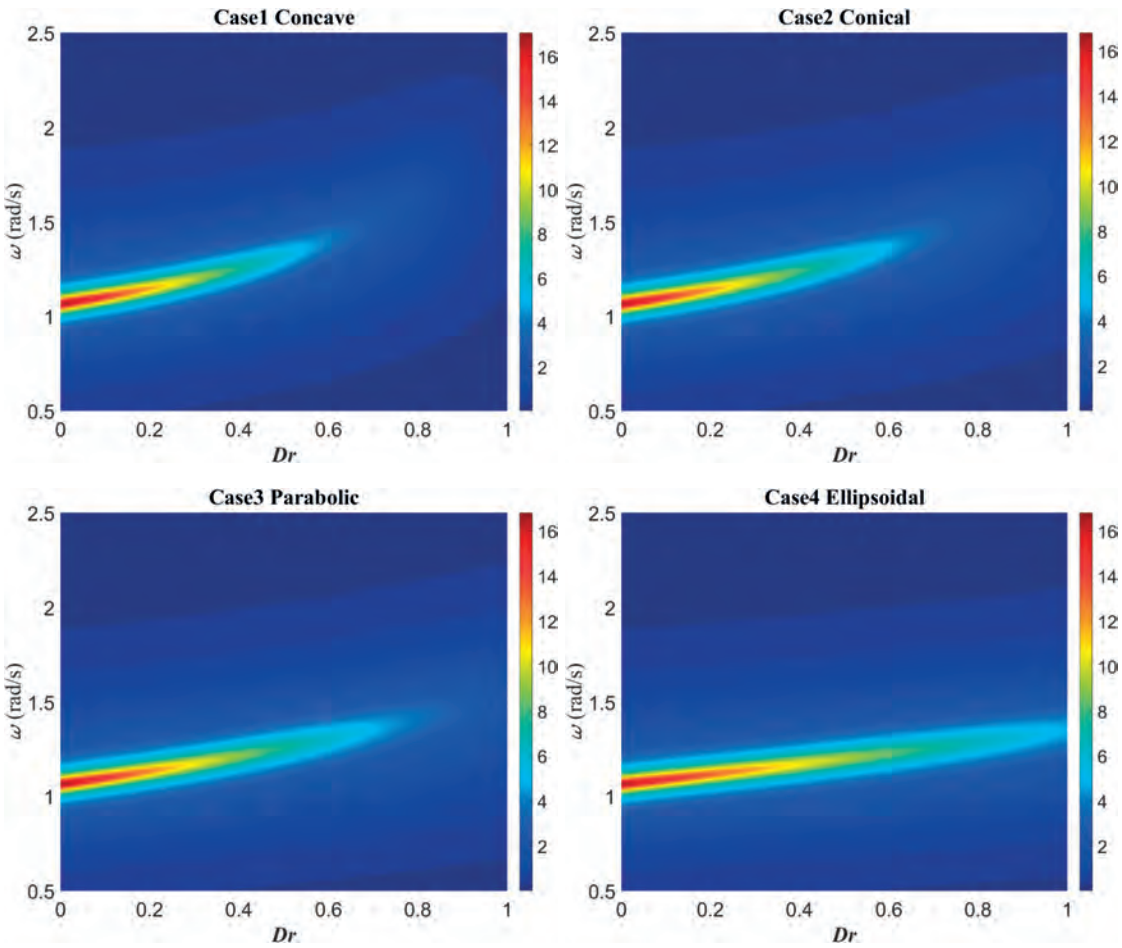

Fig. 4. Heave RAOs of the absorbers with free vibration

As shown in Fig. 5, the heave RAOs of the concave and conical buoys have no obvious peak characteristics, as well as corresponding wave-excited forces. With the increase of the draught ratio, the vertical component of the velocity potential gradient at the bottom of the float decreases, and the resulting heave excitation force also decreases. However, the radiated velocity potential comes from the forced motion of the buoys in quiescent water. The non-planar bottom caused by the draught ratio increases the external energy transfer of the radiation wave. Thus, the radiated wave forces increase along with the increase of the draught ratio. These two reasons cause the motion response of the buoys to slow down.

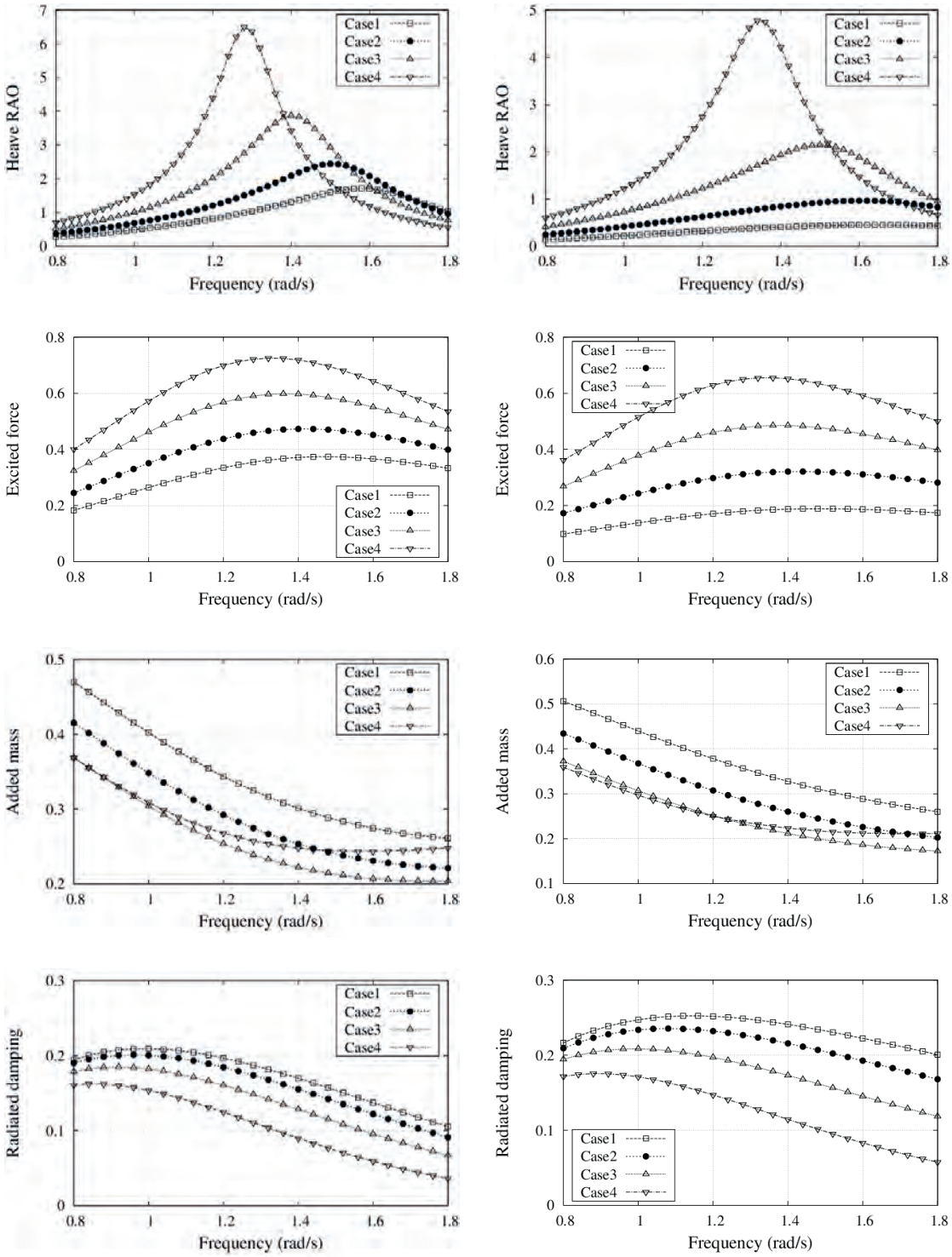

Fig. 5. Motion RAOs, excited forces, added mass and radiated damping of the absorbers in heave with dr equal to 0.8 (left) and 1.0 (right)

In addition, the motion response and hydrodynamic parameters of the floating buoys at their natural frequencies have also changed greatly. The natural frequencies of the buoys with different draught ratios are described in Table 3. Compared with the truncated cylinder, the natural frequencies of the four types of buoys are increased, and with the increase of the draught ratio, the range of increase is more obvious. In fact, this phenomenon can be explained by the wave excitation force and hydrodynamic parameters of the buoys at the natural frequency depicted in the following Fig. 6.

Tab. 3 Natural frequencies of the absorbers with free vibration

Case No.	Draught ratio					
	0.0	0.2	0.4	0.6	0.8	1.0
1	1.06	1.15	1.25	1.40	1.59	1.62
2	1.06	1.14	1.24	1.36	1.51	1.61
3	1.06	1.13	1.21	1.30	1.41	1.50
4	1.06	1.12	1.17	1.23	1.29	1.35

The natural frequencies of the free oscillating buoys are mainly decided by the generalised mass m, the stiffness coefficient k in heave and the damping coefficient c, which can be expressed as $\omega_n = \sqrt{k/m - (c/2m)^2}$. Since the four types of buoys have the same radius, the stiffness coefficient is the same. The depicted hydrodynamic parameters of the buoys with different draught ratios have little difference. The added mass of the conical and parabolic buoys even alternates. Therefore, the concave buoy with the minimum displacement has the maximum natural frequency. The motion response and wave-excited forces of the buoys at their natural frequencies are also given in Fig. 7. Both of them decrease with the increase of draught ratios. However, the motion response decreases rapidly and then flattens out, while the wave excitation force is the opposite, flattening out and then decreasing rapidly.

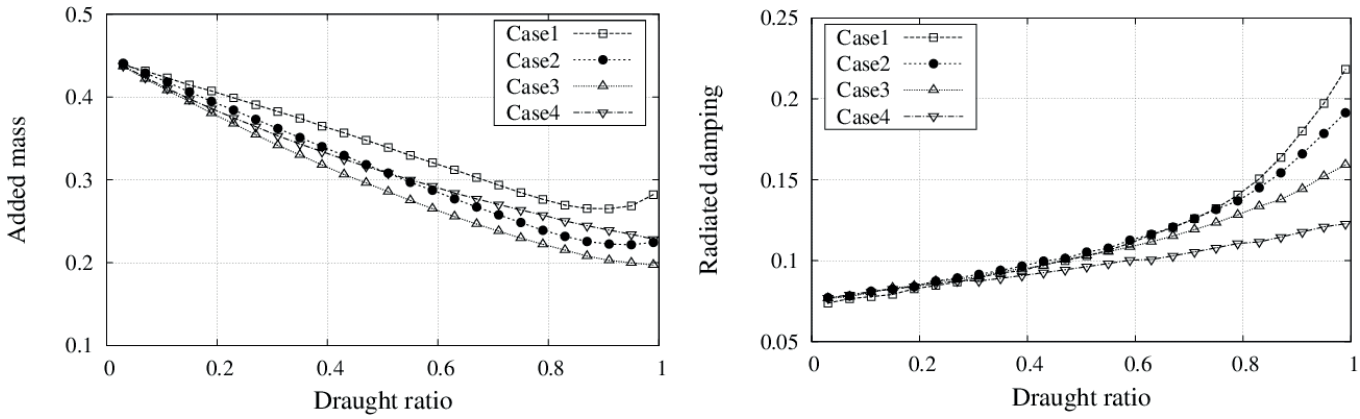

Fig. 6. Added mass and radiated damping in heave at natural frequencies of the free vibration absorbers

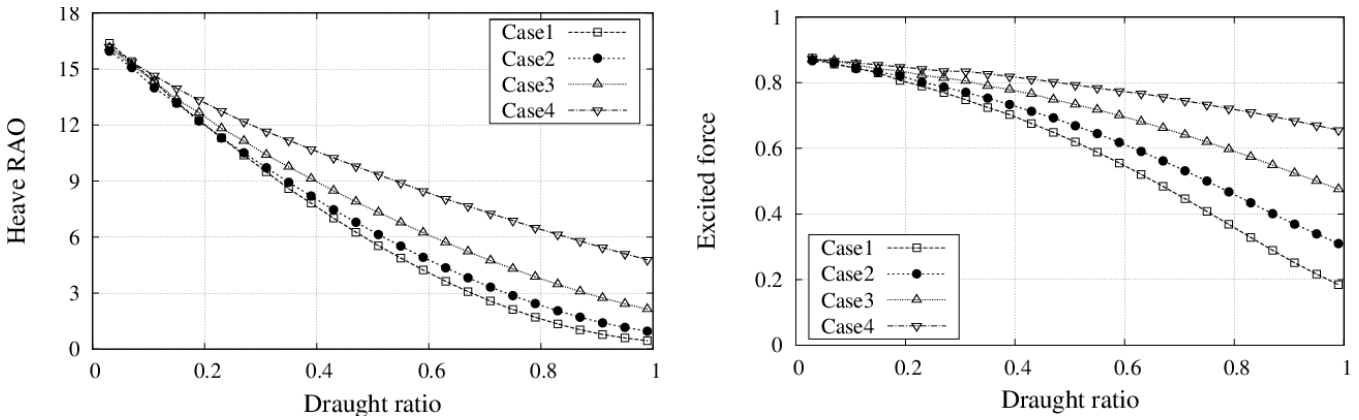

Fig. 7. Heave RAOs and excited forces at natural frequencies of the free vibration absorbers

WAVE ENERGY CONVERSION IN REGULAR WAVES

This section deals with the wave energy conversion ability of the four kinds of absorbers considered, based on the formal hydrodynamic parameters obtained. As has been mentioned before, the shape geometries of the buoys are the main factors in exploring the wave conversion characteristics. We therefore explore their effects on the natural frequencies of the buoys, which are partly decided by the viscous damping. In addition, the wave energy conversion of the buoy shows the optimal ability at the resonance frequency referring to Zhang et al. [10]. As shown in Fig. 8, the wave energy conversion efficiency of the chosen buoys with different draught ratios and PTO damping coefficients at their natural frequencies is explored and presented. For a given draught ratio, there will be a peak value of the capture width ratio with the increasing PTO damping coefficients. However, the increase of the draught ratios makes the peak value most outstanding for the ellipsoidal buoy.

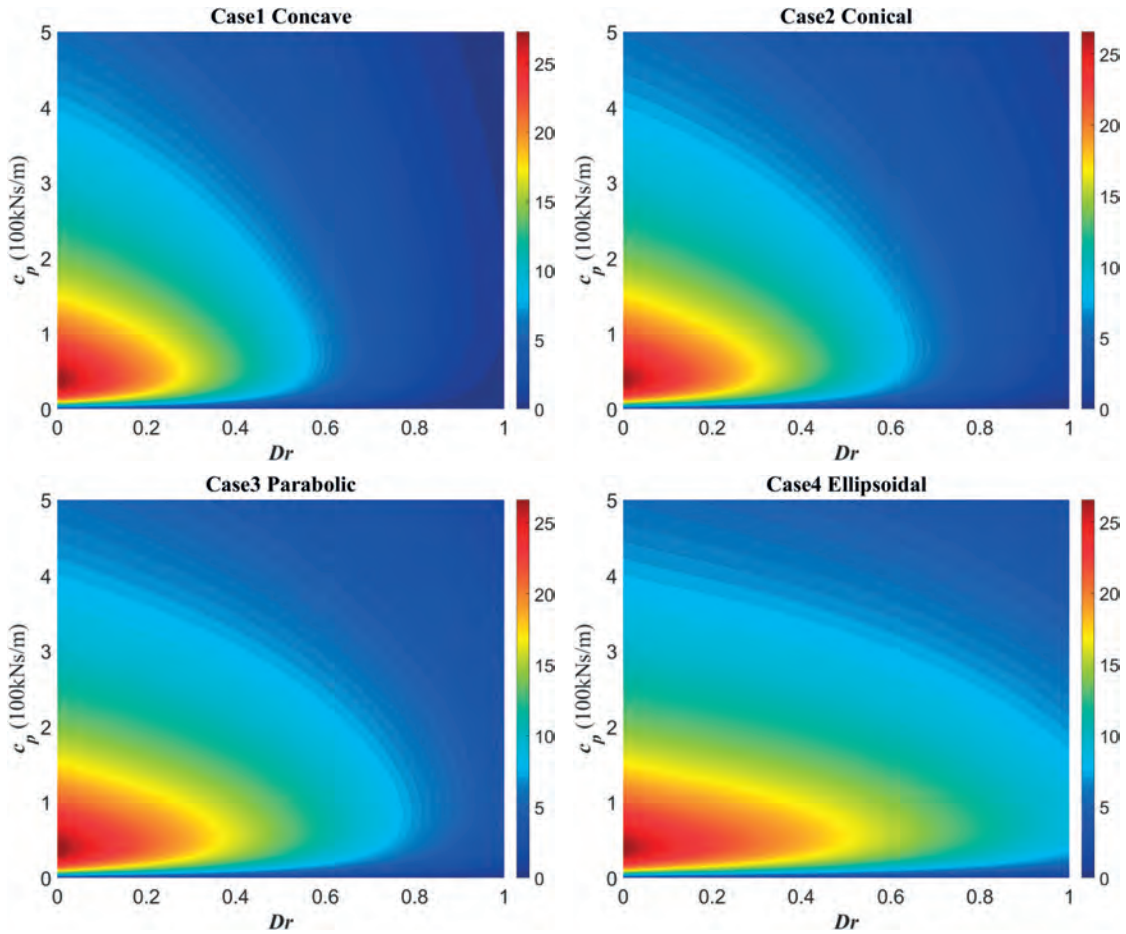

Fig. 8. Capture width ratios of the damped vibration absorbers at resonance frequencies

Of all the shapes and draught ratios, the truncated cylinder seems to have the best wave conversion ability though it may also have the narrowest frequency bandwidth. In such case, the wave energy conversion efficiency only reflects these absorbers' potential to convert waves at the resonance frequency. The conversion abilities in the whole incident wave frequency range, as well as the bandwidths of the buoys, need to be explored. For the convenience of research and description, we assume that the PTO mechanisms in this paper are adjustable and that the optimal state can be realised. Thus, the motion responses and wave capture efficiencies of the buoys with any given incident wave frequencies can be easily obtained and are depicted in the following Fig. 9.

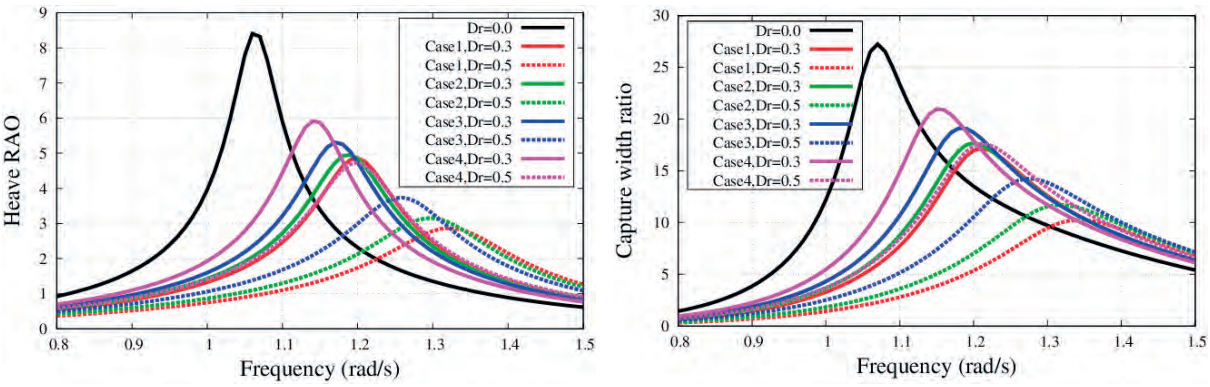

Fig. 9. Heave RAOs and capture width ratios of the damped vibration absorbers with optimal PTO damping coefficients

As shown in Fig. 9, the trend consistency between the motion response and wave power capture means that both the heave RAO and the capture width ratios for the considered shape geometries reach the optimal results at the natural frequencies. The increased draught ratios of the buoys not only decrease the optimal motion response and capture width ratio, but also increase the natural frequencies of the buoys. Though the truncated cylinder shows the best wave energy capture capability at natural frequency, its disadvantage in frequency bandwidth is also exposed. Here, the frequency bandwidth ω_{bf} is defined as the frequency range where the capture width ratios are more than half of the peak value.

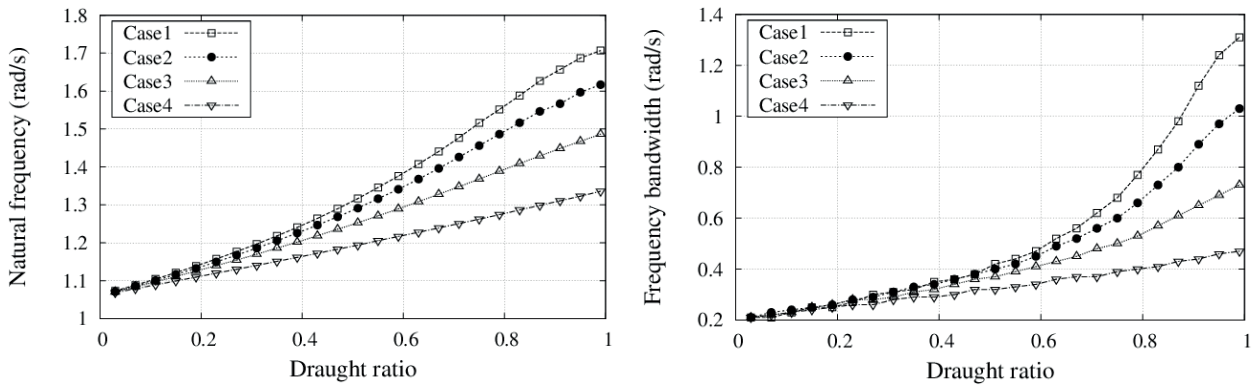

Fig. 10. Natural frequencies and frequency bandwidths of the damped vibration absorbers with optimal PTO damping coefficients

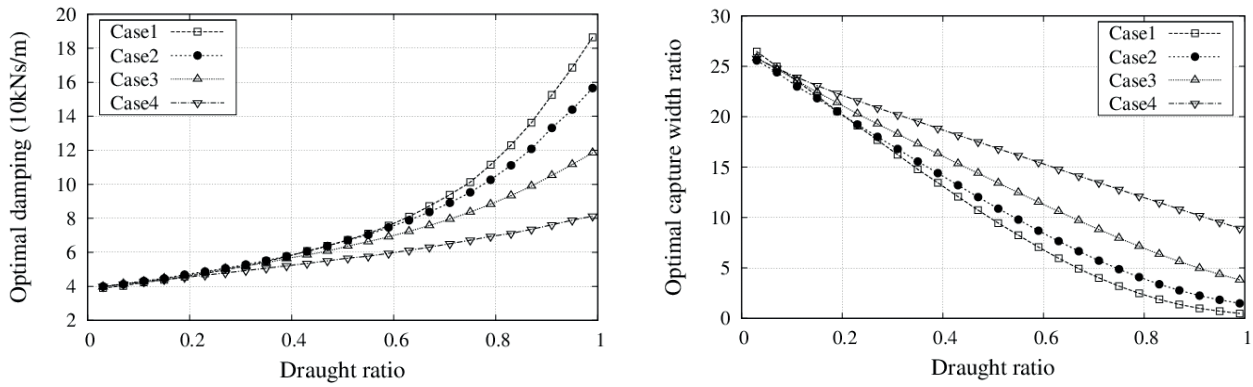

Fig. 11. Optimal PTO damping coefficients and capture width ratios of the damped vibration absorbers at natural frequencies

The natural frequencies and frequency bandwidth of the buoys with optimal PTO damping coefficients are shown in Fig. 10. It can be clearly observed that the increased draught ratio can increase the natural frequency effectively for a given shape of buoy. This conclusion can effectively improve the applicability of a buoy or beacon light to different sea areas. In addition, the concave buoy has the maximal natural frequency for a given draught ratio because of its decreased displacement. Though the concave buoy has the lowest wave conversion efficiency, it has the largest frequency bandwidth for a given draught, especially when the draught ratio is close to one. It is noteworthy that the natural frequencies and bandwidth are almost linear to the draught ratio, which is also presented in the optimal PTO damping coefficients and capture width ratios of the ellipsoidal buoy shown in Fig. 11. Special attention should also be given to the PTO mechanism, that the optimal damping coefficients and the relative optimal wave conversion efficiencies represent an obvious inverse correlation. In addition, a similar phenomenon also occurs between the frequency bandwidth and wave energy conversion efficiency.

To further explore the effect of the geometry and shape on the wave power conversion ability and eliminate the influence of the drainage volume difference at the same time, buoys with the same displacement are considered and the ellipsoidal buoy with a draught ratio equal to 1 is regarded as the reference criterion for displacement. In such case, the draught ratios of the concave, conical and parabolic buoys will be 0.417, 0.5 and 0.667, respectively. The calculation results of the buoys with the same displacement are given in Table 4. It can be observed that the natural frequencies of the forced vibrated buoys with optimal PTO damping coefficients have only a small difference. It should be stressed that, for the given four kinds of absorber, there is a perfect inverse correlation between the frequency bandwidth and the capture width ratios. This means that, though the shapes of the buoys are different, when their radius, draught and displacement are identical, the adaptabilities of their wave transformation have similar advantages. Certainly, this conclusion comes from the adjustability assumption of the optimal PTO damping coefficients for any given wave frequency. To further evaluate their wave conversion abilities, the irregular wave condition should be considered.

Tab. 4. Resonance and wave energy conversion characteristics of the buoys with same displacement

Case No.	Draught ratio	Natural frequency (rad/s)	Bandwidth (rad/s)	Optimal damping (10 kNs/m)	Optimal capture width ratio
1	0.417	1.258	0.36	5.960	12.413
2	0.500	1.286	0.40	6.587	11.196
3	0.667	1.328	0.45	7.575	9.702
4	1.000	1.339	0.48	8.211	8.786

WAVE ENERGY CONVERSION IN IRREGULAR WAVES

The above overall numerical results come from the assumption that the PTO damping can be adjusted to the optimal condition for a given incident wave frequency. However, in the real sea environment, a wave farm is complex and the frequencies are not isolated. In such case, the wave energy conversion abilities of buoys with manifold geometries and shapes should be further explored and evaluated. In this work, the JONSWAP spectrum [31] is selected to describe the incident wave spectrum and defined as

$$S(\omega)=\frac{\alpha g^2}{\omega^5}\exp\left\{-1.25(\omega_p/\omega)^4\right\}\cdot\gamma^{\exp\left\{-0.5(\omega-\omega_p/\sigma\omega_p)^2\right\}} \tag{25}$$

with

$$\begin{aligned}&\alpha=5.061(\frac{\omega_p}{2\pi})^4 H_s^2(1-0.287\log\gamma)\\&\sigma=0.07\quad\omega<\omega_p\\&\sigma=0.09\quad\omega\geq\omega_p\end{aligned} \tag{26}$$

where ω_p and H_s are the peak frequency and significant wave height, respectively. The peak elevation parameter γ is constant and typically given as 3.3 [26], whereas ω is the general incident wave frequency. As the axial-symmetric floater is not sensitive to the wave direction, the directional spectrum is not introduced here. According to the above wave absorption function , the converted wave power for the buoy in irregular waves can be obtained and expressed as

$$P_{am}=\int_0^{+\infty}c_p\omega^2\left|RAO(\omega)\right|^2 S(\omega)d\omega \tag{27}$$

Similarly, the inserted wave power for irregular waves can also be obtained according to function and given as

$$\begin{aligned}&P_{0m}=\int_0^{+\infty}\rho gBS(\omega)V(\omega)d\omega\\&V(\omega)=\omega/(4k_0)\cdot(1+2k_0h/\sinh 2k_0h)\end{aligned} \tag{28}$$

Then, the capture width ratio η_m of the buoy in irregular waves can be given as

$$_m\quad P_{am}/P_m \tag{29}$$

In such case, the optimal PTO damping and corresponding optimal capture width ratios can also be obtained by setting the partial derivative of the capture width ratio to the damping as zero. However, the motion RAOs of the buoys are also the implicit equations about the PTO damping coefficients. In such case, in this paper, the golden section search method [27] is employed to search for the optimal PTO damping coefficients for given peak frequencies and draught ratios.

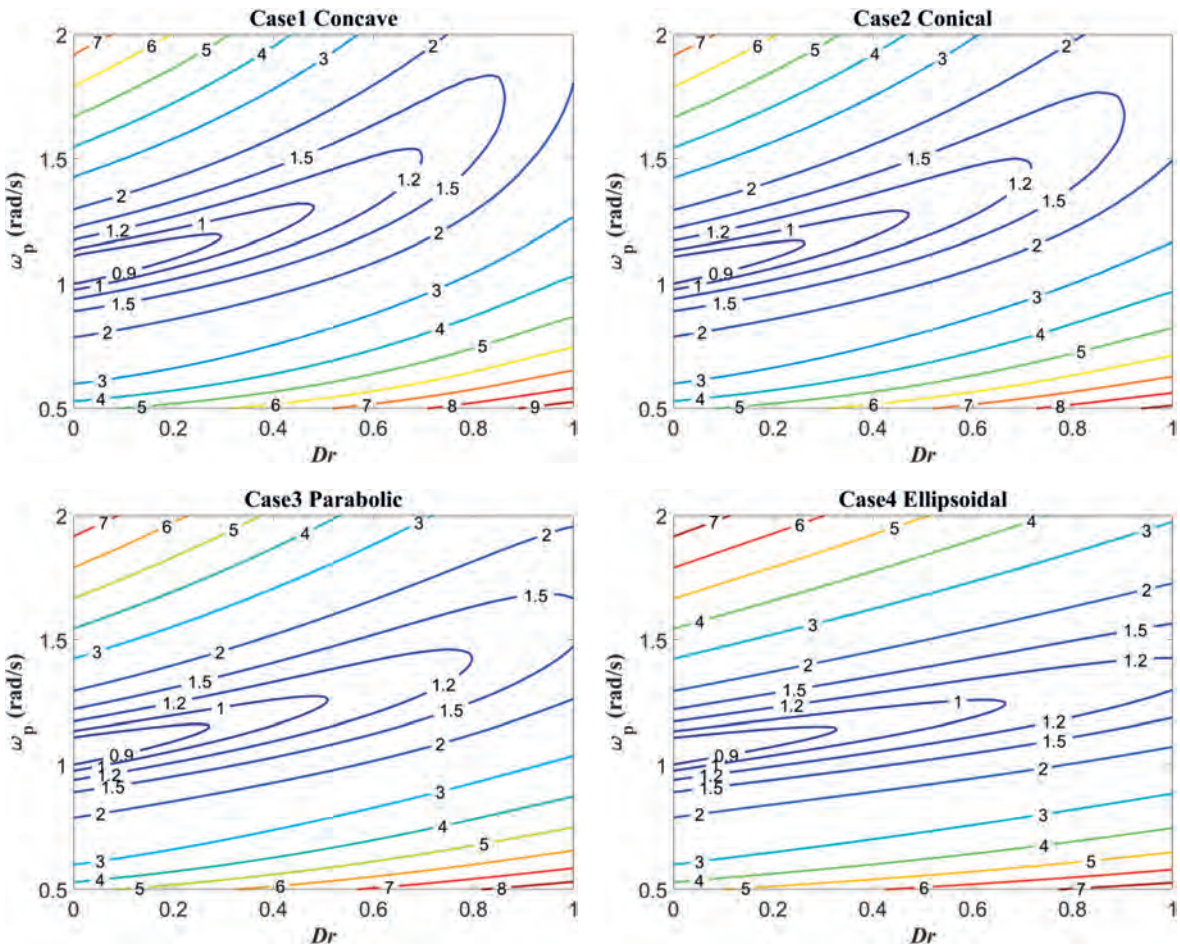

Fig. 12. Optimal PTO damping coefficients of the damped vibration absorbers at given peak frequencies ω_p and draught ratio D_r

The optimal PTO damping coefficients (100 kNs/m) for various peak frequencies and draught ratios are shown in Fig. 12. The display area of the optimal PTO damping coefficients is divided into two parts by the minimum values for the given draught ratios and peak frequencies. In the upper part, the optimal PTO damping coefficients increase with the increased peak frequencies and decreased draught ratios, while in the lower part, the coefficients show the opposite trend. From the former section in regular waves, we know that the change characteristics of the PTO damping coefficients can reflect the changing trend of energy capture to a certain extent. In such case, in real wave power conversion, the installed capacity of the device should be considered, combining the PTO mechanism and power capture. Because the PTO damping forces are limited by the hydraulic capacity or the resistive load, in this case, when the optimal PTO damping coefficients are obtained, the damping mechanism can be easily designed. The wave power capture of the buoys with optimal PTO damping coefficients in irregular wave is further explored and shown in Fig. 13. Similarly, for a given draught ratio, the capture width ratio first increases and then decreases with the increasing peak frequencies. And without considering the viscous resistance of the sea water, the truncated cylinder shows the highest wave conversion efficiency at a peak frequency equal to 1.07 rad/s. This means that, for a given working area, when the wave statistics are relatively stable and the matched wave spectrum is confirmed, the truncated cylindrical wave power absorber can be optimal, such as the 1.07 rad/s peak frequency in this paper. However, when the wave spectrum and its parameters are not stable and confirmed, the conical absorber may be the best choice for wave power conversion. For a better understanding of the effect of the geometry on the power conversion ability, buoys with the same displacement ratio are further explored. The displacement ratio here means the ratio of the absorber's displacement to that of the truncated cylinder with the same radius and draught.

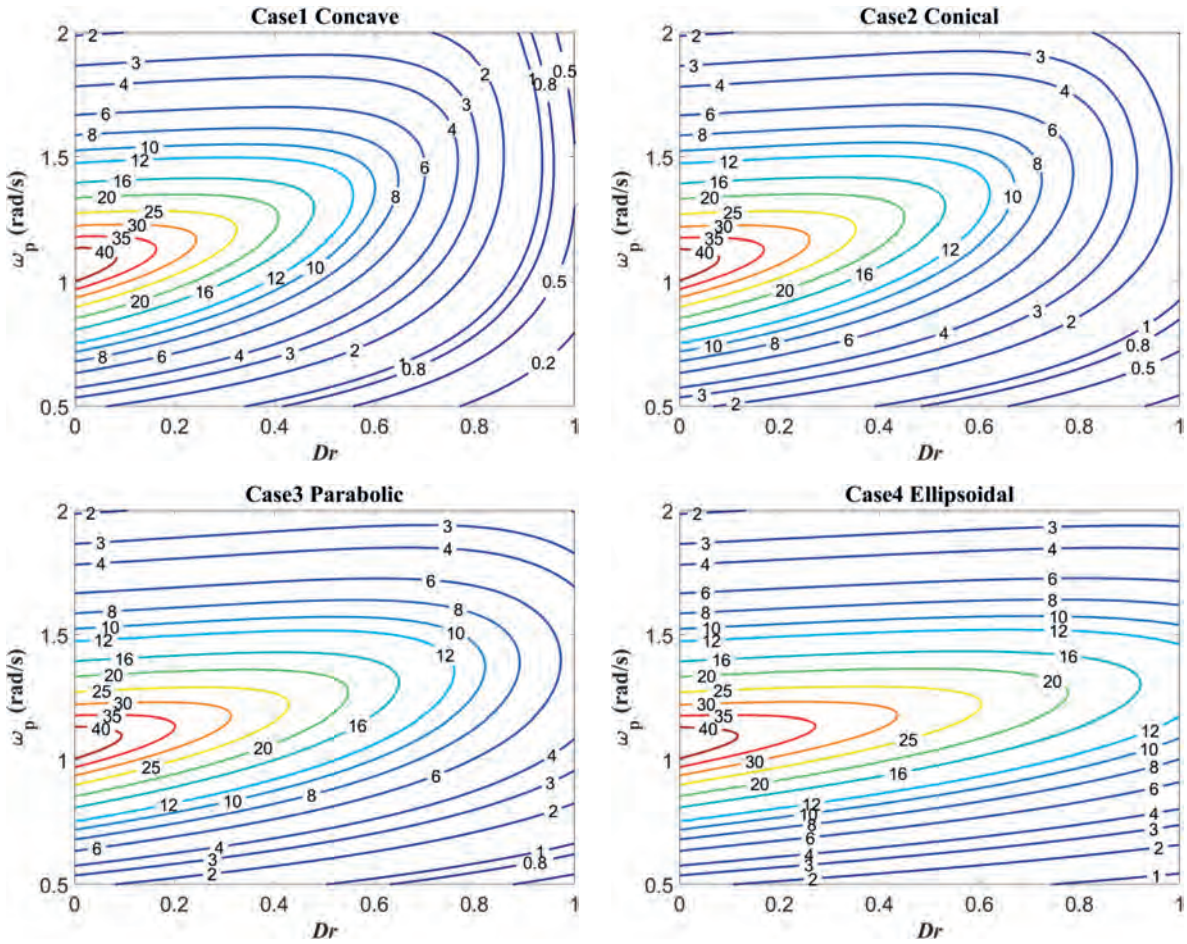

Fig. 13. Optimal capture width ratios of the damped vibration absorbers at given peak frequencies ω_p and draught ratio D_r

As shown in Fig.14, the optimal capture width ratios of the buoys with peak frequencies and displacement ratios are calculated and depicted, respectively. For different buoys with the same given displacements, the optimal capture width ratios both increase first and then decrease with the peak frequencies. However, before the capture width ratio reaches the peak value, the buoys with the same largest displacement have a better wave power conversion ability, and the concave buoy shows the best performance on the wave absorption. In addition, for the given shaped buoy with different displacements, the larger the displacement is, the better the power conversion will be. Taking the concave buoy as an example, when the peak frequency is 1.0 rad/s, the capture width ratio decreases from 28.1 when V_r is 0.9 to 12.7 when V_r is 0.7. The peak value also decreases from 37.4 to 22.1. However, it is worth noting that the relative peak frequency where the peak value occurs increases from 1.09 rad/s to 1.24 rad/s.

The buoys with different shapes and the same displacement also show interesting characteristics that the peak frequencies where the peak values occur increase in turn from the concave to the ellipsoidal buoy, and the smaller the displacement ratio, the more obvious the increase. In addition, for a given displacement, when the peak frequency reaches a certain value, the buoys with different shapes start to converge and show the same wave conversion ability. We call this particular peak frequency the assimilation frequency ω_a. It decreases with the increased displacement ratio. This means that, for a given working sea area, when the statistical wave is sure, we can choose the optimal buoy and the displacement to obtain the best wave absorption.

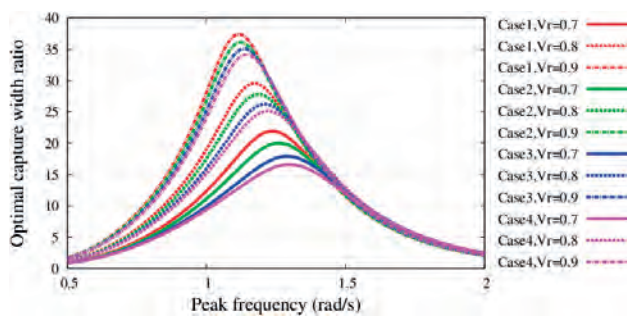

Fig. 14. Optimal capture width ratios of the damped vibration absorbers with peak frequencies ω_p at given displacement ratio V_r

DISCUSSION AND CONCLUSIONS

Four types of absorbers with different draught and displacement ratios are examined to analyse the effect of their geometries on the wave energy conversion ability, in which a semi-analytical method of decomposing the vertical axisymmetric curved surface into several ring-shaped stepped surfaces is introduced and examined. Combined with the updated body boundary characteristic, using the eigenfunction expansion matching method, the expressions of velocity potential in each domain, the added mass, radiation damping coefficients and wave-exciting forces of the oscillating buoy were obtained. The calculation results show that:

(1) The semi-analytical method by which the vertical axisymmetric curved surface is decomposed into several ring-shaped stepped surfaces can calculate accurately and investigate systematically the effect of the geometries on the hydrodynamic characteristics.

(2) In regular waves, the ellipsoidal buoy shows better wave energy conversion performance when the draught ratio reaches a relatively high value. In addition, its natural frequencies and bandwidth are almost linear to the draught ratio, as well as the optimal PTO damping coefficients and capture width ratios. When the draught ratios of all the four shaped buoys increase, their optimal motion responses, capture width ratios and natural frequencies also increase. Though the truncated cylinder shows the best wave energy capture capability at natural frequency, its disadvantage in frequency bandwidth is also exposed. The concave buoy has the maximal natural frequency for a given draught ratio because of its decreased displacement. In addition, though it has the lowest wave conversion efficiency, it has the largest frequency bandwidth for a given draught, especially when the draught ratio is close to one.

(3) In irregular waves, for a given draught ratio, the capture width ratios of all the considered shaped buoys first increase and then decrease with the increasing peak frequencies. Without considering the viscous resistance of the sea water, for a given working area, when the wave statistics are relatively stable and the matched wave spectrum is confirmed, the truncated cylindrical wave power absorber can be optimal. However, when the wave spectrum and its parameters are not stable and confirmed, the conical absorber may be the best choice for the wave power conversion.

(4) In irregular waves, when the displacements of the buoys are the same, the optimal capture width ratios both increase first and then decrease with the peak frequencies. However, before the capture width ratio reaches the peak value, the buoys with the same largest displacement have better wave power conversion ability and the concave buoy shows the best performance on the wave absorption. In addition, the peak frequencies where the peak values occur increase in turn from the concave to the ellipsoidal buoy, and the smaller the displacement ratio, the more obvious the increase.

(5) In irregular waves, for a given displacement, when the peak frequency reaches a certain value, the buoys with different shapes start to converge and show the same wave conversion ability. The assimilation frequency ω_a decreases with the increased displacement ratio, which means that, for a given working sea area, when the statistical wave is sure, we can choose the optimal buoy and the displacement to obtain the best wave absorption.

ACKNOWLEDGEMENTS

This paper is financially supported by the National Natural Science Foundation of China (No.51909111) and Natural Science Foundation of Jiangsu Province (No. BK20180980).

REFERENCES

1. F. Barbariol, A. Benetazzo, S. Carniel, and M. Sclavo, "Improving the assessment of wave energy resources by means of coupled wave-ocean numerical modeling," *Renewable Energy*, vol. 60, pp. 462-471, 2013.

2. L. Brik, "Application of constrained multi-objective optimization to the design of offshore structure hulls," *Journal of Offshore Mechanics and Arctic Engineering*, vol. 131, no. 1, p. 011301, 2009.

3. M. Liao, Y. Zhou, Y. Su, Z. Lian, and H. Jiang, "Dynamic analysis and multi-objective optimization of an offshore drilling tube system with pipe-in-pipe structure," *Applied Ocean Research*, vol. 75, pp. 85-99, 2018.

4. W. Lai, D. Li, and Y. Xie, "Simulation and experimental study of hydraulic cylinder in oscillating float-type wave energy converter," *Polish Maritime Research*, vol. 27, no. 2, pp. 30-38, 2020.

5. W. Lai, Y. Xie, and D. Li, "Numerical study on the optimization of hydrodynamic performance of oscillating buoy wave energy converter," *Polish Maritime Research*, vol. 28, no. 1, pp. 48-58, 2021.

6. E. Homayoun, H. Ghassemi, and H. Ghafari, "Power performance of the combined monopile wind turbine and floating buoy with heave-type wave energy converter," *Polish Maritime Research*, vol. 26, no. 3, pp. 107-114, 2019.

7. S. A. Mavrakos and G. M. Katsaounis, "Effects of floaters' hydrodynamics on the performance of tightly moored wave energy converters," *IET Renewable Power Generation*, vol. 4, no. 6, pp. 531-544, 2009.

8. A. P. McCabe, G. A. Aggidis, and M. B. Widden, "Optimizing the shape of a surge-and-pitch wave energy collector using a genetic algorithm," *Renewable Energy*, vol. 35, no. 12, pp. 2767-2775, 2010.

9. A. P. McCabe, "Constrained optimization of the shape of a wave energy collector by genetic algorithm," *Renewable Energy*, vol. 51, pp. 274-284, 2013.

10. W. Zhang, H. Liu, L. Zhang, and X. Zhang, "Hydrodynamic analysis and shape optimization for vertical axisymmetric wave energy converters," *China Ocean Engineering*, vol. 30, no. 6, pp. 954-966, 2016.

11. M. Shadman, S. F. Estefen, C. A. Rodriguez, and I. C. M. Nogueira, "A geometrical optimization method applied to a heaving point absorber wave energy converter," *Renewable Energy*, vol. 115, pp. 533-546, 2018.

12. S. Esmaeilzadeh and M. R. Alam, "Shape optimization of wave energy converters for broadband directional incident waves," *Ocean Engineering*, vol. 174, pp. 186-200, 2019.

13. I. O. Erselcan and A. Kükner, "A parametric optimization study towards the preliminary design of point absorber type wave energy converters suitable for the Turkish coasts of the Black Sea," *Ocean Engineering*, vol. 218, pp. 108275, 2020.

14. S. A. Mavrakos, "Hydrodynamic coefficients in heave of two concentric surface-piercing truncated circular cylinders," *Applied Ocean Research*, vol. 26, pp. 84-97, 2004.

15. E. E. Bachynskia, Y. L. Young, and R. W. Yeung, "Analysis and optimization of a tethered wave energy converter in irregular waves," *Renewable Energy*, vol. 48, pp. 133-145, 2012.

16. J. Goggins and W. Finnegan, "Shape optimisation of floating wave energy converters for a specified wave energy spectrum," *Renewable Energy*, vol. 71, pp. 208-220, 2014.

17. R. P. F. Gomes, J. C. C. Henriques, L. M. C. Gato, and A. F. O. Falcão, "Hydrodynamic optimization of an axisymmetric floating oscillating water column for wave energy conversion," *Renewable Energy*, vol. 44, pp. 328-339, 2012.

18. H. J. Koh, W. S. Ruy, I. H. Cho, and H. M. Kweon, "Multi-objective optimum design of a buoy for the resonant-type wave energy converter," *Journal of Marine Science and Technology*, vol. 20, no. 1, pp. 53-63, 2014.

19. A. Garcia-Teruel, B. DuPont, and D. I. M. Forehand, "Hull geometry optimization of wave energy converters: On the choice of the optimization algorithm and the geometry definition," *Applied Energy*, vol. 280, p. 115952, 2020.

20. A. Garcia-Teruel and D. I. M. Forehand, "A review of geometry optimization of wave energy converters," *Renewable and Sustainable Energy Reviews*, vol. 139, p. 110593, 2021.

21. S. Esmaeilzadeh and M. R. Alam, "Shape optimization of wave energy converters for broadband directional incident waves," *Ocean Engineering*, vol. 174, no. 15, pp. 186-200, 2019.

22. N. Y. Sergiienko, M. Neshat, L S. P. da Silva, B. Alexander, and M. Wagner., "Design optimisation of a multi-mode wave energy converter," in *Proc. of the 2020 39th International Conference on Ocean, Offshore and Arctic Engineering*, *2020*, *Online Virtual*.

23. M. N. Berenjkooba, M. Ghiasi, and C. G. Soares, "Influence of the shape of a buoy on the efficiency of its dual-motion wave energy conversion," *Energy*, vol. 214, p. 118998, 2021.

24. A. Claudio, C. A. Rodríguez, P. Rosa-Santos, and F. Taveira-Pinto, "Hydrodynamic optimization of the geometry of a sloped-motion wave energy converter," *Ocean Engineering*, vol. 199, p. 107046, 2020.

25. K. Kokkinowrachos, S. A. Mavrakos, and S. Asorakos, "Behavior of vertical bodies of revolution in waves," *Ocean Engineering*, vol. 13, no. 6, pp. 505-538, 1986.

26. M. Lopez, F. Taveira-Pinto, and P. Rosa-Santos, "Influence of the power take-off characteristics on the performance of CECO wave energy converter," *Energy*, vol. 120, pp. 686-697, 2017.

27. J. A. Koupaei, S. M. M. Hosseini, and F. M. Maalek Ghaini, "A new optimization algorithm based on chaotic maps and golden section search method," *Engineering Applications of Artificial Intelligence*, vol. 50, pp. 201-214, 2016.

28. J. Falnes, *Ocean waves and oscillating systems: linear interactions including wave-energy extraction*, Cambridge: Cambridge University Press, 2004.

29. R. W. Yeung, "Added mass and damping of a vertical cylinder in finite depth waters," *Applied Ocean Research*, vol. 3, no. 3, pp. 119-133, 1980.

30. A. Hulme, "The wave forces acting on a floating hemisphere undergoing forced periodic oscillations," *Journal of Fluid Mechanics*, vol. 121, pp. 443-463, 1982.

31. O. M. Faltinsen, S*ea loads on ships and offshore structures*, 1st ed. Cambridge: Cambridge University Press, 1993.

POLISH MARITIME RESEARCH 2 (118) 2023 Vol. 30; pp. 146-164
10.2478/pomr-2023-0030

UNDERSTANDING FUEL SAVING AND CLEAN FUEL STRATEGIES TOWARDS GREEN MARITIME

Van Nhanh Nguyen [1]
Krzysztof Rudzki [2]
Marek Dzida [3]
Nguyen Dang Khoa Pham [4]
Minh Tuan Pham [5*]
Phuoc Quy Phong Nguyen [4]
Phuong Nguyen Xuan [4*]
[1] Institute of Engineering, HUTECH University, Ho Chi Minh City, Viet Nam
[2] Gdynia Maritime University, Faculty of Marine Engineering, Poland
[3] Gdansk University of Technology, Poland
[4] PATET Research Group, Ho Chi Minh City University of Transport, Ho Chi Minh City, Viet Nam
[5] School of Mechanical Engineering, Hanoi University of Science and Technology, Hanoi, Viet Nam

* Corresponding authors: *phuong@ut.edu.vn (Phuong Nguyen Xuan)*
tuan.phamminh@hust.edu.vn (Minh Tuan Pham)

ABSTRACT

Due to recent emission-associated regulations imposed on marine fuel, ship owners have been forced to seek alternate fuels, in order to meet the new limits. The aim of achieving low-carbon shipping by the year 2050, has meant that alternative marine fuels, as well as various technological and operational initiatives, need to be taken into account. This article evaluates and examines recent clean fuels and novel clean technologies for vessels. The alternative fuels are classified as low-carbon fuels, carbon-free fuels, and carbon neutral fuels, based on their properties. Fuel properties, the status of technological development, and existing challenges are also summarised in this paper. Furthermore, researchers have also investigated energy-saving devices and discovered that zero-carbon and virtually zero-carbon clean fuels, together with clean production, might play an important part in shipping, despite the commercial impracticability of existing costs and infrastructure. More interestingly, the transition to marine fuel is known to be a lengthy process; thus, early consensus-building, as well as action-adoption, in the maritime community is critical for meeting the expectations and aims of sustainable marine transportation.

Keywords: Marine engine; Alternative fuel; Green maritime; Fuel savings; Low-carbon strategy

INTRODUCTION

ASo as to meet climate change goals, as well as reduce greenhouse gas (GHG) emissions, it is crucial for the shipping industry to drastically decarbonise and transition to an eco-friendlier future [1], [2]effectively promoted the marine low sulfur diesel fuel (MLSDF. Obviously, important international protocols and events, as well as academic and government agendas, all contribute to triggering and responding to the issues which this sector encounters as it strives to become more environmentally friendly and sustainable [3], [4]Most importantly, awareness of the definition of ‚decarbonisation' is critical, since it refers to the ‚reduction or entire removal of CO_2 emissions' according to reports of International Maritime Organization (IMO) [5], [6]. The fourth GHG Survey, which was released in August 2020, established significant goals for the shipping industry, including a 50% reduction in yearly GHG emissions by 2050, compared with those in 2008 [7], [8]. It is not hard to see that the IMO will attempt to reach the above-mentioned goals by using energy efficiency approaches and novel methods such as using alternative fuels that could be applied in the short, medium, and long-term [9], [10]. Fig. 1 shows the IMO's ship-enhancement strategy for reducing CO_2 emissions between 2013 and 2050 [11].

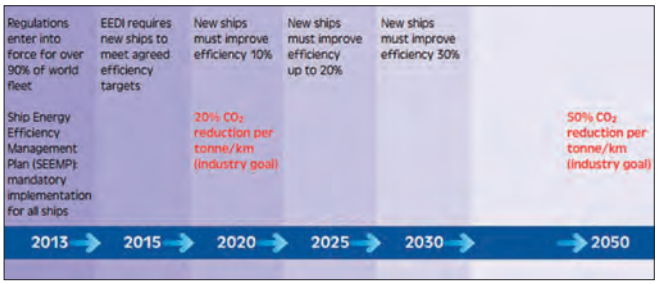

Fig. 1. IMO agreement for reduction of CO2 emission from ships [11]

In fact, international shipping's decarbonisation has been slow because of the sector's stakeholders' disparate and diversified aspirations and interests. Arguments at the IMO have been marked by sharp disagreement over how and whether this field should conform with the Paris Agreement's aims. The existing IMO GHG reduction roadmap suggested a slow decision-making process in the implementation of critical actions and regulations [12], [13]. With no precise, ambitious, and enforceable aims, the industry would have no motivation to invest in low-carbon techniques on a large scale. This could be explained by the significant risk and uncertainty related to investment in low-carbon methods, which are generally more expensive. As a result, policy uncertainty might hinder innovation in low-carbon techniques and fuels. Regarding the primary factors impeding progress in establishing an aggressive target, the lack of rigorous investigations, analysing the technical feasibility of decarbonising international maritime transportation, was mentioned, particularly in light of the Paris Agreement's more ambitious target of 1.5°C temperature limitation [14]. Significantly, shipping was identified as a substantial source of anthropogenic NOx and SOx emissions in recent research, accounting for 15% and 13% of global NOx and SOx emissions, respectively [15]–[18]. Furthermore, maritime shipping is also known as the principal source of black carbon in the Arctic Circle [19], as well as a considerable source of CO_2 and particulate matter, released through human activities [20]. For the aforementioned reasons, the IMO established goals targeted at gradually decreasing the ships and ports' carbon intensity, with general goals of decarbonising the marine field by the end of the century [21]–[23]. It has been noted that stakeholder-led initiatives, along with the regulations mentioned above, were compelling ship-owners to change their operational practices, to install on-board air contamination control devices, such as SOx scrubbers and selective catalytic reduction, as well as to diversify their fuel categories to include alternative low-carbon and low-sulphur fuels [24], [25]. Hence, the newly discovered demand for alternative fuels offers exciting potential for investment in the expansion and diversification of the blend of maritime fuels [26].

The combination of improvements in energy efficiency and a shift to energy carriers with low or zero-carbon could lead to a high probability of achieving very low (even zero) GHG emissions discharged from shipping [27]. Electricity, biofuels, and electrofuels derived from renewable sources of energy (e.g. solar, wind and biomass) are examples of energy carriers that emit little or no GHG during their life cycle [28], [29]. Energy efficient approaches, on the other hand, are those that need to go hand-in-hand with operational measures, such as:

- capacity utilisation and voyage optimisation,
- technical approaches,
- enhancements in hull design and changes in propulsion and power systems.

The emission reduction potential of various strategies have been examined and the findings show that one of the best and most gratifying approaches to achieve the required potential emission reduction is a shift to alternative fuels and the use of energy-saving techniques [30], [31]. The primary goal for this work was to look at the role of alternative fuels, as well as energy-saving measures, in decarbonising maritime transportation, which requires providing not only short-term GHG reductions but also engine solutions and tank arrangements, that could easily be adjusted to run on fuels with very low or zero carbon (if available) and are efficient in utilising fuel or technological ship operation solutions, to decrease GHG emissions.

SOLUTIONS TO MANAGE CO_2 EMISSION FROM SHIPS

Previous studies have asserted that a target of at least 50% emissions reduction should be possible at zero net cost by 2030, if low-cost energy savings were to be fully exploited in supporting investments in more costly solutions [32]. The above difference, between the energy efficiency potential and the level of realised energy efficiency, is referred to as the energy efficiency gap [33], [34]. This is an important issue that needs to be thoroughly considered if the shipping industry is to make a substantial effort in working towards a low-carbon future for global maritime transport [35], [36]. Indeed, if all available energy efficiency and carbon mitigation measures are to be implemented, the projected growth in shipping activities could achieve remarkable results, in terms of decreasing energy demands and zero-net reduction in CO_2 emissions. In other words, the reduction in emissions achieved by measures taken by various shipping companies effectively cancels out the growth in energy consumption resulting from the sector's growth [37]–[39]. To further highlight the sector's role in combating climate change, the European Commission has recently called for the global shipping industry to set a target for 2050: to achieve 40-50% CO_2 emissions reduction compared to 2005 levels [40].

Indeed, the problem of handling CO_2 emissions in current world shipping conditions is not only a technological one, but is intertwined with highly sophisticated and multifaceted governmental factors. As the main intergovernmental body governing international maritime activities, the IMO adopted two key policy measures during the 62nd meeting of its Maritime Environment Protection Committee (MEPC) in July 2011. More importantly, in order to lower CO_2 emissions released from ocean-going vessels, the EEDI (Energy Efficiency Design Index), applying exclusively to novel vessels, and the SEEMP (Ship Energy Efficiency Management Plan) needed to persuade vessel owners and operators to take CO_2 emission-cutting

measures for their fleet. Unfortunately, the rise in emissions is likely to continue, despite these actions [41]. While emission reduction is affected by other actors (e.g. port authorities) [42], [43], a substantial portion of the expected reduction is likely to come from improvements in ship compliance to the standards set by SEEMP (i.e. operational and retrofit measures to increase ship energy efficiency) [41]. When considering the goal of CO_2 emissions reduction in the shipping industry, the entire vessel and its operation should be subjected to analysis. Therefore, detailed discussions are provided on emission reduction strategies through reviewing emission control mechanisms for marine diesel engines, as the main ship engine propulsion, using the concept of EEDI given in Eq. (1). This indicates the amount of CO_2 emissions from diesel engines with CF as the conversion coefficient for CO_2 [44].

$$\text{EEDI}(g(CO_2/\text{ton/mile}) = \frac{\text{Engine power (kW) x Fuel consumption rate (g/kWh)x } C_F}{\text{DWT (ton) x Speed (mile/h)}} \quad (1)$$

In fact, the IMO implemented various technical methods to achieve the long-term goal of reducing GHG, which included the EEDI and SEEMP [45]. Notably, the EEDI required all vessels built after 2013 to have a certain minimum energy efficiency, assessed in grams of CO_2 emitted per capacity-mile. Indeed, EEDI was a regulatory measure designed to reduce the carbon intensity and enhance operating efficiency of a ship; nevertheless, the EEDI only concentrated on gate-to-gate ship emissions [46]. Significantly, critics expressed concerns that the EEDI might understate carbon reductions [47] and comprehensive systems analysis, such as the production of feedstock, raw materials acquisition, and the conversion and consumption of fuel in maritime vessels, was essential to evaluate the environmental impacts on a broad scale, as well as the advantages of alternative marine fuels [48], [49]. This life cycle viewpoint captured environmental externalities that traditional measurements could not and it could assist in offsetting unforeseen environmental implications of marine fuel usage, such as transferring environmental challenges between supply chain segments or pollutant classifications. While EEDI established performance criteria for novel ship design and construction, the SEEMP primarily addressed energy-saving options at the operating level of both current and new ships over 400 GRT. Similar to EEDI, SEEMP was made mandatory, requiring fleet owners and companies to take immediate action to improve the energy efficiency of their operations following a four-step process: i) planning, ii) implementation, iii) monitoring, and iv) self-evaluation and improvement. Moreover, the IMO created the EEOI (Energy Efficiency Operational Indicator) as an operational measuring tool to assess the energy efficiency and CO_2 emissions of vessels, in order to monitor compliance with SEEMP. Lower EEOI values indicate better ship energy efficiency and are calculated by Eq. (2):

$$\text{EEOI} = \frac{\text{Eactual } CO_2 \text{ emission}}{\text{performed transport work}} \quad (2)$$

More interestingly, with the creation of the EEOI, vessel owners and operators could access an indicator used to monitor individual ship operations in real time. As a result, any prospective alterations to the ship's structural design and operation could be evaluated according to their effects on the general efficiency performance. Although the EEOI was usually used to evaluate the energy efficiency of vessels under the SEEMP framework, there was controversy in the shipping industry because utilising such an indicator to compare ship performance was thought to be incorrect and inaccurate [50]. The IMO introduced the IMO Data Collection System in MEPC.278 (70), which came into force in 2018. This data collection system provides information about the fuel consumption of vessels. Measuring the actual transport work, in terms of tonne miles, requires information about the distance travelled and the cargo mass. The cargo on the ships is generally viewed as sensitive information and so this information is not included in the DCS. Therefore, the Annual Efficiency Ratio (AER), known to be a simple component, quantified the vessels' energy efficiency regarding GHG emissions per transportation work, which assumed a constant cargo value based on the ship's deadweight tonnage.

$$\text{AER} = \frac{\text{actual } CO_2 \text{ emission}}{\text{DWT*distance}} \quad (3)$$

In order to comprehensively evaluate the reduction measures of GHG emissions, the 5th GHG Working Group and MEPC-74 discussed the methods of approach to reduce GHG emissions given in Table 1.

Tab. 1. Measures for reducing GHG emission of IMO [51]

Measures	Main measure	Remarks
Technical measures	• Energy efficiency such as light advanced materials,waste heat recovery, optimisation of design, improvement of propulsion devices, reduction offriction. • Green/renewable/alternative energy such as biofuels, H_2, NH_3, LNG, fuel cell, renewable energy sources (solar, wind, wave and tide, geothermal); electricity.	EEDI framework
Operational measures	• Optimisation of ship speed and size, improvement of ship-port interface, enhancement of on-shore power.	SEEMP/ EEOI/EEXI
Market-based measures (MBM)	• Emission trading, efficiency incentive, GHG fund or tax.	MBM

APPLICATION OF CLEAN AND RENEWABLE ENERGY FOR SHIPS

Reducing the reliance of marine vessels on fossil fuels is part of the strategy to attain a more sustainable and low-carbon future for the global shipping industry. This is achieved via introducing alternative and cleaner fuel options to power ships [52], [53]. Ship propulsion systems (aboard commercial ships) are mostly powered by gas turbines, diesel engines, or steam, in which diesel engines accounts for the vast bulk of the available fleet [54]. In spite of their rarity, electric generators running on diesel and oil-fired boilers can be observed on

several vessels. Besides this, several kinds of vessel propulsion power systems, including gas turbines, traditional reciprocating internal combustion engines, and boilers, are investigated in the following section, for the employment of low-carbon fuels, and with the aim of replacing traditional fossil fuels. Researchers have shown interest in the possible applications of more appealing alternative fuels (such as H_2, LNG, ammonia, and biofuels) in propulsion systems of vessels and such prospective low-carbon fuels have been examined in the laboratory, as well as at pilot scales. It was noted that the fuel coefficient is determined by the carbon concentration (CC, m/m) of the fuel; this is the product of the carbon concentration and carbon fuel coefficient ($C_{FF} = C_{FC}*CC$) [55]. Fig. 2a illustrates the coefficients for various alternative and marine fuels. Among the fuels used for ships, Bouman et al. [30] discovered that biofuels had the single greatest potential in lowering CO_2 emissions among all the methods investigated. Fig. 2b depicts the life cycle GHG emissions of a variety of bio-based fuel and fossil-fuel approaches and these are documented in the paper as a series of boxplots. In spite of the wide range of results, biofuels showed a considerable ability to decrease life cycle GHG emissions, when compared to HFO, as well as fossil alternatives [56].

LNG

Because liquefied natural gas (LNG) has low carbon content, it is considered a potentially appealing fuel for the maritime sector. Furthermore, methane (CH4) is the primary chemical molecule found in natural gas, which contains a higher density of energy compared to diesel fuel derived from petroleum [63], [64]. In addition, natural gas is known to be a cleaner-burning fuel compared with diesel and HFO because it emits less SOx, NOx, and PM [26], [65]. Apart from that, because LNG has high energy density, compared to other hydrocarbons or

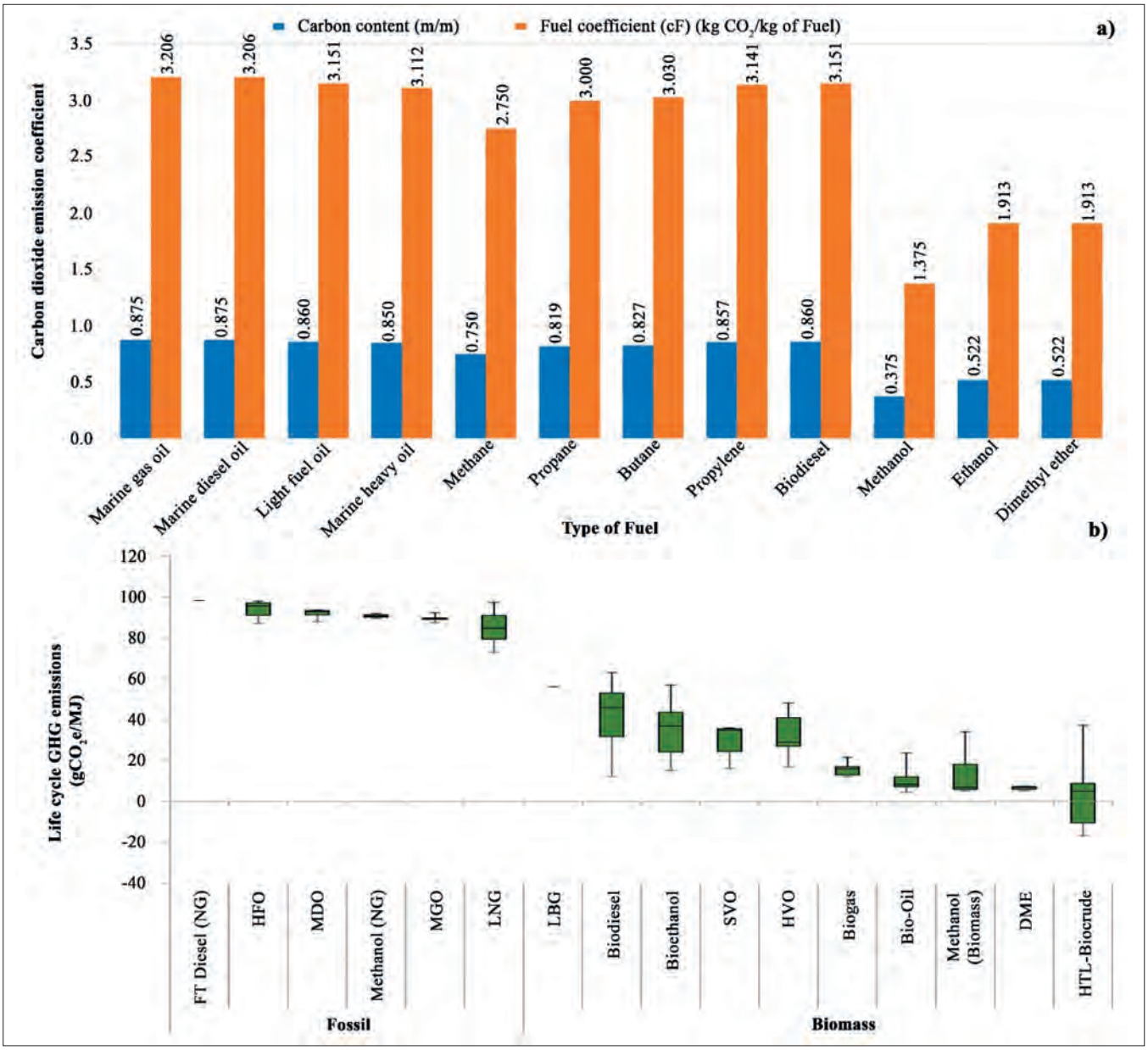

Fig. 2. (a) – CO_2 emission coefficient for various fuels used for ships [55]; (b) – Life cycle GHG emissions of various fuel types used for ships [56]–[62]

alcohol-sourced fuels, it plays a vital part in progressing the final aims. Indeed, LNG was identified as the best fossil alternative for the replacement of MGO and HFO, since it emits 30% less GHG and contains no NOx or SOx [66]. It should be noted that, although the first ship running on LNG was built in 2000, there are now 55 operating around the world; because of ECA laws, their activities are primarily in North America (38%) and Europe (57%). More importantly, for internal combustion engines running on LNG, the gas has to be stored at a temperature of –162°C [67], [68]. Nonetheless, LNG is still mostly derived from fossil fuels, so bio-LNG was suggested as a potential renewable decarbonisation source, in the document. In fact, biomass could be converted into biomethane in two ways: thermochemical gasification, known as bio-synthetic natural gas (bio-SNG), and bio-methane [69], [70], which can be liquefied and stored in tanks, to be utilised in LNG terminals [71].

The conversion of the main engine of a vessel from diesel fuel to dual-fuel (diesel and LNG) is capable of lowering CO_2 emissions by up to 10% [72]. Anderson et al. [73] studied the emission properties of a ship running on LNG with four dual-fuel engines rated as 30,400 kW at various loads. LNG's CO_2 emissions were reported to be lower, compared to those of marine fuel oils. The combustion of LNG, on the other hand, caused greater HC and CO emissions. Li et al. [74] obtained similar results with a maritime dual-fuel diesel engine at high speeds. Thus, LNG not only has a good environmental impact because of its lower CO_2 emissions, but it also brings a significant cost benefit [72], [75]. In addition, evaluating the environmental advantages of switching from HFO to natural gas by changing the average emission parameters of NOx, SOx, PM, and CO_2, for both LNG and HFO, for diesel engines with two strokes and using the same power and operating hours (in the case of an engine running on dual-fuel) were also found in studies of Banawan et al. [72] and Gerilla et al. [76]. With the use of statistical analysis, researchers discovered that switching from HFO to LNG reduced PM, SOx, CO_2, and NOx emissions by approximately 96%, 98%, 11%, and 86%, respectively [77].

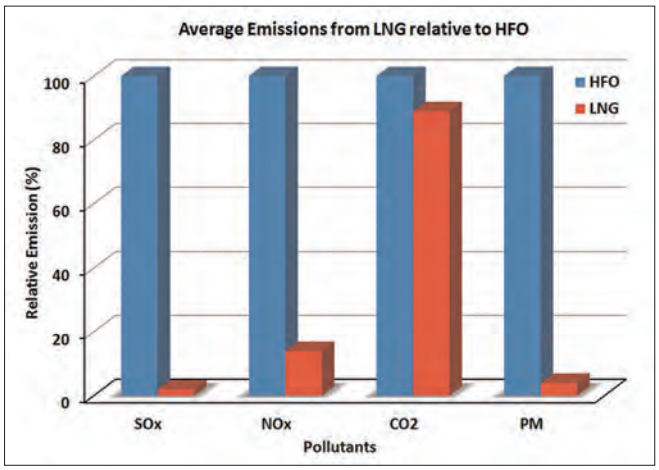

Fig. 3. Pollutants from ships using LNG compared to HFO [77]

More significantly, because of the costlier propulsion plant, related technology and procurement issues, the capital expenses for LNG-powered vessels are likely to be greater than those for conventionally powered ones. Interestingly, the LNG tank was considered the most expensive component of the additional expenditure required for all ships. According to market sources, the additional capital cost could range from 5-20 million USD, based on the tank and engine capacity [78], [79]. The key elements affecting payback time included (i) - ECA exposure, and (ii) - the price of LNG fuel. Even though the limit of global sulphur in the year 2020 or 2025 would enhance the business case, by requiring mandatory compliance for the whole journey, the uncertainty of the LNG fuel's availability and pricing makes vessel owners and operators cautious. In general, the additional expenses for a ship running on LNG (mostly applying to merchant ships like tankers, bulkers, and containers) was 15-30% of the cost of a newly built conventional ship [79]. In spite of the regulatory momentum, most major impediments to LNG adoption as a marine bunker are the financial and commercial uncertainties related to the LNG fuel price and its availability (bunkering facilities), and the considerable additional investment required. According to the current market status, the only ships that are likely to apply LNG as a fuel are those running on fixed routes such as containerships, or RoRo, and rather large ships participating in regional trades, particularly in ECAs [78], [80], [81]. Furthermore, the global sulphur restriction, which would come into effect in 2025, as well as the EU's sulphur limit for EU waters (2020), bolstered LNG's position as a marine fuel. When the afore-mentioned laws took effect, it was envisaged that larger ocean-going ships (namely tankers and bulkers) would investigate LNG as a compliance choice [79], [82].

BIODIESEL

As reported, biodiesel is considered to be one of the renewable sources of alternative energy and it has been studied by the world's oil industry because demand for fossil fuel is increasing, leading to high prices [83], [84]. Interestingly, biodiesel has nearly the same functional features as fossil fuels but is environmentally friendly, so it is regarded as a superior alternative [85]–[87]. Besides the sustainability of biodiesel production, its benefits also include a significant reduction in carbon emissions, more environment related job opportunities, a reduction in the requirement for imported fossil fuel, and a decrease in fuel costs. Furthermore, biodiesel can be used in diesel engines directly, with no modification required although some drawbacks of biodiesel should be overcome [88], [89]. It is easy to see why biodiesel gained favour as a greener alternative fuel and, recently, most scientists and researchers utilised edible and non-edible feedstocks to create more cost-effective bio-based diesel mixtures and boost the physicochemical features of the blends [90]–[93].

In fact, the study of biodiesel fuel in the marine field has been ongoing since 1998. The Great Lakes Environment Research Group conducted extensive biodiesel testing on board the NOAA Huron Explorer research ship, which was the first US vessel powered by alternative fuel and operated entirely without the use of petroleum products [94]. After eight years, the Great Lakes Maritime Research Institute conducted investigations on various technical issues related to the biodiesel fuel employed in marine engines. They stated that biodiesel served as a solvent and

might harm the rubber and elastomer components used in the engine. Moreover, in 2003, the Annis Water Research Institute carried out another investigation on Detroit and Cummins' diesel-fuelled engines, utilising the same feedstock. They claimed that using B20 soybean would have a small effect on the engine, while causing no harm to machinery equipment [95]. The BioMer Canada research team employed neat bio-based diesel on several sizes of marine ships, in October 2004; their testing resulted in a successful outcome, with a rise in engine performance of 2-3% with the use of bio-derived diesel [96]. Moreover, BV energy tested biodiesel on a MAN diesel engine with 975-kW, placed on a luxury boat in 2007. Consequently, they stressed that before transitioning from marine gasoline to bio-originated diesel, fuel filters should constantly be adjusted and fuel tanks should be cleaned [97]. The Royal Caribbean Cruise Line fleet's biodiesel initiative began with the testing of 5-100% bio-based diesel on their GE LM2500 gas turbine. The findings showed that biodiesel gasoline, soot and other pollutants greatly decreased [98], [99]. Notably, MAN Diesel Company, which is a global designer and engine manufacturer, has been working with biodiesel since 1994. They investigated various biodiesel feedstocks in order to figure out the best fuel for their engines. In Copenhagen, Denmark, the first biodiesel experiment on their low-speed engines with two strokes was conducted in 2006 [100]. In 2007, MAN Diesel utilised palm biodiesel in their medium speed engine with four strokes in Belgium, marking a new milestone. MAN Diesel currently offers a large selection of marine engines which can be ideally used with biodiesel fuel with no changes. Apart from that, Rolls-Royce, the world's largest maker of medium-speed engines, indicated that they had no experience with bio-derived diesel on their engines, but biodiesel needed to be suitable for marine engines in general. In addition, following multiple buyer requests, they wanted to devote greater attention to alternative fuel in future [94]. Caterpillar Incorporated, a marine engine manufacturer in the US, has considerable experience with the use of biodiesel. Investigations on Caterpillar ferry engines suggested that biodiesel could be utilised smoothly in the short term. Hence, additional research was conducted to determine the potential implications of using bio-derived diesel in marine engines in the long run. Most of Caterpillar's novel and older marine diesel engines could now employ up to 30% biodiesel with no adjustment [65], [99].

METHANOL

Methanol is another widely used alcoholic fuel [101], [102]. Indeed, methanol can be manufactured from natural gas or derived by gasifying biomass on an industrial scale. Because of its low CO_2 and other air pollution emissions, methanol, especially bio-methanol, was seen as a more environmentally friendly and more sustainable fuel for the maritime sector [103]. In the case of large marine engines, not only the transformation of existing engines, but also the fabrication of novel dual-fuel engines, aiming to operate methanol, was completed successfully in a few cases [104], [105]. In fact, methanol was extensively examined and utilised in spark-ignited car engines for many years, with minimal modifications necessary [106]. These days, bio-methanol and bio-ethanol generation from biomass could take advantage of a well-established supply network. Nonetheless, there are still economic hurdles that have to be solved in order to allow the afore-mentioned alternative fuels to compete with conventional petroleum-originated fuels [106]. More importantly, since the world's supply of alcoholic fuels taken from renewable resources has increased, bio-methanol and bio-ethanol have tremendous potential in the shipping sector. However, more storage space would be required because methanol has a lower energy density than fossil fuels. As reported, there are presently 13 ships running on methanol worldwide [107]. Methanol combustion, as the major fuel employed to power marine boats, has been observed to release less CO_2 and other air contaminants than HFO or MGO [108], [109]. In 2015, the MS Stena Germanica became the first marine ship to be powered by recovered methanol.

After investigating the use of methanol in a diesel engine with dual-fuel mode operations, Song et al. [110] gained great fuel economy and engine power, as well as lower levels of particulate and nitrous oxide emissions. Furthermore, Wärtsilä, a marine engine manufacturer, studied different methanol combustion methods for engine conversion on the Stena Germanica ferry and chose one in which the methanol was burnt using a moderate amount of pilot fuel [111]. Since 2015, retrofitted engines based on this design have been functioning satisfactorily [111]. The MAN engine manufacturers also tested methanol in low speed two-stroke LGI engines, employing a pilot fuel ignition approach, and the experiments were deemed a success. In 2016, the engines were mounted aboard seven novel chemical tankers [112]. In fact, methanol engines installed in smaller ships (pilot boats, road ferries, and commuter ferries) were not yet commercially viable but were being developed. Some proposals for the use of methanol in small marine engines (with power ranging from 250 to 1200 kW) were evaluated as part of the Swedish study project SUMMETH [113]. The 'Billion Miles' company, located in Singapore, developed a 100% methanol engine for harbour craft, with the prototype engine being assessed at a technical readiness level of 8-9 of 10 [114]. Therefore, various engine manufacturers, programmes and other efforts have evaluated methanol engines for marine applications, including large and small engines, with promising technical outcomes [106]. In assessing the potential application of methanol/ethanol as alternative fuels for marine vessels, an evaluation was conducted by the European Maritime Safety Agency on the benefits and challenges of these resources, in terms of the technical, operational, and economic factors, supply availability, environmental impacts, and safety regulations [115]. Despite the potential positive environmental effects, both methanol and ethanol still face considerable obstacles in their application to marine vessels, due to the lack of adequate safety instructions, operational experience, and capable infrastructure to satisfy the need for bunkering.

HYDROGEN AND HYDROGEN CARRIERS

Because of the near-zero emissions (such as PM, CO_2, and SO_2, etc.) throughout the combustion process, hydrogen (H_2) is regarded as a clean type of fuel and so it has the potential to become a cleaner alternative to traditional fossil fuels [116].

Moreover, H_2 fuel could be used in boilers, gas turbines, and internal combustion engines [117]–[119]. Spark-ignition engines, in particular, could better tolerate H2 fuel because the temperature of auto-ignition is really high (about 585°C) [120], [121].

All of the existing major shipping fuels are hydrocarbons. The H_2/carbon ratio is considered to be an important factor since a greater proportion can lead to a fuel that is more energy-efficient and discharges fewer CO_2 emissions [122], [123]. Thus, H_2 or H_2 carriers could become a zero-emission alternative for future transport [124]–[126]. Currently, the majority of vessels utilise combustion technologies in the form of diesel engines. Although H_2 could be utilised to power a diesel engine, retrofitting would necessitate major changes due to the dissimilar combustion rates of H_2 compared to the currently employed fuels [127]. However, with the proper infrastructure, de-Troya et al. [128] proposed that H_2 engine performance might outperform oil-derived fuels because of its high gravitational energy density and flammability. Significantly, a fuel cell was considered the most efficient way to extract energy from H_2. Several small vessels running on H_2 have been built with relatively low energy consumption, e.g. the Energy Observer or the Hamburg Ferry [129], [130].

In the shipping industry, H_2 has been the focus of studies into viable ship engine types, investigating the benefits from the fuel's increased power density, as well as the lower emissions of pollutants. More importantly, taking the evaluation of the life cycle into consideration, H_2 utilised in marine transportation (even as a fuel employed in a dual-fuel engine mixed with other types of fossil fuel) was observed to have the potential to decrease CO_2 emissions by up to 40% per unit of transport task [131]. Even though H_2 is largely accepted in maritime fuel cell applications, the applications of marine motors powered by H_2 remain rare. Wärtsilä tested spark-ignited engines fuelled by LNG and H_2 in two modes, including single fuel and dual fuel, and discovered that current dual-fuel marine engines could only operate with the largest amount of 25% H_2 mixture with no modification [132]. Hence, the engine had to be modified if the H2 ratios exceeded 25%. CMB's passenger ship 'Hydroville' has been recognised as the first sea-going ship fitted with dual-fuel engines, such as H_2 and diesel, in the world. More intriguingly, HyMethShip created a technique for ships to use H_2 and generate methanol through storing only methanol and CO_2 aboard, with the goal of eliminating the obstacles related to storing H_2 [133]. For liquefied H_2 storage, it demonstrated that the tank capacity for liquid H_2 was double that of LNG. Hence, with engine technologies based on methanol, the disadvantage mentioned above for H_2 marine engines can be solved, as shown in Fig. 4.

Ammonia had a pre-existing worldwide supply chain but mostly in the field of fertilisers, with a total annual production of 176 million tons in 2018 [134]. As a result, pre-existing worldwide safety regulations were considered advantageous and production scaling might be less difficult. Current ammonia generation methods typically employ fossil fuels to generate H_2 feedstock, followed by the Haber-Bosch process, which is extremely energy intensive because high pressures (20 MPa) and high temperatures (500°C) are required [135]–[137]. Consequently, ammonia generation now comprises 2% of the

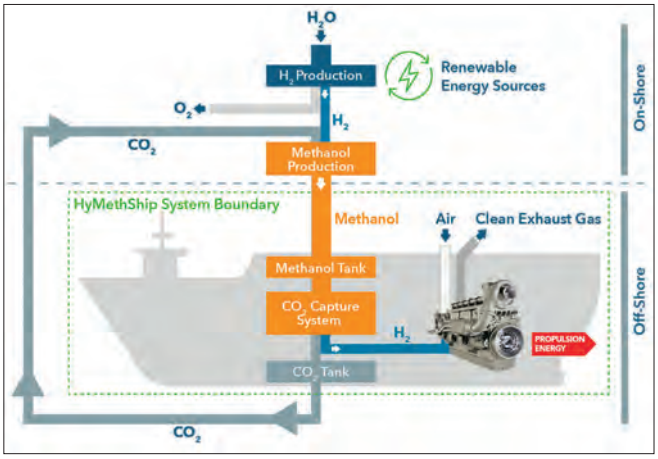

Fig. 4. HyMethShip with the engine running on H_2 and integrated in a methanol production system [133]

world's energy consumption and 1% of CO_2 emissions, making it the most energy-consuming chemical product [136]. Thus, expanding ammonia manufacturing for applications in maritime propulsion might lead to an enormous increase in emissions, unless the process can be decarbonised [130].

In dual-fuel mode, diesel fuel is mixed with ammonia fuel in order to start combustion and ammonia is partially broken to create a H_2 gas mixture. Even though ammonia can be utilised directly as a fuel in fuel cells under high temperature, the ammonia cracking process has broadened its applicability in internal combustion engines [138]. Furthermore, the ability to partially split ammonia allows internal combustion engines to operate more flexibly. In terms of maritime transportation, employing ammonia as a marine fuel in traditional marine engines is still being researched and developed, but with limited uses [139]. Indeed, the power which could be produced by a four-stroke diesel engine with ammonia acting as the fuel could match that produced by the same engine when fed conventional diesel fuel [140]. More interestingly, the world's largest diesel engine manufacturer has been developing a two-stroke diesel engine that would run on ammonia as its principal fuel [141]. According to the statistics released by the European Transportation and Environment Group, the quantity of ammonia needed for conventional marine engines aboard vessels would be in the region of 1230 MWh annually by 2050 [142]. Moreover, Bicer et al. [143] highlighted the overall environmental benefits of employing ammonia in traditional marine diesel engines without providing any particular results. Meanwhile, MAERSK [144] has stated, in a technical report, that ammonia could become one of the greatest positioned fuels for conventional marine power factories to achieve zero net emission goals.

LPG

It should be noted that the components of LPG are similar to those of LNG; however, unlike LNG, LPG liquefies at an ambient temperature and steady pressure, without the necessity for low-temperature cooling to –162°C. Apart from that, LPG has been demonstrated to be economically attractive, in terms of shorter payback periods [145], [146], lower investment expense,

and less vulnerability to fuel price variations [147], [148]. Furthermore, because most materials employed in fuel supply systems and LPG storage tanks are considered appropriate for ammonia storage, it is conceivable to reduce the compulsory methods for future conversion into ammonia fuel storage tanks [149]. There are significant commercial examples of its use in huge vessels utilising the ME-LGIP engine, built by MAN-ES and powered by LPG fuel [147], [150]. According to the World LPG Association, 71 LPG-fuelled ships were scheduled to be in operation by 2022. As for vessels of small and medium size, technological development and commercialisation is underway, with a focus on small boat outboard motors in the US and Europe. Despite this, the level of development of LPG engines that could be commercialised for ships of small to medium size, is still low [151]. In terms of volume, the small and medium vessel market is equivalent to the large vessel industry; however, it copes with significant technological challenges in the deployment of LPG in vessels, [152].

Nowadays, utilising LPG as an alternative fuel for internal combustion engines has gained popularity, despite the fact that LPG plays a trivial role in the marine industry and the shipping domain. The vast majority of diesel engines continue to use CNG and LNG as alternative fuels [153]. Nevertheless, since the 2020 IMO mandate was put into effect, LPG has received some attention because the use of LPG in marine engines powered by mono fuel lowered CO_2 emissions by roughly 10-20%, although a diesel-powered marine engine has greater thermal efficiency. Speaking of dual-fuel marine engines, it was noted that a small amount of diesel fuel is still utilised to start the ignition before switching to LPG combustion [146]. As reported, marine engines can operate using up to 3% diesel and 97% LPG fuel, resulting in low CO_2 emissions. More importantly, dual-fuel diesel engines were thought to be more efficient since they have excellent performance and dependability when compared to diesel engines that only run on diesel fuel. Wärtsilä and MAN undertook an investigation, employing LPG for tri-fuel engines that were powered by LNG, diesel, and LPG, according to a recent report. Furthermore, Wärtsilä conducted the first experiment on a container vessel with 7300 TEU. Even though these studies were preliminary, applying LPG could be a viable method for decreasing CO_2 emissions [154]. More intriguingly, the MAN B&W engine manufacturer developed a method to reduce CO_2 emissions by using both ammonia and LPG in marine engines [155]; they claim that a small adjustment to the LPG system for applying ammonia would be made, as depicted in Fig. 5.

ENERGY AND FUEL SAVINGS FOR SHIPS

As a general assumption, the relationship between the required power and the speed of the ship can be portrayed in a cubic function. For example, a 10% decrease in the ship's speed corresponds to a 27% drop in the amount of required power. Hence, it is logical to assume that by decreasing the design speed one could save on potential fuel consumption and CO_2 emissions from ships. Moreover, maintaining slower engine speeds can provide better propeller efficiency and further realise additional cost savings. As a potential strategy in reducing shipping emissions, ports can establish regulations and policy incentives to reduce vessel speeds upon entering ports that could result in lower fuel consumption and emissions [156]. Indeed, decreasing ship speed can result in an approximately 8-20% reduction in CO_2 emissions [157]. Other studies have also reached similar conclusions, in which reducing speed by as much as 10% and 20% leads to a potential fuel saving of 15-20% and 40%, respectively [158], [159]. A recent study by Ammar [160] investigated the effects of ship speed on the reduction of CO_2 emissions and the cost-effectiveness of a RO-RO cargo vessel. They indicated that approximately 78.39% of CO_2 emissions, with 287.6 $/ton CO_2 cost-effectiveness, could be reduced when

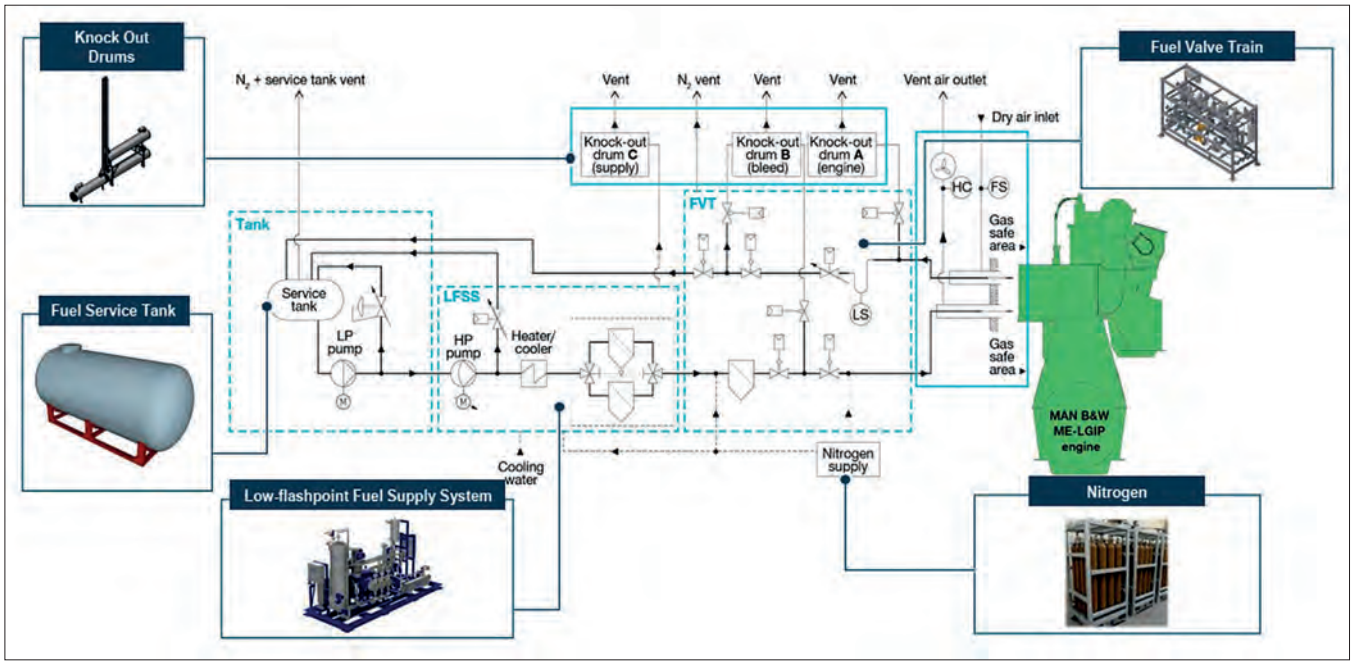

Fig. 5. Scheme of LPG and ammonia system for marine engine suggested by MAN B&W [155]

the ship speed decreased by 40%. In order for the optimisation strategy for ship speed to achieve minimum emissions in the port area, Chang et al. [161] presented a method to estimate the most suitable ship speed. They detected that 12 knots can be considered as the optimised speed to attain both low CO_2 emissions and cost-effectiveness, as shown in Fig. 6a. When combining the slow speed approach with power supply from the onshore grid, potential emission reductions can be as high as 71-91%, as ships are subjected to a 20 nautical mile speed limit within the designated area of the Port of Kaohsiung, Taiwan [161].

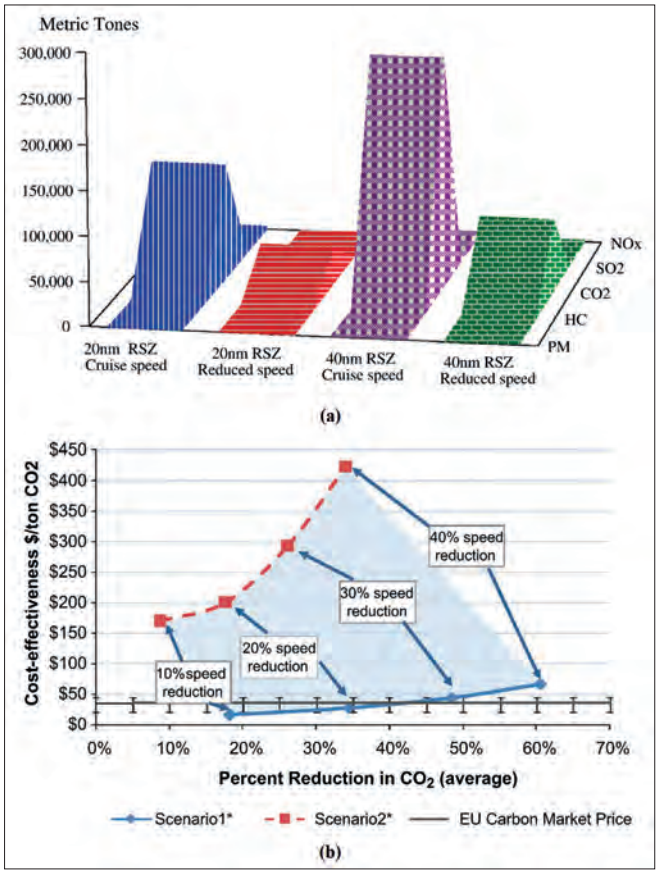

Fig. 6. (a) – Effects of the reduction of ship speed in the reduced speed-zone on emissions [161]; (b) – The marginal reduced-cost for CO_2 emissions using the change in total profit from the reduction of ship speed [162]

Moreover, Woo et al. [163] investigated the impacts of the slow steaming process on CO_2 emissions in liner shipping. They also found that more CO_2 emissions could be decreased in the case of reducing the voyage speed. More importantly, they found that around 90% CO_2 emissions could be reduced on the Asia/Europe route when the ship was operated within a speed range of 15-17 knots. Finally, the optimised result of voyage speed for CO_2 emission data and operating cost was 17.4 knots. According to Yun et al. [164], reducing speed from 24 to 8 knots could obtain up to 48.4% in CO_2 emissions reduction. However, the reduction of ship speed could negatively affect profit. Therefore, Corbett et al. [162] developed a profit-maximising function by incorporating costs relating to the ship speed reduction. They found that $150/ton for a fuel tax, combined with a reduction of ship speed of about 20–30%, resulted in a maximised reduction of CO_2 emissions of ships in US ports (Fig. 6b). In general, the reduction of speed, as well as the application of slow steaming to the ship operations in the port area, is considered a feasible approached to reduce CO_2 emissions. The effects of speed reduction or slow steaming of the ship on the decrease of CO_2 emissions in the port area are given in Table 2.

Tab. 2. Reduction level of CO_2 emissions in the port area by the application of speed reduction or slow steaming of the ship

Route/Ports	Applied strategies	CO_2 emission reduction level	References
Asia/North America	Slow steaming/ Speed reduction	29,400.10³ tons	[165], [166]
North Atlantic		5778.10³ tons	
Australasia/ Oceania		6275.10³ tons	
Latin America/ Caribbean		16,200.10³ tons	
Middle East/ South Asia		22,900.10³ tons	
Shanghai to Rotterdam		5000.10³ tons	[167]
Various ports		0 – 60%	[14], [30], [168]
Kaohsiung Port Taiwan		14% for the bulk vessel; 41% for container vessel	[169]
Port of Gothenburg		50 – 80%	[170]
North Europe–Asia		37%	[171]
Port of Rotterdam		6300 tons	[172]
Taichung Port		20 tons/1000 kW of ship power	[173]

Regarding the management of operational efficiency and emissions at the ship-port interface, measures are considered for the ports that ships are scheduled to arrive at and allowed to moor, also known as ports of call. Studies have provided comparisons of shipping GHG emissions to port emissions in the Port of Barcelona [174]: 63–78% of port emissions in the Port of Oslo [175], 61% in the Port of Gothenburg, 66% in the Port of Osaka, 8% in the Port of Sydney, 18% in the ports of Long Beach [176], and 53% of GHG emissions from the ships at berth in San Pedro Bay [177]. For UK ports, emissions from ships at berth have been observed to be ten times higher than emissions from port operations. Hence, it is suggested that ports should pay more attention and make more of an effort to reduce shipping emissions [178]. The potential of reducing shipping emissions depends on the frequency of port revisits for each vessel. The greater the number of ship calls for a particular ship, the greater the opportunity for emission reduction [176].

In most cases, the order of ships arriving and berthing at ports generally follows a first-come-first-served basis, which could lead to longer turnaround times and higher shipping emissions. In their study, Styhre et al. [176] examined four different ports and observed between 8-88% of GHG emissions from ships docking at these ports. Hence, they recommended reducing turnaround time as a potential strategy in achieving lower GHG

emissions from ports. According to Moon et al. [179], a 30% reduction in turnaround time can reduce CO_2 emissions by up to 37%. In contrast, when turnaround time increases by the same percentage, annual CO_2 emissions are observed to rise by 30.7%. In the case of Johnson et al. [180], their analysis showed that a decrease of 1-4 hours in turnaround time can yield 2-8% in energy savings. Additionally, supportive port policies can facilitate the transition toward shorter ship turnaround times in ports. Other factors that can influence turnaround time include CHE efficiency and mooring operation time [164], [178], [181], [182]. In their study, Navamuel et al. [183] found that the use of an automated mooring system could reduce up to 97% in CO_2 emissions from mooring, when analysing such activities in Ro-Ro/Pax terminals. In Piris et al. [184], automated mooring systems were proposed for the Santander port, which would reduce CO_2 emissions by as much as 76%. The application of automated mooring systems have also been found among major ports in European countries, including Finland, the Netherlands, and Denmark [183]. In another study, Gibbs et al. [178] examined the integration of virtual arrival assistance to enable the exchange of information and communication in optimising the accuracy of arrival and berthing time, vessel speed reduction, and slow steaming. The authors cited a maximum potential fuel saving of up to 27%, while the average figures could be between 12-20%. Several studies have also supported the use of 'virtual arrival' as an effective strategy in reducing shipping emissions [172], [182], [185], [186].

The major purpose of EEDI and the plan to manage vessel energy efficiency is to reduce CO_2 emissions discharged from maritime transportation [187], [188]. As shown in Table 1, the emissions reduction targets set by EEDI are listed by each implementation phase in the future. As required by EEDI standards, the IMO regulation requires ships to comply with a minimum of 20% emissions reduction by 2020, followed by a progressive increase to a 30% reduction target, beginning in 2025. Both the vessel's structural design and operations are subject to these stringent efficiency requirements [46]. Even though the majority of current energy-saving potential is held within the improvements in the structural design of the vessel body, more attention is needed to focus on the efficient operation of marine engines and the potential use of alternative low-carbon forms of energy to power ships. Indeed, the tendency towards the reduction of CO_2 emissions in the world's shipping industry was mostly driven by increasingly more stringent international rules and advancements in alternative fuel applications. Even though there is a long way to go to fully realise the practical implementations and wide adoption of zero or low-carbon fuel in powering marine vessel engines, the progress which has been made, in both the fuel and efficiency performance of current fossil-fuel-powered engines, is highly commendable and signals a positive future trend. Hence, advances in marine diesel engine efficiency improvements are critical in the current effort to achieve future emission reduction targets. It has been observed that, insofar as the EEDI served as a goal, it was not a particularly difficult one, since the EEDI achieved by newly-built vessels vastly exceeds the existing required EEDI, although they were not compulsory until 2025. This is particularly true of general cargo vessels and containerships [189], [190]. Notably, the obtained scores frequently do not represent the employment of novel electrical or mechanical technology; however, they could be obtained simply by optimising traditional machinery or changing the hull design [189], [191], [192]. It has been noted that the influence of EEDI on reducing shipping emissions was predicted to be minor: only a negligible change in CO_2 emissions has been identified between non-EEDI and EEDI scenarios [193]. More importantly, the reference years or mandated reductions need to become more ambitious, for the EEDI law to have a greater impact. Besides EEDI, technological approaches cover the technologies used on vessels to help boost their energy efficiency [14]. The techniques described in Table 3 are usually regarded as the key technological methods to boost ship energy efficiency and are covered by a number of documents.

Tab. 3. Relationship between technological solutions and fuel saving level [14], [30], [194]–[201]

Technological solutions	Potential fuel savings
Light materials	Max 10%
Slender hull design	Max 15%
Improvement devices for propulsion	Max 25%
Bulbous bow	Max 7%
Lubrication	Max 9%
Waste heat recovery	Max 4%

CHALLENGES AND OPPORTUNITIES

The use of clean fuels for maritime applications was either confined to certain vessel types or non-existent, which limited the evaluation of alternative fuels from an environmental perspective. Obviously, this reduced the credibility of the results obtained because acquiring emissions data for such an application was incredibly difficult. Remarkably, the widespread use of clean fuels, including ammonia and H_2, might be hampered or delayed because of problems associated with these relatively novel fuels' underdeveloped infrastructure and supply chains, particularly in the maritime industry; these include high production costs, requirements for special cryogenic storage, and high fuel transportation expenses.

It was necessary for HFO and MDO to be removed steadily and it was proposed that the advancement of vessels running on LNG, LPG ought to be cautious. Thus, power systems powered by H_2 and methanol could be regarded as a primary priority for future investigations and advancement, being the power resolutions for residential and short-sea shipping. Besides, double fuel compression ignition engines were recommended to be broadly applied in order to utilise H_2, methanol, biodiesels, or bioethanol as auxiliary and, after that, essential fuel. Indeed, certain flag, coastal and fuel-generating countries need to conduct more comprehensive life cycle evaluations of more alternative fuels as soon as possible. Infrastructure construction should consider the integrated use of raw materials and the recycled use of intermediate products, with the aim of producing by-products, alternative marine fuels and the cogeneration of power, heating

and cooling. It was noted that this was a significant way to lower manufacturing costs, one of the main factors limiting the widespread use of alternative marine fuels. Moreover, increasing fossil-free energy (namely solar, wind, and nuclear) in the global energy mix and increasing carbon capture, use and storage in the industrial sector on land, could directly mitigate the world's carbon emissions as well as alleviate lifecycle emissions and alternative fuel expenses. More importantly, future research assessing renewable sources of energy consisting of wind and solar power could assist in developing technological improvements to handle the obstacles that restrict the intense employment of the aforementioned energies, like energy storage resolutions, which might cause a decrease in GHG emissions released from maritime transport. Regarding the maritime community, agreement is more potent than divergent and, besides this, decisive action, with respect to the best potential methods, was more essential (as early as possible) compared to the option of waiting or hesitating. Likewise, legal frameworks at local and global scales, as well as financial incentives, need to be passed prior to other plans and, more significantly, countrywide or local regulations and pilot tasks should be prioritised.

CONCLUSIONS AND RECOMMENDATIONS

This review article provides a general overview of various approaches for lowering CO_2 emissions from ships through thorough consideration of distinct low-carbon fuels, alternative clean renewable sources of energy, and supporting regulatory frameworks. Moreover, further implementation of intelligent energy management systems, energy conversion, consumption monitoring, and battery storage could promote the potential for energy savings.

Through powerful control and operational practices aimed towards a shipping industry that was low-carbon and sustainable, ship owners could obtain effective energy, emissions mitigation and expense savings. The further deployment of clever electricity control systems, electricity transformation, battery storage, and consumption tracking could improve energy savings. Remarkably, a systematic enhancement was needed in shipping enterprises to attain energy savings. The guidelines and regulations that did not focus on the goal of decreasing emissions and obtaining electricity performance needed changing. In fact, biofuels became an appealing choice, when combined with other fuels, owing to their outstanding commercial potential. Nonetheless, the large variety of biofuels available resulted in great diversity in emissions, prices, and usability of the resources mentioned above. In spite of the numerous benefits of biodiesel, some challenges still exist, including higher expenses of generation and feedstock, cold flow features, material compatibility, fuel stability, and a shortage of marine-grade criteria. Hence, in the preceding section, effective techniques and feasible resolutions were presented to achieve the aim of this alternative fuel utilisation in the maritime sector. Also, the introduction of a novel supply of feedstock from second and third generation bio-based diesel could alleviate generation expenses and fuel economy. Recently, there has been a surge in research into novel sources, including algae and waste oil. Additionally, formal mandates from governmental and international organizations, like the IMO, could support and improve biodiesel applications in the maritime industry. Indeed, H_2 is still a viable future bunker fuel choice, since it produces more energy per unit mass, in comparison with traditional marine fuel, while emitting fewer GHGs. Nonetheless, several barriers, such as manufacturing expenses and the particular handling needs for storage and transportation, were observed, preventing the extensive use of H_2 fuel. More interestingly, ammonia is thought to be a useful H_2 storage medium because it has a greater volumetric H_2 density when compared to liquid H_2. Nevertheless, the quantity of GHG emissions related to the current ammonia manufacturing method is significant; alternative revolutionary technologies, including thermochemical processes and solid-state synthesis, are still being researched and developed. Because of their low volumetric energy densities, it was suggested that H_2, compressed natural gas, and ammonia were only suitable for domestic and short-distance transportation, while liquefied natural gas was preferred for long-distance shipping, when taking economic factors into account. In addition, one benefit of utilising ammonia fuel is that, with simple adjustments, it could readily be compatible with turbines, engines, and burners. Not only H_2 but ammonia also shows promise for totally replacing hydrocarbon fuels. In terms of both technological and economic perspectives, renewable methanol utilised in combination with a diesel engine, provided the best future world's shipping possibility. H_2 and ammonia are known as viable short-sea fuels; nonetheless, the technological routes that combine H_2 with low-temperature fuel cells and ammonia with diesel engines outperform those combining H_2 and diesel engines or ammonia with high temperature fuel cells. Obviously, the evolution of different technological paths and combinations of fuels and propulsion systems is unavoidable, and types of ships and shipping routes are considered critical elements in the majority of appropriate combinations between fuel and technology.

REFERENCES

1. Shell and Deloitte, "Decarbonising Shipping: All Hands on Deck." Shell International BV, 2020.

2. Z. Yang, Q. Tan, and P. Geng, "Combustion and Emissions Investigation on Low-Speed Two-Stroke Marine Diesel Engine with Low Sulfur Diesel Fuel," *Polish Marit. Res.*, vol. 26, no. 1, 2019, doi: 10.2478/pomr-2019-0017.

3. Z. Korczewski, "Energy and Emission Quality Ranking of Newly Produced Low-Sulphur Marine Fuels," *Polish Marit. Res.*, vol. 29, no. 4, pp. 77–87, Dec. 2022, doi: 10.2478/pomr-2022-0045.

4. O. Konur, C. O. Colpan, and O. Y. Saatcioglu, "A comprehensive review on organic Rankine cycle systems used as waste heat recovery technologies for marine applications," *Energy Sources, Part A Recover. Util. Environ. Eff.*, vol. 44, no. 2, pp. 4083–4122, Jun. 2022, doi: 10.1080/15567036.2022.2072981.

5. E. Abdelhameed and H. Tashima, "Experimental investigation on methane inert gas dilution effect on marine gas diesel engine performance and emissions," *Energy Sources, Part A Recover. Util. Environ. Eff.*, vol. 44, no. 2, pp. 3584–3596, Jun. 2022, doi: 10.1080/15567036.2022.2067603.

6. G. Mallouppas and E. A. Yfantis, "Decarbonization in Shipping Industry: A Review of Research, Technology Development, and Innovation Proposals," *J. Mar. Sci. Eng.*, vol. 9, no. 4, p. 415, Apr. 2021, doi: 10.3390/jmse9040415.

7. IMO, "Fourth IMO GHG study 2020," 2020.

8. A. Romano and Z. Yang, "Decarbonisation of shipping: A state of the art survey for 2000–2020," *Ocean Coast. Manag.*, vol. 214, p. 105936, Nov. 2021, doi: 10.1016/j.ocecoaman.2021.105936.

9. B. Bradley and R. Hoyland, "Decarbonisation and Shipping: International Maritime Organization Ambitions and Measures," 2020. .

10. A. T. Hoang and V. V. Pham, "A review on fuels used for marine diesel engines," *J. Mech. Eng. Res. Dev.*, vol. 41, no. 4, pp. 22–32, 2018.

11. International Chamber of Shipping, "Environmental Performance: IMO Agreement on Technical Regulations to Reduce Ships' CO_2," 2017. .

12. Z. Wan, A. el Makhloufi, Y. Chen, and J. Tang, "Decarbonizing the international shipping industry: Solutions and policy recommendations," *Mar. Pollut. Bull.*, vol. 126, pp. 428–435, Jan. 2018, doi: 10.1016/j.marpolbul.2017.11.064.

13. O. Cherednichenko, S. Serbin, M. Tkach, J. Kowalski, and D. Chen, "Mathematical Modelling of Marine Power Plants with Thermochemical Fuel Treatment," *Polish Marit. Res.*, vol. 29, no. 3, pp. 99–108, Sep. 2022, doi: 10.2478/pomr-2022-0030.

14. R. A. Halim, L. Kirstein, O. Merk, and L. M. Martinez, "Decarbonization pathways for international maritime transport: A model-based policy impact assessment," *Sustain.*, 2018, doi: 10.3390/su10072243.

15. IMO, "Third IMO GHG Study 2014–Executive Summary and Final Report," London, UK, 2015.

16. G. Labeckas, S. Slavinskas, J. Rudnicki, and R. Zadrąg, "The Effect of Oxygenated Diesel-N-Butanol Fuel Blends on Combustion, Performance, and Exhaust Emissions of a Turbocharged CRDI Diesel Engine," *Polish Marit. Res.*, vol. 25, no. 1, pp. 108–120, Mar. 2018, doi: 10.2478/pomr-2018-0013.

17. A. T. Hoang, V. D. Tran, V. H. Dong, and A. T. Le, "An experimental analysis on physical properties and spray characteristics of an ultrasound-assisted emulsion of ultra-low-sulphur diesel and Jatropha-based biodiesel," *J. Mar. Eng. Technol.*, vol. 21, no. 2, pp. 73–81, Mar. 2022, doi: 10.1080/20464177.2019.1595355.

18. H. P. Nguyen, P. Q. P. Nguyen, D. K. P. Nguyen, V. D. Bui, and D. T. Nguyen, "Application of IoT Technologies in Seaport Management," *JOIV Int. J. Informatics Vis.*, vol. 7, no. 1, p. 228, Mar. 2023, doi: 10.30630/joiv.7.1.1697.

19. B. Comer, "Maritime Shipping: Black Carbon Issues at the International Maritime Organization," 2021, pp. 13–25.

20. A. Astito and S. Hamdoune, "Estimating carbon dioxide and particulate matter emissions from ships using automatic identification system data," *Int. J. Comput. Appl.*, vol. 88, no. 6, 2014.

21. A. S. Alamoush, A. I. Ölçer, and F. Ballini, "Ports' role in shipping decarbonisation: A common port incentive scheme for shipping greenhouse gas emissions reduction," *Clean. Logist. Supply Chain*, vol. 3, p. 100021, Mar. 2022, doi: 10.1016/j.clscn.2021.100021.

22. S. Vakili, A. I. Ölçer, A. Schönborn, F. Ballini, and A. T. Hoang, "Energy-related clean and green framework for shipbuilding community towards zero-emissions: A strategic analysis from concept to case study," *Int. J. Energy Res.*, vol. 46, no. 14, pp. 20624–20649, Nov. 2022, doi: 10.1002/er.7649.

23. O. B. Inal, B. Zincir, and C. Deniz, "Investigation on the decarbonization of shipping: An approach to hydrogen and ammonia," *Int. J. Hydrogen Energy*, vol. 47, no. 45, pp. 19888–19900, May 2022, doi: 10.1016/j.ijhydene.2022.01.189.

24. L. Mihanović, M. Jelić, G. Radica, and N. Račić, "EXPERIMENTAL INVESTIGATION OF MARINE ENGINE EXHAUST EMISSIONS," *Energy Sources, Part A Recover. Util. Environ. Eff.*, pp. 1–14, Dec. 2021, doi: 10.1080/15567036.2021.2013344.

25. V. D. Tran, A. T. Le, and A. T. Hoang, "An Experimental Study on the Performance Characteristics of a Diesel Engine Fueled with ULSD-Biodiesel Blends.," *Int. J. Renew. Energy Dev.*, vol. 10, no. 2, pp. 183–190, 2021.

26. A. Al-Enazi, E. C. Okonkwo, Y. Bicer, and T. Al-Ansari, "A review of cleaner alternative fuels for maritime transportation," *Energy Reports*, vol. 7, pp. 1962–1985, Nov. 2021, doi: 10.1016/j.egyr.2021.03.036.

27. J. D. Ampah, A. A. Yusuf, S. Afrane, C. Jin, and H. Liu, "Reviewing two decades of cleaner alternative marine fuels: Towards IMO's decarbonization of the maritime transport sector," *J. Clean. Prod.*, vol. 320, p. 128871, Oct. 2021, doi: 10.1016/j.jclepro.2021.128871.

28. A. D. Korberg, S. Brynolf, M. Grahn, and I. R. Skov,

"Techno-economic assessment of advanced fuels and propulsion systems in future fossil-free ships," *Renew. Sustain. Energy Rev.*, vol. 142, p. 110861, May 2021, doi: 10.1016/j.rser.2021.110861.

29. W. Zeńczak and A. K. Gromadzińska, "Preliminary Analysis of the Use of Solid Biofuels in a Ship's Power System," *Polish Marit. Res.*, vol. 27, no. 4, pp. 67–79, Dec. 2020, doi: 10.2478/pomr-2020-0067.

30. E. A. Bouman, E. Lindstad, A. I. Rialland, and A. H. Strømman, "State-of-the-art technologies, measures, and potential for reducing GHG emissions from shipping – A review," *Transp. Res. Part D Transp. Environ.*, vol. 52, pp. 408–421, 2017, doi: 10.1016/j.trd.2017.03.022.

31. H. Zeraatgar and M. H. Ghaemi, "The Analysis of Overall Ship Fuel Consumption in Acceleration Manoeuvre Using Hull-Propeller-Engine Interaction Principles and Governor Features," *Polish Marit. Res.*, vol. 26, no. 1, 2019, doi: 10.2478/pomr-2019-0018.

32. P. N. Hoffmann, M. S. Eide, and Ø. Endresen, "Effect of proposed CO 2 emission reduction scenarios on capital expenditure," *Marit. Policy Manag.*, vol. 39, no. 4, pp. 443–460, Jul. 2012, doi: 10.1080/03088839.2012.690081.

33. A. B. Jaffe and R. N. Stavins, "The energy-efficiency gap What does it mean?," *Energy Policy*, vol. 22, no. 10, pp. 804–810, Oct. 1994, doi: 10.1016/0301-4215(94)90138-4.

34. H. Johnson and K. Andersson, "The energy efficiency gap in shipping – Barriers to improvement," *Int. Assoc. Marit. Econ. Annu. Conf.*, 2011.

35. K. Rudzki, P. Gomulka, and A. T. Hoang, "Optimization Model to Manage Ship Fuel Consumption and Navigation Time," *Polish Marit. Res.*, vol. 29, no. 3, pp. 141–153, Sep. 2022, doi: 10.2478/pomr-2022-0034.

36. M. Feili, M. Hasanzadeh, H. Ghaebi, and E. Abdi Aghdam, "Comprehensive analysis of a novel cooling/electricity cogeneration system driven by waste heat of a marine diesel engine," *Energy Sources, Part A Recover. Util. Environ. Eff.*, vol. 44, no. 3, pp. 7331–7346, Sep. 2022, doi: 10.1080/15567036.2022.2108167.

37. Ø. Buhaug et al., "Second IMO Greenhouse Gas Study 2009," *Int. Marit. Organ.*, 2009.

38. M. S. Eide, T. Longva, P. Hoffmann, Ø. Endresen, and S. B. Dalsøren, "Future cost scenarios for reduction of ship CO 2 emissions," *Marit. Policy Manag.*, vol. 38, no. 1, pp. 11–37, Jan. 2011, doi: 10.1080/03088839.2010.533711.

39. J. Faber *et al.*, "Technical support for European action to reducing Greenhouse Gas Emissions from international maritime transport," 2009.

40. E. C. EC, "White Paper: Roadmap to a Single European Transport Area–Towards a Competitive and Resource Efficient Transport System," *COM (2011) 144 final [online]*. European Commission Brussels, 2011.

41. Z. Bazari and T. Longva, "Assessment of IMO Mandated Energy Efficiency Measures for International Shipping," 2011.

42. A. Mellin and H. Rydhed, "Swedish ports' attitudes towards regulations of the shipping sector's emissions of CO 2," *Marit. Policy Manag.*, vol. 38, no. 4, pp. 437–450, Jul. 2011, doi: 10.1080/03088839.2011.588261.

43. H. P. Nguyen, P. Q. P. Nguyen, and T. P. Nguyen, "Green Port Strategies in Developed Coastal Countries as Useful Lessons for the Path of Sustainable Development: A case study in Vietnam," Int. J. Renew. Energy Dev., vol. 11, no. 4, pp. 950–962, Nov. 2022, doi: 10.14710/ijred.2022.46539.

44. K. Takasaki, "CO2 Reduction from Main Engine," *J. Japan Inst. Mar. Eng. Eng.*, 2015, doi: 10.5988/jime.50.198.

45. L. Čampara, N. Hasanspahić, and S. Vujičić, "Overview of MARPOL ANNEX VI regulations for prevention of air pollution from marine diesel engines," *SHS Web Conf.*, vol. 58, p. 01004, Dec. 2018, doi: 10.1051/shsconf/20185801004.

46. V. V. Pham, A. T. Hoang, and H. C. Do, "Analysis and evaluation of database for the selection of propulsion systems for tankers," 2020, doi: 10.1063/5.0007655.

47. N. L. Trivyza, A. Rentizelas, and G. Theotokatos, "A Comparative Analysis of EEDI Versus Lifetime CO2 Emissions," *J. Mar. Sci. Eng.*, vol. 8, no. 1, p. 61, Jan. 2020, doi: 10.3390/jmse8010061.

48. Hwang, Jeong, Jung, Kim, and Zhou, "Life Cycle Assessment of LNG Fueled Vessel in Domestic Services," *J. Mar. Sci. Eng.*, vol. 7, no. 10, p. 359, Oct. 2019, doi: 10.3390/jmse7100359.

49. M. H. Ghaemi and H. Zeraatgar, "Impact of Propeller Emergence on Hull, Propeller, Engine, and Fuel Consumption Performance in Regular Head Waves," *Polish Marit. Res.*, vol. 29, no. 4, pp. 56–76, Dec. 2022, doi: 10.2478/pomr-2022-0044.

50. "Brief for Eu Member States," pp. 1–9, 2013.

51. GloMEEP, "Ship Emissions Tool Kit (Guide No. 3), Development of a national Ship emissions reduction strategy," 2018.

52. J. Z. Goldstein and J. P. George, "REDUCING NAVAL FOSSIL FUEL CONSUMPTION AT SEA IN THE 21ST CENTURY." Monterey, CA; Naval Postgraduate School, 2021.

53. V. V. Pham and A. T. Hoang, "Technological perspective for reducing emissions from marine engines," *Int. J. Adv. Sci.*

Eng. Inf. Technol., vol. 9, no. 6, pp. 1989–2000, 2019, doi: 10.18517/ijaseit.9.6.10429.

54. K. Rudzki and W. Tarelko, "A decision-making system supporting selection of commanded outputs for a ship's propulsion system with a controllable pitch propeller," *Ocean Eng.*, 2016, doi: 10.1016/j.oceaneng.2016.09.018.

55. J. Herdzik, "Decarbonization of Marine Fuels—The Future of Shipping," *Energies*, vol. 14, no. 14, p. 4311, Jul. 2021, doi: 10.3390/en14144311.

56. A. Foretich, G. G. Zaimes, T. R. Hawkins, and E. Newes, "Challenges and opportunities for alternative fuels in the maritime sector," *Marit. Transp. Res.*, vol. 2, p. 100033, 2021, doi: 10.1016/j.martra.2021.100033.

57. H. Wang, D. Liu, and G. Dai, "Review of maritime transportation air emission pollution and policy analysis," *J. Ocean Univ. China*, vol. 8, no. 3, pp. 283–290, Sep. 2009, doi: 10.1007/s11802-009-0283-6.

58. S. E. Tanzer, J. Posada, S. Geraedts, and A. Ramírez, "Lignocellulosic marine biofuel: Technoeconomic and environmental assessment for production in Brazil and Sweden," *J. Clean. Prod.*, vol. 239, p. 117845, Dec. 2019, doi: 10.1016/j.jclepro.2019.117845.

59. N. Pavlenko, B. Comer, Y. Zhou, N. Clark, and D. Rutherford, "The climate implications of using LNG as a marine fuel," *Swedish Environ. Prot. Agency Stock. Sweden*, 2020.

60. TNO, "Environmental and Economic aspects of using LNG as a fuel for shipping in The Netherlands. Nederlandse Organisatie voor Toegepast Natuurwetenschappelijk Onderzoek (TNO) Report," *Delft, TNO*, vol. 48, no. July 2015, pp. 1–48, 2011.

61. D. Lowell, H. Wang, and N. Lutsey, "Assessment of the fuel cycle impact of liquefied natural gas as used in international shipping," *Int. Counc. Clean Transp.*, 2013.

62. S. Brynolf, E. Fridell, and K. Andersson, "Environmental assessment of marine fuels: liquefied natural gas, liquefied biogas, methanol and bio-methanol," *J. Clean. Prod.*, vol. 74, pp. 86–95, 2014.

63. R. Zhao et al., "A Numerical and Experimental Study of Marine Hydrogen–Natural Gas–Diesel Tri–Fuel Engines," *Polish Marit. Res.*, vol. 27, no. 4, pp. 80–90, Dec. 2020, doi: 10.2478/pomr-2020-0068.

64. J. Li, Y. Han, G. Mao, and P. Wang, "Optimization of exhaust emissions from marine engine fueled with LNG/diesel using response surface methodology," *Energy Sources, Part A Recover. Util. Environ. Eff.*, vol. 42, no. 12, pp. 1436–1448, Jun. 2020, doi: 10.1080/15567036.2019.1604859.

65. M. A. Fun-sang Cepeda, N. N. Pereira, S. Kahn, and J.-D. Caprace, "A review of the use of LNG versus HFO in maritime industry," *Mar. Syst. Ocean Technol.*, vol. 14, no. 2–3, pp. 75–84, Sep. 2019, doi: 10.1007/s40868-019-00059-y.

66. P. Balcombe, I. Staffell, I. G. Kerdan, J. F. Speirs, N. P. Brandon, and A. D. Hawkes, "How can LNG-fuelled ships meet decarbonisation targets? An environmental and economic analysis," *Energy*, vol. 227, p. 120462, Jul. 2021, doi: 10.1016/j.energy.2021.120462.

67. A. Bernatik, P. Senovsky, and M. Pitt, "LNG as a potential alternative fuel – Safety and security of storage facilities," *J. Loss Prev. Process Ind.*, vol. 24, no. 1, pp. 19–24, Jan. 2011, doi: 10.1016/j.jlp.2010.08.003.

68. P. Balcombe et al., "How to decarbonise international shipping: Options for fuels, technologies and policies," *Energy Conversion and Management*. 2019, doi: 10.1016/j.enconman.2018.12.080.

69. D. Thrän *et al.*, "Biomethane-status and factors affecting market development and trade," 2014.

70. E. Wetterlund, "System studies of forest-based biomass gasification." Linköping University Electronic Press, 2012.

71. V. A. dos Santos, P. Pereira da Silva, and L. M. V. Serrano, "The Maritime Sector and Its Problematic Decarbonization: A Systematic Review of the Contribution of Alternative Fuels," *Energies*, vol. 15, no. 10, p. 3571, May 2022, doi: 10.3390/en15103571.

72. A. A. Banawan, M. M. El Gohary, and I. S. Sadek, "Environmental and economical benefits of changing from marine diesel oil to natural-gas fuel for short-voyage high-power passenger ships," *Proc. Inst. Mech. Eng. Part M J. Eng. Marit. Environ.*, 2010, doi: 10.1243/14750902JEME181.

73. M. Anderson, K. Salo, and E. Fridell, "Particle- and Gaseous Emissions from an LNG Powered Ship," *Environ. Sci. Technol.*, 2015, doi: 10.1021/acs.est.5b02678.

74. J. Li, B. Wu, and G. Mao, "Research on the performance and emission characteristics of the LNG-diesel marine engine," *J. Nat. Gas Sci. Eng.*, 2015, doi: 10.1016/j.jngse.2015.09.036.

75. N. R. Ammar, "Environmental and cost-effectiveness comparison of dual fuel propulsion options for emissions reduction onboard lng carriers," *Brodogradnja*, 2019, doi: 10.21278/brod70304.

76. G. P. Gerilla, K. Teknomo, and K. Hokao, "Environmental assessment of international transportation of products," *J. East. Asia Soc. Transp. Stud.*, vol. 6, pp. 3167–3182, 2005.

77. M. M. Elgohary, I. S. Seddiek, and A. M. Salem, "Overview of

alternative fuels with emphasis on the potential of liquefied natural gas as future marine fuel," *Proc. Inst. Mech. Eng. Part M J. Eng. Marit. Environ.*, 2015, doi: 10.1177/1475090214522778.

78. I. Ø. Tvedten and S. Bauer, "Retrofitting towards a greener marine shipping future: Reassembling ship fuels and liquefied natural gas in Norway," *Energy Res. Soc. Sci.*, vol. 86, p. 102423, 2022.

79. O. Schinas and M. Butler, "Feasibility and commercial considerations of LNG-fueled ships," *Ocean Eng.*, 2016, doi: 10.1016/j.oceaneng.2016.04.031.

80. F. Burel, R. Taccani, and N. Zuliani, "Improving sustainability of maritime transport through utilization of Liquefied Natural Gas (LNG) for propulsion," *Energy*, 2013, doi: 10.1016/j.energy.2013.05.002.

81. M. Acciaro, "Real option analysis for environmental compliance: LNG and emission control areas," *Transp. Res. Part D Transp. Environ.*, vol. 28, pp. 41–50, May 2014, doi: 10.1016/j.trd.2013.12.007.

82. T. Iannaccone, G. Landucci, A. Tugnoli, E. Salzano, and V. Cozzani, "Sustainability of cruise ship fuel systems: Comparison among LNG and diesel technologies," *J. Clean. Prod.*, vol. 260, p. 121069, 2020.

83. H. Hadiyanto, A. P. Aini, W. Widayat, K. Kusmiyati, A. Budiman, and A. Roesyadi, "Multi-Feedstocks Biodiesel Production from Esterification of Calophyllum inophyllum Oil, Castor Oil, Palm Oil and Waste Cooking Oil," *Int. J. Renew. Energy Dev.*, vol. 9, no. 1, pp. 119–123, Feb. 2020, doi: 10.14710/ijred.9.1.119-123.

84. A. Kolakoti, M. Setiyo, and M. L. Rochman, "A green heterogeneous catalyst production and characterization for biodiesel production using RSM and ANN approach," *Int. J. Renew. Energy Dev.*, vol. 11, no. 3, pp. 703–712, Aug. 2022, doi: 10.14710/ijred.2022.43627.

85. S. Mekhilef, S. Siga, and R. Saidur, "A review on palm oil biodiesel as a source of renewable fuel," *Renew. Sustain. Energy Rev.*, vol. 15, no. 4, pp. 1937–1949, May 2011, doi: 10.1016/j.rser.2010.12.012.

86. T. Kalyani, L. S. V. Prasad, and A. Kolakoti, "Biodiesel Production from a Naturally Grown Green Algae Spirogyra Using Heterogeneous Catalyst: An Approach to RSM Optimization Technique," *Int. J. Renew. Energy Dev.*, vol. 12, no. 2, pp. 300–312, Mar. 2023, doi: 10.14710/ijred.2023.50065.

87. P. Sharma et al., "Experimental investigations on efficiency and instability of combustion process in a diesel engine fueled with ternary blends of hydrogen peroxide additive/biodiesel/diesel," *Energy Sources, Part A Recover. Util. Environ. Eff.*, vol. 44, no. 3, pp. 5929–5950, Sep. 2022, doi: 10.1080/15567036.2022.2091692.

88. A. T. Hoang, "Combustion behavior, performance and emission characteristics of diesel engine fuelled with biodiesel containing cerium oxide nanoparticles: A review," *Fuel Process. Technol.*, vol. 218, p. 106840, Jul. 2021, doi: 10.1016/j.fuproc.2021.106840.

89. A. T. Hoang et al., "Rice bran oil-based biodiesel as a promising renewable fuel alternative to petrodiesel: A review," *Renew. Sustain. Energy Rev.*, 2020, doi: 10.1016/j.rser.2020.110204.

90. M. H. Jayed, H. H. Masjuki, R. Saidur, M. A. Kalam, and M. I. Jahirul, "Environmental aspects and challenges of oilseed produced biodiesel in Southeast Asia," *Renew. Sustain. Energy Rev.*, vol. 13, no. 9, pp. 2452–2462, Dec. 2009, doi: 10.1016/j.rser.2009.06.023.

91. Y. S. M. Altarazi *et al.*, "Effects of biofuel on engines performance and emission characteristics: A review," *Energy*, vol. 238, p. 121910, Jan. 2022, doi: 10.1016/j.energy.2021.121910.

92. S. N *et al.*, "Poultry fat biodiesel as a fuel substitute in diesel-ethanol blends for DI-CI engine: Experimental, modeling and optimization," *Energy*, vol. 270, p. 126826, May 2023, doi: 10.1016/j.energy.2023.126826.

93. N. Jeyakumar et al., "Using Pithecellobium Dulce seed-derived biodiesel combined with Groundnut shell nanoparticles for diesel engines as a well-advised approach toward sustainable waste-to-energy management," Fuel, vol. 337, p. 127164, Apr. 2023, doi: 10.1016/j.fuel.2022.127164.

94. K. Kolwzan and M. Narewski, "Alternative fuels for marine applications," *Latv. J. Chem.*, vol. 51, no. 4, p. 398, 2012.

95. AWRI, "The feasibility of fuelling the research vessel D.J. Angus and W.G. Jackson with biodiesel," 2003.

96. C. Lagacé, "Biodiesel demonstration and assessment for tour boats in the old port of Montréal and Lachine canal national historic site," 2005.

97. C.-W. C. Hsieh and C. Felby, "Biofuels for the marine shipping sector," *IEA Bioenergy*, p. 86, 2017.

98. T. C. Holmseth, "Earthrace sets new world record," *Biodiesel magazine*, 2008. .

99. C. W. Mohd Noor, M. M. Noor, and R. Mamat, "Biodiesel as alternative fuel for marine diesel engine applications: A review," *Renew. Sustain. Energy Rev.*, vol. 94, pp. 127–142, Oct. 2018, doi: 10.1016/j.rser.2018.05.031.

100. MAN Diesel, "MAN B&W Stationary Engines: Alternative Fuel," 2010.

101. A. Imran, M. Varman, H. H. Masjuki, and M. A. Kalam, "Review on alcohol fumigation on diesel engine: A viable

alternative dual fuel technology for satisfactory engine performance and reduction of environment concerning emission," *Renewable and Sustainable Energy Reviews*. 2013, doi: 10.1016/j.rser.2013.05.070.

102. T. T. Truong, X. P. Nguyen, V. V. Pham, V. V. Le, A. T. Le, and V. T. Bui, "Effect of alcohol additives on diesel engine performance: a review," *Energy Sources, Part A Recover. Util. Environ. Eff.*, pp. 1–25, Dec. 2021, doi: 10.1080/15567036.2021.2011490.

103. D. Boopathi, S. Thiyagarajan, A. Sonthalia, P. Parthiban, S. Devanand, and V. Edwin Geo, "Effect of methanol fumigation on performance and emission characteristics in a waste cooking oil-fuelled single cylinder CI engine," *Energy Sources, Part A Recover. Util. Environ. Eff.*, vol. 41, no. 9, pp. 1088–1096, May 2019, doi: 10.1080/15567036.2018.1539142.

104. S. Mayer, J. Sjöholm, T. Murakami, K. Shimada, and N. Kjemtrup, "Performance and emission results from the MAN B&W LGI Low-Speed Engine Operating on Methanol," in *CIMAC Congress*, 2016, pp. 6–10.

105. T. Stojcevski, D. Jay, and L. Vicenzi, "Operation experience of world's first methanol engine in a ferry installation," in *Proceedings of the 28th CIMAC World Congress, Helsinki, Finland*, 2016, pp. 6–9.

106. M. Svanberg, J. Ellis, J. Lundgren, and I. Landälv, "Renewable methanol as a fuel for the shipping industry," *Renew. Sustain. Energy Rev.*, vol. 94, pp. 1217–1228, 2018.

107. *Technology and Applications of Autonomous Underwater Vehicles*. 2002.

108. P. Gilbert, C. Walsh, M. Traut, U. Kesieme, K. Pazouki, and A. Murphy, "Assessment of full life-cycle air emissions of alternative shipping fuels," *J. Clean. Prod.*, 2018, doi: 10.1016/j.jclepro.2017.10.165.

109. DNV GL, "Methanol as Marine Fuel: Environmental Benifits, Technology Readiness, and Economic Feasibility," 2016.

110. R. Song, J. Liu, L. Wang, and S. Liu, "Performance and Emissions of a Diesel Engine Fuelled with Methanol," *Energy & Fuels*, vol. 22, no. 6, pp. 3883–3888, Nov. 2008, doi: 10.1021/ef800492r.

111. T. Stojcevski, "Wärtsilä. Methanol as Engine Fuel: Challenges and Opportunities," 2016.

112. MAN Energy Solutions, "The Methanol-fuelled MAN B&W LGIM Engine. Application, service experience and latest development of the ME-LGIM engine.," 2021.

113. M. Túner, P. Aakko-Saksa, and P. Molander, "Engine Technology, Research, and Development for Methanol in Internal Combustion Engines: SUMMETH-Sustainable Marine Methanol, Deliverable D3. 1," 2018.

114. Bunkerworld, "Billion Miles targets methanol-fueled boats in Singapore from 2018," 2017.

115. J. Ellis and K. Tanneberger, "Study on the use of ethyl and methyl alcohol as alternative fuels in shipping," *Eur. Marit. Saf. Agency*, 2015.

116. I. A. Fernández, M. R. Gómez, J. R. Gómez, and L. M. López-González, "Generation of H2 on Board Lng Vessels for Consumption in the Propulsion System," *Polish Marit. Res.*, vol. 27, no. 1, 2020, doi: 10.2478/pomr-2020-0009.

117. A. T. Hoang and V. V. Pham, "A study on a solution to reduce emissions by using hydrogen as an alternative fuel for a diesel engine integrated exhaust gas recirculation," in *AIP Conference Proceedings*, 2020, vol. 2235, no. 1, p. 20035.

118. S. Öberg, M. Odenberger, and F. Johnsson, "Exploring the competitiveness of hydrogen-fueled gas turbines in future energy systems," *Int. J. Hydrogen Energy*, vol. 47, no. 1, pp. 624–644, Jan. 2022, doi: 10.1016/j.ijhydene.2021.10.035.

119. S. Verma, A. Suman, L. M. Das, S. C. Kaushik, and S. K. Tyagi, "A renewable pathway towards increased utilization of hydrogen in diesel engines," *Int. J. Hydrogen Energy*, vol. 45, no. 8, pp. 5577–5587, Feb. 2020, doi: 10.1016/j.ijhydene.2019.05.213.

120. A. Mohammadi, M. Shioji, Y. Nakai, W. Ishikura, and E. Tabo, "Performance and combustion characteristics of a direct injection SI hydrogen engine," *Int. J. Hydrogen Energy*, 2007, doi: 10.1016/j.ijhydene.2006.06.005.

121. M. M. Roy, E. Tomita, N. Kawahara, Y. Harada, and A. Sakane, "Comparison of performance and emissions of a supercharged dual-fuel engine fueled by hydrogen and hydrogen-containing gaseous fuels," Int. J. Hydrogen Energy, 2011, doi: 10.1016/j.ijhydene.2011.03.070.

122. B. Gopalakrishnan, N. Khanna, and D. Das, "Dark-Fermentative Biohydrogen Production," in *Biohydrogen*, Elsevier, 2019, pp. 79–122.

123. T. X. Nguyen-Thi and T. M. T. Bui, "Effects of Injection Strategies on Mixture Formation and Combustion in a Spark-Ignition Engine Fueled with Syngas-Biogas-Hydrogen," *Int. J. Renew. Energy Dev.*, vol. 12, no. 1, pp. 118–128, Jan. 2023, doi: 10.14710/ijred.2023.49368.

124. I. P. Jain, "Hydrogen the fuel for 21st century," *Int. J. Hydrogen Energy*, vol. 34, no. 17, pp. 7368–7378, Sep. 2009, doi: 10.1016/j.ijhydene.2009.05.093.

125. Y. Wang, K. S. Chen, J. Mishler, S. C. Cho, and X. C. Adroher, "A review of polymer electrolyte membrane fuel

cells: Technology, applications, and needs on fundamental research," *Appl. Energy*, vol. 88, no. 4, pp. 981–1007, Apr. 2011, doi: 10.1016/j.apenergy.2010.09.030.

126. V. G. Bui, T. M. T. Bui, A. T. Hoang, S. Nižetić, T. X. Nguyen Thi, and A. V. Vo, "Hydrogen-Enriched Biogas Premixed Charge Combustion and Emissions in Direct Injection and Indirect Injection Diesel Dual Fueled Engines: A Comparative Study," *J. Energy Resour. Technol.*, vol. 143, no. 12, Dec. 2021, doi: 10.1115/1.4051574.

127. C. WHITE, R. STEEPER, and A. LUTZ, "The hydrogen-fueled internal combustion engine: a technical review," *Int. J. Hydrogen Energy*, vol. 31, no. 10, pp. 1292–1305, Aug. 2006, doi: 10.1016/j.ijhydene.2005.12.001.

128. J. J. De-Troya, C. Álvarez, C. Fernández-Garrido, and L. Carral, "Analysing the possibilities of using fuel cells in ships," *International Journal of Hydrogen Energy*. 2016, doi: 10.1016/j.ijhydene.2015.11.145.

129. Z. E. Ships, "One Hundred Passengers and Zero Emissions: The First Ever Passenger Vessel to Sail Propelled by Fuel Cells." 2013.

130. C. J. McKinlay, S. R. Turnock, and D. A. Hudson, "Route to zero emission shipping: Hydrogen, ammonia or methanol?," *Int. J. Hydrogen Energy*, vol. 46, no. 55, pp. 28282–28297, Aug. 2021, doi: 10.1016/j.ijhydene.2021.06.066.

131. Y. Bicer and I. Dincer, "Clean fuel options with hydrogen for sea transportation: A life cycle approach," *Int. J. Hydrogen Energy*, 2018, doi: 10.1016/j.ijhydene.2017.10.157.

132. Fathom.world, "Is methanation the future of ship fuel?," 2019. .

133. HyMethShip, "Hydrogen in combustion engines," 2019.

134. F. Bird, A. Clarke, P. Davies, and E. Surkovic, *Ammonia : fuel and energy store.* 2020.

135. R. D. Milton *et al.*, "Bioelectrochemical Haber-Bosch Process: An Ammonia-Producing H 2 /N 2 Fuel Cell," *Angew. Chemie Int. Ed.*, vol. 56, no. 10, pp. 2680–2683, Mar. 2017, doi: 10.1002/anie.201612500.

136. V. Kyriakou, I. Garagounis, A. Vourros, E. Vasileiou, and M. Stoukides, "An Electrochemical Haber-Bosch Process," *Joule*, vol. 4, no. 1, pp. 142–158, Jan. 2020, doi: 10.1016/j.joule.2019.10.006.

137. R. F. Service, "Liquid sunshine," 2018.

138. P. Dimitriou and R. Javaid, "A review of ammonia as a compression ignition engine fuel," *Int. J. Hydrogen Energy*, vol. 45, no. 11, pp. 7098–7118, Feb. 2020, doi: 10.1016/j.ijhydene.2019.12.209.

139. I. S. Seddiek and N. R. Ammar, "Technical and eco-environmental analysis of blue/green ammonia-fueled RO/RO ships," *Transp. Res. Part D Transp. Environ.*, vol. 114, p. 103547, Jan. 2023, doi: 10.1016/j.trd.2022.103547.

140. N. De Vries, "Safe and Effective Application of Ammonia as a Marine Fuel Delft University of Technology," 2019.

141. MAN, "Engineering the Future Two-Stroke Green-Ammonia Engine," 2019.

142. F. Abbasov, "Roadmap to decarbonising European shipping," 2018. .

143. Y. Bicer and I. Dincer, "Environmental impact categories of hydrogen and ammonia driven transoceanic maritime vehicles: A comparative evaluation," *Int. J. Hydrogen Energy*, vol. 43, no. 9, pp. 4583–4596, 2018.

144. MAERSK, "PRESS RELEASE Alcohol , Biomethane and Ammonia are the best-positioned fuels to reach zero net emissions 24 October 2019," 2019.

145. S.-J. Yeo, J. Kim, and W.-J. Lee, "Potential economic and environmental advantages of liquid petroleum gas as a marine fuel through analysis of registered ships in South Korea," *J. Clean. Prod.*, vol. 330, p. 129955, Jan. 2022, doi: 10.1016/j.jclepro.2021.129955.

146. S. Kjartansson, "A Feasibility Study on LPG as Marine Fuel," 2012.

147. R. Laursen, "Ship operation using LPG and ammonia as fuel on MAN B&W dual fuel ME-LGIP engines," 2018.

148. E. Lindstad, B. Lagemann, A. Rialland, G. M. Gamlem, and A. Valland, "Reduction of maritime GHG emissions and the potential role of E-fuels," *Transp. Res. Part D Transp. Environ.*, vol. 101, p. 103075, Dec. 2021, doi: 10.1016/j.trd.2021.103075.

149. B. Lagemann, E. Lindstad, K. Fagerholt, A. Rialland, and S. Ove Erikstad, "Optimal ship lifetime fuel and power system selection," *Transp. Res. Part D Transp. Environ.*, vol. 102, p. 103145, Jan. 2022, doi: 10.1016/j.trd.2021.103145.

150. S.-H. Han, H.-S. Kim, B.-U. Han, and D.-J. Lee, "LPG A Study on Fuel Supply System of LPG Propulsion VLGC ME-LGIP Engine," *Bull. Soc. Nav. Archit. Korea*, vol. 56, no. 4, pp. 10–14, 2019.

151. B. Ashok, S. Denis Ashok, and C. Ramesh Kumar, "LPG diesel dual fuel engine – A critical review," *Alexandria Eng. J.*, vol. 54, no. 2, pp. 105–126, Jun. 2015, doi: 10.1016/j.aej.2015.03.002.

152. K. W. Chun, M. Kim, and J.-J. Hur, "Development of a Marine LPG-Fueled High-Speed Engine for Electric

Propulsion Systems," J. Mar. Sci. Eng., vol. 10, no. 10, p. 1498, Oct. 2022, doi: 10.3390/jmse10101498.

153. B. Ashok, S. D. Ashok, and C. R. Kumar, "LPG diesel dual fuel engine–A critical review," *Alexandria Eng. J.*, vol. 54, no. 2, pp. 105–126, 2015.

154. The WLPGA, "LPG for Marine Engines, The Marine Alternative Fuel," Charles de Gaulle, France, 2017.

155. Michael Petersen and A. Eastern, "LPG as future bunker fuel," 2019.

156. K. Cullinane and S. Cullinane, "Policy on reducing shipping emissions: implications for 'green ports,'" *Green Ports*, pp. 35–62, 2019.

157. T. Zis, R. J. North, P. Angeloudis, W. Y. Ochieng, and M. G. H. Bell, "Evaluation of cold ironing and speed reduction policies to reduce ship emissions near and at ports," *Marit. Econ. Logist*., vol. 16, no. 4, pp. 371–398, 2014.

158. R. Bergqvist and J. Monios, "Green ports in theory and practice," in *Green ports*, Elsevier, 2019, pp. 1–17.

159. F. Fung, Z. Zhu, R. Becque, and B. Finamore, "Prevention and control of shipping and Port Air emissions in china," *NRDC white Pap*., 2014.

160. N. R. Ammar, "Energy-and cost-efficiency analysis of greenhouse gas emission reduction using slow steaming of ships: case study RO-RO cargo vessel," *Ships Offshore Struct*., vol. 13, no. 8, pp. 868–876, 2018.

161. C. C. Chang and C. M. Wang, "Evaluating the effects of green port policy: Case study of Kaohsiung harbor in Taiwan," *Transp. Res. Part D Transp. Environ*., 2012, doi: 10.1016/j.trd.2011.11.006.

162. J. J. Corbett, H. Wang, and J. J. Winebrake, "The effectiveness and costs of speed reductions on emissions from international shipping," *Transp. Res. Part D Transp. Environ.*, vol. 14, no. 8, pp. 593–598, 2009.

163. J.-K. Woo and D. S.-H. Moon, "The effects of slow steaming on the environmental performance in liner shipping," *Marit. Policy Manag*., vol. 41, no. 2, pp. 176–191, 2014.

164. P. E. N. G. Yun, L. I. Xiangda, W. A. N. G. Wenyuan, L. I. U. Ke, and L. I. Chuan, "A simulation-based research on carbon emission mitigation strategies for green container terminals," *Ocean Eng*., vol. 163, pp. 288–298, Sep. 2018, doi: 10.1016/j.oceaneng.2018.05.054.

165. Alphaliner, "http://www.alphaliner.com/," 2010. .

166. P. Cariou, "Is slow steaming a sustainable means of reducing CO2 emissions from container shipping?," Transp. Res. Part D Transp. Environ., vol. 16, no. 3, pp. 260–264, 2011.

167. M. Golias, M. Boile, S. Theofanis, and C. Efstathiou, "The berth-scheduling problem: Maximizing berth productivity and minimizing fuel consumption and emissions production," *Transp. Res. Rec*., vol. 2166, no. 1, pp. 20–27, 2010.

168. L. Kirstein, R. Halim, and O. Merk, "Decarbonising Maritime Transport.—Pathways to Zero-Carbon Shipping by 2035," 2018.

169. C. C. Chang and C. W. Jhang, "Reducing speed and fuel transfer of the green flag incentive program in kaohsiung port taiwan," *Transp. Res. Part D Transp. Environ*., vol. 46, pp. 1–10, 2016.

170. H. Winnes, L. Styhre, and E. Fridell, "Reducing GHG emissions from ships in port areas," *Res. Transp. Bus. Manag.*, 2015, doi: 10.1016/j.rtbm.2015.10.008.

171. C. Kontovas and H. N. Psaraftis, "Reduction of emissions along the maritime intermodal container chain: operational models and policies," *Marit. Policy Manag*., vol. 38, no. 4, pp. 451–469, 2011.

172. R. T. Poulsen, S. Ponte, and H. Sornn-Friese, "Environmental upgrading in global value chains: The potential and limitations of ports in the greening of maritime transport," *Geoforum*, vol. 89, pp. 83–95, Feb. 2018, doi: 10.1016/j.geoforum.2018.01.011.

173. Y.-T. Tsai, C.-J. Liang, K.-H. Huang, K.-H. Hung, C.-W. Jheng, and J.-J. Liang, "Self-management of greenhouse gas and air pollutant emissions in Taichung Port, Taiwan," *Transp. Res. Part D Transp. Environ*., vol. 63, pp. 576–587, 2018.

174. G. Villalba and E. D. Gemechu, "Estimating GHG emissions of marine ports—the case of Barcelona," *Energy Policy*, vol. 39, no. 3, pp. 1363–1368, 2011.

175. S. López-Aparicio, D. Tønnesen, T. N. Thanh, and H. Neilson, "Shipping emissions in a Nordic port: Assessment of mitigation strategies," *Transp. Res. Part D Transp. Environ.*, 2017, doi: 10.1016/j.trd.2017.04.021.

176. L. Styhre, H. Winnes, J. Black, J. Lee, and H. Le-Griffin, "Greenhouse gas emissions from ships in ports – Case studies in four continents," *Transp. Res. Part D Transp. Environ.*, 2017, doi: 10.1016/j.trd.2017.04.033.

177. SPBP, "San Pedro Bay Ports Clean Air Action Plan Update. Port of Los Angeles and the Port of Long Beach," 2017.

178. D. Gibbs, P. Rigot-Muller, J. Mangan, and C. Lalwani, "The

role of sea ports in end-to-end maritime transport chain emissions," *Energy Policy*, vol. 64, pp. 337–348, 2014.

179. D. S. H. Moon and J. K. Woo, "The impact of port operations on efficient ship operation from both economic and environmental perspectives," *Marit. Policy Manag.*, 2014, doi: 10.1080/03088839.2014.931607.

180. H. Johnson and L. Styhre, "Increased energy efficiency in short sea shipping through decreased time in port," *Transp. Res. Part A Policy Pract.*, vol. 71, pp. 167–178, 2015.

181. M. Tichavska, B. Tovar, D. Gritsenko, L. Johansson, and J. P. Jalkanen, "Air emissions from ships in port: Does regulation make a difference?," *Transp. Policy*, vol. 75, pp. 128–140, 2019.

182. A. Misra, K. Panchabikesan, S. K. Gowrishankar, E. Ayyasamy, and V. Ramalingam, "GHG emission accounting and mitigation strategies to reduce the carbon footprint in conventional port activities–a case of the Port of Chennai," *Carbon Manag.*, vol. 8, no. 1, pp. 45–56, 2017.

183. E. Díaz-Ruiz-Navamuel, A. O. Piris, and C. A. Pérez-Labajos, "Reduction in CO2 emissions in RoRo/Pax ports equipped with automatic mooring systems," *Environ. Pollut.*, vol. 241, pp. 879–886, 2018.

184. A. Ortega Piris, E. Díaz-Ruiz-Navamuel, C. A. Pérez-Labajos, and J. Oria Chaveli, "Reduction of CO2 emissions with automatic mooring systems. The case of the port of Santander," *Atmos. Pollut. Res.*, 2018, doi: 10.1016/j.apr.2017.07.002.

185. P. Andersson and P. Ivehammar, "Green approaches at sea – The benefits of adjusting speed instead of anchoring," *Transp. Res. Part D Transp. Environ.*, 2017, doi: 10.1016/j.trd.2017.01.010.

186. International maritime organization, "Study of Emission Control and Energy Efficiency Measures for Ships in the Port Area," *Clim. Chang. 2013 – Phys. Sci. Basis*, 2015.

187. A. Azetsu, "Regulation of GHG Emissions and Trend of Countermeasures," *J. Japan Inst. Mar. Eng.*, vol. 51, no. 1, pp. 50–53, 2016, doi: 10.5988/jime.51.50.

188. V. V. Pham and A. T. Hoang, "Analyzing and selecting the typical propulsion systems for ocean supply vessels," 2020, doi: 10.1109/ICACCS48705.2020.9074276.

189. J. Faber and M. Hoen, *Estimated Index Values of Ships 2009-2016: Analysis of the Design Efficiency of Ships that Have Entered the Fleet Since 2009*. CE Delft, 2017.

190. T. and Environment, "Statistical analysis of the energy efficiency performance (EEDI) of new ships built in 2013-2017." 2018.

191. W. Tarełko, "The effect of hull biofouling on parameters characterising ship propulsion system efficiency," *Polish Marit. Res.*, 2014, doi: 10.2478/pomr-2014-0038.

192. X. P. Nguyen, "A simulation study on the effects of hull form on aerodynamic performances of the ships," in *Proceedings of the 2019 1st International Conference on Sustainable Manufacturing, Materials and Technologies*, 2020, p. 020015, doi: 10.1063/5.0000140.

193. T. Smith *et al.*, "CO2 Emissions from International Shipping: Possible reduction targets and their associated pathways," 2016.

194. T. Smith *et al.*, "CO2 emissions from international shipping: Possible reduction targets and their associated pathways," *UMAS London*, UK, 2016.

195. P. Gilbert, A. Bows-Larkin, S. Mander, and C. Walsh, "Technologies for the high seas: Meeting the climate challenge," *Carbon Manag.*, 2014, doi: 10.1080/17583004.2015.1013676.

196. Institute of Marine Engineering Science and Technology (IMarEST), "MEPC 62/INF.7 – Reduction of GHG emissions from ships - Marginal Abatement Costs and Cost Effectiveness of Energy-Efficiency Measures," 2011.

197. H. Lindstad and G. S. Eskeland, "Low carbon maritime transport: How speed, size and slenderness amounts to substantial capital energy substitution," *Transp. Res. Part D Transp. Environ.*, vol. 41, pp. 244–256, Dec. 2015, doi: 10.1016/j.trd.2015.10.006.

198. N. Rehmatulla, J. Calleya, and T. Smith, "The implementation of technical energy efficiency and CO 2 emission reduction measures in shipping," *Ocean Eng.*, vol. 139, pp. 184–197, Jul. 2017, doi: 10.1016/j.oceaneng.2017.04.029.

199. J. Carlton, J. Aldwinkle, and J. Anderson, "Future ship powering options: exploring alternative methods of ship propulsion," *London R. Acad. Eng.*, 2013.

200. F. Tillig, W. Mao, and J. Ringsberg, "Systems modelling for energy-efficient shipping," Chalmers University of Technology, 2015.

201. P. . Van Kluijven, L. Kwakernaak, F. Zoetmulder, M. Ruigrok, and K. de Bondt, "Contra-rotating propellers1," *Int. Shipbuild. Prog.*, vol. 3, no. 25, pp. 459–473, 2018, doi: 10.3233/isp-1956-32501.

POLISH MARITIME RESEARCH 2 (118) 2023 Vol. 30; pp. 165-187
10.2478/pomr-2023-0031

MANAGEMENT STRATEGY FOR SEAPORTS ASPIRING TO GREEN LOGISTICAL GOALS OF IMO: TECHNOLOGY AND POLICY SOLUTIONS

Thanh Tuan Le
Institute of Engineering, HUTECH University, Ho Chi Minh City, Viet Nam
Hoang Phuong Nguyen*
Academy of Politics Region II, Ho Chi Minh City, Viet Nam
Krzysztof Rudzki
Gdynia Maritime University, Faculty of Marine Engineering, Gdynia, Poland
Lech Rowiński
Gdansk University of Technology, Poland
Viet Duc Bui
PATET Research Group, Ho Chi Minh City University of Transport, Ho Chi Minh City, Viet Nam
Thanh Hai Truong
PATET Research Group, Ho Chi Minh City University of Transport, Ho Chi Minh City, Viet Nam
Huu Cuong Le
Institute of Maritime, Ho Chi Minh City University of Transport, Ho Chi Minh City, Viet Nam
Nguyen Dang Khoa Pham*
PATET Research Group, Ho Chi Minh City University of Transport, Ho Chi Minh City, Viet Nam

* Corresponding author: *khoapnd@ut.edu.vn (Nguyen Dang Khoa Pham)*
nghoangphuong11@gmail.com (Hoang Phuong Nguyen)

ABSTRACT

Recently, because of serious global challenges including the consumption of energy and climate change, there has been an increase in interest in the environmental effect of port operations and expansion. More interestingly, a strategic tendency in seaport advancement has been to manage the seaport system using a model which balances environmental volatility and economic development demands. An energy efficient management system is regarded as being vital for meeting the strict rules aimed at reducing the environmental pollution caused by port facility activities. Moreover, the enhanced supervision of port system operating methods and technical resolutions for energy utilisation also raise significant issues. In addition, low-carbon ports, as well as green port models, are becoming increasingly popular in seafaring nations. This study comprises a comprehensive assessment of operational methods, cutting-edge technologies for sustainable generation, storage, and transformation of energy, as well as systems of smart grid management, to develop a green seaport system, obtaining optimum operational efficiency and environmental protection. It is thought that using a holistic method and adaptive management, based on a framework of sustainable and green energy, could stimulate creative thinking, consensus building, and cooperation, as well as streamline the regulatory demands associated with port energy management. Although several aspects of sustainability and green energy could increase initial expenditure, they might result in significant life cycle savings due to decreased consumption of energy and output of emissions, as well as reduced operational and maintenance expenses.

Keywords: Green seaport, management strategy, clean energy, decarbonization, sustainable maritime

INTRODUCTION

Seaports have contributed significantly to global economic development [1]; they have played an important part in enabling import and export activities between nations since before the Industrial Revolution, which directly supported the development of international commerce and the world's supply chain [2][3]. However, it has been observed that energy costs are enormous for ports and facilities, so energy savings could be a significant and efficient solution to lowering these costs [4]. In addition, emission reduction contributes directly to the green viewpoint and sustainability of ports [5][6]. More interestingly, energy efficiency mainly refers to supplying similar services while using less energy, and it is frequently related to the employment of renewable and eco-friendly resources to provide such services [7][8]. Indeed, energy efficiency is critical for ports and facilities seeking to reduce energy usage and become more environmentally friendly [9]. In October 2014, the European Council established an aim of 30% energy saving and 27% renewable energy share in total energy utilisation in all industries by 2030 [10]. In particular, regulations were implemented with the goal of mitigating greenhouse gas (GHG) emissions in port waterways, inland regions, and yards, in order to foster sustainability and the green viewpoint [11][12]. Pollution reduction was a direct and obvious consequence of the electrification of equipment [13], energy efficiency [14], the employment of alternative fuels, low-sulphur fuels, and sustainable sources of energy [15][16]. The above-mentioned factors, along with working efficiency, constitute a significant portion of defining next-generation ports [17][18]. Furthermore, energy efficiency is considerably influenced by technological developments in power production, distribution, storage, consumption, and conversion [19]–[21]. Energy systems used in docks contain numerous components, such as converters, batteries, and distributors. Novel methods for enhancing grid intelligence, mentioned above, as well as novel devices, such as super-capacitors and flywheels, aim to effectively store energy and promote energy efficiency even further [22][23]. Port machinery outfitted with energy management components, for example, could greatly save energy by saving power during hoist-down, storing that energy, and then utilising it during hoist-up or travelling movements [24][25]. Notably, smart power delivery systems have the potential to improve the energy economy in the reefer industry and technological advancements significantly contribute to the efficiency of consuming energy [26][27]. Also, ports can take advantage of the development of novel fuel-efficient motors and fuel cells because green energy sources are increasingly being used and technological advancements in harnessing renewable energy are also linked to ports [28][29]. Thus, emerging technologies, including microgrid and smart grid systems for controlling the demand and supply of energy, could enhance port energy management in this situation.

Facing the problems relating to the development strategies of green ports, the motivation for this effort was to provide a thorough understanding of working strategies, techniques, and energy management systems, with the goal of achieving energy savings for sustainable and green ports. Besides, this paper presents technologies and methods to decrease GHG pollution in the shipping sector; methods for detecting and identifying energy consumption in ports are also illustrated. Research gaps are identified and research directions are proposed for future investigations. The structure of this paper includes: Section 2 focuses on the methodology for searching references in the literature; Section 3 discusses the critical factors affecting green port strategies, such as technology factors, management factors, and policy factors. Suggestions for green logistics for green ports are then analysed in Section 4. Finally, conclusions and future directions are presented in Section 5.

METHODOLOGY

In order to collect data and the most appropriate literature for this paper, some important keywords were used, including: 'renewable energy', 'clean energy', 'seaport', 'green maritime', 'green seaport', 'green logistics', 'energy plan', 'energy management for port', 'energy management in shipping', 'low-carbon energy for maritime', 'net-zero', and 'CO_2 emission'. The search was carried out on the websites of prestigious associations and organisations, as well as Google Scholar. For selected papers, they had to be peer-reviewed and published in good ISI/Scopus journals relating to energy, energy economy, maritime, port, logistics, and energy policy. After that, three filters were used to select the most relevant papers, as shown in **Fig. 1**.

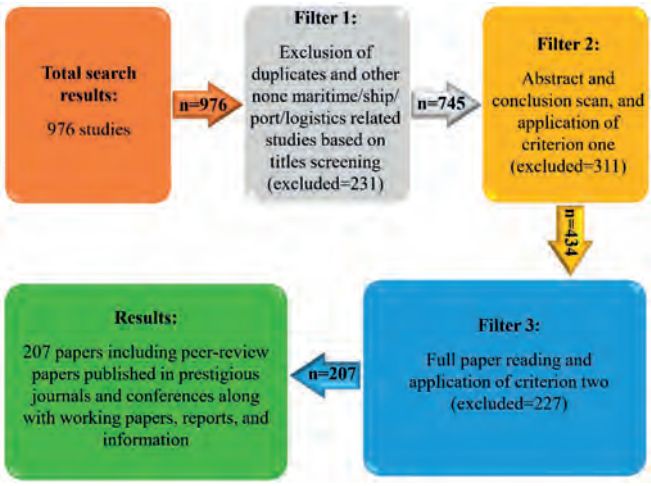

Fig. 1. Methodology used for selecting the most suitable papers/reports/information

The following criteria were used for filters. With the aim of selecting the most suitable papers/reports/information: (1) – a preliminary survey with the aforementioned keywords for the 1st filter, (2) – checking the title and abstract of papers/reports/information for the 2nd filter, (3) – checking and carefully reviewing the content of papers/reports/information for the 3rd filter. Finally, 200 of the

most relevant and suitable papers/reports/information were selected for this work.

CRITICAL FACTORS AFFECTING GREEN PORT STRATEGIES

TECHNOLOGY FACTORS

Cold-ironing technology

Cold ironing is the practice of connecting ship berths to shore-side electricity instead of operating auxiliary engines to supply electricity for ship operation [30]. Its effectiveness in reducing emissions is determined by the percentage of green energy output in that nation; therefore, nations with less ecologically favourable electricity generation simply discharge emissions elsewhere. According to Winkel et al. [31], if all ports in Europe utilised shore power, an estimated €2.94 billion in expenses could have been saved in 2020, along with an 800,000-ton decrease in carbon emissions. However, the main obstacles are the installation costs and the fact that each ship has to apply the connecting technique on board, which they only do if they expect to employ it regularly [32]–[34]. Based on the report by WPCI, there are just 28 ports, worldwide, with cold ironing installed; this indicates minimal take-up, to date [35].

There are primarily two kinds of engines in vessels: the main engine, such as the propulsion engine, and the auxiliary engine [36]. Most ships switch off their main engines upon docking. Auxiliary engines provide energy for hotelling operations including power system repair, lighting, and refrigeration. Depending on the types of fuel, these auxiliary diesel engines burn fossil fuel in the idle position and release CO_2, SO_2, and NOx [37]–[39]. Cold ironing is also known as alternative marine control, onshore power supply, and shore-side power. The grid, renewable sources, LNG, or other sources of electrical power can provide electricity which can reduce emissions if they replace burning fuels [32], [40], [41]. In general, the higher the average ship handling times are, the higher the potential ports save through cold-ironing [40]. Due to the different policies and costs in each region, emission reduction varies according to the area. By cold ironing, global carbon emissions, based on the emission intensity of port electricity supplies, are decreased by 10%, while SO_2 emissions in UK ports are decreased by 2% [40]. Similarly, there is a reduction of 57.16% in CO_2 emissions in Kaohsiung Port, Taiwan [42]. Comparisons of the supply of shore-side power with marine fuels in bulk carrier services indicate that a shore-side power supply can offer economic benefits to countries, the electricity price is less than 0.19 USD/kWh [43]. Moreover, operating expenses and energy consumption can be decreased by up to 75% through shore-side power [43], which benefits not only vessel owners but also port authorities. Cold ironing can significantly influence cruise ports due to the large amount of power needed for large vessels when several passengers are on board during hotelling [44]–[46]. Hall [47] reported that CO_2 emission reductions with shore-side power are 99.5% for the port of Oslo in Norway and 9.4% for Fort Lauderdale in the US. However, since the pricing structures of cold ironing are different, a return of investment analysis is required. More progress could be achieved through more technical, economic, regulatory, and environmental studies in the future. The integration of cold ironing with berth allocation and quay crane allotment problems can assess new trade-offs.

Refrigerated container technology

The refrigerated container trade needs the constant refrigeration of each container, so that the goods remain cool. The trade has expanded consistently and outweighed other market sectors in the liner shipping field in recent years [48]. According to various studies, the percentage of energy consumed by reefer vessels varies between 20-45% of total energy usage in ports [48]–[50]. As a result, improvements in energy efficacy in refrigerated containers is recommended. Joan et al. [51] concluded that container heating could be prevented by covered spaces for reefer containers. Furthermore, finding the number of plugs for reefers, identifying the location of the reefer zone for minimising travel distances, formulating better electrical distributing systems, developing a powerful strategy for each reefer cargo, and calculating the exact consumption of energy for reefer containers were all considered to be important research perspectives for the energy efficacy in the reefer zone [52]. Apart from that, efficient refrigerated container management fulfils ship demands, while also lowering the associated costs. Given the journey periods, operators devised an optimal plan to minimise energy usage and losses [53]. Indeed, an exterior power source was required for reefer area control in reefer containers due to their cooling power consumption. A time-space model, appropriate for moving reefer vessels, was also developed [54]. Nevertheless, the majority of the aforementioned studies were from the viewpoint of transportation. The energy flow modelling was quite simple and the energy consumption for a single container move was set as '4kWh,' which completely neglected the potential operation flexibility of scheduling transport, which facilitated the study from the perspective of flexibly managing energy [55], [56].

Lighting technology

Lighting is thought to be one of the most energy-intensive components, particularly at night. Indeed, some investigations were conducted on energy-saving lighting systems in buildings, which included the utilisation of smart lighting systems based on sensors, for future structures in California [57], as well as a lighting strategy based on occupancy for an open Dutch working environment [58]. Several previous studies researched the control of fluorescent luminaires based on sunshine [59] and the utilisation of daylight for cheap illumination [60]. Furthermore, control devices that employed daylight could save a lot of energy, particularly for interior uses [61]. Remarkably, daylight gathering utilised natural light

to counterpoint artificial lighting collected from established lighting systems, with the aim of reaching a target illumination level while lowering electric loads [62]. Moreover, controlling LED illumination systems, based on occupant position and daylight dispersal, resulted in significant energy reductions [63][64]. Nonetheless, effectively lighting an outdoor location, like a port, while also adhering to each space's unique illuminance rules, was considered a sophisticated job. Outdoor illumination in ports consumes a significant amount of energy [65], surpassing 70% of the total energy requirements of a port, in some instances [66]. Because of their complicated operations and services, ports have a high energy consumption; hence, they could be classified as small cities, communities, or villages [26]. In fact, the majority of existing port methods and technologies are out of date, but there is significant potential for considerable energy savings, along with an enormous reduction in the environmental impacts of ports [67]. Besides this, ports are required to follow stringent monitoring and societal rules in this situation [30]. The Nearly Zero Energy Port project is a hopeful step toward the sustainability of ports [9] and, simultaneously, port exterior illumination is critical for safety and comfort [68], as well as to enhance their aesthetics [69][64]. In many ports, technologies are applied to enhance lighting energy efficiency. To ensure energy efficiency, LED lamps could be used in port storage facilities, administration buildings, and lighting for outdoor terminals [50]. Assuming that 11 h of light is required, by using LED lamps an annual electricity saving of 922 MWh could be obtained [50]. In addition to LED technology, lighting levels and the design of armatures also contribute to electricity savings [51].

Other technologies

Automated mooring systems can be used as energy consumption mitigation methods and with major effects [11][70]. In this system, vessels are often vacuum-moored and locked without many manoeuvres, which decreases the motor's energy consumption. A reduction of fuel consumption between 10-15% is possible, as a result of state-of-the-art technologies, including start-stop engines for diesel equipment [71]. Many ports can use reactive power compensation methods, which compensate the reactive power consumed by various electrified equipment [71]. With the application of this system, while the power factor increases, there is a decrease in network losses. In the future, ports will be able to work in CCS systems with facilities for collecting and depositing CO_2 waste without releasing it into the air [72]. Heat exchangers, water treatment technologies, and degassing installations are used in the port of Rotterdam, to capture heat and save energy [73]. Furthermore, energy can be saved more by material recycling or waste-to-energy strategy application in ports [72][74].

In fact, automated mooring devices can have a significant effect on energy usage [11], [70]. Vessels are mostly anchored by the use of a vacuum, in this method, attached to the berth without much manoeuvring; this lowers the engines' energy usage. Moreover, advanced techniques, including start-stop engines for engines running on diesel, could reduce the consumption of fuel by 10-15%. Many terminals could benefit from reactive power compensation methods, which involve compensating for the reactive power utilised by different electrified devices, resulting in a reduction in energy consumption [75].

MANAGEMENT FACTORS

Equipment management

The organisational effectiveness of a port is determined by how well the available resources are managed; there is a positive connection between reduced operation periods, e.g. ship handling times and cargo transit times in the yard, and operational effectiveness in ports [76]. Thus, the energy economy is the result of operational effectiveness [19][77]. As a result, the majority of optimisation studies associated with improved port operation plans contribute to energy efficiency. Many of the studies in the literature considered mathematical models that had a goal function related to the energy consumption of terminals, particularly cargo terminals that were divided into three functional regions: quayside, landside, and yard side [78][79]. Also, other publications mentioned the energy-aware utilisation of quayside resources such as berths, conveyors, and quay cranes (QC) [80]–[82]. For example, the consumption of energy of QCs that existed in the objective function was used to build a combined berth allocation and QC assignment problem in [83]. Similarly, Iris et al. [84][85] addressed the reduction of QC energy consumption in relation to marginal QC output, in which QC energy consumption issues should be tackled the trade-off between energy-saving and time-saving, minimising lateness. In addition, this study also considered QCs' non-working and working energy consumption [55]. It was noticeable that working energy consumption was determined by the number of movements per hour and energy consumed throughout loading or unloading, but non-working energy consumption was determined by lighting and auxiliary units. Moreover, the QC assignment was identified by the queuing activity of automated guided vehicles (AGV) [86] and it was shown that the optimal number of QCs decreased according to the consumption of energy per QC per hour [86].

Planning on the yard side focused primarily on container transport but stacking was also considered as one of the solutions for port management, to reduce energy consumption [7], [87]–[90]. He et al. [91] discussed yard crane (YC) scheduling with energy consumption, transforming it into a variant of vehicle routing issues. They reported that, for all YCs, energy savings of 25.6% were obtained, compared to practical findings. Positions in the same row are given priority by the energy-aware planning of YCs [92]. Therefore, researchers on energy-aware planning have recently concentrated on automated container terminals. Indeed, a predictive control model for balancing the throughput and energy consumption of a single QC with AGVs and ASCs is established, in which the discrete-event and continuous-time dynamics are simulated with a hybrid

automation representation [93]. The results revealed that the proposed method achieves the same range of reduced energy consumption because the approach enables vehicles to decelerate in the yard. Another study, by Xin et al. [94], experimented with 1 QC, 2 AGVs, and 3 annualised slot capacities, indicating that an average 6.23 kWh of energy is required to load 8 containers efficiently [94]. Xin et al. [95] indicated that energy consumption of approximately 65 kWh can load 90 containers in a case of efficient energy management. In fact, emissions from port operations made fewer contributions to overall emissions but could be handled in a variety of ways, although only a trivial number of ports actually tracked their emissions. Wilmsmeier et al. [19] investigated methods to improve energy efficacy through the use of the latest handling equipment, the implementation of energy management systems, and differentiated port and terminal costs. Acciaro et al. [72] studied ports that implemented energy demand management approaches and produced their own eco-friendly energy on-site, namely solar panels, wind turbines, and heat plants. They also demonstrated that, while ports did not consider energy generation as an external revenue resource, controlling not only supply but also demand could alleviate their expenses and environmental impacts [34].

In recent years, electrification has become more common in ports because a substantial decrease in pollution from the emissions generated by electricity consumption, compared to those generated by using fossil fuels, is accompanied by cost-efficiencies when using electrical port equipment. More interestingly, peak shaving refers to practical strategies for reducing a port's peak consumption of energy and, in fact, there are numerous techniques for peak shaving. As reported, peak electricity usage was observed to account for approximately 25-30% of the monthly electricity bill [96]. Obviously, the energy bill had two major components, including an unchanging expense of electricity utilisation and a variable expense, based on the level of consumption [95]. Even though ports could not reduce the set cost, which was specified and paid yearly, lowering the variable cost could be concentrated on, which was mainly decided by peak energy use and total consumption of electricity [20]. Therefore, a high peak energy usage, such as occurs through the simultaneous utilisation of all devices, would result in high energy expenditure in the monthly bill. Several methods use the load profile curves (1) – Using any stored energy in the case of peak energy demand periods, (2) – Shifting the energy demand in the peak period to non-peak periods, (3) – Turning off non-critical loads over peak periods.

The efficient management of equipment in ports is considered as one of the solutions for achieving low energy consumption. In the ports, QCs and ship-to-shore (STS) cranes are mainly used on the quayside to load and unload cargo [97]. While rubber-tired gantries (RTG) and rail-mounted gantries (RTG) are used to stack containers, yard trucks (YT) and AGVs are used to horizontally transport containers. In recent years, highly automated equipment types are used to enhance operational efficiency, as well as decrease the involvement of humans [98]. Equipment, including automated QCs and RMGs, can be used in automated container ports and annualised slot capacities can be used for stacking operations in automated terminals. In bulk ports, cargo is mainly loaded and unloaded onto the ship by conveyors and pipelines [99], while it is stored in the yard of bulk ports in silos. Thus, increased energy efficiency and reduced emissions of GHGs are achieved in ports by electro-mobility (e-mobility) [100]. Due to its flexibility and productivity, RTG is one of the most common pieces of equipment used in yard stacking operations. Many researchers have been attracted by energy efficiency technologies for RTGs. Electrifying RTGs through electric drive systems is a crucial approach. Electrification of an RTG can be via a bus bar, touch wire, or cable reel system [100]. E-RTGs can switch between grid power and power from a diesel generator [100], and they work considerably better than conventional RTGs in connection with energy savings and reduction of CO_2. In comparison with diesel-fueled conventional RTGs, E-RTGs reduce energy expenses by 86.60% and GHG emissions by 67% [50]. More interestingly, researchers examined the installation of a flywheel with a smaller diesel engine for an RTG and predicted that fuel reductions of up to 35% were possible [101]. Similarly, Tan et al. [102] figured out that by installing a flywheel, the energy consumption was decreased by more than 30%, and the generator had a longer lifespan, less noise, and quicker system reactions. Apart from that, a power management system which considered stochastic loads reduced the use of fuel by 38%, for flywheel-installed RTGs [103]. Another proposed power management system for RTGs, based on hybridisation, could reduce fuel consumption by 20-60% [104]. By comparison with RTGs, there are fewer emissions from RMGs and ARMGs because they use electricity as an energy source [105]. Indeed, Yang et al. [106], [107] compared the energy needs of RTG, E-RTG, RMG, and ARMG. They indicated that E-RTG has the least energy consumption and RTG is the highest energy consumer. E-mobility developments greatly affected the electrification and automation of equipment in horizontal transport operations. Thus, AGVs have become more efficient, reliable, and safe [108]. Similar to the majority of other equipment, AGVs can be diesel-powered, battery-powered, or hybrid. Compared to the traditional AGVs, the use of a B-AGV fleet is recommended to charge the battery in off-peak hours [109]. The results indicate that the average energy consumption is 64% lower when B-AGV is used, as illustrated in Fig. 2.

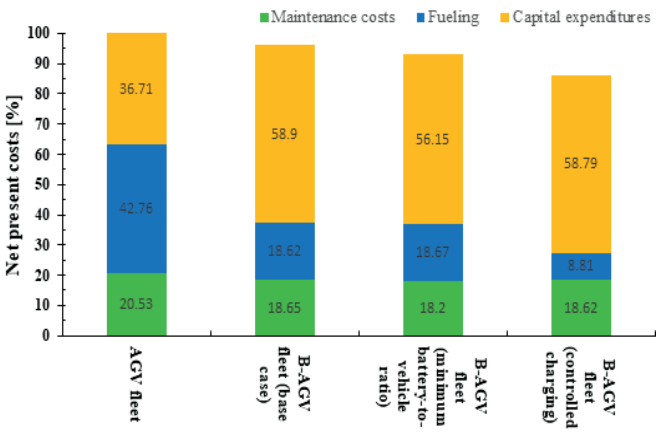

Fig. 2. Comparison of net costs for using different AGV models [109]

In fact, the impacts of electrification could be depicted using different kinds of handling, container terminals, energy costs, freight seasonality, yard sizes, and so on [110]. Economic and environmental studies are also critical for completely automated and electrified ports [111]. In future, the incorporation of electrified autonomous machinery and devices for energy storage, as well as smart meters, would broaden the potential area for further analysis [112]. In next-generation ports, electrification, automation, and smart energy management technologies would be employed [113][114]. In this respect, the functions of electrified and/or autonomous transport in smart grids for port activities should be considered in greater detail. Also, a clever energy planning system could be created by taking random energy demand and supply into account.

In general, peak shaving techniques could be employed in the processes of QCs, electrified machinery, and reefer containers. As a QC consumes a significant amount of energy at a port [96], it is necessary to restrict the number of QCs hoisting simultaneously. Additionally, while synchronising the QCs, not lifting them at the same time was seen to lower the peak electricity consumption significantly; it could raise average processing time as well as waiting duration [96]. It was also reported that, lifting 5 QCs at the same time reduced peak energy usage by 11.1%. Apart from that, employing less handling equipment and smoothing out the processes throughout peak hours could reduce maximum electricity consumption [96]. Peak demand would be reduced by 19.8% in the instance of 6 QCs, if the highest permissible energy demand was fixed to 12 MW. Simultaneously, the typical waiting time was only increased by 3.4 seconds per container. Peak shaving for QCs using twin lift and dual hoist technology was discussed by Parise et al. [20]. Indeed, the combination of crane job cycles with a strong optimisation tool, as well as an energy storage system, were two of the main operational and technological approaches suggested for peak shaving. In addition, Parise et al. [20] disclosed that, during peak times, the saved energy could be utilised, reducing peak energy demand from 10.22 MW to 2.63 MW. For reefer containers, they required variable electricity depending on the month and time of day, so peak shaving approaches were critical for lowering the peak electricity demand in the reefer area because reefer containers constituted 30-45% of overall energy utilisation [49]. The period before a reefer was hooked in, the number of reefer plugs, and the sizes of the vessels, all had an impact on reefer energy needs [49]. Therefore, the dispersal of energy between reefer batches and restricted provision of electricity to reefer batches are considered as two peak-shaving techniques. According to the experiments, the highest energy demand needed for reefers was 14.8 MW in the base scenario and this was reduced by an average of 62.8%, by the first method. Meanwhile, the latter approach had a maximal limit of 14 MW, which led to a reduction in peak demand of 7.2% [49]. Nevertheless, the connection between total operating time, energy consumption, and real idling periods for each machine were not comprehensive. Therefore, integrating the management of energy and plans for real-time operations required improvement. Indeed, a better model which could evaluate the relationship between the consumption of energy and yard traffic congestion was needed for yard activities. Therefore, it was noted that energy-aware routing and equipment scheduling was thought to be a fascinating study subject. Moreover, economic, operational, and environmental studies could be used to examine how peak-shaving techniques could be integrated into smart energy management.

Energy consumption and emission management

Since GHGs emitted from port operations are known to be a function of energy utilisation, a shortage of knowledge about energy usage might result in ambiguous information about the carbon footprint of goods through the port, as well as the total GHG emissions. According to Iris et al. [50], the primary energy consumers in ports are reefer containers (accounting for 43%), QCs (constituting 37%), and yard machinery and buildings (20%). The petroleum usage for the aforementioned ports' YTs, and RTGs comprised 32% and 58% of the overall consumption, respectively. Similarly, reefer containers and QCs each consumed 40% of the overall consumption, in a low-automation container port [52][48]; whereas, horizontal containers and YCs primarily utilised 30% and 68% of the fuel, in turn. For another example, the port of Chennai was reported to consume 6.3 million litres of gasoline, of which 59.2% and 25.5% were employed by cranes and tug vessels, respectively [115]. As reported, the port sector accounted for 3% of total global GHG pollution [70]. It was noted that several variables had an effect on the shift in energy usage, including (1) – changes in handling quantities and patterns of ship calls, (2) – fluctuation in reefer container energy requirements, and (3) – variations in port stay periods for trans-shipments, imports, reefer containers, and exports [19]. For these reasons, energy management in ports is very important, with the aim of minimising the energy used and, therefore, reducing CO_2 emissions.

Indeed, to manage the energy consumption in a port efficiently, building suitable models is very necessary.

While an instrument or device was in use for measuring energy consumption, calculations and/or observations were employed to estimate the consumption of energy. A recent Sea Terminals project examined ports in Valencia and Livorno; they suggested a smart integrated strategy in energy management towards low-CO_2 emissions, as shown in Fig. 3. They concluded that using renewable energy, integrated with smart energy management, could considerably reduce energy consumption and GHG emissions [81][116]. Grundmeier et al. [117] indicated that simulating yard and berth operations could estimate energy consumption [117]. A forecast of electrical usage in the short term and an analytical technique for one electrified RTG was given in a study by Alasali et al. [118]. Regarding emissions, they included emissions from land (such as emissions from container processing in the port) and emissions from ship activities (such as emissions from the arrival and departure of a ship, berthing, and ship manoeuvring in port waterways). All of these emissions were included in the port pollution list. The technique of determining emissions was primarily based on a bottom-up strategy, in which all emission sources made an equal contribution to overall emission values. Indeed, inputs in the various studies included size of port, cargo capacity, and the quantity of equipment investigated [119], [120]. Furthermore, the kind of engine, fuel type, port stay period, and sailing pace were all factors considered in the studies regarding ship-based emissions [115], [120]–[123]. Also, research concentrating on the GHG emissions from machinery and zones took into account scheduling, gridlock, and routing in the yard. It also addressed how port selection affected CO_2 pollution [106], [124], [125]. Liao et al. [126] suggested an emission model based on the activity for measuring emissions between Taiwan's hinterlands and various towns, and demonstrated that when trans-shipped goods were moved to a new port, emissions were reduced.

Smart grid management

The working characteristics of seaports promoted the application of smart energy management methods because smart energy management approaches could supply controllability and flexibility in operation strategy. These could be efficiently used to coordinate production and load demand and, at the same time, alleviate uncertainty or volatility [56]. Aside from the development of electrification, flourishing cold chain transport and cruise ships also led to heating and cooling demands for the port. Furthermore, high-voltage shore connection devices for passenger ships and large cargo ships were used in ports [127]. In this context, future ports will have integrated transport energy systems, and energy management is considered critical in forming the future economic and environmental behaviour of marine transport [54][56]. Buiza et al. [128] investigated smart energy systems employed in ports, in order to evaluate the present scenario in terms of operation, energy, and environmental factors. The research showed how efficient energy management could play an important part in port operations, by allowing interaction

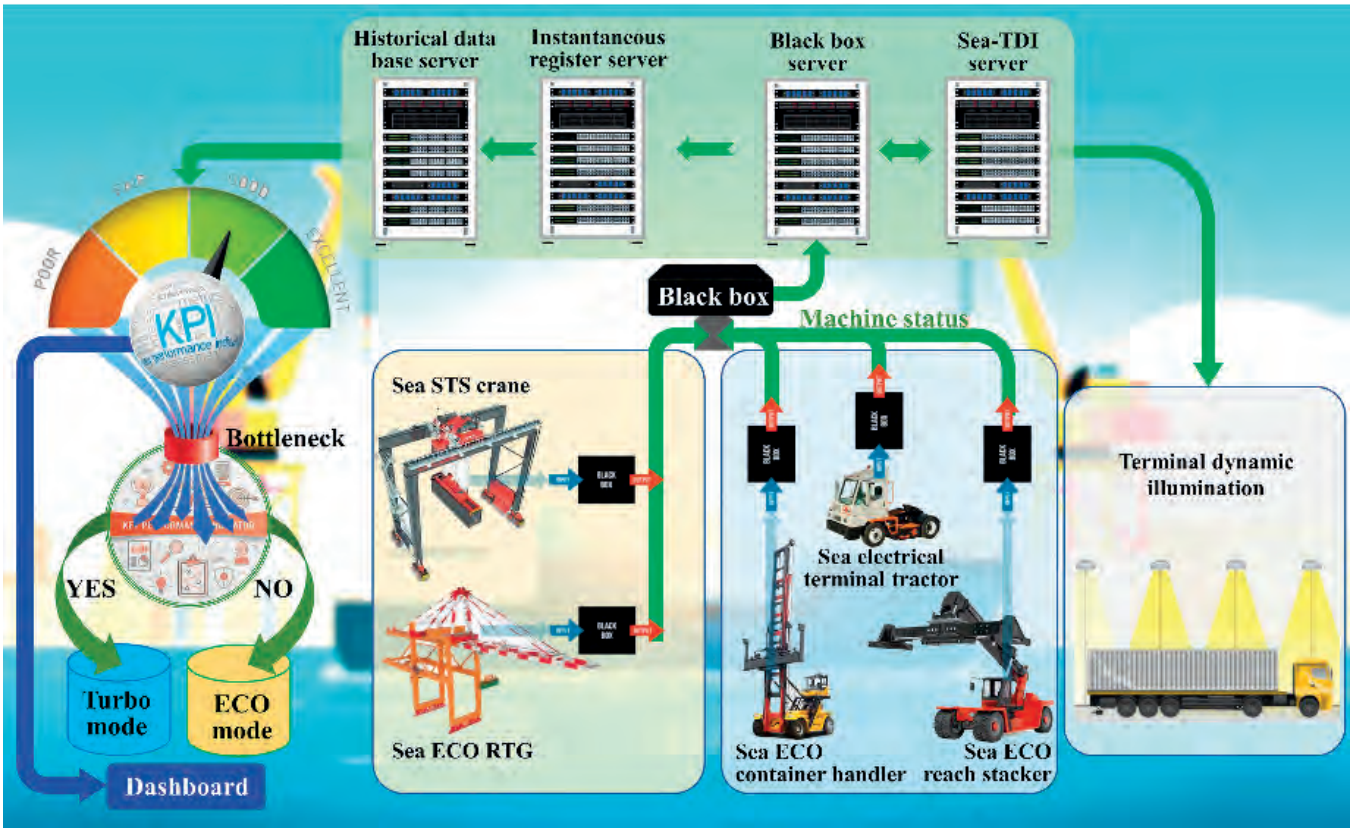

Fig. 3. Integrated energy systems smart management strategy and renewable energy [81][116]

with green sources of energy to guarantee self-consumption and decrease carbon emissions. According to comparable research by Parise et al. [129], smart grid approaches could improve the electrical efficiency of port energy management systems. Also, port authorities and stakeholders were advised to employ more informed approaches to managing energy, in order to maximise port and community benefits. The idea of a smart seaport microgrid was suggested [130], which required effective energy management techniques to handle multiple energy supplies, while satisfying port energy demand.

An energy management system could regulate, supervise, and optimise the activities of smart nanogrids and microgrids [131][132]. In fact, it comprises a high-level controller, as well as a group of lower-level controllers, linked by a communication system [133]. The motivation for developing the seaport microgrid was to use it as an energy district, so as to promote the penetration of renewable energy and grid storage capacity through selling power to the market via the main grid. Parise et al. [129] depicted an idea that was newly suggested for managing a port, called a seaport microgrid. Besides this, Lamberti et al. [134] indicated that the port region was regarded as a distinct zone with its own energy strategy. In fact, two microgrid port projects were manifested in depth in Genoa (Italy) and Hamburg (Germany), and the working data demonstrated their validity [72]. Fig. 4 shows an example of a standard seaport microgrid layout, in which the port was linked to a major grid and a variety of green energy sources were incorporated. Indeed, the seaport would provide on-shore electricity provision (cold-ironing), as well as berth location services to ships when berthing. Interestingly, the seaport's central control would send messages to each subsystem in the port for both energy and logistical management [54]. In general, a port microgrid employs microgrid techniques to enhance its operational behaviour.

The port microgrid was described as a system for managing all energy-related problems in a port area [72][129]. Because the ships were berthing in and out constantly, there would be constant plug-and-play activities, which might result in large loading pulses [135]–[137]. Port microgrids include a range of important and adaptable electrical loads such as cranes, winches, reefer systems, shore power delivery to berthed-in vessels, and electric cars, as well as the ability to incorporate local energy sources. Many studies have indicated that the increased use of electricity, with the incorporation of renewable energy and energy storage systems, will be the main factor in achieving better environmental sustainability in future ports [50], [54], [134], [138]. Nevertheless, because of the intermittent and volatile nature of non-dispatchable renewable energy systems, along with the incorporation of novel kinds of electrical loads, port area operation planning has become considerably challenging [50], [54]. In fact, with a greater prevalence of offshore renewable energy systems held by seaport owners, they would run their dispersed production and energy storage system units in order to profit economically, by selling back the energy to the main grid [139]. Thus, in this regard, the port operation differs from that of a typical grid-supported (and isolated) microgrid, with the primary goal being to handle the system's load demand by depending on power delivery from the main grid [140]. A smart grid system is needed to fulfil the requirements of four sectors: (1) QCs, (2) on-shore, (3) infrastructure and storage, and (4) equipment. As reported, energy storage systems, as well as conventional grid systems, were known as the primary components of the smart grid. Wind power and solar energy were also used to augment sustainable energy sources. Clearly, the smart grid was at the core of the system, performing functions including energy multidirectional flow centralisation distribution, control, and time data handling [54]. In general, the connections between the components of the grid control system at a seaport are depicted in Fig. 5.

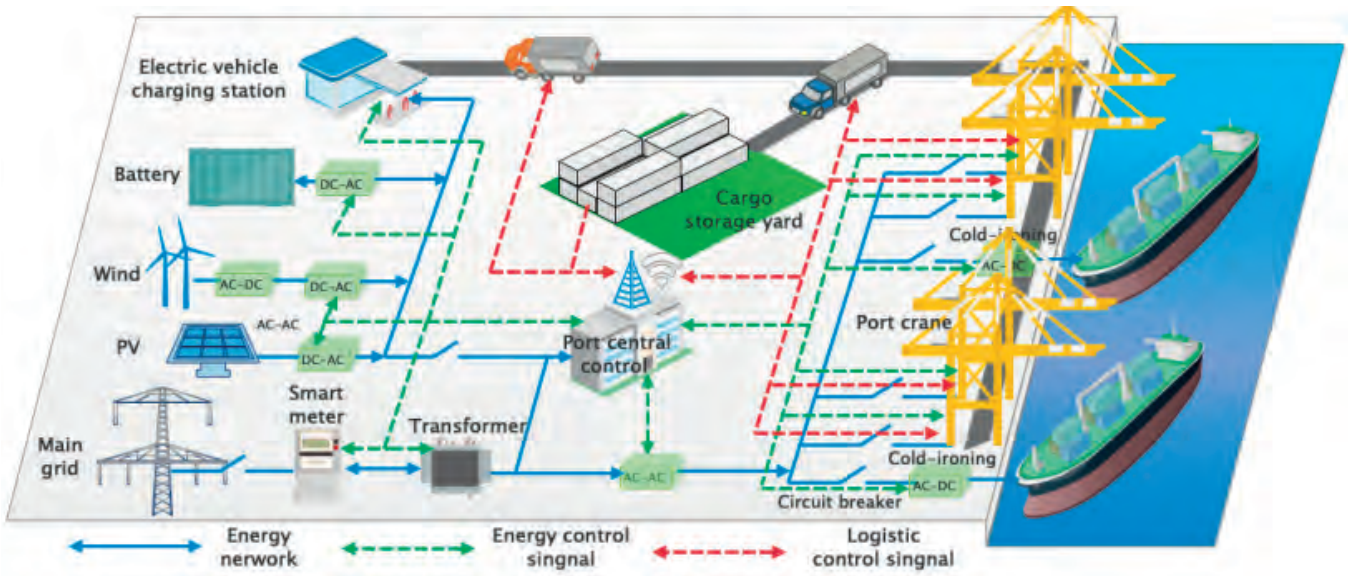

Fig. 4. Seaport grid for energy management plan [54]

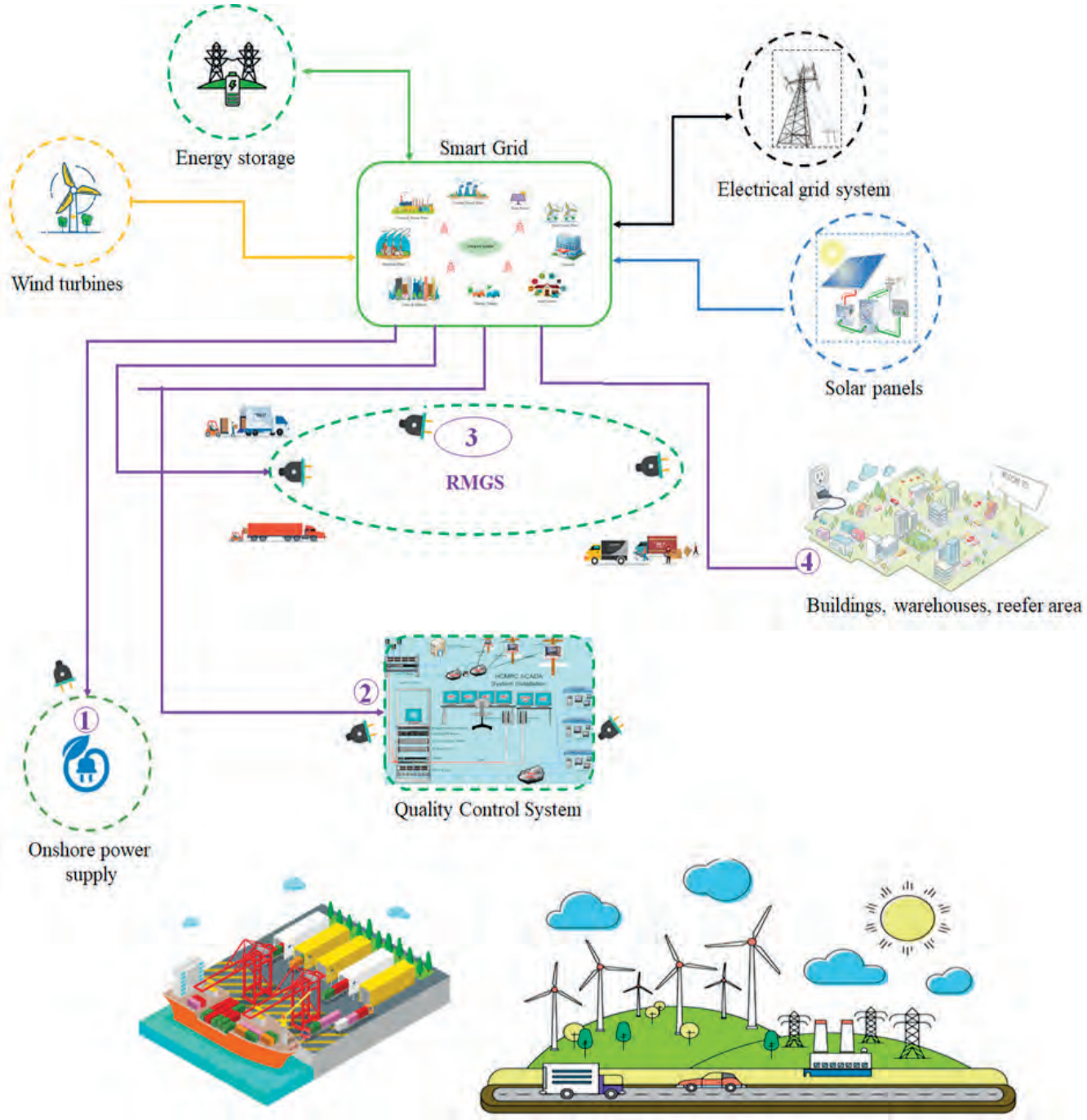

Fig. 5. Model of smart grid management at seaports [141]

POLICY FACTORS

The significance of consuming energy at ports stems from the large energy requirements of seaport activities. Energy efficiency is regarded as a problem for port authorities, since more energy usage results in more carbon emissions and higher operating expenses [52]. As a result, most seaport organisations advocate for port officials to enact port laws aiming to mitigate energy consumption, while increasing renewable sources of energy. This would also help to lower carbon pollution and energy expenses for the operating systems of ports [142]. Various innovations have sought to define and establish environmental performance metrics to assist port officials in alleviating and eliminating the influence of environmental impacts [143]–[145]. Regarding the diversity of port authorities, they were observed to differ significantly in their aims, institutional frameworks, functions, market power, financial capabilities, competencies, knowledge, and

skills, as well as energy and environmental concerns, which were heavily influenced by the specific position and properties of each seaport zone [10]. Importantly, there were three levels of potential intervention from the viewpoint of environmental management by a seaport authority, with various potential effects and impacts at each level: (1) – those under the port authority's responsibility (limited effect, high influence), (2) – other interventions in the port zone (reasonable effect and influence), as well as (3) – interventions at the transportation and logistics chain levels [10]. Therefore, a model of energy management is suggested, with the aim of optimising energy consumption, thereby reducing GHG emissions, as depicted in Fig. 6.

green policies and initiatives [149][150]. A good example is the green purchasing policy, which requires ports to acquire and buy goods from ecologically favourable sectors [151], [152]. Seaports, such as the ports of Zeebrugge and Houston, purchase green dredging and towage, as well as green power generated from renewable energy [153]. Furthermore, the green travel program also promotes and incentivises port workers and residents to utilise public transportation, carpooling, biking, vanpooling, and even constructed bicycle parking and storage [151], [154]. Moreover, ports implement policies aiming to reduce freight and port vehicle idling periods via eco-driving and vessel idling times by designating quicker berths for green boats, such as the green

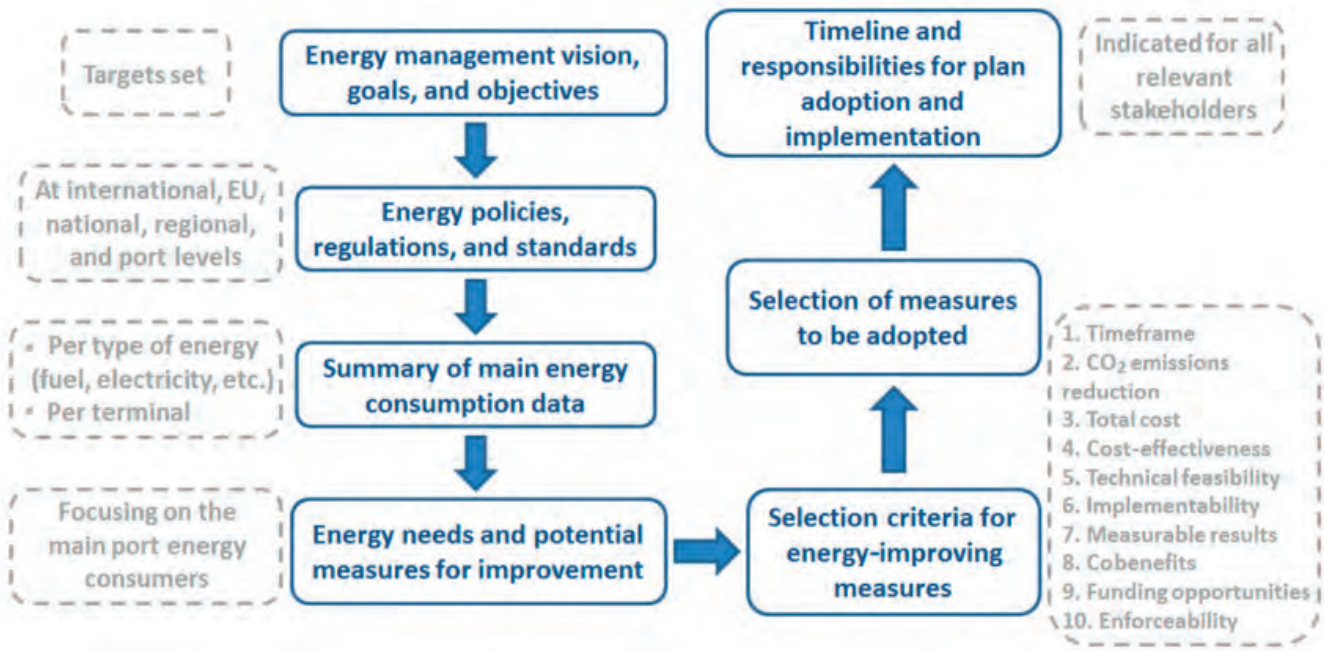

Fig. 6. Energy management planning to get low costs and low CO_2 emissions [10]

Noticeably, the impact level that a seaport authority had in taking actions for enhancing a port's energy and environmental performance differed across the three levels and was determined by the administrative structure, functions, and goals, along with the seaport authority's general competence [146]. Seaport officials, at least those of the landlord kind, took responsibility for the possible incorporation of environment-related factors in the terminal granting process to private operators, in addition to their involvement in seaport environmental management [147] [148]. Furthermore, seaport authorities might include more stringent construction guidelines for the modal split targets, infrastructure and superstructure of ports, and specific methods, such as using a minimal proportion of green energy or installing cold ironing or LNG facilities in the concession agreement [10].

In fact, seaports could go beyond technological and operational emission reduction steps by implementing various

berth allocation at the Panama Canal. More appealingly, ports recently emerged as key participants in carbon capture and storage [72]. Apart from that, ports create verdant buffer zones that enhance the look of a city; for instance, ports of Long Beach planted trees to optimise carbon sequestration [151], [154]. Thus, the carbon captured through carbon capture and utilisation could be used to supply other products [155]. Table 1 summarises the suggested policy for energy management at seaports around the world.

Tab. 1. Suggested policy for energy management plan in ports

Port and country	Input	Facilities	Policy proposal	Reference
Rotterdam, Netherlands	– The overall trans-shipment performance; – Modal split, terminal layout; – Terminal configuration (QCs, BCs, RCs, RS, ASCs, RSCs, AVGs).	Cargo handling, cranes, vehicles, trucks.	– Construct compact terminals; – Fast replacement of (diesel-powered) terminal equipment; – Blending biofuels.	[119]
Barcelona, Spain	– Consumption of electricity; – Consumption of natural gas, gasoline, diesel oil, and jet fuel; – Consumption of waste.	Cargo handling, cranes, vehicles, trucks, arrival vessel, departure vessel, hotelling, manoeuvring.	– Compatible with existing city inventories; – The consequences of GHG emissions might be more than global-scale climate change.	[156]
UK ports	– Time for staying at the port; – Type of vessel; – Type of engine; – Type of fuel.	Cargo handling, cranes, vehicles, trucks, arrival vessel, departure vessel, hotelling, manoeuvring.	– Developing both individually and collectively port working policies of reduction in emissions; – Encouraging shipping companies.	[11]
EU ports	– Number of lights, equipment, and cooling systems; – Throughput of containers; – Working time per day; – Time for staying at port.	Cargo handling, cranes, vehicles, trucks, cooling systems, lighting, and generators.	– Instead of allocating the equation of CO_2 to containers; – Handling a reference system combining weight and volume might be required;	[71]
Qingdao, Shanghai, and Tianjin terminals, China	– Container throughput; – Berth length; – Number of equipment; – Type of fuel.	Cargo handling, cranes, vehicles, trucks, heaters, water & solid waste treatment.	– Making appropriate policies for GHG emission mitigation; – A dual method to calculate GHG emissions from various sources.	[120]
Tianjin Port, China	– Type of engine, fuel; – Installed power; – Operating time; – Emission factor.	Arrival vessel, departure vessel, hotelling, manoeuvring, fairways, berth, anchorage areas.	– Emission measurement in port with both high temporal and spatial resolution is available.	[157]
Chennai Port, India	– Number of equipment; – Type of engine, fuel; – Speed of approach in port.	Cargo handling, cranes, hotelling, manoeuvring, arrival and departure vessel.	– Implementing energy conservation measures and renewable energy technologies.	[115]
Tianjin, Ningbo, Guangzhou, and Dalian ports, China	– Number of QCs, YCs, arrival vessel; – Type of fuel, vessel.	Berth, cargo handling, cranes, vehicles, trucks, hotelling, manoeuvring, arrival and departure vessel.	– Stochastic DEA can be used for future economic planning and policy evaluation.	[122]

SUGGESTIONS FOR GREEN PORTS TOWARD GREEN LOGISTICS

It is easy to see the enormous opportunities for renewable energy applications in ports, which contribute to meeting a portion, or even all, of the port's electricity consumption, thereby reducing carbon emissions. In a study by Mishra et al. [70], carbon emissions were calculated for different port activities, showing that port operations produced approximately 280,558 tons of CO_2 per year. So as to alleviate CO_2 emissions, several methods were suggested for integrating renewable sources of energy [158], [159]. However, the important issue is the desire of the port managers/owners to use renewable energy to meet their energy requirements [160]. Indeed, seaports are known as logistic nodes aiming to accommodate ships/vessels [161]. Ports, as extensively global nodes, could generate adverse effects on the climate via their logistical and industrial functions. Hence, ports play an important role in green supply chain management [162]. Indeed, the structure of green supply chain management associated with port functions can be illustrated as Fig. 7.

Fig. 7. Role of ports in green supply chain management [162]

As reported, the renewable sources of energy that could be advanced in ports include: the wind technology installed in electric forklifts and cranes; off-shore, photovoltaic techniques integrated into buildings to meet the energy demand of electric vehicles, offices, and garage facilities; small-scale wind power used in buildings, to fulfil the energy demand of garage facilities, offices, and electric transport; biodiesel for an internal fleet; and ocean energy for electric forklifts and cranes [163]. When the use of renewable energy is not feasible, ports could buy power from the Renewable Energy Purchase Initiative to mitigate GHG emissions [151]. Furthermore, ports engage in and collaborate with other businesses through renewable energy cooperatives, to broaden the extent of renewable energy employment. For this reason, port authorities should increase the penetration rate of renewable energy to energy systems, in order to achieve the goals of green port logistics and green maritime in the near future.

Indeed, Hentschel et al. [164] examined how to expand renewable energy cooperatives in the Port of Rotterdam. In addition, the EU's 'E-ports' initiative researched the possible use of renewable energy in EU ports [165] and a The World Association for Waterborne Transport Infrastructure described renewable energy techniques and their potential [166]. When combining renewable energies, the overall energy usage and CO_2 emissions were seen to greatly decrease. In a study by Fahdi et al. [167], diverse renewable energy was compared for various Asian ports, discovering energy savings ranging from 12-84% and CO_2 reductions ranging between 2.7-80.0%. Some studies addressed the significance of green energy sources in establishing a viable port [51]. In this context, "the proportion of energy from renewable sources" was utilised as a key performance indicator (KPI) for smart and sustainable ports [50], [168], [169]. Apart from that, the significance of RE was also emphasised in a German marine industry report [170]. In this regard, Hamburg Port erected over 20 wind turbines with a total capacity of 25.4 MW, with seven additional turbines scheduled to be installed in 2017 [171]. Although offshore turbines were usually placed in offshore wind farms, they were too large to be incorporated into the port's infrastructure, and so ports have entered into power purchase deals with wind farm operators [166]. More significantly, Li et al. [172] investigated the optimisation of offshore wind production and storage for container ports. In fact, current wind energy producers operate in the ports of San Francisco, New York/New Jersey, San Diego, Zeebrugge, Baltimore, Hamburg and Long Beach, while significant wind developments can also be found in the ports of Rotterdam (200 MW), Amsterdam (28.2 MW), and Antwerp (45 MW) [173].

Ocean energy exploits the energy generated by tides, ocean waves, salinity, and temperature variations [173], and yet it is limited because of navigational and biological challenges. The present state and potential prospects of ocean sources of energy were examined in [174]. Ocean energy could be exploited in two ways: tidal energy and wave energy. Tidal energy converters harness the kinetic energy of the tide's nearshore in passes, islands, and straits. Some investigations looked into the utilisation of tidal turbines in various ports, such as the port of New Jersey in the United States of America [175] and some ports in Spain [160][176]. Wave energy utilisation was investigated for different ports, including Port Leixes in Portugal [177] and various Italian ports [178]. Furthermore, the evolution of the conversion of wave energy in port breakwaters was examined by [179] [155]. Another study, by Alvarez et al. [180], offered a techno-economic analysis of using tidal energy to satisfy the energy requirements of ports and local communities. According to the research, utilising tidal energy was a viable choice in terms of expense and sustainability. The research also investigated tidal turbine generator design while evaluating the economic viability of implementing the system.

Solar energy is considered to be a potential renewable energy source and solar energy can be used to produce electricity or to heat water etc. [181][182]. In particular, PVs were employed in off-grid applications, including remote signals, navigation aids, and buoys. Solar panels were installed in open areas when the land was available, and on the roofs of

buildings, cruise ports, cold storage warehouses, and normal warehouses, as evident at ports such as Rijeka, Venice, and West Sacramento [10][155]. Additionally, PV electricity has been utilised in the ports of Genoa, Amsterdam, Felixstowe, Tokyo, San Diego, and Antwerp [72]. Significant pollution reduction could be realised if the OPS was powered by wind turbines and PVs [183]; thus, PVs have been suggested as a low-carbon green port strategy [184]. Meanwhile, panels are placed on the rooftops of port buildings, lowering the energy expenses associated with heating canteens, buildings, warehouses, and bathrooms [185][155].

Another sustainable source of energy, under consideration for ports, is geothermal energy [72]. Geothermal energy could be employed to produce electricity and, along with cold stores, the heat can also be utilised for heating and cooling workplaces, buildings, and warehouses. Furthermore, near-surface geothermal energy is used in EU ports [173] such as Antwerp and Hamburg [72]. Combined heat and power facilities, also known as co-generation, could offer a significant opportunity for ports [129][186]. It has been noted that combined heat and power could be operated in a heat-controlled mode, employing a waste heat recovery device, from the in-house utilisation of port buildings [171]. Notably, heat exchangers, degassing systems, and water purification technologies are used by the Port of Rotterdam to save energy and collect heat [73]. Material recycling for ports also contribute to additional energy savings [72]. In addition, ports could serve as carbon capture systems in the future, with facilities collecting excess CO_2 from activities and depositing it, without discharging it into the atmosphere [72]. Moreover, Balbaa et al. [187] suggested statistical techniques for combining solar-based farms and biomass energy, with the aim of satisfying electricity requirements in port locations. The effect of such integration was found to have 50% power consumption optimisation with local renewable energy production [188]. In general, green ports should include a core principle relating to Energy-Environment-Economy (3E), as depicted in Fig. 8 [189].

In order to have a high rate of renewable energy in the energy systems of ports, Green Efforts initiatives, sponsored by the EU, recommend: (1) – external provision of regenerative energy and (2) – energy generation from sustainable resources for ports [75]. In the first case of, ports could serve as a great negotiator, grouping all minor customers around the port and negotiating with electricity providers, and then, the supply energy can be distributed to consumers [50]. Even though the use of renewable energy in ports shows a variety of supplied energy source possibilities to target the green port goals, it should take account into the efficiency of using which green energy that is considered the most potential at those ports. Table 2 illustrates various capabilities of renewable energies [155].

Tab. 2. Power capabilities of various renewable energy sources [190][155]

Renewable energy sources	Power produced
Wind turbine	Max 6 MW
Solar PV – rooftop	Max 2 MW
Solar PV – on-ground	Max 50 MW
Tidal energy converters	Max 750 kW
Wave energy converters	Max 250 MW

Fig. 8. Energy-Environment-Economy principle for green ports [189]

In addition to renewable energy applications in ports, sustainability and energy economy goals are encouraged when choosing port machinery; this will cause fewer pollutants to be discharged [4], [5]. In this regard, renewable fuels, such as LNG-based dual-fuel, biodiesel, hydrogen, and fuel cells, and others, are critical in shipping and ports [191]–[193]. Ports can have an impact on reducing pollutants and GHGs by employing renewable fuels in their machinery. As part of the EU-sponsored Green Crane initiative [50], a number of European ports assessed LNG fuel-powered terminal tractors, LNG dual-fuel RSs, dual-fuel RTGs, and LNG. With NOx emissions, the projected CO_2 decrease for terminal tractors based on LNG was 16%. In contrast to fossil fuels, the use of LNG was expected to decrease CO_2 emissions by 25% [122]. In addition, as part of the EU-funded SEA ports initiative [50], hybrid, as well as LNG dual-fuel RTGs, were tested as prototypes. The port at Valencia will eventually employ LNG-fueled engines, along with other 'green' efforts [71]. Because of the growing demand for LNG as a fuel, it is observed that LNG bunkering infrastructure, LNG delivery network, and LNG storage sites all play important parts in ports [50][72]. In addition to LNG, biodiesel is one of the efficient alternatives that could be used in vehicles in ports. For example, the Port of Rotterdam, which obtained a biofuel yield of 4.8 million tons in 2016 and became the top import and export centre, presents clean fuels that are a blend of bio-derived fuels (30%) and diesel fuel. Interestingly, port wastes are used to produce biofuel from natural sources [194]. Furthermore, utilising H_2 fuel cells in terminal machinery is a brand-new method and has been studied in recent years. According to McDowall et al. [195], the Port of Hamburg examined H_2 generated from green resources for fuel cells in forklifts, and the Port of Bremerhaven analysed upgrading engines to H_2-powered combustion engines. Whereas, the Port of Los Angeles and the Port of Long Beach, have evaluated the commercial fuel cell in conjunction with H_2 acting as a clean source of energy for a range of machinery [196].

CONCLUSION

In this work, operational approaches, energy management methods, and technologies for seaport green energy efficacy were all examined. Furthermore, all techniques, measures, and technologies were also analysed and contrasted in this paper. The findings highlighted that, in addition to electrifying the equipment, the employment of renewable energy and biofuels could be investigated in future green ports. Besides this, seaports could improve energy distribution, create better power strategies, and employ a variety of other techniques for reefer containers. In addition, the ports could save energy and reduce emissions by implementing energy management, operational enhancements, and state-of-the-art technologies. Nonetheless, port authorities should make significant efforts in this regard, establishing suitable policy frameworks, implementing novel operational practices, and investing in modern techniques, in order to realise additional energy savings and promote their present energy performance. Moreover, studies in the literature clarify the employment of green energy, although there are no studies on its economic impact, best practices, feasibility, or applicability. Hence, further investigations should assess existing renewable energy initiatives in ports around the world; this would significantly contribute to the literature. In this respect, port areas with renewable energy possibilities could be highlighted. In addition, hydrogen fuel cells are employed in many vehicles in the transportation sector, including yard trucks and other port machinery. Ports might benefit from future advancements in this technology. Therefore, further studies should examine the technical, operational, environmental, and economic factors of hydrogen fuel cells in this context. Last but not least, greater commitments to energy saving are required and an appropriate voluntary certification system might be able to effectively advance the process of shifting to green energy, green logistics and maritime.

REFERENCES

1. H. P. Nguyen, "Sustainable development of logistics in Vietnam in the period 2020-2025," Int. J. Innov. Creat. Chang., vol. 11, no. 3, pp. 665–682, 2020.

2. T. E. Notteboom * and J.-P. Rodrigue, "Port regionalization: towards a new phase in port development," Marit. Policy Manag., vol. 32, no. 3, pp. 297–313, Jul. 2005, doi: 10.1080/03088830500139885.

3. M. Gogas, K. Papoutsis, and E. Nathanail, "Optimization of Decision-Making in Port Logistics Terminals: Using Analytic Hierarchy Process for the Case of Port of Thessaloniki," Transp. Telecommun. J., vol. 15, no. 4, pp. 255–268, Dec. 2014, doi: 10.2478/ttj-2014-0022.

4. M. Acciaro et al., "Environmental sustainability in seaports: a framework for successful innovation," Marit. Policy Manag., vol. 41, no. 5, pp. 480–500, Jul. 2014, doi: 10.1080/03088839.2014.932926.

5. J. S. L. Lam and T. Notteboom, "The Greening of Ports: A Comparison of Port Management Tools Used by Leading Ports in Asia and Europe," Transp. Rev., vol. 34, no. 2, pp. 169–189, Mar. 2014, doi: 10.1080/01441647.2014.891162.

6. E. C. Shin, J. K. Kang, S. H. Kim, and J. J. Park, "Construction technology of environmental sustainable shore and harbor structures using stacked geotextile tube," KSCE J. Civ. Eng., vol. 20, no. 6, pp. 2095–2102, Sep. 2016, doi: 10.1007/s12205-015-0792-3.

7. H. Johnson and L. Styhre, "Increased energy efficiency in short sea shipping through decreased time in port," Transp. Res. Part A Policy Pract., vol. 71, pp. 167–178, 2015.

8. A. Di Vaio, L. Varriale, and F. Alvino, "Key performance indicators for developing environmentally sustainable and energy efficient ports: Evidence from Italy," Energy Policy, vol. 122, pp. 229–240, Nov. 2018, doi: 10.1016/j.enpol.2018.07.046.

9. J. Martínez-Moya, B. Vazquez-Paja, and J. A. Gimenez Maldonado, "Energy efficiency and CO_2 emissions of port container terminal equipment: Evidence from the Port of Valencia," Energy Policy, vol. 131, pp. 312–319, Aug. 2019, doi: 10.1016/j.enpol.2019.04.044.

10. M. Boile, S. Theofanis, E. Sdoukopoulos, and N. Plytas, "Developing a Port Energy Management Plan: Issues, Challenges, and Prospects," Transp. Res. Rec., vol. 2549, no. 1, pp. 19–28, Jan. 2016, doi: 10.3141/2549-03.

11. D. Gibbs, P. Rigot-Muller, J. Mangan, and C. Lalwani, "The role of sea ports in end-to-end maritime transport chain emissions," Energy Policy, vol. 64, pp. 337–348, 2014.

12. H. Winnes, L. Styhre, and E. Fridell, "Reducing GHG emissions from ships in port areas," Res. Transp. Bus. Manag., 2015, doi: 10.1016/j.rtbm.2015.10.008.

13. J. Kim, M. Rahimi, and J. Newell, "Life-Cycle Emissions from Port Electrification: A Case Study of Cargo Handling Tractors at the Port of Los Angeles," Int. J. Sustain. Transp., vol. 6, no. 6, pp. 321–337, Nov. 2012, doi: 10.1080/15568318.2011.606353.

14. M. Luo and T. L. Yip, "Ports and the environment," Marit. Policy Manag., vol. 40, no. 5, pp. 401–403, Sep. 2013, doi: 10.1080/03088839.2013.797122.

15. V. D. Tran, A. T. Le, and A. T. Hoang, "An Experimental Study on the Performance Characteristics of a Diesel Engine Fueled with ULSD-Biodiesel Blends.," Int. J. Renew. Energy Dev., vol. 10, no. 2, pp. 183–190, 2021.

16. A. T. Hoang, V. D. Tran, V. H. Dong, and A. T. Le, "An experimental analysis on physical properties and spray characteristics of an ultrasound-assisted emulsion of ultra-low-sulphur diesel and Jatropha-based biodiesel," J. Mar. Eng. Technol., vol. 21, no. 2, pp. 73–81, Mar. 2022, doi: 10.1080/20464177.2019.1595355.

17. J.-K. Woo, D. S. H. Moon, and J. S. L. Lam, "The impact of environmental policy on ports and the associated economic opportunities," Transp. Res. Part A Policy Pract., vol. 110, pp. 234–242, 2018.

18. J. M. . Low and S. W. Lam, "Evaluations of port performances from a seaborne cargo supply chain perspective," Polish Marit. Res., vol. 20, no. Special-Issue, pp. 20–31, Jul. 2013, doi: 10.2478/pomr-2013-0024.

19. G. Wilmsmeier and T. Spengler, "Energy consumption and container terminal efficiency," 2016.

20. G. Parise, L. Parise, A. Malerba, F. M. Pepe, A. Honorati, and P. Ben Chavdarian, "Comprehensive peak-shaving solutions for port cranes," IEEE Trans. Ind. Appl., vol. 53, no. 3, pp. 1799–1806, 2016.

21. E. Sdoukopoulos, M. Boile, A. Tromaras, and N. Anastasiadis, "Energy Efficiency in European Ports: State-Of-Practice and Insights on the Way Forward," Sustainability, vol. 11, no. 18, p. 4952, Sep. 2019, doi: 10.3390/su11184952.

22. A. E. Tironi, B. M. Corti, and C. G. Ubezio, "A novel approach in multi-port DC/DC converter control," in 2015 International Conference on Clean Electrical Power (ICCEP), Jun. 2015, pp. 48–54, doi: 10.1109/ICCEP.2015.7177599.

23. X. P. Nguyen and A. T. Hoang, "The Flywheel Energy Storage System: An Effective Solution to Accumulate Renewable Energy," 2020 6th Int. Conf. Adv. Comput. Commun. Syst., pp. 1322–1328, Mar. 2020, doi: 10.1109/ICACCS48705.2020.9074469.

24. L. Xu, Y. Zhang, and X. Wen, "Multioperational Modes and Control Strategies of Dual-Mechanical-Port Machine for Hybrid Electrical Vehicles," IEEE Trans. Ind. Appl., vol. 45, no. 2, pp. 747–755, 2009, doi: 10.1109/TIA.2009.2013575.

25. X. Ren, D. Li, R. Qu, W. Kong, X. Han, and T. Pei, "Analysis of Spoke-Type Brushless Dual-Electrical-Port Dual-Mechanical-Port Machine With Decoupled Windings," IEEE Trans. Ind. Electron., vol. 66, no. 8, pp. 6128–6140, Aug. 2019, doi: 10.1109/TIE.2018.2870395.

26. N. Sifakis, S. Konidakis, and T. Tsoutsos, "Hybrid renewable energy system optimum design and smart dispatch for nearly Zero Energy Ports," J. Clean. Prod., vol. 310, p. 127397, Aug. 2021, doi: 10.1016/j.jclepro.2021.127397.

27. K.-L. A. Yau, S. Peng, J. Qadir, Y.-C. Low, and M. H. Ling, "Towards Smart Port Infrastructures: Enhancing Port Activities Using Information and Communications Technology," IEEE Access, vol. 8, pp. 83387–83404, 2020, doi: 10.1109/ACCESS.2020.2990961.

28. A. Manos, "How the Vision of a Distribution System Operator Encompasses the Green Energy Transformation of Ports [Technology Leaders]," IEEE Electrif. Mag., vol. 11, no. 1, pp. 6–91, Mar. 2023, doi: 10.1109/MELE.2022.3232922.

29. G.-Y. Gan, H.-S. Lee, Y.-J. Tao, and C.-S. Tu, "Selecting Suitable, Green Port Crane Equipment for International

Commercial Ports," Sustainability, vol. 13, no. 12, p. 6801, Jun. 2021, doi: 10.3390/su13126801.

30. T. P. V. Zis, "Prospects of cold ironing as an emissions reduction option," Transp. Res. Part A Policy Pract., 2019, doi: 10.1016/j.tra.2018.11.003.

31. R. Winkel, U. Weddige, D. Johnsen, V. Hoen, and S. Papaefthimiou, "Shore Side Electricity in Europe: Potential and environmental benefits," Energy Policy, 2016, doi: 10.1016/j.enpol.2015.07.013.

32. E. A. Sciberras, B. Zahawi, and D. J. Atkinson, "Electrical characteristics of cold ironing energy supply for berthed ships," Transp. Res. Part D Transp. Environ., vol. 39, pp. 31–43, 2015.

33. A. Innes and J. Monios, "Identifying the unique challenges of installing cold ironing at small and medium ports–The case of Aberdeen," Transp. Res. Part D Transp. Environ., vol. 62, pp. 298–313, 2018.

34. R. Bergqvist and J. Monios, "Green ports in theory and practice," in Green ports, Elsevier, 2019, pp. 1–17.

35. WCPI, "Existing Fleet and Current Orderbooks," 2018. .

36. Z. Korczewski, "Energy and Emission Quality Ranking of Newly Produced Low-Sulphur Marine Fuels," Polish Marit. Res., vol. 29, no. 4, pp. 77–87, Dec. 2022, doi: 10.2478/pomr-2022-0045.

37. A. T. Hoang, "Applicability of fuel injection techniques for modern diesel engines," in International Conference on Sustainable Manufacturing, Materials and Technologies, ICSMMT 2019, 2020, p. 020018, doi: 10.1063/5.0000133.

38. Z. Yang, Q. Tan, and P. Geng, "Combustion and Emissions Investigation on Low-Speed Two-Stroke Marine Diesel Engine with Low Sulfur Diesel Fuel," Polish Marit. Res., vol. 26, no. 1, 2019, doi: 10.2478/pomr-2019-0017.

39. V. V. Pham and A. T. Hoang, "Technological perspective for reducing emissions from marine engines," Int. J. Adv. Sci. Eng. Inf. Technol., vol. 9, no. 6, pp. 1989–2000, 2019.

40. T. Zis, R. J. North, P. Angeloudis, W. Y. Ochieng, and M. G. H. Bell, "Evaluation of cold ironing and speed reduction policies to reduce ship emissions near and at ports," Marit. Econ. Logist., vol. 16, no. 4, pp. 371–398, 2014.

41. T. Coppola, M. Fantauzzi, S. Miranda, and F. Quaranta, "Cost/benefit analysis of alternative systems for feeding electric energy to ships in port from ashore," in 2016 AEIT International Annual Conference (AEIT), 2016, pp. 1–7.

42. C.-C. Chang and C.-M. Wang, "Evaluating the effects of green port policy: Case study of Kaohsiung harbor in Taiwan," Transp. Res. Part D Transp. Environ., vol. 17, no. 3, pp. 185–189, 2012.

43. K. Yiğit, G. Kökkülünk, A. Parlak, and A. Karakaş, "Energy cost assessment of shoreside power supply considering the smart grid concept: a case study for a bulk carrier ship," Marit. Policy Manag., vol. 43, no. 4, pp. 469–482, 2016.

44. P.-H. Tseng and N. Pilcher, "A study of the potential of shore power for the port of Kaohsiung, Taiwan: to introduce or not to introduce?," Res. Transp. Bus. Manag., vol. 17, pp. 83–91, 2015.

45. F. Ballini and R. Bozzo, "Air pollution from ships in ports: The socio-economic benefit of cold-ironing technology," Res. Transp. Bus. Manag., vol. 17, pp. 92–98, 2015.

46. S. Gucma, "Conditions of Safe Ship Operation in Seaports – Optimization of Port Waterway Parameters," Polish Marit. Res., vol. 26, no. 3, pp. 22–29, Sep. 2019, doi: 10.2478/pomr-2019-0042.

47. W. J. Hall, "Assessment of CO_2 and priority pollutant reduction by installation of shoreside power," Resour. Conserv. Recycl., vol. 54, no. 7, pp. 462–467, 2010.

48. M. Acciaro and G. Wilmsmeier, "Energy efficiency in maritime logistics chains," Res. Transp. Bus. Manag., no. 17, pp. 1–7, 2015.

49. J. H. R. R. van Duin, H. H. Geerlings, A. A. Verbraeck, and T. T. Nafde, "Cooling down: A simulation approach to reduce energy peaks of reefers at terminals," J. Clean. Prod., vol. 193, pp. 72–86, 2018.

50. Ç. Iris and J. S. L. Lam, "A review of energy efficiency in ports: Operational strategies, technologies and energy management systems," Renew. Sustain. Energy Rev., vol. 112, pp. 170–182, 2019.

51. J. C. Rijsenbrij and A. Wieschemann, "Sustainable container terminals: a design approach," in Handbook of terminal planning, Springer, 2011, pp. 61–82.

52. G. Wilmsmeier, J. Froese, A. Zotz, and A. Meyer, "Energy consumption and efficiency: emerging challenges from reefer trade in South American container terminals," FAL Bull., vol. 1, no. 329, p. 9, 2014.

53. S. Hartmann, "Scheduling reefer mechanics at container terminals," Transp. Res. Part E Logist. Transp. Rev., vol. 51, pp. 17–27, 2013.

54. S. Fang, Y. Wang, B. Gou, and Y. Xu, "Toward future green maritime transportation: An overview of seaport

microgrids and all-electric ships," IEEE Trans. Veh. Technol., vol. 69, no. 1, pp. 207–219, 2019.

55. J. He, "Berth allocation and quay crane assignment in a container terminal for the trade-off between time-saving and energy-saving," Adv. Eng. Informatics, vol. 30, no. 3, pp. 390–405, Aug. 2016, doi: 10.1016/j.aei.2016.04.006.

56. A. Mao, T. Yu, Z. Ding, S. Fang, J. Guo, and Q. Sheng, "Optimal scheduling for seaport integrated energy system considering flexible berth allocation," Appl. Energy, vol. 308, p. 118386, Feb. 2022, doi: 10.1016/j.apenergy.2021.118386.

57. C. Basu et al., "Sensor-Based Predictive Modeling for Smart Lighting in Grid-Integrated Buildings," IEEE Sens. J., vol. 14, no. 12, pp. 4216–4229, Dec. 2014, doi: 10.1109/JSEN.2014.2352331.

58. A. Rosemann, "The Energy Saving Potential of Occupancy-Based Lighting Control Strategies in Open-Plan Offices: The Influence of Occupancy Patterns," Energies, vol. 11, no. 1, p. 2, Dec. 2017, doi: 10.3390/en11010002.

59. S. Bunjongjit and A. Ngaopitakkul, "Feasibility Study and Impact of Daylight on Illumination Control for Energy-Saving Lighting Systems," Sustainability, vol. 10, no. 11, p. 4075, Nov. 2018, doi: 10.3390/su10114075.

60. R. Bardhan and R. Debnath, "Towards daylight inclusive bye-law: Daylight as an energy saving route for affordable housing in India," Energy Sustain. Dev., vol. 34, pp. 1–9, Oct. 2016, doi: 10.1016/j.esd.2016.06.005.

61. Y. Gao, Y. Cheng, H. Zhang, and N. Zou, "Dynamic illuminance measurement and control used for smart lighting with LED," Measurement, vol. 139, pp. 380–386, Jun. 2019, doi: 10.1016/j.measurement.2019.03.003.

62. C. Yin, S. Dadras, X. Huang, J. Mei, H. Malek, and Y. Cheng, "Energy-saving control strategy for lighting system based on multivariate extremum seeking with Newton algorithm," Energy Convers. Manag., vol. 142, pp. 504–522, Jun. 2017, doi: 10.1016/j.enconman.2017.03.072.

63. S. Gorgulu and S. Kocabey, "An energy saving potential analysis of lighting retrofit scenarios in outdoor lighting systems: A case study for a university campus," J. Clean. Prod., vol. 260, p. 121060, Jul. 2020, doi: 10.1016/j.jclepro.2020.121060.

64. N. Sifakis, K. Kalaitzakis, and T. Tsoutsos, "Integrating a novel smart control system for outdoor lighting infrastructures in ports," Energy Convers. Manag., vol. 246, p. 114684, Oct. 2021, doi: 10.1016/j.enconman.2021.114684.

65. G. P. Gobbi, L. Di Liberto, and F. Barnaba, "Impact of port emissions on EU-regulated and non-regulated air quality indicators: The case of Civitavecchia (Italy)," Sci. Total Environ., vol. 719, p. 134984, Jun. 2020, doi: 10.1016/j.scitotenv.2019.134984.

66. M. Halper, "Dutch Port Taps Smart Street Lighting," 2017.

67. N. Sifakis and T. Tsoutsos, "Can a medium-sized Mediterranean port be green and energy-independent?," 2021.

68. W. Pan and J. Du, "Impacts of urban morphological characteristics on nocturnal outdoor lighting environment in cities: An empirical investigation in Shenzhen," Build. Environ., vol. 192, p. 107587, Apr. 2021, doi: 10.1016/j.buildenv.2021.107587.

69. P. Zajac and G. Przybylek, "Lighting lamps in recreational areas – Damage and prevention, testing and modelling," Eng. Fail. Anal., vol. 115, p. 104693, Sep. 2020, doi: 10.1016/j.engfailanal.2020.104693.

70. A. Misra, K. Panchabikesan, S. K. Gowrishankar, E. Ayyasamy, and V. Ramalingam, "GHG emission accounting and mitigation strategies to reduce the carbon footprint in conventional port activities–a case of the Port of Chennai," Carbon Manag., vol. 8, no. 1, pp. 45–56, 2017.

71. J. Froese, S. Toter, and I. Erdogan, "Green and effective operations at terminals and in ports (Green EFFORTS) project," GreenPort Mag. Hampsh., 2011.

72. M. Acciaro, H. Ghiara, and M. I. Cusano, "Energy management in seaports: A new role for port authorities," Energy Policy, vol. 71, pp. 4–12, 2014.

73. R. M. A. Hollen, F. A. J. Van Den Bosch, and H. W. Volberda, "Strategic levers of port authorities for industrial ecosystem development," Marit. Econ. Logist., vol. 17, no. 1, pp. 79–96, 2015.

74. J. Bakker, D. M. Frangopol, and K. Breugel, Life-Cycle of Engineering Systems: Emphasis on Sustainable Civil Infrastructure. London: CRC Press, 2016.

75. E. I. Froese Jens, Toter Svenja, "Green and effective operations at terminals and in ports, green efforts project Technical report 2014," 2014.

76. B. Hu, "Application of Evaluation Algorithm for Port Logistics Park Based on Pca-Svm Model," Polish Marit. Res., vol. 25, no. s3, pp. 29–35, Dec. 2018, doi: 10.2478/pomr-2018-0109.

77. M. Budzyński, D. Ryś, and W. Kustra, "Selected Problems of Transport in Port Towns – Tri-City as an Example,"

Polish Marit. Res., vol. 24, no. s1, pp. 16–24, Apr. 2017, doi: 10.1515/pomr-2017-0016.

78. D. Steenken, S. Voß, and R. Stahlbock, "Container terminal operation and operations research-a classification and literature review," OR Spectr., vol. 26, no. 1, pp. 3–49, 2004.

79. C. Bierwirth and F. Meisel, "A follow-up survey of berth allocation and quay crane scheduling problems in container terminals," Eur. J. Oper. Res., vol. 244, no. 3, pp. 675–689, 2015.

80. P. Alderton and G. Saieva, Port management and operations. Taylor & Francis, 2013.

81. A. T. Hoang et al., "Energy-related approach for reduction of CO_2 emissions: A critical strategy on the port-to-ship pathway," J. Clean. Prod., vol. 355, p. 131772, Jun. 2022, doi: 10.1016/j.jclepro.2022.131772.

82. M. Wei, J. He, C. Tan, J. Yue, and H. Yu, "Quay crane scheduling with time windows constraints for automated container port," Ocean Coast. Manag., vol. 231, p. 106401, Jan. 2023, doi: 10.1016/j.ocecoaman.2022.106401.

83. D. Chang, Z. Jiang, W. Yan, and J. He, "Integrating berth allocation and quay crane assignments," Transp. Res. Part E Logist. Transp. Rev., vol. 46, no. 6, pp. 975–990, 2010.

84. Ç. Iris, D. Pacino, S. Ropke, and A. Larsen, "Integrated berth allocation and quay crane assignment problem: Set partitioning models and computational results," Transp. Res. Part E Logist. Transp. Rev., vol. 81, pp. 75–97, 2015.

85. Ç. Iris, D. Pacino, and S. Ropke, "Improved formulations and an adaptive large neighborhood search heuristic for the integrated berth allocation and quay crane assignment problem," Transp. Res. Part E Logist. Transp. Rev., vol. 105, pp. 123–147, 2017.

86. D. Liu, Z. Shi, and W. Ai, "An improved car-following model accounting for impact of strong wind," Math. Probl. Eng., vol. 2017, 2017.

87. C. C. Chang and C. W. Jhang, "Reducing speed and fuel transfer of the green flag incentive program in kaohsiung port taiwan," Transp. Res. Part D Transp. Environ., vol. 46, pp. 1–10, 2016.

88. Y. Du, Q. Chen, J. S. L. Lam, Y. Xu, and J. X. Cao, "Modeling the impacts of tides and the virtual arrival policy in berth allocation," Transp. Sci., vol. 49, no. 4, pp. 939–956, 2015.

89. G. Venturini, Ç. Iris, C. A. Kontovas, and A. Larsen, "The multi-port berth allocation problem with speed optimization and emission considerations," Transp. Res. Part D Transp. Environ., vol. 54, pp. 142–159, 2017.

90. D.-H. Lee, Z. Cao, and Q. Meng, "Scheduling of two-transtainer systems for loading outbound containers in port container terminals with simulated annealing algorithm," Int. J. Prod. Econ., vol. 107, no. 1, pp. 115–124, 2007.

91. J. He, Y. Huang, and W. Yan, "Yard crane scheduling in a container terminal for the trade-off between efficiency and energy consumption," Adv. Eng. Informatics, vol. 29, no. 1, pp. 59–75, 2015.

92. M. Sha et al., "Scheduling optimization of yard cranes with minimal energy consumption at container terminals," Comput. Ind. Eng., vol. 113, pp. 704–713, 2017.

93. J. Xin, R. R. Negenborn, and G. Lodewijks, "Hybrid MPC for balancing throughput and energy consumption in an automated container terminal," in 16th International IEEE Conference on Intelligent Transportation Systems (ITSC 2013), 2013, pp. 1238–1244.

94. J. Xin, R. R. Negenborn, and G. Lodewijks, "Energy-aware control for automated container terminals using integrated flow shop scheduling and optimal control," Transp. Res. Part C Emerg. Technol., vol. 44, pp. 214–230, 2014.

95. J. Xin, R. R. Negenborn, and G. Lodewijks, "Event-driven receding horizon control for energy-efficient container handling," Control Eng. Pract., vol. 39, pp. 45–55, 2015.

96. H. Geerlings, R. Heij, and R. van Duin, "Opportunities for peak shaving the energy demand of ship-to-shore quay cranes at container terminals," J. Shipp. Trade, vol. 3, no. 1, pp. 1–20, 2018.

97. B. Wen, W. Xia, and J. M. Sokolovic, "Recent advances in effective collectors for enhancing the flotation of low rank/oxidized coals," Powder Technol., vol. 319, pp. 1–11, 2017.

98. A. H. Gharehgozli, D. Roy, and R. De Koster, "Sea container terminals: New technologies and OR models," Marit. Econ. Logist., vol. 18, no. 2, pp. 103–140, 2016.

99. T. Robenek, N. Umang, M. Bierlaire, and S. Ropke, "A branch-and-price algorithm to solve the integrated berth allocation and yard assignment problem in bulk ports," Eur. J. Oper. Res., vol. 235, no. 2, pp. 399–411, 2014.

100. Y.-C. Yang and W.-M. Chang, "Impacts of electric rubber-tired gantries on green port performance," Res. Transp. Bus. Manag., vol. 8, pp. 67–76, 2013.

101. M. M. Flynn, P. McMullen, and O. Solis, "Saving energy using flywheels," IEEE Ind. Appl. Mag., vol. 14, no. 6, pp. 69–76, 2008.

102. K. H. Tan and F. F. Yap, "Reducing Fuel Consumption Using Flywheel Battery Technology for Rubber Tyred Gantry Cranes in Container Terminals," 2017.

103. S. Pietrosanti, I. Harrison, A. Luque, W. Holderbaum, and V. M. Becerra, "Net energy savings in Rubber Tyred Gantry cranes equipped with an active front end," in 2016 IEEE 16th International Conference on Environment and Electrical Engineering (EEEIC), 2016, pp. 1–5.

104. M. Antonelli, M. Ceraolo, U. Desideri, G. Lutzemberger, and L. Sani, "Hybridization of rubber tired gantry (RTG) cranes," J. Energy Storage, vol. 12, pp. 186–195, 2017.

105. M. B. Lazic, "Is the Semi-Automated or Automated Rail Mounted Gantry Operation a Green Terminal?," Am. Assoc. Port Authorities, 2006.

106. Y.-C. Yang and C.-L. Lin, "Performance analysis of cargo-handling equipment from a green container terminal perspective," Transp. Res. Part D Transp. Environ., vol. 23, pp. 9–11, 2013.

107. Y.-C. Yang, "Operating strategies of CO_2 reduction for a container terminal based on carbon footprint perspective," J. Clean. Prod., vol. 141, pp. 472–480, 2017.

108. D. Bechtsis, N. Tsolakis, D. Vlachos, and E. Iakovou, "Sustainable supply chain management in the digitalisation era: The impact of Automated Guided Vehicles," J. Clean. Prod., vol. 142, pp. 3970–3984, 2017.

109. J. Schmidt, C. Meyer-Barlag, M. Eisel, L. M. Kolbe, and H.-J. Appelrath, "Using battery-electric AGVs in container terminals—Assessing the potential and optimizing the economic viability," Res. Transp. Bus. Manag., vol. 17, pp. 99–111, 2015.

110. S. Anwar, M. Y. I. Zia, M. Rashid, G. Z. de Rubens, and P. Enevoldsen, "Towards Ferry Electrification in the Maritime Sector," Energies, vol. 13, no. 24, p. 6506, Dec. 2020, doi: 10.3390/en13246506.

111. L. Zhen, L. H. Lee, E. P. Chew, D.-F. Chang, and Z.-X. Xu, "A comparative study on two types of automated container terminal systems," IEEE Trans. Autom. Sci. Eng., vol. 9, no. 1, pp. 56–69, 2011.

112. B. M. Al-Alawi and T. H. Bradley, "Review of hybrid, plug-in hybrid, and electric vehicle market modeling studies," Renew. Sustain. Energy Rev., vol. 21, pp. 190–203, 2013.

113. N. P. Reddy et al., "Zero-Emission Autonomous Ferries for Urban Water Transport: Cheaper, Cleaner Alternative to Bridges and Manned Vessels," IEEE Electrif. Mag., vol. 7, no. 4, pp. 32–45, Dec. 2019, doi: 10.1109/MELE.2019.2943954.

114. H. A. Gabbar, A. H. Fahad, and A. M. Othman, "Design of Test Platform of Connected-Autonomous Vehicles and Transportation Electrification," in Recent Trends in Intelligent Computing, Communication and Devices. Advances in Intelligent Systems and Computing, 2020, pp. 1035–1046.

115. A. Misra, K. Panchabikesan, E. Ayyasamy, and V. Ramalingam, "Sustainability and environmental management: Emissions accounting for ports," Strateg. Plan. Energy Environ., vol. 37, no. 1, pp. 8–26, 2017.

116. Fundacion Valencia port, "SEA TERMINALS – SMART, ENERGY EFFICIENCY AND ADAPTIVE PORT TERMINALS," 2015. .

117. N. Grundmeier, A. Hahn, N. Ihle, S. Runge, and C. Meyer-Barlag, "A simulation based approach to forecast a demand load curve for a container terminal using battery powered vehicles," in 2014 International Joint Conference on Neural Networks (IJCNN), 2014, pp. 1711–1718.

118. F. Alasali, S. Haben, V. Becerra, and W. Holderbaum, "Analysis of RTG crane load demand and short-term load forecasting," Int J Comput Commun Instrumen Eng, vol. 3, no. 2, pp. 448–454, 2016.

119. H. Geerlings and R. Van Duin, "A new method for assessing CO_2-emissions from container terminals: a promising approach applied in Rotterdam," J. Clean. Prod., vol. 19, no. 6–7, pp. 657–666, 2011.

120. Y. Tian and Q. Zhu, "GHG emission assessment of Chinese container terminals: a hybrid approach of IPCC and input-output analysis," Int. J. Shipp. Transp. Logist., vol. 7, no. 6, pp. 758–779, 2015.

121. Y.-T. Chang, Y. Song, and Y. Roh, "Assessing greenhouse gas emissions from port vessel operations at the Port of Incheon," Transp. Res. Part D Transp. Environ., vol. 25, pp. 1–4, 2013.

122. J.-H. Na, A.-Y. Choi, J. Ji, and D. Zhang, "Environmental efficiency analysis of Chinese container ports with CO_2 emissions: An inseparable input-output SBM model," J. Transp. Geogr., vol. 65, pp. 13–24, 2017.

123. K. Rudzki, P. Gomulka, and A. T. Hoang, "Optimization Model to Manage Ship Fuel Consumption and Navigation Time," Polish Marit. Res., vol. 29, no. 3, pp. 141–153, Sep. 2022, doi: 10.2478/pomr-2022-0034.

124. H. Yu, Y.-E. Ge, J. Chen, L. Luo, C. Tan, and D. Liu, "CO_2 emission evaluation of yard tractors during loading

at container terminals," Transp. Res. Part D Transp. Environ., vol. 53, pp. 17–36, 2017.

125. W. Li, W. Liu, X. Xu, and Z. Gao, "The Port Service Ecosystem Research Based on the Lotka-Volterra Model," Polish Marit. Res., vol. 24, no. s3, pp. 86–94, Nov. 2017, doi: 10.1515/pomr-2017-0109.

126. C.-H. Liao, P.-H. Tseng, K. Cullinane, and C.-S. Lu, "The impact of an emerging port on the carbon dioxide emissions of inland container transport: An empirical study of Taipei port," Energy Policy, vol. 38, no. 9, pp. 5251–5257, 2010.

127. A. Rolan, P. Manteca, R. Oktar, and P. Siano, "Integration of Cold Ironing and Renewable Sources in the Barcelona Smart Port," IEEE Trans. Ind. Appl., vol. 55, no. 6, pp. 7198–7206, Nov. 2019, doi: 10.1109/TIA.2019.2910781.

128. G. Buiza, S. Cepolina, A. Dobrijevic, M. del Mar Cerbán, O. Djordjevic, and C. González, "Current situation of the Mediterranean container ports regarding the operational, energy and environment areas," in 2015 International Conference on Industrial Engineering and Systems Management (IESM), 2015, pp. 530–536.

129. G. Parise, L. Parise, L. Martirano, P. Ben Chavdarian, C. L. Su, and A. Ferrante, "Wise port and business energy management: Port facilities, electrical power distribution," IEEE Trans. Ind. Appl., 2016, doi: 10.1109/TIA.2015.2461176.

130. S. G. Gennitsaris and F. D. Kanellos, "Emission-Aware and Cost-Effective Distributed Demand Response System for Extensively Electrified Large Ports," IEEE Trans. Power Syst., vol. 34, no. 6, pp. 4341–4351, Nov. 2019, doi: 10.1109/TPWRS.2019.2919949.

131. J. Prousalidis et al., "The ports as smart micro-grids: development perspectives," Proc. HAEE, pp. 12–16, 2017.

132. A. Alzahrani, I. Petri, Y. Rezgui, and A. Ghoroghi, "Optimal control-based price strategies for smart fishery ports micro-grids," in 2021 IEEE International Conference on Engineering, Technology and Innovation (ICE/ITMC), Jun. 2021, pp. 1–8, doi: 10.1109/ICE/ITMC52061.2021.9570267.

133. M. Canepa, G. Frugone, and R. Bozzo, "Smart Micro-Grid: An Effective Tool for Energy Management in Ports," in Trends and Challenges in Maritime Energy Management, 2018, pp. 275–293.

134. T. Lamberti, A. Sorce, L. Di Fresco, and S. Barberis, "Smart port: Exploiting renewable energy and storage potential of moored boats," in OCEANS 2015 - Genova, May 2015, pp. 1–3, doi: 10.1109/OCEANS-Genova.2015.7271376.

135. S. Mumtaz, S. Ali, S. Ahmad, L. Khan, S. Hassan, and T. Kamal, "Energy Management and Control of Plug-In Hybrid Electric Vehicle Charging Stations in a Grid-Connected Hybrid Power System," Energies, vol. 10, no. 11, p. 1923, Nov. 2017, doi: 10.3390/en10111923.

136. J. Y. Yong, V. K. Ramachandaramurthy, K. M. Tan, and N. Mithulananthan, "Bi-directional electric vehicle fast charging station with novel reactive power compensation for voltage regulation," Int. J. Electr. Power Energy Syst., vol. 64, pp. 300–310, Jan. 2015, doi: 10.1016/j.ijepes.2014.07.025.

137. L. Tan, B. Wu, V. Yaramasu, S. Rivera, and X. Guo, "Effective Voltage Balance Control for Bipolar-DC-Bus-Fed EV Charging Station With Three-Level DC–DC Fast Charger," IEEE Trans. Ind. Electron., vol. 63, no. 7, pp. 4031–4041, Jul. 2016, doi: 10.1109/TIE.2016.2539248.

138. N. B. Ahamad, M. Othman, J. C. Vasquez, J. M. Guerrero, and C.-L. Su, "Optimal sizing and performance evaluation of a renewable energy based microgrid in future seaports," in 2018 IEEE International Conference on Industrial Technology (ICIT), Feb. 2018, pp. 1043–1048, doi: 10.1109/ICIT.2018.8352322.

139. J. Kumar, O. Palizban, and K. Kauhaniemi, "Designing and analysis of innovative solutions for harbour area smart grid," in 2017 IEEE Manchester PowerTech, Jun. 2017, pp. 1–6, doi: 10.1109/PTC.2017.7980870.

140. K. Hein, Y. Xu, W. Gary, and A. K. Gupta, "Robustly coordinated operational scheduling of a grid-connected seaport microgrid under uncertainties," IET Gener. Transm. Distrib., vol. 15, no. 2, pp. 347–358, Jan. 2021, doi: 10.1049/gtd2.12025.

141. V. Duc Bui, H. Phuong Nguyen, X. Phuong Nguyen, and H. Chi Minh city, "Optimization of energy management systems in seaports as a potential strategy for sustainable development," J. Mech. Eng. Res. Dev., vol. 44, no. 8, pp. 19–30, 2021.

142. H. Jiang, W. Xiong, and Y. Cao, "A Conceptual Model of Excellent Performance Mode of Port Enterprise Logistics Management," Polish Marit. Res., vol. 24, no. s3, pp. 34–40, Nov. 2017, doi: 10.1515/pomr-2017-0102.

143. A. Alzahrani, I. Petri, Y. Rezgui, and A. Ghoroghi, "Decarbonisation of seaports: A review and directions for future research," Energy Strateg. Rev., vol. 38, p. 100727, Nov. 2021, doi: 10.1016/j.esr.2021.100727.

144. B. Akgul, "Green Port / Eco Port Project - Applications and Procedures in Turkey," IOP Conf. Ser. Earth Environ. Sci., vol. 95, p. 042063, Dec. 2017, doi: 10.1088/1755-1315/95/4/042063.

145. L. Fobbe, R. Lozano, and A. Carpenter, "Assessing the coverage of sustainability reports: An analysis of sustainability in seaports," SPONSORS, p. 609, 2019.

146. European Sea Ports Organization, "ESPO Green Guide: Towards Excellence in Port Environmental Management and Sustainability," EcoPorts Publications, 2012. .

147. V. D. Bui and H. P. Nguyen, "Role of Inland Container Depot System in Developing the Sustainable Transport System," Int. J. Knowledge-Based Dev., vol. 12, no. 3/4, p. 1, 2022, doi: 10.1504/IJKBD.2022.10053121.

148. H. P. Nguyen, "What solutions should be applied to improve the efficiency in the management for port system in Ho Chi Minh City?," Int. J. Innov. Creat. Chang., vol. 5, no. 2, pp. 1747–1769, 2019.

149. T. T. M. Nguyen, H. P. Nguyen, and V. D. Bui, "Recent Applications for Improving the Last-Mile Delivery in Urbanism Logistics," Int. J. Knowledge-Based Dev., vol. 12, no. 3/4, p. 1, 2022, doi: 10.1504/IJKBD.2022.10052410.

150. V. D. Bui and H. P. Nguyen, "A Systematized Review on Rationale and Experience to Develop Advanced Logistics Center System in Vietnam," Webology, vol. 18, pp. 89–101, 2021.

151. IAPH, "IAPH Tool Box for Greenhouse Gasses," EIA, 2008. .

152. H. P. Nguyen, P. Q. P. Nguyen, and T. P. Nguyen, "Green Port Strategies in Developed Coastal Countries as Useful Lessons for the Path of Sustainable Development: A case study in Vietnam," Int. J. Renew. Energy Dev., vol. 11, no. 4, pp. 950–962, Nov. 2022, doi: 10.14710/ijred.2022.46539.

153. Organisation for Economic Cooperation and Development, The Competitiveness of Global Port-Cities. Paris, France: OECD, 2014.

154. M. Hermans, W. Haynes, and J. Childs, "Port of Portland's Changes in Maintenance Dredging: Barge Unloading and the New Dredged Material Rehandling Facility," in Dredging '02, Oct. 2003, pp. 1–15, doi: 10.1061/40680(2003)95.

155. A. S. Alamoush, F. Ballini, and A. I. Ölçer, "Ports' technical and operational measures to reduce greenhouse gas emission and improve energy efficiency: A review," Mar. Pollut. Bull., vol. 160, p. 111508, Nov. 2020, doi: 10.1016/j.marpolbul.2020.111508.

156. G. Villalba and E. D. Gemechu, "Estimating GHG emissions of marine ports—the case of Barcelona," Energy Policy, vol. 39, no. 3, pp. 1363–1368, 2011.

157. D. Chen et al., "Estimating ship emissions based on AIS data for port of Tianjin, China," Atmos. Environ., 2016, doi: 10.1016/j.atmosenv.2016.08.086.

158. A. T. Hoang, V. V. Pham, and X. P. Nguyen, "Integrating renewable sources into energy system for smart city as a sagacious strategy towards clean and sustainable process," J. Clean. Prod., vol. 305, p. 127161, Jul. 2021, doi: 10.1016/j.jclepro.2021.127161.

159. I. S. Seddiek, "Application of renewable energy technologies for eco-friendly sea ports," Ships Offshore Struct., vol. 15, no. 9, pp. 953–962, Oct. 2020, doi: 10.1080/17445302.2019.1696535.

160. V. Ramos, R. Carballo, M. Álvarez, M. Sánchez, and G. Iglesias, "A port towards energy self-sufficiency using tidal stream power," Energy, vol. 71, pp. 432–444, Jul. 2014, doi: 10.1016/j.energy.2014.04.098.

161. T. Notteboom, "The adaptive capacity of container ports in an era of mega vessels: The case of upstream seaports Antwerp and Hamburg," J. Transp. Geogr., vol. 54, pp. 295–309, Jun. 2016, doi: 10.1016/j.jtrangeo.2016.06.002.

162. T. Notteboom, L. van der Lugt, N. van Saase, S. Sel, and K. Neyens, "The Role of Seaports in Green Supply Chain Management: Initiatives, Attitudes, and Perspectives in Rotterdam, Antwerp, North Sea Port, and Zeebrugge," Sustainability, vol. 12, no. 4, p. 1688, Feb. 2020, doi: 10.3390/su12041688.

163. A. Molavi, G. J. Lim, and B. Race, "A framework for building a smart port and smart port index," Int. J. Sustain. Transp., vol. 14, no. 9, pp. 686–700, Jul. 2020, doi: 10.1080/15568318.2019.1610919.

164. M. Hentschel, W. Ketter, and J. Collins, "Renewable energy cooperatives: Facilitating the energy transition at the Port of Rotterdam," Energy Policy, 2018, doi: 10.1016/j.enpol.2018.06.014.

165. The Pure Energy, "Innovative Green Technologies for a Sustainable Harbour: E-Harbours towards Sustainable, Clean and Energetic Innovative Harbour Cities in the North Sea Region," 2012.

166. PIANC, "Renewables and Energy Efficiency for Maritime Ports - MarCom WG Report n° 159-2019. The World Association for Waterborne Transport Infrastructure," Brussels, Belguim, 2019.

167. S. FAHDI, M. ELKHECHAFI, and H. HACHIMI, "Green Port in Blue Ocean: Optimization of Energy in Asian Ports," in 2019 5th International Conference on Optimization and Applications (ICOA), Apr. 2019, pp. 1–4, doi: 10.1109/ICOA.2019.8727615.

168. G. Buiza, S. Cepolina, A. Dobrijevic, M. del Mar Cerban, O. Djordjevic, and C. Gonzalez, "Current situation of the Mediterranean container ports regarding the operational, energy and environment areas," in International Conference on Industrial Engineering and Systems Management (IESM), Oct. 2015, pp. 530–536, doi: 10.1109/IESM.2015.7380209.

169. B. Ports and O. Conference, Smart energy efficient and adaptive port terminals (Sea Terminals), no. December 2014. Estonia, Spain, Italy, the Netherlands, 2015, p. 1.

170. Federal Ministry for Economic Affairs and Energy, "Maritime Agenda 2025," 2017.

171. HPA, "Energy cooperation, port of Hamburg," 2015.

172. X. Li et al., "A method for optimizing installation capacity and operation strategy of a hybrid renewable energy system with offshore wind energy for a green container terminal," Ocean Eng., vol. 186, p. 106125, Aug. 2019, doi: 10.1016/j.oceaneng.2019.106125.

173. G. Efforts, "Green and Effective Operations at Terminals and in Ports -deliverable 12.1- Recommendations Manual for Terminals. European Commission," 2014.

174. M. Melikoglu, "Current status and future of ocean energy sources: A global review," Ocean Engineering. 2018, doi: 10.1016/j.oceaneng.2017.11.045.

175. H. S. Tang, K. Qu, G. Q. Chen, S. Kraatz, N. Aboobaker, and C. B. Jiang, "Potential sites for tidal power generation: A thorough search at coast of New Jersey, USA," Renew. Sustain. Energy Rev., vol. 39, pp. 412–425, 2014.

176. R. Espina-Valdés, E. Álvarez Álvarez, J. García-Maribona, A. J. G. Trashorras, and J. M. González-Caballín, "Tidal current energy potential assessment in the Avilés Port using a three-dimensional CFD method," Clean Technol. Environ. Policy, 2019, doi: 10.1007/s10098-019-01711-2.

177. P. Rosa-Santos et al., "Experimental Study of a Hybrid Wave Energy Converter Integrated in a Harbor Breakwater," J. Mar. Sci. Eng., vol. 7, no. 2, p. 33, Feb. 2019, doi: 10.3390/jmse7020033.

178. F. Arena, G. Malara, G. Musolino, C. Rindone, A. Romolo, and A. Vitetta, "From green-energy to green-logistics: A pilot study in an Italian port area," 2018, doi: 10.1016/j.trpro.2018.09.013.

179. D. Vicinanza, E. Di Lauro, P. Contestabile, C. Gisonni, J. L. Lara, and I. J. Losada, "Review of Innovative Harbor Breakwaters for Wave-Energy Conversion," J. Waterw. Port, Coastal, Ocean Eng., 2019, doi: 10.1061/(asce)ww.1943-5460.0000519.

180. E. A. Alvarez, A. N. Manso, A. J. Gutiérrez-Trashorras, J. F. Francos, and M. R. Secades, "Obtaining renewable energy from tidal currents in the Aviles port: New services for citizens," 2013, doi: 10.1109/SmartMILE.2013.6708175.

181. S. Nižetić, M. Jurčević, D. Čoko, M. Arıcı, and A. T. Hoang, "Implementation of phase change materials for thermal regulation of photovoltaic thermal systems: Comprehensive analysis of design approaches," Energy, vol. 228, p. 120546, Aug. 2021, doi: 10.1016/j.energy.2021.120546.

182. Z. Said et al., "Application of novel framework based on ensemble boosted regression trees and Gaussian process regression in modelling thermal performance of small-scale Organic Rankine Cycle (ORC) using hybrid nanofluid," J. Clean. Prod., vol. 360, p. 132194, Aug. 2022, doi: 10.1016/j.jclepro.2022.132194.

183. A. M. Kotrikla, T. Lilas, and N. Nikitakos, "Abatement of air pollution at an aegean island port utilizing shore side electricity and renewable energy," Mar. Policy, 2017, doi: 10.1016/j.marpol.2016.01.026.

184. J. S. L. Lam, M. J. Ko, J. R. Sim, and Y. Tee, "Feasibility of implementing energy management system in ports," in 2017 IEEE International Conference on Industrial Engineering and Engineering Management (IEEM), 2017, pp. 1621–1625.

185. E.-H. Electric, "Innovative Green Technologies for a Sustainable Harbour. E-Harbours towards sustainable, clean and energetic innovative harbour cities in the North Sea Region," 2012.

186. Siemens, "Innovative power distribution for ports & harbors Concept for profitable and safe electric power distribution. Technical report," 2017.

187. A. Balbaa and N. H. El-Amary, "Green energy seaport suggestion for sustainable development in Damietta Port, Egypt," WIT Trans. Ecol. Environ., 2017, doi: 10.2495/ECO170071.

188. A. Alzahrani, I. Petri, Y. Rezgui, and A. Ghoroghi, "Developing Smart Energy Communities around Fishery Ports: Toward Zero-Carbon Fishery Ports," Energies, vol. 13, no. 11, p. 2779, Jun. 2020, doi: 10.3390/en13112779.

189. S. Vakili, A. I. Ölçer, A. Schönborn, F. Ballini, and A. T. Hoang, "Energy-related clean and green framework for shipbuilding community towards zero-emissions: A strategic analysis from concept to case study," Int. J. Energy Res., vol. 46, no. 14, pp. 20624–20649, Nov. 2022, doi: 10.1002/er.7649.

190. PIANC, "Renewables and Energy Efficiency for Maritime Ports - MarCom WG Report n° 159-2019," Brussel, 2019.

191. M. Subramanian et al., "A technical review on composite phase change material based secondary assisted battery thermal management system for electric vehicles," J. Clean. Prod., vol. 322, p. 129079, Nov. 2021, doi: 10.1016/j.jclepro.2021.129079.

192. O. Aneziris, I. Koromila, and Z. Nivolianitou, "A systematic literature review on LNG safety at ports," Saf. Sci., vol. 124, p. 104595, Apr. 2020, doi: 10.1016/j.ssci.2019.104595.

193. L. Van Hoecke, L. Laffineur, R. Campe, P. Perreault, S. W. Verbruggen, and S. Lenaerts, "Challenges in the use of hydrogen for maritime applications," Energy Environ. Sci., vol. 14, no. 2, pp. 815–843, 2021, doi: 10.1039/D0EE01545H.

194. A. Misra, G. Venkataramani, S. Gowrishankar, E. Ayyasam, and V. Ramalingam, "Renewable energy based smart microgrids—A pathway to green port development," Strateg. Plan. Energy Environ., vol. 37, no. 2, pp. 17–32, 2017.

195. W. McDowall and M. Eames, "Towards a sustainable hydrogen economy: A multi-criteria sustainability appraisal of competing hydrogen futures," Int. J. Hydrogen Energy, vol. 32, no. 18, pp. 4611–4626, 2007.

196. P. P. Edwards, V. L. Kuznetsov, W. I. F. David, and N. P. Brandon, "Hydrogen and fuel cells: towards a sustainable energy future," Energy Policy, vol. 36, no. 12, pp. 4356–4362, 2008.

POLISH MARITIME RESEARCH 2 (118) 2023 Vol. 30; pp. 188-196
10.2478/pomr-2023-0032

MATHEMATICAL MODEL OF FLEXIBLE LINK DYNAMICS IN MARINE TETHERED SYSTEMS CONSIDERING TORSION AND ITS INFLUENCE ON TENSION FORCE

Konstantin Trunin *
Admiral Makarov National University of Shipbuilding, Mykolaiv, Ukraine

* Corresponding author: *trunin.konstantin.stanislav@gmail.com (K. Trunin)*

ABSTRACT

The rigidity in bending of a flexible link (is an important characteristic that should be considered during regular service conditions. The tension and bending with torsion of wire ropes are also significant factors. This study proposed a method to calculate the vectors of the generalised forces of bending of flexible links. One of the causes of torsional stresses in the power plant of underwater tethered systems is the interaction with ship equipment, such as spiral winding on the winch drum, friction on the flanges of the pulleys or winch drums, and bends on various blocks and rolls that cause torsion. The source of torsional stresses in the FL may also be related to manufacturing, storage, transportation, and its placement on the ship's winch drums. Torsion can lead to a decrease in the tensile strength due to load redistribution between power elements, or even a violation of their structure. In some cases, torsion significantly affects the movement of the underwater tethered system as a whole. The development of a mathematical model to describe the marine tethered systems dynamics, taking into account the effect of torsion, is important and relevant. The mathematical model of the marine tethered systems dynamics was improved and solved by accounting for the generalised forces of the torsion rigidity of the flexible link, using an algorithm and computer program. The influence of the bending and torsional rigidity of the FL on its deflection and tensile strength were considered based on the example of two problems. The developed program's working window image shows the simulated parameters and the initial position of the flexible link. The results show that torsion has almost no effect on the shape of the a flexible link's deflection in the X0Z plane, but leads to a deviation from the X0Z plane when calculating the static deflection of the flexible link. When the carrier vessel is stationary and the submersible vehicle has no restrictions on movement and has positive buoyancy, torsion leads to a three-dimensional change in the shape of the flexible link both in the X0Z plane and in the X0Y plane. The tension force of the flexible link along its length is distributed unevenly, and the torsion of the flexible link can lead to significant changes in its shape, the trajectory of towed objects, and the forces acting on the elements of the marine tethered systems

Keywords: underwater tethered system, flexible links, rigidity, submersible vehicle

INTRODUCTION

When calculating or choosing the design of the flexible links (FL) of marine tethered systems (MTS), account must be taken of the conditions in which they will be operated. The FLs of MTS are used in a wide range of operating modes (different depths, currents, a large number of links in the MTS, their mutual influence, etc.). Complex and difficult (extreme) modes of operation of FLs require special study and determination of the forces acting on them, taking into account the nonlinearity

of the governing equations, the possibility of losing the stability of equilibrium and the study of the system behaviour in supercritical states.

During the operation of the FLs of an underwater tethered system (UTS), there is the possibility of damage to the tow-cable (TC) as a result of repeated bends in the rollers, blocks, winch drums and elements of the lowering and lifting devices [1, p. 5]. In the process of long-term operation, for example, trawler winches, which are designed for uniform laying of FL on their drums, cease to fulfill their purpose after a certain period of operation due to wear of their friction pairs.

Mathematical models (MM) of the FL dynamics of MTS have been developed and improved, complemented by taking into account the generalised forces of the torsion rigidity of the FL and with the help of an algorithm and computer program which were solved by carrying out mathematical modelling of the MTS dynamics, including the influence of the torsion of the FL.

The study of the torsional rigidity (TR) of FLs in operating conditions thus becomes important. Although in some industries these issues have been previously addressed in the operation of FLs, for example, in towing and in UTS, these issues remain virtually unexplored due to the high cost of field experiments, lack of specialists, and the control and measurement complexity. In addition, the existing mathematical models (MM) describing the dynamics do not take into account the TR or allow it to be used in engineering calculations [2, p. 58].

To date, these studies have not received the necessary development due to the lack of reliable MM, which could, however, be quite simply and effectively implemented in the form of algorithms and programs for numerical solutions to these problems.

The aim of the study is to improve the previously developed MM of the FL dynamics in a MTS, taking into account the effect of the torsional rigidity and torsional forces of the FL on its deflection and tensile strength.

As concerns the research methods used in this study, analysis, synthesis, generalisation, analogy as an epistemological basis of modelling, modelling (study of the original object) by creating and studying a copy (the model) that has common properties with the original, are all used as general scientific research methods.

The object of study is the FL of a MTS (based on the example of a UTS). The subject of this research adds to and improves the previously developed method for the MM of the dynamics of the FL of a MTS by determining the vectors of the generalised torsional forces of the FL.

ANALYSIS OF RECENT RESEARCH AND PUBLICATIONS

The elements of a rope (wire) experience tension, bending and contact loads together with torsion [3]. Torsion causes additional stresses that add to the main stress. These stresses have been studied by Glushko [4], Roslik [5, 6], Chukmasov [7], and Jacobson [8].

Glushko [4], considering the helical winding of the rope on the drum, obtained the torsional stress of the helical winding line. By analogy, Roslik [6] obtained the torsional tension of the helix, based on the assumption that it is equal to the torsion of the rope in the pulley system. In the bending of rope on blocks and drums, supplementary tensions appear, which cause axis and twist deformations. Roslik obtained an expression for the definition of the stress of torsion of the rope.

As Egorov [9] believed, in choosing the strength of the wire for the rope, one cannot be guided only by the calculated tension of the rope. The ropes used in the cable part of towed systems (TS) operate in conditions of vibration, which appear as a result of the action of the hydrodynamic forces that occur when towing ropes in water. It is noted that one of the causes of tensile stresses in the power plant of the UTS is the interaction with ship equipment, in which the spiral winding on the winch drum, friction on the flanges of the pulleys or winch drums, or bends in the blocks and rolls cause torsion. As the source of torsional stresses in the FL, there may be technological reasons related to both the manufacture and storage, transportation and placement on the ship's winch.

Poddubniy, Shamarin and other authors [10] considered the problem of equilibrium in the flow of a heavy FL, the bearing part of which consists of twisted flexible tensile elements and which resists torsional deformations. As an example, the towing of a deep-water vehicle, which consists of a submersible vehicle (SV) and a TC with two-and-half power armour, is considered. It is noted that the torsion of the TC leads to a redistribution of the total tension between the outer and inner layers of the armour so that the wires of the inner layer are more loaded than the outer layers. Most unfavourable is the case of free rotation of the running end of the FL, resulting in an estimated loss of tensile strength that reaches 15%. Torsion can cause a decrease in the tensile strength of the FL due to redistribution of load between the power elements, or may even lead to a violation of their structure. In some cases of torsion, the FL significantly affects the nature of the UTS movement as a whole.

In article [11], the matrix method of analysis of the system was widened to take into account the dynamics reaction of the towed system, using the method of equivalent linearisation and perturbation disturbance keys, of the angles of the towed body. Two examples were considered: the first uses the fundamental limitations of the passive compensation of the tow-rod and the second touches on the use of floating communications for dynamics relief. The FL modeling uses a differential approximation with a local disturbance in the form of the FL. This dynamics model is measured without taking account of the bending rigidity of the FL, and without interval elements of the FL.

Work [12] explores a method of motion control for a towed submersible vehicle (TSV) with movable wings. The TSV is affected by the non-linearity and uncertainty of the position of the flexible towing cable, hydrodynamic forces, parametric fluctuations, and external disturbances. The cable is approximated by the method of concentrated masses, where the number of cable segments determines the order of the system. Direct consideration of the non-linear dynamics is one of the main features of the cited work. However, the effect of hydrodynamic compression on the cable during its spatial movement is not considered. A way out of this situation could be an approach that implies creating a comprehensive model for the description of the UTS dynamics.

Article [13] considers a model of flexible segments adopted for dynamics calculations. In this model, the cable is divided into a certain number of flexible segments and is described by the non-linear equations at moments of the uniform segment movement. In a given example, the dynamics modelling was also performed in a two-coordinate system, which is currently insufficient to describe the dynamics of the spatial motion of the UTS.

Study [14] considers the application of a method of dynamic optimisation of the trajectory of a free-floating cable in the water depth. The model was considered in a three-dimensional system of coordinates, splitting the FL into the interrelated elements. The cable is modelled as a chain of rods connected to each other by hinges with two degrees of freedom, which could describe the bend of the cable in two planes (three coordinates). The cable is considered to be very flexible, but not able to be lengthened. The proposed model provides an opportunity to obtain the motion trajectory of a vessel and a cable, but does not take into consideration the change in the hydrodynamic characteristics of the cable, meaning that it is insufficient to fully study the dynamics of the FL.

In [15], Drag investigated the method of dynamics optimisation of a drill column which was attached by means of anchoring it at one end on the bottom, by analogy with the method proposed in [16]. This model takes into account the loading from bending and torsion of the drill column. However, the approach in this model does not take account of the cable lines.

Paper [17] considers the application of a dynamic optimisation method for a drill column fixed at one end on the seabed. The model presented takes into consideration the loads from the stretching and rotation of the drill column. However, the specified model is unsuitable for use in cable line calculations.

In [18], a lumped-mass method is used to establish the numerical model for evaluating the performance of a mooring line with embedded chains. To validate the numerical model, comparisons of the numerical results with the analytical formulas and the experimental data are conducted. Good agreement of the profile and the tension response is obtained. Then, the effect of the embedded chains on the static and dynamic response of the mooring line is evaluated, and the dynamic behaviour of the mooring system considering the embedded chains for a net cage system is investigated. The results indicate that the soil resistance on the embedded chains should be included to predict the mooring line development and the load on the embedded anchors in the numerical simulations.

The author tried to find information on the study of the torsion and torsional stresses of FLs and the creation of MMs that describe them, but such literature, as can be seen from the review, is virtually non-existent. It is obvious that the topic of developing a MM for the description of the dynamics of the MTS, taking into account the effect of torsion, is important and relevant.

RESULTS OF THE STUDY

The author examined more than 80 articles from research on the existing MMs of MTS. In some articles there was a lack of research on the dynamic interaction between the FL and MTS, as a whole, with obstacles in the water. In many cases, relatively little movement of the FL was modelled with the assistance of partial differential equations. Not one of the examined works made use of generalised coordinates, and the proposed MMs did not model the movement of the FL with great displacements and torsions.

Some articles used the finite element method (FEM) of the FL, which include methods addressing the rigidity of the bars and of the localised mass. As distinct from the method of generalised coordinates, these methods make the major mistake of approximating the form of the FL, which essentially restricts their use in describing the dynamics of a FL with big displacements and especially the fracture of the FL, which inevitably arise in the process of interaction of the FL with obstacles.

In many works, the presence of the FL is not taken into account at all, and some authors assigned the form of the FL a priori. In some works, the authors used simpler and more approximate methods of describing the statics of the FL of the MTS. To simplify the MM, some authors of articles in which they were presented examined the dynamics of the FL without some essential assumptions by neglecting the tension of the FL, its bending rigidity and the rigidity of FL torsion.

In many works, the movement of the FL was examined by the authors in two dimensions. Only in two works did the authors examine major bending of the FL in three coordinates. For improvement of the MM, the Authors of [16] used the method of generalised coordinates, which allows modelling of the motion of the FL with big movements and torsions. As distinct from the examined works, the method of generalised coordinates used in the development of the proposed MM makes such modelling of the motion of the FL with big movements and torsions possible.

Analysis of the existing dynamics models of the FL of a MTS has shown that, in most models, the elements of the FL in the MTS consider the dynamics of the FL at rather small displacements and bends, which testifies to the urgency of developing the proposed mathematical model of the dynamics of the elements of the FL to allow the consideration of big displacements of the FL as a part of the MTS. Previously, the equations of the dynamics of the elements of the FL of the MTS were obtained [16], which makes it possible to describe the significant values of its displacements. Creating the MM of the two related elements of the FL of the MTS allows an algorithm to be developed for calculating the FL dynamics at large displacements. More detailed descriptions of the MM of the FL are listed in [2, 16, 19].

Let us supplement the MM addressing the FL of the MTS through the method of determining the vectors of the generalised torsional forces of the FL. In Fig. 1 bent item FL indicates the angle of rotation of the final cross-section of the FL element

The angle β is determined along the FL centreline ($p \in [0; l]$). Using interpolation,

$$\beta\,(p) = \beta_0 \cdot (1 - p/l) + \beta_l \cdot p/l\,, \tag{1}$$

where β_k are the angles of rotation of the cross-sections of the FL at the end points of the element relative to the normal n of the Frenet reference of the centreline [20, 21].

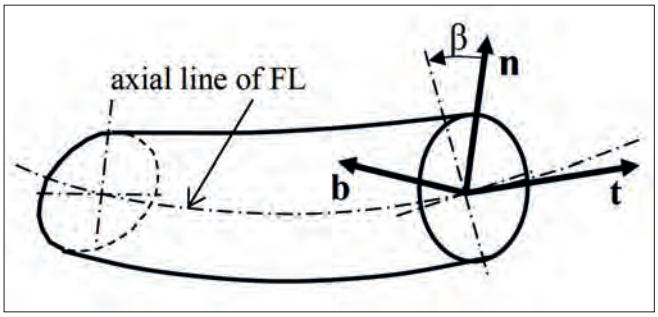

Fig. 1. Rotation of the final cross-section of the FL element relative to the normal axis

Hermitian functions are used as the functions of the FL form:

$$s_1(p) = s_3(l-p) = 1 - 3\xi^2 + 2\xi^3\,, \tag{2}$$

$$s_2(p) = s_4(l-p) = l\cdot(\xi - 2\xi^2 + \xi^3)\,, \tag{3}$$

$$s_3(p) = 3\xi^2 - 2\xi^3\,, \tag{4}$$

$$s_4(p) = l\cdot(\xi^3 - \xi^2)\,, \tag{5}$$

$$\xi = p/l\,, \tag{6}$$

allowing the shape of the FL element to be approximated by the magnitude and derivative of the radius vector of the FL:

$$x(p) = s_1(p)\cdot x_0 + s_2(p)\cdot x_0' + s_3(p)\cdot x_l + s_4(p)\cdot x_l'\,, \tag{7}$$

$$y(p) = s_1(p)\cdot y_0 + s_2(p)\cdot y_0' + s_3(p)\cdot y_l + s_4(p)\cdot y_l'\,, \tag{8}$$

$$z(p) = s_1(p)\cdot z_0 + s_2(p)\cdot z_0' + s_3(p)\cdot z_l + s_4(p)\cdot z_l'\,, \tag{9}$$

where $x_0, y_0, z_0, x_l, y_l, z_l$ are the coordinates of the final points of the FL element; and $x_0', y_0', z_0', x_l', y_l', z_l'$ are the coordinates of the derivative of the final points of the axis lines of the FL element.

The vectors of the generalised bending and torsion forces ($\vec{Q}^{\chi}_{i-1}, \vec{Q}^{\chi}_{i_1}, \vec{Q}^{\chi}_{i_2}, \vec{Q}^{\chi}_{i+1}, \vec{Q}^{\tau}_{i-1}, \vec{Q}^{\tau}_{i_1}, \vec{Q}^{\tau}_{i_2}, \vec{Q}^{\tau}_{i+1}$) are included in Eq. (10):

$$\begin{gathered}\mathbf{M}_1\cdot\ddot{\vec{e}}_{i-1}+\mathbf{M}_2\cdot\ddot{\vec{e}}_{i}+\mathbf{M}_3\cdot\ddot{\vec{e}}_{i+1}+\mathbf{K}_1\cdot\vec{e}_{i-1}+\mathbf{K}_2\cdot\vec{e}_{i}+\mathbf{K}_3\cdot\vec{e}_{i+1}+\\ +\vec{Q}^{\chi}_{i-1}+\vec{Q}^{\chi}_{i_1}+\vec{Q}^{\chi}_{i_2}+\vec{Q}^{\chi}_{i+1}+\vec{Q}^{\tau}_{i-1}+\vec{Q}^{\tau}_{i_1}+\vec{Q}^{\tau}_{i_2}+\vec{Q}^{\tau}_{i+1}=\vec{Q}_i\end{gathered}\,, \tag{10}$$

determined by formula (11) for the bending reaction forces of the FL:

$$\vec{Q}^{\chi}_i = EJ\int_0^l \chi\frac{\partial\chi}{\partial\vec{e}_i}dp = \frac{EJ\cdot l}{2}\int_0^1\frac{\partial\chi^2}{\partial\vec{e}_i}d\xi \tag{11}$$

and by formula (12) for the torsional reaction forces of the FL:

$$\vec{Q}^{\tau}_i = \frac{\partial U^{\tau}}{\partial\vec{e}_i} = G\cdot J_P\int_0^l \tau\frac{\partial\tau}{\partial\vec{e}_i}dp = \frac{G\cdot J_P\cdot l}{2}\int_0^1\frac{\partial\tau^2}{\partial\vec{e}_i}d\xi\,. \tag{12}$$

The curvature χ of the centreline with respect to the major axes of inertia of the cross-sectional area with bending stiffness EJ is expressed as follows:

$$\chi = \frac{|\vec{r}\,'\times\vec{r}\,''|}{|\vec{r}\,'|^3}\,. \tag{13}$$

The vectors of the generalised bending and torsion forces ($\vec{Q}^{\chi}_{i-1}, \vec{Q}^{\chi}_{i_1}, \vec{Q}^{\chi}_{i_2}, \vec{Q}^{\chi}_{i+1}, \vec{Q}^{\tau}_{i-1}, \vec{Q}^{\tau}_{i_1}, \vec{Q}^{\tau}_{i_2}, \vec{Q}^{\tau}_{i+1}$) can be calculated by formulas (151) – (158) in reference [10], but the process of determining them is associated with major problems in calculating the derivatives and integrals in analytical form, due to the great complexity of the formulas. This makes this process very time-consuming and does not always enable the integrals to be calculated in analytical form.

To solve this problem, a method for determining the vectors $\vec{Q}^{\chi}_{i-1}, \vec{Q}^{\chi}_{i_1}, \vec{Q}^{\chi}_{i_2}, \vec{Q}^{\chi}_{i+1}, \vec{Q}^{\tau}_{i-1}, \vec{Q}^{\tau}_{i_1}, \vec{Q}^{\tau}_{i_2}, \vec{Q}^{\tau}_{i+1}$ has been developed using numerical methods for calculating the derivatives and integrals included in formulas (11) – (12), by using the vector of generalised coordinates in the nodal points of the FL (14).

Taking account of the introduced matrix equation for the FL element with nodal points i_{-1} and i_1, and also with nodal points i_2 and i_{+1}, the system of equations is rearranged. Taking into account that in the nodal point $i = i_1 \equiv i_2$, the following equality is carried out:

$$\vec{e}_i = \vec{e}_{i_2} = \vec{e}_{i_1}\,, \tag{14}$$

then the generalised variables at nodal point i are substituted into $\vec{e}_i$ and with the exception of bonds in the nodal point *i* from other equation. The system of equations obtained is defined and correlated with three of the neighbouring nodal points of the FL, but to account for the boundary conditions in this case it is necessary to correct the matrix using Lagrange factors. But defining these complicates the solution of the task and also demands transformation of the matrix of mass near the borders of the FL. In order to secure the impossibility of these problems, the vector of generalised coordinates is written down only to the i-nodal point of the FL:

$$\vec{e}_i = \{\vec{r}_i^{\,0T}\,\vec{r}_i^{\,1T}\,\beta_i\}^T\,, \tag{15}$$

or, in coordinate form,

$$\vec{e}_i = \{x_i\,y_i\,z_i\,x_i'\,y_i'\,z_i'\,\beta_i\}^T\,. \tag{16}$$

Function χ_τ included in formula (13) is represented as the ratio of vector products by the formula

$$\chi_\tau = \frac{b^T r'''}{b^T b} = \frac{x'''(y'\cdot z''-y''\cdot z') + (y'\cdot z''-z'\cdot y'')^2 + y'''(z'\cdot x''-z''\cdot x') + z'''(x'\cdot y''-x''\cdot y')}{+(z'\cdot x''-x'\cdot z'')^2 + (x'\cdot y''-y'\cdot x'')^2}\,. \tag{17}$$

Then, in formula (1), the relative angle of torsion of the dihedral section of the FL taking account of the angle of torsion of the dihedral section β is:

$$\tau = \chi_\tau + \partial\beta/\partial p\,, \tag{18}$$

and may be expressed as

$$\tau = \frac{b^T r'''}{b^T b} + \partial\beta/\partial p\,. \tag{19}$$

For the derivative of function τ at the generalised coordinates (20), we write the vector of the generalised coordinates only down to the i-nodal point of the FL:

$$\vec{e}_i = \{\vec{r}_i^{\,0T}\,\vec{r}_i^{\,1T}\,\beta_i\}^T\,, \tag{20}$$

or, in coordinate form,

$$\vec{e}_i = \{x_i\, y_i\, z_i\, x'_i\, y'_i\, z'_i\, \beta_i\}^T\,, \tag{21}$$

and they take the form

$$\frac{\partial\tau}{\partial e_i^T} = -\frac{b^T r'''}{(b^T b)^2}\left\{2\left[\frac{\partial b}{\partial e_i^T}\right]^T b\right\} + \\ + \frac{1}{b^T b}\left\{\left[\frac{\partial b}{\partial e_i^T}\right]^T r''' + \left[\frac{\partial r'''}{\partial e_i^T}\right]^T b\right\}. \tag{22}$$

$$\frac{\partial\tau}{\partial\beta_0} = -\frac{\partial\tau}{\partial\beta_l} = -\frac{1}{l}\,. \tag{23}$$

Taking account of the approximation of the coordinates of the FL and of their derivatives, we define the derivatives and functions within Eq. (22). The integrals (12) were calculated by the Simpson method.

The derivatives and functions that are included in Eq. (11) were calculated similarly. The square of the curvature χ of the axial line with respect to the main axes of inertia of the cross-sectional area with bending stiffness EJ, taking into account the notation of the numerator and denominator of the fraction, has the form

$$\chi^2 = \frac{a}{b} = \\ = \frac{(y'\cdot z''-z'\cdot y'')^2+(z'\cdot x''-x'\cdot z'')^2+(x'\cdot y''-y'\cdot x'')^2}{(x'^2+y'^2+z'^2)^3} \tag{24}$$

The derivative of the function (24) is determined by the formula:

$$\frac{\partial\chi^2}{\partial\vec{e}_i} = \frac{\frac{\partial a}{\partial\vec{e}_i}b - a\frac{\partial b}{\partial\vec{e}_i}}{b^2}\,. \tag{25}$$

The calculation of the derivatives of formulas (22), (23) and (25) produced a small error in the calculation of the reactions of the FL to bending and torsion, and also the stability of the process of mathematical modeling of the dynamics of the FL and the MTS as a whole.

PRACTICAL VERIFICATION OF SIMULATION RESULTS: THE INFLUENCE OF THE TORSIONAL RIGIDITY OF THE FL ON ITS DEFLECTION AND TENSILE STRENGTH

The influence of the torsional rigidity of the FL on the dynamics of the MTS are considered through the example of two tasks. In both tasks, the initial length of the FL was taken as 100 m. The FL is in the water. The root end of the FL is still. The density of the material of the FL is 7800 kg/m³ and its Young's modulus is $2 \cdot 10^{11}$ Pa. The diameter of the FL is 40 mm and it is divided into 10 elements. The normal coefficient of hydrodynamic resistance of the FL is equal to 1.35, and the tangential is 0.04.

Consider these tasks:

1. calculation of the static deflection of the FL;
2. calculation of the tensile strength: the carrier vessel (CV) is stationary, and the submersible vehicle (SV) has no restrictions on movement and has positive buoyancy.

TASK 1. Calculation of the static deflection of the FL is performed by the method of establishing motion using the developed mathematical model. The root and running ends of the FL at the initial moment of time were motionless, and were on the surface of the sea at a distance of 100 m. The tensile strength of the FL at the initial time is zero. Under the action of gravity, the FL sagged to a steady state. In the absence of torsion of the FL, its deformation occurred only in the X0Z plane.

In the second version of this problem, it was assumed that the root end of the FL was twisted by 10 turns. Torsion of the FL has almost no effect on the shape of the deflection of the FL in the X0Z plane (Fig. 2), but leads to deviation of the FL from the X0Z plane (Fig. 3).

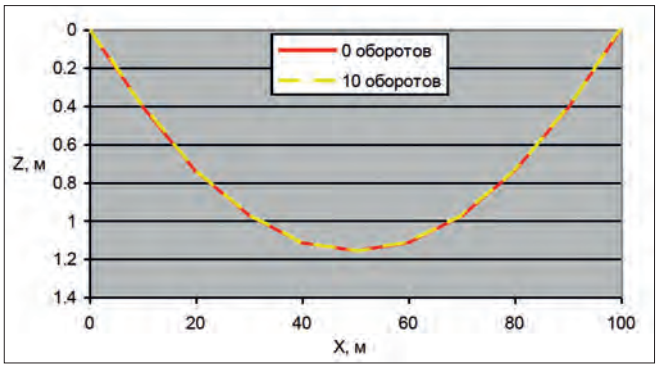

Fig. 2. The final shape of the deflection of FL in the X0Z plane

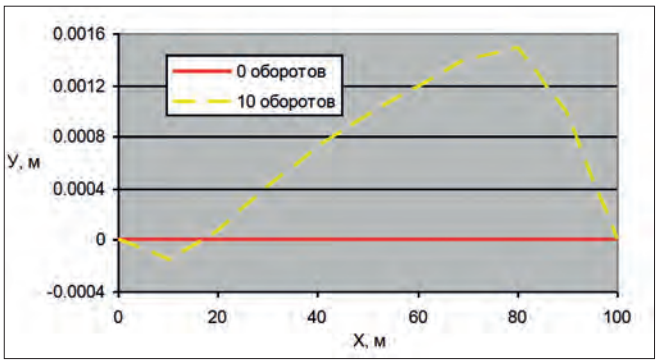

Fig. 3. The final shape of the deflection of FL in the X0Y plane

As a result of the torsion of the FL, even with fixed ends, the FL acquires a three-dimensional shape.

TASK 2. The CV is immobile, and the SV has no restrictions on movement, has positive buoyancy and is connected to the CV at the FL length of 100 m. At the initial moment of time, the FL has no tension and is located along the sea surface. In the course of modelling, the FL sags under the action of gravity and causes the underwater towed vehicle (UTV) to move along the sea surface to the CV. In the absence of FL torsion, the process of FL and SV movement occurs in the X0Z plane (Fig. 4).

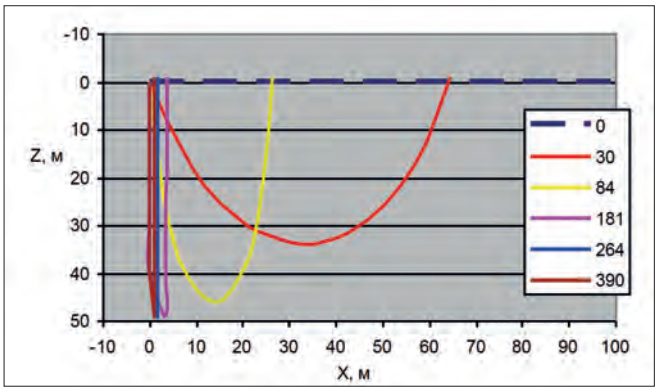

Fig. 4. Form of FL at different points in time (curves are indicated by the corresponding points in time in seconds from the beginning of the process)

The tension force of the FL is distributed unevenly along its length (Fig. 5).

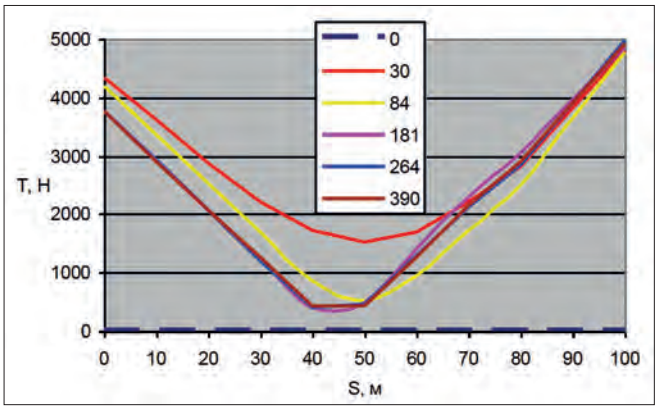

Fig. 5. Tensile strength of FL by its length at different points in time (curves are denoted by the corresponding points in time in seconds from the beginning of the process)

The second version of this task considered the process of release of the FL from the drum of the winch located on the CV, where its root end receives torsion on 10 turns and maintains it in the course of modelling. The angle of rotation of the running end of the FL on the UTV is zero.

Torsion of the FL leads to a three-dimensional change in its shape both in the X0Z plane and in the X0Y plane (Fig. 6 and Fig. 7), respectively.

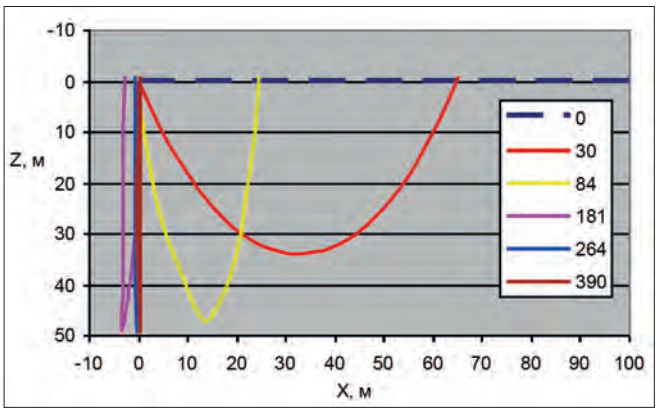

Fig. 6. Form of FL at different times

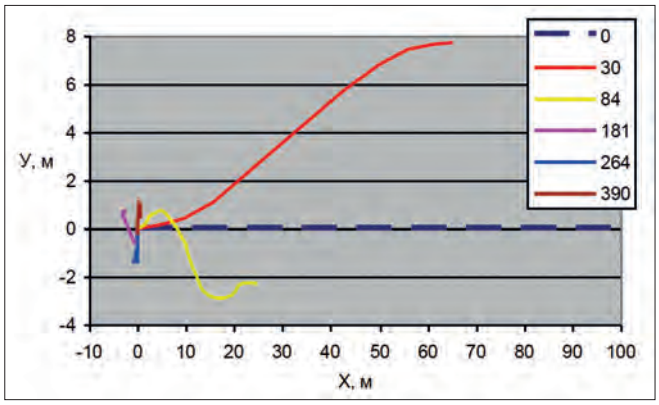

Fig. 7. Form of FL at different times

The tension force of the FL is distributed unevenly along its length (Fig. 8).

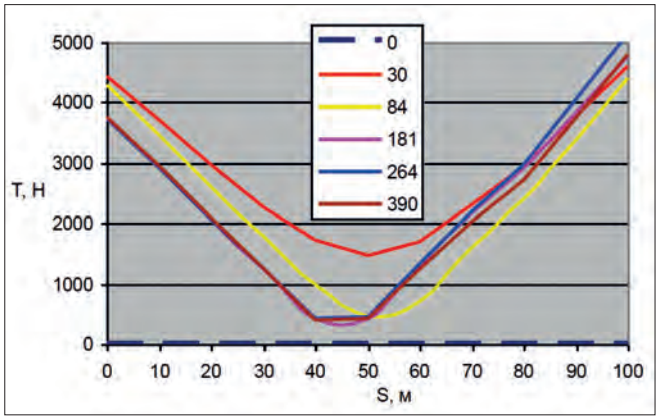

Fig. 8. Tensile strength of FL along its length at different points in time (curves are indicated by the corresponding points in time in seconds from the beginning of the process)

The maximum deviation of the FL and the SV from the X0Z plane is 7.7 m 30 seconds after the start of simulation. In the following moments of time, projection of the FL on the X0Y plane significantly changes its shape in the process of approaching the UTV to the CV, crossing the X0Z plane many times, as well as circulating around the CV (Z axis).

In the Z0X plane, the form of the FL after its rotation is also markedly different from its shape in the absence of torsion (Fig. 9).

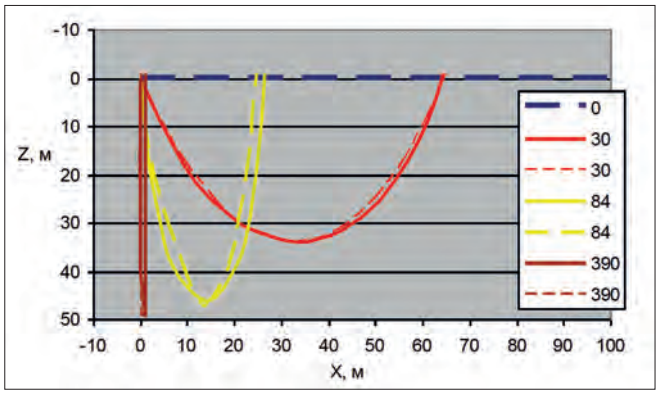

Fig. 9. Form of FL at different points in time (curves are denoted by the corresponding points in time in seconds from the beginning of the process, the dashed lines correspond to the torsion FL)

To a lesser extent, torsion of the FL affects the distribution of tensile force along its length (Fig. 10).

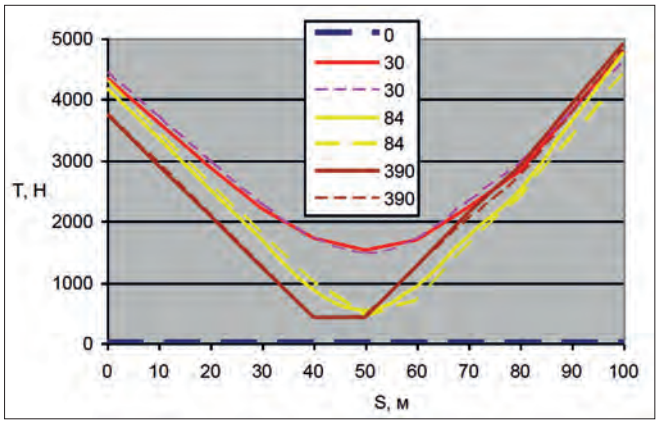

Fig. 10. Tensile strength of FL by its length at different points in time (curves are denoted by the corresponding moments of time in seconds from the beginning of the process, dashed lines correspond to torsion of FL)

Based on these data, we can conclude that, for correct modelling of the dynamics of the FL, taking into account its torsion, it is necessary to carry out a three-dimensional statement of the problem. In this case, assumptions that simplify the idea of the movement of the FL only in the X0Z plane can lead to qualitatively and quantitatively incorrect conclusions.

DISCUSSION OF RESULTS

The created MM of the element dynamics of the FL makes it possible to take into account large movements of the FL as part of the MTS and take into account also the following:

1. The movement of the CV, which is determined by the following factors: sea surface turbulence; kinematic characteristics of CV motion, and sea current velocity [16];
2. Design features of the FL affecting the functional characteristics of the MTS and which are determined by the following factors: the length and change in the length of the FL in the process of moving the CV; the elasticity and strength of the FL; positive or negative buoyancy of the FL, as well as cargo, floats and buoys associated with it; the hydrodynamic resistance forces of the FL in the process of its movement in water; and forces acting on the root and running ends of the FL [16];
3. The movement of the UTV, which is determined by the following factors: the mass and buoyancy of the UTV; the relative location of the UTV in relation to the VC and the kinematic characteristics of its motion; the forces of hydrodynamic resistance of the SV in the course of its movement in water;
4. The impact of obstacles on the movement of the UTV and FL, which is determined by the following factors: the location of obstacles in the water; the size of the obstacles; kinematic characteristics of the movement of obstacles [22–24].

The mathematical modelling of two related elements of the FL of the MTS made it possible to develop an algorithm for calculating the dynamics of the FL during large movements and to solve some problems which were not considered in the existing MM [25]:

1. To determine the change of form of the FL and forces of its tension in the process of manoeuvring of the CV and UTV, taking into account sea waves, underwater currents, wind loads on the CV, the sea depth and its changes in a given water area, and the mass and elastic properties of the FL;
2. To determine the relative position of the CV and SV in the process of their manoeuvring;
3. To determine the modes of manoeuvring of the MTS, which leads to the formation of loops ("pegs") on the FL (usually formed on the stretched FL when there is a "slack" and the presence of torque, which depends on the tension of the FL);
4. To determine the regimes of manoeuvring of that MTS that reduce the vibration of bad flow of FL at the inflow;
5. To determine the tensile, bending [26] and torsional forces in the FL;
6. To determine the system of equations describing the dynamics of the element under load and rotation;
7. To develop an algorithm for modelling the dynamics of the FL, which makes it possible to perform calculations of the dynamics of the FL of the MTS.

By means of practical tests of the modelling results on the influence of the torsion rigidity of the FL on its flexure and tension force, the conclusion may be reached that, for correct modelling of the dynamics of the FL accounting for its torsion, a complete three-dimensional formulation of the problem is necessary. In this case, assumptions taken in earlier work that simplify the movement of the FL as occurring only in the X0Z plane mean that qualitatively and quantitatively accurate conclusions cannot be obtained.

With the developed MM of the dynamics of the FL and the algorithm established, the computer program description of the dynamics of the FL of the MTS will allow the designer of the MTS, which includes the FL, to more efficiently and quickly design almost all classes of MTS [27]. The originality of the MM of the FL dynamics is that the modelled dynamics of the MTS with the FL includes not only equations for the FL, but also the equation of the dynamics of the CV and towed SV, the motion of which determines the boundary conditions in the nodes of the FL, with numbers i = 0 and i = N.

CONCLUSIONS

Based on the study, the following main conclusions can be drawn:

1. Torsion of the FL can lead to a significant change in the shape of the FL and the trajectory of towed objects, as well as changes in the forces acting on the elements of the MTS.
2. The advanced MM, as well as the algorithm and computer program make it possible to perform mathematical modelling of the dynamics of the MTS, taking into account the torsion of the FL.

3. For correct modelling of the FL dynamics, taking into account its rotation, it is necessary to establish a three-dimensional statement of the problem. In this case, simplifying the assumptions about the FL moving only in the X0Z plane can lead to qualitatively and quantitatively incorrect conclusions.

Thus the generalised forces of torsion of the FL in Eq. (10) are used, which, together with Eq. (12), allow the possibility of taking into account the influence of the torsional rigidity of the FL in its dynamics.

Examples of modelling of the FL dynamics which were examined show the possibility of registering the rigidity of torsion of the FL in an improved MM, and also its essential influence on the functional characteristics of the MTS.

The scientific novelty of this MM of the dynamics of the FL of the MTS is that it is complex, allowing us to study the FL taking into account its stretching, bending and torsion and operating conditions as a part of practically all classes of MTS.

Thus the aim of research is achieved: a method that allows us to complete the previously developed MM of the dynamics of the FL of the MTS and account for the rigidity of the FL is proposed.

REFERENCES

1. K. S. Trunin, "Designing ship deck winches for marine mooring systems with flexible connections using mathematical models to describe their dynamics (in Russian)," *Shipbuilding & Marine Infrastructure*, vol. 13, no. 1, pp. 4–16, 2020. DOI: https:// doi.org./10.15589/smi2020.1(1).1.

2. V. Blintsov and K. Trunin, "Construction of a mathematical model to describe the dynamics of marine technical systems with elastic links in order to improve the process of their design," *Eastern-European Journal of Enterprise Technologies*, vol. /1/9 (103), pp. 56–66, 2020. DOI: 10.15587/1729-4061.2020.197358. pp. 56-66, p. 74.

3. S. T. Sergeev, *Reliability and durability of lifting cables* (in Russian). Kiev: Tekhnika; 1968.

4. M. F. Glushko, *Steel lifting cables* (in Russian). Kiev: Tekhnika; 1966.

5. A. I. Roslik, *Experimental investigations of twisting of crane cables. Collection "Steel Cables", Issue 1*. (in Russian). Kiev: Tekhnika; 1964.

6. A. I. Roslik, *Twisting of crane cables during operation. Collection "Steel Cables", Issue 4* (in Russian). Kiev: Tekhnika; 1967.

7. S. F. Chukmasov and A. I. Roslik, *Twisting of crane cables due to additional elongation during bending. Collection "Steel Cables", Issue 2* (in Russian). Kiev: Tekhnika; 1965.

8. A. I. Yakobson, *Twisting of cables on blocks and drums. Collection "Steel Cables", Issue 3* (in Russian). Kiev: Tekhnika; 1966.

9. V. I. Egorov, *Underwater towed systems: A textbook* (in Russian). *Leningrad. Sudostroienie*; 1981.

10. V. I. Podubnyj, Yu. E. Shamarin, et al. *Dynamics of underwater towed systems* (in Russian). *St. Petersburg: Судостроение*; 1995.

11. F. S. Hover, M. A. Grosenbaugh, and M. S. Triantafyllou, "Calculation of dynamic motion and tensions in towed underwater cables," *IEEE Journal of Oceanic Engineering*, vol. 19, no. 3, pp. 449–457, 1994. Retrieved from: https://core.ac.uk/ download/ pdf/4385954.pdf.

12. M. Asuma and T. Masayoshi, "A high-gain observer-based approach to robust motion control of towed underwater vehicles," *IEEE Journal of Oceanic Engineering*, vol. 44, no. 4, pp. 997–1010, 2018. http://www.ieee.org/publications.standards/publications /rights/index.html.

13. X.-S. Xu, S.W. Wang, L. Lian, "Dynamic motion and tension of marine cables being laid during velocity change of mother vessels," *China Ocean Engineering*, vol. 27, no. 5, pp. 629–644, 2013. DOI: 10.1007/s13344-013-0053-5

14. Ł. Drag, "Application of dynamic optimization to the trajectory of a cable-suspended load," Nonlinear Dynamics, vol. 84, iss. 3, pp. 1637–1653, 2016. DOI: 10.1007/s11071-015-2593-0.

15. Ł. Drag, "Application of dynamic optimisation to stabilise bending moments and top tension forces in risers," *Nonlinear Dynamics*, vol. 88, iss. 3, pp. 2225–2239, 2017. DOI: 10.1007/s11071-017-3372-x

16. K. S. Trunin, *Flexible connections in marine mooring systems: Monograph. Mykolaiv: Torubara Publisher*. B.B; 2019.

17. W.-S. Yoo, O. Dmitrochenko, S.-J. Park, and O.-K. Lim, "A new thin spatial beam element using the absolute nodal coordinates: Application to a rotating strip," *Mechanics Based Design of Structures and Machines*, vol. 33, pp. 399–422, 2005.

18. H.-M. Hou, G.-H. Dong, T.-J. Xu, Y.-P. Zhao, and C.-W. Bi, "Dynamic analysis of embedded chains in mooring line for fish cage system," *Polish Maritime Research*, vol. 25, no. 4, pp. 83–97, 2018. DOI:10.2478/pomr-2018-0135.

19. K. S. Trunin, "The three-dimensional motion of marine tethered system at example buoy of neutral floating (in Uk," *Shipbuilding & Marine Infrastructure*, vol. 11, no. 1, pp. 18–31, 2019. DOI: https:// doi.org./10.15589/smi2019.1(11).3

20. R. Schwertassek, "Flexible bodies in multibody systems," in *Computational methods in mechanical systems: mechanism*

analysis, synthesis and optimization. Jorge Angeles, Evtim Zakhariev, Eds. (NATO ASI series. Series F, Computer and systems sciences; vol. 161), 1998, pp. 329–363.

21. A. A. Shabana and R. Y. Yakoub, "Three dimensional absolute nodal coordinate for beam elements; Theory," *Journal of Mechanical Design*, vol. 123, pp. 606-621, 2001.

22. V. Blintsov and K. Trunin, "Improving the designing of marine tethered systems using the principles of Shipbuilding 4.0," *Eastern-European Journal of Enterprise Technologies*, vol. 1/13 (109), pp. 35-48, 2021. DOI: 10.15587/1729-4061.2021.225512.

23. V. Blintsov, K. Trunin, and W. Tarelko, "Determination of additional tension in towed streamer cable triggered by collision with underwater moving object," Abstract Book the 2nd Mediterranean Geosciences Union Annual Meeting (MedGu 2022). 27-30 November 2022. Marrakech, Morocco. Springer – Publishing Partner.

24. V. Blintsov, K. Trunin, and W. Tarelko, "Determination of additional tension in towed streamer cable triggered off by collision with underwater moving object," *Polish Maritime Research*, vol. 27, no. 2, pp. 58-68, 2020.

25. K. S Trunin, "Mathematical model of two interconnected elements of a flexible connection in a marine mooring system" (in Russian). Collection of scientific works of NUK, №2, pp. 3–10, 2017. DOI: 10.15589/jnn20170201.

26. K. S. Trunin, "Mathematical model of the dynamics of a marine mooring system taking into account the influence of flexural stiffness of the flexible connection (in Ukrainian)," Shipbuilding & Marine Infrastructure, vol. 15, no. 1, pp. 4-23, 2021. DOI: https:// doi.org./10.15589/smi2021.1(15).1.

27. K. S. Trunin, "Application of a specialized modeling toolkit for the design of marine mooring systems with flexible connections (in Ukrainian)" Collection of scientific works of NUK, №1, pp 3-13, 2021. DOI: https:/doi.org/10.15589/znp2021.1(484).2.

POLISH MARITIME RESEARCH 2 (118) 2023 Vol. 30; pp. 197-206
10.2478/pomr-2023-0033

COMMENTS ON EXISTING ANALYTICAL SOLUTIONS TO THE WAVE-INDUCED CYCLIC RESPONSE OF A POROUS SEABED OF INFINITE THICKNESS

Waldemar Magda*
Gdańsk University of Technology, Faculty of Civil and Environmental Engineering,
Department of Geotechnical and Hydraulic Engineering, Poland

* Corresponding author: *waldemar.magda@pg.edu.pl (Waldemar Magda)*

ABSTRACT

This paper deals with the wave-induced cyclic response of a porous seabed (by means of oscillating parameters: pore-fluid pressure, soil displacement components, effective normal stress and shear stress components) due to a surface sinusoidal water-wave propagating over a seabed of infinite thickness. The main existing analytical solutions to the governing problem are critically discussed, pointing out their meaningful errors and doubtful items. A phase-lag phenomena is particularly studied as an immanent part of any complex-valued analytical solutions having a cyclic nature.

Keywords: porous seabed, infinite seabed thickness, cyclic response, soil saturation, sinusoidal progressive wave, phase-lag phenomenon, analytical solutions

INTRODUCTION

The wave-induced response of a porous seabed loaded by a progressive sinusoidal surface water-wave is still an interesting subject in many coastal engineering problems. In order to solve them, it is necessary to treat the problem either numerically, especially when a certain engineering structure is involved, or analytically by using one of the existing theories and their solutions to the wave-induced cyclic seabed response, particularly when a pure case of the seabed without presence of any structure founded on or embedded in seabed sediments is concerned. These analytical solutions can be further used in many scientific and engineering analyses of the wave-induced seabed instability due to wave-induced momentary liquefaction or/and wave-induced residual liquefaction of the upper part of seabed as a result of continuous build-up of the wave-induced pore-fluid pressure within seabed sediments. But above all, anyone needs to be reminded of the fact that analytical solutions serve very often as an important reference for validation of appropriate numerical solutions.

Assuming only the pore-fluid to be compressible, Moshagen and Tørum [12] presented an analytical solution for the pore-fluid pressure obtained for both infinite and finite thicknesses of the seabed. Following research works pertained to a more advanced case where both phases of the seabed (i.e. pore-fluid and soil skeleton) are considered to be compressible and, thereby, the relative compressibility of the two-phase seabed medium started to become of great importance from the practical point of view. This type of analytical solutions is based on Biot's consolidation theory, Hooke's law (the soil has linear, reversible, isotropic and non-retarded mechanical properties) and Darcy's law for the pore-fluid flow through a porous medium. The obtained solutions are given in terms of six (in case of the two-dimensional space) complex-valued wave-induced and cyclically varying parameters (pore-fluid pressure, two soil displacement components, two soil effective normal stress components and one shear stress component), or at least some of them, assuming simultaneously plain strain and partly saturated soil conditions.

Basically, an infinite thickness of the seabed was studied by Yamamoto et al. [19], Madsen [6] and Okusa [13]. Yamamoto et al. [19] assumed a hydraulically isotropic seabed and presented the final solution only with respect to the wave-induced pore-fluid pressure and soil displacement components. However, Yamamoto et al. [19] presented

additionally two simplified approximate solutions for: (a) soils completely saturated with seawater and for most soils except for dense sand, and (b) partially saturated dense sand and sandstones. Only case (a) was associated with a set of final equations obtained for all six wave-induced parameters. Madsen [6], treating the seabed as a hydraulically anisotropic medium, derived the governing partial differential equation of the 6th order and obtained the final solution in terms of all the above mentioned wave-induced parameters. Madsen [6] considered a special simplified case of a fully saturated, isotropic, dense soil and presented appropriate equations only for the pore-fluid pressure and soil stress components. Okusa [13], similarly to Yamamoto et al. [19], assumed the seabed to act as a hydraulically isotropic medium. After solving the governing partial differential equation of the 4th order, Okusa [13] obtained equations for the wave-induced pore-fluid pressure, effective normal stress and shear stress components within the soil skeleton. The general solution (i.e. before applying boundary conditions) was presented in two forms: exact and simplified (the approximation was obtained after identification of negligibly small terms). However, the particular solution (i.e. after applying boundary conditions), presented by Okusa [13], was based only on his simplified general solution. Similarly to his forerunners, Okusa [13] considered a special case of fully saturated soil conditions and presented adequate final equations. Yamamoto et al. [19] and Okusa [13] were kind to discuss the question of phase-lag phenomenon, presenting vertical distributions of this parameter with respect to pore-fluid pressure oscillations. Yamamoto et al. [19] made a comparison with some experimental data and values calculated after Moshagen and Tørum [12], whereas Okusa [13] illustrated graphically two different computational cases and presented, as a bonus, an equation for the phase-lag of pore-fluid pressure oscillations derived from his simplified approximate solution.

In the next step, the "infinite thickness" two-phase compressible seabed model was adopted and extended into a more general "finite thickness" model together with its analytical solutions derived by many researchers, among others: Richwien and Magda [15], Magda [7], Hsu and Jeng [2], Jeng and Hsu [5] and Jeng [3, 4]. Very often, based on their "finite thickness" analytical solutions, the authors formulated also, as a special simpler case, equations reflecting the conditions of infinite thickness of a porous and elastically deformable seabed. Besides that, it is also worth noting that Mei and Foda [9] elaborated a very sophisticated "boundary layer theory". Its easily applicable analytical solution was found to be a useful tool in many seabed response analyses, where, among others, the problem of extrication of large objects from the seabed is particularly studied [1]. This very interesting engineering challenge is still of great importance, as documented in recent works by Michalski [10, 11].

A solid mechanics sign convention for strains and stresses was usually applied in the above mentioned analytical solutions. Only Okusa [13] hold entirely with a soil mechanics sign convention, whereas Madsen [6] presented a kind of "hybrid method". The consistency of mathematical formulations and analytical solutions to the governing problem, based on different sign conventions for strains and stresses, was thoroughly studied by Magda [8].

Using the above mentioned first group of "infinite thickness" analytical solutions in practice, some important drawbacks have been found by the Author of the present paper. Therefore, after a brief description of mathematical models of the wave-induced cyclic seabed response, a critical assessment of some selected "infinite thickness" analytical solutions will be presented in the following, pointing out their weaknesses and mistakes.

All of the errors in the analytical methods under consideration have been detected personally by the Author of the present paper. The entire mathematical procedures, associated with the analytical solutions presented originally by Moshagen and Tørum [12], Yamamoto et al. [19] and Okusa [13], have been repeated from soup to nuts by the Author. The results of all derivative procedures performed by the Author have been compared with the published matter and the differences have been indicated and depicted in details. Additional computations have been executed using the questionable solutions and the corrected equations. Moreover, the computational results obtained from the corrected equations have been collated with appropriate results computed according to the originally perfect analytical solution published by Madsen [6]. All the computations have been performed by the Author of the present paper using his own computer programs written in Fortran.

A CRITICAL REVIEW OF THE EXISTING ANALYTICAL SOLUTIONS

Basic definition sketch of the two-dimensional governing problem is illustrated in Fig. 1. A porous (permeable) and elastically deformable seabed is loaded by a progressive sinusoidal surface water-wave travelling above it. This causes wave-induced cyclic variations of six seabed response parameters, i.e.: pore-fluid pressure, two soil displacement components, two effective normal stress components and one shear stress component.

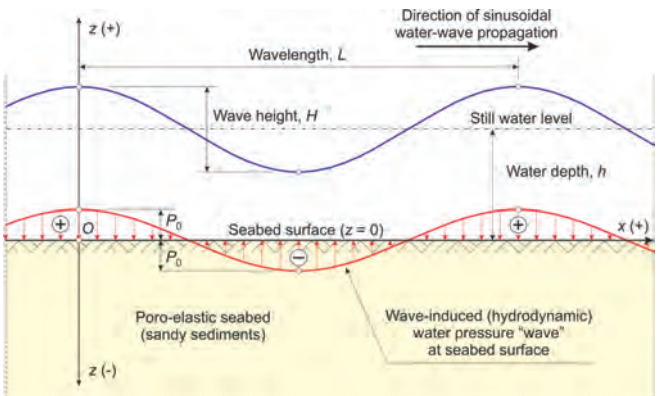

Fig. 1. Definition sketch for analysis of the wave-induced cyclic response of a poro-elastic sandy seabed of infinite thickness

A porous seabed is considered as a two-phase medium, consisting of the soil skeleton and the pore-fluid. Taking into account solutions most interesting from the practical point of view, at least one of the two component phases must be assumed to be compressible. Therefore, the so-called potential model, developed by Putnam [14], where both phases are treated as incompressible media and the problem is governed by the Laplace equation, is out of scope of the present paper. And thus, the following two models of the wave-induced seabed response are applicable, namely:

- diffusion model (governed by the continuity equation in the form of Fick's second law diffusion partial differential equation; only the pore-fluid is assumed to be compressible and the soil skeleton does not obey elastic deformations),
- storage model (governed by the coupled equations of static force and moment equilibrium together with the continuity equation in the form of storage partial differential equation proposed by Verruijt [18]; both the pore-fluid and the soil skeleton are treated as compressible media).

Different analytical solutions to the governing problem, according to the above mentioned mathematical models of the wave-induced seabed response, were treated analytically and numerically by many researchers. However, this paper deals only with some milestone analytical solutions listed in Tab. 1. The present selection of the analytical solutions published in the scientific literature was a consequence of their high citation level. And thus, according to the "Google Scholar" web search engine data from the 14th of March, 2023, the papers by: Moshagen and Tørum [12], Yamamoto et al. [19], Madsen [6], Okusa [13], Hsu and Jeng [2], Jeng and Hsu [5], Jeng [3, 4] are associated with the following number of citations: 133, 877, 714, 393, 390, 162, 208 and 66, respectively. Additionally, it has to be emphasized that the analytical solutions by Yamamoto et al. [19], Madsen [6] and Okusa [13] are used frequently by other researchers, e.g. Sumer [16], Sumer and Fredsøe [17], Jeng [3, 4], in their works and many comparative analyses.

Tab. 1. Chronological list of some milestone theories and their analytical solutions to the wave-induced cyclic response of a porous seabed of infinite thickness

Author/Authors (Year of publication)	Soil skeleton				Pore-fluid
	Compressibility		Hydraulic anisotropy		Compressibility
	No	Yes	No	Yes	Yes
Moshagen and Tørum [12]	x			x	x
Yamamoto et al. [19]		x	x		x
Madsen [6]		x		x	x
Okusa [13]		x	x		x
Hsu and Jeng [2]		x		x	x
Jeng and Hsu [5]		x		x	x
Jeng [3, 4]		x		x	x

It is very characteristic that all the wave-induced seabed response analytical solutions were achieved in the form of complex functions.

SOLUTION BY MOSHAGEN AND TØRUM [12]

An analytical solution to the diffusion problem, describing the wave-induced pore-fluid pressure response in a rigid and porous seabed under the assumption of pore-fluid compressibility, was obtained by Moshagen and Tørum [12] who, using suitable boundary conditions, presented two types of their analytical solution. The first one, more general, is the solution for a finite thickness of a porous seabed layer – the so-called "finite thickness solution". Afterwards, applying $d \to \infty$ (where d denotes the thickness of a porous seabed layer), a special case thereof was also obtained as the "infinite thickness solution"

$$\tilde{p} = P_0 \exp\left(\mu\sqrt{\frac{K_x}{K_z}}z\right)\exp[i(kx - \omega t)] \tag{1}$$

where: $\tilde{p}$ = wave-induced pore-fluid pressure (complex-valued) [kPa], P_0 = amplitude of the hydrodynamic pressure at the seabed surface ($z = 0$) [kPa], μ = parameter (complex-valued) [1/m], K_x and K_z = coefficients of soil permeability in horizontal and vertical directions, respectively [m/s], k = wave number ($k = 2\pi/L$) [1/m], L = wavelength [m], ω = wave angular frequency ($\omega = 2\pi/T$) [rad/s], T = wave period [s], t = time [s], x and z = horizontal and vertical coordinates of the two-dimensional Cartesian coordinate system Oxz, respectively [m], i = imaginary unit ($i = \sqrt{-1}$).

The complex-valued parameter μ can be presented using the following well-known trigonometric form of a complex number

$$\mu = |\mu|(\cos\varphi + i\sin\varphi) \tag{2}$$

(where: $|\mu|$ = absolute value (or modulus or magnitude) of μ [1/m], $\varphi \equiv \arg(\mu)$ = the argument (or phase) of μ [rad].

Moshagen and Tørum [12] gave the following formulas for the absolute value and the argument of complex-valued parameter μ, respectively (see the original Eqs. (15) and (16) in [12], p. 53):

$$|\mu| = \left[k^4 + \left(\frac{\omega n \beta \gamma_w}{K_x}\right)^2\right]^{1/4} \tag{3a}$$

$$\varphi \equiv \arg(\mu) = \frac{1}{2}\arctan\left(\frac{\omega n \beta \gamma_w}{K_x k^2}\right) \tag{3b}$$

where, additionally: n = porosity of soil [-], β = compressibility of pore-fluid [m²/kN], γ_w = unit weight of pore-fluid (seawater) [kN/m³].

When using Eq. (1) in an analysis of the hydrodynamic uplift force acting on a submarine pipeline buried in seabed sediments, the Author had noticed some unexpected problems with the phase-lag of wave-induced pore-fluid pressure oscillations. This was the reason why the Author went through the entire derivation procedure in order to find the reason thereof. The comparison of the Author's derivation with the matter printed in [12] has led to the conclusion that the analytical solution by Moshagen and Tørum [12] is burdened with an error which can be easily detected and proved.

And thus, by introducing the "infinite thickness solution" (Eq. (1)) into the governing partial differential equation of the diffusion type (see the original Eq. (8) in [12], p. 51) and performing some additional mathematical operations, one should be able to reach the following expression

$$\mu^2 = k^2 - i\frac{\omega n \beta \gamma_w}{K_x} \tag{4}$$

Next, by raising both sides of Eq. (2) to the power of 2, and keeping in mind the double-angle formulas, one has

$$\mu^2 = |\mu|^2 \cos 2\varphi + i|\mu|^2 \sin 2\varphi \tag{5}$$

And now, by analogy between Eq. (4) and Eq. (5), and performing some simple mathematical operations, it becomes possible to prove that the absolute value of μ is described by exactly the same equation as given in [12] (see Eq. (3a)) but the equation for the argument of μ should be rather given as follows

$$\varphi \equiv \arg(\mu) = \frac{1}{2}\arctan\left(-\frac{\omega n \beta \gamma_w}{K_x k^2}\right) = \tag{6a}$$

$$= -\frac{1}{2}\arctan\left(\frac{\omega n \beta \gamma_w}{K_x k^2}\right) \tag{6b}$$

After comparing Eqs. (3b) and (6b) it is worth noting that the solution for the argument $\phi \equiv \arg(\mu)$ of complex-valued parameter μ is wrongly given in the original Eq. (16) by Moshagen and Tørum [12], p. 53, where the argument of arcus tangent is positively signed, whereas a correct form of the equation should contain a negative value of the argument of inverse trigonometric function, as presented in the above derived Eq. (6a). As a consequence of this fundamental error, sinusoidal oscillations of the pore-fluid pressure in the seabed precede sinusoidal oscillations of the surface water-wave and the hydrodynamic pressure "wave" at the seabed surface ($z = 0$), which stays in contradiction to the phase-lag definition in case of the progressive surface water-wave moving above the seabed. As indicated by many other analytical solutions, e.g. [6, 13, 19], the pore-fluid pressure oscillations within the seabed (at least in its uppermost zone) must always follow the hydrodynamic pressure "wave" irrespectively of the direction of the surface water-wave propagation, as illustrated in Fig. 2.

Apart from Eq. (2), the complex-valued parameter μ can be also represented by the most general defining form

$$\mu = \Re\{\mu\} + i\Im\{\mu\} \tag{7}$$

where: $\Re\{\mu\}$ and $\Im\{\mu\}$ = real and imaginary parts of μ, respectively [1/m]. After introducing this notation to Eq. (1), assuming hydraulically isotropic soil conditions ($K_x = K_z$), and performing some simple mathematical manipulations, the "infinite thickness solution" by Moshagen and Tørum [12] can be presented in the following form

$$\tilde{p} = P_0 \exp(\Re\{\mu\}z)\exp[i(kx - \omega t + \Im\{\mu\}z)] \tag{8a}$$

the real part of which can be written as (see also the original Eq. (17) in [12], p.53)

$$\Re\{\tilde{p}\} = P_0 \exp(\Re\{\mu\}z)\cos(kx - \omega t + \Im\{\mu\}z) \tag{8b}$$

On the other hand, still assuming the same traditional direction of surface water-wave propagation as done by Moshagen and Tørum [12] (see Figs. 1 and 2(a)), the wave-induced pore-fluid pressure oscillations within a porous seabed can be represented by the following most general equations:

$$\tilde{p} = P(z)\cos\left[kx - \left(\omega t - \delta_p\right)\right] = \tag{9a}$$

$$= P(z)\cos\left(kx - \omega t + \delta_p\right) \tag{9b}$$

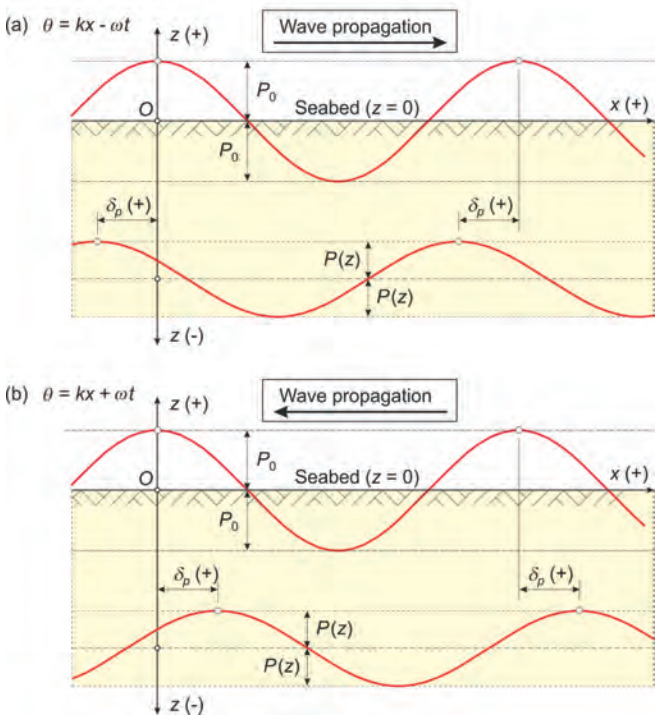

Fig. 2. Graphical presentation of the phase-lag, δ_p, in pore-fluid pressure "travelling" sinusoidal oscillations within the seabed for two opposite directions of surface water-wave propagation

where: $\tilde{p}$ = wave-induced momentary pore-fluid pressure (real-valued) [kPa], $P(z)$ = amplitude of the wave-induced cyclic pore-fluid pressure oscillations [kPa], δ_p = phase-lag (or phase-shift or phase-delay) of the wave-induced cyclic pore-fluid pressure oscillations [rad]. In general, the phase-lag, δ_p, is defined to be positively signed when a "wave" of any oscillating parameter (here the pore-fluid pressure) within the seabed follow the surface water-wave and, as a consequence, the hydrodynamic pore-fluid pressure "wave" at the seabed surface ($z = 0$), as presented in Fig. 2(a).

Because the phase-lag phenomenon is very often misunderstood, a general definition of the phase-lag in pore-fluid pressure sinusoidal oscillations, considered for the case of two opposing directions of surface water-wave propagation, is clearly illustrated in Fig. 2 in a two-dimensional Cartesian coordinate system Oxz. By analogy with Eqs. (9a) and (9b), the application of opposite direction of the surface water-wave propagation (i.e. according to the negative Ox-axis direction) would require the following general equation (see Fig. 2(b)):

$$\tilde{p} = P(z)\cos\left[kx + \left(\omega t - \delta_p\right)\right] = \quad \textbf{(10a)}$$

$$= P(z)\cos\left(kx + \omega t - \delta_p\right) \quad \textbf{(10b)}$$

A short comparison of Eqs. (8b) and (9b) leads to the conclusion that the "infinite thickness solution", obtained by Moshagen and Tørum [12], is associated by the phase-lag of wave-induced pore-fluid pressure increasing linearly with depth ($\delta_p = \Im\{\mu\}z$) which seems to be a rather rough approximation of the real behaviour of wave-induced pore-fluid pressure cyclic oscillations within the seabed.

In order to illustrate the meaning of the error detected, comparative computations have been performed, using the following set of input-data chosen arbitrary in the present paper: wave period $T = 9.78$ s, water depth $h = 10$ m, wavelength $L = 90.04$ m (sinusoidal wave theory), coefficient of soil permeability $K_x = K_z = 10^{-4}$ m/s (fine sand), compressibility of pore-water (seawater) $\beta_w = 5.0\times10^{-7}$ m^2/kN, degree of soil saturation $S_r = 1.0$ (fully saturated soil conditions; $\beta = \beta_w$), unit weight of seawater $\gamma_w = 10.06$ kN/m^3 (for mean World Ocean salinity equal to 35‰) and porosity of soil $n = 0.4$. The results of computations of the phase-lag of wave-induced pore-fluid pressure are illustrated in Fig. 3.

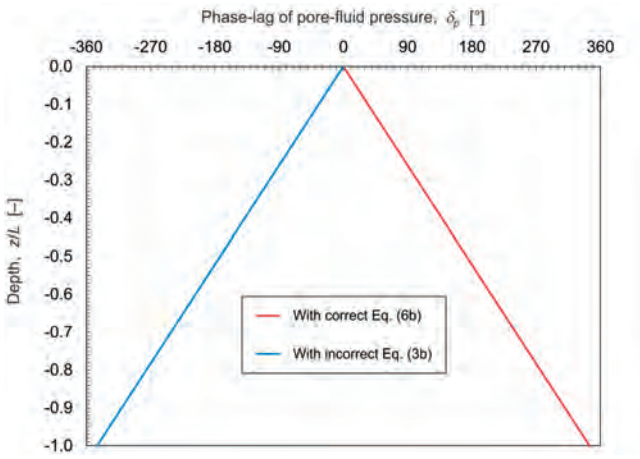

Fig. 3. Vertical distributions of the phase-lag of wave-induced pore-fluid pressure oscillations computed with the incorrect Eq. (3b) by Moshagen and Tørum [12] and the Author's correct Eq. (6b)

Using the erroneous Eq. (3b), one obtains:

$$\mu = (9{,}6631601\text{E}-02,\ -6{,}6852028\text{E}-02)\ \ [\text{m}^{-1}] \quad \textbf{(11a)}$$

$$\Im\{\mu\} = -6.685\times10^{-2}\ \ \text{m}^{-1} \quad \textbf{(11b)}$$

whereas, taking the correct Eq. (6b), one should calculate:

$$\mu = (9{,}6631601\text{E}-02,\ 6{,}6852028\text{E}-02)\ \ [\text{m}^{-1}] \quad \textbf{(12a)}$$

$$\Im\{\mu\} = 6.685\times10^{-2}\ \ \text{m}^{-1} \quad \textbf{(12b)}$$

The phase-lag values obtained using the correct Eq. (6b) are exactly additive inverses of the appropriate results calculated using the incorrect Eq. (3b) (see Fig. 3).

SOLUTION BY YAMAMOTO ET AL. [19]

Yamamoto et al. [19] were the first researchers (paper published on July 12, 1978) who presented a theory of the wave-induced cyclic seabed response together with an "infinite thickness" analytical solution, assuming compressibility of both of the two-phase seabed components (i.e. soil skeleton and pore-fluid; see Tab. 1). The solution was presented in the form of complex-valued wave-induced pore-fluid pressure and soil displacement components. Assuming a special simplified case of fully saturated and dense soils, Yamamoto et al. [19] showed also the final equations obtained this time with respect to all six wave-induced parameters.

A sign convention applied by Yamamoto et al. [19] for the wave-induced soil stress components, $\tilde{\sigma}_x'$, $\tilde{\sigma}_z'$ and $\tilde{\tau}_{xz}$ [the original Eqs. (2.7)–(2.9) in [19], p. 196, respectively], is typical for solid mechanics which is opposite to traditionally applied soil mechanics sign convention [8]. Fortunately, Yamamoto et al. [19] were consequent and applied the same solid mechanics sign convention also in case of two equations of equilibrium and the storage equation (the original Eqs. (2.4)–(2.5) and Eq. (2.1) in [19], p. 195, respectively).

Exclusively from all the Authors considered in the present paper, only Yamamoto et al. [19] took the direction of positive *Oz*-axis vertically downwards from the seabed surface. One has to be aware of some consequences thereof when comparing to the other wave-induced seabed response theories and their solutions. Firstly, vertical coordinates of points within the seabed introduced into a computational procedure obviously must not be negative ($z \geq 0$). Secondly, one has also to remember that such assumption will influence the sign of the wave-induced vertical displacement of soil skeleton as well as effective vertical normal stress and the shear stress components within the soil matrix, as discussed by Magda [8].

A boundary condition for the hydrodynamic bottom pressure oscillations is usually taken in the following form

$$\tilde{p} = P_0 \exp[i(kx - \omega t)] \tag{13}$$

where the minus sign in the term $-\omega t$ denotes the water-wave movement from left to right (i.e. along the positive *Ox*-axis direction). Yamamoto et al. [19] decided to introduce an opposite direction of water-wave propagation (i.e. adequately to the negative *Ox*-axis direction); this condition is represented by the positive sign in the term $+\omega t$ within the surface water-wave phase-angle expression $\Theta = kx + \omega t$. If one does not take it into account, the sign of phase-lag can be erroneously read out. The sequence of the wave-induced oscillating soil shear stress can also be changed. For instance, assuming $t = T/4$, the wave-induced shear stress is usually positive for the right-side directed water-wave (of course, after assuming the solid mechanics sign convention and $z \geq 0$ in the seabed) but the computations according to [19] will bring a negative value of the soil shear stress component, as discussed in [8].

Performing an extended comparative analyses of different analytical solutions published in the literature, the Author has found unexpected differences between the solutions by Yamamoto et al. [19] and Madsen [6] (the quality of Madsen's [6] solution had been already proved by the Author through repeating the entire Madsen's [6] analytical derivation procedure). This was the reason why the Author decided to get down to reproducing the whole Yamamoto's [19] analytical derivation procedure which finally has led to the conclusion that the general solution (i.e. before applying the boundary conditions) for the vertical displacement of soil skeleton is wrong, as given by (see the original Eq. (3.8b) in [19], p. 198; please note that the original notation is kept)

$$\begin{aligned} W = i\left[a_2 + \frac{a_4}{\lambda}\frac{1+(3-4\nu)m}{1+m}\right]\exp(-\lambda z) + \\ + i a_4 z \exp(-\lambda z) + i\frac{\lambda}{\lambda'}\, a_6 \exp(-\lambda' z) \end{aligned} \tag{14}$$

and the correct equation should take the following form

$$\begin{aligned} W = i\left[a_2 + \frac{a_4}{\lambda}\frac{1+(3-4\nu)m}{1+m}\right]\exp(-\lambda z) + \\ + i a_4 z \exp(-\lambda z) + i\frac{\lambda'}{\lambda} a_6 \exp(-\lambda' z) \end{aligned} \tag{15}$$

The above two equations differ in the form of their third terms which are correlated by the following expression

$$\frac{\lambda'}{\lambda} = \frac{\lambda}{\lambda'}\left(1 - \frac{\omega'}{i\lambda^2}\right) \tag{16}$$

After applying the boundary conditions to the general solution, Yamamoto et al. [19] presented a particular solution for both components of the soil skeleton displacement and the pore-fluid pressure. Unfortunately, based on the above mentioned Author's derivation procedure applied to Yamamoto's [19] way of solution, it has been found that the particular solution for the vertical displacement of soil skeleton is wrong as well, as given consequently by (see the original Eq. (3.13b) in [19], p. 198; please note that the original notation is kept)

$$\begin{aligned} w = \Bigg\{\left[1 + m\frac{1+(1-2\nu)(-\lambda''+i\omega'')}{-\lambda''+i(1+m)\omega'}\right]\exp(-\lambda z) + \\ -\left[1 - \frac{m\lambda''}{-\lambda''+i(1+m)\omega''}\right]\lambda z \exp(-\lambda z) + \\ -\frac{m(1+\lambda'')}{-\lambda''+i(1+m)\omega'}\exp(-\lambda' z)\Bigg\}\frac{p_0}{2\lambda G}\exp[i(kx+\omega t)] \end{aligned} \tag{17}$$

whereas the correct equation should be presented as follows

$$\begin{aligned} w = \Bigg\{\left[1 + m\frac{1+(1-2\nu)(-\lambda''+i\omega'')}{-\lambda''+i(1+m)\omega'}\right]\exp(-\lambda z) + \\ +\left[1 - \frac{m\lambda''}{-\lambda''+i(1+m)\omega''}\right]\lambda z \exp(-\lambda z) + \\ -\frac{m(1+\lambda'')}{-\lambda''+i(1+m)\omega'}\exp(-\lambda' z)\Bigg\}\frac{p_0}{2\lambda G}\exp[i(kx+\omega t)] \end{aligned} \tag{18}$$

The difference between Eqs. (17) and (18) can be seen by comparing their second terms in curly brackets; the second term in the wrong Yamamoto's [19] Eq. (17) is negatively signed whereas the second term in the correct Eq. (18), derived solely by the Author, must be signed positively.

The above mentioned two errors could not be discovered by Yamamoto et al. [19] probably because they presented results of computations only with respect to the pore-fluid pressure (both amplitude and phase-lag of pore-fluid pressure oscillations). However, if one wants to derive the wave-induced effective normal stress components, $\tilde{\sigma}'_x$ and $\tilde{\sigma}'_z$, and the wave-induced shear stress component, $\tilde{\tau}_{xz}$, based on the wrong particular solution published by Yamamoto et al. [19], the results obtained will be consequently burdened with an error.

In order to illustrate the meaning of the second error discovered, illustrative and comparative computations were performed, using the formerly presented set of input-data together with the following additional parameters and their values: shear modulus of soil $G = 10^4$ kPa, degree of soil saturation S_r = 1.0, 0.999, 0.99, 0.9, and Poisson's ratio of soil $\nu = 0.33$. Vertical distributions of the relative

(and dimensionless) amplitude of wave-induced vertical displacement of soil, $\bar{u}_z = \tilde{u}_z/[P_0/(2Gk)] = 2Gk\tilde{u}_z/P_0$, are shown in Fig. 4 for different soil saturation conditions modelled by the degree of soil saturation. The pore-fluid compressibility was computed using the following formula proposed by Verruijt [18]

$$\beta = \beta_w + \frac{1 - S_r}{P_h} \quad \text{for} \quad S_r \geq 0.85 \tag{19}$$

where: β = compressibility of pore-fluid [m²/kN], β_w = compressibility of pure pore-water (seawater without air-bubles content) [m²/kN], S_r = degree of soil saturation [-], $P_h = p_{at} + p_h$ = absolute hydrostatic pressure at the computational point in the seabed (usually at the seabed surface) [kPa], p_{at} = atmospheric pressure (p_{at} = 101,325 kPa), p_h = hydrostatic pressure at the computational point in the seabed (usually at the seabed surface for for which $p_h = \gamma_w h$) [kPa], γ_w = unit weight of seawater [kN/m³], h = water depth [m].

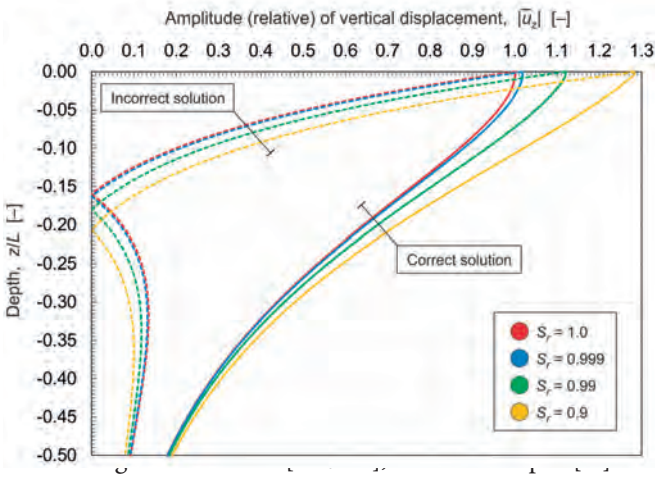

Fig. 4. Vertical distributions of the amplitude of wave-induced vertical displacement of soil skeleton; solid lines — Author's corrected solution given in Eq. (18), dashed lines — incorrect original solution by Yamamoto et al. [19] given in Eq. (17)

The difference between the wrong solution by Yamamoto et al. [19] (see Eq. (17)) and the correct solution obtained by the Author of the present paper (see Eq. (18)) is obvious and very meaningful. The quality of the Author's computations has been proved by performing additional computations based on Madsen's [6] analytical solution where a full agreement has been achieved.

SOLUTION BY MADSEN [6]

Madsen [6], as the second scientist (paper published in December 1978), presented a theory of the wave-induced cyclic seabed response and derived his own "infinite thickness" analytical solution, assuming the two-phase seabed medium to be compressible (see Tab. 1). Madsen [6] was also the first who published resultant equations of the particular solution for a full set of six wave-induced parameters: pore-fluid pressure, two soil displacement components, two effective normal stress components and one shear stress component.

According to the best knowledge of the Author of present paper, Madsen's [6] theory and his analytical solutions for the above mentioned wave-induced parameters are perfect (clearly presented and completely free of errors) in relation with all other similar solutions considered and discussed in the present paper. Although the final equations are perfect, it is interesting to emphasize that Madsen [6] used a kind of "hybrid method" when formulating the governing problem; the solid mechanics sign notation for strains was used whereas the stress-strain relationships were obtained by artificial "attaching" a negative sign (-) to the right-hand sides of the stress-strain equations, allowing thereby switching into the soil mechanics sign convention, as described in [3, 8].

SOLUTION BY OKUSA [13]

Okusa [13], followed the work by Yamamoto et al. [19] and Madsen [6] and, assuming hydraulically isotropic seabed consisting of two compressible phases (see Tab. 1), presented his own "infinite thickness" analytical solution obtained only for the wave-induced pore-fluid pressure and effective normal and shear stress components.

Jeng [3, 4] noted that the considerations presented by Okusa [13] had been based on plane stress conditions (see in [3], p. 11, and repeatedly in [4], p. 8). It has to be stressed that this statement is completely wrong; a closer study of the paper by Okusa [13] reveals that the volumetric strain of soil skeleton, appearing in the equation of mass conservation of fluid (so-called the storage equation), is given under plain strain conditions (see the original Eq. (2) in [13], p. 519); exactly the same situation is with the compatibility equation (see the original Eq. (8) in [13], p. 520) which reflects the plain strain conditions evidently.

The equations for the real-valued wave-induced pore-fluid pressure and the phase-lag of pore-fluid pressure oscillations (see the original Eq. (48) in [13], p. 525), obtained by Okusa [13] as a simplified approximate solution (due to abandoning the negligibly small terms), are as follows (please note that the original notation is kept):

$$U = \left\{\left[\left(1 - B_1'\right)\exp(\kappa_1 z)\sin(\kappa_2 z)\right]^2 + \right. \\ \left. + \left[B_1'\exp(az) + \left(1 - B_1'\right)\exp(\kappa_1 z)\cos(\kappa_2 z)\right]^2\right\}^{\frac{1}{2}} \times \\ \times \cos\left(ax - \omega t - \delta\right) \tag{20a}$$

$$\tan\delta = \frac{(1 - B_1')\exp(\kappa_1 z)\sin(\kappa_2 z)}{B_1'\exp(az) + (1 - B_1')\exp(\kappa_1 z)\cos(\kappa_2 z)} \tag{20b}$$

Based on the computational analysis performed by the Author, it must be stressed that the momentary pore-fluid pressure results, obtained by using Eq. (20a) together with Eq. (20b), are correct. However, these equations separately

must be evaluated as incorrect from the formal analytical point of view. The term cos $(ax - \omega t - \delta)$ informs that the pore-fluid pressure oscillations within the seabed precede the hydrodynamic pressure oscillations at the seabed surface ($z = 0$) which, of course, contradicts with formerly described phase-lag definition (see Eq. (9b)). The momentary pore-fluid pressure, computed from the combination of Eqs. (20a) and (20b), are coincidentally correct just because Eq. (20b) gives the values which are opposite to those which are really expected from the derivation procedure performed properly.

The equation for the momentary pore-fluid pressure, written in terms of a complex function, has the following form (see the original Eqs. (23) and (42) in [13], pp. 521 and 523, respectively; please note that the original notation is kept) [13]

$$U = B_1' \exp(az) \exp[i(ax + \omega t)] + \\ +(1 - B_1') \exp(\kappa_1 z) \exp[i(ax - \omega t - \kappa_2 z)] \tag{21}$$

Based on Eq. (21), adopting the form of Eq. (9b), using the fundamental equations for the absolute value and the argument of a complex number, remembering that the cosine function is an even function and the sine function is an odd function, and assuming a convenient value of the water-wave phase angle $\Theta = kx - \omega t = 0$, the following should be easily derived:

$$U = \left\{\left[\left(1 - B_1'\right) \exp(\kappa_1 z) \sin(\kappa_2 z)\right]^2 + \right. \\ \left. + \left[B_1' \exp(az) + \left(1 - B_1'\right) \exp(\kappa_1 z) \cos(\kappa_2 z)\right]^2\right\}^{\frac{1}{2}} \times \\ \times \cos(ax - \omega t + \delta) \tag{22a}$$

$$\tan \delta = -\frac{(1 - B_1') \exp(\kappa_1 z) \sin(\kappa_2 z)}{B_1' \exp(az) + (1 - B_1') \exp(\kappa_1 z) \cos(\kappa_2 z)} \tag{22b}$$

If positive values of the phase-lag of wave-induced pore-fluid pressure oscillations should classically denote a certain delay of the pore-fluid pressure oscillations with respect to the surface water-wave oscillations (or the hydrodynamic pressure oscillations at the seabed surface; see Fig. 2) — and this is the case confirmed by graphical presentation in the original Figs. 6 and 7 in [13], pp. 526–527 — the phase-angle term, responsible for the cyclic character of the phenomena under consideration, should be rather written as $(ax - \omega t + \delta_p)$ (please note that $\delta_p \equiv \delta$), as presented in Eqs. (9b) and (22a), and not in the form of $(ax - \omega t - \delta_p)$ used by Okusa [13] (see Eq. (20a)).

In order to perform illustrative computations of the wave-induced pore-fluid pressure, the following set of input-data was chosen after Okusa's [13] paper: wave period $T = 15$ s, water depth $h = 20$ m, wavelength $L = 197.53$ m (sinusoidal wave theory), volume compressibility of soil $\alpha = 9.18 \times 10^{-4}$ m^2/kN, porosity of soil $n = 0.5$, Poisson's ratio of soil $\nu = 0.3$ and Skempton's pore-fluid pressure coefficient $B = 1.0, 0.9, 0.8, 0.7, 0.6, 0.5$. The values of other required parameters: K, β_w, γ_w and p_{at} were assumed as in the previously presented computational examples. A family of vertical distributions of the relative (and dimensionless) amplitude of wave-induced pore-fluid pressure, $\bar{p} = \tilde{p}/P_0$, is shown in Fig. 5 for several different soil saturation conditions modelled by Skempton's coefficient, B.

A comparison analysis has revealed that Okusa's [13] results, obtained from his simplified approximate solution and presented in a graphical form, are lacking in accuracy. The original Fig. 4 in [13], p. 524, and also the original Fig. 5 in [13], p. 525 (obtained for another set of input data), do not show a very characteristic disturbance of monotonicity of the curves in the uppermost zone of the seabed, as indicated in Fig. 5(a) of the present analysis. As far as the distribution of phase-lag of the wave-induced pore-fluid pressure oscillations is concerned (see Fig. 5(b)), maximum values are underestimated by factor one-third in Okusa's [13] illustrations, presented in the original Fig. 6, p. 526, and also in the original Fig. 7, p. 527 (obtained for another set of input data). It seems that these meaningful discrepancies can be explained by insufficient hardware computational capabilities existing almost four decades ago. As before, the quality of the Author's computations has been proved by additional computations based on Madsen's [6] analytical solution, achieving a highly satisfactory agreement.

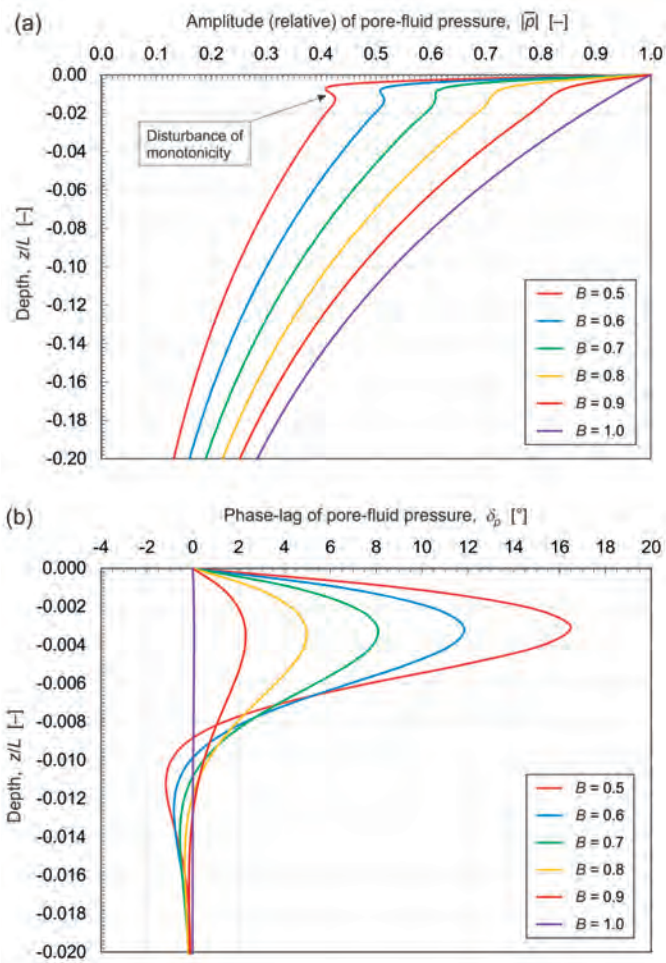

Fig. 5. Vertical distributions of the amplitude and the phase-lag of wave-induced pore-fluid pressure oscillations computed using Okusa's [13] exact and approximate forms of his analytical solution

SOLUTIONS BY HSU AND JENG [2], JENG AND HSU [5], JENG [3, 4]

Hsu and Jeng [2] and Jeng and Hsu [5] presented the three-dimensional governing partial differential equations (the static force and moment equilibrium equations together with the storage equation), clearly indicating the use of the solid mechanics sign convention for stresses throughout their papers; this was also certified by the stress block in the original Fig. 2 in [2], p. 789. The form of equations for the wave-induced effective normal stress and shear stress components also indicate the use of the solid mechanics sign convention. Surprisingly, Jeng and Hsu [5], p. 430, wrote: "A positive sign is used in the present paper, as in equations (7)–(12), i.e. compressive stresses are defined as positive". Nothing could be further from the truth. The form of equilibrium equations and equations for the wave-induced stress components, given by Jeng and Hsu [5], indicates clearly that the solid mechanics sign convention was used by them. Therefore, the solution obtained by Jeng and Hsu [5] for a fully saturated and isotropic soil of infinite thickness should follow strictly the solution presented by Yamamoto et al. [19], of course after transformation of the latter to the positive z-axis directed upwards and setting the water-wave propagation direction to be consistent with the positive Ox-axis direction. This finding makes a clear contradiction between what Jeng and Hsu [5] wrote in the text (please recall the above citation) and what they presented in the equations of their original paper.

Jeng [3] used exactly the same assumptions as Hsu and Jeng [2] and Jeng and Hsu [5]. However, among seven basic assumptions indicated in his book there is no any information regarding the sign convention applied. Again, it can only be deducted from the form of the equilibrium equations (see the original Eqs. (3.10)–(3.12) in [3], pp. 37–38) and the stress block in the soil element, presented in the original Fig. 3.2 in [3], p. 38, that the solid mechanics sign convention is used throughout Chapter 3 of the book by Jeng [3]. Jeng's [3] solution, obtained for fully saturated and hydraulically isotropic seabed of infinite thickness, after transforming it into the two-dimensional case and real-valued functions, and adopting the notation used in the present paper, can be presented as follows:

$$\overline{\sigma}'_x \stackrel{\text{def}}{=} \frac{\widetilde{\sigma}'_x}{P_0} = -kz\exp(kz)\cos(kx-\omega t) \quad \textbf{(23a)}$$

$$\overline{\sigma}'_z \stackrel{\text{def}}{=} \frac{\widetilde{\sigma}'_z}{P_0} = -kz\exp(kz)\cos(kx-\omega t) \quad \textbf{(23b)}$$

$$\overline{\tau}_{xz} \stackrel{\text{def}}{=} \frac{\widetilde{\tau}_{xz}}{P_0} = -kz\exp(kz)\sin(kx-\omega t) \quad \textbf{(23c)}$$

It can be easily recognised that the above solution differs from the solution given in the original Eqs. (47), (49) and (50), pp. 432–433, published formerly by Jeng and Hsu [5]. The wave-induced effective vertical normal stress, $\overline{\sigma}'_z$, which should obviously be compressive under the wave crest (e.g. for the surface water-wave phase-angle $\Theta = kx - \omega t = 0$), this time will always have non-negative values for $z \leq 0$, as it is always in the case of soil mechanics sign convention. But this is not the sign convention used by Jeng [3]. The solution to the wave-induced effective vertical normal stress in the soil, given in Eq. (23b), must be evaluated as a wrong one. The signs of other stresses, $\overline{\sigma}'_x$ and $\overline{\tau}_{xz}$, described by Eqs. (23a) and (23c), are in line with the solid mechanics sign convention. Such mixture of two different sign conventions in one set of solution equations is unacceptable, leading very often to many misunderstandings and mistakes, and is not recommended for any practical use.

It has also been found that the original Eqs. (2.46)–(2.48) in [4], p. 45, describing the soil stress components in terms of complex functions, are erroneous because: there is a conflict of units in Eq. (2.46), and the common coefficient C_1^{∞}, appearing in the original Eqs. (2.46)–(2.48) and given in the original Eq. (2.51) in [4], p. 46, does not become equal to unity as it should be when fully saturated soil conditions (practically denoting incompressibility of the pore-fluid) are assumed.

CONCLUSIONS

A closer look has been taken at some selected analytical solutions of the wave-induced cyclic response of a porous seabed of infinite thickness to the sinusoidal surface water-wave loading. A thorough analysis has indicated the following items:

- a perfectly correct analytical solution was published by Madsen [6] and obtained for the entire set of six wave-induced seabed response parameters (pressure, stress and displacement components),
- some minor corrections are required in the analytical solutions delivered by Moshagen and Tørum [12] and Okusa [13] as far as the equations for the phase-lag of wave-induced pore-fluid pressure oscillations are concerned,
- unfortunately, there are two meaningful errors in the analytical solution given by Yamamoto et al. [19]: one in the general solution (i.e. before applying boundary conditions) and one in the particular solution (i.e. after applying boundary conditions) for the vertical component of soil displacement, which makes the Reader impossible to obtain, by means of further differentiations, correct forms of the linked equations for the soil stress components,
- unexpected errors in the analytical "infinite thickness solutions" can be caused by problems with a correct identification or with a lack of consequences in using only one and the same sign convention for stresses in the soil matrix, as found in [3]; the other errors detected especially in [4], are quite inexplicable.

The correct forms of the erroneous equations has been derived personally by the Author and they are included in the present paper for comparison purposes.

REFERENCES

1. M. Foda, "On the extrication of large objects from the ocean bottom (the breakout phenomenon)", Journal of Fluid Mechanics, Vol. 117, 1982, pp. 211–231, DOI: 10.1017/S0022112082001591.

2. J. R. C. Hsu and D.-S. Jeng, "Wave-induced soil response in an unsaturated anisotropic seabed of finite thickness", International Journal for Numerical and Analytical Methods in Geomechanics, Vol. 18, Issue 11, 1994, pp. 785–807, DOI: 10.1002/nag.1610181104.

3. D.-S. Jeng, Porous Models for Wave-seabed Interactions, Berlin and Heidelberg: Springer, 2013, DOI: 10.1007/978-3-642-33593-8.

4. D.-S. Jeng, Mechanics of Wave-Seabed-Structure Interactions. Modelling, Processes and Applications, Cambridge: Cambridge University Press, 2018, DOI: 10.1017/9781316672266.

5. D.-S. Jeng and J. R. C. Hsu, "Wave-induced soil response in a nearly saturated sea-bed of finite thickness", Géotechnique, Vol. 46, No. 3, 1996, pp. 427–440, DOI: 10.1680/geot.1996.46.3.427.

6. O. S. Madsen, "Wave-induced pore pressures and effective stresses in a porous bed", Géotechnique, Vol. 28, No. 4, 1978, pp. 377–393, DOI: 10.1680/geot.1978.28.4.377.

7. W. Magda, "Analytical solution for the wave-induced excess pore-pressure in a finite-thickness seabed layer", Proc. of the 24th Conference on Coastal Engineering (ICCE 1994), American Society of Civil Engineers, 23–28 October 1994, Kobe, Japan, pp. 3111–3125, DOI: 10.1061/9780784400890.225.

8. W. Magda, "On importance of sign conventions on analytical solutions to the wave-induced cyclic response of a poro-elastic seabed", Archives of Civil Engineering, Vol. 69, Issue 4, 2023 (submitted for publication).

9. C. C. Mei and M. A. Foda, "Wave-induced responses in a fluid-filled poro-elastic solid with a free surface — a boundary layer theory", Geophysical Journal of the Royal Astronomical Society, Vol. 66, Issue 3, September 1981, pp. 597–631, DOI: 10.1111/j.1365-246X.1981.tb04892.x.

10. J. P. Michalski, "Parametric method applicable in calculating breakout force and time for lifting axisymmetric objects from seabed", Polish Maritime Research, Vol. 26, No. 3, 2019, pp. 147–152, DOI: 10.2478/pomr-2019-0055.

11. J. P. Michalski, "Parametric method applicable in assessing breakout force and time for lifting slender bodies from seabed", Polish Maritime Research, Vol. 27, No. 2, 2020, pp. 69–75, DOI: 10.2478/pomr-2020-0028.

12. H. Moshagen and A. Tørum, "Wave induced pressures in permeable seabeds", Journal of the Waterways, Harbors and Coastal Engineering Division, Proc. of the American Society of Civil Engineering (ASCE), Vol. 101, No. WW1, February 1975, pp. 49–57. DOI: 10.1061/AWHCAR.0000271.

13. S. Okusa, "Wave-induced stresses in unsaturated submarine sediments", Géotechnique, Vol. 35, No. 4, 1985, pp. 517–532, DOI: 10.1680/geot.1985.35.4.517.

14. J. A. Putnam, "Loss of wave energy due to percolation in a permeable sea bottom", Transactions, American Geophysical Union, Vol. 30, No. 3, 1949, pp. 349–356, DOI: 10.1029/TR030i003p00349.

15. W. Richwien and W. Magda, Design Levels for Offshore Structures. State-of-the-Art and Instantenous Pore-Pressure Model, Forschungsbereich aus dem Fachbereich Bauwesen, Universität – Gesamthochschule Essen, Heft 63, Essen, September 1994. https://drive.google.com/file/d/1kqLPL_s_MM3Q8oLR5iU5ACPri_YStU3b/view.

16. M. Sumer, Liquefaction Around Marine Structures, Advanced Series on Ocean Engineering – Vol. 39, Singapore: World Scientific Publishing, 2014, DOI: 10.1142/7986.

17. B. M. Sumer and J. Fredsøe, "The Mechanics of Scour in the Marine Environment", Advanced Series on Ocean Engineering – Vol. 17, Singapore: World Scientific Publishing, 2002, DOI: 10.1142/4942.

18. A. Verruijt, "Elastic storage of aquifers", in: Flow Through Porous Media, ed. De Wiest, New York and London: Academic Press, 1969, pp. 331–376. https://www.researchgate.net/publication/258354880.

19. T. Yamamoto, H. L. Koning, H. Sellmeijer and E. van Hijum, "On the response of a poro-elastic bed to water waves", Journal of Fluid Mechanics, Vol. 87, 1978, pp. 193–206, DOI: 10.1017/S0022112078003006.